Nanosilicon

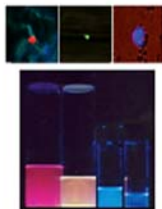
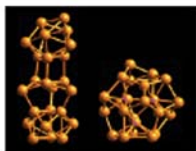
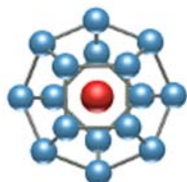
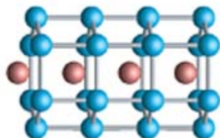
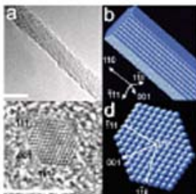
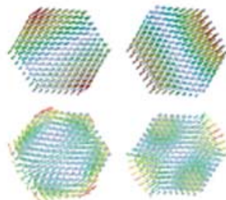
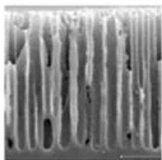
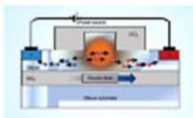
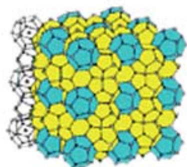

Vijay Kumar

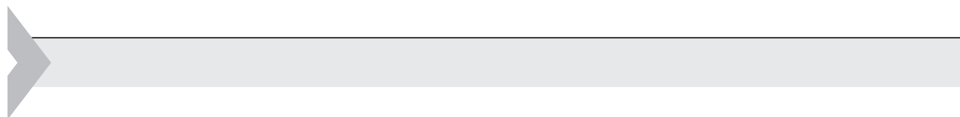

NANOSILICON

This page intentionally left blank

NANOSILICON

Edited by

VIJAY KUMAR
Dr. Vijay Kumar Foundation, Chennai, India

ELSEVIER

Amsterdam • Boston • Heidelberg • London • New York • Oxford
Paris • San Diego • San Francisco • Singapore • Sydney • Tokyo

Elsevier
Linacre House, Jordan Hill, Oxford, OX2 8DP, UK
84 Theobald's Road, London WC1X 8RR, UK

First edition 2007

Copyright © 2007 Elsevier Ltd. All rights reserved

No part of this publication may be reproduced, stored in a retrieval system
or transmitted in any form or by any means electronic, mechanical, photocopying,
recording or otherwise without the prior written permission of the publisher

Permissions may be sought directly from Elsevier's Science & Technology Rights
Department in Oxford, UK: phone (+44) (0) 1865 843830; fax (+44) (0) 1865 853333;
e-mail: permissions@elsevier.com. Alternatively you can submit your request online by
visiting the Elsevier web site at http://elsevier.com/locate/permissions, and selecting
Obtaining permission to use Elsevier material

Notice
No responsibility is assumed by the publisher for any injury and/or damage to persons
or property as a matter of products liability, negligence or otherwise, or from any use or
operation of any methods, products, instructions or ideas contained in the material herein.
Because of rapid advances in the medical sciences, in particular, independent verification
of diagnoses and drug dosages should be made

British Library Cataloguing in Publication Data
Nanosilicon
1. Silicon 2. Nanostructure materials
2. I. Kumar, Vijay
3. 620.1'93

Library of Congress Number: 2007926933

ISBN: 978-0-08-044528-1

For information on all Elsevier publications
visit our web site at books.elsevier.com

Typeset by Charon Tec Ltd (A Macmillan Company), Chennai, India
www.charontec.com

Printed and bound in China

07 08 09 10 11 11 10 9 8 7 6 5 4 3 2 1

Working together to grow
libraries in developing countries

www.elsevier.com | www.bookaid.org | www.sabre.org

ELSEVIER BOOK AID International Sabre Foundation

Dedicated To My Father

This page intentionally left blank

Contents

Preface xv

1 Silicon Nanoparticles: New Photonic and Electronic Material at the Transition Between Solid and Molecule **1**

Munir H. Nayfeh and Lubos Mitas

1.1 Introduction 3
1.2 Synthesis 3
1.2.1 Physical Techniques 3
1.2.2 Physico-Chemical Techniques 4
1.2.3 Chemical Techniques 4
1.2.4 Electrochemical Techniques 4
1.2.5 Discretely Sized Si Nanoparticles 6
1.3 Functionalization 8
1.3.1 Initial Surface Condition 9
1.3.2 Alkylated Particles 11
1.3.2.1 Alcohol 11
1.3.2.2 Alkylamine 13
1.3.2.3 Alkene 14
1.3.2.4 Carboxy 14
1.3.2.5 Alkyl and Alkoxy 15
1.3.3 Aggregation and Solubility 15
1.3.4 Stability in Acid 17
1.4 Spectroscopic Characterization 17
1.4.1 Fourier Transform Infrared Spectroscopy 17
1.4.2 Nuclear Magnetic Resonance 19
1.4.3 Gel Permission Chromotography 20
1.4.4 X-Ray Photospectroscopy 21
1.4.5 Auger Electron Spectroscopy 21
1.4.6 Transmission Electron Microscopy 21
1.5 Optical Properties 22
1.5.1 PL and Detection of Single Nanoparticles 22
1.5.2 PL Lifetime 26
1.5.3 Cathodoluminescence and Electroluminescence 27
1.5.4 Photostability Under UV and Infrared Radiation 29
1.6 Reconstitution of Particles in Films 29
1.6.1 Precipitation Spray 30
1.6.2 Electrodeposition: Composite Films of Metal and Nanoparticles 31

1.6.3 Silicon Sheet Roll into Tubes 32
1.6.4 Self-Assembly 33
1.7 Nonlinear Optical Properties 34
1.7.1 Stimulated Emission 34
1.7.2 Second Harmonic Generation 39
1.7.3 Gain and Optical Nonlinearity 39
1.8 Effect of Functionalization on Emission 41
1.9 Structure of Particles 41
1.9.1 Luminescence Models 42
1.9.2 Computational Methods for Electronic Structure of Nanoclusters 43
1.9.2.1 DFT Methods 44
1.9.2.2 Quantum Monte Carlo 45
1.9.2.3 Variational Monte Carlo 45
1.9.2.4 Diffusion Monte Carlo 46
1.9.2.5 Applications to Si Clusters 46
1.9.3 Prototype of Hydrogenated Particles (Supermolecule) 49
1.9.4 H_2O_2 Effect on Surface Reconstruction 51
1.9.5 Novel Si—Si Bonds (Molecular-Like Behaviour) 52
1.9.6 Structural Stability of the Prototype 54
1.9.7 Material Properties: Dielectric Constant and Effective Mass 55
1.9.8 Excited States (Molecular-Like Bands) 57
1.9.9 Collective Molecular Surface 57
1.9.10 Phonon Structure: Collective Molecular Vibration Modes 59
1.9.11 Molecular-Like Emission: Direct versus Indirect Process 60
1.9.12 X-Ray Form Factors 61
1.9.13 Effect of Termination on the Band Gap 63
1.10 Device Applications 63
1.10.1 Photoelectric Conversion/UV Photodetector 64
1.10.2 Metal Oxide Silicon Memory Devices 66
1.10.3 Biophotonic Imaging 68
1.10.4 Amperometric Detection 69
1.10.5 Nanosolar Cell 71
1.10.6 Nanoink Printing 72
1.10.7 Single Electron Transistor Devices 73
1.11 Conclusion 73
Acknowledgements 74
References 74

2 Cluster Assembled Silicon Networks 79
P. Mélinon, X. Blase, A. San Miguel and A. Perez

2.1 Introduction 80
2.2 Isolated Silicon Clusters 81

2.2.1 Small Si_N Clusters ($N < 14$) 81
2.2.2 Medium-Sized Clusters ($20 < N < 100$): the Case of Si_{33} 82
2.2.3 Large Clusters ($N > 100$) 82
2.3 Si-Cluster-Assembled Materials 83
2.3.1 Introduction 83
2.3.2 Si-Cluster-Assembled Films 83
2.3.2.1 Gas-Phase Synthesis of Si_N Clusters: Experimental Methods 83
2.3.2.2 Structure and Morphology 86
2.3.2.3 Electronic Structure 90
2.3.2.4 Vibrational Structure 90
2.3.2.5 Optical Properties 92
2.3.2.6 New Bonding for Silicon 93
2.3.3 Bulk Si-Cluster-Assembled Materials from Fullerenes: Clathrate Phases 97
2.3.3.1 Silicon Clathrate Structures 98
2.3.3.2 Synthesis Methods 100
2.3.3.3 Electronic Properties of Empty Silicon Clathrates 100
2.3.3.4 Vibrational Properties 101
2.3.3.5 Cohesive Energy and Stability Under Pressure of Si-34 103
2.3.3.6 Endohedral Doping in Clathrates 104
2.4 Conclusion 110
Acknowledgements 110
References 111

3 Metal Encapsulated Clusters of Silicon: Silicon Fullerenes and Other Polyhedral Forms 114

Vijay Kumar

3.1 Introduction 115
3.2 Clusters of Elemental Silicon 118
3.3 Metal Encapsulation: A New Paradigm 121
3.3.1 Silicon Fullerenes 121
3.3.2 Metal Size Dependent Encapsulated Silicon Structures 122
3.3.3 The Electronic Factor and the Isolated Rhombus Rule 124
3.3.4 Reactivity as a Probe of Metal Encapsulation 137
3.3.5 Vibrational Properties 137
3.3.6 Empty and Endohedral Hydrogenated Fullerene Cages of Silicon 139
3.3.7 Absorption Spectra 142
3.3.8 Magnetic Clusters of Silicon 142
3.4 Summary 144
Acknowledgments 145
References 145

4 Porous Silicon – Sensors and Future Applications **149**
James L. Gole and Stephen E. Lewis

4.1 Introduction 150
4.2 Kinds of PS 151
4.2.1 Pore Structure in PS 151
4.2.2 PL from PS 153
4.2.2.1 Photoluminescent Enhancement and Stabilization 155
4.2.2.2 PL-Induced Metallization 155
4.3 PS Sensors 157
4.3.1 PS Humidity Sensors 157
4.3.2 PS Chemical Sensors 161
4.3.3 PS Gas Sensors 161
4.3.3.1 NO_2 Sensors 162
4.3.3.2 Hydrocarbon Sensors 164
4.3.3.3 Low-Cost Multi-application Gas Sensors 164
4.4 Future Technology 168
4.4.1 Nanoparticle Photocatalytic Coating of PS 168
4.4.2 Lithium Electrolyte-Based PS Microbattery Electrodes 170
4.5 Conclusions 172
References 172

5 Silicon Nanowires and Nanowire Heterostructures **176**
Zhaohui Zhong, Chen Yang and Charles M. Lieber

5.1 Introduction 177
5.2 Silicon Nanowires 177
5.2.1 Rational Synthesis and Structural Characterization of SiNW 177
5.2.1.1 Overview of SiNW 1D Growth 178
5.2.1.2 Structural Characterization of SiNWs 180
5.2.1.3 Rational Control of SiNW Diameters 182
5.2.2 Electronic Properties of SiNWs 182
5.2.2.1 Room Temperature Electronic Properties of SiNWs 183
5.2.2.2 Fundamental Transport Studies of SiNWs 186
5.2.3 SiNWs for Nanoelectronics 190
5.2.3.1 Crossed Nanowire Structures and Devices 191
5.2.3.2 Crossed Nanowire-Based Logic Gates 191
5.2.3.3 Nanowire Crossbar Arrays as Address Decoders 193
5.2.3.4 SiNW Electronics on Non-conventional Substrates 194
5.2.4 Large-Scale Hierarchical Organization of SiNW Arrays 195
5.2.4.1 Langmuir–Blodgett-Based Assembly of Nanowires 196
5.2.4.2 Scalable Integration of Nanowire Devices 197
5.2.4.3 High-Frequency Nanowire Circuits 199

5.2.5 SiNWs as Nanoscale Sensors 200
5.2.5.1 Nanowire Field-Effect Sensors 201
5.2.5.2 Single Virus Detection 202
5.2.5.3 Multiplexed Detection at the Single Virus Level 203
5.3 SiNW Heterostructures 204
5.3.1 NiSi/SiNW Heterostructures 204
5.3.2 Modulation Doped SiNWs 204
5.3.2.1 Synthesis and Characterization of Modulation Doped SiNWs 205
5.3.2.2 Novel Applications of Modulation Doped SiNWs 208
5.3.3 Branched and Hyper-Branched SiNWs 209
5.4 Summary 213
References 214

6 Theoretical Advances in the Electronic and Atomic Structures of Silicon Nanotubes and Nanowires 217

Abhishek Kumar Singh, Vijay Kumar and Yoshiyuki Kawazoe

6.1 Introduction 218
6.2 Computational Approach 220
6.3 Silicon Nanotubes 220
6.3.1 Metal Encapsulated Nanotubes of Silicon 222
6.3.2 Electronic Structure and Bonding Nature 225
6.3.3 Magnetism in Metal Encapsulated SiNTs 228
6.4 Germanium Nanotubes 231
6.4.1 Metallic and Semiconducting Nanotubes of Ge 233
6.5 Silicon Nanowires 235
6.5.1 Non-Crystalline Pristine SiNWs 237
6.5.2 Crystalline Pristine SiNWs 238
6.5.3 Band Structure of SiNWs 243
6.6 Hydrogenated Nanowires 244
6.6.1 Electronic Structure of Hydrogenated SiNWs 249
6.6.2 Effects of Doping and H Defects 251
6.7 Nanowire Superlattices 253
6.8 Conclusion and Perspective Remarks 254
Acknowledgements 255
References 255

7 Phonons in Silicon Nanowires 258

Kofi W. Adu, Humberto R. Gutierrez and Peter C. Eklund

7.1 Introduction 259
7.2 Theoretical Models for Confined Phonons 261
7.2.1 Lattice Dynamics of Si Nanowires 261

7.2.2 The Richter Model for Raman Scattering from Confined Phonons 267
7.3 Experimental Evidence of Confined Phonons in Silicon 269
7.3.1 Acoustic Phonons 269
7.3.2 Optical Phonons 273
7.3.3 Thermal Conductivity 275
7.4 Effects of Inhomogeneous Laser Heating on Raman Lineshape 278
7.4.1 Stokes–AntiStokes Ratio as a Probe of Laser Heating of Si Nanowires 279
7.4.2 Evolution of the Raman Band Asymmetry with Laser Flux 280
7.4.3 Modification of Richter's Lineshape Function to Include Inhomogeneous Heating 282
7.5 Summary and Conclusions 285
Acknowledgements 285
References 286

8 Quasi-One-Dimensional Silicon Nanostructures 289
Yu Lin, Nevill Gonzalez Szwacki and Boris I. Yakobson

8.1 Introduction 290
8.2 Silicon Nanowires 290
8.2.1 Pentagonal Silicon Wires 290
8.2.1.1 Wulff's Construction Generalized 291
8.2.1.2 Pentagonal Shape SiNW 291
8.2.1.3 Ground State of the Thinnest SiNW 292
8.2.1.4 Kinetic Advantages of $P_{||}$ SiNW 296
8.2.2 Hydrogen-Passivated Silicon Wires 297
8.3 Metal Silicide 300
8.3.1 Endohedral Silicon Nanotubes 301
8.3.2 Yttrium Silicide NW 307
8.3.3 Energy Decomposition 308
Acknowledgements 311
References 312

9 Low-dimensional Silicon as a Photonic Material 314
N. Daldosso and L. Pavesi

9.1 The Need of a Silicon-Based Photonics 314
9.2 Various Approaches to a Silicon Light Source 316
9.2.1 Silicon Raman Laser 317
9.2.2 Bulk Silicon Light Emitting Diodes 319
9.3 Optical Gain in Silicon Nanocrystals 321
9.3.1 CW and TR Measurements 322
9.3.2 Gain Model: Four-Level System 325

9.3.3 Other Key Ingredients 327
9.4 Er Coupled Si Nanocrystal Optical Amplifiers 328
9.4.1 Er^{3+} Internal Transition 329
9.4.2 Er^{3+} and Si-nc Interactions 330
9.4.3 Er^{3+} Cross Sections 330
9.5 Conclusions 332
Acknowledgements 333
References 333

10 Nanosilicon Single-Electron Transistors and Memory 335
Z. A. K. Durrani and H. Ahmed

10.1 Introduction 335
10.1.1 Single-Electron and Quantum Confinement Effects 337
10.2 Nanosilicon SETs 341
10.2.1 Conduction in Continuous Nanocrystalline Silicon Films 341
10.2.2 Silicon Nanowire SETs 343
10.2.3 Point-Contact SETs: Room Temperature Operation 346
10.2.4 “Grain-Boundary” Engineering 350
10.2.5 Single-Electron Transistors Using Silicon Nanocrystals 351
10.2.6 Comparison with Crystalline Silicon SETs 352
10.3 Electron Coupling Effects in Nanosilicon 352
10.3.1 Electrostatic Coupling Effects 354
10.3.2 Electron Wavefunction Coupling Effects 354
10.4 Nanosilicon Memory 356
References 358

Index 361

Preface

Silicon is a wonderful material for modern electronic devices and there has been intense research on various aspects, both fundamental as well as applications. The continuously shrinking size of silicon devices (currently around 65 nm) has raised interest about the properties of silicon at the nanoscale, either in the form of clusters and nanoparticles or quasi-one-dimensional structures such as nanowires. These nanosilicon forms add a new desired feature to silicon that it becomes useful as an optical material. Bright luminescence in silicon was first discovered in the form of porous silicon and since then numerous studies have been carried out on nanoparticles as well as nanowires to understand the origin of photoluminescence and a vast variety of applications have emerged. In recent years it has become possible to produce silicon nanowires with a control on diameter. Such one-dimensional structures have potential for the development of silicon based very small devices such as sensors, logical gates, memories, and systems for optoelectronic and biological applications. Molecular level detection of gases and viruses, single electron transistors, memories, light sources, and logical circuits are among the applications that have been already achieved.

An important aspect of nanostructures such as those of clusters and nanoparticles is that the atomic structures as well as compositions could be very different from the corresponding bulk and the properties are size and shape dependent due to quantum confinement. These novel features could lead to the possibilities of designing materials with desired properties. Soon after the discovery of carbon fullerenes, there have been efforts to produce similar structures of silicon. However, elemental silicon does not favour empty cage or tubular structures, though interlinked fullerene cages of silicon exist in clathrates. In recent years much progress has been made from computer simulations and it has been shown that fullerene and nanotube structures of silicon can be stabilized by metal encapsulation or by hydrogen capping. Some of these forms have recently been realized in laboratory and a new paradigm has emerged in silicon research which can bring new possibilities for the applications of silicon at the nanoscale as well as the development of their novel assemblies.

This book is an effort to compile many such developments on nanosilicon. The Chapter by Nayfeh and Mitas covers many aspects of nanoparticles of silicon: synthesis, functionalization, spectroscopic characterization, optical properties, and the finding of bright luminescence from size selected hydrogenated nanoparticles, device applications as well as theoretical understanding of the atomic structures and optical properties from quantum Monte Carlo calculations. Melinon *et al.* discuss the production of gas phase silicon clusters and nanoparticles as well as the developments of cluster-assembled materials. In bulk form, silicon clathrates are examples of cluster assembled materials whose properties can be tailored by doping. The Chapter by Kumar covers the recent developments of metal encapsulated structures of silicon

clusters, the discovery of silicon fullerenes and other polyhedral forms as well as their properties. Lewis and Gole discuss photoluminescence from porous silicon and applications to gas sensors. Lieber and coworkers cover developments of silicon nanowires, their assemblies and heterostructures, applications to logical gates, sensors, and other devices. Singh *et al.* cover the developments of the stabilization of silicon nanotube structures by encapsulation of metal atoms from assemblies of metal encapsulated silicon clusters. Such nanotubes are very thin. Experimentally silicon nanowires are produced with a diameter of a few nanometres. Since silicon surfaces have reconstruction, it is important to understand atomic scale changes in nanowires and their effects on the properties. Pristine silicon nanowires are often metallic while hydrogenated silicon nanowires are semiconducting. Several studies have therefore been made in recent years to understand the properties as a function of size, morphology, and growth direction. Singh *et al.* discuss the atomic and electronic structures of pristine and hydrogenated silicon nanowires, as well as the effects of morphology and electron or hole doping on the electronic structure. Confinement of phonons in silicon nanowires has been discussed by Gutierrez *et al.*, while Lin *et al.* present progress in the understanding of the ground state structures of silicon nanowires, and the nanostructures from metal silicides which are related to silicon nanotubes. Daldosso and Pavesi present developments related to silicon as a photonic material, silicon laser, silicon nanocrystal amplifiers, etc. Durrani and Ahmed cover the developments on nanosilicon single electron transistors and memories.

The idea of the book emerged from a public lecture I gave in Tokyo in 2003 on nanosilicon and I am very grateful to Nan Chen to have organized that at the Asian Technology Information Program (ATIP) in association with GLOCOM as well as to Ken Goretta for the support. The past few years have seen many exciting developments on nanosilicon and there is renewed hope for the usefulness of silicon at the nanoscale as well as its new applications which have been covered in this book. Some of these developments took place at the Institute for Materials Research (IMR), Tohoku University, Sendai where I spent several years and I am very grateful to Y. Kawazoe to have given me all the support and the excellent facilities there, to my coworkers and all the group members with whom I enjoyed many discussions. I am particularly indebted to T.M. Briere, H. Kawamura, C. Majumdar, F. Pichierri, A.K. Singh, Marcel Sluiter, and Q. Sun with whom I shared many stimulating thoughts that led to many developments. I am also grateful to T. Sakurai and A. Kasuya for their support. The staff of the Center for Computational Materials Science, IMR provided me excellent support and I express my sincere gratitude to them. R. Note gave all the support for efficiently running big jobs. Parts of the book were completed during my stay at the Research Institute for Computational Sciences, AIST, Tsukuba, and the Institute of Mathematical Sciences, Chennai. I am very grateful to K. Terakura, T. Ikeshoji, G. Baskaran, and R. Shankar who gave me all the support. I am thankful to Abinav Saket and Vinu Lukose who helped me to prepare the final manuscripts. I thankfully acknowledge the hospitality at the International Frontier Center for Advanced Materials (IFCAM) of IMR and the support of M.W. Chen. I sincerely thank the Elsevier staff to have taken the project and provided all the cooperation and support. Special thanks to Kristi Green to have done excellent coordination at the final stages. Last but least, I acknowledge the great support given by my wife, Brij Bala Gupta and my children Smita, Preeti and Gaurav.

Vijay Kumar

CHAPTER ONE

Silicon Nanoparticles: New Photonic and Electronic Material at the Transition Between Solid and Molecule

Munir H. Nayfeh[1] and Lubos Mitas[2]

Contents

1.1 Introduction 3
1.2 Synthesis 3
 1.2.1 Physical Techniques 3
 1.2.2 Physico-Chemical Techniques 4
 1.2.3 Chemical Techniques 4
 1.2.4 Electrochemical Techniques 4
 1.2.5 Discretely Sized Si Nanoparticles 6
1.3 Functionalization 8
 1.3.1 Initial Surface Condition 9
 1.3.2 Alkylated Particles 11
 1.3.3 Aggregation and Solubility 15
 1.3.4 Stability in Acid 17
1.4 Spectroscopic Characterization 17
 1.4.1 Fourier Transform Infrared Spectroscopy 17
 1.4.2 Nuclear Magnetic Resonance 19
 1.4.3 Gel Permission Chromotography 20
 1.4.4 X-Ray Photospectroscopy 21
 1.4.5 Auger Electron Spectroscopy 21
 1.4.6 Transmission Electron Microscopy 21
1.5 Optical Properties 22
 1.5.1 PL and Detection of Single Nanoparticles 22
 1.5.2 PL Lifetime 26
 1.5.3 Cathodoluminescence and Electroluminescence 27
 1.5.4 Photostability Under UV and Infrared Radiation 29

[1] Department of Physics, University of Illinois at Urbana-Champaign, Urbana, IL, USA.
[2] Department of Physics, North Carolina State University, Raleigh, NC, USA.

Nanosilicon
9780080445281
Copyright © 2007. Elsevier Ltd.
All rights reserved.

1.6 Reconstitution of Particles in Films 29
1.6.1 Precipitation Spray 30
1.6.2 Electrodeposition: Composite Films of Metal and Nanoparticles 31
1.6.3 Silicon Sheet Roll into Tubes 32
1.6.4 Self-Assembly 33
1.7 Nonlinear Optical Properties 34
1.7.1 Stimulated Emission 34
1.7.2 Second Harmonic Generation 39
1.7.3 Gain and Optical Nonlinearity 39
1.8 Effect of Functionalization on Emission 41
1.9 Structure of Particles 41
1.9.1 Luminescence Models 42
1.9.2 Computational Methods for Electronic Structure of Nanoclusters 43
1.9.3 Prototype of Hydrogenated Particles (Supermolecule) 49
1.9.4 H_2O_2 Effect on Surface Reconstruction 51
1.9.5 Novel Si—Si Bonds (Molecular-Like Behaviour) 52
1.9.6 Structural Stability of the Prototype 54
1.9.7 Material Properties: Dielectric Constant and Effective Mass 55
1.9.8 Excited States (Molecular-Like Bands) 57
1.9.9 Collective Molecular Surface 57
1.9.10 Phonon Structure: Collective Molecular Vibration Modes 59
1.9.11 Molecular-Like Emission: Direct versus Indirect Process 60
1.9.12 X-Ray Form Factors 61
1.9.13 Effect of Termination on the Band Gap 63
1.10 Device Applications 63
1.10.1 Photoelectric Conversion/UV Photodetector 64
1.10.2 Metal Oxide Silicon Memory Devices 66
1.10.3 Biophotonic Imaging 68
1.10.4 Amperometric Detection 69
1.10.5 Nanosolar Cell 71
1.10.6 Nanoink Printing 72
1.10.7 Single Electron Transistor Devices 73
1.11 Conclusion 73
Acknowledgements 74
References 74

Abstract

Unlike bulk silicon, a spectacularly dull material, ultrasmall silicon nanoparticles are spectacularly efficient at emitting light in RGB colours. In addition to being ultrabright, reconstituted films of particles exhibit stimulated emission. Light-emitting Si devices could eventually result in a laser on a chip, new generation of Si chips, and extend the functionality of Si technology from microelectronics into optoelectronics and biophotonics. We present in this review experimental as well as theoretical and simulations results discussing the synthesis, structure, and the wide-ranging optical, electronic, mechanical and (derivatized) biocompatible properties and applications of the particles. We discuss the basic mechanism behind the multi-novel properties in terms of silicon–hydrogen configurations of filled fullerene. With a tetrahedral core and a strong molecule-like reconstruction of the surface, the particles constitute a new phase or “supermolecule” that exhibits solid-like behaviour as well as molecule-like behaviour.

1.1 Introduction

The area of nanoparticles (nanocrystallites (nc) or quantum dots) is one of the most active areas of science today. In particular, silicon nanoparticles is a burgeoning and fascinating area of science and one that has significant technological implications. This new charge of interest came nearly a decade after the exciting discovery by Canham in 1990 [1,2] of visible red photoluminescence (PL) at room temperature with a quantum efficiency of few percent, from electrochemically etched silicon (porous silicon (PS) layer). Although in the ensuing years, the quantum efficiency remained practically small, dashing hopes for optoelectronics integration from this development stimulated a variety of physical, chemical, physiochemical, and electrochemical techniques to produce dispersions of luminescent nanometre sized silicon crystallites. The research led by Nayfeh at Illinois in 2000 has shown that reducing the size of an elemental Si crystal to a few tens of atoms (~1 nm), without altering its chemical composition, effectively creates a new material, a nanoparticle with novel properties – both electronic and non-electronic, including ultrabright ultrastable luminescence – that were not available before [3–22]. This research demonstrated that single-element Si particles – an abundant, stable, environmentally benign, malleable nanomaterial – have versatile and wide-ranging optical, electronic, and (derivatized) biocompatible properties. These properties have drawn the interest of engineering, physics, chemistry, material science, and biology, and medical researchers alike.

Ultrabright silicon structures are particularly intriguing for several reasons. First, bulk Si is spectacularly inefficient at emitting light. Second, light-emitting nanoparticles can be synthesized at very low cost, without resort to either the costly lithographic or epitaxial techniques. Third, the most technologically important and abundant material, Si, is the backbone of the microelectronics industry, dominating the microelectronics revolution. Light-emitting Si devices could eventually result in a new generation of Si chips and in a laser on a chip, and extend the functionality of Si technology from microelectronics into optoelectronics and biophotonics.

We discuss the synthesis, structure, origin of brightness, and the wide-ranging optical, electronic, and (derivatized) biocompatible properties of the family. Finally we present a number of device applications in electronics, optoelectronics, and biophotonics.

1.2 Synthesis

Several procedures have been developed throughout the last decade for the synthesis of luminescent Si nanoparticles [3–47]. These include physical, physiochemical, chemical, and electrochemical procedures. We will discuss the procedures, size, uniformity in size, throughput, cost, and amenability to mass production, and recovery.

1.2.1 Physical Techniques

A variety of *physical techniques* were developed in the last decade. First, Si nanoclusters were formed, for example, in the matrices of glass [23,24] and SiO_2 [25]. In

these efforts, luminescent nanocrystals of ~3 nm across embedded in quartz by implanting high-energy Si ions into quartz, followed by annealing at 1100°C were created. Second, silicon wafers were dispersed by ablation using a variety of agents to produce isolated Si particles [42]. These agents included spark and laser ablation [26]. In laser ablation [27], a focused high-power laser radiation is used as a brute force to blast the wafer, heat evaporate, or break chunks of the material. The broken pieces are transported downstream from the laser/material target by an inert gas jet, to be collected by filters. The particles are then recovered from the filter. These ablation techniques suffer from low throughput and cost, lack of control on the size and quality of the particles produced.

1.2.2 Physico-Chemical Techniques

Isolated particles were obtained by the gas-phase preparation from silanes via slow combustion [28,29], thermal decomposition [30], microwave plasma [31], gas-evaporation [32], or chemical vapour deposition (CVD) [33,34]. Such methods may involve particle formation in a discharge of gas mixtures that include the highly toxic silane (SiH_4), followed by collection in filters and recovery from filters. These techniques suffer from low throughput and cost, lack of control on the size and shape of the particles. Although the decomposition of silanes produces nanoparticles with a relatively small size distribution, it does not lend itself to the easy manipulation of the surface of the particles, covered with SiO_2, or to their large-scale manufacturing.

1.2.3 Chemical Techniques

Recently Si nanoclusters in the range 2–10 nm were synthesized *chemically* via a reduction of anhydrous ionic salts SiX_4 (X = Cl, Br), dispersed in water-free reverse-micelles solutions, with $LiAlH_4$ [35]. A certain degree of control over the Si cluster size was achieved by variation of the micelles size, intermicellar interaction, and reaction chemistry. Unlike the *physical preparations*, which produce impure Si crystallites that contain a large amount of SiO_2 on the surface, this method produces Si particles with the surface terminated by hydrogen from metal hydride. However, the formed Si particles are stable for long time (6 months to 1 year) only in a glove box under Ar. They would undergo degradation upon exposure to oxygen, presumably due to surface oxidation.

Finally, organic capping of nanoparticles has been used as a means to achieve some degree of control over the particle size, directly during the synthesis step. This has been achieved in solution synthesis procedures using molecular silicon compounds. Methods of chemical reduction of Si(IV) compounds such as SiR_nCl_{4-n} (R = H, alkyl) to Si(0) have been shown to directly produce organic-monolayer-stabilized Si particles.

1.2.4 Electrochemical Techniques

The best technique developed to date for generating stable H-passivated particles is electrochemical dispersion of bulk silicon. Electrochemical etching was first used in 1956, but resulted in electropolishing rather than in nanomaterial structure [36]. Electrochemical dissolution of silicon followed by a means to separate particles, such

as *ultrasonic fracturing*, produces colloidal suspension of particles in a variety of organic solvents. This etching technique is an interfacial process involving a two-electron transfer through an overall electrochemical reaction, involving HF molecules [37]:

$$\mathrm{Si\ (surface) + 2HF + nh^+ \rightarrow SiF_2\ (surface) + 2H^+ + (2-n)e^-}$$

The divalent silicon species formed on the surface is then oxidized to tetravalent silicon ions in the form of SiF_6^{2-} (solution) through a redox reaction in solution:

$$\mathrm{SiF_2\ (surface) + 4HF \rightarrow H_2SiF_6\ (solution) + H_2}$$

with the partial reactions being:

$$\mathrm{SiF_2 + 4F^- \rightarrow SiF_6^{2-} + 2e^- \quad and \quad 2H^+ + 2e^- \rightarrow H_2}$$

The resulting porous layer (formed under electrochemical anodization of crystalline Si wafers in HF-containing electrolysis bath) has a highly complex nanoscale architecture made up of one-dimensional crystalline nanowires and zero-dimensional nanocrystallites as shown in Fig. 1.1. It is to be noted that these layers are hydride terminated (containing very little SiO_2), with mono- ($\equiv$SiH), di- ($=SiH_2$) and tri- ($-SiH_3$) hydride groups in a variety of different local orientations and environments, owing to the complex porous nature of the material [38,39].

Ultrasonic dispersion of electrochemically etched Si wafers in a variety of solvents results in a colloidal suspension of Si particles. The size distribution depends on the anodization time and the composition of the electrolysis bath solution. Unlike the gas-phase preparation of colloidal particles, this technique is more convenient and starts from high-purity semiconductor-grade substrates. More importantly, the resulting H-passivation of the surface minimizes its contamination by SiO_2 and other impurities. Due to dispersion and fracturing in the ultrasonication step, some of the bare silicon will be exposed, resulting in some degree of hydrocarbon contamination and oxidation as it was demonstrated by recent Fourier transform infrared spectroscopy (FTIR) investigation [40].

The ultrasonic fracturing of PS in toluene and acetonitrile resulting in colloid suspension of Si-nc was first reported in 1992 [41]. PS was prepared from *n*-type (P-doped) and *p*-type (B-doped) single-crystal polished Si(100) wafers by galvanostatical etching at current densities between 0.1 and 5 mA/cm^2, adjusted by illuminating with a 300 W tungsten lamp, in a solution of aqueous HF and ethanol. The infrared spectra of anodized wafers, rinsed with water and air dried, displayed strong Si—H stretches in the 2050–2150 cm^{-1} region and lacked discernible peaks for

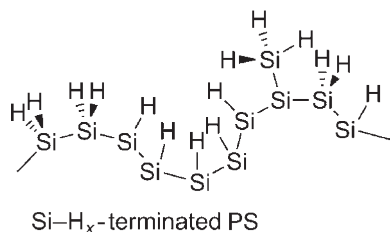

Figure 1.1 Schematic presentation of H-terminated surface of PS layer (Reproduced with permission from Buriak [51] copyright RCS 1999).

surface Si—O, indicative of the clean, H-terminated Si surface characteristic of freshly etched PS [38,39]. The presence of residual SiO_2 on the surface of nanoclusters has been observed in some studies, however [42,43]. Ultrasonication was carried out under dry N_2 atmosphere, using purified, dried solvents, added to the flasks with anodized Si wafers. Typically, after sonication the solution was allowed to settle for 1 h, and the supernatant was removed from the settled solids. The particles were irregularly shaped and ranged in size from many micrometres down to the resolution limit of the TEM. In some cases, high-resolution transmission electron microscopy (HRTEM) studies of colloidal suspensions showed that the size of the particles ranges from 50 nm and smaller up to 2 nm. Addition of ethanol to electrolyte solution and the increase in anodization time resulted in producing more uniform crystallites in the size range of 10 nm or less. It was found that the bigger size objects are actually agglomerate of several small crystallites 7–11 nm in diameter as shown in Fig. 1.2. The smallest crystallites in agglomeration are about 2 nm. In addition to these relatively big aggregates of crystallites, small individual crystallites were also observed.

In contrast to the physical methods for preparation, the anodization procedures and ultrasound are straightforward and inexpensive. Unfortunately, the effort, required for control of the size distribution and quantitative characterization, is prohibitive for large-scale synthesis and surface manipulation is limited.

1.2.5 Discretely Sized Si Nanoparticles

Significant progress in the dispersion of single-crystal silicon wafers into ultrasmall Si nanoparticles with uniform size and large throughput was recently achieved. The method uses aqueous HF/ethanol electrolyte bath that additionally incorporates the highly oxidative, catalytic, and cleansing agent of hydrogen peroxide, H_2O_2 [3–22]. The silicon samples used were (100) oriented, 1–10 Ω-cm resistivity, *p*-type

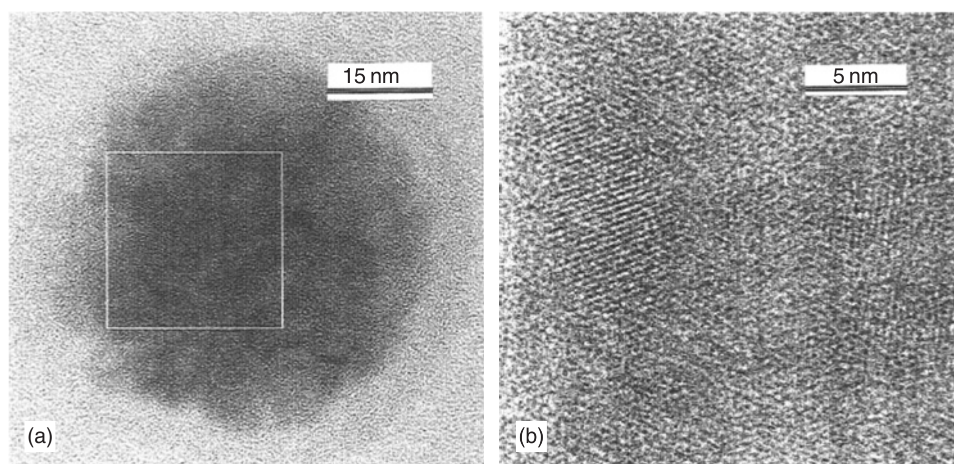

Figure 1.2 (a) HRTEM micrograph of a typical cluster of Si crystallites with an outer amorphous layer between 3 and 4 nm and (b) an enlargement of the outline region shown in (a). The lattice spacing of 0.31 nm indicates this is a view down a <100> axis showing [111] interplanar spacing (Reproduced with permission from Ref. [40] copyright American Chemical Society (ACS) 1996).

boron-doped silicon wafers. The silicon substrate is used as the anode, and a platinum wire facing is used as the cathode. An anodizing current density was fixed at 5 mA/cm^2. We gradually advance the wafer into the chemical etch bath at a low speed while etching is taking place. A meniscus forms as a very thin slice of the wafer that is at the interface of etching solution and air. The slow advance of the wafer creates a large section, which is meniscus-like. The process enriches the ultrasmall substructure. Moreover, it makes the top skin material extremely fragile. Larger particles are less amenable to dispersion due to stronger interconnections. We use a post-HF treatment to weaken those. The Si wafer is then immersed in an ultrasound acetone (ethanol, methanol, or any other solvent) bath for a brief period of time. Under the ultrasound treatment, the very top layer of the luminescent film, a weakly interconnected nanostructure network dislodges into ultrasmall particles which may then be separated and recovered. We used commercial gel permeation chromatography to separate the particles. The particles are separated into four vials each contains particles of uniform size, with near 90–100% efficiency. A thin graphite grid is immersed in the colloid and imaged by HRTEM [10,18]. Figure 1.3 (left) shows that particles are nearly spherical and classify into a small number of sizes. These include 1.0 (see inset), 1.67, 2.15, 2.9, and 3.7 nm. Figure 1.3 (right) shows the atomic planes in closeups of the 1.67, 2.15, 2.9 and 3.7 nm particles. It is to be noted that, we can predominantly produce the 1 nm blue luminescent particles with 95% purity using high anodizing current. On the other hand under low current we can produce 2.85 nm red luminescent particles with 85% purity. A soup of the particles is produced at intermediate currents.

The existence of magic sizes is in contrast to what has been known. It has been known that the abundance spectrum of self-terminated clusters Si_n [44–46] with $n > 20$ exhibits neither special features nor discrete magic numbers [47]. The smallest four are ultrabright blue, green, yellow, and red luminescent particles, respectively. Fabricating size-, shape-, and orientation-controlled fluorescent Si nanoparticles in the range 1–3 nm (30–1000 atoms), with reproducibility would be critical to the

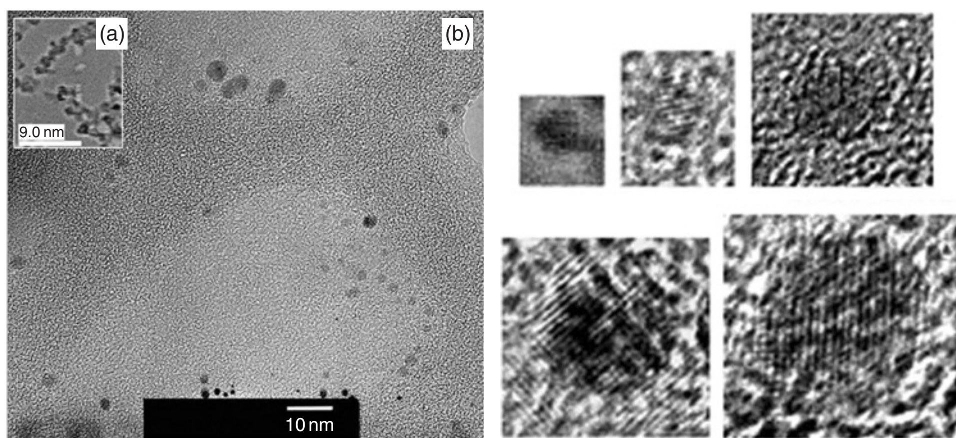

Figure 1.3 (Left) (a) and (b) TEM images of particles on a graphite grid. The particles are nearly spherical and can be classified into a small number of discrete sizes. (Right) Closeup TEM images of the 1.0, 1.67, 2.15, 2.9 and 3.7 nm particles (from Ref. [18]).

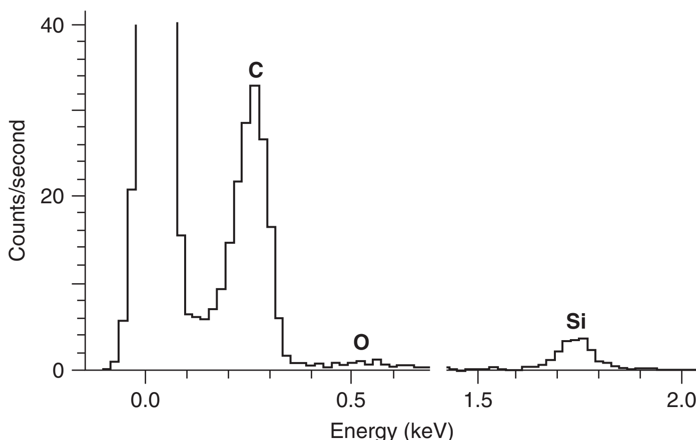

Figure 1.4 Electron PL spectrum of dried film of the Si particles deposed on thin graphite grid. The particles were obtained through ultrasonication of PS sample anodized in with H_2O_2:HF mixture (from Ref. [9]).

understanding of nanostructures and would be of significant interest to the microelectronics, optoelectronics, and biomedical industries. The availability of discrete sizes and distinct emission in the red, green, and blue range is useful for biomedical tagging, RGB displays, and flash memories. Moreover, size uniformity is important for applications that require superlattices, high-quality films, or single nanoparticle-based devices, such as fluorescent imaging and tagging.

The incorporation of H_2O_2 in the anodization mixture brings several features and advantages. It produces electronically and chemically high-quality particles with a homogeneous monohydride stretching phase on the surface, with no defect-like trihydrides and dihydrides. The process also reduces the crystallite size, and reduces impurities. Moreover, it produces substructure that is very loose, requiring very brief period of time for sonication with very little fracturing, hence subsequent oxidation.

The size of the smallest particle was also confirmed by two-photon autocorrelation fluctuation spectroscopy (FCS) in the colloid in which we determined the autocorrelation function of the luminescence and compared it to a fluorescein dye molecule standard with known density, diffusion coefficient, and size [3]. Previous differential excitation measurements and TEM of the solid before sonication showed structures of $\sim$1 nm [19]. Moreover, material analysis using electron PL shown in Fig. 1.4 shows that the particles are composed of silicon with $<$10% oxygen.

1.3 Functionalization

Present-day medical and biological fluorescent imaging is significantly constrained by the use of dye markers – the only markers currently available [48]. Dyes, especially the blue ones, are not photostable – they decompose under room light or higher temperatures. Efforts are being directed to produce different classes of markers,

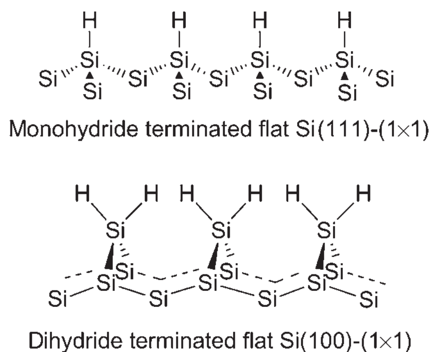

Figure 1.5 Schematic presentation of the Si(111) and Si(100) silicon-hydride-terminated surfaces (Reproduced with permission from Ref. [51] copyright RCS 1999).

such as semiconductor particles. CdS nanoparticles have recently been proposed as fluorescent markers [49,50].

Because the Si particles are ultrasmall, ultrabright, photostable, and do not blink, they show significant potential for creation of robust, highly PL organic–inorganic nanosemiconductors, constituting the next generation of ultrabright markers for ultrasensitive fluorescence analysis [4]. Organic groups on the surface of the particles provide several features, including an increase in the resistance towards oxidation, an opportunity to control particle's interaction and hence particle's arrangement on surfaces, the stabilization of the electronic and/or optical properties of the particles, and improved solubility (preventing bulk aggregation). The linkage facilitates the attachment of organic functional groups capable of recognizing specific analytes such as proteins, DNA, or viruses. The exceptional optical properties, ultrasmall size (approximately small molecules), uniformity of size, low cost and photostability provide the ultimate sensitivity and spatial resolution in imaging capabilities.

1.3.1 Initial Surface Condition

In general, SiO_2 overlayer completely inhibits the chemical activity of silicon. On the other hand, Si—H and Si—Si bonds on the particle's surface can be reactive. Indirectly in ultrasmall species, Si—O bonds may increase the reaction ability of silicon nanosurface because those bonds tend to polarize Si—Si and Si—H bonds, rendering them more amenable to functionalization.

Surfaces of Si nanoparticles may constitute the chemical analogue of continuous surfaces (Si flat and PS wafers). However, they have several particularities, which require the adjustment of the modification strategies applied to bulk Si surfaces. Therefore we present in Figs. 1.5–1.8 a number of examples of functionalized Si surfaces with organic layers, attached through Si—C, Si—O—C, Si—N—C, etc. [51]. A catalogue of different schemes is shown in Fig 1.9. The reaction ability of the nanosurface can be higher than the surface of the bulk material due to a higher surface curvature and consequently more defected surface composed of stressed Si—Si bonds. For instance, ultrasmall (~1 nm) Si nanoparticles have highly radiative surface

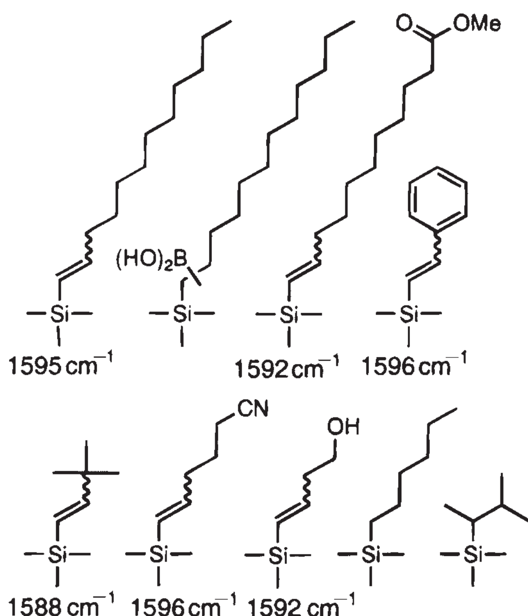

Figure 1.6 Functional groups covalently attached to the PS surface through Lewis acid mediated hydrosilylation with $EtAlCl_2$ of alkenes and alkynes. The numerical values correspond to the ν (C=C) of the surface-bound vinyl group as measured by transmission FTIR (Reproduced with permission from Buriak et al. [51] copyright ACS 1998).

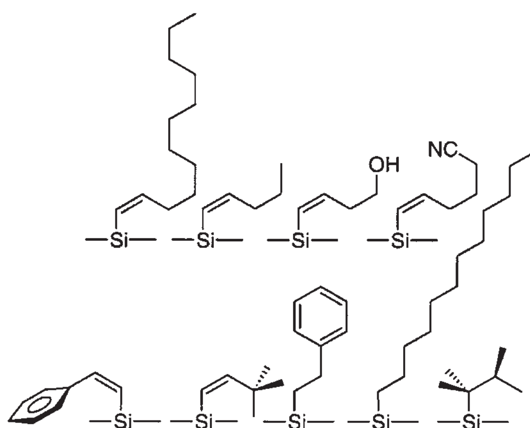

Figure 1.7 Examples of the surface termination possible through $EtAlCl_2$ Lewis acid mediated hydrosilylation of alkenes and alkynes on PS surfaces. Reaction with alkynes affords cis-conformation of attached chain. With permission from Buriak et al. [51] copyright ACS 1999.

reconstructed Si—Si network, found only in ultrasmall nanoparticles, on which excited excitons are self-trapped [17,52]. Preserving the optical activity is key to selection of strategies for semiconductor surface modification. The chemistry chosen for the modification [3,10] must therefore involve only replacement of hydrogen of Si—H groups and not the cleavage of Si—Si bonds.

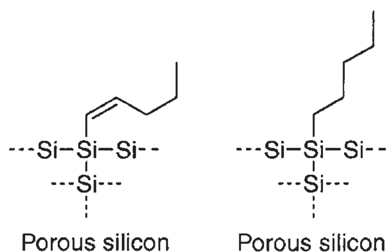

Figure 1.8 Packing of alkenyl and alkyl species on PS surface. Because of cis-stereochemistry of alkenyl groups formed through alkyne hydrosilylation it occupies more space than the corresponding alkyl group with the same number of carbons and cannot pack as well (Reproduced with permission from Buriak et al. [51] copyright ACS 1999).

Electrochemical-based synthesis of silicon nanoparticles results in nanosurfaces that are to a large extent H-passivated [41]. Because of its unique and simple structure, the hydride passivation opens a unique opportunity for manipulation of the surface of particles. The alcohols included 1-undecanol (UD-OH), 1-hexadecanol (HD-OH), 1-octanol (OC-OH), and 1,12-dodecanediol (DD-$(OH)_2$). The colloid dispersions of H-terminated silicon nanoparticle in several organic solvents (Cl–benzene, xylenes, heptane, THF) were not stable and rapidly formed amorphous precipitates [53]. A resonication restored their transparency only for short time. The colloids of the alkylated particles [12,53] dispersed in the same organic solvents were stable for months. For better biocompatibility and control, we readily replaced the hydrogen coating and capped the particles with an oxide at room temperature under ordinary conditions by immersion in H_2O_2 [10,11]. Figure 1.10 gives the molecular vibrations of as-is particles and after capping with oxygen. In the as-is we see mainly hydrogen, but after capping we see hydrogen being replaced by oxygen. Upon oxygen termination, the spectrum suffers only minor changes, while the brightness drops only by a factor of two. SiO_2 overlayer inhibits the chemical activity of the continuous crystalline silicon surfaces (flat Si wafers and PS) to functionalization.

1.3.2 Alkylated Particles

Silicon nanoparticles have been functionalized with alcohol, butylamine, 1-pentene, carboxyl acid, thiol groups, etc.

1.3.2.1 Alcohol

Thermally activated reactions of several alcohols with Si nanoparticle's colloid in toluene have been shown to result in the formation of alkoxy-coated particles [43]. Primary alcohols $C_nH_{2n+1}OH$ were dissolved in toluene, and added to a colloid of Si particles. The reaction was then carried out in a water bath at 95–100°C under a stream of nitrogen. After completion of the reaction, the excess solvent is evaporated. After cooling to room temperature, some toluene was added to disperse the particles. It was found that the heating process induces covalent bonding of the alcohol molecules to the surface and thereby produces alkoxy-capped Si particles (Si—O—R) where R = UD, HD, OC. The modified particles exhibited superior qualities; there was persistent observation of lower oxidation level for the modified samples.

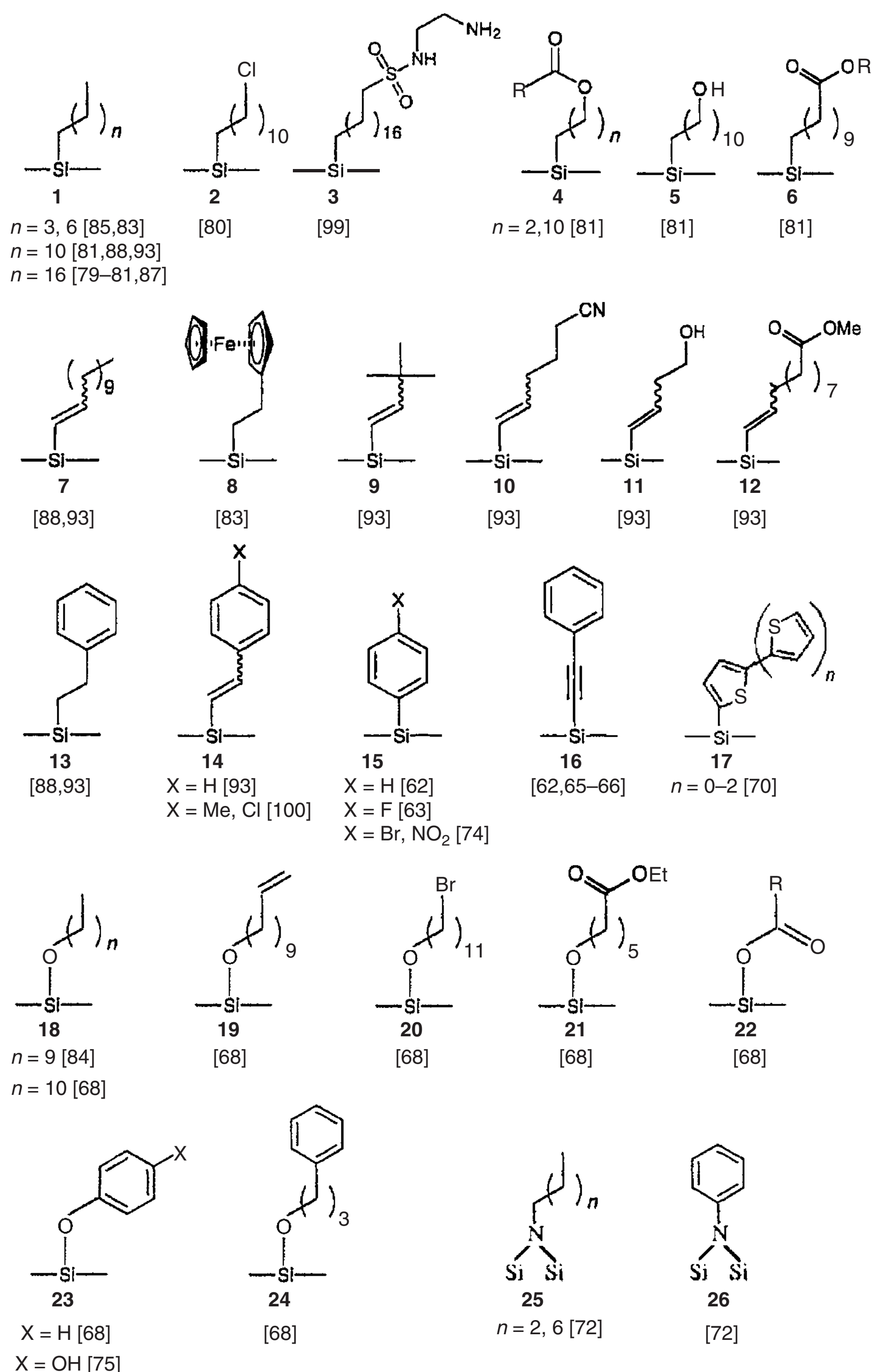

Figure 1.9 Examples of functionalized Si surfaces with organic layers attached through Si—C, Si—O—C and Si—N—C linkages (after Ref. [4], the numbers in square brackets refer to reference numbers in Ref. 4).

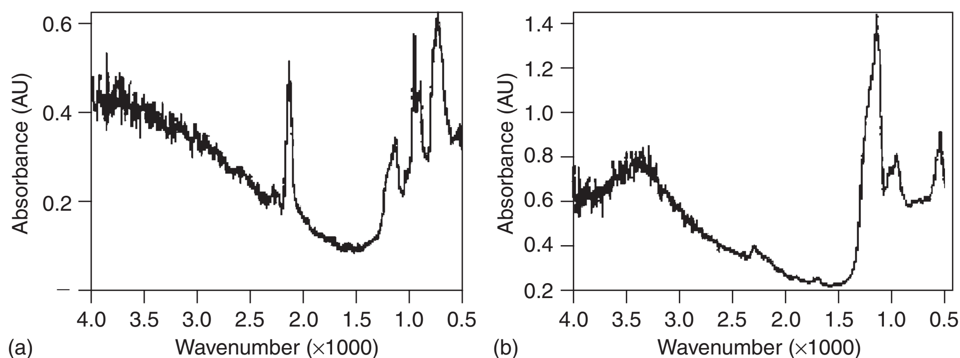

Figure 1.10 FTIR spectra of (a) as anodized PS sample before ultrasonication and (b) after oxidation by immersion in H_2O_2 (after Ref. [10]).

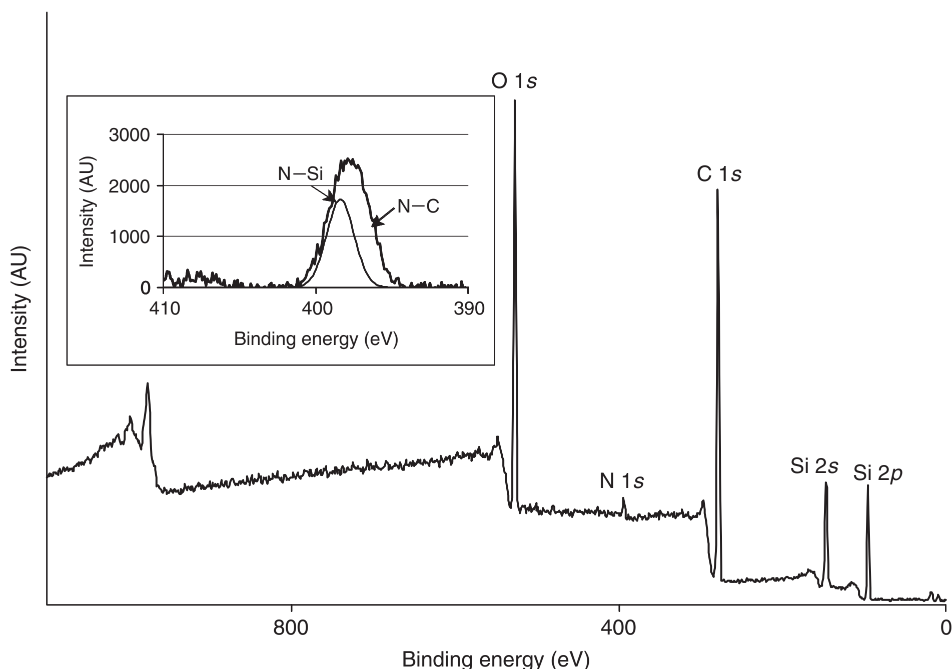

Figure 1.11 XPS survey spectrum of film reconstructed from aminized particles showing that the particles have nitrogen and carbon peaks at ~400 and 300 eV, respectively. A fit of the binding energy of the 400 eV peak in terms of two components is given in the insert.

1.3.2.2 Alkylamine

Aminization of particles was also accomplished via Si—N linkage. A chlorobenzene colloid of particles is saturated with Cl_2 gas at a temperature of −10°C [12,54,55]. The dissolved chlorine gas chlorinates the particles by electrophilic replacement of hydrogen with chlorine [56,59]. Fresh distilled butylamine ($C_4H_9NH_2$) was then added to the dried particles and was heated and stirred. The dried particles were redispersed in heptane. Figure 1.11 is an X-Ray photospectroscopy (XPS) survey

spectrum of a film reconstructed from aminized particles showing that the particles indeed has a nitrogen peak at ~300 eV.

1.3.2.3 Alkene

Pentene was reacted with the particles via Si—C linkage. Dispersion of ultrasmall silicon nanoparticle [3,10,57,58] in xylenes was reacted with 1-pentene at 135–140°C for 24 h [53]. The residue was dried under vacuum and dispersed in heptane. The alkylated particles dispersed in d_8-THF were also directly analysed by nanoprobe H NMR, showing that about 25% of Si—H groups were involved into hydrosilylation. In Fig. 1.12 we show the proposed mechanism of thermal hydrosilylation of terminal alkenes in colloid dispersion of the particles.

1.3.2.4 Carboxy

Carboxylic groups on the surface of ultrasmall H-passivated silicon nanoparticle were introduced by reaction with derivatives of 4-pentenoic acid (4-PA) via a Si—C linkage [3,10]. This is a bi-functional molecule containing terminal double bond and terminal acid group. Since both ends of the bi-functional acid molecule are active to reaction with the particles under hydrosilylation conditions [53,57], the acid group was ester protected during the reaction. The acid group was protected

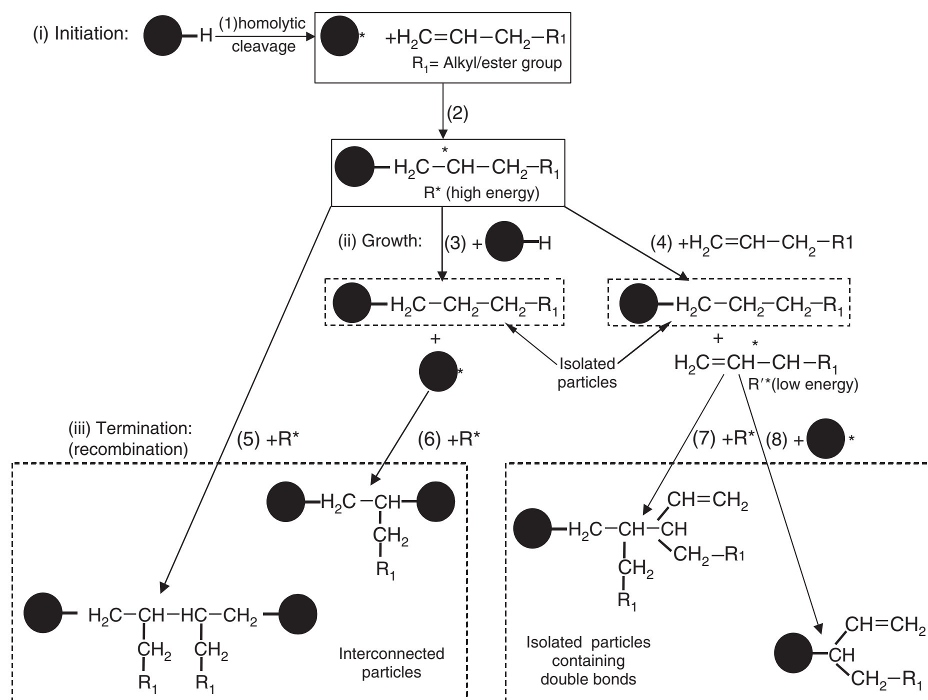

Figure 1.12 Proposed mechanism of thermal hydrosilylation of terminal alkenes in colloid dispersion of H-terminated Si particles (from Ref. [53]).

during the process of attachment to the particles by either tert-butyl (t-Bu) or methyl (Me) ester. After completion of the reaction, the ester groups were converted to —COOH groups by hydrolysis in acidic (basic) media. It is to be noted that t-Bu ester is not thermally stable under the temperature conditions of the procedure, whereas Me-ester is of sufficient stability.

1.3.2.5 Alkyl and Alkoxy

Organic alkyl-monolayer-coated nanoparticles may be synthesized also directly during liquid solution-phase synthesis procedures utilizing molecular silicon compounds via Si—C linkage. For instance, the reaction $SiCl_4 + RSiCl_3 + Na \rightarrow$ Si nanoclusters (diamond lattice) + NaCl in the presence of sodium metal (Na) produces mostly hexagonal-shaped Si single crystals. The choice of R provides some size selectivity. With R = H, a wide size distribution (5–3000 nm) is produced. With $R = C_8H_{17}$, alkyl-coated Si nc were produced [60] with the size being controlled to a diameter of 5.5 ± 2.5 nm.

The specific crystal structure allows alkali silicon salts ASi (A = Na, K) to interact with $SiCl_4$ to form Cl-capped Si nanoclusters [40,61]:

$$4n\text{ASi} = n\text{SiCl}_4 \rightarrow \text{Cl-capped particle} + 4n\text{ACl}$$

This is followed by the reaction:

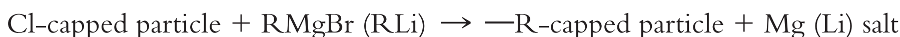

$$\text{Cl-capped particle} + \text{RMgBr (RLi)} \rightarrow \text{—R-capped particle} + \text{Mg (Li) salt}$$

to produce alkyl capping (Si—C linker) from surface passivation with alkyl Li or Grignard reagents (R = methyl, ethyl, butyl and octyl) [61]. This method gives some advantages such as soft reaction conditions and some control over surface termination. Because termination of the particles stops their growth, control of the reaction time before termination offers a degree of size control. On the other hand, larger (40–130 nm) tetrahedral-shaped butyl-capped Si nanoclusters were obtained by room temperature reduction of $SiCl_4$ with Na naphtalenide followed by termination with butyl lithium [62].

Finally, thermally degrading the Si precursor diphenyl silane (SiH_2Ph_2) in the presence of octanol under supercritical fluid conditions produces alkoxy capping via Si—O—C linkage. These are robust, highly crystalline, octyloxi-terminated Si nanocrystals (Si—O—C linker). Relatively size-monodisperse sterically stabilized Si nanocrystals ranging from 1.5 to 4.0 nm in diameter were obtained in significant quantities [63].

1.3.3 Aggregation and Solubility

Alkylation of the particles significantly increases their solubility in organic solvents and the stability of colloid dispersions [12–53]. The aminized and alkylated Si nanocrystals in organic solvents (heptane, THF, CH_2Cl_2) were found to remain stable for months, indicating an increase in solubility and reduction of bulk aggregation [12]. The colloid dispersions of H-terminated silicon nanoparticles in several organic solvents (Cl–benzene, xylenes, heptane, THF) were not stable and rapidly formed amorphous precipitates [53]. A resonication restored their transparency only for short time. The colloids of the alkylated particles [12,53] dispersed in the same

organic solvents were stable for months. In contrast to particles alkylated with butylamine [12] and 1-pentene [53], the acid-functionalized particles were not dissolvable in heptane. However, they completely dissolved in CH_2Cl_2 and THF and more polar methanol, forming colloids that are stable for months. The higher thermal stability of Me ester of PA compared to t-Bu ester has diminished cross-linking, but not completely suppressing it.

The aggregation of *the particles* was characterized by gel permission chromatography (GPC) in THF at 365 nm (see Fig. 1.13). Prior to the modification GPC showed a single monodispersion but there is observed aggregation which may be explained by interconnection of the particles through H-bonding of Si—OH species formed because of partial oxidation of the surface, which results in Si—O—Si covalent bridges

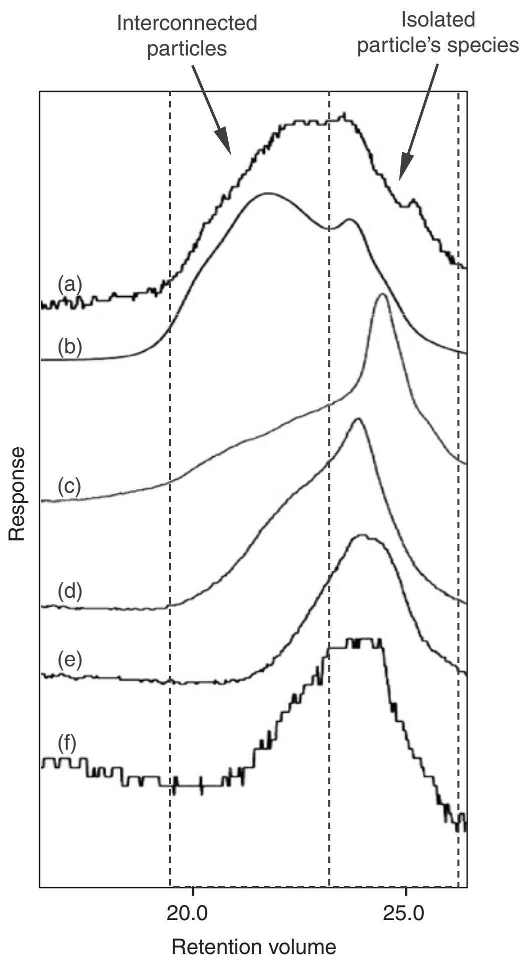

Figure 1.13 GPC plots of dispersions of Si particles of 1 nm in diameter: (a) H-terminated, (b) modified with t-Bu ester of 4-PA, (c) alkylated with 1-pentene and (d–f) modified with Me-ester of 4-PA, (d) the ester-modified sample and (e–f) after hydrolysis of the ester units of the sample (d) (e: "THF" fraction, f: "water" fraction). UV detector recorded absorption of the colloids in THF at 365 nm (after Ref. [4]).

between particles in the dried sample. Contrary to the H-terminated particles, the GPC plot of particles functionalized with butylamine (Si—NH—C_4H_9) showed a much narrower peak. This narrowing points to the absence of bulk aggregates (even after vacuum drying). The GPC of 1-pentene treated particles showed a weak broad shoulder to a sharp peak. Low intensity of this shoulder is evidence of low possibility of cross-linking for the hydrosilylation of 1-alkenes. The low polydispersity of silicon nanoparticles after modification [12,53] may have resulted from an increased resistance of alkylated Si surface of nanoparticles to oxidation, which likely is the main reason of aggregation of H-terminated Silicon nanoparticle. The GPC of the acid-functionalized particles dispersed in THF showed monodispersion but contains some cross-linked particle's aggregates. The aggregation is believed to be due to a side reaction of the Si particles with the —COOH groups that [57] are liberated due to the partial thermal decomposition of the t-Bu ester groups. Moreover, free radicals on the different particles may recombine, resulting in interconnected particles.

1.3.4 Stability in Acid

Because of the presence of acid groups on the surface, the solubility of the modified particles was sensitive to pH. For example, aggregation was observed upon lowering of the pH of the water colloid to $pH < 5$, but increasing the pH to the original value restored its transparency. HCl interacts with carboxylated particles in basic water solution [59] if there is residual Si–H (incomplete functionalization) groups. After keeping the aqueous sample with $pH = 2$ for 2 months, its PL was completely quenched [60]. The sample hydrolysed under softer acidic conditions (starting pH equal to 4.9 and self-increased up to 7 at the end of the experiment) lost the PL after 5 months.

1.4 Spectroscopic characterization

To assess the effectiveness of the chemical and biological reactions, particles must be subjected to several diagnostics and interactions. These include Fourier transform infrared spectroscopy (FTIR), nuclear magnetic resonance (NMR), gel permission chromatography (GPC), X-ray photospectroscopy (XPS), Auger electron spectroscopy (AES), transmission electron spectroscopy (TEM), and optical absorption, and emission and excitation spectroscopy. This will help zero on the procedures that may be adopted.

1.4.1 Fourier Transform Infrared Spectroscopy

We use FTIR to examine the chemical termination. Transmission mode data in normal incidence was taken in air using an ATI-Mattson Galaxy model GL-5020. To examine the quality of the samples, we measured the infrared absorption of hydrogen bonds in the Si—H stretch region ($2100\,cm^{-1}$) as well as in the vibration and bending region ($600–900\,cm^{-1}$). From these spectra the relative importance of different hydride species, and hence the type of passivation can be deduced. Figures 1.14a–d compares the absorption spectra of samples prepared under conditions of

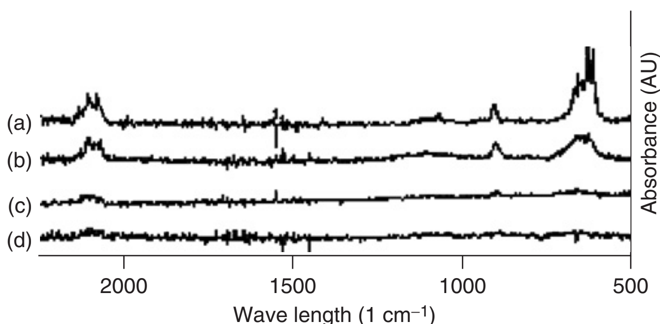

Figure 1.14 FTIR spectra for samples prepared under conditions of different H_2O_2 solution concentrations: (a) was prepared in a 0:1:1 solution for 90 min, during the last 10 of which the sample was exposed to UV radiation to induce the PL activity and (b–d) were prepared in 1:8:0, 2:1:2, and 5:1:1 solutions, respectively. The silicon substrate signal has been subtracted for all these spectra (after Ref. [14]).

different H_2O_2 solution proportions. Figure 1.14a shows the sample prepared in a 0:1:1 solution for 90 min., during the last 10 of which, the sample was exposed to UV radiation to induce the PL activity. The result shows a typical electrochemically etched silicon FTIR spectra; it shows strong hydrogen signal and a weak oxygen signal (in the 1100 cm^{-1} region), indicating a high degree of H-passivation. The bond assignments are 615–619 cm^{-1} due to Si—H or Si—Si bulk vibrations; 623 cm^{-1} due to Si—H or Si—Si bulk vibrations; and 905–910 cm^{-1} due to Si—H_2 scissors or Si—H_3 symmetric or anti-symmetric deformation. Other peaks in the range 2070–2090 cm^{-1} are characteristic of other stretching monohydrides (coupled H—Si—Si—H or H attached to Si atoms with Si—Si bonding arrangements different than for bulk Si). The latter are reconstructed Si—Si bond between closest lateral Si atoms [14]. We note the stretch hydrogen signal is only 10% of the bending region; thus there is a high density of defect modes, which are coupled monohydride M and di-hydride D that characterize the surface.

The samples of Figs. 1.14b–d were prepared in 1:8:0, 2:1:2, and 5:1:1 solutions of HF:H_2O_2:methanol, respectively. The results indicate two features. First, there is an overall drop in the infrared activity with the proportion of the peroxide due to thinning rather than depassivation of the layer. Second, the ratio of the stretch signal to the bending region rises with the proportion of the peroxide. For a proportion of peroxide to HF > 2, the samples show the character of ideal passivation.

FTIR analysis can be used to analyse amine, 1-pentene and acid-functionalized particles (Fig. 1.15c). The spectrum of the aminized particles showed significant increase in the intensity of the 2800–3000 cm^{-1} band, where the peaks at 2869, 2881, 2931, and 2966 cm^{-1} are characteristics of C—H stretch vibrations in butyl groups. The spectrum displayed also strong N—H stretch at $\sim$3300 cm^{-1}, and Si—N stretching mode at 860 cm^{-1}. These results provided support for the formation of single Si—N bond linkage. The presence of hydrogen-nitrogen bond is a strong indication of the single Si—N formation as compared to the formation of a bridge double bond linkage Si—N—Si during the aminization of silicon flat or porous surfaces using a similar chemical treatment [54].

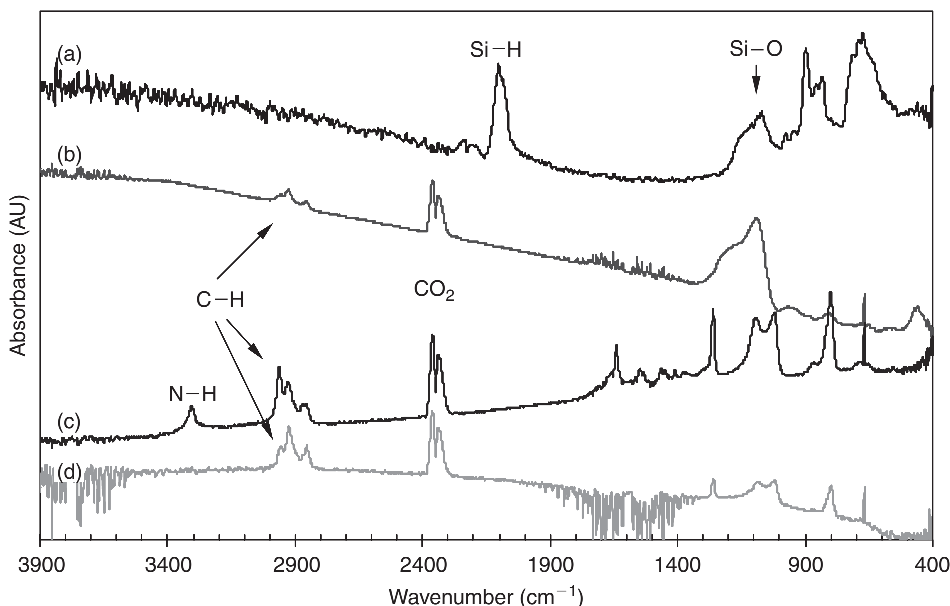

Figure 1.15 Absorption FTIR spectra of (a) PS sample, (b) Si particles produced from (a) through ultrasonication and (c–d) modified particles, alkylated through (c) chlorination/reaction with butylamine and (d) thermal hydrosilylation of 1-pentene (from Ref. [53]).

A few drops of heptane solution of 1-pentene treated particles were vacuum dried on a Si substrate, forming a thin film. Those were characterized by FTIR spectroscopy (Fig. 1.15d). The spectrum showed the presence of the familiar alkyl tail, composed of a set of peaks at 2800–3000 cm^{-1} (2862 and 2871 cm^{-1} $\nu(CH_3)$, 2925 and 2855 cm^{-1} $\nu(CH_2)$). It also showed peaks at 1376 cm^{-1} ($\delta(CH_3)$) and 1465 cm^{-1} ($\delta(CH_2)$). Those are assigned to pentyl fragments on the surface of particles.

Functionalization with carboxyl acid produces an oil-like residue after vacuum drying the particles [53]. The residue was characterized with FTIR. The spectrum confirmed the functionalization process.

1.4.2 Nuclear Magnetic Resonance

To confirm H-passivation of Si nanoparticles, a nanoprobe H NMR study of fresh prepared particle's dispersion in d-THF was performed [53]. The spectrum displays a strong proton signal of Si—H groups (2.5–2.6 ppm), which is direct confirmation of the presence of Si—H species in the solution. The spectrum contains also proton's signals of Si—CH_2— (0.1 ppm) and methyl (0.9 ppm) and methylene (1.2–1.4 ppm) groups attributed to a hydrocarbon contamination [40]. The ratio of the integral intensities of Si—CH_2— protons to the protons of Si—H fragments characterizing contamination degree was found to be equal to 0.17, which corresponds to a $Si_{29}H_{24}$ particle [3,10] containing 22 Si—H and 2 Si—alkyl bonds [53].

The chemical structure of alkylated particles dispersed in d_8-THF was also directly analysed by nanoprobe H NMR. As we noted before, for H-terminated particles prior to modification, the ratio of the integral intensities of Si—CH_2— protons

to the protons of Si—H fragments was found equal to 2:22 (0.17). This ratio increased up to 0.64 for the alkylated sample, which corresponds to a particle containing 18 Si—H and 6 Si—alkyl groups on the surface. These results indicate that about 25% of Si—H groups were involved into hydrosilylation. Additionally, the spectrum of pentyl-modified particles did not show any proton signals of terminal double bonds usually observed at 5–6 ppm, confirming FTIR data.

1.4.3 Gel Permission Chromatography

The solubility and aggregation of H-terminated and alkylated *particles* was characterized by GPC (Styragel column with THF as elluent), using a polystyrene standard for calibration [53]. A UV detector measured absorption of the dispersion of the particles in THF at 365 nm (Fig. 1.13).

The GPC plot of a polystyrene standard fraction with $M_n = 955$, and for the particles prior to the modification are shown in Fig. 1.13a and b. The particles show a single broad peak. Since the colloid consisted of a single size, namely 1 nm silicon nanoparticle [3,10], the wide distribution indicates formation of bulk aggregates of interconnected particles. Previous TEM study of dried film prepared from the dispersion of H-terminated silicon nanoparticle in acetone showed the presence of linear-shape aggregates of the interconnected 1 nm size silicon nanoparticle (Fig. 1.3). The observed aggregation may be explained by interconnection of the particles through H-bonding of Si—OH species formed because of partial oxidation of the surface, which results in Si—O—Si covalent bridges between particles in the dried sample.

Contrary to the H-terminated particles, the GPC plot of particles functionalized with butylamine (Si—NH—C_4H_9) (Fig. 1.13c) showed a much narrower peak. This narrowing points to the absence of bulk aggregates (even after vacuum drying). The slight polydispersity may be in part explained by different degrees of H-replacement on the surface of particles.

The 1-pentene treated particles were also examined by GPC (Fig. 1.13d) [53] and compared to that for aminized particles (Fig. 1.13c) [12]. Apart from a weak broad shoulder, the observed narrow peak was close to the R_V value for particles modified with butylamine. The similarities are reasonable, since pentyl (—CH_2—C_4H_9) and aminobutyl (—NH—C_4H_9) tails have approximately the same length and structure. The shoulder was assigned to interconnected particle's aggregates. However an interconnection of the particles resulting from surface oxidation is unlikely for the alkylated particles because alkylated Si surfaces are characterized by increased resistance to oxidation. Moreover, the colloids of pentyl-terminated particles are as stable as butylamine-terminated samples as evidenced by a narrow GPC peak. But these alkylated samples were obtained through different synthetic routes, which might be a reason for the different size distribution.

The acid-functionalized particles obtained by reaction with the t-Bu ester was characterized by GPC. The GPC chromatogram of the modified particles dispersed in THF (Fig. 1.13b) showed a broad peak. However, unlike non-modified particles (Fig. 1.13a), the response was composed of two overlapping peaks. The weak but narrow peaks of the alkylated particles (Fig. 1.13c) correspond to isolated modified particle's species. The second peak, which is broad and shifted (Fig. 1.13b), appears due to cross-linked particle's aggregates.

1.4.4 X-Ray Photospectroscopy

We present analysis of the aminized particles [12]. XPS spectra of the particle films (Fig. 1.11) showed that the aminized particles are characterized by the nitrogen and carbon peaks at ~400 and 285 eV, respectively. A fit of the binding energy of the 400 eV peak, given in the inset, gives two components at 397.12 and 398.44 eV with 1.76 and 1.88 FWHM and 43.9 and 56.1 percentage mass concentration, respectively. These may be associated with the N_{1s} peak of bulk silicon nitride and amine molecules (typically at 399 eV), respectively. The low-energy one is consistent with well-established chemistry of the absorption of NH_3 on silicon surfaces and in the atomic layer growth of the Si_3N_4. These binding energies lend support to binding in terms of a Si—N linkage. It is to be noted that XPS taken after air exposure did not show significant change in the N_{1s} or C_{1s} peaks.

1.4.5 Auger Electron Spectroscopy

Material analysis using AES may be performed and the atomic concentration percentages and the depth profile were recorded. The thickness of the particle layers can be estimated using the AES data. We used this procedure to study the effect of hydrogen peroxide on the particle quality [14]. Figure 1.16a and b gives the measurements for two samples prior to sonification and particle dispersion, one prepared in HF and the other in an HF hydrogen peroxide mixture. The results show that the sample prepared using the peroxide procedure is much cleaner, namely it has much less oxygen and carbon contamination than the one prepared by conventional procedures. Moreover, material analysis using electron PL can be used. Figure 1.4 shows that the particles are composed of silicon with $<10\%$ oxygen [10].

1.4.6 Transmission Electron Microscopy

The size of the particles may be determined by direct imaging, using HRTEM. A thin graphite grid is coated with the smallest particles obtained in the synthesis by immersion in the colloid and quickly transferred to the vacuum compartment of the TEM [10]. Figure 1.3 shows the particles are 1 nm in diameter. A size histogram of particles which did not aggregate shows roughly 10% dispersion. A thin graphite grid is immersed in the colloid of the mix of discrete family of particles and imaged by HRTEM [14,15]. Figure 1.3 (left) shows that particles are nearly spherical and classify into a small number of sizes. These include 1.0 (see inset), 1.67, 2.15, 2.9, and 3.7 nm. Figure 1.3 (right) shows the atomic planes in closeups of the 1.67, 2.15, 2.9, and 3.7 nm particles.

Previously TEM images of Si colloidal suspensions prepared by HF alone clearly showed crystalline, overlapping Si particles. The particles were irregularly shaped and ranged in size from many micrometres down to the resolution limit of the TEM (about 0.2 nm). HRTEM studies of obtained colloidal suspensions showed that a size of the particles ranges from 50 nm and smaller up to 2 nm. It was found that the bigger size objects are not single crystalline and in reality are agglomerate of several small crystallites ~7–11 nm in diameter as shown in Fig. 1.2. The smallest crystallites in agglomeration are about 2 nm. More importantly, there was not amorphous

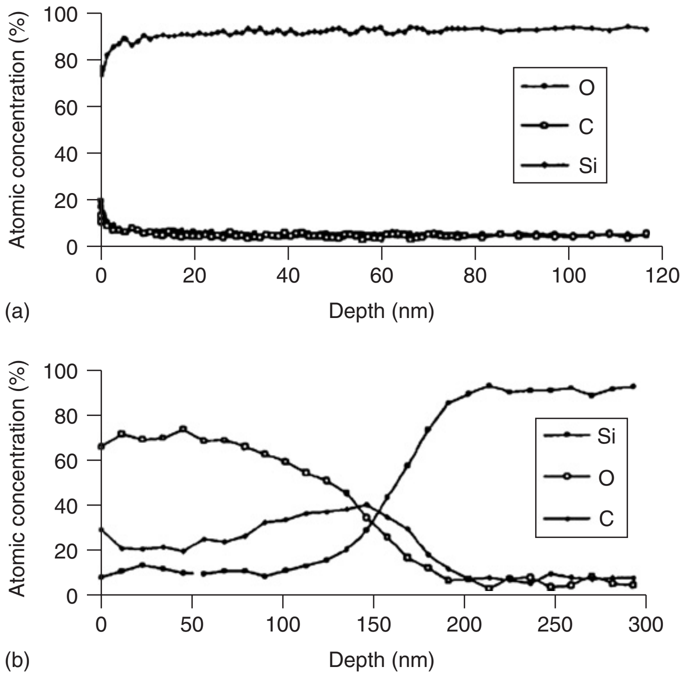

Figure 1.16 AES of two samples: (a) prepared with H_2O_2 in an HF mixture and (b) prepared under UV illumination (after Ref. [14]).

layer visible for the crystallites ranging in size from 2 to 10 nm in diameter although it can be explained by too small thickness of this layer, making it not distinguished on the amorphous layer of supporting substrate.

1.5 Optical properties

Particles may be stimulated optically or electrically. Most of the studies that have been performed focused on optical excitation (PL).

1.5.1 PL and Detection of Single Nanoparticles

Colloids of the particles have been prepared. When a colloid of the 1 nm particles with a concentration of ~10 nM is excited by 355 nm pulsed radiation, blue emission is observable with the naked eye, in room light [10], as shown in Fig. 1.17. Figure 1.18 gives the spectrum for excitation wavelength at 330, 350, 365, and 400 nm from an incoherent Xe lamp, showing a strong blue band that maximizes for 350 nm excitation. Figure 1.19 (bottom) gives a photo of colloids of the magic sizes under the irradiation from an incoherent low intensity commercial UV lamp at 365 nm, showing the characteristic red, yellow, green, blue colours [20].

We studied the absorption and emission gaps of the members of the 1.0, 1.67, 2.15, and 2.9 nm family. The excitation, i.e. the absorption monitored at a specific

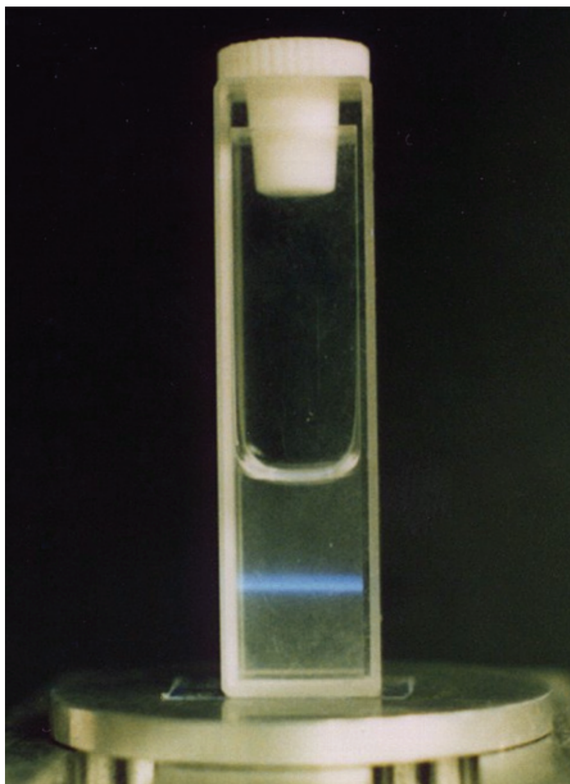

Figure 1.17 A photo of a Si colloid excited by 355 nm radiation (after Ref. [10]).

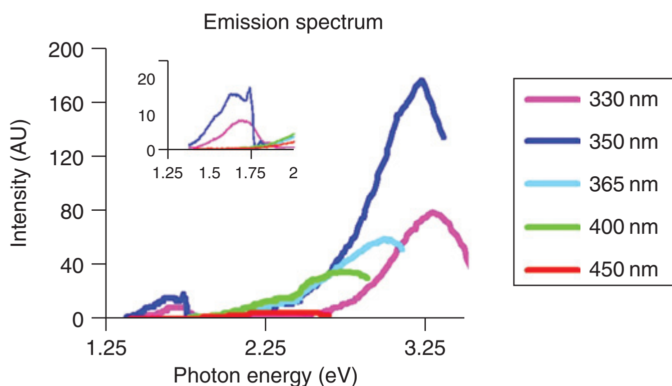

Figure 1.18 Emission spectra of the dispersed particles in acetone excited at several excitation wavelengths (330, 350, 365, and 400 nm). Inset: excitation spectra of the dispersed particles in acetone while monitoring the emission at several visible wavelength (400, 500, and 600 nm) (after Ref. [10]).

emission wavelength (product of absorption and emission) was recorded on a photon counting spectrofluorometer with an Xe arc lamp light source and 4 nm band-pass excitation and emission monochrometers. We mapped out the excitation in the range 250–800 nm, while monitoring the emission in the range 400–700 nm.

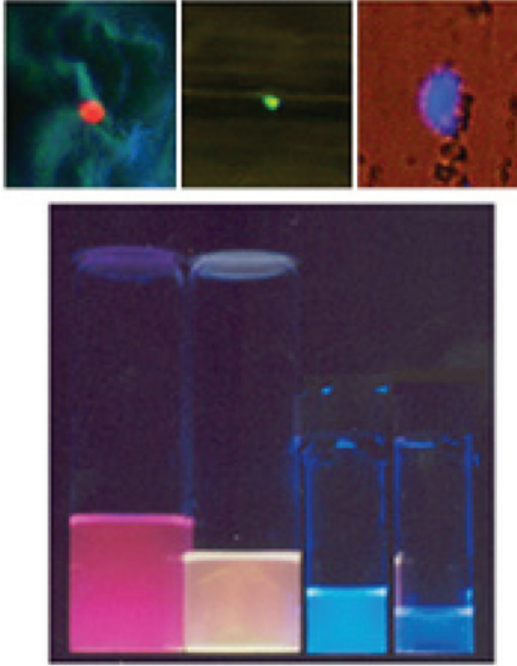

Figure 1.19 (Bottom, right to left) Emission of colloids of four members of the magic family 1.0, 1.67, 2.15, and 2.9 nm in diameter, after they have been separated, under excitation using a commercial low-intensity UV source with an average wavelength of 365 nm. (Top view) Emission from blue, green, and red colloidal crystals segregated according to magic sizes 1.0, 1.67, and 2.9 nm diameters. The crystals are illuminated by light from a mercury lamp. The background is due to a weak bright field (after Ref. [20]).

We used the mapping to identify the resonance excitation structure [20]. Figure 1.20, which presents the excitation, shows a resonance structure at 3.44 ± 0.1, 2.64, 2.39, and 2.11 eV. This resonance structure produces emission bands with maxima at 410, 540, 570, and 600 nm, respectively. We associate the resonance energies with the highest occupied and lowest unoccupied molecular orbital (HOMO–LUMO) edge E_g. According to quantum confinement, the absorption and emission photon energies correlate with the size. We pair the diameter d (in nm) with excitation resonance E_g (in eV) as follows (d, E_g): (1.0, 3.44); (1.67, 2.64); (2.15, 2.39); and (2.9, 2.11). However, we did not record an excitation/emission resonance that can be associated with the 3.7 nm diameter particles. This may be due to low abundance or/and diminished brightness. A power law fit gives $E_g = 3.44/d^{0.5}$.

UV is not friendly to biological molecules, thus for biomedical applications we tested the excitation of the particles using two-photon excitation processes at near-infrared wavelengths. Because they exhibit nonlinear properties, the particle sums two photon quanta and emits blue radiation. The process requires high peak power from a picosecond or a femtosecond source, however. We used this two-photon excitation (780 nm, 150 fs duration at 80 MHz) to determine the particle's brightness by FCS [3]. The raw traces of emission are recorded. Figure 1.21 gives (at 780 nm) the

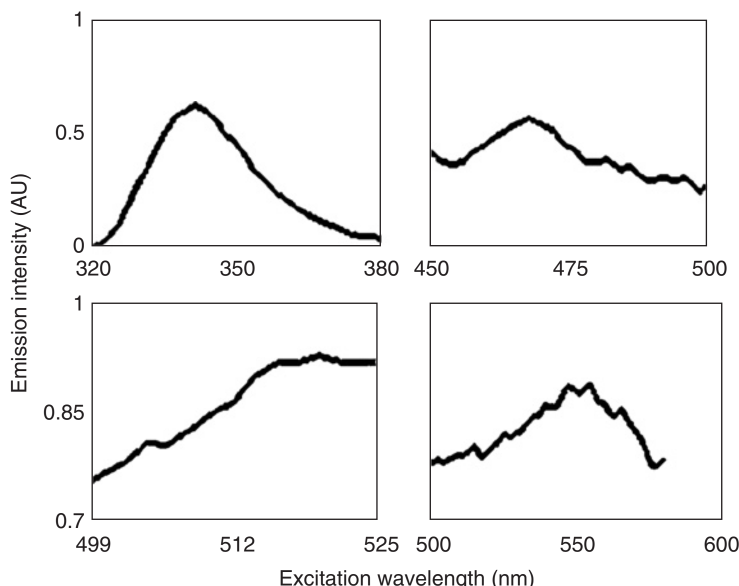

Figure 1.20 Excitation spectra of the 1.0, 1.67, 2.15, and 2.9 nm diameter particles monitored at emission wavelengths of 400, 540, 570, and 600 nm, respectively. They show local resonance structures at 3.44, 2.64, 2.39, and 2.11 eV, respectively (after Ref. [20]).

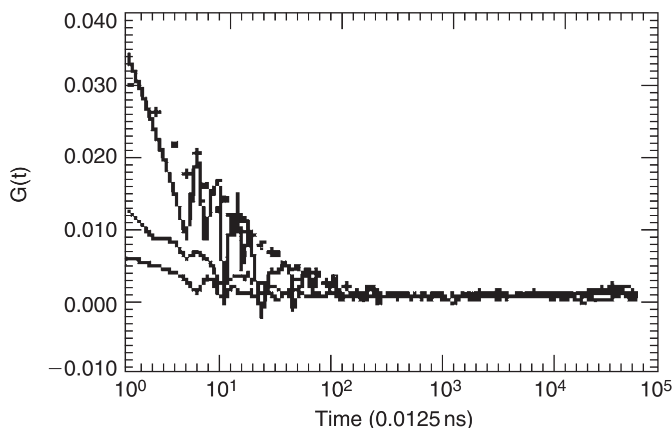

Figure 1.21 Autocorrelation of 5.4, 2.75, 0.75 Si particles and 1.5 fluorescein molecules (after Ref. [3], American Institute of Physics (AIP)).

autocorrelation function of the fluctuating time series of the luminescence with progressive dilution to demonstrate the sensitivity of the detection: Si with 5.4 particles; a fluorescein standard with 1.5 molecule; Si with 2.75 particles; and Si a single particle (0.75) in the focal volume. The measurements yield a particle size of ~1 nm, consistent with direct imaging by TEM. They also yield a brightness 4-fold larger than that of fluorescein.

1.5.2 PL Lifetime

We have performed time-resolved PL measurements on suspensions of silicon nanoparticles using near-infrared two-photon femtosecond excitation [64]. The excitation employs a two-photon process at 760–800 nm, corresponding to an effective single photon process at 380–400 nm. We used a mode locked femtosecond Ti-Sapphire near-infrared laser system, generating pulses of <150 fs duration at a repetition rate of 80 MHz (12 ns duty cycle). At the target, the average power, 20 mW, is focused to a beam waist of ~0.5 μm, giving an average intensity of 10^7 W/cm^2 (peak pulse intensity of 10^{12} W/cm^2). In the measurement of the time dynamics we did not employ wavelength resolution; all of the PL in the blue band of the 1 nm particles or in the red band of the 2.85 nm particles was collected using a photomultiplier.

Figure 1.22 gives time-resolved PL of 1 and 2.85 nm particle colloids. It was taken under 780 nm excitation. The working range of the free decay is ~2–11 ns within the 0–12 ns duty cycle. The flat steady-state background the free decay is riding on is due to accumulation resulting from decay rates with long characteristic time scale. For 1 nm, the background is ~10% of the maximum yield. This value of background shows that the 1 nm nanoparticle has predominantly short lifetimes <12 ns. For 2.85 nm, the fluorescence decays to near 50% level within the detection time window (12 ns). This implies that the nanoparticle has fast decay channels as well as considerably slower decay channels with times >12 ns. Our results for 1 nm particles show wide bandwidth but indicate full conversion to direct-like behaviour, with a few nanosecond time characteristic (2.6 ± 0.3 ns) for the lifetime, corresponding to oscillator strength comparable to those in direct semiconductors. In addition to fast nanosecond decay of 1.6 ns, the PL from 2.85 nm nanoparticle exhibits considerably slower decay of ~38 ns with amplitudes of 1:2, consistent with a transition regime to direct-like behaviour.

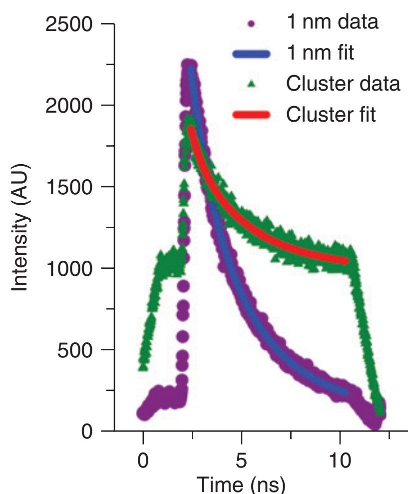

Figure 1.22 Time dynamics of luminescence after two photon excitation with pulsed femtosecond radiation at 780 nm for 1 and 2.85 nm particle colloids.

1.5.3 Cathodoluminescence and Electroluminescence

The electrical excitation of quantum-confinement-based visible luminescence in silicon nanostructures by low-energy (eV) electrons (electroluminescence EL) or by keV electron beams (cathodoluminescence, CL) has been of great interest for electronic applications and complements the work of PL in PS.

Electroluminescence of nanoscale silicon structures is useful for optoelectronics device application. However, charge carrier injection at the electrodes and charge carrier transport through layers of silicon nanoparticles present problems or challenges. Several reports of EL may be found in the literature; they give very low quantum efficiency (<0.01–0.0001%) due to a large reduction in electron mobility in the layer. Types of electroluminescence diode (ED) devices reported include p-n homojunctions, p-n heterojunctions, and Schottky junctions. The Schottky junction metal/p-type devices reported (schematically shown in Fig. 1.17) are constructed by sandwiching a layer of nanoparticles between a silicon substrate electrode and a metal film electrode. They are basically the same except for the type of the nanomaterial active layer used. Variations in device operation may depend on the quality of the film (average size and dispersion of the particles, termination of the particles, method of deposition, doping, thickness of film, etc.). Silicon and germanium nanocrystallites may be used as the active layer.

There have been relatively few studies of the visible CL from nanostructures in electrochemically etched silicon (PS) and in addition, it has been difficult to conduct correlation tests between the PL and CL to elucidate the basic mechanisms. Studies are hampered by the fact that for freshly etched material, CL is weak, much weaker than the PL, and is extremely unstable. We recently presented measurements from 1 nm nanoparticles giving blue luminescence bands and red luminescence from 2.85 nm nanoparticles [65], and contrasted them with their room temperature PL response.

Figure 1.23a gives an isometric view of the CL spectrum for a film of 1 nm blue PL particles with 10% 2.85 nm red PL over the temperature range of 300–25 K. There is a far red band at 750 nm which increases gently with cooling. A second red band, near 620 nm, fades during cooling. There are two blue bands at 420 and 450 nm which fade away initially with cooling, but re-intensify at the lower temperatures (<120 K). Figure 1.23b gives the CL spectral data for a film of 2.85 nm red PL particle with 10% blue luminescent 1 nm particles over the temperature range of 300–25 K. It shows a far red band at 750 nm growing gently with cooling. A very strong second red band near 620 nm fades during cooling. It has two blue bands at 430 and 450 nm that appear at lower temperatures.

The PL of dispersions of the silicon particles was studied at room temperature. The spectra were recorded on a photon counting spectro-fluorometer with a Xe arc lamp light source and 4 nm bandpass excitation and emission monochrometers. Additional data, especially of the infrared components, were obtained with a fibre-optic spectrometer. This uses optical fibres to transport the excitation and to extract the emission, and a holographic grating with groove density of 600 mm^{-1} with a blaze angle of 1 μm for dispersion. Overall there is a good correlation between the CL and PL responses of dispersed silicon nanoparticles. The preferred model is that the features observed are related to quantum confinement induced bands in nanostructures, rather

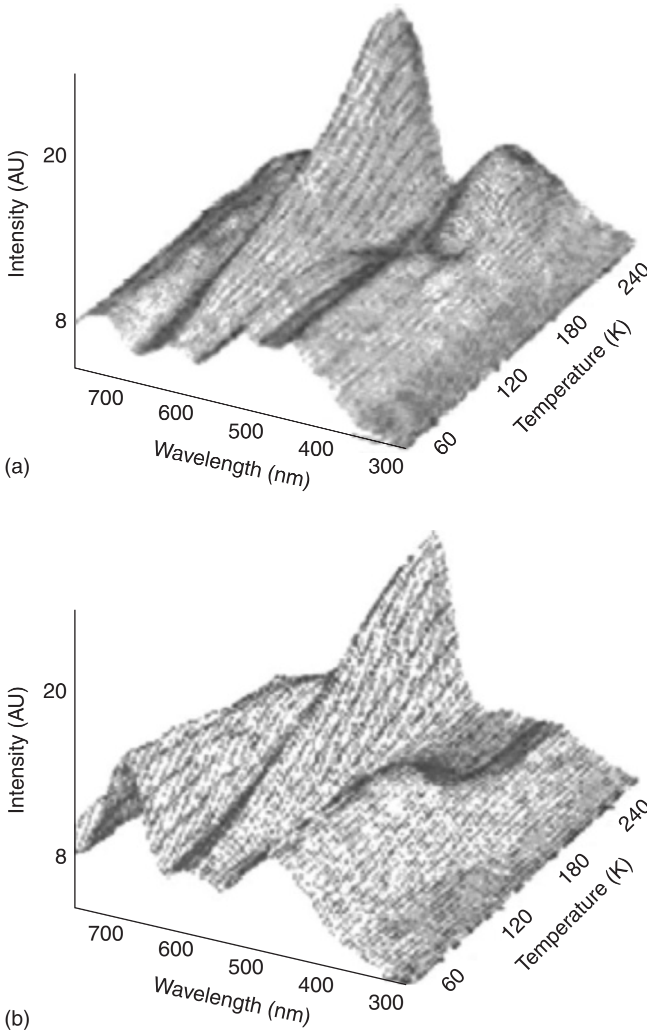

Figure 1.23 (a) The temperature behaviour of the CL spectrum for a film of 1 nm size nanoparticles primarily a blue responsed. (b) The CL spectrum for a film of 2.85 nm particles primarily a red responsed (after Ref. [65]).

than being associated with defects in the hydrogen passivation (such as the presence of a single oxygen site). For instance, the CL of fused silica or heavily oxidized porous layers is known to fade with cooling. But, the CL of the nanoparticle films is found to exhibit luminescence that variously fade away or grow with cooling, i.e. nanoparticle films have additional features that do not behave like oxides. Thus the approximate coincidence of the peak energy observed for the PL and CL spectra, along with the double temperature behaviour of the CL points to a contribution from spatial quantum confinement at nanostructures.

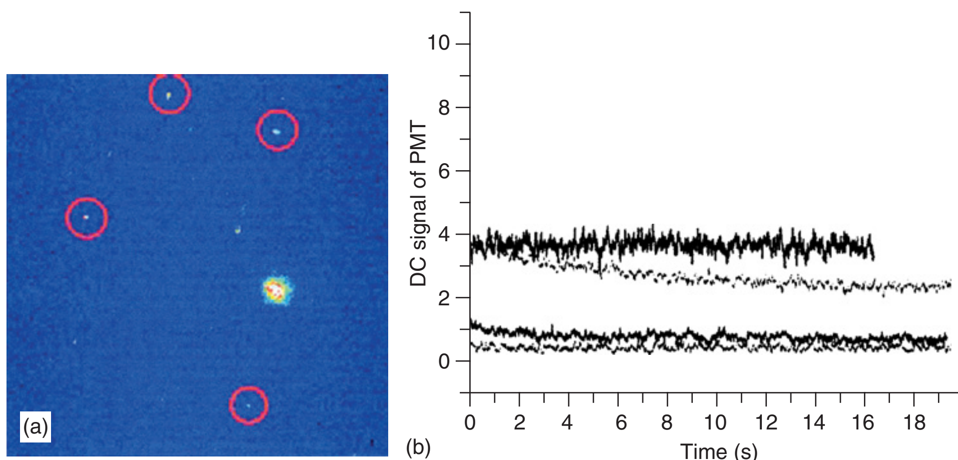

Figure 1.24 Frozen Si particles in a gel. (a) Luminescent images, demonstrating the ability to observe/image single ones and (b) "Parking" the excitation beam on stationary particles shows that they are photostable.

1.5.4 Photostability Under UV and Infrared Radiation

The photostability under infrared irradiation was tested by targeting stationary particles frozen in a gel. We used two-photon excitation at 750–850 nm. This range, unlike UV radiation, is biology friendly and often used for imaging and interrogation of biological material. A small number of particles were mixed in an agarose gel. Figure 1.24a gives examples of luminescent images of some clusters of the particles in the gel. Using calibration data, a few of the clusters consist of single particles whereas few others consist of two and three particles. The measurement demonstrates the ability to observe/image clusters of one to three particles. "Parking" the excitation beam, focused to an average intensity as high as 10^6 W/cm^2, on stationary clusters shows that the particles are photostable (see Fig. 1.24b) [4]. The photostability was also tested by targeting stationary particle clusters immobilized on a quartz plate, and compared to similarly immobilized red dye molecules. Again the particles showed superior stability.

The particles are expected to be less stable under UV radiation than infrared radiation. A 1 cm^3 colloid of particles in propanol was placed in a small cell. The colloid was irradiated by 30 ns, 30 pulses pps, pulsed laser radiation at 355 nm with an average power of 20 mW and an interaction volume of 1 cm^3. The emission intensity dropped by 50% after 3 h of irradiation. Under the same irradiation condition and geometry, blue dyes such as coumarin and stilbene decay at 8- and 50-fold faster.

1.6 Reconstitution of Particles in Films

In addition to the novel properties that the individual particles provide, there is a potential to engineer additional properties by synthesizing two- and three-dimensional arrays of the particles. The ability to produce monosize particles gives us the opportunity to manipulate interspacing with atomic precision to tailor new

elemental silicon-based material with unique optical and electrical properties. The band gap of the new material is governed by the particle size. The conductivity is controlled by the interspacing (tunnelling spacing). The transport is governed by the size, termination, and dielectric properties (charging) of the particles.

1.6.1 Precipitation Spray

We used precipitation from a volatile solvent to reconstitute the particles into thin films. By gentle evaporation, microcrystallites is demonstrated on high-quality Si or silicon oxide, or in free standing mode [4,6]. The structures are optically clear. Optical imaging in initial experiments show colloidal crystals of 5–50 μm across (see Fig. 1.25). We experimented with slower growth rates using slower evaporation rates at reduced temperatures to produce larger, flatter, clearer, and more uniform films. Careful regulation of the temperature allows precise adjustment of the destabilization.

The particles may also be sprayed onto a substrate using a jet/nozzle using differential pressure. The volatile liquid evaporates in flight allowing the particles to land on the substrate.

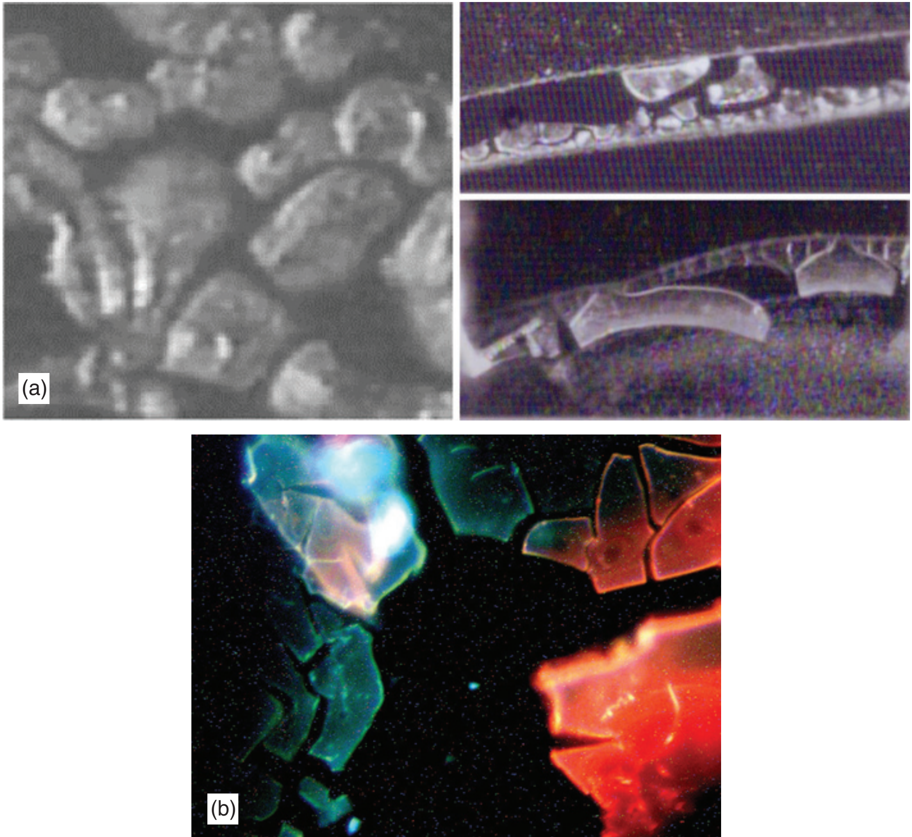

Figure 1.25 Reconstitution of silicon nanoparticles into crystals by simple evaporation from a volatile solvent (a) in acetone, (b) in water (after Ref. [6]).

1.6.2 Electrodeposition: Composite Films of Metal and Nanoparticles

We recently developed a procedure for delivery of nanoparticles, using electrochemical-plating processes, analogous to metal plating [21]. In the method, a conducting substrate is immersed in a solution in which the particles have been dissolved. Biasing the substrate positively draws the particles to the substrate, forming a film. Thin coatings of the particles on metals, foils, or silicon substrates are demonstrated.

Figure 1.26b shows a post-deposition fluorescent image of a section of stainless steel plate under UV illumination at 365 nm, showing a red luminescent particle film. We have also used the same procedure to deposit 1 nm blue luminescent particles. A variety of patterns on Si and several metallic objects, such as an aluminium alligator clip (shown in Fig. 1.26e), were successfully coated, demonstrating the versatility of the method. The process is self-limiting because the particles are essentially nonconducting; under doping of 10^{15} mL^{-1} boron, less than one particle in a million contains a boron atom. We believe the mechanism of the deposition of the particles is that of the well-known electrophoresis. In the process, the particles get attached to negative alcohol ions $(ROHSi)^-$. Alcohol is known to ionize to produce the negative ion in the presence of even trace amount of water. The slow down of the deposition of the smallest particles may be a result of a smaller surface area.

We added metal Al salt ($AlCl_3$) to the particle colloid. The particle density is a 3–5% of the ion density. In this case the particles get deposited on the negatively biased electrode. The reversed direction indicates that the process proceeds largely in terms of the attachment of the silicon particles to metal ions, rather than by attachment to alcohol ions. The deposition results in a composite thin film of metal and partially oxidized (capped) nanoparticles. Finally, we masked the substrate to spatially control the deposition process. A thermal oxide layer of 300 nm was grown on the *p*-type Si (100) substrate. Patterns in the oxide were etched away to provide current paths. The substrate was then coated. Figure 1.26d shows that the particles are selectively deposited within the etched pattern area (error bar). The same process was tested successfully using an erbium salt to generate a composite film of silicon nanoparticles and erbium.

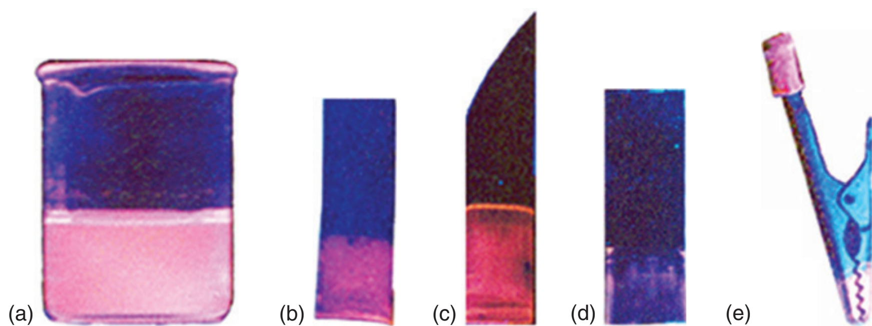

Figure 1.26 A series of images of (a) a colloid of red fluorescing silicon nanoparticles and objects that have been electroplated with particles from this colloid, (b) stainless steel substrate, (c) silicon wafer, (d) selective deposition on a silicon wafer, and (e) alligator clip (after Ref. [21]).

1.6.3 Silicon Sheet Roll into Tubes

We recently showed that we can make hollow tubes from self-assemblies of electrodeposited fluorescent silicon nanoparticles [66]. When a colloidal dispersion of the nanoparticles in alcohol is subjected to an electric field, the nanoparticles are driven to the surface of a positively biased conducting substrate, where they form a thin film. Upon drying the film delaminates from the surface of the substrate and rolls up into tubes. By applying a force on the tubes using atomic force microscopy (AFM), we estimate the Young's modulus of the film and find it to be close to that of rubber.

In the method, a conducting substrate electrode is horizontally immersed in a colloid of the nanoparticles, and a counter rod electrode is vertically immersed. We used a 5 mm diameter stainless steel rod as the cathode and a silicon wafer as the anode substrate. A colloid of blue luminescent nanoparticles of 1 nm diameter in alcohol is used. A current of 0.3 mA is established between the electrodes. Under the electric field, particles are driven towards the anode substrate where they get deposited. Thin films obtained are near circular patches of about 100–200 μm in diameter. The sample is then removed from the bath. Upon drying, the film rolls up into uniform tubes of a diameter ranging from 2 to 5 μm. Figure 1.27 presents examples of the tubes. The tubes or pipes are hollow. They are transparent enough to see through them. They are transparent because of the wide band gap characteristics of the constituent particles. They can be seen with the aid of an optical microscope that they are indeed hollow. The tubes are large enough to be seen with an optical microscope.

We have measured the thickness of the wall of the nanotube by measuring the thickness of the precursor film using an AFM. The film thickness is found to be 32 nm. Parking the tip of AFM over several points on the film showed that these

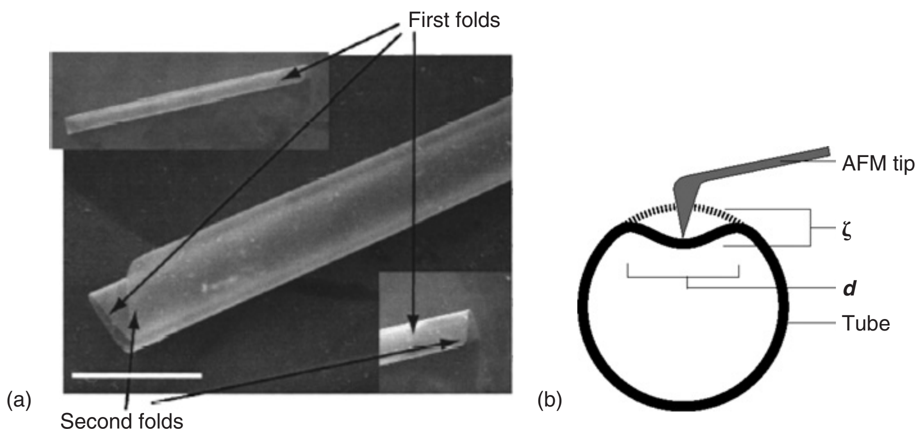

Figure 1.27 (a) (Left inset) Films made of deposited silicon nanoparticles delaminate and roll up upon drying. (Right) A closeup of a nanotube. Besides its transparency, notice the folds inside the tube which can be seen across the film. The film is hollow as emphasized from the inset in the upper right and lower right. The scale bar is 8 μm. (b) A schematic of an AFM tip poking a cylindrical tube (an end view). The deflection is exaggerated and is not to scale. The corresponding AFM arm deflection versus vertical displacement of the piezo of the AFM showed a 66 nm deflection of the film (after Ref. [66]).

films are smooth. Tube diameters ranging from 2 to 5 μm have been achieved, while tube walls in the range of 20–50 nm have been achieved.

1.6.4 Self-Assembly

Organization or self-assembly requires size uniformity. Under certain conditions, the particles segregate according to size upon crystallization. Over time, 5–100 μm crystals have formed in a water colloid. Colloidal crystallites were placed on glass and illuminated with light from a mercury lamp. Emission is detected in the backward direction and detected by an RGB filter/prism-based dispersive charge coupled device (3CCD) [20]. Figure 1.19 (top row) shows examples of blue, green, and red segregated crystals. Recrystallization to form yellow or green crystals takes place but they are less frequent compared to the blue and red.

Figure 1.28a presents a wide-angle scanning electron microscopy image of the deposit, showing a variety of formations [67]. Figure 1.29a and b shows three sets of selections of such structures. The images clearly show that there is a preferred angle of branching. Tips are found to branches at an angle between 90° and 120°, with most of them closer to 120°. It is interesting to note that the building block of tree formations are not individual nanoparticles, rather particle clusters of ~150 nm in diameter. The clusters making up the trees have the characteristic blue/green emission of 1 nm particles.

It is not clear what the basic mechanism of the assembly is. But if one attempts to discuss it in terms of an optimality principle, then one notes that the Si particles are essentially nonconducting since dispersion of a wafer with 10^{15} mL^{-1} doping (4 Ω-cm) leaves only 10^{-6} dopants per particle. Thus the particles would not strive for resistance minimization. Another prospective underlying principle of optimality is

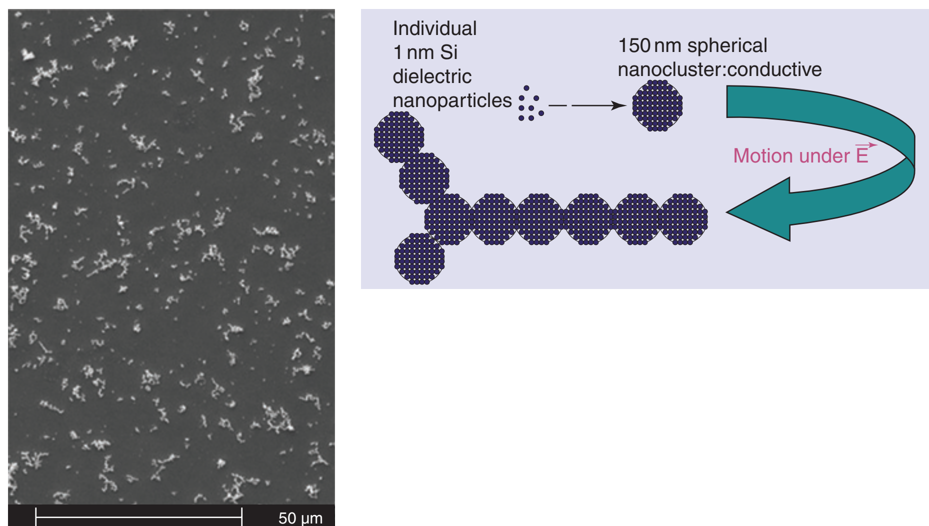

Figure 1.28 (a) Wide-angle images of the self-assembly formations on a substrate. It shows an intricate network of formations that show a high degree of branching and (b) a schematic of the proposed stages of the assembly (after Ref. [67]).

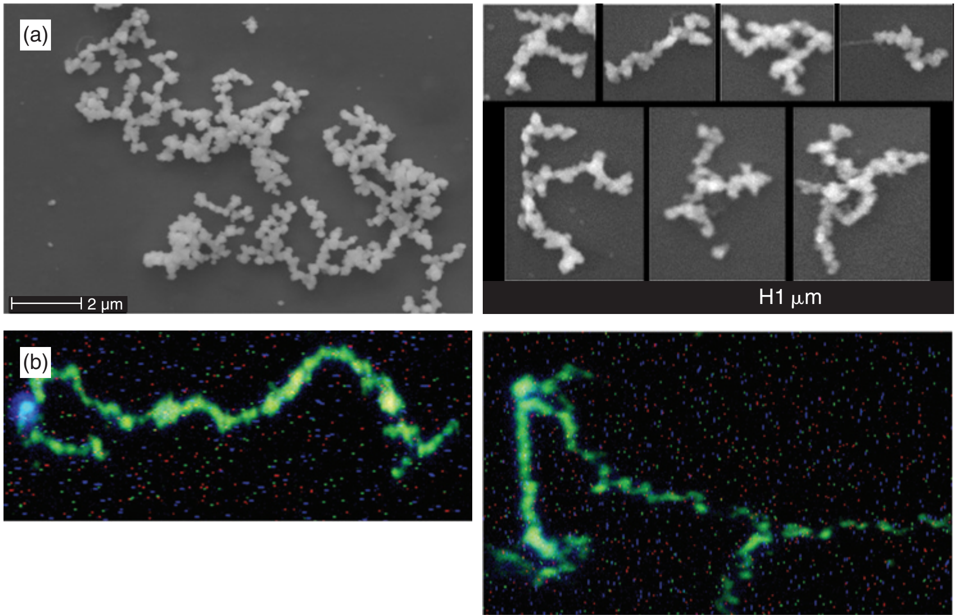

Figure 1.29 (a) Closeups of several isolated formations, showing that the growth avoids closed loops, and a preferred branching angle of 90–120°. (b) A fluorescent image of a formation. The network is illuminated with Hg UV lamp and detected in reverse direction. The image shows that the clusters making up the trees have the characteristic blue/green emission of individual 1 nm Si nanoparticles (after Ref. [67]).

the minimization of electric flux. In fact, polarizable particles have been known to form chains in an external electric field, like pearls on a string, as a result of the dipole–dipole attraction that aligns dipoles in the same direction. Single chains migrate towards nearby parallel chains to make thicker columns. Fibre formation has been observed in 1 nm silica particle colloids under an electric field of a few kV/cm. Large particles are preferred, and they are more amenable to self-assembly because of the larger Van de Waals interaction and polarizability. However, there were no tree formations or clusters observed.

Based on the doping level of the precursor wafer from which the particles were dispersed, a cluster of 150 nm in diameter may contain on the average ∼1–2 boron dopants. If close packing induces electrical connection between the constituent nanoparticles, then clusters may become conducting, displaying the resistivity of the precursor wafer. As a result, an optimality based on the minimization of the electrical resistance may come into play.

1.7 Nonlinear optical properties

1.7.1 Stimulated Emission

In the last 2 years, there have been several reports of progress towards efficient nonlinear light emission from silicon, suggesting that Si-based material is of great potential

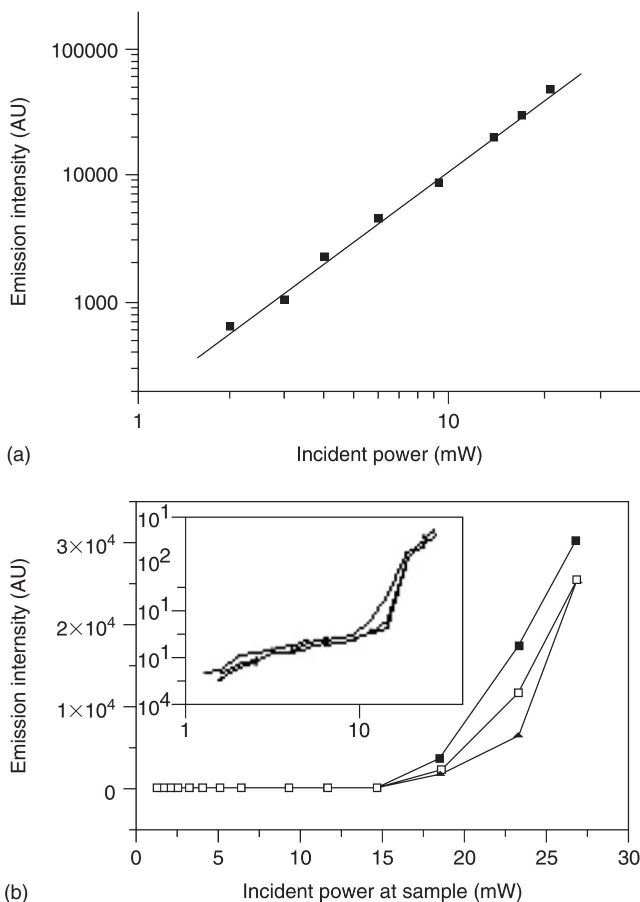

Figure 1.30 (a) Power dependence of emission of dispersed particles. (b) The emission intensity under femtosecond pulsed excitation as a function of the average power of the incident radiation for several individual micron size bright spots. The inset is the log-log of the data with the same axis labels. An average power of 15 mW corresponds to an average intensity of $5 \times 10^5\,W/cm^2$ (after Ref. [5]).

value for a new generation of light sources. In one effort [42], luminescent nanocrystals of ~3 nm across embedded in quartz by implanting high-energy Si ions into quartz, followed by annealing at 1100°C were created. Optical amplification of a weak beam at the emission wavelength, traversing the medium while the medium is being excited was reported. Earlier [68], superlinear emission in the range 600–1400 nm from PS, oxidized at elevated temperatures was reported, but it was long lived (ms), unstable, and was attributed to heat.

We tested aggregates or microcrystallites of our ultrasmall nanoparticles under high peak power from femto- and picosecond laser radiation in the near infrared in a two-photon excitation process. The response exhibited emission with highly nonlinear characteristics, suggesting stimulated emission [4,5]. We first examined dispersed particles (under a single-particle condition) in a colloid as a base case. We performed power dependence studies of the emission. Figure 1.30a shows quadratic dependence

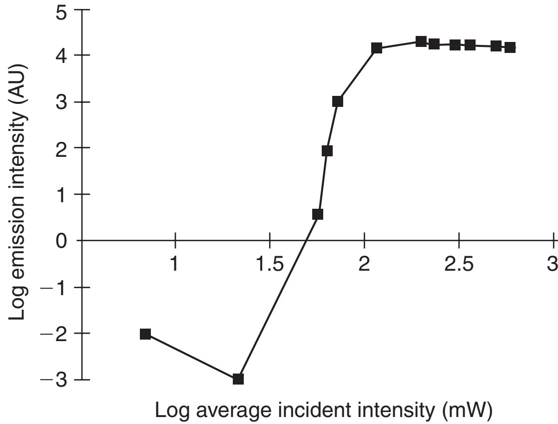

Figure 1.31 Emission intensity as a function of the average incident intensity for a reconstructed thin film of Si nanoparticles (after Ref. [6]).

as in two-photon processes. Next we examined the dependence from aggregates of particles. Aggregates are found on the solid precursor before sonification and dispersion into individual particles. The intensity of the emission from such aggregates has a sharp threshold, with highly nonlinear emission, rising by several orders. Figure 1.30b shows the emission intensity under femtosecond pulsed excitation as a function of the average power of the incident radiation. The inset is the log-log of the data.

The region that exhibits the threshold behaviour on the solid precursor [5] is abundant, but it is spotty, shallow, and uncontrollable. We created large, thick, and uniform layers by reconstituting the dispersed particles as described above. Figure 1.31 gives the emission intensity from such films as a function of the average incident intensity. It is typical of the response from any part of the film. For low intensity, the emission is finite, but at an average intensity of $\sim 10^6\,\mathrm{W/cm^2}$ (~20–25 mW) exhibits a sharp threshold, rising by many orders of magnitude. Beyond the threshold, there sets in a low-order power dependence that saturates at the highest intensities [6].

Figure 1.32 displays the interaction of the incident beam with the microcrystallites. It is normally incident (normal to the plane of the figure). The four examples in Fig. 1.32a show that directed blue beams emerge, propagating in the interior of the crystallite, in the plane of the sample, locally normal to the closest side. Due to re-absorption and scattering, it gets narrower as it fades away, propagating only 5–10 μm. Figure 1.32b shows two cases when the opposite faces of a crystallite are close. The beam, in this case, strikes the opposite face forming a weaker bright spot. The blue beams are characterized by a threshold. When the incident intensity is reduced, the beam fades away, and disappear, while the interaction spot remains bright (frames in Fig. 1.33).

Recently [7], we reported the observation of laser oscillation at ~610 nm in aggregates of ultrasmall elemental 2.9 nm silicon nanoparticles. The aggregates are excited by continuous wave radiation at 560 nm from a mercury lamp. Intense directed beams, with a threshold, manifest the emission (see Fig. 1.34). We observe line narrowing, Gaussian beams, and speckle patterns, indicating spatial coherence (see Fig. 1.35). This microlasing constitutes an important step towards the realization of a laser on a chip, hence optoelectronics integration and optical interconnects.

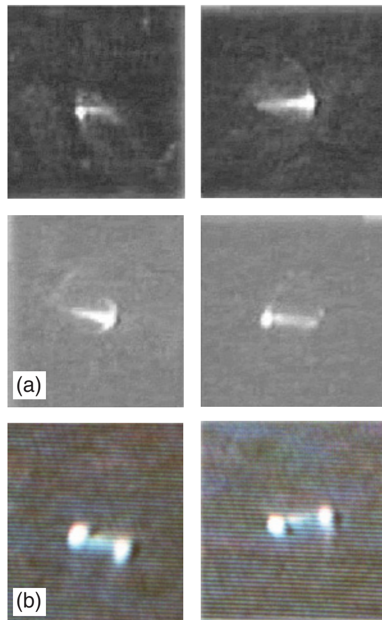

Figure 1.32 PL from the microcrystallite. The excitation beam focused to 1 μm spot is normally incident (normal to the plane of the figure). The interaction spots appear as "white blue" spot. 20 μm × 20 μm images showing examples of a blue beam. The beam is in the plane of the sample (normal to the incident beam), propagating in the interior of the crystallite, locally normal to its side (after Ref. [6]).

Figure 1.33 12 μm × 12 μm PL images from the microcrystallites region, showing a blue beam between opposite faces, under decreasing incident intensity starting left to right, top to bottom (after Ref. [6]).

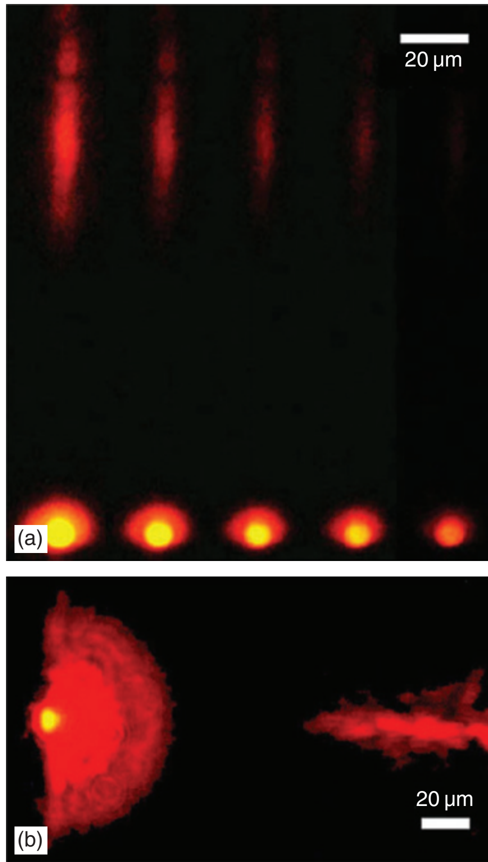

Figure 1.34 (a) Interaction of the incident beam from a mercury lamp at ~560 nm with the active silicon nanoparticles aggregate with decreasing pumping intensity (left to right). In each, the lower bright spot is the aggregate under illumination. The upper is a red beam spot that emerges above a certain incident intensity. (b) Closeup of an interaction spot (rotated 90°) (after Ref. [7]).

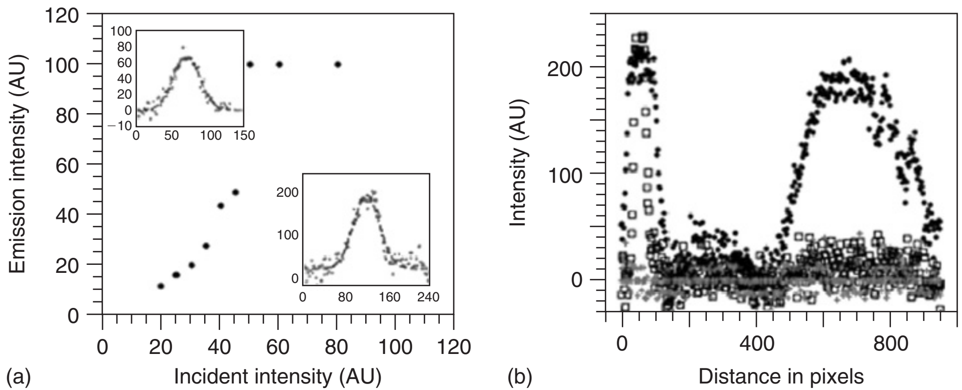

Figure 1.35 (a) Intensity of the generated beam as a function of the incident pumping intensity (solid circle). Line profile across the beam at a low intensity (upper-left-hand side inset), and at higher intensity (lower-right-hand side inset) fitted to Gaussian profiles (distance in arbitrary units). (b) RGB spectral analysis of a line profile along the beam through the interaction spot (solid circle) red component (open square) green component, and blue component (cross) (after Ref. [7]).

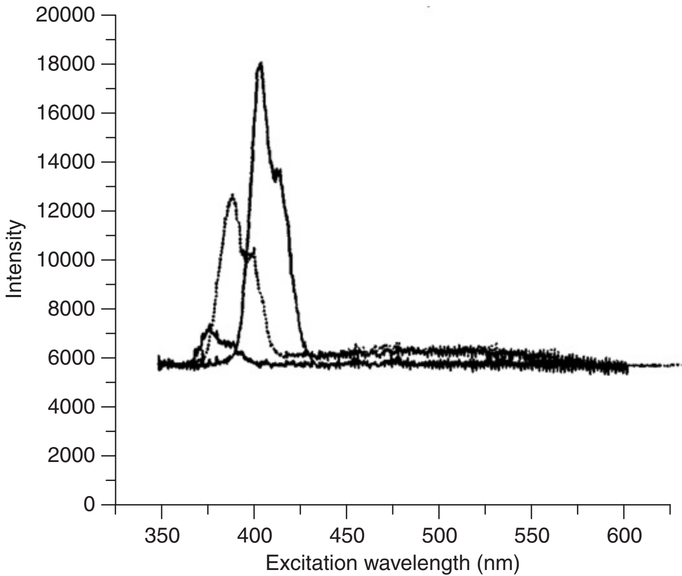

Figure 1.36 Emission spectra for the three excitation wavelength 780 nm (solid), 800 nm (dot) and 832 nm (dense dot) (at different incident intensities). Each shows a peak with a shoulder on the red wing. The shoulders are set at 390, 400, and 416 nm, respectively (after Ref. [8]).

1.7.2 Second Harmonic Generation

Bulk Si is known to have negligible nonlinearity, being zero at the second-order level (not allowed because of centrosymmetry), and very small at the third-order level. We recently reported the first observation of second harmonic generation in films of ultra-small silicon nanoparticles. Figure 1.36 gives the emission spectra for the three excitation wavelengths 780, 800, and 832 nm (not of the same intensity). Each shows a peak with a shoulder on the red wing [8]. The shoulders are at 390, 400, 416 nm, half the wavelengths of the incident beam. The peaks in the spectra are at 380, 390, and 406 nm, i.e. blue shifted by 10 nm from the shoulder in each of the spectra. Those and other measurements show that the emitted wavelength tracks the incident wavelength. These results point to a mechanism in ultrasmall particles that break the centrosymmetry of bulk Si, the symmetry that inhibits second harmonic generation.

1.7.3 Gain and Optical Nonlinearity

Silicon nanoparticle material may provide a stimulated emission channel and hence may constitute an optical gain media, which may be used to construct lasers or optical amplifier. Novel Si—Si bonds have been suggested as a possible origin of the emission. Moreover, they may provide optical gain. The molecular-like structure of the dimer bonds is shown in Fig. 1.37. They will be discussed in Section 1.9.3–1.9.5. We now examine the prospect of gain. The initial gain coefficient [6] is $\gamma = \Delta N\lambda^2 \Delta\nu/(8\pi n_r^2\tau)$ where $\Delta N = N_2 - N_1$ is the population inversion, n_r is the refractive index, $\Delta\nu$ is the emission width, λ is the emission wavelength, and τ is spontaneous lifetime. Measurements in the precursor colloid show several emission channels with

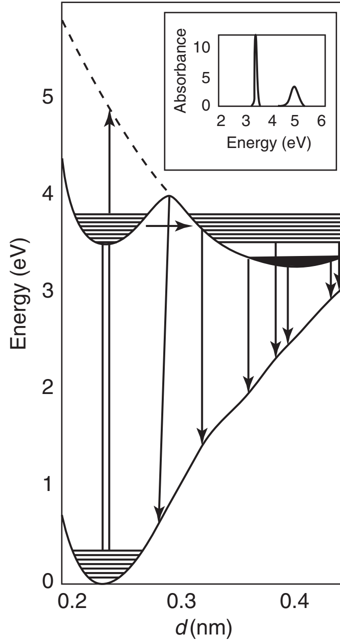

Figure 1.37 Interatomic potential of the dimers in 1.03 nm crystallites, showing ground and the first excited electronic states, along with the pathways for excitation and emission. *d* is the bond length of the Si-Si dimer. The inset is the transition probability in absorption (from Refs. [52,17]).

lifetimes of 1–5, 10–15 ns, and ~100 μs, with most of the blue emission being in the 10–15 ns time scale. With near saturated absorption, followed by strong transfer to the outer well, we expect the density of the excited emitters to be nearly 25% of the atomic solid density $\sim 1.5 \times 10^{22}\,\mathrm{cm}^{-3}$. We use $\tau = 0.01$–$1\,\mu\mathrm{s}$, $\lambda = 400\,\mathrm{nm}$, $n_r = 2$, and $\Delta\nu = 100\,\mathrm{nm}$ ($\sim 10^{14}\,\mathrm{Hz}$). With these parameters, $\gamma \sim 1.5 \times 10^3$ to $1.5 \times 10^5\,\mathrm{cm}^{-1}$. This gain allows considerable growth over microscopic distances. The number of spontaneous emission modes is given by $p = 8\pi\Delta\nu n_r^3 V/\lambda^2 c$ where V is the active volume. Using an active cross-section of $(2\,\mu\mathrm{m})^2$ and an active sample thickness of $0.2\,\mu\mathrm{m}$, we get $p \sim 10^3$, sizable even for such microscopic volume.

There has been interest in the nonlinear optical response in silicon nanostructures despite the fact that bulk silicon is known to have negligible nonlinearity, being zero at the second-order level (not allowed), and very small at the third-order level. The restructured Si—Si bonds provide an harmonicity and optical nonlinearity. To make an estimate, we expand the interatomic potential as a function of the bond length (Fig. 1.37) about its minimum: $V(r) = ar^2 + Dr^3$ where r is from the potential minimum. The fit gives $m_e D \sim 5.1 \times 10^{13}\,\mathrm{V/m}^3$, where m_e is the mass of the electron [8]. From D we can determine the frequency independent nonlinear optical coefficient $\delta = m_e D/2e^3N^2$, where N is the density of electrons that contribute to the polarization. The polarization at the second harmonic is proportional to δ and to the susceptibilities at ω and 2ω: $P^{(2\omega)} = 1/2\, d^{(2\omega)}\, E_0^2 \cos 2\omega$, where $d^{(2\omega)} = \delta(\chi^{(\omega)})^2\chi^{(2\omega)}$, and $\chi^{(\omega)}$ is the linear susceptibility at frequency ω. This gives $\delta \sim 7 \times 10^{13}$ for $N = 6 \times 10^{28}\,\mathrm{m}^{-3}$. Note that the mean value of the parameter δ

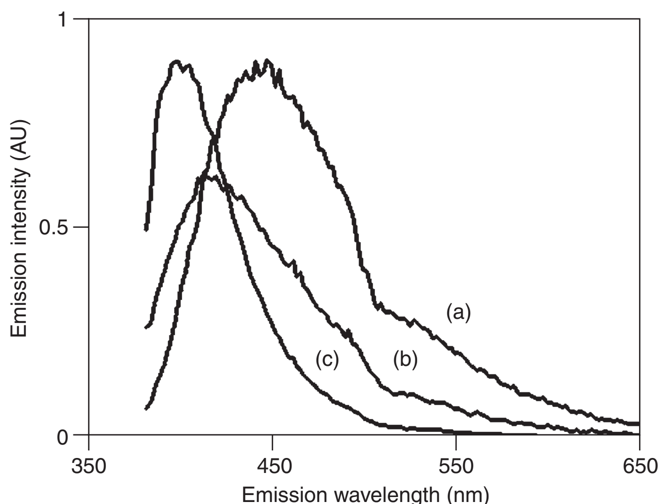

Figure 1.38 The emission spectra at 365 nm of the dispersed (a) Si—N, (b) Si—C, and (c) Si—H terminated particles (after Ref. [22]).

for 25 non-centrosymmetric crystals known for second harmonic generation is 2×10^9. The blue peak (shifted by 10 nm from the second harmonic) suggests a higher-order nonlinear coherent process such as stimulated anti-Stokes scattering.

1.8 Effect of functionalization on emission

Figure 1.38 gives the emission spectrum at 365 nm of the dispersed Si—H, Si—N, and Si—C passivated particles. In the H-terminated case, the spectrum is dominated by a strong blue band with a tail band that extends into the visible, diminishing at ~600 nm. Apart from a shift in the blue band, the spectra have similar shape for the aminized particles [12]. For instance, the peak of the blue band emission of the hydrogenated particle shifts from 410 nm to 450 nm upon aminization. On the other hand, in the case of Si—C, the figure shows that the process narrows the emission band by dimishing the red wing, causing a minor blue shift of 5–10 nm. Similarly carboxyl-functionalized particles retain luminescence. The HOMO–LUMO absorption edge is calculated to be 3.5 ± 0.3, 3.25 ± 0.3, and 3.55 ± 0.3 eV for H-, N-, and C-termination, respectively, indicating that measured emission correlates with the band gaps [22]. FCS was used to determine the brightness after functionalization [3,12]. From the photon counting histograms, we find the brightness to be 2-fold smaller than coumarin.

1.9 Structure of particles

In this section, we describe theoretical properties of nanoparticles. We will cover a discussion of bulk silicon, models for emission from nanoparticles, and simulation of their structure.

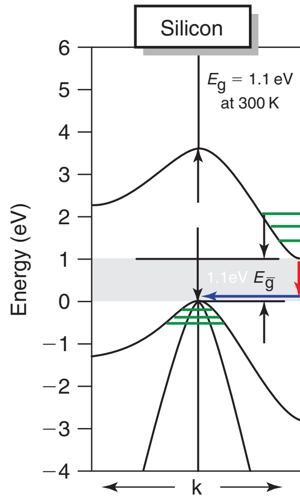

Figure 1.39 Band gap diagram of bulk silicon showing the direct as well as the indirect band gap. The figure also shows the quantized energy levels in the conduction as well as in the valence bands.

1.9.1 Luminescence Models

There are several mechanisms that have been proposed for the origin of visible PL. The "chemical agents" model attributes the PL to chemical species like siloxene. However, there is now consensus that quantum confinement is the main cause. In an infinite silicon crystal, the band structure is as depicted in Fig. 1.39. Silicon is an indirect gap semiconductor, and requires a phonon in addition to a photon for excitation to the lowest minimum in the conduction band at 1.1 eV. This is a weak second-order process. The first direct gap, which requires no phonon for excitation, is at 3.3 eV. In a nanocrystallite, the energy levels become quantized due to confinement. Also, the crystallite surface can provide momentum and hence the crystal momentum is not conserved (Fig. 1.39). So, photons can, alone, excite electron–hole pairs. Subsequent relaxation/decay to the lowest state of the quantum dot is followed by radiative recombination of the pair to produce the PL. In the crudest approximation for the electron–hole confinement energy, we assume a spherical crystallite of radius R with infinite barriers, and electron and hole masses m_e and m_h, respectively. Then, the total energy is:

$$E_{eh} = 1.1 + h^2/(8m_eR^2) + h^2/\ (8m_hR^2)$$

For a 2.5 nm diameter crystallite, the confinement shift is approximately 0.7 eV; this shifts the gap from 1.1 eV, in the infrared, to 1.8 eV, in the visible part of the spectrum. The successful explanation of the shift of the emission to the visible is the major achievement of this model. In addition, the model predicts a Stokes shift (emitted photons are of lower energy than exciting photons) but the shift is not as big as has been measured in experiments. However, this model fails to explain the large bandwidth of the emission. Moreover, it predicts too strong a dependence of emission wavelength on crystallite size. Supporters of this model attribute the large bandwidth to size broadening.

The second postulate is the radiative surface states model. Until recently, there had been no information about their nature or origin. Recently, it was theoretically demonstrated [52] that such states indeed exist on the nanocrystallite surface, and to a lesser degree in the interior, under the form of "self-trapped excitons" on Si—Si dimers. Those are stabilized because of the widening of the gap due to quantum confinement. Using local density approximation (LDA) and tight binding (TB) methods, Allan *et al.* [52] calculated the interatomic potentials of these species, for two sizes. Nayfeh *et al.* [17] studied the pathways for photoexcitation processes involved in populating the dimer states, and calculated the PL.

1.9.2 Computational Methods for Electronic Structure of Nanoclusters

Computational studies of nanosystems such as clusters and nanocrystals have become an exciting direction in physics, chemistry, and materials research. New materials based on nanosystems open a novel window of opportunity to develop unique materials by tuning the properties of the constituent nanosystem building blocks. Nanosystems exhibit a plethora of effects which are not present in common materials such as solids, molecular, or polymer systems. Nanosystems often exhibit a variety of properties and phenomena which challenge our imagination and also our understanding of the underlying physics. Nanoclusters are particularly interesting since one can exploit the enormous variability in size, shape, composition, and environment in order to influence the cluster properties. For example:

- Boundary conditions can vary between free (gas phase), surface depositions, solid embeddings, artificial confinements, solutions, etc.
- Clusters span sizes from a few to thousands of atoms; however, clusters do not qualify as typical molecules since they show a number of unusual effects such as "closed structural shell" effects or "magic sizes", large number of very different isomers with almost the same energies, transitions between structural regimes and patterns, etc.
- Clusters often exhibit combinations of electron shell-filling together with variety of many-body effects and a significant impact of electron–electron correlation.

Nanosystems therefore do not comfortably fit our traditional paradigms such as periodicity and band structure used for describing the basic properties of solids or molecular orbital picture of traditional molecular physics. The mentioned variety of phenomena makes the theoretical investigations difficult and challenging. In particular, very often details in atomic and electronic structures can appreciably influence optical, magnetic, dielectric and conductivity properties, chemical reactivity, and stability of nanosystems.

The atomic and electronic structures are often investigated by a combination of methods. For very large clusters, molecular dynamics and/or Monte Carlo methods with interatomic pair potentials are typically employed. For intermediate sizes say, clusters with the number of atoms between several tens and hundreds TB methods are used, sometimes combined with sophisticated optimizations such as genetic algorithms in order to efficiently find the most promising candidates for structures of ground states. The density functional methods based on density functional theory (DFT) [69] are commonly used for sizes up to a few dozens of atoms with the

time-dependent density functional theory (TDDFT) applied to study excited states and optical spectra. More advanced methods for excited states are based on the GW approach augmented with Bethe–Salpeter equation which captures excitonic (two-particle) effects [70,71]. Some of the most accurate calculations which have been carried out for these systems are based on the quantum Monte Carlo (QMC) methods [72–76]. Let as briefly describe the DFT and QMC approaches from the perspective of their applicability to nanosystems.

1.9.2.1 DFT Methods

In the two seminal papers of the DFT [69] Walter Kohn and his collaborators have shown that the ground state total energy of the system of electrons in the external field can be expressed as a functional of the single-particle electron density. Such an exact functional is claimed to exist and to be universal but it is unknown. Although at present the exact functional is out of reach, a number of approximate functionals have been suggested and proved very useful in practice. Historically the first one is the LDA based on the homogeneous electron gas model. In LDA the electron density is locally represented by the homogeneous electron gas of the same density. The properties of the homogeneous electron gas and its energy, in particular, are known, so one can write the total energy as an integral over the energy density of the homogeneous electron gas. The approach was then improved by incorporating the gradient of the electron density into the total energy in the form of the so-called generalized gradient approximation (GGA) [77].

The GGA functionals take into account, in an approximate way, the spatial variation of electron density and in most cases provide significantly improved estimations for energy differences and other quantities. Unfortunately, these improvements are not systematic and the quality of predictions can vary from system to system. The DFT methods proved to be remarkably productive and established themselves as a "sweet spot" which very successfully balanced the conflicting demands on computational speed and accuracy of predictions. The DFT methods have been tested on a full scale of electronic structure systems such as molecules, solids, surfaces, etc. over the last three decades. It is also clear that the success of the approximate DFT functionals stems from the cancellation of errors between exchange, correlation, and the component of kinetic energy related to the electron–electron interaction. It is not difficult to verify that these three terms tend to compensate each other as the sum of exchange and correlation is smoother than each of them separately and the kinetic energy contribution from electron–electron interaction decreases the amplitude of the exchange–correlation having the opposite sign. The compensation works very well when comparing systems which have similar bonding patterns, charge densities, etc. such as a solid or a molecule close to equilibrium geometry. The DFT methods therefore often provide excellent description for equilibrium geometries. The cancellation is less effective when the variation in electron densities in the system are significant or when strongly localized states (such as *d*-electrons in transition elements) energetically compete with states which are more delocalized. In such cases, with typical examples being transition metal oxide solids, the DFT methods need to be modified either by *ad hoc* approaches such as LDA + U or by high-level perturbational methods such as self-consistent GW approach. Very often, even change of bonding pattern, bond-breaking or non-equilibrium geometries can produce significant errors in the DFT predictions [78–82].

The DFT theory was originally presented as a ground-state approach, nevertheless, its use was extended to estimations of excited state properties as well. For example, one particle eigenvalues of the Kohn–Sham formalism can be interpreted as approximate quasiparticle energies and therefore enable to extract estimations of band gaps. Although it was early recognized that the DFT gaps are lower than the true ones, typically by 30–50%, they provided reasonable starting guesses for many sp insulators. The extension of DFT to the TDDFT is based on similar ideas as the random phase approximation and configuration interaction with single (CIS) excitations in the post-Hartree–Fock methods [83]. The key difference is in the effective potential which in CIS method is the Fock potential with the corresponding orbital occupation while in the TDDFT the Fock potential is replaced by the corresponding GGA/LDA effective potential. In the simplest version the TDDFT theory exhibits similar underestimations of gaps as the quasiparticle eigenvalues. To correct for the DFT bias for excited states it is necessary to include more sophisticated approaches such as the GW method and beyond (see, for example, [70,71]).

1.9.2.2 Quantum Monte Carlo

The QMC method is based on solving the quantum many-body problem, or, more precisely, on using the stochastic techniques for sampling the wave functions and for solving the corresponding quantum many-body problem, i.e. the stationary Schrodinger equation [72–76]. This approach enables us to achieve high accuracy by describing the electron correlation effects explicitly and directly. In particular, QMC treats with an unprecedented efficiency the dynamical correlation such as electron–electron cusp which is very difficult to describe by more traditional methods based on expansions in basis sets. In a certain sense the QMC methods are complementary to the traditional correlated wave function approaches developed in quantum chemistry community, since what is easy in QMC is difficult in traditional approaches and vice versa [72–76]. We will briefly describe the two basic QMC approaches.

1.9.2.3 Variational Monte Carlo

In the variational Monte Carlo (VMC) method, the expectation values are estimated from stochastic samples of electron configurations in real space. For example, the variational energy of an arbitrary trial wave function is given by an average of the local energy. The stochastic method of integration is the key ingredient since it enables us to explore explicitly correlated trial wave functions. The correlated trial wave function depends on the interelectronic distances and includes electron–electron cusps which are so difficult to capture by traditional basis set expansion methods. For very accurate calculations the VMC correlation part includes also the most important triple correlations of the electron–electron–ion type [75]. The commonly used VMC trial wave function is a product of linear combination of one (or a few) Slater determinant(s) and a correlation factor. Calculations done by us and others demonstrate that this procedure works for a whole range of systems such as atoms, molecules, solids, surfaces, etc. In many cases already this level of correlation is capable of providing very unique information such as accurate cohesive energies of diamond and silicon solids [76]. However, the choice of the trial function and its optimization using stochastic samples of electron configurations could be a source of variational bias. This is particularly important for comparison of two different systems

(e.g. molecule and isolated atoms for estimation of atomization energies) because the bias can and often does vary from system to system.

1.9.2.4 Diffusion Monte Carlo

In order to eliminate a major part of variational bias we employ the diffusion Monte Carlo (DMC) method. It is based on the projection operator, which projects out the ground state of a given symmetry from any trial function with nonzero overlap. We note that DMC works also for excited states which are ground states of different symmetries. It can be applied also to genuine excited states, i.e., which are not the ground states of the given symmetry, although the computational demands are significantly higher.

1.9.2.5 Applications to Si Clusters

The pure silicon clusters were studied quite intensively over the last 15 years or so. The investigations focused on electronic and atomic structures [84], chemical reactivity, and other properties. For example, one of the first real materials applications by QMC methods was the binding energy estimations of small silicon clusters in our work from mid-90s [81].

The key experiments which brought the silicon clusters to the forefront of materials and chemistry research were the mobility measurements which provided insights into the structural properties at small to intermediate sizes, i.e. between 10 and 50 atoms. In particular, the experiments revealed an onset of a structural transition from prolate to oblate structures at the size of $\sim$20 atoms and oblate structures were clearly dominant beyond 25 atoms [84]. The nature of transition remained unclear for some time until low-energy structural isomers were found by a combination of theoretical methods in several groups. Our group has carried out accurate studies of the Si clusters in the range of intermediate sizes [82] between 20 and 25 atoms which bracket the range of the structural transition. The DFT energy differences from various functionals were not accurate enough since the accuracy varied from isomer to isomer. The DMC results have shown that from the investigated isomers the elongated one was the lowest in energy in contradiction, for example, with the PW91 functional results [81]. The structures for Si_{25} which we have found are in Fig. 1.40. Combination of QMC and the Car–Parrinello method enabled us to explain the structural transition as being associated with the formation of irregular cages with small number of highly coordinated "internal" atoms which enabled fast structural relaxations by rapid bond-breaking and rebonding with the atoms on the cluster surface.

There have been a number of papers over the past decade devoted to the hydrogenated Si clusters since it was discovered that they actually appear to be extremely promising as new optical materials. As explained elsewhere, unlike bulk silicon which is an indirect gap material, the bond-saturated silicon nanocrystals in the range of sizes from one to a few nanometres show interesting optical behaviour such as strong luminescence across the visible spectrum, nonlinear effects, etc. We have carried out both DFT and QMC calculations for several types of hydrogenated Si clusters with different degrees of surface hydrogenations and surface reconstructions. We have analysed the lowest energy states and also excitations in order to understand the optical absorption spectra. More detailed information can be found in an earlier review and in relevant publications [85–87].

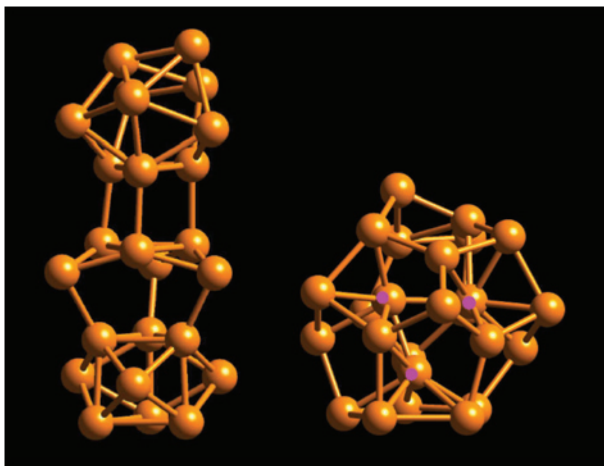

Figure 1.40 Prototypes of Si_{25} elongated and spherical-like cluster isomers. The spherical-shape cluster is formed around a few internal Si atoms with high coordinations which enable the cluster to relax into a low-lying structural conformation (after Ref. [81]).

Very recently, a new research avenue has been opened by rather remarkable experimental results on doped Si clusters, cage-like, clusters with encapsulated transition metal atoms [88,89]. In particular, Ohara *et al.* produced TM = Ti, Hf, Mo, and W embedded TM@Si_{12} clusters [89] while the group of Hiura was able to produce TM@Si_nH_x (TM = Hf, Ta, W, Re, Ir, Nb, Mo, Co, Ni) clusters in an external quadrupole static attraction ion trap [88]. The maximum value of n depends on the particular transition metal atom, for which completely dehydrogenated clusters were found. A simple electron counting shows that the most stable clusters observed seem to fulfil the "18-electron rule" originating in a simplified model of the cluster as a sphere with TM being at the centre ("Ar-like atom"). They also found that for W@Si_{12}, a regular hexagonal prism Si_{12} cage with a W atom at the centre has the lowest energy. The 6-fold symmetry prism structure was quite unexpected since Si clusters usually show very different structural patterns in this range of sizes.

Our calculations [90] show that the structural frame of the hexagonal prism cage (Fig. 1.41a) is remarkably stable regardless of the type of the central transition metal atom. Analysis of the one-electron states indicates varying degree of *pd* hybridization with corresponding changes in the stability and character of ground and lowest excited states. For example, the energy differences between singlet and triplet states depend on the type of the TM atom and, in fact, for Ti, the triplet is the lowest energy state. Altogether we have carried out electronic structure calculations of TM@Si_{12} with TM = Sc, Ti, V, Cr, Mn, Fe, Co, Ni, Cu, Zr, Mo, W, Re, Os, Pt, and Au. Qualitatively, one expects the TM *d*-states to hybridize with the *p*-states of the Si atoms and the resulting spins to be smaller than those of highly spin-polarized TM atoms in the middle of the *d*-series. This was indeed the case for the TM atoms with an odd number of electrons. We found that ground states are doublets for all such elements we studied, namely Sc, V, Mn, Co, Cu, Re, and Au.

One of the interesting features is the character of the singly occupied electronic state in the majority spin channel. We found that this level is invariably and predominantly

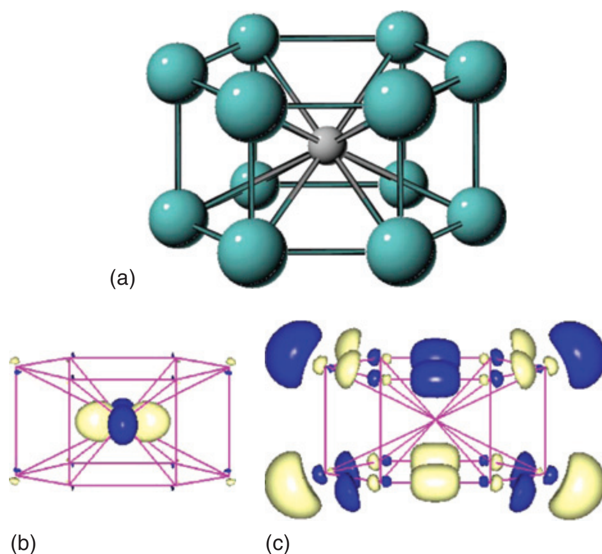

Figure 1.41 (a) The hexagonal prism cage structure of 12 Si atoms with D_{6h} symmetry with a TM atom at the centre. (b) The singly occupied state in the majority spin channel for V@Si_{12} localized on the TM atom. (c) The LUMO level for the same cluster (after Ref. [90]).

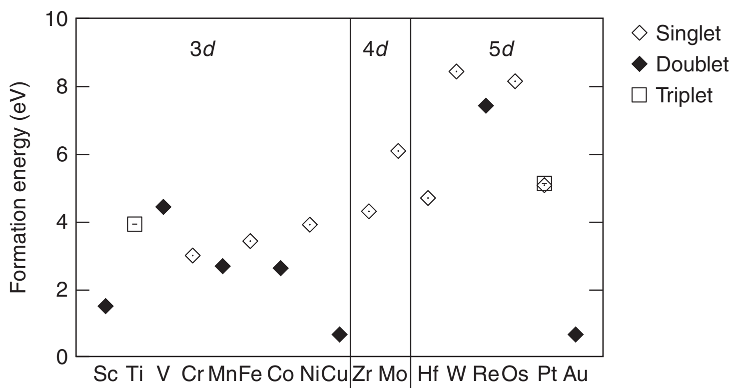

Figure 1.42 The formation energies of the TM@Si_{12} clusters with various TMs from 3*d*-, 4*d*-, and 5*d*- series. Note that the most stable clusters form with the middle of the 5*d*- series atoms (after Ref. [90]).

d-like, localized on the TM atom, and almost completely enclosed in the cage (Fig. 1.41b). In case of Co@Si_{12} and Re@Si_{12} this state is the HOMO level. In rest of the doublet systems, this state is slightly lower in energy than HOMO, which happens to be a bonding state of the Si cage consisting of Si *p*-states.

A measure of the relative stabilities of various clusters is the energy gain in forming TM@Si_n starting with the lowest known Si_n cluster isomer and an isolated TM atom. This formation energy is given by FE = E (Si_n, the lowest isomer) + E (TM) − E (TM@Si_n) where E denotes the calculated ground state total energy of a given system. A summary of our estimations of FEs within B3LYP functional is shown in Fig. 1.42.

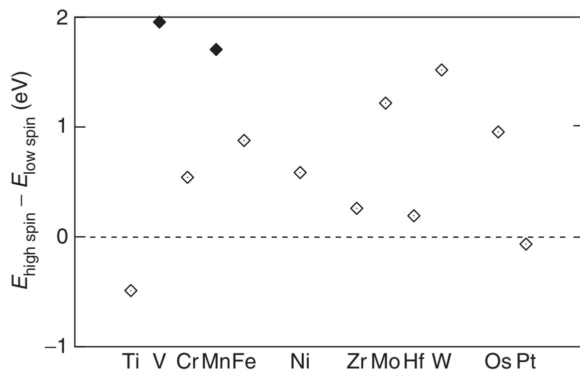

Figure 1.43 The energy difference between the high- and low-spin states of the TM@Si_{12} clusters. The results suggest that from the clusters we study, only the Ti-embedded atom leads to a high-spin (triplet) state which is lower than the zero-spin singlet. This was verified by the QMC calculations which confirmed the DFT result for this case.

For the lowest isomer of Si_{12} cluster (structurally very different from the hexagonal cage) we used the geometry obtained by Shvartsburg *et al.* [84] which was further optimized within the DFT methods. Perhaps the most surprising fact is that all TM atoms we have studied form stable TM@Si_{12} clusters. However, the amount of formation energy varies considerably. While the TM atoms at the beginning or end of a series (Sc, Cu, Au) lead to marginal stability, those towards the middle are clearly more stable. Note that the comparison between the high- and low-spin states revealed that only one TM atom resulted in a high-spin state being more stable (Fig. 1.43).

The example of TM@Si_{12} clusters has shown that there is an unexplored and possibly very fruitful window of opportunity to find new nanosystems (see Chapter Three) with unique properties for applications. It seems that the most exciting experimental discoveries happen when new methods of preparation are explored for compositions which are unusual in traditional chemistry or materials research. These results also beautifully illustrate how limited is our understanding of the physics and chemical behaviour of these systems. Indeed, the key structural features, such as the double Si hexagon arrangement and its chemical properties, were unknown before the experimental discovery. It is clear that there is a number of such discoveries which will be made in the future and some of them will for sure find their way into useful devices or device components.

1.9.3 Prototype of Hydrogenated Particles (Supermolecule)

The search [13] for a realistic structural prototype started from a spherical piece of a crystalline Si which, for the experimentally observed size of ~1 nm, contains 29 atoms (magic number for the T_d symmetry and spherical shape) (see Fig. 1.44). All of the 36 dangling bonds were terminated by hydrogen. However, the corresponding electronic energy gap was >6 eV, suggesting that the observed clusters possess smaller number of terminating hydrogen/oxygen, with a part of the dangling bonds saturated by a nanocrystal surface reconstruction. By eliminating 12H atoms we

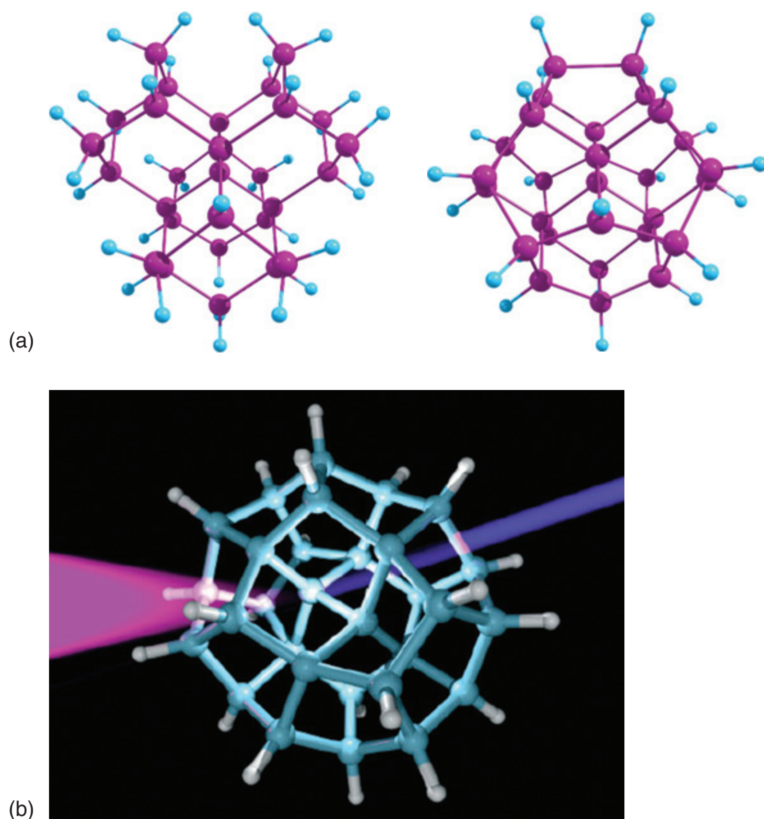

Figure 1.44 Schematic of the prototypes of the bulk-like unconstructed $Si_{29}H_{36}$ configuration and the filled fullerene reconstructed $Si_{29}H_{24}$ particle. The figure also shows a cartoon of the PL from the particle (Reproduced with permission from Draeger et al. [93] copyright Wiley-VCH 2003).

arrived at a structure of $Si_{29}H_{24}$ with six reconstructed surface Si—Si dimers similar to Si(001) surface 2×1 reconstruction. The resulting $Si_{29}H_{24}$ system was then relaxed using the DFT with the PW91 exchange–correlation functional, giving, after correcting for the well-known DFT gap underestimation, a band gap of 3.5 eV, close to the one observed.

We should also note that the surface of a $Si_{29}H_{24}$ cluster can be represented as a 28-atom cage (12 pentagons, 4 hexagons) with a single silicon atom in the centre, bonded to four surface atoms (related by T_d symmetry) to form a five-atom tetrahedral core. The remaining surface atoms are passivated with hydrogen.

The relaxed configuration, shown in Fig. 1.44, with five atoms constituting a single tetrahedral core and 24 constituting a H-terminated reconstructed surface ($Si_{29}H_{24}$, with six reconstructed dimers) provides the best agreement with the measurements. The coordinates of the $Si_{29}H_{24}$ particle (x, y, z) in angstroms are summarized as follows. There are 12 Si atoms at (-2.720, -2.720, -0.0197) and their permutations. Another 12 atoms are at (-3.932, 0.886, -0.886) and their

permutations. Four atoms are at (−1.394, −1.394, −1.394) and their permutations. Finally the centre atom is at (0.000, 0.000, 0.000). The surface is highly wrinkled or puckered system of hexagon and pentagon rings. The prototype gives a diameter of 0.9 nm for the Si core and 1.066 nm including the H-termination, and an absorption edge of 3.5 ± 0.3 eV. The surface Si atoms form four hexagonal rings. Three atoms from the surface with three of the internal tetrahedral unit (one is the centre atom) form a hexagonal ring. There are a total of eight such hexagons; those slice the particle as deep as the centre, creating ridges. There is also a total of eight pentagon rings, each is formed by four surface atoms and one of the tetrahedral internal atoms (excluding the centre atom). The participation of the internal atoms in ring formation makes the particle highly wrinkled- or "puckered-ball".

We next calculated the optical absorption spectrum. The resulting spectrum with a Gaussian broadening of 0.14 eV, which qualitatively represent the temperature and size averaging, shows agreement with our measurement. We also evaluated the cluster polarizability, a uniquely defined property, giving ~793 a.u. A general definition of a dielectric constant in semiconductor nanoparticles is not possible since the energy levels are discrete. To arrive at an effective "dielectric constant" one has to define an appropriate "cluster interior volume". For an effective interior radius (~4.2 Å) we get a dielectric constant of ~5.7. This value is close to estimations done before by Allan *et al.* [52] and Wang and Zunger [91]. The Penn's model-based analysis [91] gives, for a diameter of 0.8 nm, a more reduced static dielectric constant of 2.

The silicon–hydrogen prototype of the particle $Si_{29}H_{24}$ represent in some sense a new phase between solid and molecule. With a tetrahedral core and a strong molecule-like reconstruction of the surface, the new phase or supermolecule may exhibit solid-like behaviour as well as molecule-like behaviour, which may account for the multitude of novel optical and electronic properties of our nanoparticles.

1.9.4 H_2O_2 Effect on Surface Reconstruction

The formation of these reconstructions is favourable under our dispersion conditions. H_2O_2 in our etchant is critical for controlling the amount and configuration of hydrogen on the surface, hence the reconstruction. The reaction $Si_nH_m \rightarrow Si_nH_{m-2} + H_2$ has a barrier of 0.6 eV. However, the reaction $Si_nH_m + H_2O_2 \rightarrow Si_nH_{m-2} + 2H_2O$ proceeds followed by reconstruction to form novel radiative Si—Si dimer bonds while gaining an energy of 0.25 eV [92].

In the analysis H_2O_2 gets in the gap stripping two hydrogens and the bonds connect as shown in Fig. 1.45 (top). Those reconstructions can take place more readily in ultrasmall particles for which the elasticity drops. This makes the atoms amenable to large movement. For instance, in the model, some surface Si atoms in 1 nm particles move by >0.65 Å from their bulk positions to reconstruct into novel radiative Si—Si dimers, with a binding energy of 0.75 eV, much larger than the thermal agitation energy of 0.025 eV. If additional hydrogen below 24 total atoms and reconstruction takes place, sp^2 symmetry begins to set in, and the band gap of the particle begins to drop fast eventually collapsing resulting in a graphite-like structure (conduction system) (Fig. 1.45, middle).

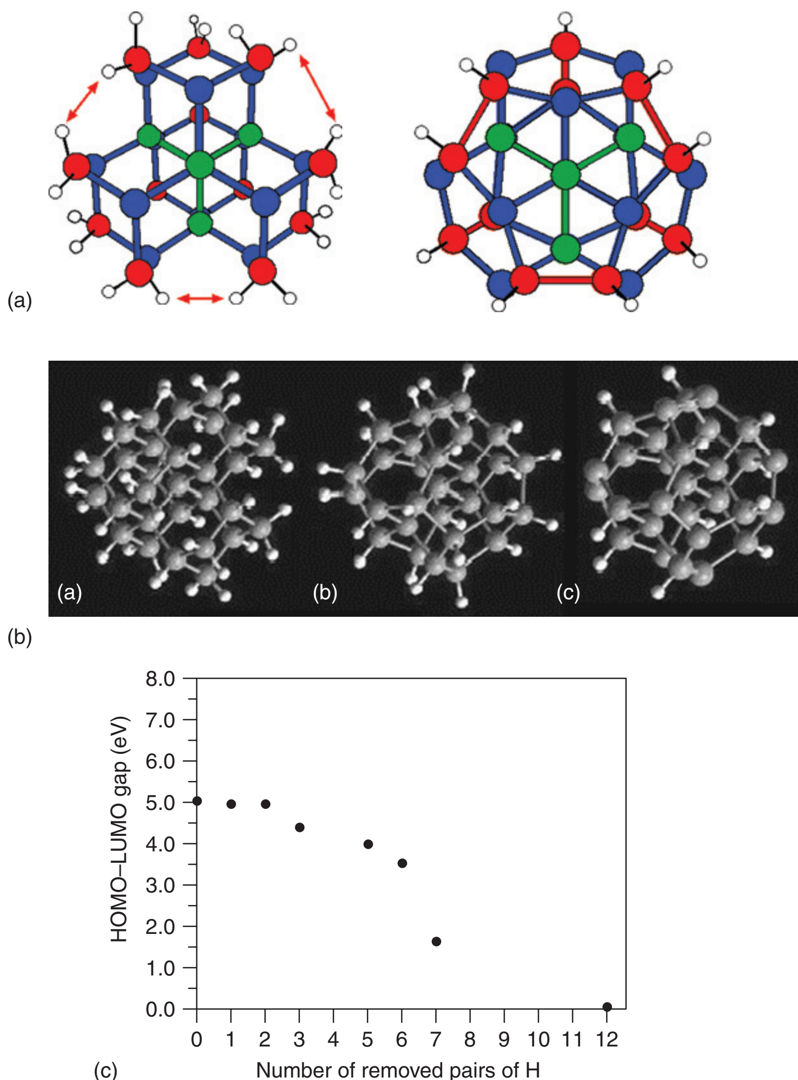

Figure 1.45 (Top) Schematic of the reconstruction of $Si_{29}H_{36}$ to $Si_{29}H_{24}$ in which 12 hydrogen atoms are stripped by H_2O_2 molecules to form water molecules. (Middle) Configuration structures of a particle that contains 29 atoms (magic number for the T_d symmetry and spherical shape) with silicon atoms (grey) and hydrogen atoms (white). (a) All dangling bonds are saturated with hydrogen. (b) Twenty-four of the 36 dangling bonds are terminated by hydrogen with six reconstructed surface Si dimers. (c) Twelve of the 36 dangling bonds are terminated by hydrogen with 12 reconstructed surface Si dimers. (Bottom) The calculated band gap of H-terminated particles as a function of the number of H atoms on the particle (adopted from Refs. [13,22]).

1.9.5 Novel Si—Si Bonds (Molecular-Like Behaviour)

As discussed in the previous section and with the aid of Figure 1.45a, there are six pairs of surface atoms, each of which has two broken bonds that are saturated with hydrogen. The atoms in each pair are at 4.84 Å interspacing. When each of those

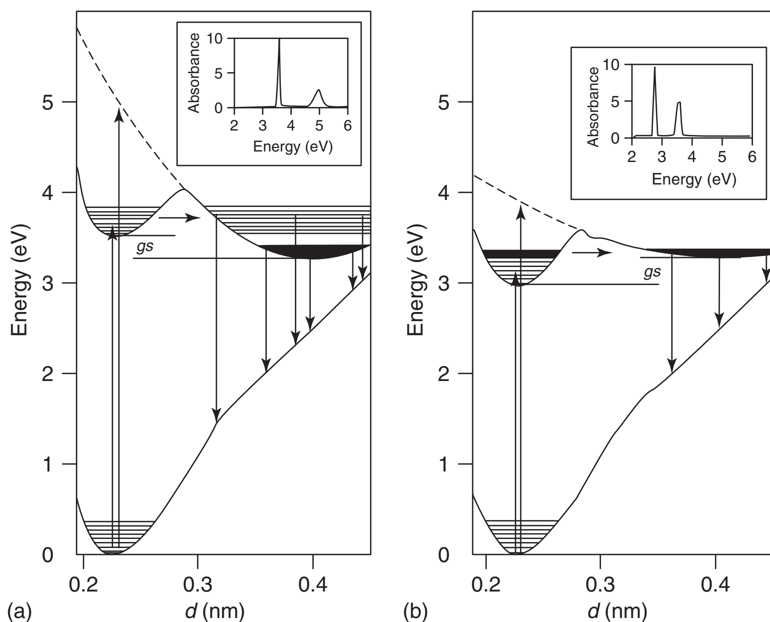

Figure 1.46 Partial energy-level diagram of the Si–Si surface dimers in nanocrystals crystallite showing the ground and the first excited electronic states. (a) In 1.03 nm crystallite, it schematically shows excitation into the inner well via double-well vibrational states, and above-barrier excitation into the outer well, along with emission from the double-well states and from the relaxed single outer well. (b) In 1.67 nm crystallite, it shows excitation into the inner well and above-barrier excitation into the outer well, along with emission from the double-well states and from the relaxed single outer well (after Ref. [17]).

atoms gets stripped from one hydrogen, the atoms move closer from 3.84 Å interspacing to form a Si-Si molecule-like dimer bond at 2.35 Å, the tetrahedral distance.

Allan *et al.* focused their attention on a single Si—Si molecule-like dimer on the Si_{29} particle. Figure 1.46 gives a schematic of the interatomic potential of the Si—Si reconstructed bond [52] calculated by this group using LDA in the 1.03 nm diameter particle as well as in 1.67 nm particle, and the various pathways for absorption and emission calculated by Nayfeh *et al.* [17]. The excited state is a double well with a potential barrier. The inner well (at 2.35 Å) is associated with the tetrahedral configuration and radiates on a long time scale of milliseconds. The outer well, a new state found only in ultrasmall nanoparticles, is a trap well (at 3.85 Å) that radiates with lifetimes of 5 ns to 100 μs. The calculations were performed with the silicon atoms terminated by hydrogen. Only minor changes such as a shift of the bottom of the outer well inward are expected for oxygen-terminated dimers since they are less amenable to expansion. The state to which the outer well radiates vertically down is the ground electronic state. But, at extended bond lengths, the ground state is high lying and unpopulated, hence this system constitutes a stimulated emission/gain channel. The blue emission proceeds at an interatomic distance at the top of the barrier (∼3 Å), where the lifetime is in the nanosecond regime and mixing between the two states is most significant. Emission from near the bottom of the outer well is of longer time characteristic and of longer wavelength (in the red or near infrared).

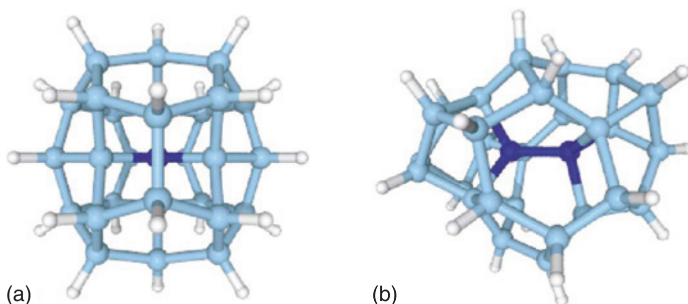

Figure 1.47 Computer prototype of Si_{29} particles with a single-core and double-core configurations: in white hydrogen, in grey silicon and in black is the silicon core (Reproduced with permission from Draeger et al. [93] copyright American Physical Society (APS) 2003).

According to the Frank–Condon principle for molecular transitions, absorption proceeds vertically up into the inner well at a bond of 2.35 Å, followed by transfer into the outer by bond expansion via tunnelling or thermal activation (i.e. self-trapping) as in Fig. 1.46. Also, above-barrier absorption, followed by relaxation populates the trapping well. For sizes less than a critical size of ~1.4 nm, the trapping edge is lower than the absorption edge, allowing strong transfer to the outer well [17]. The potential barrier was demonstrated by manipulation of the material by metal and oxide coatings [19].

1.9.6 Structural Stability of the Prototype

Draeger and colleagues at Lawrence Livermore National Laboratory (LLNL) employed a combination of first principles molecular dynamics (FPMD) and QMC calculations to determine the structural and optical properties of 1 nm silicon particle [93]. In addition to the symmetrical single-core configuration presented above, they found other stable but asymmetric configurations consisting of a two-atom core configuration as depicted in Fig. 1.47. They set out to determine the stability of our nanoparticle configuration against hydrogen saturation. They studied the number of hydrogens required to maintain a single-core crystalline structure in a 29-atom silicon cluster. They performed FPMD simulations in which a number of neighbouring hydrogen atoms were removed from a tetrahedrally symmetric $Si_{29}H_{24}$ nanocrystal. The cluster was then heated to $T = 600$ and 1000 K. At $T = 1000$ K, removal of only six hydrogen atoms ($Si_{29}H_{18}$) resulted in a persistently stable, single-core structure. When 12 hydrogen atoms were removed ($Si_{29}H_{12}$), the silicon cluster formed a double core within 0.5 ps. When 18 hydrogen atoms were removed ($Si_{29}H_6$), the cluster again formed a double core within 0.5 ps, but also exhibited dynamics consistent with an amorphous cluster, as shown by the exchange of interior core and surface atoms on a time scale of roughly 1 ps. They found that 14 neighbouring hydrogen atoms ($Si_{29}H_{14}$) are required to maintain a single tetrahedral core. At $T = 600$ K, similar behaviour is observed, although the double core formed more slowly than at $T = 1000$ K. These findings suggest that the retention of a crystalline core depends on both the fraction of dangling bonds at the surface and the passivation time scale.

The calculations also yielded two other configurations of the single-core particles $Si_{29}H_{24}$ with a different hydrogen distribution. The surface of a $Si_{29}H_{24}$ cluster can be

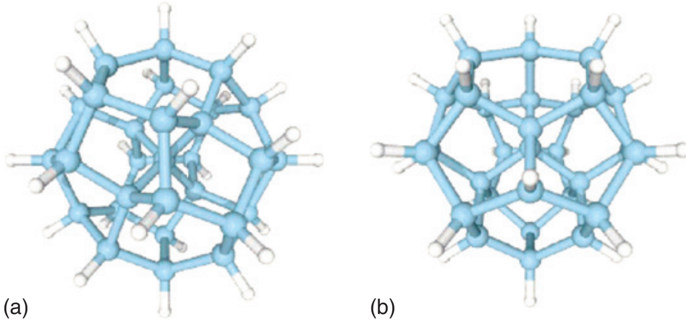

Figure 1.48 Computer prototype of a single-core $Si_{29}H_{24}$ with two different ways of distribution of hydrogen that are different from that in Fig. 47 particles (Reproduced with permission from Draeger et al. [93] copyright APS 2003).

represented as a 28-atom cage (12 pentagons, 4 hexagons) with a single silicon atom in the centre, bonded to four surface atoms (related by T_d symmetry) to form a five-atom tetrahedral core. The remaining surface atoms are passivated with hydrogen. The first configuration is our bulk-like surface reconstruction of crystalline $Si_{29}H_{36}$ to $Si_{29}H_{24}$ and found to have an optical gap in agreement with an experimentally measured optical gap of 3.44 eV [16]. The two other ways to connect the interior core atom to the surface and maintain a tetrahedral core are shown in Fig. 1.48a and b. These are *unique to a curved nanostructure*, and have no bulk analogue. In these configurations, partial reconstruction takes place in which silicon atoms from the inner shell strip hydrogen atoms from their neighbours in the outer shell, which then bond to the central core atom, resulting in "isosize" distorted configurations. Exchange of one or two hydrogen atoms between the two shells was found to change the band gap from 3.5 to 4.5 or 4.1 eV, respectively [93].

1.9.7 Material Properties: Dielectric Constant and Effective Mass

Bulk properties of semiconductor systems rely on the periodicity of the atoms in the crystal, thus for smaller and smaller particles, there is a point where the particle can no longer support several unit cells of the crystal, destroying the periodicity and translational symmetry, hence commencing the transition from bulk-like to molecule-like properties [91]. Moreover, as the size of the crystal decreases, the elasticity drops, especially in the surface layers, allowing appreciable restructuring to occur, accelerating the transition. The breakdown of bulk-based properties is not entirely unexpected, but the manner and the size at which it happens are unknown. Elucidating this transition is important since the structure governs the dielectric and optical constants, effective mass, and phonon structure, hence much of the electronic and optical behaviour of the particle. The 1–3 nm regime may truly be a transition between the bulk-like and amorphous-like or molecule-like structure. Yet, there exists little systematic testing in this size regime.

Particles are evaporated on *p*-type Si substrate. The tip of a scanning tunnelling microscope (STM) is placed over the silicon particle film at a constant height for injection of charge. Figure 1.49a gives the *I*–*V* spectra taken at room temperature under dark condition. Figure 1.49b, taken under light irradiation, shows a high visibility regular step structure, for negative tip biasing [9]. Under standard doping of

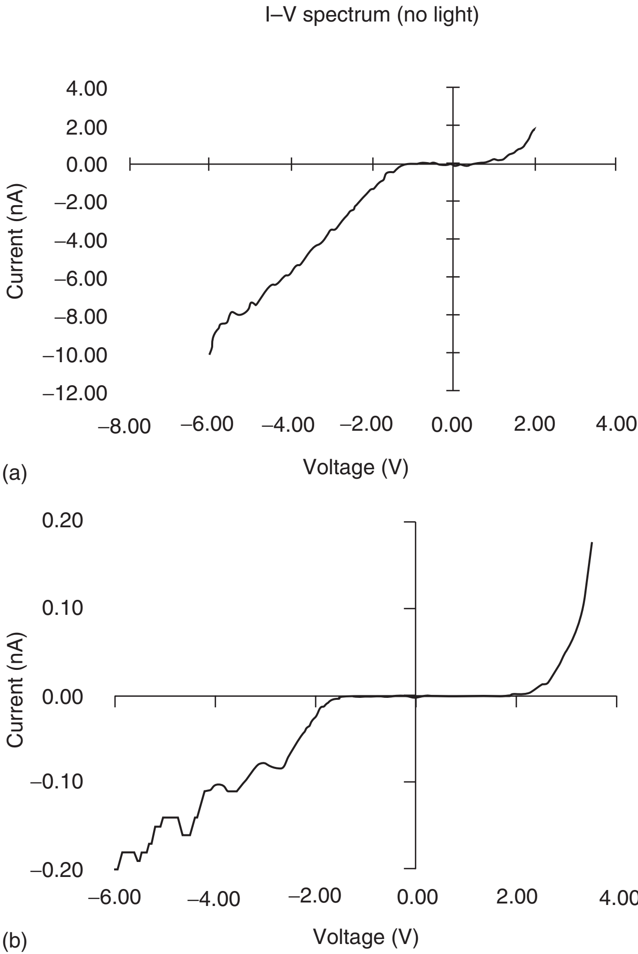

Figure 1.49 The *I–V* response for a film of nanoparticles on a device-quality silicon substrate (a) taken in the dark. (b) Taken under light illumination from a mercury lamp. The tip potential was varied with respect to the (grounded) sample (from Ref. [9]).

$\sim 10^{15}\,\mathrm{cm}^{-3}$, as in this sample, 1 nm particles contain less than one in a million holes, hence they behave as undoped, with the number of electrons in the conduction states extremely small. Laboratory temperatures are not sufficient to induce holes. Light irradiation, however, creates holes for the process to proceed. Measurements with size may yield the dielectric constant and the effective mass. In preliminary measurements, we find a transition at the size of 2.15 nm that demarks a critical size, which separates particles with bulk-like properties from those with molecular-like properties. Resonant tunnelling and the Coulomb blockade effect were used to examine the effective mass of holes created in Si nanoparticles as well as the particle's dielectric constant. We find that the effective mass approximation fails for particles with sizes below the critical size, while the dielectric constant is found to drop sharply at this critical size.

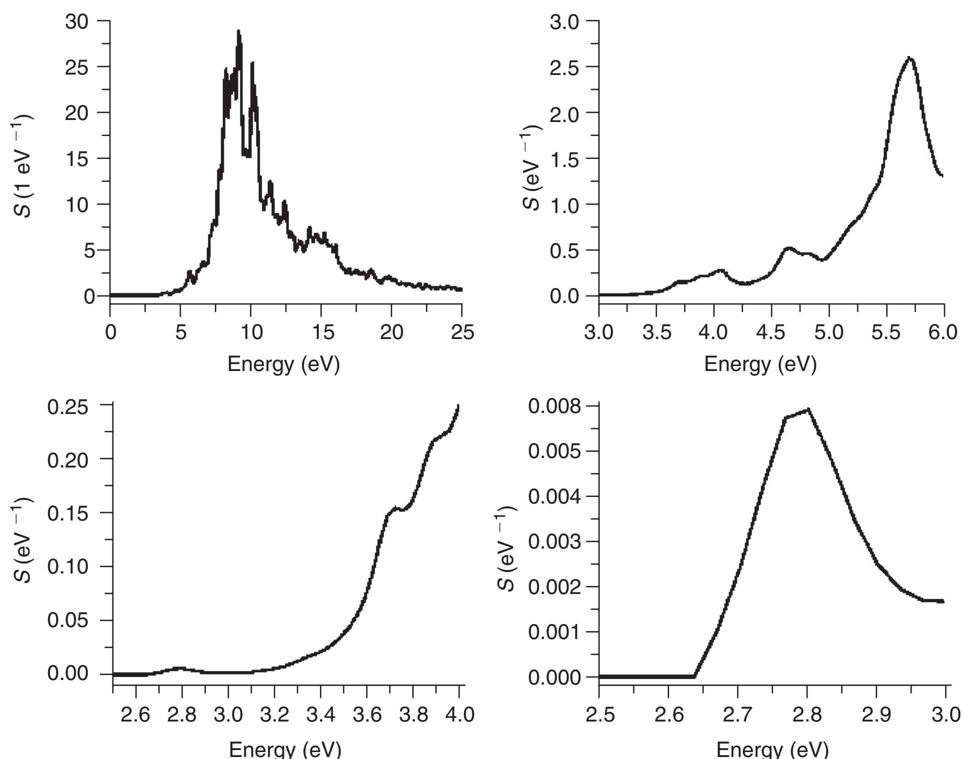

Figure 1.50 The absorption spectrum of the ideal bulk-like configuration of $Si_{29}H_{24}$ for different photon energy ranges (after Ref. [94] copyright APS 2004).

1.9.8 Excited States (Molecular-Like Bands)

In collaboration with Prof. Richard Martin we conducted a theoretical calculation and measurements to test this theory for each particle size [94]. We will analyse all isosize reconstruction configurations of $Si_{29}H_{24}$, which may be produced using QMC and time-dependent density functional therapy (TDDFT). Figure 1.50 gives the calculated absorption of the 1 nm particle. It shows overlapping bands. The lowest few bands occur at 350, 310, and 275 nm. We conducted measurements that map out all bands. The excitation wavelength was varied between 250 and 400 nm, while collecting the emission in the range 250–600 nm at each excitation wavelength. The results for the 1 nm particles are shown in Fig. 1.51. Distinct emission bands can be identified with peaks at 310, 360, and 400 nm, in agreement with the calculated TDDFT spectra. Moreover, the above calculations of Fig. 1.50 have shown that the particles behave in some sense also as “supermolecules”, with excited electronic states from which higher-energy bands may originate.

1.9.9 Collective Molecular Surface

The particle may actually represent the transition between solid and molecule phases. Instead of forming only a single dimer on the particle, Mitas *et al.* examined the

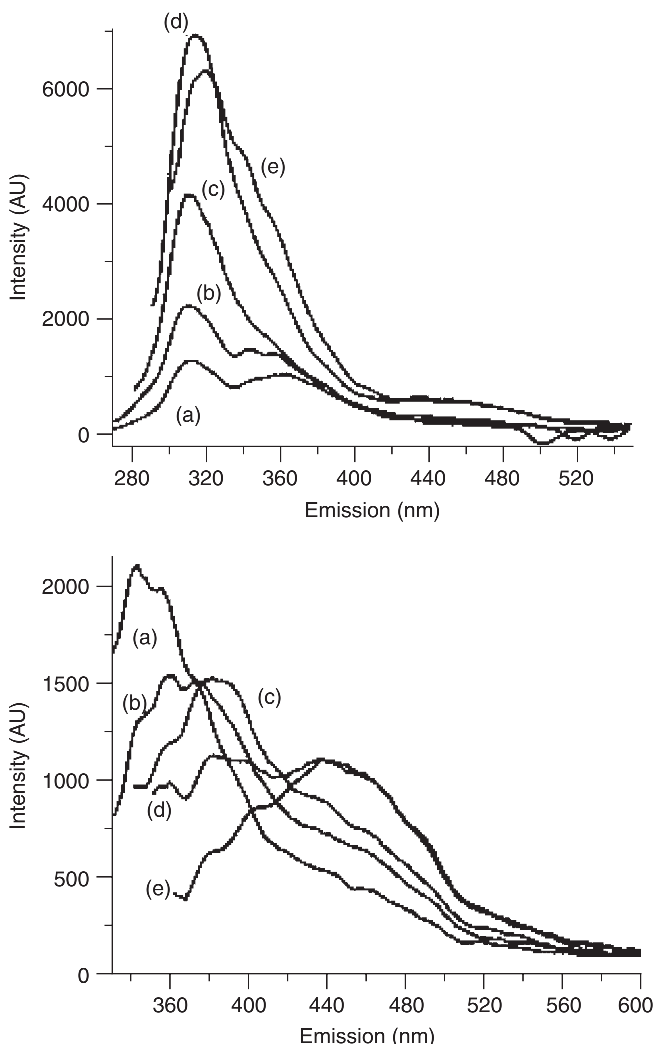

Figure 1.51 A series of emission line profile spectra for a typical sample with corresponding excitation wavelength: (Top) (a) 250, (b) 260, (c) 270, (d) 280, (e) 290 nm; (Bottom) (a) 310, (b) 320, (c) 335, (d) 340, and (e) 350 nm. Distinct emission bands are observed centered at 310, 360, 390, and 440 nm. The curves Top (d), Bottom (a), Bottom (c), and Bottom (e) represent the optimal response of the bands with excitation wavelengths of 275, 310, 335, and 355 nm, respectively, or 4.5, 4.0, 3.7, and 3.5 eV. The center of weight of the overlapping band of 390 and 440 nm at 410 nm maximizes for excitation at 3.6 eV (after Ref. [94] copyright APS 2004).

situation where the whole surface is reconstructed into the dimer molecule-like phase, as in the experimental synthesis. To calculate the molecular electronic structure of the silicon nanoparticle, the group used DFT for determining geometries of molecules, and the QMC method provides a significantly more accurate approach of calculating the energy differences such as the optically active excitations. Some of these calculations have been done in collaboration with a research group and supercomputers at LLNL led by Giulia Galli. One of the most interesting questions

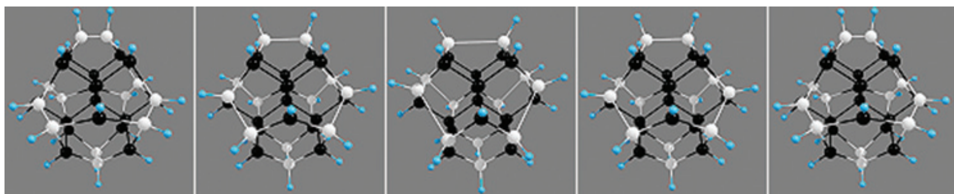

Figure 1.52 Animation of the vibration of $Si_{29}H_{24}$ nanoparticle. It shows the mode in which all six dimers (white balls) stretch coherently in a collective manner.

was whether the excited state was localized within the molecule and how much the excitation could affect the atomic geometries [92]. Because QMC was capable of describing the excitonic effects very well, the team found that the excited electrons were delocalized across the whole structure. They also found that the excitation causes very small changes to the structure of the molecule. They also carried out calculations of the Stokes shift, or the difference between the energy absorbed by the molecule-like and the energy that the molecule emits afterward, for the excitation at the absorption edge of the molecule. The Stokes shift was in excellent agreement with the experimental data showing the actual difference in frequencies between absorbed and emitted energy. In particular, they were able to predict changes in the colour of the emitted light upon attaching additional molecules such as methyl and ammonia groups to nanocrystals. The results of their QMC simulations of chemical doping were in excellent agreement with physical experiments.

1.9.10 Phonon Structure: Collective Molecular Vibration Modes

The hypothesis of excitation and emission at single Si—Si dimers or collectively on all the dimers simultaneously was examined. Detailed first principles calculation without an assumption of dispersion relations was carried out using Hartree–Fock theory through the GAMESS quantum chemistry package, developed for molecules, to calculate the normal vibration modes and the Raman spectrum of the 1 nm particle [95]. Because of the significantly larger number of atoms contained in the 2.2 nm diameter structure, it is not presently feasible to conduct these calculations for this size. We analysed the modes further by the utilization of Chemcraft, a graphical interface for GAMESS that images the nanoparticle and animates its normal modes. We determined the atomic configuration and symmetry, frequency, reduced mass, and the Raman amplitude of the Si—H and Si-based modes. The calculations indicate the presence of coherent vibration modes localized on pairs on opposite sides of the particle or collectively on all the surface dimers as shown in Fig. 1.52.

We also performed Raman spectroscopy on 1 nm silicon nanoparticles suspended in liquid. The Raman spectroscopy (in solution) was conducted using an Nd:YAG continuous wave laser at 532 nm as the excitation source. The power at the focus was ~50 mW. The detector is a triple grating spectrometer (SPEX 1000 Triplemate) equipped with a charge coupled device. At the optimal settings for this experiment, the resolution of the system is $\sim 3\ cm^{-1}$. The 1 nm particle colloid solution was placed in a quartz cuvette with the detector at 90° to the excitation. Polarized Raman was

collected by placing linear polarizers at the excitation source and in front of the detector such that the excitation light was polarized in the scattering plane.

The measurement agrees with calculated vibrations in the $Si_{29}H_{24}$ structural prototype and confirms the presence of surface dimer reconstruction, and high symmetry collective vibrations localized on those dimers. This confirms electronic excitations on the dimers that were recently proposed as the source of the strong optical activity, and basis of the transformation of the particles into direct-like behaviour. The peak positions and FWHMs, along with calculations of the normal modes, suggest that the nanoparticle exhibits strong molecular behaviour despite its derivation from a bulk structure.

Finally, we conducted low-temperature PL measurements. The measurements confirmed coupling of vibronic processes at the dimers and PL excitonic processes, which provided a valuable tool for elucidating the role of the bulk, surface scattering, and surface molecular traps in luminescent Si nanostructures [96]. The results showed the collective vibrational imprint of the whole surface.

1.9.11 Molecular-Like Emission: Direct versus Indirect Process

The recombination of spatially confined excitons in the bulk of nanocrystals, analysed by Hybertsen using an effective mass procedure [97], shows that for sizes <1.5–2.0 nm the oscillator strength of zero-phonon transition dominates that of phonon-assisted transitions. In this size regime, losses due to non-radiative processes drop. However, the luminescent excitons are found to have an oscillator strength of 0.002 in nanocrystallites of 1.5 nm diameter corresponding to luminescence lifetime of a few microseconds. Sundholm obtained an oscillator strength of 0.0017 for luminescence from a fully non-reconstructed bulk Si_{29} (1 nm) cluster configuration (see Fig. 1.44a) [98]. In those calculations, the molecular structures of the ground and the lowest excited state, hence the electronic absorption and emission energy were optimized at the DFT level using the time-dependent perturbation theory (TDDFT) approach. Other calculations of spherical clusters [99] used linear combination of atomic orbital framework. The calculations showed that the nature of the transition, i.e. A_1T_2, T_2T_2, or E–T_2 in the representation of the T_d point group, can change quickly with respect to a small change in the crystallite size. In the range of 1.3–1.5 nm diameter, for instance, the calculation gives oscillating rates of recombination that span over two decades (10^6–10^8 Hz), which correspond to 0.001–0.1 range of oscillator strength, with the upper limit approaching our experimental result.

A viable explanation of the fast decay rates observed involves molecular-like trap states. If the trapped states are shallow states, the picture will not essentially change [97]. This is due to the fact that shallow trapping changes the zero-phonon and phonon-assisted oscillator strengths in roughly the same way. If only deep traps are really involved in the PL process and act as a decisive factor, fast decay is expected and little change in oscillator strength with cluster size could be observed. The model presented by Allan *et al.* involves intrinsic radiative Si self-traps [52], which is based on molecule-like Si—Si surface reconstruction. The wave functions of these states are not extended throughout the bulk of the nanoparticles, but rather concentrated on local sites of atomic dimensions [99,52,17]. Those reconstructions can take place more readily in ultrasmall particles for which the elasticity drops. This makes

the atoms amenable to large movement from their bulk positions to reconstruct into novel radiative Si—Si dimers, with a binding energy of 0.75 eV, much larger than the thermal agitation energy of 0.025 eV. The binding energy (depth of trap) drops from 0.75 eV for 1 nm to 0.25 eV in 1.7 nm particles, and is expected to be a shallow condition of ~0.03 eV for 3 nm particles, comparable to the thermal agitation energy.

The fully reconstructed bulk-like Si_{29} (1 nm) cluster configuration with a total of six dimers was shown in Fig. 1.44a [13]. The large binding of the trap may explain the domination of the fast fluorescence decay time in 1 nm particles. But the shallow binding of the trap in 2.85 nm particle may explain the presence of a fast as well as a slow decay channel. The slow components may be associated with radiative recombination of electron-hole pairs in the bulk of the particle, i.e. under spatial bulk-like localization in the particle. Allan *et al.* presented an example of recombination on traps. Detailed calculations of the oscillator strength or lifetime for transitions in the HOMO–LUMO gap in 1.67 nm cluster gave lifetimes as short as 100 ns [52]. There is no corresponding calculation for the 1 nm particle, or for the 2.85 nm particle. Such calculations should be most helpful for detailed comparison with the experimentally observed lifetimes.

Our results for 1 nm particles show wide bandwidth but indicate full conversion to direct-like behaviour, with a few nanosecond time characteristic, corresponding to oscillator strength comparable to those in direct semiconductors. In addition to fast nanosecond decay, the PL from 2.85 nm nanoparticle suspension exhibit considerably slower decay, consistent with a transition regime to direct-like behaviour. The quantum yield is measured to be ~0.48, 0.55, 0.3 for excitation at 254, 310, and 365 nm, respectively, for the blue 1 nm particles, and ~0.16, 0.28, and 0.3 for the red 2.85 nm particles. The direct-like characteristics are strong evidence molecular-like behaviour. They point to localization on radiative deep molecular-like Si—Si traps with size-dependent depth.

1.9.12 X-Ray Form Factors

The structure of the nanoparticles using X-ray diffraction may elucidate the transition from bulk-like to molecule-like properties [100]. We numerically calculated the single particle molecular scattering of 1.543 Å X-rays for all members of the discrete family. The molecular form factor of the 1 nm particle shows molecular-like scattering at small angles, but amorphous-like at large angles. With size, the molecular-like structure shows an increase in the number of sub-peaks, narrowing, and shifting to forward scattering, but the amorphous-like structure transforms into polycrystalline scattering. The transition from amorphous/molecular-like to polycrystalline-like behaviour occurs at 2.2 nm. Computed electron diffraction patterns of an array of the 1 nm particles show residual crystalline-like patterns for large scattering angle, but small angles show very little resemblance to crystalline scattering [13].

Figure 1.53 (top) gives the calculated molecular structure factor at 1.543 Å using the bulk-like interatomic spacing. It consists of three broad peaks centred at $2\theta = 49°, 28°$, and 16°. The scattering is similar to amorphous scattering. The peaks are broad, indicating that the particle has only a limited number of atomic planes. The band at 49° appears as a doublet and is associated with scattering from the tetrahedral bond lengths 2.3 Å. For reference, crystalline or polycrystalline have

peaks at 56.25° and 47.5° due to scattering from the 220 and 331 planes. For amorphous silicon, a single broad peak replaces the two peaks at 49°. The band at 28°, due to scattering from the next nearest neighbour bond length centred at 3.9 Å, is the precursor to scattering from the 111 crystalline plane. Additionally, there is high-order but weaker and somewhat unresolved broad resonance in the region ~70–90°. In this angular region, crystalline or polycrystalline have peaks at 69.2°, 76.4°, and 88.1° due to scattering from the 400, 331, and 422 planes. Finally, the scattering band in the low-angle region has a peak at 16°; it is associated with pure surface atoms and has no crystalline or amorphous correspondence.

We next examined the fluorescent 1 nm particle ($Si_{29}H_{24}$), reconstructed from the bulk-like 1 nm cluster ($Si_{29}H_{36}$) as a result of surface relaxation. It has been proposed as a source of the optical activity observed recently [52,17]. The calculated molecular structure factor of the reconstructed particle (Fig. 1.53, bottom) consists of the same amorphous-like broad peaks of bulk-like clusters, however shifted, broadened, and less resolved. The 49° complex shifts to 48°, with the shoulder on the peek essentially disappearing. The substructure of the high-order complex of peaks is washed out further. The 27° band shifts to 29.5°. Finally, the strength of the large angle scattering diminishes with respect to the strength of the small angle scattering upon relaxation and reconstruction.

Figure 1.53 (top to bottom) displays the development of scattering with increasing bulk particle size 1, 1.67, 2.15, 2.9, 3.7, 5.0, and 6.0 nm. We do not show results

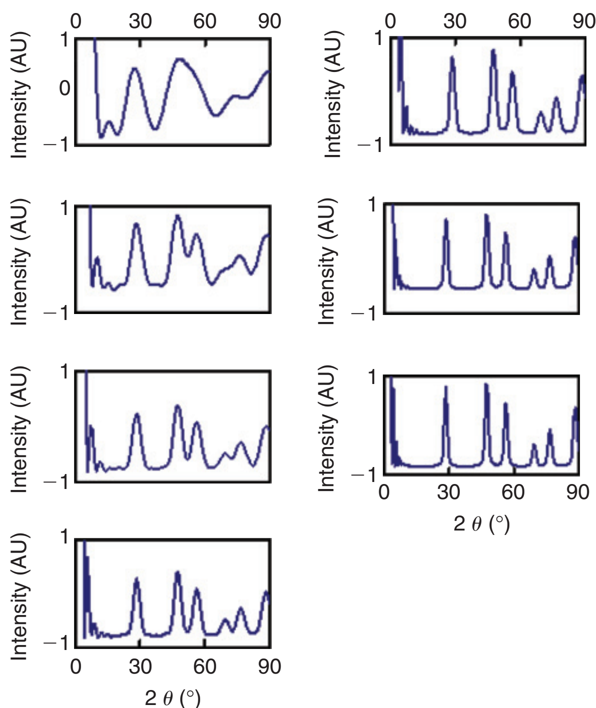

Figure 1.53 Calculated scattering top to bottom (left) for 1.0, 1.67, 2.15, and 2.9 nm and (right) for 3.7, 5.0, and 6.0 nm diameter clusters using the interatomic spacing of bulk (after Ref. [100]).

for diameters >6 nm since we find very little change in the spectra beyond 6 nm. However, for particles >2.15 nm, scattering from all of the above planes is resolved. Thus the particle size of 2.15 nm among the above discrete set of sizes may represent a demarcation of the transition from amorphous/molecular-like to polycrystalline-like behaviour. There is no experimental study on the size effects or the existence of critical size in silicon in this important size regime (1–4 nm).

1.9.13 Effect of Termination on the Band Gap

The LDA/QMC treatment was also used to predict changes in the colour of the emitted light upon attaching additional molecules such as methyl and ammonia groups to nanocrystals. The results of their QMC simulations of chemical doping were in excellent agreement with physical experiments. For the doping by —NH_2 and —CH_3 groups, the positions of the Si atoms are very similar to the pure H-terminations and the corresponding shifts are small, of the order 0.1 Å. The HOMO–LUMO absorption edge is calculated to be 3.5 ± 0.3, 3.25 ± 0.3, and 3.55 ± 0.3 eV for H-, N-, and C-termination, respectively [22]. The N-termination down-shifted the band gap by 0.25 eV relative to the H-termination, whereas C-termination shifted it by a smaller amount to the blue side. The large ± uncertainty is due to a common correction, but the relative shifts between the three terminations are more accurate. As expected, the emission spectra correlate with the size of the band gap. The N atom, in the Si—N termination, is of negative valence, i.e. a Lewis base that acts as a hole trap. Trapping the Si hole onto the N site may cause recombination outside the Si material. On the other hand C repels the hole, and recombination continues to be on Si sites. N-termination may be viewed as softening of the confinement. The C-termination, on the other hand, results in a slight strengthening of the confinement.

1.10 Device applications

Ultrasmall silicon nanoparticle may offer applications in fields as diverse as paint, electronics, and medicine. The impetus of the applications stems from the fact that we can produce commercial amounts of high-quality nanoparticles at low cost. Advanced device concepts that utilize nanomaterial put stringent conditions on the quality of the particles and the matrix in which they are embedded, as well as on the uniformity of the particle density distribution. To date, there is no significant advance in the use of nano-silicon to structure devices; due either to particle size non-uniformity, low yield, distribution non-uniformity, matrix inhomogeniety, or interference with the flow of the silicon conventional complementary metal oxide semiconductor (CMOS) device fabrication process. For instance, procedures for production of nanoparticles such as CVD, aerosol, plasma assisted, ion implantation, and laser ablation do not produce nanoparticles or dots of constant size and shape. The difficulties are compounded in methods that produce particles *in situ*, such as CVD, plasma assisted, or ion implantation. These involve high-temperature anneals that may interfere with the standard CMOS fabrication process flow, which may result in non-uniform layering and defects. On the other hand, because they

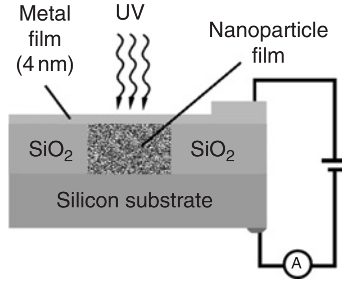

Figure 1.54 A schematic of a Schottky-like diode constructed by sandwiching a layer of silicon nanoparticles between a silicon substrate electrode and a metal film electrode.

involve growth on a surface, CVD or plasma-assisted processes produce nonspherical structures (hemispherical), which compromise quality. Finally, in *in situ* procedures, temperature conditions for narrow size distributions are often diabolic with conditions for uniform density distributions, which hamper independent control of either.

The procedure we developed alleviates these difficulties. We achieved production of commercial amounts of constant size/shape, highly fluorescent ultrasmall silicon nanoparticles and their reconstitution from colloids into high-quality thin films that coat surfaces or solid objects. For flat surfaces, such as silicon wafers, we use spin. For solid conducting objects or flexible surfaces we use electrodeposition, an analogous process to electroplating. Electrodeposition is also used to produce composite films/coating of silicon nanoparticles and metal. A spray system using a volatile solvent has been constructed and is used to produce thin coatings on conducting as well as nonconducting surfaces. In particular, using spin coating, the *ex situ* the particles can be incorporated at room temperature in advanced devices with uniform distributions, at the right depth and thickness, while maintaining the standard CMOS fabrication process.

We describe here some of the applications we have already demonstrated.

1.10.1 Photoelectric Conversion/UV Photodetector

We constructed UV photodetectors with ultrasmall uniform 1.0 nm Si nanoparticles as the active medium [101,102]. The detectors exhibit high-responsivity and good-visible blindness. We start with a device-quality *p*-type Si(100) wafer of resistivity 4–8 Ω cm ($\sim 10^{15}$ dopants/cm^3) as the substrate. A 500 nm SiO_2 layer is then grown on the substrate, and a single pattern or an array of patterns is etched using HF/NH_4F. We immerse the wafer in a suspension of nanoparticles in alcohol, positively biased relative to a platinum electrode. A current is established, depositing nanoparticles in the hole/array, producing a film $\sim$500 nm thick with an active circular region, 5 mm in diameter. Semitransparent gold of 4 nm thickness is deposited on the nanoparticle film. Gold pads $\sim$300 nm thick are subsequently deposited on the semitransparent gold layer and on the back of the substrate, to provide means to bias the device. Details of the device structure are shown in Fig. 1.54.

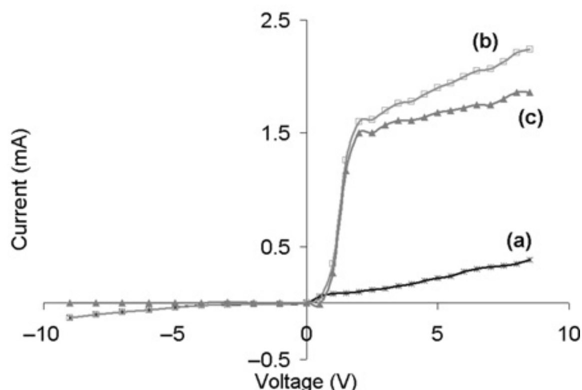

Figure 1.55 I–V spectra at room temperature: (a) taken under dark condition, (b) taken under light irradiation. It shows a high visibility regular step structure, for negative tip biasing, and (c) the difference of (b) and (a)

We focused the Hg lamp of a fluorescence microscope at powers of 1–3 mW on the active film region to a spot 2 mm in diameter. Figure 1.55a–c shows the I–V spectra of the detector under dark conditions, irradiation with 2 mW at 365 nm, and the difference. The ratio of the forward to reverse current under irradiation at 2.0 V bias is 160, compared to 7 in darkness. Upon irradiation, the forward current is enhanced by a factor of ~20, while the reverse current is essentially unaffected. The device is operating as a photoconductor in series with a diode junction. The semi-transparent-gold/nanoparticle-film forms a quasi-ohmic photoconducting medium, while the nanoparticle-film/silicon-substrate forms the diode-like behaviour. The open circuit impedance of the device under darkness is a few MΩ. We attribute the photoconduction to UV-generated hole states in the silicon nanoparticle film. At 1.0 V bias, the responsivity is ~150 mA/W, which is nearly an order of magnitude improvement to some commercial thin film UV detectors. The responsivity rises to a local maximum of 750 mA/W at ~2.0 V. The gain, $G = 2.6$ at 2.0 V, is calculated from $R = \lambda \cdot \eta \cdot e \cdot G/h \cdot c$, where λ is the wavelength of the incident radiation, h is Planck's constant, e is the electronic charge, c is the light speed, η is the quantum efficiency (number of electrons generated per incident photons), assuming $\eta \sim 1$. The response of single particles under injection of electrons from an STM is shown in Fig. 1.49.

The device has good visible blindness. At 390 nm irradiance, the gain or responsivity drops to 0.3 of that at 355 nm, and drops to 0.036 at 560 nm. We also tested the detector at shorter UV wavelengths than 355 nm, namely at 200, 250, and 300 nm using a Xe lamp. These measurements yielded a gain of 1, 22, and 7, respectively, as compared to 2.6 at 365 nm. Due to propagation problems of deep UV, the gain at 200 nm is underestimated.

We find that device performance depends among other factors on the quality of the nanoparticle film (uniformity, thickness, packing). Other devices tested showed wider saturation regions (plateau), with softer rises. Responsivities ranging from 80 to 180 mA/W at 1.0 V, and 350–750 at 2.0 V have been measured for different deposition conditions.

1.10.2 Metal Oxide Silicon Memory Devices

We constructed metal oxide silicon (MOS) capacitors with ultrasmall uniform Si nanoparticles sandwiched in the oxide for potential applications in memory devices [103]. Fig. 1.56 gives the schematic of the MOS capacitor device. We start with boron-doped substrate at a level of $\sim 1.05 \times 10^{15}\,\mathrm{cm}^{-3}$. Thin SiO_2 tunnel oxide ($\sim$4.2 nm) was grown by dry oxidation at 800°C for 20 min. The thickness and uniformity were characterized by UV ellipsometry. We have then spread colloidal Si nanoparticles in isopropanol (IPA) on the oxide using spin coating. Standard variable speed photoresist spinner was utilized. We used AFM along with ellipsometry to test uniformity and to estimate the film thickness. At high concentration we get thick films with a mound at the edge of the wafer (the edge effect). AFM image of an edge as high as 20 nm just inside the bare wafer rim allowed us to estimate the film thickness. We used several particle colloids with decreasing molar concentration that were prepared by successive dilutions. Uniform distribution of nanoparticles is achieved near the central part of the wafer. We measured a combined particle/oxide film thickness of 8, 6, 5, and 4.5 nm. The latter indicates the approach to sub-monolayer coatings. After spin coating the particles, $a \sim 10$ nm SiO_2 cap layer was deposited by low-pressure CVD at 400°C. Thin ($\sim$500 nm) Al films were then deposited. The wafers were patterned and capacitors were defined and chemically etched. Al contact on the wafer backside was deposited. Finally the devices were annealed in N_2/H_2 at 450°C for 10 min. Control MOS capacitors containing no particles were also fabricated using the same procedure.

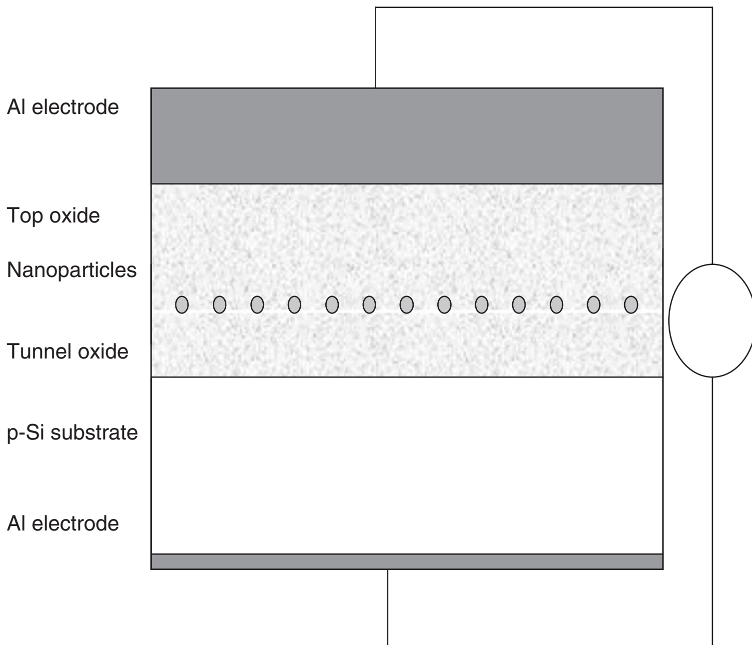

Figure 1.56 Schematic of a nanocapacitor with nanoparticles embedded in the silicon oxide.

We analysed the charge storage in the MOS devices using capacitance–voltage (CV) at a frequency of 1 MHz. Figure 1.57 presents the CV hysteresis curves for an active device with nanoparticles, control device, and an ideal simulated CV curve that assumes no interface states. The control device has a slight counter-clockwise hysteresis of ~0.01 V; however, the active device now has a clockwise hysteresis of ~0.8 V. The hysteresis curve shows that the positive half voltage of the cycle involves charging while the negative half involves erasing, with the residual hysteresis pointing to an asymmetric write/erase process. The negligible hysteresis in control samples indicates that the effect is nanoparticle related. We estimated by integration of the CV, a particle density of $\sim 5 \times 10^{11}\,cm^{-2}$ in the active device, which corresponds to an interparticle spacing of ~14 nm. We also measured the hysteresis loops for a diluted sample that shows a drop in the shift from ~0.8 to ~0.2 V. Based on these measurements, the dynamic range for voltage shift available could grow from about 1 V for 15 nm spacing to several volts for an interspacing of 5 nm. We also compared the control and active CV curves with an ideal simulated CV (Fig. 1.57) of a control structure that assumes no interface states. The similarity in control, active, and simulated curves, in regards to the absence of kinks, humps, or differences in slope point to the fact that the active device charging is most likely due to charging of the nanoparticles and not to charging of interface states between the nanoparticles and the adjacent SiO_2, or at interface states between the tunnelling oxide and capping oxide, or between the Si substrate and tunnelling oxide. Moreover, the use of H_2/N_2 annealing greatly reduces the interface state density at the Si/SiO_2 interface, and at the silicon nanoparticle and the adjacent oxide interface [5].

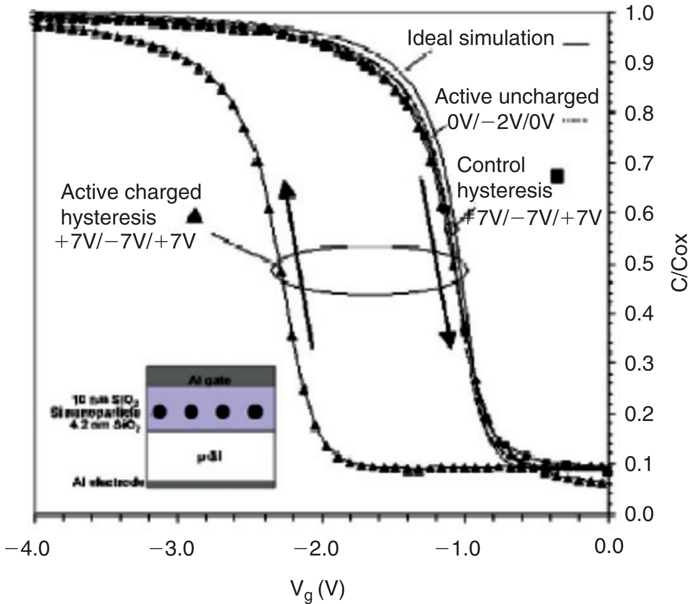

Figure 1.57 *C-V* hysteresis loops of control (squares) and active (triangles) devices with hole charge density $4.8 \times 10^{11}\,cm^{-2}$. The ideal simulated *C-V* (dark solid). The inset shows a schematic of the MOS capacitor system. C is the capacitance of the device. Cox is the maximum capacitance or the capacitance of the oxide.

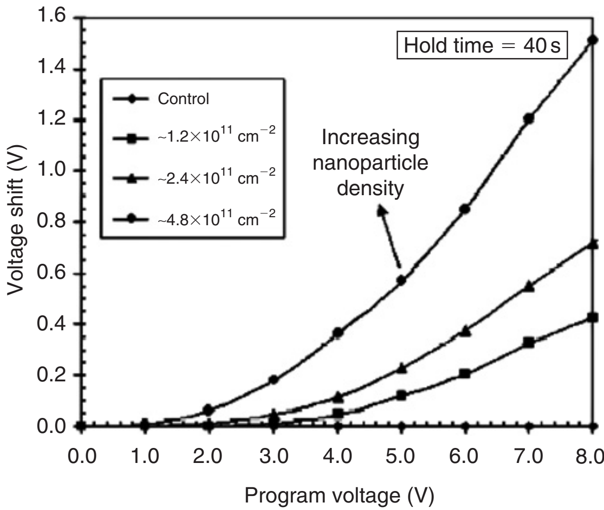

Figure 1.58 Shift in voltage as a function of the program voltage for a control device (zero nanoparticles), and active devices with varying nanoparticle densities, achieved by the dilution of the starting nanoparticle solution. After programming with 7.0 V, we estimate stored hole charge densities of 4.8×10^{11}cm^2, 2.4×10^{11}, and $\sim 1.2 \times 10^{11}$, and negligible charging for the control device.

Measurements of the programming characteristics were performed by applying a positive programming voltage for ~40 s, and then sweeping forward and backward between 0 and $V_o = -2$ V (uncharged conditions). The shift in the threshold voltage was recorded as a function of the programming voltage. Figure 1.58 shows the programming characteristics of devices with different densities of nanoparticles along that of the control device. As can be seen in the figure, the shift in threshold voltage correlates with the density of nanoparticles in a near linear behaviour, whereas negligible charging occurs for the control device over the entire range of programming voltages.

We have tested the charge retention characteristics of several devices. We first obtained a quasi-neutral curve at the much reduced voltage range of 0 to −0.8 V, and then programmed the device at +7 V for ~40 s. We analysed the threshold voltage shift as a function of time while holding voltage at −0.8 V. An example is given in Fig. 1.59 in a logarithmic scale. Based on the slope of the response we extrapolate to a retention time of several years.

1.10.3 Biophotonic Imaging

We examined the staining or uptake/permeability by cancer as well as healthy cells. We demonstrated that particles stain kidney, breast, stem, and bacteria cells (see Figs. 1.60 and 1.61). Si particles of ~1 nm diameter are functionalized with carboxyl groups. Kidney cells are incubated in a suspension of the particles. The cells are imaged and the emission spectra are recorded by two-photon near-infrared fs imaging at 800 nm [104]. The result shows that staining renders the otherwise invisible cells visible, and the fluorescence from the stained cells is characteristic of the particle's blue emission. Three-dimensional sectioning shows that the particles indeed penetrated into the cell. We also

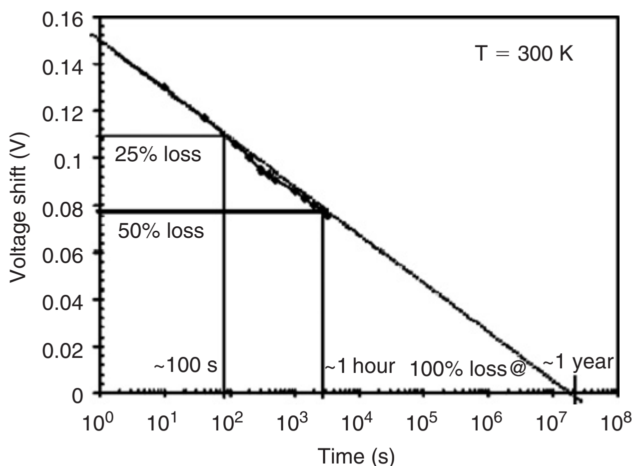

Figure 1.59 The charge retention on a log plot. By extrapolation, the device should retain charge for a year (after Ref. [103]).

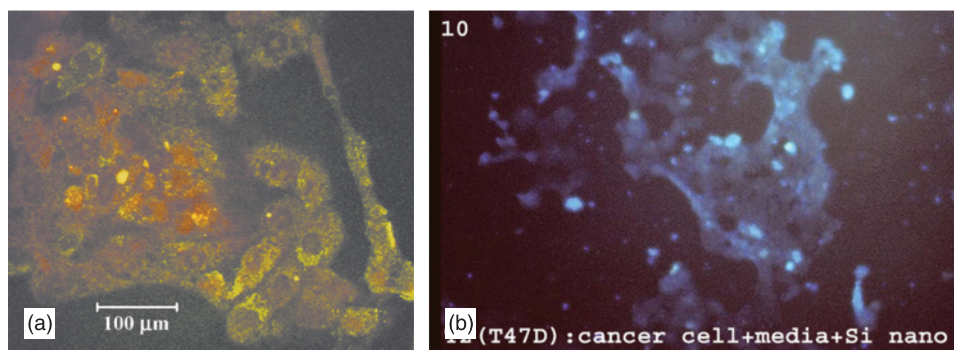

Figure 1.60 Staining cells with Si nanoparticles (a) kidney cells imaged by laser scanning microscopy and (b) breast cancer cells imaged by a fluorescence microscope (after Ref. [104]).

incubated breast cancer cells as well as bacteria in particles prepared in water. In this case the particles aggregate into 20–30 nm clusters. TEM of the aggregate is shown in Fig. 1.61b. TEM images of the bacteria show the clusters (Fig. 1.61a). Fluorescence microscopy of cancer cells shows the particles (Fig. 1.60b).

1.10.4 Amperometric Detection

Heavily doped ($\rho < 0.005\,\Omega$-cm) n-type silicon wafers were used to support Si_{29} particles as sensing elements for electrochemical detection. The wafer with its surface containing the native oxide was cleaned with ethanol, isopropanol, and de-ionized water. The wafer surface was covered with a mask to achieve a working area of about $1\,mm \times 1\,mm$. A drop of 0.1 ml of the Si_{29} colloid was spread on the wafer surface, and the sample was incubated for 10 h and then rinsed with de-ionized water. The

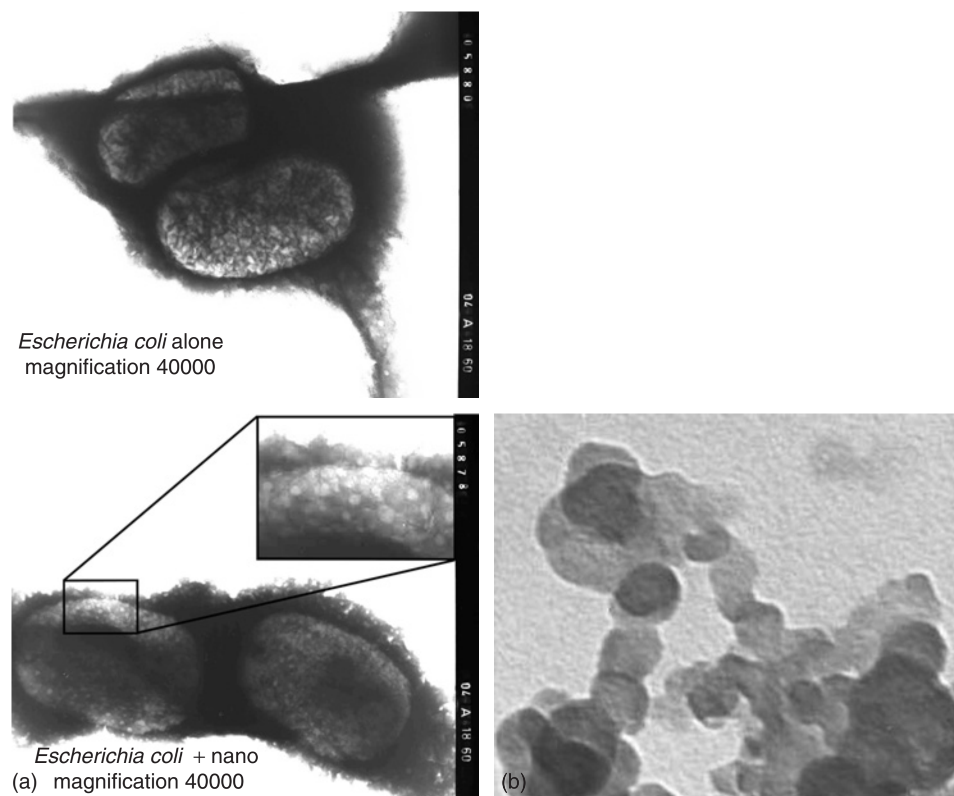

Figure 1.61 *Escherichia coli* bacteria incubated in silicon nanoparticles and imaged by TEM with particle clusters (see inset) (after Ref. [104]).

particle-covered wafer was used as the working electrode in a typical three-electrode electrochemical cell for cyclic voltammetry measurements [105]. An Ag/AgCl electrode was used as the reference electrode. Substances to be detected using the Si_{29}—Si electrode were dissolved in a phosphate buffer solution (PBS) and introduced into the cell for measurements. Note that the bare silicon wafer showed no electrochemical response to the substances used in this work up to a potential as high as 1.6 V.

We demonstrated the amperometric electrochemical detection of several biomedically important substances using the newly discovered ultrasmall (1 nm) Si_{29} particles that were deposited on a silicon wafer. The particle-covered (Si_{29}—Si) electrode showed amperometric responses to dopamine, hydrogen peroxide, and glucose. We have obtained exclusive detection of dopamine and glucose in the presence of interfering species within the physiological concentration ranges of these substances. The observed reversibility in the electrode's response indicates negligible electrode poisoning due to adsorption of reaction intermediates. The Si_{29} particle, thus behaves as a catalyst, bringing about the oxidation reaction in a potential range, in which no electrochemical reactions of the substances occur with the bare silicon wafer. A comparison between the glucose detection characteristics of the Si_{29}—Si electrode and a glucose oxidase-immobilized electrode shows an

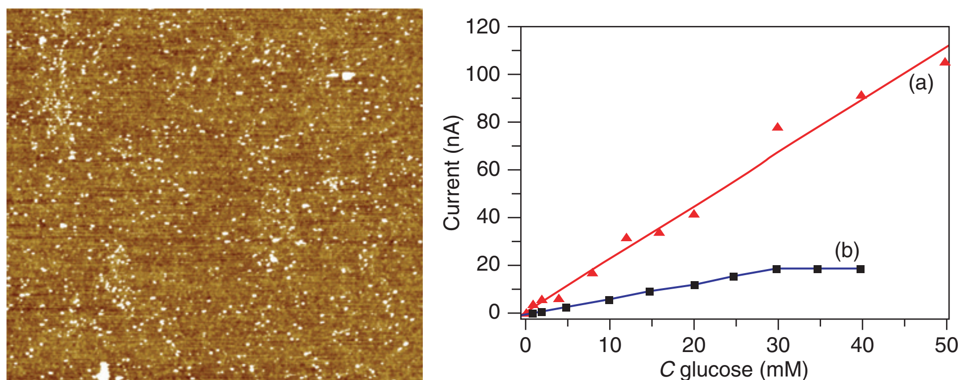

Figure 1.62 A comparison of the glucose responses of the Si_{29}—Si electrode and the GOx electrode. (a) AFM image (2 μm × 2 μm) of the surface of the Si_{29}—Si electrode made using the water-based Si_{29} particles. The 1 nm particles appear as individual bright spots. (b) Amperometric responses of the Si_{29}—Si electrode and the GOx electrode to glucose. The current values were measured at a potential of 0.7 V for both electrodes (after Ref. [105]).

enhanced amperometric response of the particle electrode, which also shows significantly larger rate constants for electron transfer and material conversion processes (see Fig. 1.62). Our results reveal several advantages of using the Si_{29} particle as an inexpensive material in bioelectronics, including effective signal transduction or energy harvest and device miniaturization.

1.10.5 Nanosolar Cell

We integrated ultrathin films of luminescent Si particles in photovoltaic Si solar cells. We use a polycrystalline Si cell made by BP Solarex. The cell is *p*-type Si with a thin *n*-type Si layer on top. It is coated with a very thin Si_3N_4, a coating that filters out heat generating infrared radiation. The units are sheets with dimensions 12 × 12 cm. Across each sheet there are 50 grid lines and two thicker buss lines (made of a silver/copper alloy), which are designed to collect the current generated over the entire sheet. The topography of the cell was analysed by a surface texture measuring system (Dectak); it shows that the thickness of the silver/copper grid lines is larger than that of the nitride coating. Thus the laid-down nanocrystal film is not electrically isolated from the underlying device.

We improved performance by converting the otherwise damaging UV light with high quantum conversion into visible light as well as electron-hole pairs [106]. We enhanced the power performance of commercial polycrystalline Si solar cells by ~60–70% in the UV (see Fig. 1.63). Films of 2.85 nm red luminescent Si particles also provide additional enhancement of 7–13% in the visible due to a confinement band gap of 2.15 eV. We also show that the films exhibit long-term stability under UV irradiation. The good performance is likely related to the fact that the film was applied directly without a glass or polymer matrix and that the particles are identical which leads to self-assembly of closely packed films. These characteristics provide

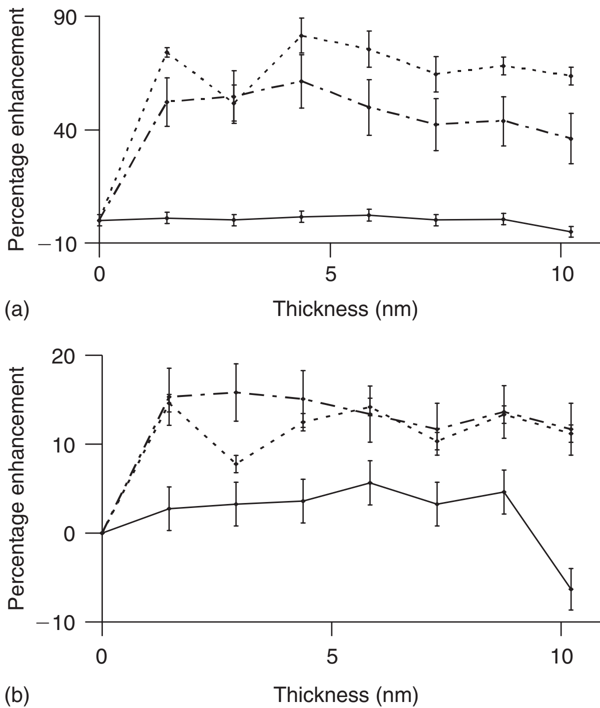

Figure 1.63 The response of a polycrystalline Si solar cell with a film of 1 nm nanoparticles on top. (a) The enhancement in open circuit voltage. (b) The enhancement in short circuit current. The enhancements are measured versus the thickness of the nanofilm for excitation at (dot) 254 nm, (dash) 310 nm, and (solid) 550–630 nm. Error bars represent the standard error in measurement (after Ref. [106]).

efficient charge separation and transport, and better optical confinement and index of refraction matching as well as reduced scattering or fluorescence losses with enhanced anti-reflection. Research is ongoing to dope the particles with Ge or Er to tune their band gap. Finally, although there are no measurements, we expect this film to be effective for crystalline Si cells as well.

1.10.6 Nanoink Printing

Inks commonly employed in ink-jet technologies utilizes either dyes or pigments as colourants. The capability of ink-jet printing technology to controllably dispense a wide range of materials of interest to MEMS and BioMEMS fabrication has been demonstrated. Materials dispensed include optical polymers, solders, thermoplastics, light-emitting polymers, semiconductor and conducting particles, biologically active fluids, and precursors for chemical synthesis. In addition to the wide range of suitable materials, the inherently data-driven nature of ink-jet printing technology makes it highly suited for both prototyping and flexible manufacturing. We printed

patterns (physical incorporation) out of these silicon nanoparticles with ink-jet equipment on silicon substrates. A cartridge of an aqueous organic solvent in which the colloid of alkyl-functionalized particles are dissolved operates as a fluorescent nano-silicon-organic ink. We can use this method to produce electronic and other devices such as displays based on ink-jet deposition of the silicon nanoparticles. Hybrid gold–silicon nanoparticle inks were developed using thiol linkages.

1.10.7 Single Electron Transistor Devices

Si nanoparticles may be incorporated into a gate stack of a MOSFET nanotransistor. The composite system (MOSFET + particles) offers advanced nanotechnology in terms of room temperature, single electronics and non-volatile flash memory cell – a nanoflash cell. The use of crystalline Si 5–10 nm in size is currently under development in a number of industrial laboratories such as Lucent, Motorola, Intel for this application in 0.18 or 0.12 μm technology. We envision producing isolated cells using 25–50 nm line-rules with 1 nm scale nanoparticles. The proposed gate stack, which can be incorporated into 25–50 nm gate length MOSFETs, consists of a 2 nm thick gate oxide, a layer of isolated (ideally a regular array) nanoparticles (with a density of $5\text{–}20 \times 10^{11}\,\text{cm}^{-2}$), surrounded by a CVD deposited dielectric 5 nm thick, and a polysilicon control electrode. The nanoflash cell operates by biasing the control electrode relative to the source-drain and channel to permit quantum mechanical tunnelling to the channel inversion layer. Ideally, the charge stored on the nanoparticle screens the control electrode and shifts the threshold voltage of the MOSFET by an amount related to the particle size. Subsequent read operations at a fixed control voltage will sample an exponentially reduced drain current corresponding to the shift in threshold indicating a logical "0". The efficacy of using nanoparticles this small ($\sim$1 nm) must be investigated, however. Naively, because of the small diameter, a 1–10 V shift of the threshold voltage in a 25 nm gate length MOSFET would be anticipated after a WRITE operation, but experience with 1 nm thick films indicates that the dielectric and electrical properties of the nanoparticle will be substantially different from bulk.

1.11 Conclusion

Processes for converting bulk silicon into ultrasmall nanoparticles have been developed. Particles are nearly spherical and classify into a small number of sizes of 1.0 nm (Si_{29}), 1.67 nm (Si_{123}), 2.15 nm, and 2.9 nm that are ultrabright blue, green, yellow, and red luminescent particles, respectively. This is unlike the abundance spectrum of uncapped clusters Si_n which has been known to exhibit no discrete magic numbers for $n > 20$. The particles can be formed into colloids, crystals, films, and collimated beams for unique applications in the electronics, optoelectronics and biomedical industries. Unlike bulk Si, an optically dull indirect gap material, ultrasmall Si nanoparticles are spectacularly fluorescent material, exceeding the level of common dyes, produce stimulated emission with collimated beams, and exhibit harmonic generation.

Because our silicon nanoparticles have novel optical as well as electronic and chemical properties, such coatings provide the component or application with new functions. Our current research is focusing on several features in this regard. For instance a thin coating of the nanoparticles on a silicon solar cell extends its operation and efficiency into the UV, prolongs its working lifetime because it also minimizes the damage that the UV would otherwise induce, and acts as an anti-reflecting coating. A thin film also provides sensitive photodetection or filtering in the UV. Ultrathin coatings embedded in nanomemory capacitors have enhanced their memory characteristics. A thin coating of the nanoparticles on highly doped silicon may act as an amperometric sensor for biomedically important substances.

The availability of ultrabright silicon structures is particularly revolutionary. Unlike bulk silicon, which is spectacularly inefficient at emitting light, there are specific silicon configurations (particles) that form, at very low cost without resort to either the costly lithographic or epitaxial techniques, within a discrete family that is spectacularly efficient at emitting light in RGB colours. Light-emitting Si devices could eventually result in a new generation of Si chips and extend the functionality of Si technology from microelectronics into optoelectronics, and biophotonics. Single electronics for consumer electronics, charge-based nanomemory devices, nano-transistors, switches, displays, sensors and assays, fluorescent labelling, laser on a chip, optical interconnect, etc.

Finally, there have been signatures of silicon nanoparticles in a wide range of astrophysical environment in terms of extended red emission (ERE) or in terms of the more recent blue extended emission [107–110]. The red component was first detected in the Red Rectangle, but it was subsequently detected in many kinds of objects such as reflection nebula, planetary nebula, HII regions, halos of galaxies, and in the diffuse interstellar medium (DISM), indicating a general spectroscopic feature. The blue component so far has been observed in the Red Rectangle proto planetary nebula by Vijh *et al.* [108].

Acknowledgements

The authors acknowledge the State of Illinois Grant IDCCA No. 00-49106, the US NSF Grant BES-0118053, the US DOE Grant DEFG02-ER9645439, NIH Grant RR03155, Motorola, and the University of Illinois at Urbana-Champaign as well as the NSF Grants DMR-0102668 and DMR-0121361.

REFERENCES

1. L.T. Canham, *Appl. Phys. Lett.* **57**, 1046 (1990).
2. A.G. Cullis, L.T. Canham and P. Calcott, *J. Appl. Phys.* **82**, 909 (1997).
3. O. Akcakir, J. Therrien, G. Belomoin, N. Barry, E. Gratton and M. Nayfeh, *Appl. Phys. Lett.* **76**, 1857 (2000).
4. M.H. Nayfeh, E. Rogozhina and L. Mitas, *Synthesis, Functionalization, and Surface Treatment of Nanoparticles*, Ed. M.-I. Baratron (American Scientific Publishers, Valenc 2002); M.H. Nayfeh,

J. Therrien, G. Belomoin, O. Akcakir, N. Barry and E. Gratton, *Proc. Mat. Soc.* **638**, F9.5.1-12 (2000); J. Therrien, G. Belomoin and M.H. Nayfeh, *Proc. Mat. Soc.* **582**, 11.4.1-6 (1999); D.A. Eckhoff, J.N. Stuart, J.D.B. Sutin, Jonathan V. Sweedler, E. Gratton, *J. Chem. Phys.* **125**, 081103 (2006); E.V. Rogozhina, D.A. Eckhoff, E. Gratton, P.V. Braun *J. Mat. Chem.* **16**, 1421 (2006); D.A. Eckhoff, *J. Sutin*, R.M. Clegg, E. Gratton, E.V. Rogozhina, P.V. Braun, *J. Phys. Chem. B* **109**, 19786 (2005).

5. M. Nayfeh, O. Akcakir, J. Therrien, Z. Yamani, N. Barry, W. Yu and E. Gratton, *Appl. Phys. Lett.* **75**, 4112 (1999).
6. M.H. Nayfeh, N. Barry, J. Therrien, O. Akcakir, E. Gratton and G. Belomoin, *Appl. Phys. Lett.* **78**, 1131 (2001).
7. M.H. Nayfeh, S. Rao, N. Barry, J. Therrien, G. Belomoin, A. Smith and S. Chaieb, *Appl. Phys. Lett.* **80**, 121 (2002).
8. M.H. Nayfeh, O. Akcakir, G. Belomoin, N. Barry, J. Therrien and E. Gratton, *Appl. Phys. Lett.* **77**, 4086 (2000).
9. J. Therrien, G. Belomoin and M. Nayfeh, *Appl. Phys. Lett.* **77**, 1668 (2000).
10. G. Belomoin, J. Therrien and M. Nayfeh, *Appl. Phys. Lett.* **77**, 779 (2000).
11. H. Thompson, Z. Yamani, L. AbuHassan, O. Gurdal and M.H. Nayfeh, *Appl. Phys. Lett.* **73**, 841 (1998); W.H. Thompson, Z. Yamani, L.H. Abuhassan, J.E. Greene and M. Nayfeh, *J. Appl. Phys.* **80**, 5415 (1996).
12. E. Rogozhina, G. Belomoin, J. Therrien, P. Braun and M.H. Nayfeh, *Appl. Phys. Lett.* **78**, 3711 (2001).
13. L. Mitas, J. Therrien, G. Belomoin and M.H. Nayfeh, *Appl. Phys. Lett.* **78**, 1918 (2001).
14. Z. Yamani, H. Thompson, L. AbuHassan and M.H. Nayfeh, *Appl. Phys. Lett.* **70**, 3404 (1997).
15. D. Andsager, J. Hilliard, J.M. Hetrick, L.H. AbuHassan, M. Plisch and M.H. Nayfeh, *J. Appl. Phys.* **74**, 4783 (1993).
16. Z. Yamani, S. Ashhab, A. Nayfeh and M.H. Nayfeh, *J. Appl. Phys.* **83**, 3929 (1998).
17. M. Nayfeh, N. Rigakis and Z. Yamani, *Phys. Rev. B* **56**, 2079 (1997); *MRS* **486**, 243 (1998).
18. G. Belomoin, J. Therrien, A. Smith, S. Rao, R. Twesten, S. Chaieb, L. Wagner, L. Mitas and M. Nayfeh, *Appl. Phys. Lett.* **80**, 841 (2002).
19. Z. Yamani, N. Rigakis and M.H. Nayfeh, *Appl. Phys Lett.* **72**, 2556 (1998); Z. Yamani, O. Gurdal, A. Alaql and M. Nayfeh, *J. Appl. Phys.* **85**, 8050 (1999); M.H. Nayfeh, Z. Yamani, O. Gurdal and A. Alaql, *Proc. Mat. Res. Soc.* **536**, 191 (1998); Z. Yamani, A. Alaql, J. Therrien, O. Nayfeh and M. Nayfeh, *Appl. Phys. Lett.* **74**, 3483 (1999).
20. G. Belomoin, J. Therrien, A. Smith, S. Rao, S. Chaieb and M.H. Nayfeh, *Appl. Phys. Lett.* **80**, 841 (2002).
21. A Smith, G. Belomoin, M.H. Nayfeh and T. Nayfeh, *Chem. Phys. Lett.* **372**, 415 (2003).
22. G. Belomoin, E. Rogozhina, J. Therrien, P.V. Braun, L. Abuhassan, M.H. Nayfeh, L. Wagner, L. Mitas, *Phys. Rev. B* **65**, 193406 (2002).
23. S.H. Risbud, L.-C. Liu and J.F. Shackelford, *Appl. Phys. Lett.* **63**, 1648 (1993).
24. M. Fujii, S. Hayashi and K. Yamamoto, *Jpn. J. Appl. Phys.* **30**, 687 (1991).
25. J.G. Zhu, C.W. White, J.D. Budal, S.P. Withrow and Y. Chen, *J. Appl. Phys.* **78**, 4386 (1995).
26. W.A. Saunders, P.C. Sercel, R.B. Lee, H.A. Atwater, K.J. Vahala, R.C. Flagan, E.J. Escorcia-Aparcio, *Appl. Phys. Lett.* **63**, 1549 (1993).
27. T. Yoshida, T. Takeyama, Y. Yamada and K. Mutoh, *Appl. Phys. Lett.* **68**, 1772 (1996).
28. A. Fojtik, H. Weller, S. Fiechter and A. Henglein, *Chem. Phys. Lett.* **134**, 477 (1987).
29. A. Fojtik and A. Henglein, *Chem. Phys. Lett.* **221**, 363 (1994).
30. J.J. Wu and R.C. Flagan, *J. Appl. Phys.* **73**, 407 (1993).
31. H. Takagi, H. Ogawa, Y. Yamazaki, A. Ishizaki and T. Nakagiri, *Appl. Phys. Lett.* **56**, 2379 (1990).
32. R. Okada and S. Iijima, *Appl. Phys. Lett.* **58**, 1662 (1991).
33. D.J. DiMaria, *et al.*, *J. Appl. Phys.* **56**, 401 (1998).
34. S. Berger, L. Schächter and S. Tamir, *Nanostruct. Mater.* **8**, 231 (1997).
35. J.P. Wilcoxon, G.A. Samara and P.N. Provencio, *Phys. Rev. B* **60**, 2704 (1999).
36. A. Uhlir, *Bell. Syst. Technol. J.* **35**, 333 (1956).
37. Y.H. Xie, W.L. Wilson, F.M. Ross, J.A. Mucha, E.A. Fitzgerald, J.M. Macaulay and T.D. Harris, *Appl. Phys. Lett.* **71**, 2403 (1992).
38. R.C. Anderson, R.S. Muller and C.W. Tobias, *J. Electrochem. Soc.* **140**, 1393 (1993).
39. A. Grosman and C. Ortega, *Properties of Porous Silicon*, Ed. L.T. Canham (INSPEC, London, 1997), p.145.

40. R.A. Bley, S.M. Kauzlarich, J.E. Davis and H.W.H. Lee, *Chem. Mater.* **8**, 1881 (1996).
41. J.L. Heinrich, C.L. Curtis, G.M. Credo, K.L. Kavanagh and M.J. Saylor, *Science* **255**, 66 (1992).
42. L. Pavasi, L. Del Negro, C. Mazzoleni, G. Franzo and F. Priolo, *Nature* **408**, 440 (2000); A. Borgensi, A. Sasella, B. Pivas and L. Pavesi, *Solid State Commun.* **87**, 1 (1993).
43. B. Sweryda-Krawiec, T. Cassagneau and J.H. Fendler, *J. Phys. Chem. B* **103**, 9524 (1999).
44. W. Brown, R. Freeman, K. Raghavachari and M. Schulter, *Science* **235**, 860 (1987); L. Bloomfield, R. Freeman and W. Brown, *Phys. Rev. Lett.* **54**, 2246 (1985).
45. K. Raghavachari, *Phase Transit.* **24–26**, 61 (1990).
46. U. Rothlisberger, W. Andreoni and M. Parrinello, *Phys. Rev. Lett.* **72**, 665 (1994); W. Andreoni and G. Pastore, *Phys. Rev. B* **41**, 10243 (1990); U. Rothlisberger, W. Andreoni and P. Ginnozzi, *J. Chem. Phys.* **96**, 1248 (1992).
47. L. Anderson, S. Muruyama and R. Smalley, *Chem. Phys. Lett.* **176**, 348 (1991); H. Kroto, J. Heath, S. O'Brian, R. Curl and R. Smalley, *Nature (London)* **318**, 162 (1985).
48. E.P. Diamandis and T.K. Christopoulos, Eds. *Immunoassays* (Academic Press, New York, 1996); P.G. Issac, Ed. *Protocols for Nucleic Acid Analysis by Nonradioactive Probes* (Humana, Totowa, NJ, 1994); L.J. Kricka, Ed. *Nonisotropic Probing, Blotting, and Sequencing* (Academic Press, New York, 1995).
49. M. Bruchez Jr., M. Morrone, P. Gin, S. Weiss and A.P. Alivisatos, *Science* **281**, 2013 (1998).
50. W. Chan and S. Nie, *Science* **281**, 2016 (1998).
51. J.M. Buriak and M.J. Allen, *J. Am. Chem. Soc.* **120**, 1339 (1998); J.M. Buriak, M.P. Stewart, T.W. Geders, M.J. Allen, H.C. Choi, J. Smith, D. Raftery and L. Canham, *J. Am. Chem. Soc.* **121**, 11491 (1999); J.M. Buriak, *Chem. Commun.* Vol. 12, 1051 (1999).
52. G. Allan, C. Delerue and M. Lannoo, *Phys. Rev. Lett.* **76**, 2961 (1996).
53. E.V. Rogozhina, G.A. Belomoin, M.H. Nayfeh and P.V. Braun, *MRS Conference*, Boston, MA, November 26–30, 2001, Book of Abstracts, W 6.10; E.V. Rogozhina, G.A. Belomoin, J.M. Therrien, M.H. Nayfeh and P. V. Braun, *J. Am. Chem. Soc.* (in preparation).
54. W.F. Bergerson, J.A. Mulder, R.P. Hsung and X.-Y. Zhu, *J. Am. Chem. Soc.* **121**, 454 (1999).
55. A. Taylor and B. De G. Walden, *J. Am. Chem. Soc.* **66**, 842 (1944).
56. A.B. Sieval, A.L. Demirel, J.W.M. Nissink, M.R. Linford, J.H. van der Maas, W.H. De Jeu, H. Zuilhof and E.J.R. Sudhölter, *Langmuir* **14**, 1759 (1998).
57. A.B. Sieval, R. Linke, H. Zuilhof and E.J.R. Sudhölter, *Adv. Mater.* **12**, 1457 (2000).
58. I. Fleming, "Organic silicon silicon", in D. Barton and W.D. Ollis, *Comprehensive Organic Chemistry*, Ed. D.N. Jones Part 3 (Pergamon Press, London, 1979), p. 578.
59. I. Flemming, "Organic silicon chemistry", in D. Barton, W.D. Ollis, *Comprehensive Organic Chemistry*, Vol. 3 (Pergamon Press 1979), p. 566; I. Flemming, "Organic silicon chemistry" in D. Barton, W.D. Ollis, Comprehensive Organic Chemistry, Vol. 3 (Pergamon Press, London, 1979), p. 563; M.E. Havill, I. Joffe, H.W. Post, *J. Org. Chem.* **13**, 280 (1948).
60. J.R. Heath, *Science* **258**, 1131 (1992).
61. Ch.-S. Yang, R.A. Bley, S.M. Kauzlarich, H.W.H. Lee and G.R. Delgado, *J. Am. Chem. Soc.* **121**, 5191 (1999).
62. R.K. Baldwin, K.A. Pettigrew, J.C. Garno, P.P. Power, G. Liu and S.M. Kauzlarich, *J. Am. Chem. Soc.* **124**, 1150 (2002).
63. J.D. Holmes, K.J. Ziegler, R.C. Doty, L.E. Pell, K.P. Johnston and B.A. Korgel, *J. Am. Chem. Soc.* **123**, 3743 (2001).
64. A. Smith, Z. Yamani, J. Turner, S. Habbal, S. Granick and M.H. Nayfeh, *Phys. Rev. B* **72**, 205307 (2005).
65. L. Abuhassan, M. Khanlary, P. Townsend and M.H. Nayfeh, *J. Appl. Phys.* **97**, 104314 (2005).
66. S. Chaieb, M. Nayfeh and A. Smith, *Appl. Phys. Lett.* **87**, 062104-1-3 (2005).
67. A Smith, S. Chaieb, A. Alaql, M. Alsalhi and M.H. Nayfeh, *J. Nanosci. Nanotech.* **2**, 471 (2002).
68. H. Koyama and P. Fauchet, *Appl. Phys. Lett.* **73**, 3259 (1998); H. Koyama, L. Tsybeskov and P. Fauchet, *J. Lumines.* **80**, 99 (1999); H. Koyama and P. Fauchet, *J. Appl. Phys.* **87**, 1788 (2000); H. Koyama and P. Fauchet, *MRS* **536**, 9 (1999).
69. P. Hohenberg and W. Kohn, *Phys. Rev.* **136**, B864 (1964); W. Kohn and L.J. Sham, *Phys. Rev.* **140**, A1133 (1965).
70. M.S. Hybertsen and S.G. Louie, *Phys. Rev. Lett.* **55**, 1418 (1985); *Phys. Rev.* B **34**, 5390 (1986).
71. M. Rohlfing and S.G. Louie, *Phys. Rev. Lett.* **80**, 3320 (1998); J.C. Gorssman, M. Rohlfing, L. Mitas, S.G. Louie and M.L. Cohen, *Phys. Rev. Lett.* **86**, 472 (2001).

72. D.M. Ceperley and M.H. Kalos, "Quantum many-body problems", in *Monte Carlo Methods in Statistical Physics*, Ed. K. Binder (Springer, Berlin, 1979) pp. 145–194; K.E. Schmidt and D.M. Ceperley, "Monte Carlo techniques for quantum fluids, solids and droplets", in *Monte Carlo Methods in Statistical Physics II*, Ed. K. Binder (Springer, Berlin, 1984), pp. 279–355.
73. B.L. Hammond, W.A. Lester Jr. and P.J. Reynolds, *Monte Carlo Methods in Ab Initio Quantum Chemistry* (World Scientific, Singapore, 1994).
74. J.B. Anderson, "Exact quantum chemistry by Monte Carlo methods", in *Understanding Chemical Reactivity*, Ed. S.R. Langhoff (Kluwer, Dordrecht, 1995), pp. 1–45.
75. D.M. Ceperley and L. Mitas, "Quantum Monte Carlo methods in chemistry", in Advances Chemical Physics, Vol. XCIII, Ed. I. Prigogine and S.A. Rice, (Wiley, New York, 1996), pp. 1–38.
76. M.W.C. Foulkes, L. Mitas, R.J. Needs and G. Rajagopal, *Rev. Mod. Phys.* **73**, 33 (2001).
77. See M. Ernzerhof, J.P. Perdew and K. Burke, "Density functionals: Where do they come from, why do they work"?, in *Topics in Current Chemistry*, Vol. 180, Ed. R.F. Nalewajski (Springer, Berlin, 1996).
78. J.C. Grossman and L. Mitas, *Phys. Rev. Lett.* **79**, 4353 (1997).
79. T. Torelli and L. Mitas, *Phys. Rev. Lett.* **85**, 1702 (2000).
80. L. Mitas and R.M. Martin, *Phys. Rev. Lett.* **72**, 2438 (1994).
81. J.C. Grossman and L. Mitas, *Phys. Rev. Lett.* **74**, 1323 (1995); L. Mitas, J.C. Grossman, I. Stich and J. Tobik, *Phys. Rev. Lett.* **84**, 1479 (2000).
82. J.C. Grossman, L. Mitas and K. Raghavachari, *Phys. Rev. Lett.* **75**, 3870 (1995).
83. S. Hirata, M. Head-Gordon and R.J. Bartlett, *J. Chem. Phys.* **111**, 10774 (1999); I. Vasiliev, S. Ogut and J.R. Chelikowsky, *Phys. Rev. Lett.* **86**, 1813 (2001).
84. M.F. Jarrold, *J. Phys. Chem.* **99**, 11 (1995); A.A. Shvartsburg, M.F. Jarrold, B. Liu, Z.-Y. Lu, C.-Z. Wang and K.-M. Ho, *Phys. Rev. Lett.* **81**, 4616 (1998).
85. M. Nayfeh, O. Rogozhina and L. Mitas, "Silicon nanoparticles: next generation of ultrasensitive fluorescent nano-organic markers", in *Synthesis, Functionalization and Surface Treatment of Nanoparticles*, Ed. M.-I. Baraton (American Scientific Publishers, Los Angeles, CA, 2003).
86. G. Belomoin, E. Rogozhina, J. Therrien, P.V. Braun, L. Abuhassan, M.H. Nayfeh, L. Wagner and L. Mitas, *Phys. Rev. B* **65**, 193406 (2002).
87. L. Mitas, J. Therrien, G. Belomoin and M.H. Nayfeh, *Appl. Phys. Lett.* **78**,1918 (2001).
88. H. Hiura, T. Miyazaki and T. Kanayama, *Phys. Rev. Lett.* **86**, 1733 (2001).
89. M. Ohara, K. Koyasu, A. Nakajima and K. Kaya, *Chem. Phys. Lett.* **371**, 490 (2003).
90. P. Sen and L. Mitas, *Phys. Rev. B* **68**, 155404 (2003).
91. L.W. Wang and A. Zunger, *Phys. Rev. Lett.* **73**, 1039 (1994); R. Tsu, L. Ioriatti, J. Harvey, H. Shen and R. Lux, *Mater. Res. Soc. Symp. Proc.* **283**, 437 (1993); G. Allan, C. Delerue, M. Lannoo and E. Martin, *Phys. Rev. B* **52**, 11982 (1995); D.R. Penn, *Phys. Rev.* **128**, 2093 (1962).
92. L. Wagner, A. Puzder, A.Williamson, Z. Helms, J. Grossman, L. Mitas, G. Galli and M. Nayfeh, *The Structure and Stokes Shift of Hydrogenated Silicon Nanoclusters*, cond-mat/0403226 (2004).
93. P. Puzder, A. Williamson, F. Reboredo and G. Galli, *Phys. Rev. Lett.* **91**, 157405 (2003); E. Draeger, A.J. Grossman, A. Williamson and G. Galli, *Phys. Stat. Sol. B* **239**, 11 (2003); *Phys. Rev. Lett.* **90**, 167402 (2003).
94. S. Rao, J. Sutin, R. Clegg, E. Gratton, S. Habbal, M.H. Nayfeh, A. Tsolakidis and R. Martin, *Phys. Rev. B* **69**, 205319 (2004); A. Tsolakidis and R. Martin, *Phys. Rev. B* **71**, 125319 (2005).
95. S. Rao, K. Mantey, J. Therrien, A. Smith and M.H. Nayfeh (to be published).
96. M. Rosenbauer, S. Finkbeiner, E. Bustarret, J. Weber and M. Stutzmann, *Phys. Rev. B* **51**, 10539 (1995); P. Calcott, K. Nash, L. Canham, M. Kane and D. Brumhead, *J. Phys. Condens Mat.* **5**, L91 (1993); T. Lee and J. Kanicki, *Appl. Phys. Lett.* **73**, 3866 (1998); V. Volodin, M. Effremov, V. Gritsenko and S. Kochubei, *Appl. Phys. Lett.* **73**, 1212 (1998); J. Diener, M. Ben-Chorin, D. Kovalev, S. Ganichev and F. Koch, *Phys. Rev. B* **52**, R8617 (1995).
97. M.S. Hybertsen, *Phys. Rev. Lett.* **72**, 1514 (1994).
98. D. Sundholm, *Nano Lett.* **3**, 847 (2003); D. Sundholm, *Phys. Chem. Chem. Phys.* **6**, 2044 (2004); O. Lehtonen and D. Sundholm, *Phys. Rev. B* **72**, 085424 (2005).
99. J.P. Proot, C. Delerue and G. Allan, *Appl. Phys. Lett.* **61**, 1948 (1992).
100. G. Belomoin, M. Alsalhi, A. Al Aql and M.H. Nayfeh, *J. Appl. Phys.* **95**, 5019 (2004).
101. O. Nayfeh, S. Rao, A. Smith, J. Therrien and M. Nayfeh, *Photon. Technol. Lett. IEEE* **16**, 1927 (2004).
102. M. Nayfeh, S. Rao, O. Nayfeh, A. Smith and J. Therrien, IEEE Trans. Nanotech. **4**, 660 (2005).

103. O. Nayfeh, D. Antoniadis, K. Mantey and M.H. Nayfeh, *Appl. Phys. Lett.* **90**, 153105 (2007); *Nanoelectronics Workshop*, (Honolulu, HI, 2006).
104. W. Yu, H. Malkawai, M. Hassouna, L. Abuhassan, K. Alshraideh and M.H. Nayfeh, *J. Microsc.* (submitted).
105. Y. Gang, K. Mantey, M.H. Nayfeh and S. Yau, *Appl. Phys. Lett.* **89**, 243901 (2006).
106. M. Stupka, M. Nayfeh, M. Alsalhi and T. AlSaud (*MRS* Boston, Warrendale, PA 2005).
107. G. Ledoux, M. Ehbrecht and O. Guillois, *A&A* **333**, L39 (1998); A.N. Witt, K. Gordon and D.G. Furton, *APJL* **501**, L111 (1998); G. Ledoux, O. Guillois, F. Huisken, B. Kohn, D. Porterat and C. Reynaud, *A&A* **377**, 707 (2001).
108. U.P. Vijh, A.N Witt and K.D. Gordon, *ApJ* **606**, L65 (2004).
109. S. Rifai Habbal, M. Arndt, M. Nayfeh, J. Arnaud, J. Johnson and S. Hegwer, *Astrophys. J.* **592**, L87 (2003).
110. M.H. Nayfeh, S. Habbal and S. Rao, *Astrophys. J.* **621**, L121 (2005).
111. D.A. Eckhoff, J.N. Stuart, J.D.B. Sutin, Jonathan V. Sweedler, E. Gratton, *J. Chem. Phys.* **125**, 081103 (2006).
112. E.V. Rogozhina, D.A. Eckhoff, E. Gratton, P.V. Braun, *J. Mat. Chem.* **16**, 1421 (2006).
113. D.A. Eckhoff, J. Sutin, R.M. Clegg, E. Gratton, E.V. Rogozhina, P.V. Braun, *J. Phys. Chem.* **B109**, 19786 (2005).

CHAPTER TWO

Cluster Assembled Silicon Networks

P. Mélinon, X. Blase, A. San Miguel and A. Perez

Contents

2.1 Introduction 80
2.2 Isolated Silicon Clusters 81
  2.2.1 Small Si_N Clusters ($N < 14$) 81
  2.2.2 Medium-Sized Clusters ($20 < N < 100$): the Case of Si_{33} 82
  2.2.3 Large Clusters ($N > 100$) 82
2.3 Si-Cluster-Assembled Materials 83
  2.3.1 Introduction 83
  2.3.2 Si-Cluster-Assembled Films 83
  2.3.3 Bulk Si-Cluster-Assembled Materials from Fullerenes : Clathrate Phases 97
2.4 Conclusion 110
Acknowledgements 110
References 111

Abstract

In this chapter we briefly review the structure and properties of various nanostructured silicon phases built from small silicon nanoclusters: Si-clusters assembled films prepared by deposition of low-energy cage-like nanoclusters preformed in the gas phase (low-energy cluster beam deposition (LECBD) technique), and silicon clathrates exhibiting a crystalline structure formed by the periodic arrangement of Si dodecahedral fullerenes (Si_{20}, Si_{24}, Si_{28}) sharing faces. In the first case, two specific features relevant to the size effect (presence of odd-member rings and packing structure) are at the origin of the original properties of the corresponding cluster films. The clathrate structure compared to the diamond structure contains a large fraction of pentagons (up to 86%) and is amenable to a large doping by intercalation of guest atoms at the centre of the cage, leading to attractive properties such as superconductivity, electronic band-gap opening, high hardness, etc. Novel silicon–carbon phases obtained by deposition of mixed SiC clusters are also reported.

Laboratoire de Physique de la Matière Condensée et Nanostructures, Université Claude Bernard Lyon 1 and CNRS, F-69622 Villeurbanne, France.

Nanosilicon
9780080445281

Copyright © 2007. Elsevier Ltd.
All rights reserved.

2.1 Introduction

The properties of silicon clusters are ordinarily catalogued with respect to their size, at least in the regime below 10 nm. Earlier works devoted to crystalline, para crystalline, porous or amorphous silicon structures suggested a phase transition close to 2–3 nm [1]. Silicon networks or silicon clusters are crystalline beyond this size and amorphous-like below. This frontier remained unexplained until 1990. During the past two decades, the renewed interest for the electronic structure of small silicon clusters has partially solved the origin of this transition. For large clusters, the features are similar to those in the crystalline phase: silicon is four-fold hybridized and the compact (111) and (100) surfaces are reconstructed [2,3] (see Fig. 2.1). Near 5 nm, the lattice exhibits deviations from the bulk spacing [4]. Below 2–3 nm, the surface reconstruction plays a dominant role, involving the breakdown of the lattice symmetry (amorphous-like transition). Below 1 nm, because of Laplace's law (melting temperature decreases as $1/D$, D being the diameter), clusters become liquid at room temperature, leading to a close packed structure as predicted in the standard Si phase diagram.

In the first part of this chapter (Section 2.2), we briefly review the structure and properties of small isolated Si clusters. We then report, in Section 2.3.2, on some selected properties of Si-cluster-assembled films in the 1.5–3 nm regime where close packed structures do not take place. In this regime, the key parameter is the Si-rings parity, as governed by the surface reconstruction (see Fig. 2.1). In Section 2.3.3, well-crystallized 3D phases composed of face-sharing Si_N ($N = 20, 24, 28$) clusters, the clathrates, will be presented and their properties analysed. We will show in particular that, upon doping by intercalation, unique properties such as stabilization under pressure, superconductivity or band-gap opening can be obtained.

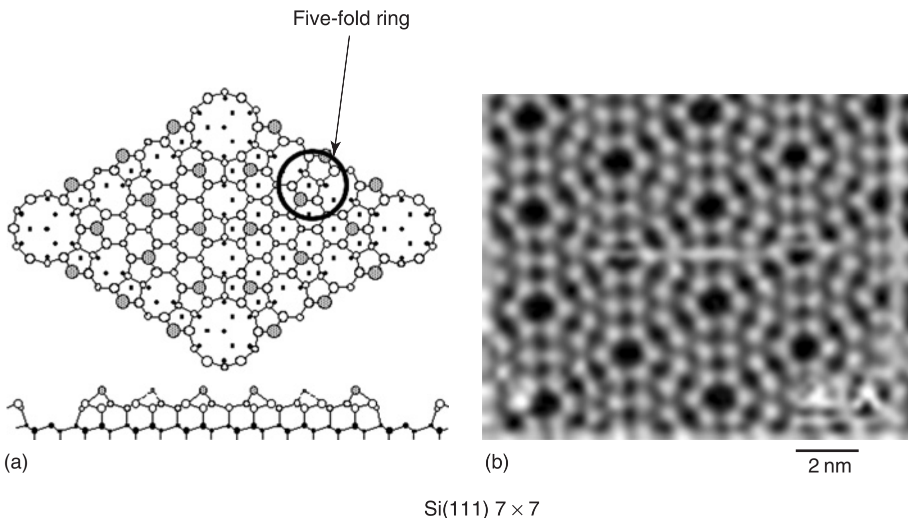

Figure 2.1 (a) Top and side views of the Si(111) 7×7 reconstruction as described by the dimer-adatom stacking fault model of Takayanagi *et al*. [3]. The circle shows a pentagonal ring. (b) Empty-state AFM images of the same reconstructed surface obtained by Erlandsson *et al*. [2] (Reproduced with permission, Ref. [3] Copyright 1985. AVS The Science & Technology Society, Ref. [2] Copyright 1996 APS).

2.2 Isolated silicon clusters

Two families of isolated silicon clusters can be synthesized: hydrogen-free silicon clusters and passivated clusters. The passivation with atomic hydrogen leaves the crystalline Si skeleton unchanged. As a consequence, the electronic properties are readily understood in terms of quantum size effects (opening of the band gap) and exciton confinement. We discuss here the second family where passivation does not take place. From an experimental point of view, such clusters need ultra high vacuum (UHV) and/or encapsulation in inert matrices. A change of the structural properties of silicon clusters is expected once the size is reduced to the nanometer scale. All predictions suggest that open structures become energetically more stable than close packed ones below a critical size of about 30–100 atoms [5]. Close packed structures are experimentally confirmed up to 14 atoms [6,7] and are corroborated by *ab initio* calculations [8] or empirical methods [9]. Photo-ionization spectra, reactivity trends [10] and gas phase chromatography [11] support the idea of a transition in medium-sized clusters near 30 atoms. Concerning the electronic properties, and as compared to passiv-ated structures, the band gap can vary strongly with size, compacity and isomeric shape. Several attempts to relate band gap and compacity, or band gap and size have been proposed, but the results remain elusive [12].

2.2.1 Small Si_N Clusters ($N < 14$)

Using surface plasmon polariton-enhanced Raman spectroscopy, Honea *et al.* [6] have studied small Si clusters isolated in an inert matrix. Si_4, Si_6 and Si_7 show sharp well-defined vibrations assigned to a planar rhombus, a distorted octahedron and a pentagonal bipyramid, respectively (see Fig. 2.2). For these latter two atoms are

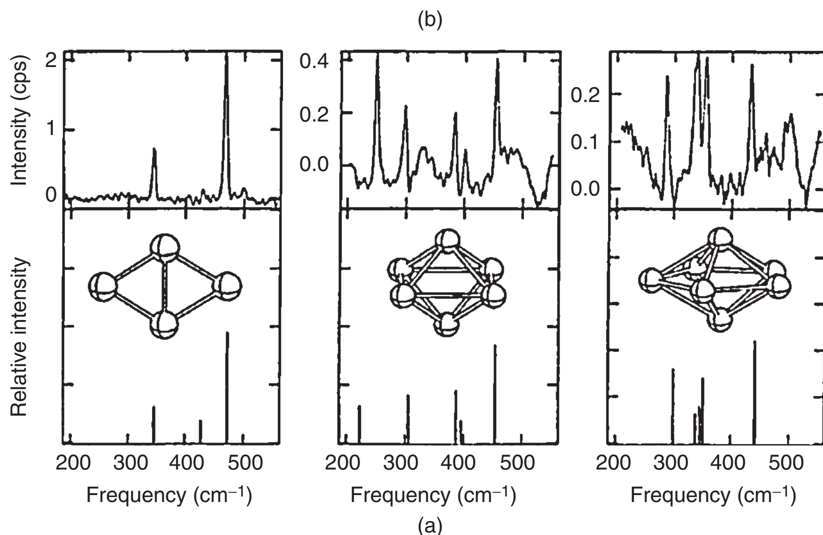

Figure 2.2 Measured Raman spectra of three clusters (Si_4, Si_6 and Si_9). The structure is deduced from the agreement between calculation (a) and experiment (b) after Honea *et al.* [6] (Reproduced with permission, Copyright 1999 AIP).

five-fold coordinated supporting the closed packed structure idea. The structure depends on the size since all the atoms are located on the surface. Numerous isomer sets are possible since the shift in cohesive energy is weak.

2.2.2 Medium-Sized Clusters ($20 < N < 100$): the Case of Si_{33}

The phase transition near 30 atoms, between open and close packed structure, is not well defined. Contrary to carbon, no magic numbers corresponding to an excess of stability are observed in mass spectra. This indicates that the stability and/or the cohesive energy is not the salient parameter which explains an expected phase transition. However, the experiments have shown that the cluster shape changes from prolate-like to spherical-like near 27 atoms. On the other hand, reactivity of Si_{33}, Si_{39} and Si_{45} [13–15] is particularly low as compared to the bulk phase one. These features are in agreement with a fullerene-like cluster filled by atoms in the inner shells. From this point of view, Si_{33} is the most interesting example and can be considered as the template of the C_{60} fullerene. This cluster is composed by an Si_{28} T_d fullerene with four hexagons and twelve pentagons surrounding a Si_5 tetrahedron cell (Fig. 2.3). The Si_{28} cluster will also be shown to be an important building block of some clathrates as it will be detailed later in this chapter. The position of the Si_5 is not well defined leading to several isomers [13–16]. As mentioned above, this structure does not ensure an excess of stability but the large highest occupied and lowest unoccupied molecular orbital (HOMO–LUMO) separation indicates a low reactivity. From a structural point of view, such structures are characterized by a spherical shape, an over coordination (>4 for a few atoms) and five-fold rings. However most of the atoms keep the tetrahedron structure at short-range order. This tetrahedron structure as observed in the diamond phase is the common signature of the sp^3 hybridization. Figure 2.3 displays two selected isomers for Si_{33} with a mean coordination ranging between $\bar{N} = 3.6$ and $\bar{N} = 4.2$ much more than the one expected for a diamond phase ($\bar{N} = 3.0$ for 33 atoms).

2.2.3 Large Clusters ($N > 100$)

There is less information on very large clusters as accurate theoretical calculations become enormously difficult. However, with growing size, the diamond phase

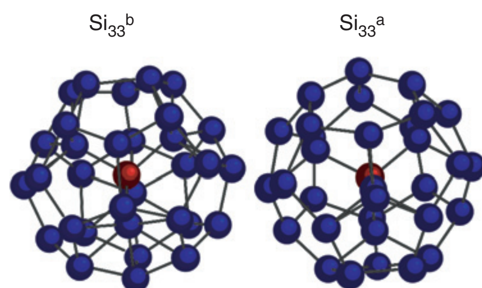

Figure 2.3 Two possible isomers for the Si_{33} structure. Both isomers differ from the position of the Si_5 inside the Si_{28} fullerene cage (Reproduced with permission from Ref. [16]).

becomes the most probable structure and the surface reconstruction observed in the (100) or (111) facets of the crystalline phase are assumed to be valid. The band gap is probably reduced by the Urbach's tail which characterizes the amplitude of the disorder and the density of the dangling bonds. Nevertheless, the band gap width is still larger than the one observed in bulk phase as the indirect band gap of bulk silicon does not survive in the clusters. This is also observed in amorphous silicon where the band gap is about 1.8–1.9 eV as compared to the one in Si diamond phase (1.17 eV).

2.3 Si-Cluster-assembled materials

2.3.1 Introduction

Two kinds of materials can be synthesized. In the first one, films are obtained from the deposition of preformed clusters with adjustable sizes. In the soft landing regime, the ballistic deposition and the spread in cluster sizes lead to the lack of medium- and long-range order. The so-called memory effect ensures a short-range order limited to the cluster itself. Such films characterized by a very low density due to pores are analysed with the same framework developed for amorphous silicon. In the second, a crystalline phase named clathrate [17] can be obtained through the 3D periodic arrangement of selected Si fullerenes sharing their common faces. Such structures are prepared from a precursor namely XSi_2, X being a metal. The two types of Si-cluster-assembled materials will be discussed respectively in Sections 2.3.2 and 2.3.3.

2.3.2 Si-Cluster-Assembled Films

2.3.2.1 Gas-Phase Synthesis of Si_N Clusters: Experimental Methods

Silicon clusters are generated in a standard laser vapourization source as schematically described in the Fig. 2.4. An Nd:YAG laser (532 nm, 10 Hz) is used to create a high temperature plasma from a nearly undoped silicon wafer target (resistivity $\rho > 10^3\,\Omega\,\mathrm{cm}$) [18]. The quenching of the plasma by a pulsed high pressure helium burst (high purity 99,9999%) insures the cluster growth in the source chamber until the cluster-carrier gas mixture is expanded through a conical nozzle. The cluster size distribution is studied using a reflectron time of flight (TOF) mass spectrometer sets perpendicular to the incoming cluster beam. For that purpose, nascent ions and/or photo ionized neutral clusters are analysed in the spectrometer. Anion, cation and neutral species give roughly the same abundance spectra except the magic sequence numbers. We denote that contrary to carbon, magic numbers are not the signature of an excess of thermodynamic stability. The gain in cohesive energy remains small except for the smallest sizes ($N < 10$ atoms) [19]. Mean cluster size is mainly controlled by the helium pressure and the laser intensity. Figure 2.5 displays a size distribution observed in the TOF spectrometer. As depicted in the insert, oxygen and hydrogen pollution are weakly present and may be neglected. The size distribution has more or less a Gaussian shape with a FWMH of about $<N>$, $<N>$ being the mean size.

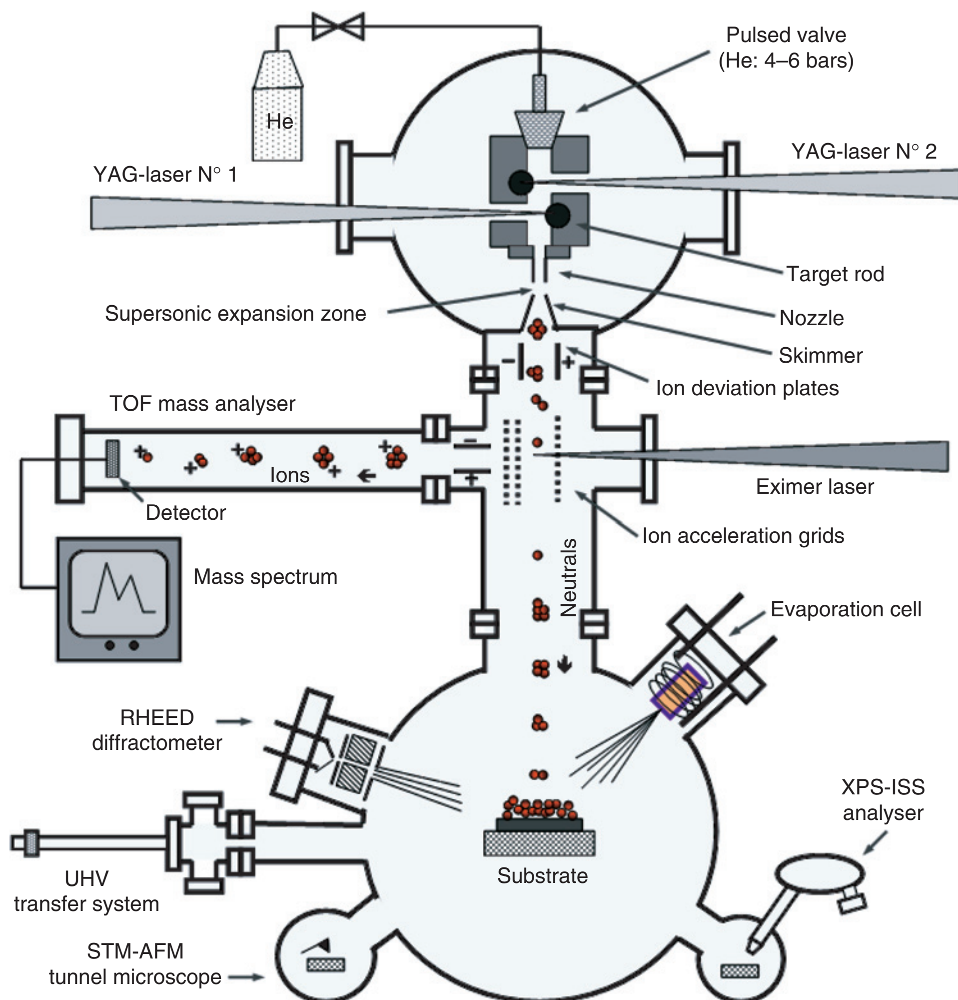

Figure 2.4 Schematic view of the cluster generator based on a combined laser vapourization/inert gas condensation source, associated to a TOF mass spectrometer for the studies of free clusters and a UHV-deposition chamber for cluster-assembled film preparations. The source can operate with one or two independent laser/target arrangements for the production of pure clusters as well as mixed clusters. Some characterization techniques of the films are available *in situ* in UHV: RHEED diffractometry, STM-AFM near field microscopy, XPS-ISS spectrometry. A UHV-transfer system is used for sample transfers to *ex situ* equipments. An electron-beam evaporator *in situ* in UHV is used for co-deposition experiments to produce films of clusters embedded in various media.

The obtained free clusters can be deposited following different techniques. In this general context, the low-energy cluster beam deposition (LECBD) technique extensively developed in the past 20 years has demonstrated its unique potentialities to prepare nanostructured thin films with original properties [20]. The technique consists in deposition of low-energy nanoclusters preformed in the gas phase on various substrates in controlled conditions. In the low-energy regime characteristic

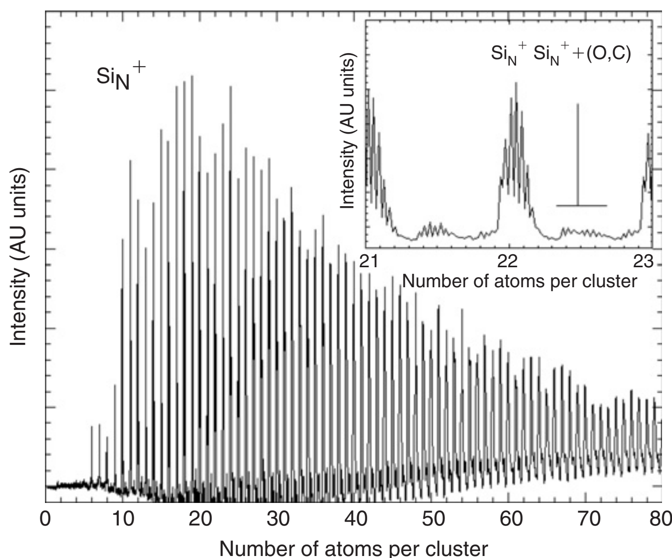

Figure 2.5 Mass abundance spectrum of silicon clusters produced using a combined laser vapourization – rare gas condensation source. The insert gives a detail of the spectrum. The resolution is high enough to separate the combination between Si isotopes. The presence of oxygen and carbon is weak enough to be neglected. Note that the simulation of this spectrum using a multimodal Poisson law fits perfectly this curve. This underlines that such clusters are hydrogen free. Incorporation of hydrogen in the gas source changes drastically the distribution of the peaks.

of LECBD experiments, clusters are not fragmented upon impact on the substrate leading to the formation of cluster-assembled films which retain the original properties of the incident-free clusters. A typical experimental set-up for the preparation of cluster-assembled films by LECBD is presented in Fig. 2.4. Free cluster analysis in the TOF mass spectrometer prior to deposition (see Fig. 2.4) is an important stage in LECBD experiments, especially to control the nature of the elementary bricks which are used in a second stage to grow films. At this last stage, neutral-free clusters, having the very low energy gained in the supersonic expansion at the exit of the source are deposited on substrates in UHV to grow films. Since neutral species are only deposited, nascent ions are electrostatically deviated from the beam axis. UHV conditions are really necessary, especially in the case of Si-cluster films because of the highly reactive nature of such nanostructured/ nanoporous materials. Therefore, cluster films are studied without any air transfer. Samples are directly analysed in the deposition chamber or transferred through a portative UHV suitcase into other devices. Silicon clusters are deposited on silver-coated silicon wafers prepared *in situ*. Auger and photoemission spectroscopies are obtained *in situ*. Si K-edge X-ray absorption spectra (EXAFS) were also recorded. Alternatively, *ex situ* experiments were also performed after coating the cluster-film by LiF. These experiments include Raman SERS (surface enhanced Raman spectroscopy), absorption spectroscopy (IR, visible and near UV) and HRTEM (high resolution transmission electron microscopy).

2.3.2.2 Structure and Morphology

The nucleation and growth process characteristic of the LECBD films have been extensively studied in the past 10 years, experimentally as well as theoretically, especially to allow the control of the specific nanostructured morphologies of the cluster-assembled films and the resulting properties. A comprehensive review article on the subject of LECBD-film formation was published by P. Jensen in 1999 [21], with a kinetic Monte Carlo model: the DDA model (Deposition–Diffusion–Aggregation) well suited for the simulations of cluster-assembled nanostructure morphologies obtained from deposited clusters in the LECBD regime, taking into account of all the elementary processes which take place: cluster impact, supported cluster diffusion, cluster–cluster coalescence. First of all, it is clearly demonstrated from experimental observations on various types of cluster deposits: metallic clusters [21–23], or carbon [24,25], silicon [26] and mixed SiC clusters [27], and molecular dynamics simulations in the case of metallic clusters [22,28] or carbon clusters [29,30] depositions that low-energy clusters (kinetic energy per atom < 1 eV) are not fragmented upon impact on the substrate. Depending on the cluster-substrate interaction related with the nature of both systems and the deposition conditions, clusters can diffuse more or less on the surface. Consequently, for deposited thicknesses lower than the 2D-percolation threshold of the film, isolated supported cluster [22] or cluster-assembled islands [22,27] can be observed in the cases of non-diffusing or diffusing clusters, respectively. Note that the supported nanostructures from clusters presented in Fig. 2.6 are randomly distributed since they are formed after trapping at nucleation sites of the surface (i.e. defects). When the deposited thicknesses increase above the 2D-percolation threshold, nanostructured thick films formed by the random stacking of incident free-clusters are obtained.

Note that the highly nanoporous character of such cluster-assembled materials leads to a reduced density which is generally not higher than 50–60% of the corresponding bulk material's density. Moreover, it appears that under certain deposition conditions the coalescence effects between adjacent clusters are limited leading to cluster-film morphologies resulting from a random stacking process of incident-free clusters. In this case, incident-free clusters act as building blocks on a nanometer scale to form nanostructured thin films which retain their intrinsic properties. Such a process is the most important feature of the low-energy cluster deposition method to produce novel nanostructured materials with unique properties. Note that the experimental results reported above are concerned with clusters of rather high melting temperature materials deposited on substrates at rather low temperature (i.e. room temperature). However, in the cases of low melting temperature materials (i.e. Bi-clusters) [31] or/and high substrate temperatures, strong cluster–cluster coalescence effects can be observed leading to the formation of larger supported particles which could loss the memory of the original free-cluster structures and properties.

Microscopy patterns reveal an inhomogeneous structure with a collection of small grains ranging in the nanoscale (Fig. 2.7).

The inner structure observed by direct imaging or by electron diffraction appears amorphous like. The density of the films is about 50–70% times the one observed in crystalline phase that supports a stacking of silicon nano grains with a lot of voids and cracks. The LECBD strongly differs from other deposition methods (direct

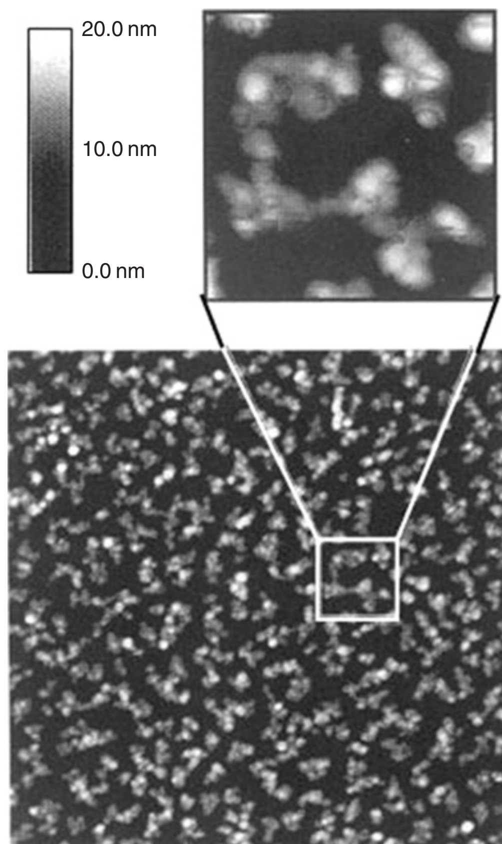

Figure 2.6 TMAFM image (2000 nm × 2000 nm) of a SiC-cluster film deposited on HOPG-graphite substrate at room temperature. The characteristic morphology of ramified islands with cluster-assembled branches is observed as well as in inset (300 nm × 300 nm) with the corresponding height scale.

evaporation, chemical vapour deposition ...). In these latter cases, films are nearly homogeneous. The most common model is the continuous random network (CRN) model where bond and dihedral angle distortions affect the tetrahedral diamond structure. In addition, strong constraints into the network are partially released by introducing some defects such as odd-membered rings, dangling bonds or few over coordinated atoms (coordination > 4). In this way, Si-cluster-assembled films can be compared with porous silicon structure having the same primitive bricks. Nevertheless, Si-cluster-assembled films are hydrogen free while porous structures present a large hydrogen content (up to 120% and more). Si K-edge NEXAFS data (near extended X-ray absorption fine structure) do not report Si—O bonding in Si-cluster-assembled films. Locally ordered structures are observed from EXAFS oscillations and their analysis through the standard procedure [32]. Figure 2.8 displays the pseudo radial distribution obtained for the Si-cluster-assembled films (Fig. 2.8b) compared to crystalline phases (diamond Si-2

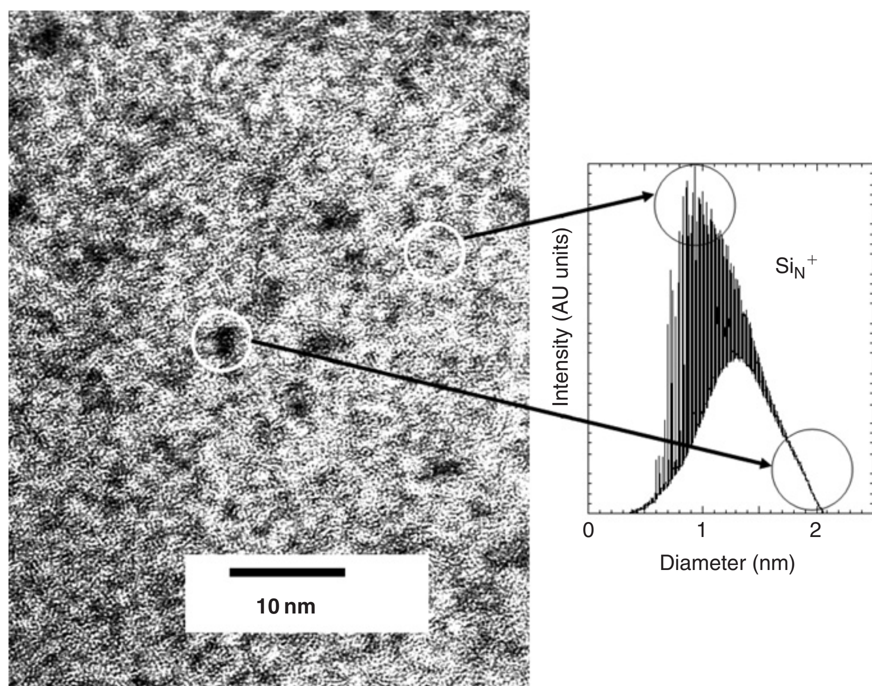

Figure 2.7 HRTEM micrograph obtained with a 20 nm thick Si_{50} film deposited on a a-C coated grid. The corresponding size distribution is drawn as a function of the diameter ($D \simeq <N> 0.34 <N>^{1/3}$, D the diameter in nm, $<N>$ the mean cluster size). The film is continuous beyond the percolation threshold. The dark grains correspond to the tail of the size distribution with well-crystallized particles (beyond 2 nm diameter). These particles present a more intense phase contrast with respect to the small disordered grains (after Ref. [33]).

and clathrate Si-34 phases) (Fig. 2.8a), amorphous structures (a-Si:H)(Fig. 2.8b) and porous silicon (Fig. 2.8c). Locally ordered structures are seen from the second- and third-neighbour shells appearing at 3.4 and 4.1 Å in Si-2 and 3.6 Å for the second shell in Si-34, respectively. This ordering is absent in Si-cluster-assembled films and amorphous structures due to static disorder. Nevertheless, this ordering is more or less present in porous structure as reported by Schuppler *et al.* [34]. In such samples where silicon is passivated with H and/or O, the structure corresponds to the diamond phase. The granular structure remains identical in porous structure and in cluster-assembled films, and densities are yet comparable in both phases assuming the same size for the elementary brick (i.e. the Si cluster). One observes a similar reduction of first neighbour Fourier transform peak intensities at 2 Å in porous, a-Si:H and cluster-assembled films. This is understood by a low coordination in such samples compared to crystalline phases ($\bar{N} = 4$). The under coordination in a-Si:H has already been observed [35,36] and has been assigned [35] to Si—H bonds not detected by EXAFS. However, the reduction of the first shell intensity is larger for porous silicon as compared with cluster-assembled films (sample labelled "Si_N film" has a comparable size for the elementary brick (1–1.5 nm)). The same conclusion

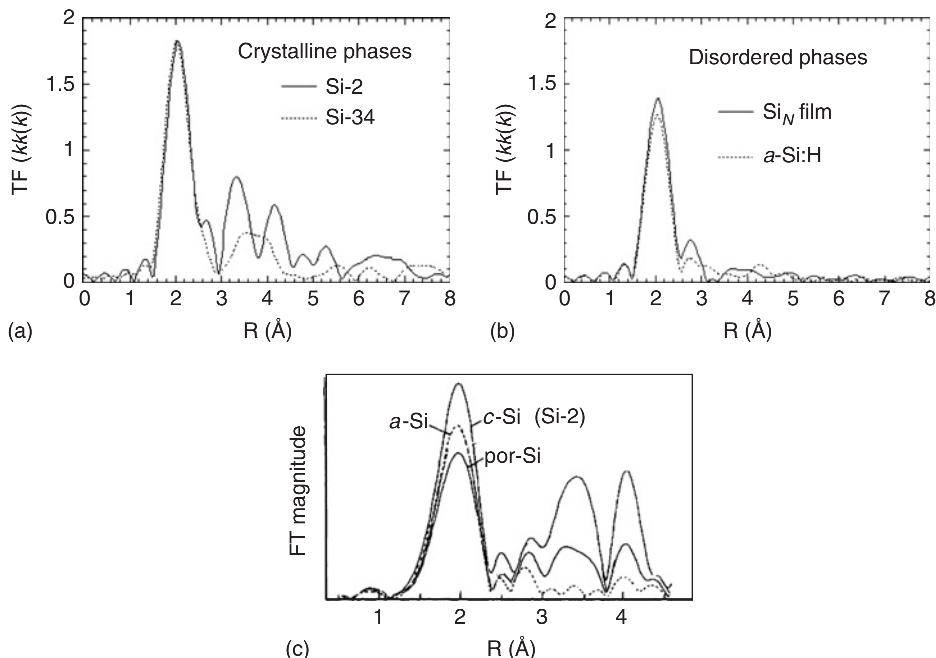

Figure 2.8 (a) Fourier transforms of edge-truncated k multiplied with background substracted data, for diamond phase labelled Si-2 (continuous line) and clathrate phase labelled Si-34 (dashed line). Such curves are assimilated to pseudo radial distributions. The position of the first peak appears at about 2 Å while the true neighbouring distance in Si is 2.35 Å. This difference is due to the uncorrected phase shift. Second and third shells present an artificial low amplitude due to the Debye–Waller factor and multiscattering effects, (b) Fourier transforms of edge-truncated k multiplied, background subtracted data for Si cluster-assembled films Si_N (continuous line) and hydrogenated amorphous silicon labelled a-Si:H (dashed line). For the Si cluster-assembled films, the mean cluster size and the distribution are given in Fig. 2.5. The intensity of the first peak is less than the curves depicted on (a) indicating a reduction of the coordination. Second and third shells are not observed owing to the disorder at medium range. (c) Fourier transforms of edge-truncated k^2 multiplied and background subtracted data for diamond phase labelled c-Si, amorphous silicon labelled (a-Si) and porous silicon labelled por-Si. The original figure is published by Schuppler *et al*. [34]. (Reproduced with permission copyright APS 2004) Following the authors, the cluster size is about 1–1.5 nm close to the one observed in Si cluster-assembled films. The mismatch between the amplitude of the second and third shell observed in (a) and (c) for the diamond phase is due to the k weighting $k\chi(k)$ in (a) and $k^2\chi(k)$ in (c).

is extended to the comparison between Si-cluster-assembled films and a-Si:H. Both phases have a large difference in densities since a-Si:H is nearly homogeneous while Si-cluster-assembled films are strongly inhomogeneous with void cavities. Since *EXAFS* gives the mean coordination averaged for all silicon atoms, we can assume that silicon clusters are partially connected to each others and probably over coordinated with respect to the ideal value of 4 in crystalline phases. This agrees with the over coordination expected in silicon clusters such as Si_{33} cluster for example.

Structural informations are also obtained from reactivity. In this case, cluster films are exposed to oxygen and subsequently studied by (XPS), IR, Raman and XAS spectroscopies. Contrary to passivated porous or amorphous structures, Si-cluster-assembled films are strongly sensitive to oxygen underlining the presence of a lot of lone orbitals at the surface (i.e. dangling bonds). We find the signature of Si—O bonding where Si atom is bonded to one O atom and no more. This strongly differs from the oxidation of a diamond surface which is characterized by the well-known $Si—O_4$ tetrahedron cell as observed in SiO_2 or native oxidation in diamond phase. The oxidation limited to SiO even with high oxygen exposure is related to a possible signature of the Si cluster surface. From a topological point of view, the $Si—O_4$ cell building needs a flat surface for the Si before starting oxidation while spherical clusters just accommodate one oxygen atom per dangling bond. The sub stoichiometry can be also assigned to a different electron transfer between clusters and diamond phase.

2.3.2.3 Electronic Structure

The valence band is sensitive to details of the chemical bonding which can provide information at a length scale much smaller than that addressed by electron diffraction or microscopy. Electronic structure is readily probed by XPS near the Fermi level. The following curves have been corrected for inelastic loss scattering from the raw data. However, the true e-DOS needs a correction for the 3*s*-3*p* cross section modulation. Nevertheless, this correction is not important for the following discussion. Figure 2.9a displays the valence band (e-*DOS*) for the Si-cluster-assembled film compared to Si-2 and Si-34 clathrate. [37] This latter is interesting since clathrate is formed by a triplicate periodic arrangement of Si cages with 87% of five-fold rings (Si-2 being formed by six-fold rings). The positions of the 3*s* and 3*p* bands are affected by the oddness and give us a reference for the five-fold defects in Si-cluster film (we have to remember that five-fold rings are present in small clusters such as Si_{33}). The e-*DOS* in Si-film is similar to the one observed in *a*-Si with a *p*-like, *sp*-like bands merging. This is unambiguously attributed to the five-fold/six-fold rings mixture in our Si-films [37]. Over coordinated atoms may also play a role in the merging. As discussed for EXAFS experiments, it is worthwhile comparing with porous structures where the individual bricks are crystallized in fcc phase. Following Vasquez *et al.* [38], porous structures give similar band features (see Fig. 2.9b) but the merging is rather less pronounced due to the low percentage of odd rings.

2.3.2.4 Vibrational Structure

Raman spectroscopy is a powerful tool for probing the electronic structure through the analysis of the phonon density of states. For very large clusters (D being the diameter of the particle) selection rules holds $qD \sim 1$ and then $q \sim 0$. The Raman intensity for the diamond lattice is:

$$I(\omega) = I(\omega_M) = I(\Gamma'_{25}) \tag{2.1}$$

When the Raman coherence length is comparable with the cluster size, selection rules do not hold. In other words, the phonon wave function is confined into

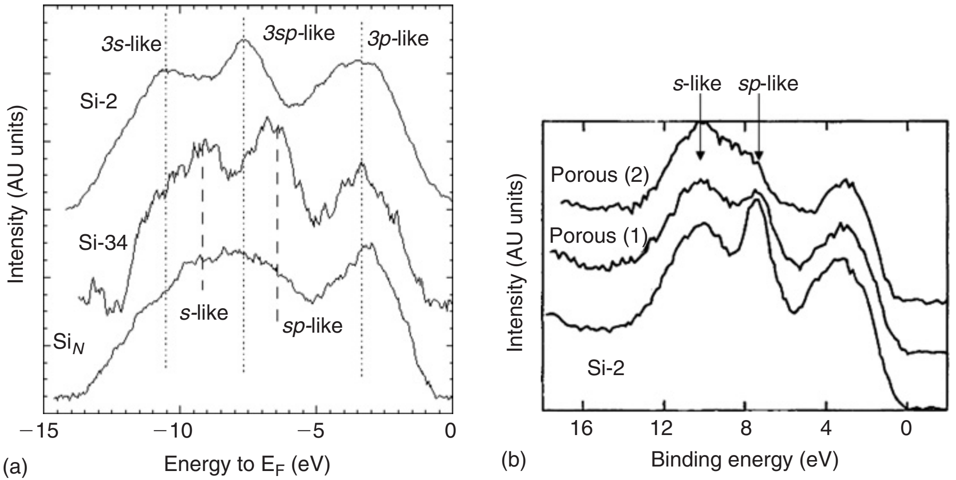

Figure 2.9 (a) Core level observed near the Fermi level by XPS for various Si samples: diamond phase (Si-2), clathrate phase (Si-34), cluster film (Si_N) and nanoporous Si (porous). The bands located near −3 eV are assigned to 3*p*-like states, the bands located near −11 eV are assigned to 3*s*-like states. The band around −7 eV corresponds to the mixing between *s*-like and *p*-like states (hybridization). The s band is strongly affected by the oddness. The narrowing of the total spectrum observed in clathrate (Si-34) is due to the frustration in five-fold rings. The valence band in Si cluster-assembled films presents a merging of the *s*-like and *sp*-like bands. This is due to the superposition of the *p*-like states with odd and even parity. This superposition fills the valley between both the *s*-like and *sp*-like bands observed in crystalline phases. For the Si cluster-assembled films, the mean cluster size and the distribution is given on Fig. 2.5. (b) Core levels observed for two crystallized porous silicon structures prepared by chemical etching of *p*-type Si wafers of (111) orientation (labelled "porous (1)") and (100) orientation (labelled "porous (2)"), respectively. The original figure is published by Vasquez *et al*. [38]. Both arrows on top show the reminiscence of the *s*-like and *sp*-like bands. The merging of the *s*-like and *sp*-like bands in Si cluster-assembled films is much more pronounced indicating a large part of odd rings in the cluster films as compared to porous structures (Reproduced with permission of AIP).

the crystallite structure. The intensity of the Raman signal $I(\omega)$ is crudely given by the following expression:

$$I(\omega) \sim (n(\omega) + 1)\frac{4D^4}{q^2(2\pi)^4}\int \frac{\Gamma/\pi}{[\omega(\mathbf{q}) - \omega]^2 + \left(\dfrac{\Gamma}{2}\right)^2}\frac{\sin^2(\mathbf{q}D/2)}{(4\pi^2 - q^2D^2)^2}\, d \tag{2.2}$$

The first term is the Böse–Einstein factor, the second term is the Lorentzian response with a Γ factor. $\omega(\mathbf{q})$ is the dispersion law of the optical phonon branch and the last term is the confinement factor that depends on the amplitude of the $\mathbf{q}D$ factor. The Raman shift $\delta(\omega_M)$ is related to the cluster size through the analytical form [39]:

$$\delta(\omega_M) = -52.3\left(\frac{0.543}{D}\right)^{1.586} \tag{2.3}$$

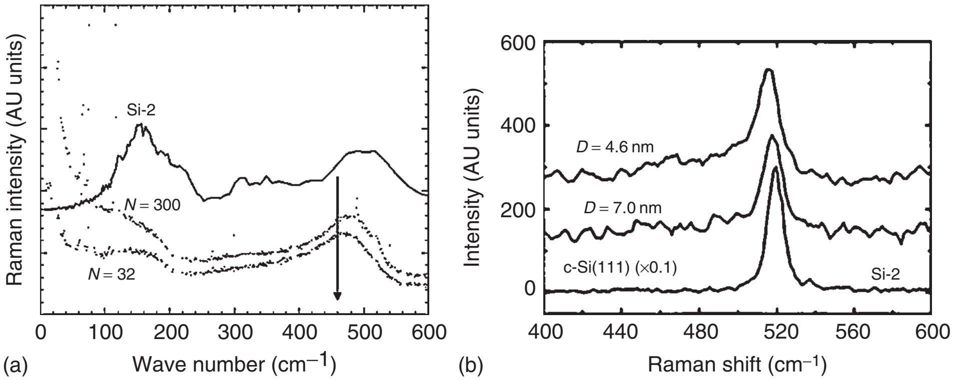

Figure 2.10 (a) Raman spectra of cluster-assembled films with a mean size of $N = 32$ ($D = 1.25\,\text{nm}$) and $N = 300$ atoms ($D = 2.0\,\text{nm}$), respectively. The size $N = 32$ corresponds to Fig. 2.9. The figure labelled (Si-2) is the ph-DOS measured by inelastic neutron scattering spectroscopy. In this case, selection rule is fully broken while the Fig. 2.10b reports the peak at $521\,\text{cm}^{-1}$ for Si-2 observed by Raman spectroscopy. In this case, the selection rule gives a single peak corresponding to the optical mode, (b) Raman spectra of Si cluster-assembled films with a mean size of $D = 4.6\,\text{nm}$ and $D = 7.0\,\text{nm}$ respectively. The original figure in this last case is published by Paillard *et al.* [39] (Reproduced with permission of AIP).

Upper limit is reached when the cluster is fully disordered like amorphous silicon a-Si. In this case, at room temperature, the reduced first-order Raman spectra (raw spectra divided by ω) is a more or less template of the phonon density of states [40] (ph-DS) $g(\omega)$ measured by inelastic neutron scattering for example (see Fig. 2.10a).

$$I(\omega) \sim \sum_{\text{overall the bands}} (n(\omega) + 1)\omega^{-1} g(\omega) \tag{2.4}$$

Figure 2.10a shows the first order Raman spectra for Si-cluster-assembled films as the function of the cluster size. Figure 2.10b shows for comparison, resonant Raman spectra of Si-cluster-assembled films obtained by Paillard *et al.* [39]. In such experiments, cluster sizes are larger (4.6 and 7.0 nm) and fully crystallized. For moderate sizes when the phonon is confined, the position of the Raman peak is related to the cluster size. This holds in Fig. 2.10b. In our case, the Raman spectra are close to the phonon density of states for silicon and can be compared to amorphous silicon. A careful analysis gives a slight shift of the main band as a function of the cluster size. The shift observed for small clusters as compared to a-Si shows a short-range order limited to the cluster which depends on the size. Nevertheless, the presence of odd rings [41] in the structure contributes to the softening of the optical phonon energies getting a Raman intensity dependence with the size.

Table 2.1 reports the experimental values for Si-cluster-assembled films.

2.3.2.5 Optical Properties

For a piece of Si diamond, the confinement of the electrons into the cluster induces a broadening of the band gap both theoretically predicted (see Fig. 2.11) by empirical model [33] or *ab initio* calculations [42] and experimentally [43].

Table 2.1 Cluster size deduced from TOF mass spectroscopy, red shift and size deduced from Raman scattering according to Eq. (2.3). For amorphous silicon (a-Si) the mean cluster size is limited to the first neighbouring shell. For the smallest sizes (down to 2 nm), Eq. (2.3) is not valid.

D in nm deduced from TOF	Red shift $\delta(\omega_M)$	*D* in nm (Eq. (2.3))
∞ (Si-2)	0	∞
[1] 7.0	−0.9	7.1
[1] 4.6	−1.6	4.9
2.0	−44	–
1.25	−51	–
<0.5 (a-Si)	−59	–

[1] Values are from Ref. [39].

Photoluminescence (PL) energy E_{PL} is blue shifted with respect to the band gap of bulk silicon and obeys to the empirical law [44]:

$$E_{PL}(D) = E_0 + \frac{3.73}{D^{1.39}} \tag{2.5}$$

where D is the diameter in nm and E_0 the band gap in crystal (1.17 eV). This law has a physical meaning assuming a total passivation. When dangling bonds are unsatisfied, localized states in the band gap introduce trapping states and luminescence totally disappears. A small luminescence is observed in Si-clusters assembled films at an unusually low value (about 1.6 eV)(see Fig. 2.12). This luminescence strongly increases when oxygen is introduced. The increasing of the luminescence yield is probably due to the decreasing of the dangling bonds (see Fig. 2.11). This clearly indicates that Equation (2.5) does not hold for the smallest clusters. The increasing of the PL yield has been also reported in Si-rich SiO_2 films upon annealing by Hayashi [45] *et al.* In addition, oxidation does not change the PL energy. This behaviour could be assigned to the competition between two antagonist effects. Oxidation with the formation of Si–O_4 tetrahedron cell leads to a gap increasing since SiO_2 has a bandgap larger than Si. However, Vasiliev *et al.* [46] have reported that limited oxidation at the surface induced the presence of localized oxygen level stated in the band gap. In this case, the authors claim a large decreasing of the band gap (about 2 eV between Si_NH_M and Si_NOH_{M-2}).

2.3.2.6 New Bonding for Silicon

In summary, the hybridization of the silicon atoms in the cluster films is close to the one in bulk phase. Two specific features are yet relevant to the size effect: ring oddness and packing structure. Some of the atoms belong to five-fold rings and are affected by the oddness (see the clathrate as reference). Few atoms are over coordinated with a metal-like character. Nevertheless, the main features are close to the

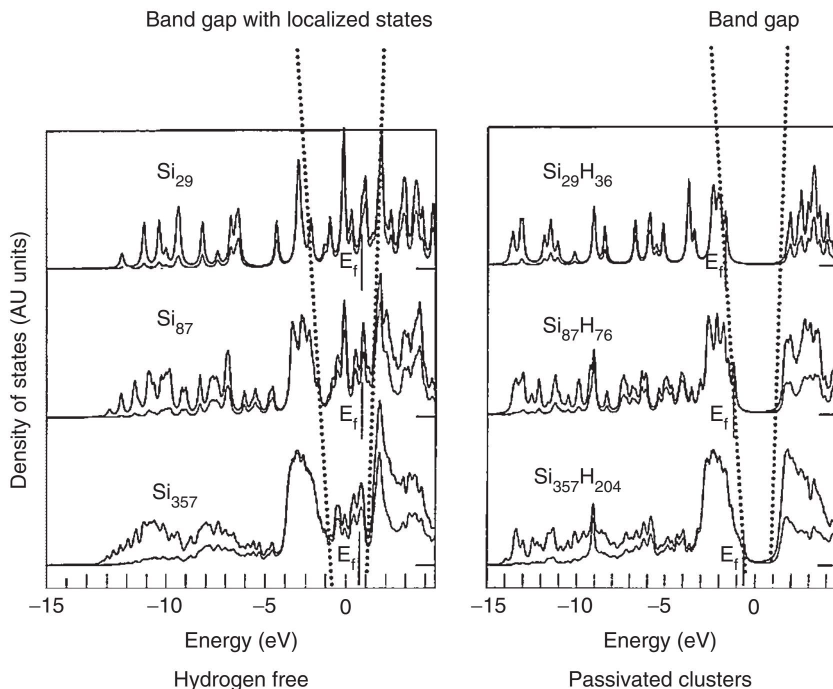

Figure 2.11 Theoretical electronic e-DOS [33] for several free Si clusters (left panel) and hydrogenated Si clusters having the diamond structure (right panel). The calculation is done in the tight binding framework with five basis orbitals per Si site, s, p_x, p_y, p_x and $s^{\star}$. For hydrogenated clusters, one additional s orbital per H site is considered. Hydrogen terminates all the dangling bonds at the surface. The highest occupied level E_F is indicated by a vertical line. For the figure in the left panel, the thick-line curves (on top) correspond to the complete e-DOS, while the thin-line curves (on bottom) display the contribution of the p-like orbital. For the figure in the right panel, the thick-line curves correspond to the complete e-DOS without the s-like orbital of the atomic hydrogen, while the thin-line curves display the contribution of the p-like orbital. The band gaps for the three passivated clusters are 3.44, 2.77 and 199 eV for $Si_{29}H_{36}$, $Si_{87}H_{76}$ and $Si_{357}H_{204}$ respectively. We clearly observe the increasing of the bad gap as the cluster size decreases and the localized states into the band gap for the hydrogen-free clusters. The striking result is the likeness between the e-DOS of pure Si clusters and passivated clusters (except the localized states). Such localized states are also reported in hydrogen-free a-Si networks.

diamond lattice with more or less disorder. A question could be addressed now: is it possible to modify the nature of the bonding for a silicon atom? The answer is yes so long as silicon is bonded with foreign atoms, carbon for example. We briefly discuss two examples of a new bonding state between Si and C. Both elements belong to the same column and SiC lattice is a crude template of the common diamond lattice (we do not discuss polytypes) with an iono-covalent bonding between Si and C according to the difference in electronegativities between both elements. Moreover, what happens when clusters are prepared with different stoichiometries? The answer is complicated due to two antagonist effects: silicon (in small clusters) prefers a dense packing structure while carbon adopts a geometry (fullerene) with a three-fold configuration.

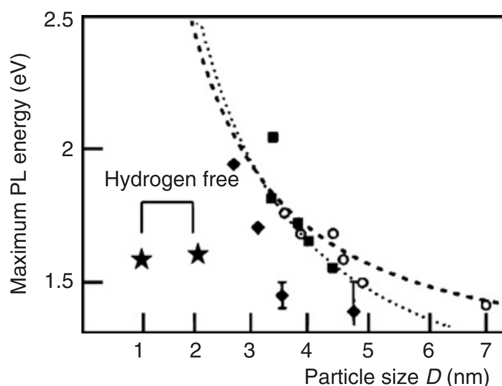

Figure 2.12 Position of the PL maximum as a function of the size of Si nanoclusters deduced from TOF mass spectroscopy. Squares and diamond symbols are deduced from the work of Ledoux *et al*. [44]. Open circles are measured by Ehbrecht *et al*. [47]. The dashed curve represents the theoretical data of Delerue *et al*. [48]. The dotted curve includes the correction due to the lattice relaxation Ref. [44]. For further explanation, see the original Fig. 2.7 published by Ledoux *et al*. [44]. The stars present our data.

SiC Heterofullerenes The geometry becomes strongly sensitive to the stoichiometry. When carbon and silicon are in the same ratio, one observes a complete phase separation with a core shell structure for the corresponding clusters. For a low percentage of silicon, carbon adopts a geometry close to the fullerene where a few Si atoms (<12) are substituted to carbon atoms in the fullerene structure [49,50]. Figure 2.13 displays the symbolic ball and stick models for two heterofullerenes with one and two silicon atoms, respectively, C_{60} being the template. Selected energy levels are studied by *ab initio* calculations within the density functional theory (DFT) framework. Figure 2.13 reports the region near the gap (HOMO–LUMO region). The striking result is the analogy with doped semiconductors. HOMO–LUMO separation in heterofullerenes are weakly affected by Si atoms compared to pure C_{60} fullerenes. The Si-related orbitals (dashed lines) can be described in terms of defect levels. Because Si and C belong to the same column, Si atom introduces two levels with acceptor-like and donor-like characters keeping the neutral stability. For two Si atoms substituted in C_{60}, the mechanism is the same except the splitting of each donor level in two levels. The validity of the standard defect level model is surprising since the basic hypothesis (low concentration) is not assumed. Furthermore, a careful observation of Si_2C_{58} structure (see Fig. 2.13) shows a Si pair. This pair ensures a gain of stability since the two neighbouring lonely orbitals couple together bringing a stabilizing hybridization energy. This energy counterbalances the classical polarization energy as observed in SiC bulk phase where a perfect SiC alternance is observed.

C_{60}-Si-Based Nanostructures Silicon atom can be incorporated between two C_{60} molecules. For that purpose, we use a sophisticated double target (Si and C_{60}) laser vapourization source [51]. Bridging C_{60} is deduced in free phase by

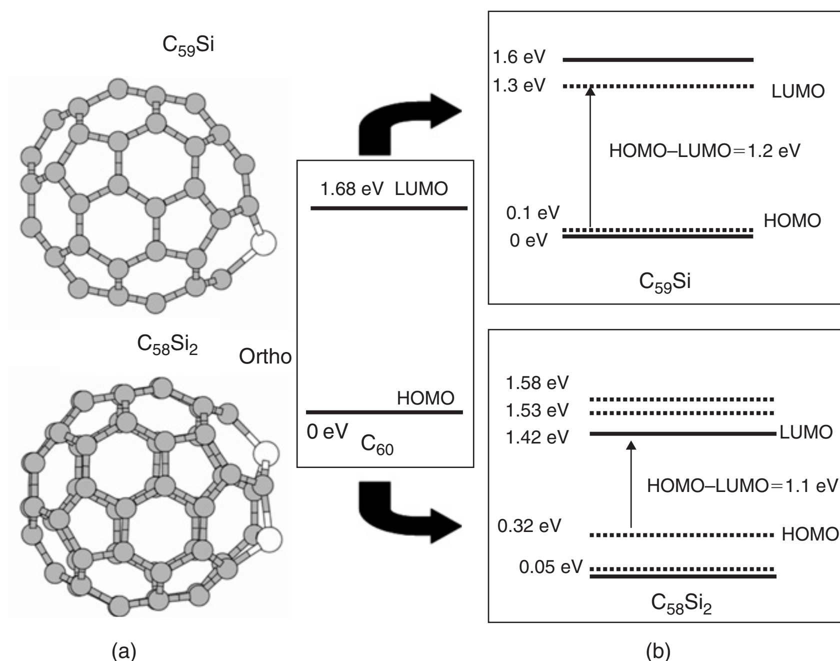

Figure 2.13 (a) Symbolic ball and stick representation of SiC_{59} and meta $C_{58}Si_2$ structures. Geometries are deduced from DFT-LDA calculations and relaxed following the standard conjugate gradient scheme (see Ref. [50]). The white spheres are the silicon atoms. (b) Selected energy levels near the HOMO–LUMO region. Full lines and dotted lines indicate the carbon- and silicon-related orbitals, respectively. Taking only carbon-related orbitals, the HOMO–LUMO separation is respectively 1.68, 1.60 and 1.58 eV for C_{60}, $C_{59}Si$ and $C_{58}Si_2$ respectively. The arrow gives the HOMO–LUMO separation. In this way, the HOMO–LUMO separation is 1.2 and 1.1 eV in $C_{59}Si$ and $C_{58}Si_2$ respectively.

photofragmentation experiments [51] and cluster-assembled films by EXAFS spectroscopy performed at the Si K-edge [52]. Figure 2.14 displays a selected mass spectrum in the region corresponding to $(C_{60})_7Si_m$ with $1 < m < 4$. After mass selection, clusters can be warmed up by irradiation with a UV laser operating at 4 eV. The corresponding evaporation mass spectra exhibits the sequential loss of $C_{60}Si_m$ monomer with $m = 0$ and 1. Hypothetic geometric arrangement for $(C_{60})_6Si_4$ cluster is also displayed in Fig. 2.14. In summary, such experiments are compatible with a silicon atom bridging two C_{60} molecules. Such a bridging is corroborated by EXAFS experiments. Figure 2.15 displays the experimental EXAFS signal $\chi(k)$ of various samples: C_{60}Si-cluster-assembled films, hexagonal SiC carbide and Si diamond. The striking features are a well-structured signal for C_{60}Si cluster-assembled films that indicates a locally well-ordered environment around silicon atoms and the large difference between $\chi(k)$ for C_{60}Si-cluster-assembled films and other crystalline phase (Si-2 and SiC). EXAFS simulation is performed within *ab initio* self-consistent real space multiple scattering code FEFF8 [53] with self-consistent scattering potentials. Different geometries are tested and the best configuration for the fit corresponds to a silicon atom bridging two C_{60}.

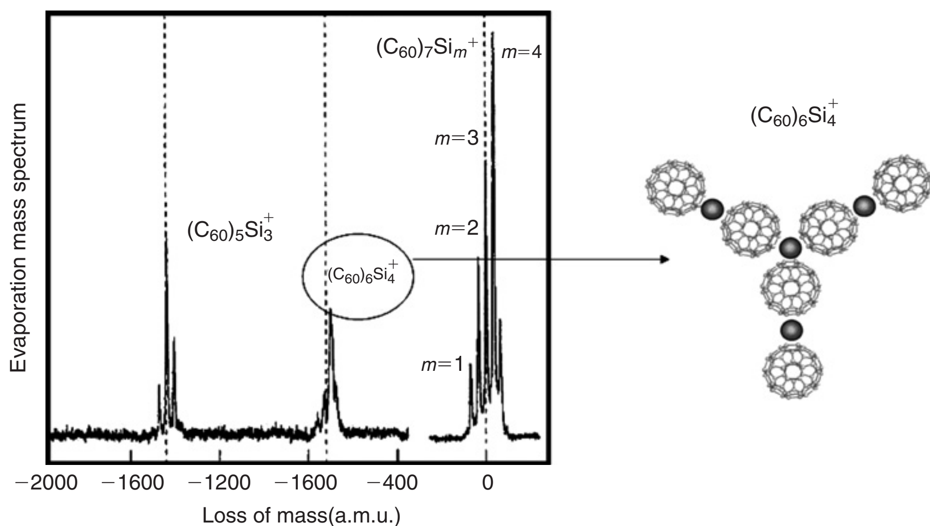

Figure 2.14 Evaporation mass spectrum showing the first steps of the unimolecular decomposition of $(C_{60})_7Si_m^+$ clusters previously warmed using a UV laser. The dotted lines give the expected position for the sequential loss of one C_{60} neutral cluster. The time reference for the origin just coincides with the particular case $(C_{60})_7Si_3^+$. The figure also displays a ball and stick proposed representation of a selected cluster $(C_{60})_6Si_4^+$. This structure is compatible with the observed evaporation channels (Reproduced from Ref. [51] with permission of AIP Copyright 2000).

Figure 2.15 displays the configuration where two nearest C_{60} face the silicon atom with a pentagonal phase. In this case, we have 10 neighbours located at 2.52 Å as compared to 4 neighbours located at 1.88 Å in SiC carbide. In this case, the geometry around silicon suggests an unusual bonding close to intercalated graphite rather than a sp^3 basic set.

Figure 2.16 reports a comparison between energy levels in C_{60}, C_{60}—Si (Si exohedral) and $C_{59}Si$ (Si substituted) deduced from *ab initio* calculations. Stable configuration for C_{60}—Si corresponds to a silicon atom bonded to a hexagon–hexagon edge [54]. The predicted distance between the silicon atom and the two nearest carbon atoms is 1.91 Å close to the one in SiC carbide. However the dihedral angle is 48°26′ much smaller than the 109°28′ value for an usual sp^3 configuration. Nevertheless, the energy levels near the HOMO–LUMO region shows the same behaviour: silicon introduces two levels with acceptor-like and donor-like characters. However the exohedrally doping (C_{60}—Si) introduces two symmetric levels and strongly decreases the band gap as compared to substitutional doping ($C_{59}Si$). The main difference is the nature of the SiC bonding. In C_{60}—Si, the C—Si covalent bond needs the π character C═C double bond breakdown while in heterofullerene, Si replaces a carbon atom with a strong σ character.

2.3.3 Bulk Si-Cluster-Assembled Materials from Fullerenes: Clathrate Phases

After reviewing Si-cluster-assembled films produced by the deposition of preformed clusters, we discuss now some selected properties of Si-cluster-assembled

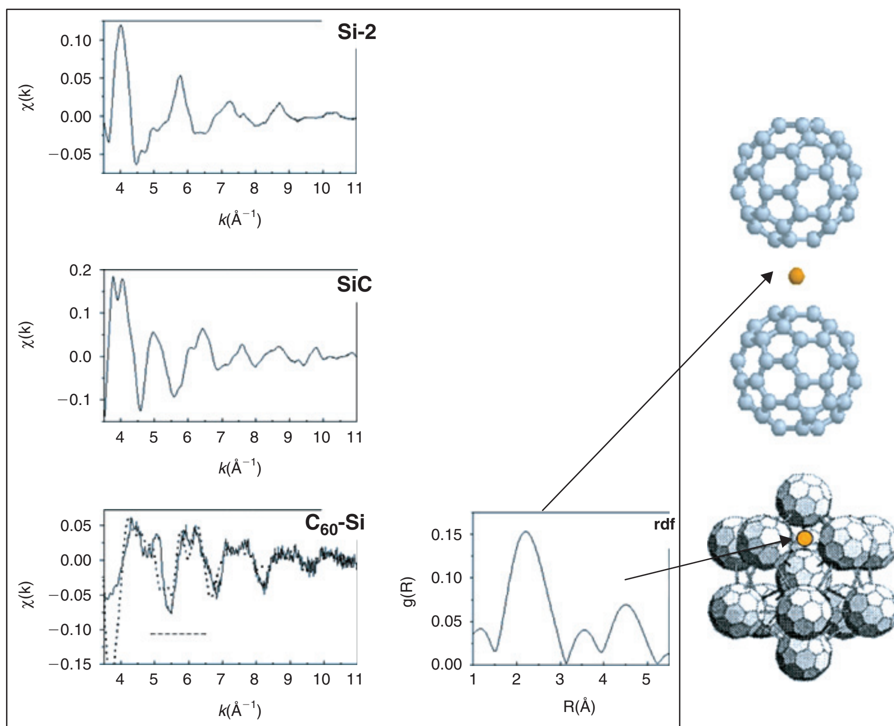

Figure 2.15 Experimental EXAFS signals $\chi(k)$ of silicon diamond (Si-2), silicon carbide SiC (hexagonal phase) and C_{60}-Si cluster-assembled film. The pseudo radial distribution function g(R) is given for C_{60}-Si cluster-assembled film. The dotted line is the *ab initio* simulation with the structure given on the figure. The first peak corresponds to the silicon bridging two C_{60} and the second peak could be assigned to the contribution of C_{60} molecules in the perpendicular plane. In this case, the cluster structure will be compact as observed in the icosahedron proposed structure (adopted from Ref. [52]).

materials built up by the periodic arrangement of well-defined Si fullerenes sharing a common face.

2.3.3.1 Silicon Clathrate Structures

Si-clusters assembled films are amorphous-like, porous and the electronic properties are widely tuned by the mean cluster size (the elemental brick). As mentioned in the Introduction, it is however possible to synthesize well-organized Si clusters packed into crystalline phases. Silicon clathrates are 3D periodic networks of Si dodecahedral fullerenes with either Si_{24} or Si_{28} polyhedral cage-like nanoclusters respectively. In type-I clusters, only Si_{20} and Si_{24} can be found, while the so-called type-II phases contain Si_{20} and Si_{28}. The silicon clusters are sharing faces, giving rise to full sp^3-based networks of slightly distorted tetrahedra (Fig. 2.17). [55] As such, the clathrate structure can be compared to the well-known diamond phase, with the difference that it contains a large fraction of pentagons (up to 86%), and is amenable to a large doping by intercalation of guest atoms at the centre of the cages (endohedral doping). Indeed, as mentioned above, the nano-polyhedra form around

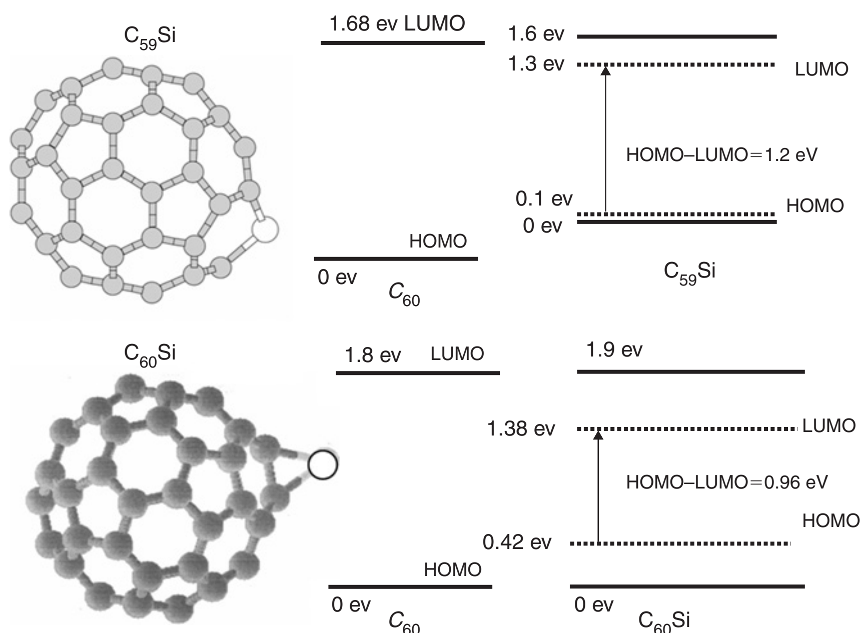

Figure 2.16 Energy levels of C_{60}, $C_{60}Si$ [54] and $C_{59}Si$ [50]. The difference in the primitive bandgap for C_{60} differs from 0.12 eV. This shift is explained by the difference in the *ab initio* codes used by the authors. Big white balls correspond to Si atoms as in Fig. 2.13.

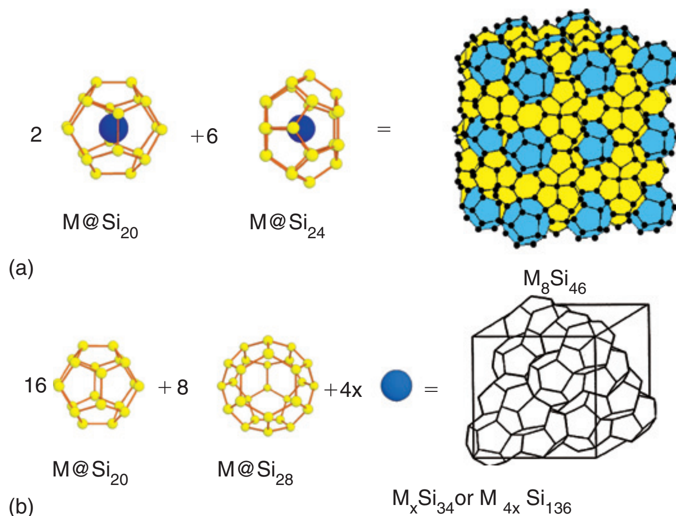

Figure 2.17 The structure of Si clathrates. The structure of silicon clathrate of type-I (a) and II (b) an be viewed as cubic 3D arrangements of face-sharing fullerene like nanoclusters (after Ref. [55].

guest atoms (M) [17,56]. The silicon clathrate structure is isomorphous with ice or silica clathrates and has M_xSi_{46} stoichiometry for the type-I (space group $Fd\bar{3}m$) and M_ySi-34 (often noted by the Bravais lattice as $M_{4y}Si_{136}$) for the type-II (space group $Pm\bar{3}n$). Experimentally, guest atoms can be alkali metals [17], barium [56], strontium

[57], iodine [58] and tellurium[59,60] in the type-I, but only Na or Cs are encountered in the type-II. In type-I clathrates, $6.6 \leqslant x \leqslant 8$ is encountered, whereas for type-II guest intercalation varies as $0 \leqslant y \leqslant 6$. In both cases, the maximum x or y values correspond to the case where all silicon clusters are endohedrally doped with one atom per cage. It is noticeable that whereas it is possible to synthesize the empty type-II clathrate [17,61,62], the empty type-I silicon clathrate has never been observed and only theoretical calculations are possible in this case.

2.3.3.2 Synthesis Methods

There are two routes for clathrate synthesis. The common point between the two methods is the construction of Si-cages around a template atom, usually an alkali metal. The historical method [17,63,24] (the "chemical" approach) is based on thermal decomposition of silicide precursors (XSi_2, X doping atom) at moderate temperatures (700–1000 K). For the clathrate I phase (two Si_{20} and six Si_{24} per unit cell), the silicide is heated under argon pressure. Clathrate II (two Si_{28} and four Si_{20} per unit cell) are prepared by heating the silicide under vacuum. During the heating process, the samples lose metal. Another route has been recently developed [64–66]. The silicide phase is mixed with silicon powder and placed in an h-BN cell. The synthesis occurs at 1000 K under high pressure (1–5 GPa). The sample is quenched at room temperature before the pressure is slowly released. This last method has only allowed the obtention of type-I clathrates. It is possible to reduce the content of the guest atoms through heating under vacuum. With this method, it has been observed that the stability of the type-I clathrate, M_xSi_{46}, is limited to a minimum value of $x = 6.6$. In the case of M_ySi-34, values close to $y = 0$ have been obtained [61,67].

2.3.3.3 Electronic Properties of Empty Silicon Clathrates

In the absence of angle-resolved photoemission data, the band structure of clathrates has been discussed on the basis of tight-binding [68] and *ab initio* DFT [69,70] calculations [41,68,71–74]. In particular, DFT studies within the local density approximation [75] (LDA) predict [67,71,73] that the Si-34 phase displays a "nearly direct" band gap which is ~0.7 eV larger than the one of bulk Si-2 diamond. Such a large band gap has been attributed to the presence of pentagons which frustrates the formation of completely bonding states between Si-3*p* orbitals at the top of the valence bands, thus reducing the *p*-band width as shown in Fig. 2.18.

DFT-based band structure calculations are however known to lead to large discrepancies as compared to experimental results. The most documented problem is related to the magnitude of the band gap of semiconductors and insulators which is significantly underestimated [76]. An alternative approach is the so-called quasiparticle approach within the *GW* approximation which has been shown to yield for semiconductor bulk [77], surfaces [78–80] or clusters [81], quasiparticle energies accurate to within 0.1 eV as compared to experiment. In this approach, the standard LDA (or GGA) exchange-correlation potential is replaced by a non-local and energy-dependent term, the self-energy operator Σ, that can be built from the screened Coulomb interaction (W) and the electronic Green's function (G):

$$\begin{aligned}[\hat{T} + V_{\mathrm{ext}}(\mathbf{r}) + V_{\mathrm{H}}(\mathbf{r})]\Psi^{qp}(\mathbf{r}) \\ + \int d^3\mathbf{r} \sum(\mathbf{r}, \mathbf{r}'; E^{qp})\Psi^{qp}(\mathbf{r}') = E^{qp}\Psi^{qp}(\mathbf{r})\end{aligned} \tag{2.6}$$

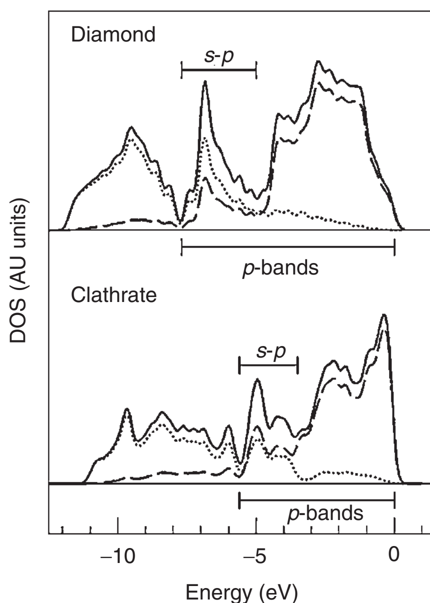

Figure 2.18 Electron density of states in silicon diamond (Si-2) and Si-34 clathrate (adopted from Refs. [37,82]).

where $\hat{T}$ is the kinetic energy operator, V_{ext} the ionic potential, and V_H a mean field electron–electron interaction potential (the Hartree potential in this case). More details can be found in Refs. [77,83,84].

Within such an approach, and as a reference, the indirect band gap of bulk silicon (diamond phase) is found to be 1.2 eV, in much better agreement with the 1.17 eV experimental value than the 0.5–0.6 eV predicted by DFT calculations [77]. The band structures of Si-34 and Si-46 has been studied within the GW approach [82] and the corresponding quasiparticle band structures are provided in Fig. 2.19. The nature of the band gap and the ordering of the states is qualitatively similar to what can be obtained within DFT but the band gap is ~1.9 eV, that is in much better agreement with the 1.8 eV experimental value [67], as compared to ~1.2 eV DFT value. As a result, the band gap of clathrates enters the visible range (red light) and the band gap can be direct in the case of the Si-34 phase. Such a result suggests that Si-clathrate could be used in opto-electronic applications, thus providing a route for an all integrated Si-technology. Unfortunately, the calculation of the dipole matrix elements shows that the direct band gap at L in Si-34 is optically forbidden. Similar results have been found for the Hex-Si40 phase [71].

2.3.3.4 Vibrational Properties

Phonon density of states (ph-DOS) are usually probed by inelastic neutron scattering where selection rules do not hold contrary to Raman spectroscopy which probes phonons located at Γ point. Figure 2.20 displays ph-DOS recorded for diamond and Si-34 phases.

In addition, selected vibrational modes probed by first Raman spectroscopy are also displayed. The large number of Raman modes observed in clathrate phase is

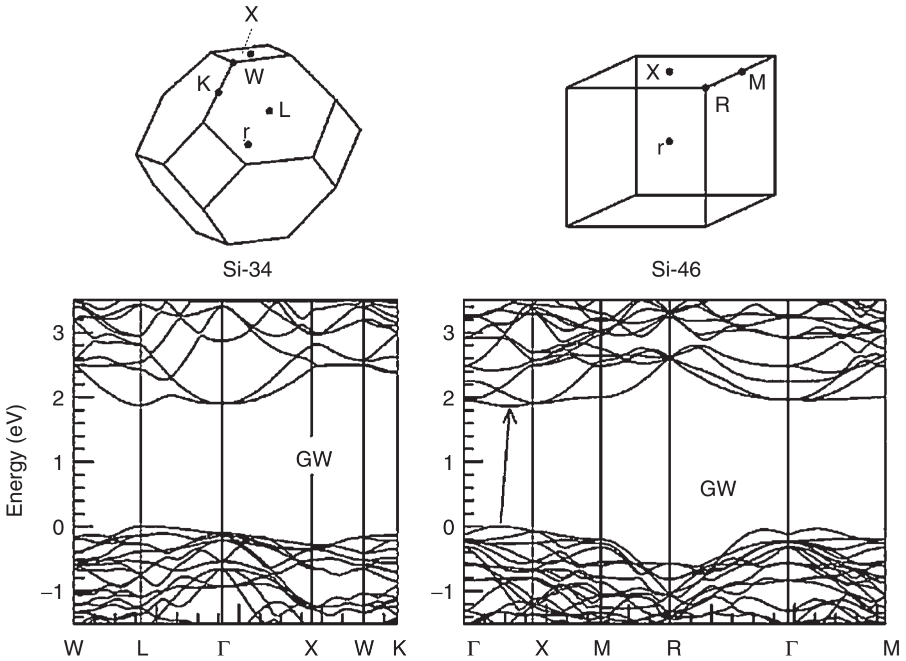

Figure 2.19 Quasiparticle band structures of Si-34 and Si-46 clathrates along high-symmetry directions of the Brillouin zone. Energies are in eV. The zero has been set to the top of the valence bands [82].

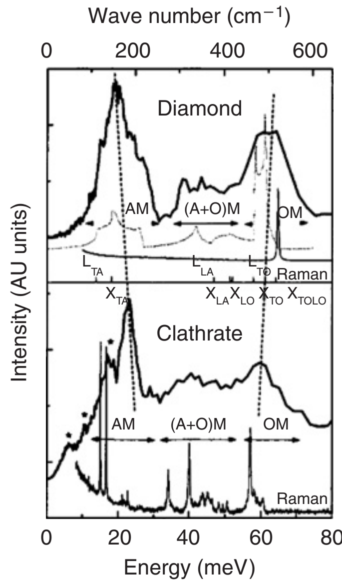

Figure 2.20 Phonon density of states deduced from neutron scattering and Raman scattering spectra of silicon diamond and Si-34 phase. To guide the eye, calculated ph-DOS for diamond is also displayed in dashed line [85,86]. OM, AM and (A+O) M are related to acoustic, optical and mixed modes, respectively.

directly related to the high number of atoms in the primitive cell for clathrate (34 atoms versus 2 in diamond). For the ph-DOS, clathrates and diamond phases present similar features with three regions attributed to acoustic modes, optical modes and mixed states. A slight red shift of the optical branches towards low energy in the clathrate with respect to the diamond phase is attributed to the softening of the Si—Si bond. This is well understood taking the fact that optical modes are not eigen values in odd-membered rings. This is one of the effect attributed to the frustration. Conversely, a blue shift of the acoustic modes is still reported. The network is formed by sphere (i.e. the cages) packing, ensuring an high "mechanical" rigidity [87] with respect to an homogeneous deformation of the medium. As a consequence, the narrowing of the ph-DOS is consistent with the narrowing of the electron DOS as supported by a classical tight binding scheme.

2.3.3.5 Cohesive Energy and Stability Under Pressure of Si-34

The binding energy of silicon clathrates is found, [68] on the basis of *ab initio* calculations, to lie within 0.1 eV/atom of the one of the diamond phase (see Fig. 2.21). It is in particular more stable than the high-pressure phases of silicon, such as the *sh* or beta-tin (β-tin) phases [88].

The lower density of the cage-based networks explains that the bulk modulus of clathrates is 8 ± 5% smaller than the one of the silicon diamond structure [89]. It is to be noted however that the Si bonds are slightly expanded as compared to the diamond phase, thus providing another reason for lower elastic constants [90]. Other factors, such as the presence of pentagons or strained angles, could also explain such an observation.

At ambient pressure, the high temperature stability of the empty silicon clathrate is limited to temperatures below 730 K from which the transformation into diamond silicon is observed. At ambient temperature, the high pressure phase diagram

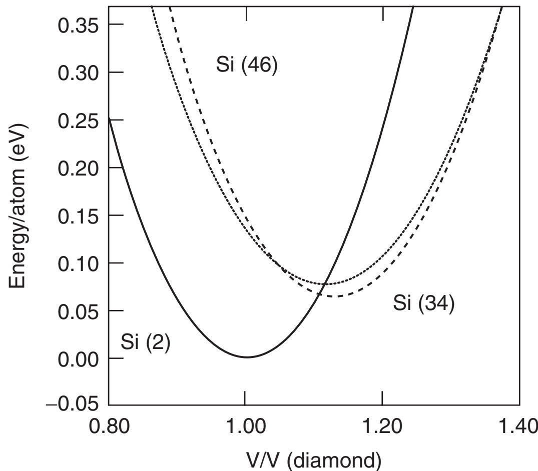

Figure 2.21 Calculated phase diagrams for Si-34, expected Si-46 and Si-2 structures [68]. Contrary to high-pressure phases, the clathrate corresponds to an expanded structure with an equivalent negative pressure as compared to diamond phase. The difference in cohesive energy for β-tin structure is about 0.25 eV. For convenience, the volume is normalized to the diamond one (Reproduced with permission copyright APS 1994).

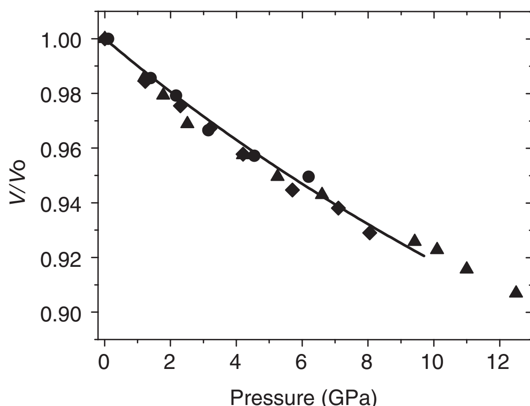

Figure 2.22 Experimental pressure variation of the reduced volume of Si-34 (symbols) and Si-2 Murnaghan equation of state (line) (adopted from Ref. [89]).

of the empty silicon clathrate is totally equivalent to the one of diamond silicon (see Fig. 2.22). The transition towards the same denser phase (β-tin type) at the same pressure of 11.5 Gpa [89] is observed.

It is remarkable that the volume change associated to this phase transition represents one-third of the total volume at the transition. There is presently no model for the transition path (martensitic, reconstructive) between the clathrate structure and the β-tin, even if the presence of an intermediate phase has been evoked [91].

2.3.3.6 Endohedral Doping in Clathrates

Doping in semiconductors is the key of many applications. Most of the semiconductors are doped by substitution. However, cage-like based materials permit a new type of bonding with guest atom endohedrally incorporated inside the cage. This type of doping is promising, since the donor concentration can reach unusual values (up to 17%). Further, the "size" and electronic structure of the guest atom can differ significantly from the one of the host lattice, without inducing misfits and dislocations. As such, endohedral (or intercalation) doping allows for much flexibility, provided that the precursor be found for the synthesis. Besides the evolution under doping of the pressure-related phase diagram, of the electronic and superconducting properties, that we discuss below, intercalation has been shown to yield interesting thermoelectric properties [92–94], low electronic affinity materials for field-emission devices [95] or novel magnetic compounds [96].

Intercalated atoms occupy in general the centre of the cages. For example, in the case of the type-I silicon clathrate Ba_8Si_{46}, the Ba-atoms appear to keep the central position in both Si_{20} and Si_{24} cages (Fig. 2.23b). However, when the atom is "small" enough, it can shift off centre, breaking thus the symmetry of silicon host network. This has been demonstrated in the case of the type-II clathrates Na_xSi-34 for $x = 2$ and 6 [97,98] where the evolution of the "Na-expanded sublattice" was interpreted in terms of a Peierls distortion [99]. EXAFS (Extended X-ray absorption fine structure) studies show that the Na atom is shifted up to 1.0 Å from the central position in the large Si_{28} cage (Fig. 2.23a).

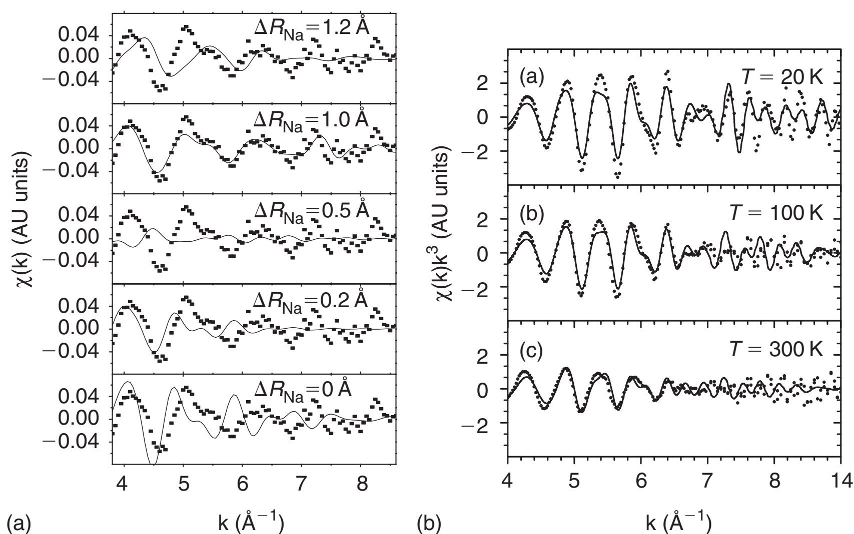

Figure 2.23 EXAFS study of the symmetry breaking in endohedrally doped clathrates. (a) $\chi(k)$ in Na_2Si_{34} at the Na K-edge. In this structure only the larger Si_{28} clusters are filled. Dots give the experimental data and the continuous line, the simulation. The best fit is obtained for a 1.0 Å shift ΔR_{Na} of the Na atom. (b) $\chi(k)$ of Ba_8Si_{46} at the Ba K-edge at different temperatures (a) $T = 20$ K, (b) $T = 100$ K, (c) $T = 300$ K. The best fits correspond to the same structural model with the Ba atoms at the centre of both the Si_{20} and Si_{24} nanocages ([after Refs. [97,100]).

Intercalation of clathrates also modify the phonon DOS as reported in Fig. 2.24 (assuming that both Si-46 and Si-34 phases are similar enough, we can compare their ph-DOS in the Figs. 2.24 and 2.20). In the case of Na doping, we notice first the presence of low-energy sharp peaks attributed to Einstein-like modes related to the intercalated atoms. This clearly indicates the weak coupling between doping atoms and host lattice. In addition, a softening of the optical branches is well observed. This is due to the increase of the electron density of states at the Fermi level and the corresponding screening effect.

Tailoring Band Gap by Doping The doping of clathrates by elements such as Na or Ba leads to *n*-type doped silicon networks. With the increase of interest in such phases, incorporation of other elements inside the cages has been attempted. In particular, the synthesis of Si-46 clathrates doped by iodine has been achieved [58]. The initial interest in such a system is that doping would be of *p*-type (as iodine is more electronegative than silicon), thus enlarging the possibilities of Si-clathrate-based electronic devices. This was confirmed by *ab initio* calculations [101] predicting that in the "ideal" $I_8@Si_{46}$ compound, the Fermi level would be located $\sim$0.26 eV below the top of the valence bands (Fig. 2.25 shows the results for Si-34 clathrate from Ref. [100]). The density of states integrated between E_F and the top of the valence bands yields exactly four states/cell, which corresponds exactly to the eight electrons that the iodine atoms in one cell need to fill up their 5*p* shells. The density of states at the Fermi level $N(E_F) \sim 44$ eV/states cell is large, equivalent to that of $Ba_8@Si$-46, suggesting that superconductivity can be obtained with other type of dopant than Ba (see Fig. 2.25).

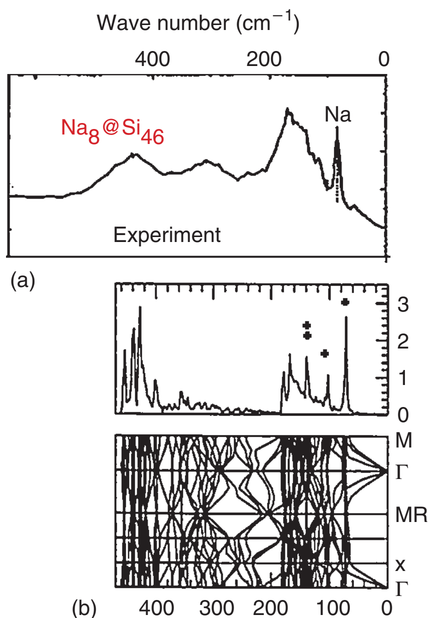

Figure 2.24 ph-DOS deduced from neutron scattering in $Na_8@Si_{46}$ (a) compared to theoretical ph-DOS (middle) and corresponding dispersion curves along high-symmetry directions of the Brillouin zone (b). For convenience, wavenumbers in abscissa of all figures are aligned.

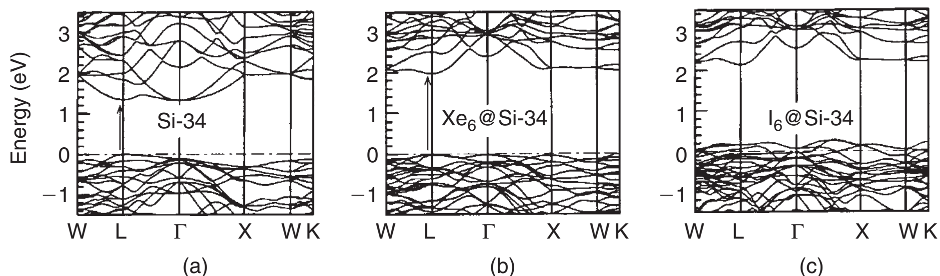

Figure 2.25 DFT-LDA band structure of (a) Si-34, (b) $Xe_6@Si$-34 and (c) $I_6@Si$-34 along high symmetry directions of the Brillouin zone. Energies are in eV. The zero of energy has been set to the top of the valence bands for Si-34 and $Xe_6@Si$-34 and to the Fermi level for $I_6@Si$-34. The arrows indicate the nature of the gap (direct) (after Ref. [102]).

While $N(E_F)$ is indeed an important quantity, the evolution of the band gap under doping has hardly been addressed. In the case of $I_8@Si_{46}$, an important observation [101] is that the band gap opens from 1.8 to 2.4 eV (GW value). Such a large value of the band gap, corresponding to the green light, confirms the potentiality of clathrates in optoelectronic devices. The origin of the band gap opening in $I_8@Si_{46}$ is not related to the ionic character of the I—Si bond. Indeed, the (hypothetical) $Xe_8@Si_{46}$ – an intrinsic semiconductor with no charge transfer – displays a similar ~2.4 eV band gap. Group theory analysis [101] allows to verify that the (s,p)-I or Xe orbitals can couple with the bottom of the conduction bands but not with the top of the valence bands (they do not belong to the same irreducible representation).

The opening of the band gap stems therefore from the repulsion of the low-lying conduction bands to higher energy. It is interesting to note that the same symmetry-selection rules hold both for Si-34 and Si-46 systems even though their point group is different. In the case of the $Xe_6@Si_{34}$ compound (see Fig. 2.25), the band gap is found to be direct. Further, similar results have been found for intercalated $X@H_NSi_N$ ($N = 20, 24, 28$ and $X = $ Xe, I) endohedrally doped H-passivated clusters, [102,103] even though, again, the point groups of such systems are very different.

Unfortunately for applications in optoelectronic, the band gap of e.g. $Xe_8@Si_{46}$, even though direct, is found to be optically forbidden (similar results hold for intercalated H_NSi_N cages). Further, recent analysis [66] suggest that iodine atoms not only intercalate the Si cages, but also enter in substitution in the Si network. The $I_8@Si_{46-x}I_x$ ($x \sim 1.8$ atoms in substitution) compound seems to display electronic properties significantly different from those of the ideal $I_8@Si_{46}$ network [66].

Origin of the Superconductivity in Doped Clathrates The superconductivity in doped clathrates is a surprising phenomenon as it refers to the superconducting properties of the covalent column IV sp^3 semiconductors for which such a transition has never been discussed until recently. The clathrates are actually the precursor of the so-called covalent superconductor family [104], which contains also MgB_2 [105] and doped diamond [106,107]. Superconductivity has been reported for $Ba_8@Si_{46}$ [56], $Na_xBa_{8-x}@Si_{46}$ [65], $Sr_xBa_{8-x}@Si_{46}$ [57], $Ba_8@[Ga_{16}Ge_{30}]$ [108] and $Ba_8@[TM_xSi_{46-x}]$ (TM = Au, Ag, Cu) [109] clathrates with a maximum T_c of 8 K for $Ba_8@Si_{46}$. The origin of superconductivity in doped clathrates has been studied within the Bardeen–Cooper–Schrieffer (BCS) theory of phonon-mediated superconductivity. Concerning the case of Ba_8@Si-46, the role of Ba has been recognized in early calculations [110] as being responsible for the large value of the density of states $N(E_F)$ at the Fermi level. However, a complete understanding of the superconducting state requires as well a study of the $(\mathbf{q},\nu)$-phonons (wavevector $\mathbf{q}$ and band ν) responsible for the pairing of electrons in Cooper pairs and the evaluation of the average electron–phonon (e–ph) interaction parameter λ:

$$\lambda = 2N(E_F)\sum_{\nu} << |g_{q\nu}|^2 >> / h\omega_{q\nu}$$

where $<<|g_{\mathbf{q}\nu}|^2>>$ is related to the $(\mathbf{k},\mathbf{k}')$-averaged electron–phonon coupling matrix elements for $(\mathbf{k},\mathbf{k}')$ electronic states on the Fermi surface [111]. The calculated value for Ba_8@Si-46 was $\lambda = 1.05$, in excellent agreement with the experimental measurement [112]: $0.8 \leqslant \lambda^{\exp} \leqslant 1.2$, suggesting that the superconductivity is indeed of BCS type in the strong coupling limit. The $\lambda \sim 1$ value can be compared to the typical $\lambda \sim 0.6$ in fullerides.

The knowledge of λ allows to compute the superconducting transition temperature T_C following McMillan [113]:

$$T_C = \frac{h\omega_{\log}}{1.2\,k_B}\exp\left[\frac{-1.04(1+\lambda)}{(\lambda - \mu^{\star}(1+0.62\lambda)}\right]$$

where $\omega_{\log} = \exp(\Sigma_{q\nu} \log(\omega_{q\nu})\lambda_{q\nu}/\Sigma_{q\nu}\lambda_{q\nu})$ is the calculated effective temperature, $\mu^\star$ is the effective electron–electron repulsive interaction (retarded and screened Coulomb interaction) which opposes the formation of Cooper pairs.

The value of $\mu^\star$ is one of the main problem in the calculation of T_C and is usually taken as a fitting parameter. Using the fact that $\mu^\star$ varies slowly with applied pressure [111], experimental measurement of the evolution of T_C under applied pressure was performed. T_C was found to quickly decrease with decreasing volume (Fig. 2.26). Adjusting $\mu^\star$ to the value needed to obtain $T_C = 8$ K at ambient pressure, the entire T_C versus pressure experimental curve could be reproduced very accurately by recalculating λ for each lattice parameter. The fitted $\mu^\star = 0.24$ value can be compared to 0.1 for typical good metals and 0.2–0.3 for fullerides. Both the agreement between theory and experiment over a large range of T_C values, and the good agreement with the experimental value of $\mu^\star$ ($0.2 \leqslant \mu^{\star\exp} \leqslant 0.3$), suggest again that the BCS–McMillan approach, fed with the calculated λ and $\omega_{\log}$ parameters, can capture the physics of superconductivity in such systems.

Beyond the numerical results, an important outcome of this calculation was to show that the phonons responsible for the superconducting e–e coupling were essentially Si-related modes. As a matter of fact, it was shown that the e–ph potential $V^{\mathrm{ep}} = \lambda/N(E_F)$ was nearly independent of the intercalated atom and that doping within a rigid-band-model yields similar e–ph potential. This means that the superconductivity is not the specific property of the "Ba_8@Si-46 alloy", but really an intrinsic property of the sp^3 silicon network doped by Ba atoms. As a matter of fact, numerical calculations for Si-diamond, doped within a rigid-band-model, yields similar T_C values.

The actual value of T_C in Si-clathrates is not of much practical interest. However, numerical calculations [114,115] predicted that in the case of the hypothetical carbon

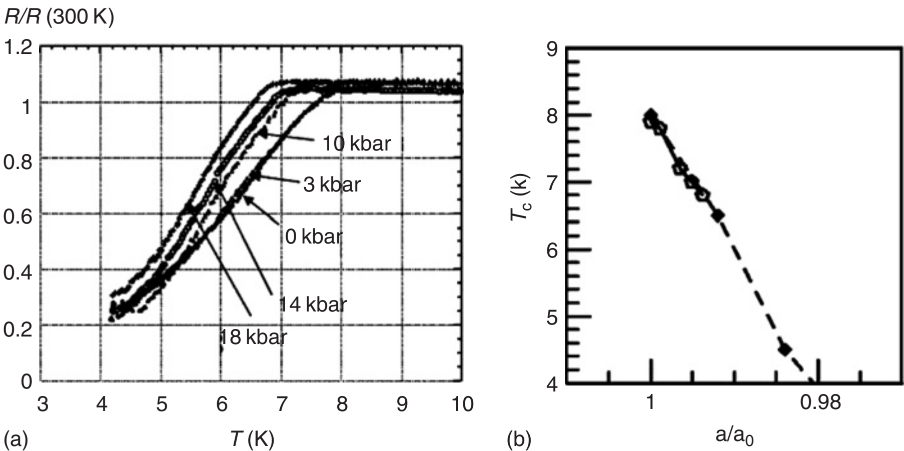

Figure 2.26 (a) Evolution of the resistivity (normalized by its value at 300 K) of Ba_8@Si–46 as a function of temperature for different pressures. (b) Evolution of T_c under pressure as a function of the a/a_0 lattice parameter ratio (a_0 ambient pressure lattice parameter). The empty circles represent the experimental data and the black squares the theoretical values. The dashed line is a guide to the eyes (Ref. [114]).

clathrates, the electron–phonon coupling potential would be extremely large, and in particular much larger than the typical 60–70 meV of fullerides. This suggests that, if properly doped, carbon sp^3 systems could display interesting properties. A few months after these predictions, a superconducting transition in B-doped diamond was discovered [106,116]. The difficulty of doping the "dense" diamond phase limits $N(E_F)$ (and thus T_C). Carbon clathrates, if ever synthesized, could provide a carbon-based sp^3 system much easier to dope than the diamond phase.

Compressibility and Pressure Stability of Doped Clathrates The experimental and theoretical study of endohedral doping of silicon clathrates at high pressures shows that even if the bulk modulus (B_0) modification is limited to a maximum of ~10%, convenient doping can raise its value up to the one of the silicon diamond phase [117]. This is the case of iodine intercalation or even better of tellurium doping. The hybridization between the guest atom and the silicon cages is crucial to understand such a behaviour. This is well demonstrated by the hypothetical Xe-intercalation. Xe-size is similar to I, but its calculated B_0 is 6% smaller than the one of I_8@Si-46 and expected to be chemically inert. This demonstrates that the lower compressibility of I_8@Si-46 is not related to a steric effect but to electronic mixing. This chemical host–guest coupling can be decomposed in a covalent and a ionic part. Their contribution to the B_0 was tested by considering the hypothetical Sn_8@Si-46 for which we obtain a bulk modulus value of 97 GPa, that is the same as in silicon diamond and larger than for the iodine-doped clathrate. Hence, covalent coupling is the predominant factor leading to improved elastic properties in doped silicon clathrates.

In all studied cases [117–120], doping has also a stabilizing effect on the clathrate structure under pressure. In fact first-order phase transition leading to the clathrate structure destabilization has only been observed in Na_8@Si-46 [117] for which the hexagonal phase of silicon was detected above about 15 GPa. As it can be seen in Fig. 2.27, in the case of Ba, K or I doped clathrates, doping prevents the

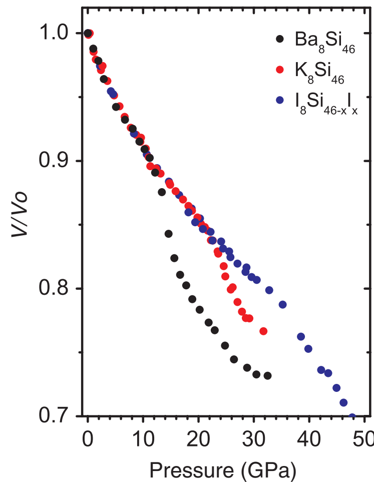

Figure 2.27 Pressure evolution of the reduced volume of Ba, K and I intercalated clathrates (adopted from Ref. [121]).

collapse of the cage structure up to pressures at least three times higher than in the empty clathrate (or of the silicon diamond structure). At the highest pressures attained, the irreversible amorphization of the clathrate structure was observed. The atomic size difference between Na and the other studied guests atoms, let us figure out the predominant role of the steric barrier in the doped clathrate stability. Nevertheless the pressure evolution of electronic interaction between silicon and the guest atom, dramatically influences the compressibility of the structure at high pressures. In Fig. 2.27 we observe the presence of an isostructural volume collapse in which pressure strongly depends on the guest atom. The detailed X-ray diffraction study of this isostructural phase transition [121] shows that full homothety is maintained all over the volume collapse. As a consequence, the cage-type silicon clusters are preserved in the full compressive process, allowing to obtain tetrahedral silicon with record interatomic distances as low as 2.13 Å. The detailed high-pressure evolution of the doped clathrate structure evidence the presence of a further isostructural change at relatively low pressures [118] that can be associated to changes in the coupling between the guest and host atoms in the larger Si_{24} cages [118,120,121]. On the other side, a change in the guest-silicon coupling of the $M@Si_{20}$ cluster could be at the origin of the observed high pressure induced compressibility catastrophe of doped silicon clathrates [121].

2.4 Conclusion

We have reviewed recent advances in the synthesis and properties of cluster-assembled networks. Crystallized or amorphous-like networks present novel properties with respect to the diamond Si phase. Most of the reviewed properties are related to the elemental bricks themselves that compose the network. These bricks which are built up from the assembling of individual atoms limited to the nanoscale give rise to the novel-observed features.

The main common feature of the 2D and 3D cluster assemblings discussed in this chapter is the sp^3 character that governs their physical properties. In the cluster-assembled films, dangling bonds lead to a surface reconstruction, having as consequence a local over coordination for a certain number of atoms. In the 3D-clathrate cluster assembling, the full-covalent interconnection leads to a four-fold coordination. The particular topology of the network is based on small fullerene-type clusters which can host different atom types. This endohedral intercalation allows for the heavily degenerated doping of the structure leading to such unusual properties as the silicon superconductivity.

Acknowledgements

The authors are indebted to G. Guiraud and O. Boisron for technical assistance to perform Si cluster deposition experiments using the cluster generator of the "Centre interlaboratoire lyonnais de recherche sur les agrégats". Christian Cros and Michel Pouchard from ICMCB-Bordeaux, France, who discovered the silicon clathrates are warmly thanked for all the scientific discussions as well as for their

personal implication in part of the work here presented. We thank Prof. Yamanaka (University of Hiroshima, Japan) for many discussions as for providing some of the clathrate samples studied. We would like to thank all the colleagues from our laboratory that have participated in one way or another to obtain the results presented (Ch. Adessi, A. Aouzierat, D. Connétable, P. Kéguélian, S. Le Floch, B. Masenelli, A. Merlen, P. Toulemonde, F. Tournus). We thank also our colleagues from synchrotron radiation (ESRF-Grenoble, France, LURE-Orsay, France) and neutron sources (ILL-Grenoble, France) who have contributed to the measurements.

REFERENCES

1. Z. Iqbal and S. Vepřek, *J. Phys. C: Solid State Phys.* **15**, 377 (1982).
2. R. Erlandsson, L. Olsson and P. Martensson, *Phys. Rev. B* **54**, (1996).
3. K. Takayanagi, Y. Tanishiro, M. Takahashi and S. Takahashi, *J. Vac. Sci. Technol. A* **3**, 1502 (1985).
4. H. Hofmeister, F. Huisken and B. Kohn, *Europ. Phys. J. D* **9**, 137 (1999).
5. J.R. Chelikowsky, *Phys. Rev. Lett.* **60**, 2669 (1988).
6. E.G. Honea, A. Ogura, D.R. Peale, C. Félix. C.A. Murray, K. Raghavachari. W.O. Sprenger, M.F. Jarrold and W.L. Brown, *J. Chem. Phys.* **110**, 12161 (1999).
7. C. Xu, T.R. Taylor, G.R. Burton and D.M. Neumark, *J. Chem. Phys.* **108**, 1395 (1997).
8. A.A. Shvartsburg, B. Liu, M.F. Jarrold and K.M. Ho, *J. Chem. Phys.* **112**, 4517 (2000).
9. S.N. Behera, B.K. Panda, S. Mukherjee and P. Entel, *Phase Transit.*, **75**, 41 (2002).
10. J.M. Alford, R.T. Laaksonen and R.E. Smalley, *J. Chem. Phys.* **94**, 2618 (1990).
11. M.F. Jarrold and V.A. Constant, *Phys. Rev. Lett.* **67**, 2994 (1991).
12. B. Marsen, M. Lonfat, P. Scheier and K. Sattler, *Phys. Rev. B* **62**, 6892 (2000).
13. E. Kaxiras, *Phys. Rev. Lett.* **64**, 551 (1990).
14. M.V. Ramakrishna and J. Pun Pan, *J. Chem. Phys.* Vol. 101, 8108 (1994).
15. U. Rothlisberger, W. Andreoni and M. Parinello, *Phys. Rev. Lett.* **72**, 665 (1994).
16. P. Mélinon, P. Keghélian, B. Prével, A. Perez, G. Guiraud, J. LeBrusq, J. Lermé, M. Pellarin and M. Broyer, *J. Chem. Phys.* **107**, 10278 (1997).
17. C. Cros, M. Pouchard and P. Hagenmuller, *Compt. Red. de l'Académie des Sci.* **260**, 4764 (1965).
18. Si target can be replaced by a rod shaped target of a well-defined Si: C composition. A sophisticated double target laser vaporization source with C_{60} and Si targets is used for $C_{60} - Si$ system.
19. D. Tománek and M.A. Schlüter, *Phys. Rev. Lett.* **56**, 1055 (1986).
20. *Cluster beam synthesis of nano-structured materials.* Eds. P. Milani and S. Iannotta. *Springer series in Cluster Physics* (Springer Verlag, Berlin-Germany 1999).
21. P. Jensen, *Rev. Mod. Phys.* **71**, 1695 (1999).
22. L. Bardotti, B. Prével, M. Treilleux, P. Mélinon and A. Perez, *Appl. Surf. Sci.* **164**, 52 (2000).
23. C. Brechignac, P. Cahuzac, F. Carrier, M. De Frutos, A. Masson, C. Mory, C. Colliex and B. Yoon, *Phys. Rev. B* **57**, 2084 (1998).
24. C.S. Casari, A. Li Bassi, L. Ravagnan, F. Siviero, C. Lenardi, P. Piseri, G. Bongiorno, C.E. Bottani and P. Milani, *Phys. Rev. B* **69**, 75422 (2004).
25. V. Paillard, P. Mélinon, V. Vouis, J.P. Perez, A. Perez and B. Champagnon, *Phys. Rev. Lett.* **71**, 4170 (1993).
26. P. Mélinon, B. Masenelli, A. Perez, M. Pellarin and M. Broyer, *C.R. Physique* **3**, 273 (2002).
27. P. Mélinon, P. Kéghélian, A. Perez, J.L. Rousset, A.M. Cadrot, A. Malhomme and A. Renouprez, *Phil. Mag. A* **80**, 143 (2000).
28. H. Haberland, Z. Insepov and M. Moseler, *Phys. Rev. B* **51**, 11061 (1995).
29. A. Canning, G. Galli and J. King, *Phys. Rev. Lett.* **78**, 4442 (1997).
30. D. Donadio, L. Colombo, P. Milani and G. Benedek, *Phys. Rev. Lett.* **83**, 776 (1999).
31. M. Treilleux, G. Fuchs, F. Santos Aires, P. Mélinon, A. Hoareau and B. Cabaud, *Z. Phys.* **20**, 263 (1991).
32. Fourier transform and filtering, atomic absorption modelized by a sixth order polynomial expression, normalisation following Lengeler-Eisenberg algorithm.

33. P. Mélinon, P. Kéghélian, B. Prével, V. Dupuis, A. Perez, B. Champagnon, Y. Guyot, M. Pellarin, J. Lermé, M. Broyer, J.L. Rousset and P. Delichère, *J. Chem. Phys.* **108**, 4607 (1998).
34. S. Schuppler, S.L. Friedman. M.A. Marcus, D.L. Adler, Y.H. Xie, F.M. Ross, T.D. Harris, W.L. Brown, Y.J. Chabal, L.E. Brus and P.H. Citrin, *Phys. Rev. Lett.* **72**, 2648 (1994).
35. A. Filipponi, F. Evangelisti, M. Benfatto, S. Mobilio and C.R. Natoli, *Phys. Rev. B* **40**, 9636 (1989).
36. M. Wakagi, K. Ogata and A. Nakano, **50**, 10666 (1994).
37. P. Mélinon, P. Kéghélian, X. Blase, J. LeBrusc, A. Perez, E. Reny, C. Cros and M. Pouchard, *Phys. Rev. B*, **58**, 12590 (1998).
38. R.P. Vasquez, R.W. Fathauer, T. George, A. Ksendzov and T.L. Lin, *Appl. Phys. Lett.* **60**, 1004 (1992).
39. V. Paillard, P. Puech, M.A. Laguna, R. Carles, B. Kohn and F. Huisken, *J. Appl. Phys.* **86**, 1921 (1999).
40. R. Shuker and R.W. Gammon, *Phys. Rev. Lett.* **25**, 222 (1970).
41. P. Mélinon, P. Kéghélian, A. Perez, B. Champagnon, Y. Guyot, L. Saviot, E. Reny, C. Cros, M. Pouchard and A.J. Dianoux, *Phys. Rev. B* **59**, 10099 (1998).
42. I. Vasiliev, S. Öğüt, and J.R. Chelikowsky, *Phys. Rev. Lett.* **86**, 1813 (2001).
43. T. Van Buuren, L.N. Dinh, L.L. Chase, W.J. Siekhaus and L.J. Terminello, *Phys. Rev. Lett.* **80**, 3803 (1998).
44. G. Ledoux, O. Guillois, D. Porterat, C. Reynaud, F. Huisken B. Kohn and V. Paillard, *Phys. Rev. B* **62**, 15942 (2000).
45. S. Hayashi, T. Nakareda, Y. Kanzawa and K. Yamamoto, *J. Appl. Phys.* **32**, 3840 (1993).
46. I. Vasiliev, J.R. Chelikowsky and R.M. Martin, *Phys. Rev. B* **65**, 121302 (2002).
47. M. Ehbrecht, B. Kohn, F. Huisken, M.A. Laguna and V. Paillard, *Phys. Rev. B* **56**, 6958 (1997).
48. C. Delerue, G. Allan and M. Lannoo, *Phys. Rev. B* **48**, 11024 (1993).
49. M. Pellarin, C. Ray, J.L. Vialle, M. Broyer, X. Blase, P. Kéghélian, P. Mélinon and A. Perez, *J. Chem. Phys.* **110**, 6927 (1999).
50. C. Ray, M. Pellarin, J. Lermé, J.L. Vialle, M. Broyer, X. Blase, P. Mélinon, P. Kéghélian and A. Perez, *Phys. Rev. Lett*, **80**, 5365 (1998).
51. M. Pellarin, C. Ray, J.L. Vialle, M. Broyer and P. Mélinon, *J. Chem. Phys.* **112**, 8436 (2000).
52. F. Tournus, B. Masenelli, X. Blase, A. Perez, M. Pellarin, M. Broyer, A.M. Flank and P. Lagarde, *Phys. Rev. B* **65**, 165417 (2002).
53. A.L. Ankudinov, B. Ravel, J.J. Rehr and S.D. Conradson, *Phys. Rev. B* **58**, 7565 (1998).
54. B. Masenelli, F. Tournus, P. Mélinon, A. Perez and X. Blase, *J. Chem. Phys.* **117**, 10627 (2002).
55. A. San-Miguel, *Chem. Soc. Rev.* **35**, 876 (2006).
56. S. Yamanaka, E. Enishi, H. Fukuoka and M. Yasukawa, *Inorg. Chem.* **39**, 56 (2000).
57. P. Toulemonde, A. San-Miguel, X. Blase, C. Adessi and J.L. Tholence, *Phys. Rev. B* **71**, 094504 (2005).
58. E. Reny, S. Yamanaka, C. Cros and M. Pouchard, *Chem. Commun.* **24**, 2505 (2000).
59. N. Jaussaud, M. Pouchard, G. Goglio, C Cros, A. Ammar, F. Weill and P. Gravereau, *Solid State Sci.* **5,** 1193 (2003).
60. N. Jaussaud, P. Toulemonde, M. Pouchard, A. San-Miguel, P. Gravereau, S. Pechev, G. Goglioa and C. Cros, *Solid State Sci.* **6**, 401 (2004).
61. N. Jaussaud, *Ph.D. Thesis*, University of Bordeaux-1 (France), 2003.
62. J. Gryko, P.F. MacMillan, R.F. Martzke, G.K. Ramachandran, D. Patton and S.K. Deb and O.F. Sankey, *Phys. Rev. B* **62**, R7707 (2000).
63. C. Cros, M. Pouchard and P. Hagenmuller, *J. Solid. State Chem.* **2**, 570 (1970).
64. H. Fukuoka, K. Ueno and S. Yamanaka, *J. Organomet. Chem.* **611**, 543 (2000).
65. H. Kawaji, H. omi Horie, S. Yamanaka and M. Ishikawa, *Phys. Rev. Lett.* **74**, 1427 (1995).
66. E. Reny, S. Yamanaka, C. Cros and M. Pouchard, *J. Phys. Condens. Mat.* **14**, 11233 (2002).
67. J. Gryko, R.F. McMillan, R.F. Marzke, G.K. Ramachandran, Patton, S.K. Deb and O.F. Sankey, *Phys. Rev. B* **62**, R7707 (2000).
68. G.B. Adams, M. O'Keefe, A.A. Demkov, O.F. Sankey and Y.M. Huang, *Phys. Rev. B* **49**, 8048 (1994).
69. P. Hohenberg and W. Kohn, *Phys. Rev.* **136**, 864 (1964).
70. W. Kohn, *Rev. Mod. Phys.* **71**, 1255 (1999).
71. E. Galvani, G. Onida, S. Serra and G. Benedek, *Phys. Rev. Lett.* **77**, 3573 (1996).
72. K. Moriguchi, M. Yonemura, A. Shintani and S. Yamanaka, *Phys. Rev. B* **61**, 9859 (2000).
73. S. Saito and A. Oshiyama, *Phys. Rev. B* **51**, 2628 (1995).
74. V.I. Smelyansky and J.S. Tse, *Chem. Phys. Lett.* **264**, 459 (1997).
75. W. Kohn and L.J. Sham, *Phys. Rev.* **140**, 1133 (1965).

76. L.J. Sham and M. Schlüter, *Phys. Rev. Lett.* **51**, 1888 (1994).
77. M. Hybertsen and S.G. Louie, *Phys. Rev. B* **34**, 5390 (1985).
78. X. Blase, X. Zhu and X. Louie, *Phys. Rev. B* **49**, 4973 (1994).
79. O. Pulci, G. Onida, R. Del Sole and L. Reining, *Phys. Rev. Lett.* **81**, 5374 (1998).
80. M. Rohlfing, P. Krüger and J. Pollmann, *Phys. Rev. B* **52**, 1905 (1995).
81. S. Ishi, K. Ohno, Y. Kawazoe and S.G. Louie, *Phys. Rev. B* **65**, 245109 (2002).
82. X. Blase, *Phys. Rev. B* **67**, 35211 (2003).
83. L. Hedin, *Phys. Rev.* **139**, A796 (1965).
84. L. Hedin and S. Lundqvist, *Solid State Phys.* **23**, 1 (1969).
85. P. Giannozzi, S. de Giroucouli, P. Pavone and S. Baroni, *Phys. Rev. B* **43**, 7231 (1991).
86. P. Melinon, P. Keghelian, A. Perez, B. Champagnon, Y. Guyot, L. Saviot, E. Reny, C. Cros, M. Pouchard and A.J. Dianoux, *Phys. Rev. B* **59**, 10099 (1999).
87. M. Widow, *Phys. Rev. B* **34**, 756 (1986).
88. M.T. Yin and M.L. Cohen, *Phys. Rev. Lett.* **45**, 1004 (1980).
89. A. San-Miguel and P. Kéghélian, X. Blase, P. Mélinon, A. Perez, J.P. Itié, A. Polian, E. Reny, C. Cros and M. Pouchard, *Phys. Rev. Lett.* **83**, 5290 (1999).
90. M.L. Cohen, *Phys. Rev. B* **32**, 7988 (1985).
91. P. Mac Millan, private communication.
92. J.L. Cohn, G.S. Nolas, V. Fessatidis, T.H. Metcalf and G.A. Slack, *Phys. Rev. Lett.* **82**, 1999 (1999).
93. J. Dong, O.F. Sankey and C.W. Myles, *Phys. Rev. Lett.* **86**, 2361 (2001).
94. J.S. Tse, K. Uehara, R. Rousseau, A. Ker, C.I. Ratcliffe, M.A. White and G. Mackay, *Phys. Rev. Lett.* **85**, 114 (2000).
95. V. Timoshevskii, D. Connétable, and X. Blase, *Appl. Phys. Lett.* **80**, 1385 (2002).
96. Y. Li and J.H. Ross Jr., *Appl. Phys. Lett.* **83**, 2866 (2003).
97. B.F. Brunet, P. Mélinon, A. San-Miguel, P. Kéghélian, A. Perez, A.M. Flank, E. Reny, C. Cros and M. Pouchard, *Phys. Rev. B* **61**, 16550 (2000).
98. F. Tournus, B. Masenelli, P. Mélinon, D. Connétable, X. Blase, A.M. Flank, P. Lagarde, C. Cros and M. Pouchard, *Phys Rev. B* **69**, 035204 (2004).
99. H. Libotte, J.P. Gaspard, A. San-Miguel and P. Mélinon, *Euro. Phys. Lett.* **64**, 757 (2003).
100. E. Reny, A. San-Miguel, Y. Guyot, B. Masenelli, P. Mélinon, L. Saviot, S. Yamanaka, B. Champagnon, C. Cros, M. Ponchard, M. Borowski and A. J. Diamonx, *Phys. Rev. B* **66**, 14532 (2002).
101. D. Connétable, V. Timoshevskii, E. Artacho and X. Blase, *Phys. Rev. Lett.* **87**, 206405 (2001).
102. D. Connetable, PhD thesis, university of Lyon, France (2003) and *Phys. Rev. B* **75**, 125202 (2007).
103. V. Kumar and Y. Kawazoe, *Phys. Rev. B* **75**, 155425 (2007).
104. V.H. Crespi, *Nature Mater.* **2**, 650 (2003).
105. J. Nagamatsu, *et al.*, *Nature* **410**, 63 (2001).
106. E.A. Ekimov, V.A. Sidorov, E.D. Bauer, N.N. Mel'nik, N.J. Curro, J.D. Thompson and S.M. Stishov, *Nature* **428**, 542 (2004).
107. X. Blase, *et al., Phys. Rev. Lett.* **93**, 237004 (2004).
108. J.D. Bryan, V.I. Srdanov, G.D. Stucky and D. Schmidt, *Phys. Rev. B* **60**, 3064 (2000).
109. R.F.W. Herrmann, K. Tanigaki, S. Kuroshima and H. Suematsu, *Chem. Phys. Lett.* **283**, 29 (1998).
110. S. Saito and A. Oshiyama, *Phys. Rev. B* **51**, 2628 (1995).
111. M.M. Dacarogna and M.L. Cohen, *Phys. Rev. Lett.* **55**, 837 (1985).
112. K. Tanigaki, *Nature Mater.* **2**, 653 (2003).
113. W.L. McMillan, *Phys. Rev.* **167**, 331 (1968).
114. D. Connétable, V. Timoshevskii, B. Masenelli, J. Beille, J. Marcus, B. Barbara, A.M. Saitta, G.-M. Rignanese, P. Mélinon, S. Yamanaka and X. Blase, *Phys. Rev. Lett.* **91**, 247001 (2003).
115. I. Spagnolatti, M. Bernasconi and G. Benedek, *Eur. Phys. J. B* **34**, 63 (2003).
116. X. Blase, Ch. Adessi and D. Connétable, *Phys. Rev. Lett.* **93**, 237004 (2004).
117. A. San Miguel, P. Mélinon, D. Connetable, X. Blase, F. Tournus, E. Reny, S. Yamanaka and J.P. Itié, *Phys. Rev. B* **65**, 054109 (2002).
118. T. Kume, H. Fukuoka, T. Koda, S. Sasaki, H. Shimizu and S. Yamanaka, *Phys. Rev. Lett.* **90**, 155503 (2003).
119. T. Kume, T. Koda, S. Sasaki, H. Shimizu and J.S. Tse, *Phys. Rev. B* **70**, 2101 (2004).
120. J.S. Tse, S. Desgreniers, Z.Q. Li, M.R. Ferguson and Y. Kawazoe, *Phys. Rev. Lett.* **89**, 195507 (2002).
121. A. San-Miguel and P. Toulemonde, High Pressure Research **25**, 159 (2005).

CHAPTER THREE

Metal Encapsulated Clusters of Silicon: Silicon Fullerenes and Other Polyhedral Forms

Vijay Kumar

Contents

3.1 Introduction 115
3.2 Clusters of Elemental Silicon 118
3.3 Metal Encapsulation: A New Paradigm 121
3.3.1 Silicon Fullerenes 121
3.3.2 Metal Size Dependent Encapsulated Silicon Structures 122
3.3.3 The Electronic Factor and the Isolated Rhombus Rule 124
3.3.4 Reactivity as a Probe of Metal Encapsulation 137
3.3.5 Vibrational Properties 137
3.3.6 Empty and Endohedral Hydrogenated Fullerene Cages of Silicon 139
3.3.7 Absorption Spectra 142
3.3.8 Magnetic Clusters of Silicon 142
3.4 Summary 144
Acknowledgments 145
References 145

Abstract

Calculations on encapsulation of a metal atom in silicon clusters have led to the predictions of novel forms of nanosilicon and the discovery of silicon fullerenes. There is renewed interest in the study of silicon nanoclusters and the understanding of the effects of doping with metal atoms. Experiments on doped clusters of silicon as well as other group 14 elements have led to the realization of some of the predictions. Here we review this progress. Encapsulation of a metal atom enhances the stability of nanoclusters and often leads to a striking preference for a specific size. This can facilitate the design and production of nanoclusters of silicon with specific properties in high abundance and the development of assemblies of such species. We discuss the electronic origin of the stability of such species as well as their magnetic, vibrational, and optical properties. Hydrogen termination has been used to predict empty cage silicon fullerenes as

Dr. Vijay Kumar Foundation, 45 Bazaar Street, K.K. Nagar (West), Chennai 600078, India.
The Institute of Mathematical Sciences, Taramani, Chennai 600113, India.
Research Institute for Computational Sciences (RICS), National Institute of Advanced Industrial Science and Technology (AIST), AIST Tsukuba Central 2, Tsukuba, Japan.

Nanosilicon
9780080445281
Copyright © 2007. Elsevier Ltd.
All rights reserved.

well as their endohedral and exohedral forms that could have potential for the development of many derivatives and functional materials similar to carbon fullerenes as well as their interesting optical and magnetic properties for nanoscale applications.

3.1 Introduction

The continuous downsizing of the silicon based devices and the finding of bright luminescence from porous silicon [1] have led to a major thrust in the understanding of the nanostructures of silicon in recent years. Fundamental research on small silicon clusters started about two decades ago with the advent of cluster sources using laser ablation or thermal evaporation methods [2–9]. Several experimental studies have been performed on abundance of silicon clusters and the dependence on source and nucleation conditions, effects of reactions with gases [8,9], ionization potential (IP), electron affinity (EA) [10], photoemission [11], and vibrational spectra [12,13] and the understanding of the shape from ion mobility measurements [14]. Simultaneously quantum mechanical calculations [15–17] have been performed to determine the structures of very small clusters having only a few atoms. In the early days of these developments, it was a difficult task to understand the structures of Si_n clusters even with a few (n up to about 10) atoms. The reconstruction of the atomic structure of a bulk fragment due to the presence of dangling bonds makes compact structures favourable and these are very different from bulk. There are possibilities of the simultaneous occurrence of isomers which could have quite different properties. Also in experiments clusters are generally observed in charged state. Therefore it is important to understand the properties of charged clusters as a higher energy neutral isomer could become lower in energy in a charged state. It has therefore been an important task to understand the evolution of the structures and properties with an increase in size and the changes due to charging. The difficulty of the task could be imagined from the fact that even now cluster sizes that have been well studied quantum mechanically are limited to a few tens of atoms [18–30] and only in a few cases nanoparticles with a few hundred atoms have been explored (e.g. see Refs. [31–34]) in spite of the great advances in computer power. Theoretically it is almost impossible in most cases to know if one has achieved the true ground state for a given number of atoms. Experimental data from photoemission, IP, EA as well as vibrational and optical absorption spectra have been used to support theoretical findings and vice versa. These studies have demonstrated that the properties of clusters could change very significantly with size and with shape (in case more than one isomer is produced). For applications, one would like to produce clusters with size selectivity. However, mass abundance spectra of silicon clusters do not show any striking preference of size beyond 10 atoms (Figs. 3.1 and 3.2). A way to change this behaviour could be technologically advantageous so that silicon clusters and nanoparticles could be mass produced with a control on size.

An important aspect of the nanoscale structures of silicon has been the discovery [1] of bright luminescence from porous silicon in 1991 because bulk silicon is a bad emitter of light due to its indirect band gap. This finding led to the hope of using silicon as an optical material and great attention has been paid to the understanding as

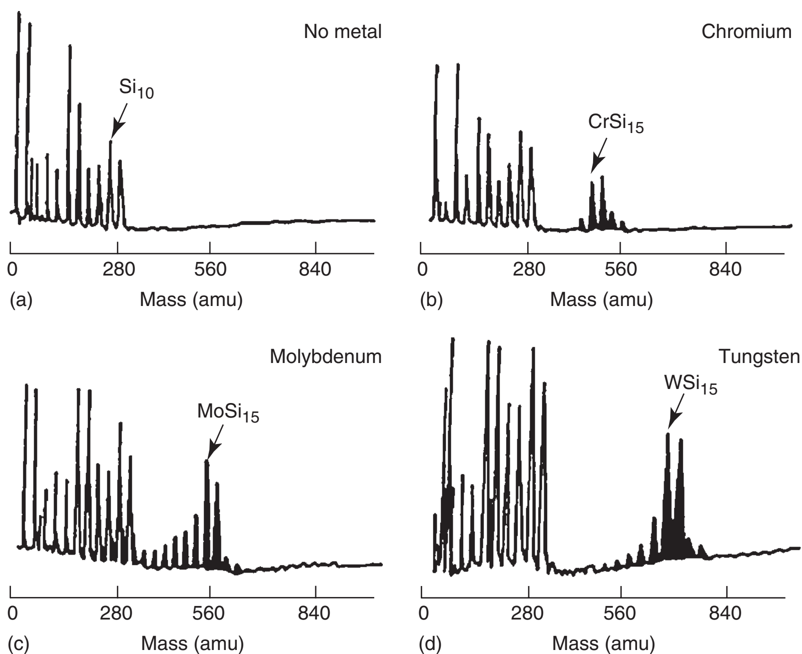

Figure 3.1 193 nm (6.4 eV) ArF laser photoionization time of flight mass spectra showing: (a) bare silicon clusters formed by laser vaporization of a silicon wafer followed by supersonic expansion, (b) reaction products formed in supersonic nozzle between chromium atoms and silicon to form $CrSi_n$ clusters, (c) $MoSi_n$, and (d) WSi_n. The metal atom-silicon cluster peaks in each spectrum are darkened for emphasis. Undarkened peaks represent bare silicon clusters. ArF laser fluence in each case was about 1 mJ/cm^2. At this fluence very little intensity is seen for elemental silicon clusters with more than 11 atoms (Reproduced with permission from Ref. [76], copyright AIP 1989).

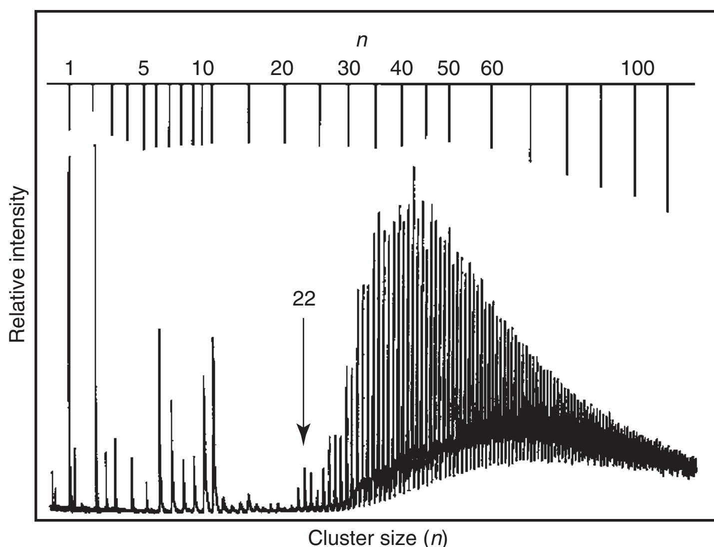

Figure 3.2 Photoionization mass spectrum of silicon clusters, Si_n, n = 1–120, obtained with the cold cluster source and 6.42 eV (ArF) radiation (Reproduced with permission from Fuke *et al*. Ref. [10], copyright AIP 1993, courtesy K. Fuke).

well as applications of porous silicon. Porous silicon has nanostructures that are nanoparticles and nanowires. Several theoretical studies have been carried out on nanoparticles and nanowires of silicon in which the dangling bonds have been saturated by H atoms to understand the effects of quantum confinement on the electronic structure. These studies did show the possibility of a direct band gap in nanowires (see the Chapter by Singh *et al.*) and absorption by nanoparticles in the visible range. Further experimental and theoretical studies on the properties of silicon nanoparticles of varying sizes and the effects of capping with different species (e.g. see Refs. [31, 35–38]) have led to significant progress in our understanding of silicon nanostructures. Recently size selected hydrogenated clusters of silicon have been produced [39] which exhibit photoluminescence with RGB colours. These developments have been discussed in Chapter One by Nayfeh and Mitas.

A decade later, in 2001 an experimental study [40] on reaction of silane gas with metal monomers and dimers showed that no hydrogen was associated with $Si_{12}W$ cluster presumably due to encapsulation of W atom within silicon. Calculations did show a hexagonal prism structure with W at the centre to be most favourable. This was an interesting finding. Extensive theoretical work [41] on the role of metal encapsulation in the stabilization of silicon clusters has shown that metal encapsulation is a novel way to produce size selected clusters of silicon and other materials in large quantities with tailor made properties. It has led to the predictions of silicon fullerene [42] and many other polyhedral structures as well as created wide interest in the understanding of these systems [43–74]. Much before these developments in 1987 Beck [75,76] studied doping of silicon clusters with Cr, Mo, and W atoms in order to get an insight about Schottky barrier formation. As shown in Fig. 3.1 he obtained strikingly high abundances of $Si_{15}M$ and $Si_{16}M$ clusters with $M =$ Cr, Mo, and W and low abundances of other sizes of metal doped silicon clusters. In order to understand the abundance spectra, he even postulated a possible scenario where metal atom acts as a seed and silicon atoms form a shell structure with a specific number of atoms around the metal atom. Calculations [42,45–47,53,54,58] indeed support this conjecture.

The remarkable results of Beck [75,76] remained buried in literature for a long time. It is presumably due to the fact that (1) an understanding of the atomic structures and properties of elemental silicon clusters was itself evolving and (2) the treatment of clusters with transition metal atoms was difficult. The finding [40] of $Si_{12}W$ cluster attracted renewed interest because much progress has already been made [77] in the understanding of the structures and properties of clusters of Si and a variety of other elements including transition metals. A detailed study of these systems became possible also due to a big jump in computer power in these years. It led to the understanding of the stability of 15- and 16-atom Si clusters [45] with doping of Cr, Mo, and W atoms as well as to the prediction of many other magic clusters [42,46,47,54,58,59]. It is noteworthy that earlier calculations [78] on a Zr atom in Si_{20} dodecahedral cage showed a large gain in energy. However, this structure was later shown [42] to be unstable when optimized and a $Si_{16}Zr$ fullerene was predicted to be optimal. Following these initial successes of predicting metal encapsulated silicon clusters, several experimental studies have been made [68–71] and the predictions [42] of the magic behaviour of $Ti@Si_{16}$ as well as some other clusters [46,47] have been confirmed [70,71]. Further theoretical studies on reaction of hydrogen showed a possibility of stabilizing cage structures of silicon [41,67], and

their endohedral [79,80] as well as exohedral [81] derivatives. This could lead to novel possibilities of functionalization of silicon fullerenes as well as the development of nanostructures with useful magnetic and optical properties. Similar to carbon fullerenes [82] these findings have opened up a new way of using silicon at the nanoscale as well as assembling novel structures [83] similar to solid C_{60}. In this Chapter we present these developments and review briefly the results on elemental silicon clusters in the next section for reference. The reader is referred to the Chapters by Melinon *et al.* as well as by Nayfeh and Mitas for more information on nanoparticles of silicon. Also a related chapter by Singh *et al.* deals with the assemblies of metal encapsulated clusters and the findings of silicon nanotubes.

3.2 Clusters of elemental silicon

The mass abundance spectrum of cation silicon clusters shows a few prominent peaks in the small size range such as for Si_6^+, Si_{10}^+, and Si_{11}^+ but in the intermediate and large size range the abundances could be quite different depending on the nucleation, ionization, and photofragmentation conditions (Figs. 3.1 and 3.2). For Si_n cation clusters ($n > 20$) there is a rather smooth variation in the abundance of clusters with no particular magic size (Fig. 3.2). However, in Fig. 3.1 little intensities are seen for clusters with $n > 11$ because in this experiment larger clusters fragmented into smaller ones. Independent fragmentation studies [4,6,10] on Si clusters have also shown breaking of clusters with more than 10 atoms into subclusters. This is in contrast to the behaviour of metal clusters in which atom by atom removal is generally most favourable. Reactivity [8,9] of oxygen, H_2O, NO_2, and other molecules has been used to find magic clusters. Measurements [10] of the IP and EA show high values of approximately 6.8–8.0 eV for IP with local maxima at $n = 6, 7$, and 10 and low values (approximately in the range of 2.3–3.0 eV) of EA. These results also support high stability of Si_6 and Si_{10}. A change in the values of the IP has been seen beyond $n = 21$ and this has been suggested to indicate a change in the atomic growth pattern (see Fig. 3.3a). Ion mobility experiments [14] also showed prolate shape of clusters in the range of 20–27 atoms beyond which the shape becomes spherical. The prolate structures are made up [30,84] of smaller clusters such as Si_9, Si_{10} or Si_6 with variations in linking. Recent photoemission experiments [11] also support a structural transition with increasing size. It has been found [85,86] (Fig. 3.3b) that the dissociation energy of clusters increases rapidly with size in the range of $n \leqslant 10$ and becomes nearly flat in the range of $n = 11$–25 and then increases nearly linearly as a function of $n^{-1/3}$ towards the bulk value. The constant behaviour of the binding energy has also been related to the formation of prolate structures whereas a linear behaviour with $n^{-1/3}$ suggests more spherical shape of clusters. There have been suggestions [19] of fullerene like structures (Fig. 3.3a) of silicon clusters in the range of $n > 30$. In recent years there has been renewed interest in understanding the atomic structures and new closed packed isomers based on stuffed fullerene structure of carbon have been found [30]. In the prolate structures, the surface energy is higher which decreases in the more compact spherical isomers with increasing size. Horoi and Jackson [86] compared the flattening of the binding energy curve around the size of $n = 10$–25 with the binding

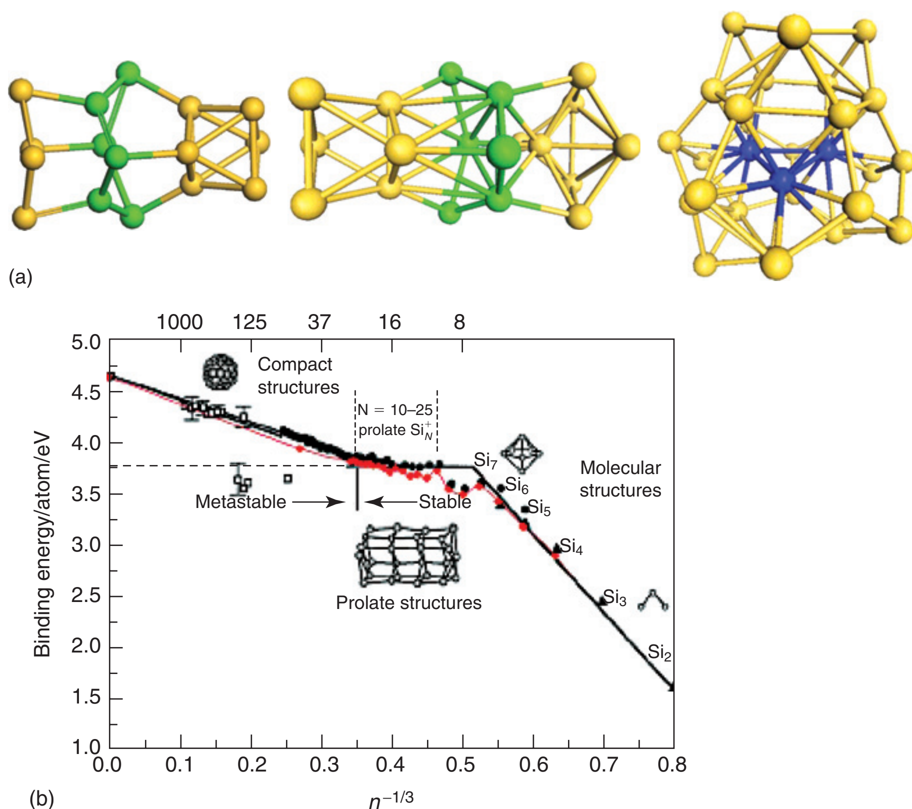

Figure 3.3 (a) Representative structures of small Si_n clusters, $n = 16$, 20, and 31. For $n = 16$ and 20 elongated structures are favored. For larger clusters elongated and three-dimensional structures based on stuffed fullerenes start competing. One such structure is shown for $n = 31$. Green balls show six-atom unit sandwiched between Si_4 and Si_6 in Si_{16} and Si_6 and Si_8 in Si_{20}. Blue balls show Si atoms inside the cage. (Courtesy X. C. Zeng) (b) Binding energy per atom versus $n^{-1/3}$ for neutral silicon clusters from different calculations. The line shows the trend: rapidly increasing from very small clusters till $n \sim 7$, nearly flat for $n \sim 10$–25 and then increasing linearly for larger sizes (after Ref. [86], courtesy M. Horoi and K.A. Jackson).

energy per nucleon of samarium chain of isotopes. Also for Sn clusters Majumder *et al.* [87] obtained flattening of the binding energy versus $n^{-1/3}$ for small clusters with $n > 10$.

As silicon is reactive with oxygen, oxygen etching reactions have been used [88] on cation and anion clusters to determine their relative stability. Cation clusters with $n = 4, 6, 9, 13, 14$, and 23 and anion clusters with $n = 18, 21, 24, 25$, and 28 were found to be magic, though the conclusion of the magic nature was not strong. In general the reactivity of silicon clusters is lower by 2–3 orders of magnitude compared with the most stable Si surface, Si(111) 7×7 and there is a minimum in the reactivity of annealed [7] Si_n clusters with $n = 33, 39$, and 45.

A large number of theoretical studies have been performed to understand the growth behaviour and the atomic structures of Si clusters. These include calculations

based on quantum chemical methods [15,21,27], density functional theory [17–19,22,28–30,32,33] and simpler methods such as those based on a tight binding approach [16,21,23,27] as well as the most modern quantum Monte Carlo (QMC) methods [24,26,31]. Since the structures of small clusters are very different from the tetrahedral bonded bulk structure, it is a difficult task to find the most favourable atomic structure for a given size. The simulated annealing method which is very successful for metal clusters is generally inappropriate in the case of silicon though good results have been obtained [17] particularly for small size clusters. Genetic algorithm [84] has also been used and this has led to the finding of lower energy structures. In Fig. 3.3a we have shown representative structures of small clusters. Up to a size of about 10 atoms, the structures are closed packed except for Si_4 which is a rhombus. In the range of 10–25 atoms, the atomic structures tend to have a prolate shape. Beyond $n = 25$ the clusters have spherical shaped distorted fullerene-like cage structures with pentagons and hexagons and a core of silicon atoms inside [19,24,28,89,90]. Atoms in the core have high coordination as these are connected to the cage. The interconnection between the cage and the core leads to distortions in the sp^2 bonding of the fullerene cage which is driven by the sp^3 hybridization. The presence of core also saturates partially the dangling bonds of the fullerene cage. This saturation may be optimal for clusters with $n = 33$, 39, and 45 leading to their low reactivity. Different structures of the low energy isomers of 33-, 39-, and 45-atom clusters have been suggested [19,28,30,90]. One possible way is 28 cage + 5 atoms inside, 32 cage + 7 atoms inside, and 36 cage + 9 atoms inside, respectively, but other isomers with different ways of the distribution of cage and core atoms are possible. Different sets of isomers were suggested such as Si_{28+n_c}, Si_{32+n_c}, Si_{36+n_c}, and Si_{38+n_c}, where n_c is the number of atoms in the core. For each cage size, there may be an n_c value that will optimally saturate the dangling bonds on the cage and among these some cages could be more stable with less reactivity. The core-cage isomers were shown to be significantly lower in energy than other structures predicted before. Yoo *et al.* [30] have recently studied the optimal combinations of the core and cage units and found the carbon fullerene cages to be most favourable in the range of $n = 27$–39. Some of the most favourable combinations were reported to be $Si_3@Si_{24}$, $Si_3@Si_{28}$, $Si_3@Si_{30}$, $Si_4@Si_{32}$, $Si_4@Si_{34}$, and $Si_5@Si_{34}$. More recently spherical shaped quantum dots of pristine Si were made [33] by joining tetravalent semiconductor fragments into an icosahedral particle. It has been shown from calculations that such icosahedral nanoparticles are more favourable than bulk fragments for diameters of less than 5 nm. As shown in Fig. 3.4, these quantum dots have tetrahedral bonding and a Si_{20} fullerene at the core. Further recent studies using molecular dynamics calculations [34] on nanoparticles of Si with 274, 280, and 323 atoms have shown that such nanoparticles do form an icosahedral structure as suggested by Zhao *et al.* [33]. These studies also support the measurements of the binding energies of silicon clusters which suggest closed packed spherical structures for large clusters. Calculations [13,91] on the vibrational spectra of small clusters have shown good agreement with the values obtained from Raman [12] and infrared [13] spectroscopies such as in the case of Si_7. Several researchers [11] have compared the measured and calculated photoelectron spectra and the EA values to obtain support for the calculated lowest energy structures of silicon clusters.

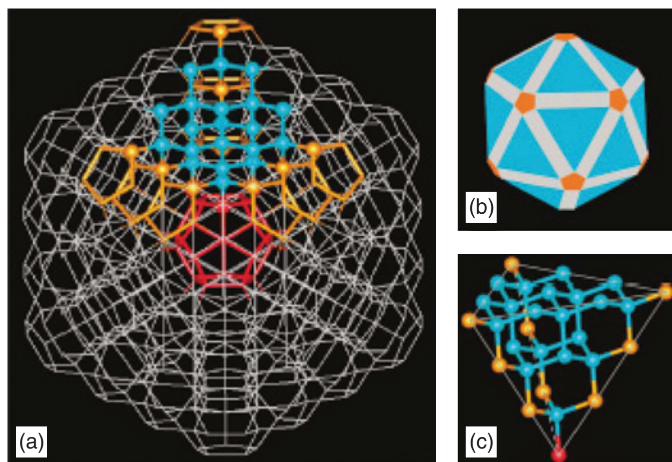

Figure 3.4 (a) An icosahedral tetrahedrally bonded network for a quantum dot of silicon with 600 atoms, (b) surface morphology, and (c) tetrahedron building block truncated from the bulk. Apex atoms of the tetrahedra form a dodecahedron, and edge atoms form radial channels of pentagonal rings (after Ref. [33], courtesy S.B. Zhang).

3.3 Metal encapsulation: a new paradigm

3.3.1 Silicon Fullerenes

The discovery of carbon fullerenes [82] led to curiosity if similar structures could be stable for silicon. For carbon, C_{60} is the most prominent. However, no such cluster/molecule has been found for silicon, though efforts have been made [92] to look for such possibilities. The reason for this failure is understandable. The bonding nature in C_{60} is predominantly sp^2 type. However, silicon favours sp^3 bonding as π bonding in silicon is weaker than in carbon. Therefore, silicon does not exist in graphite phase and isolated cage structures of elemental silicon are generally unstable. In bulk form fullerene cages of Si_{20} and Si_{24} or Si_{28} exist in silicon clathrates [93]. The cages are interlinked and this makes the bonding in clathrates close to sp^3 type. In 2001 Kumar and Kawazoe [42] studied from *ab initio* calculations the stabilization of dodecahedral Si_{20} fullerene using encapsulation of a Zr atom. When the structure was optimized, the dodecahedral fullerene structure deformed as shown in Fig. 3.5. Taking a clue from the experimental shrinking of carbon cages [94] with laser evaporation of dimers, calculations were performed using the strategy of an atom removal and cage shrinking approach which showed $Si_{16}Zr$ to be an optimally bonded cluster. Figure 3.5 shows the intermediate stages of the atom removal from the cage in which Si_{20} cage shrinks to Si_{19} and then to Si_{17} cluster with a Si_{16} cage. Zr@Si_{16} cluster has D_{4h} symmetric fullerene structure with 8 pentagonal and two square faces. Each silicon atom on the cage is 3-fold coordinated as in carbon fullerenes. However, because the size is smaller than 20 atoms needed to have all the pentagonal faces in the fullerene, there are rhombi in this 16-atom silicon fullerene and the pentagons are not regular. This result was simply very striking and very beautiful as it showed that symmetric fullerene structures of

silicon can be stabilized by encapsulation of a metal atom. Therefore a new paradigm emerged where novel nanostructures of silicon could be prepared with encapsulation of metal atoms. The Si_{16} fullerene cage is completely different from the structure of elemental Si_{16} cluster (Fig. 3.3a). There is a gain of ~14 eV when Zr atom is embedded in the cage due to very tight bonding between metal and Si atoms. The strong bonding is responsible for the total transformation of the structure of elemental silicon clusters. Therefore the bonding and stability of metal encapsulated silicon clusters is improved as compared to elemental Si clusters. It is expected that the fragmentation of the metal encapsulated silicon clusters will be quite different as compared to elemental silicon clusters in which case fragmentation in two subclusters is generally most favorable. Indeed recently photodissociation of cation Cr doped silicon clusters with $n = 15$ and 16 [94] has been shown to proceed via silicon evaporation resulting in to smaller Cr doped Si clusters while for Cu and Ag doping, dissociation of metal atom is favored. The highest occupied–lowest unoccupied molecular orbital (HOMO–LUMO) gap for $Zr@Si_{16}$ is about 1.58 eV within the generalized gradient approximation (GGA) for the exchange-correlation energy. The large value is also good for the stability of the silicon fullerene.

3.3.2 Metal Size Dependent Encapsulated Silicon Structures

Studies [42] on encapsulation of a Ti atom, isoelectronic with Zr, showed a tetrahedral Frank-Kasper (FK) polyhedron (Fig. 3.5) to be lower in energy than the fullerene isomer. This result showed that a small difference in the size of Ti and Zr atoms makes a significant difference in the stabilization of silicon structures. It is because encapsulation of a metal atom is highly exothermic with very strong bonding between metal and Si atoms. As Ti is a slightly smaller atom than Zr, a more compact cage with closed

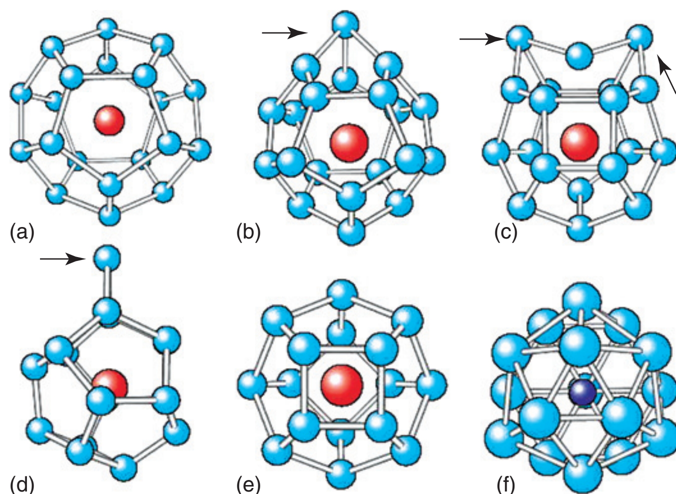

Figure 3.5 Shrinkage of the Si_{20} cage. (a) Dodecahedral Zr-encapsulated $Zr@Si_{20}$, (b)–(e) optimized structures of $Zr@Si_{20}$, $Zr@Si_{19}$, $Zr@Si_{17}$, and $Zr@Si_{16}$, respectively. The arrows indicate the atoms that were removed. (f) The Frank-Kasper polyhedral structure of $Ti@Si_{16}$. The light blue balls represent Si atoms and the metal atom is inside the cage. For clarity, bonds connecting the metal atom to the cage are not shown (after Ref. [42]).

packed structure becomes lower in energy. The dependence of the cage on the size of the metal atom was further confirmed when still smaller atoms such as Mo and Fe were doped and the cage structures with 15 and 14 Si atoms, respectively were found [42,45] to be optimal. One can also do a reverse experiment of increasing the size of the cage. It was found that for Ge, a FK isomer had [53] lower energy even for Zr doping because Ge atom is about 4% bigger in size than a Si atom. In this case again in the FK isomer the Ge cage becomes more compact to make optimal bonding with Zr atom. These calculations showed that with metal encapsulation it is possible to design novel nanostructures of silicon and other materials that could be much different from those of elemental material and have desired properties and size. The latter can be manipulated by choosing the right metal (dopant) atom. In metal encapsulated clusters of silicon, the metal atom holds the key for the lowest energy structure and optimal size and it can change the properties very significantly. This is seen from the fact that the GGA value of the HOMO–LUMO gap for $Ti@Si_{16}$ is 2.35 eV which is much larger than the value for $Zr@Si_{16}$. $Zr@Si_{16}$ and $Ti@Si_{16}$ have been predicted [57] to be luminescent in red and blue regions due to their very different HOMO–LUMO gaps. The large HOMO–LUMO gap of $Ti@Si_{16}$ makes it very stable. For another isoelectronic atom, Hf, both the fullerene and the FK cages are nearly degenerate. In this case, however, a small change occurs in the FK structure such that a triangle of 3 Si atoms along a 3-fold rotation axis gets rotated by 60°. Following these developments, Ohara *et al.* [68] performed experiments on anion clusters doped with M = Ti, Hf, Mo, and W atoms. MSi_{15}^- and MSi_{16}^- clusters were generally found to be strongly abundant and this was more special for the case of Ti. Also experiments on reactivity of water with Ti doped clusters showed little intensities of clusters having a water molecule beyond $n = 12$ suggesting that the metal atom was incorporated into a cage. Recently the prediction of the high stability of the FK $Ti@Si_{16}$ cluster was confirmed [70] when it was produced almost exclusively in high abundance (Fig. 3.6) in a way similar to C_{60} by fine tuning the source conditions, laser fluences, and the flow rate of the He career gas.

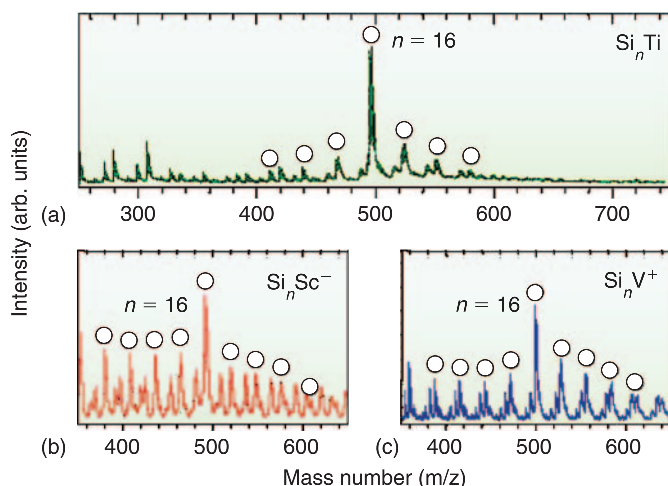

Figure 3.6 Mass spectra showing size-selective formation of (a) $TiSi_{16}$ neutrals, (b) $ScSi_{16}$ anions, and (c) VSi_{16} cations (Reproduced with permission from Ref. [70], copyright ACS 2005, courtesy A. Nakajima).

Photoelectron spectroscopy was also used to measure the EA of these clusters and the HOMO–LUMO gap. For $TiSi_{16}$ the EA is particularly low ($\sim$2 eV) and the HOMO–LUMO gap is large as also predicted. In order to check the role of the electronic structure, experiments were performed on Sc doped anion and V doped cation clusters. As shown in Fig. 3.6, in both these cases $n = 16$ cluster has high abundance but there are smaller intensities of clusters of other sizes also.

Subsequent to the above discoveries, extensive *ab initio* calculations [43–67] have been performed on encapsulation of different metal atoms which have led to the findings of a variety of new structures of Si and other materials such as Ge, Sn, and Pb. Kawamura *et al.* [55] have studied the growth behaviour of Ti, Zr, and Hf doped silicon clusters. Figure 3.7 shows the growth behaviour of Ti doped silicon clusters. For clusters with $n \geqslant 13$, Ti atom is encapsulated in a cage. As shown in Fig. 3.8, the binding energy of the Ti doped Si clusters increases monotonically [55,95] till $n = 16$ which leads to the high abundance of $Ti@Si_{16}$ clusters. On the other hand for Cr, it has been shown [56] that for 12 Si atoms, Cr atom is encapsulated in a cage and that $n = 12$, 15, and 16 clusters are special, though the abundance of the clusters was found to depend on the charged state. Interestingly clusters of these three sizes have been produced in experiments, though with different routes. $Si_{12}W$ was produced by Hiura *et al.* [40] while 15- and 16-atom clusters by Beck [76] as well as Ohara *et al.* [68]. For Ni, 10 Si atoms are sufficient to form a cage [54]. Therefore depending upon the relative atomic sizes of the metal (M) and the cage (X) atoms, a certain cluster size(s) is particularly favoured as only a specific number of atoms can generally be accommodated in a cage optimally due to the strong M-cage interactions. This leads to the size selectivity of the cages. The strong bonding of the metal atom with the X cage also quenches the magnetic moment of the M atom in most cases.

The effects of the relative atomic sizes of the M and X atoms on the abundance of the metal encapsulated clusters has been demonstrated [71] recently in experiments on Cr, Mn, Cu, and Zn doped clusters of Si, Ge, Sn, and Pb. As shown in Fig. 3.9, for Cr doping $n = 15$ and 16 clusters are most abundant similar to the results of Beck [75,76]. However, in the case of Cr doping in Ge clusters, $n = 14$, a smaller size cluster, also becomes significantly abundant and the highest intensity is for $n = 15$. For Sn and Pb, the spectra change very significantly. One can see that several sizes become significantly abundant and smaller clusters with $n = 7$, 10–12 also have relatively high intensities. When Cr is replaced by Mn, one can see the effects of the number of electrons on the transition metal atom. Figure 3.10 shows that for Mn doping in Si and Ge, the distribution becomes broader with several metal doped clusters becoming abundant though $n = 15$ and 16 are still most prominent. However for Pb, $n = 12$ cluster is very special. Special stability of isoelectronic $MnSn_{12}$ has been predicted [47].

3.3.3 The Electronic Factor and the Isolated Rhombus Rule

In general more than one type of atoms may have nearly the same atomic size and the electronic configuration of the metal atom determines which atomic structure could have the best stability. Different symmetries may need different metal atoms for nearly the same relative atomic sizes of M and X, and the number of the X atoms. This strategy was used by Kumar and coworkers to find suitable combinations for

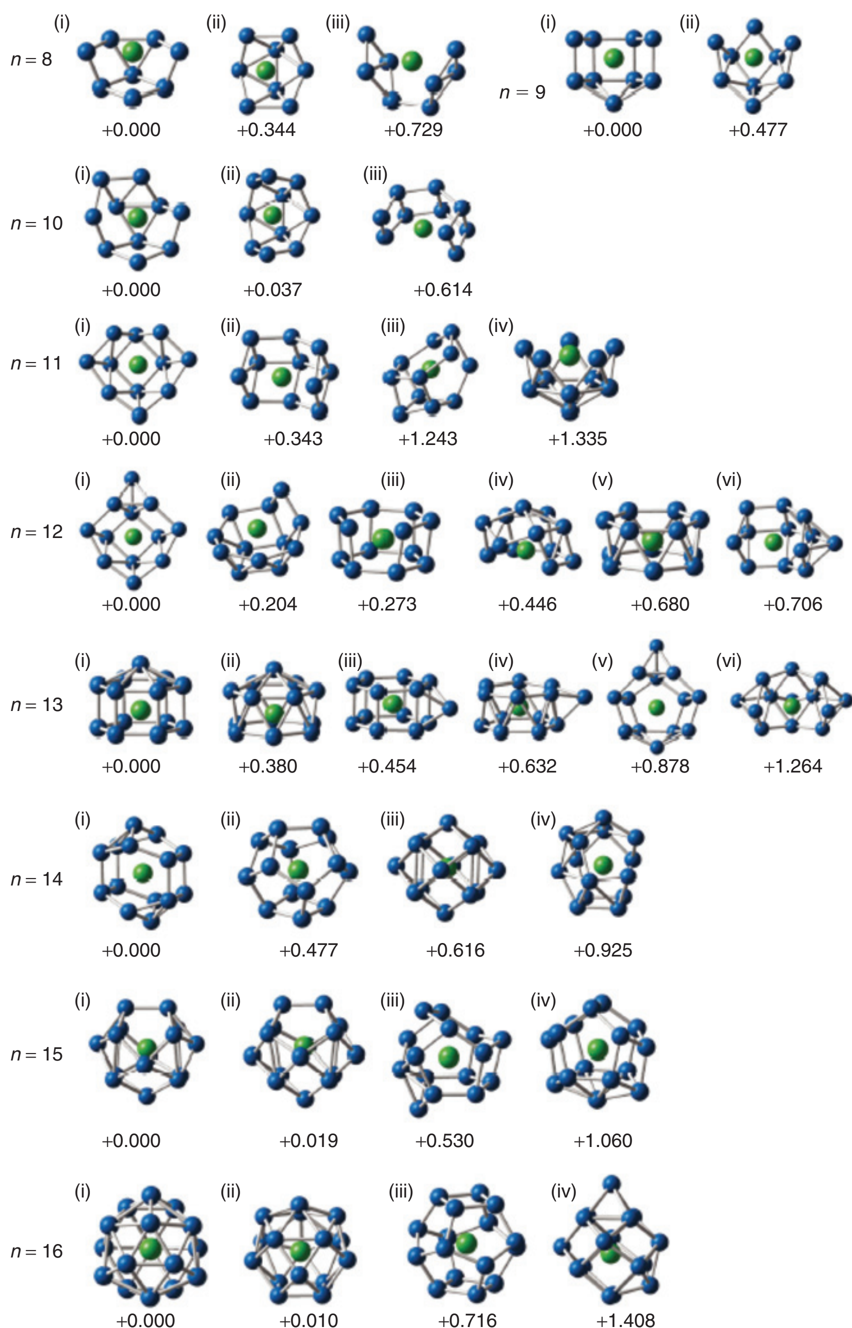

Figure 3.7 Structures and differences of the total energies from the most favourable isomer in each size for Ti@Si_n, $n = 8$–16 obtained by using the plane-wave pseudopotential method with GGA. Almost the same structures have been obtained for M@Si_n, M = Zr and Hf and $n = 8$–16. Isomers 10(i) and 10(ii) as well as 15(i) and 15(ii) are nearly degenerate. In addition, under experimental conditions of finite temperatures, a few other isomers may coexist such as those with an energy difference of about 0.2 eV in this figure. Green (blue) balls show M (Si) atoms [after Ref. [55]).

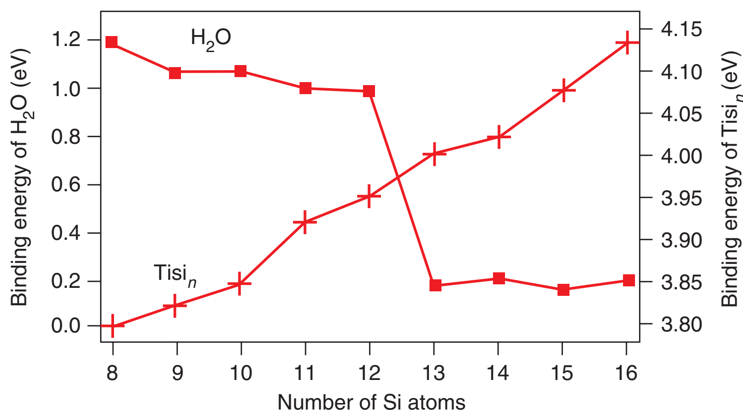

Figure 3.8 Interaction energies (left scale) between $TiSi_n$ and H_2O, n = 8–16. The right scale shows the binding energy per atom of $TiSi_n$ clusters. Experiments show little abundance of $TiSi_n$ clusters with H_2O molecules beyond n = 12 (after Ref. [95]).

$M@X_n$, n = 8–20 clusters in which encapsulation may be possible. Figures 3.11 and 3.12 show some of the interesting combinations of metal encapsulated silicon clusters of different sizes. The resulting clusters could be characterized to have either fullerene-like structures shown in Figs. 3.11a and b (coordination of each Si atom on the cage being 3 such as a cube for n = 8 with all square faces and dodecahedron for n = 20 with all pentagonal faces, silicon fullerenes of intermediate sizes with n = 10, 12, 14, and 16 have a mixture of rhombi and pentagons) or closed packed structures (coordination of silicon atoms on the cage being 4 or more) shown in Fig. 3.12 such as a bicapped tetragonal antiprism (n = 10), hexagonal antiprism, or icosahedron (n = 12), and 14-, 15-, and 16-atom FK as well as other polyhedral forms. The metal encapsulated fullerene structures of $M@X_n$ can be represented by (r,p) where r and p represent the number of rhombi and pentagons on the cage. Accordingly the n = 8, 10, 12, 14, 16, and 20 fullerenes will be denoted by (6, 0), (5, 2), (4, 4), (3, 6), (2, 8), and (0, 12), respectively.

The $W@Si_{14}$ and $Zr@Si_{16}$ fullerenes are symmetric and have large HOMO–LUMO gaps of 1.1 and 1.58 eV, respectively. On the other hand a higher symmetry dodecahedral Si_{20} fullerene cage has been stabilized recently by encapsulation of lanthanide and actinide elements [58,59], but the HOMO–LUMO gap is lower due to the partial occupation of the states as we shall discuss later. This is the largest cage that can be stabilized with one metal atom. In the case of Th encapsulation, the silicon fullerene has icosahedral symmetry and it is an ideal cage for silicon as C_{60} is for carbon. Both $Th@Si_{20}$ and C_{60} have nearly the same size. All the faces in $Th@Si_{20}$ are regular pentagons (Fig. 3.11b) which optimize sp^3 bonding in these structures. The $Th@Si_{20}$ fullerene has the highest binding energy among all the metal encapsulated silicon clusters that have been studied. Contrary to it the smallest carbon fullerene, C_{20} has the lowest stability among carbon fullerenes due to the change in the bonding character from predominantly sp^2 in larger fullerenes to sp^3 type in C_{20}. In carbon fullerenes hexagons are most preferred and pentagons are the places of strain. Therefore C_{20} fullerene with all the pentagonal faces is maximally

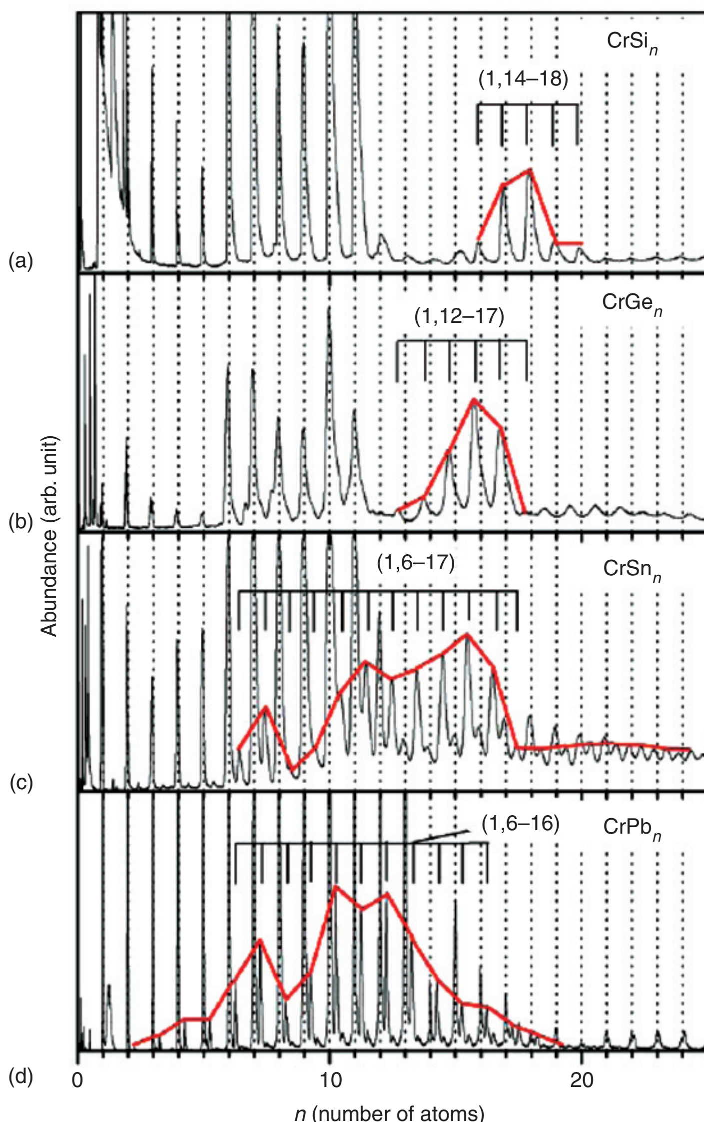

Figure 3.9 Mass abundance spectra of Cr doped clusters after 6.4 eV laser ionization. Cr doped (a) Si_n (900 μJ/cm^2), (b) Ge_n (830 μJ/cm^2), (c) Sn_n (520 μJ/cm^2), and (d) Pb_n (400 μJ/cm^2). The peaks at the dotted lines correspond to elemental Si clusters. The peaks for the doped clusters are connected and a bar is placed to identify n (Reproduced with permission from Ref. [71], courtesy S. Neukermans and P. Lievens).

strained. On the other hand in silicon fullerenes rhombi are the places of strain. Carbon fullerenes favour isolated pentagon rule while silicon fullerenes favour isolated rhombus rule [41]. Similar to C_{20}, a cube is the limit for silicon fullerenes in which all faces become square such as for Be@Sn_8 (Fig. 3.11b). Decahedron (2 pentagons and 5 rhombi) for 10 X atoms, 12-atom fullerene cage with 4 pentagons and 4 rhombi, 3-fold symmetric 14-cage with 6 pentagons and 3 rhombi, 16-cage

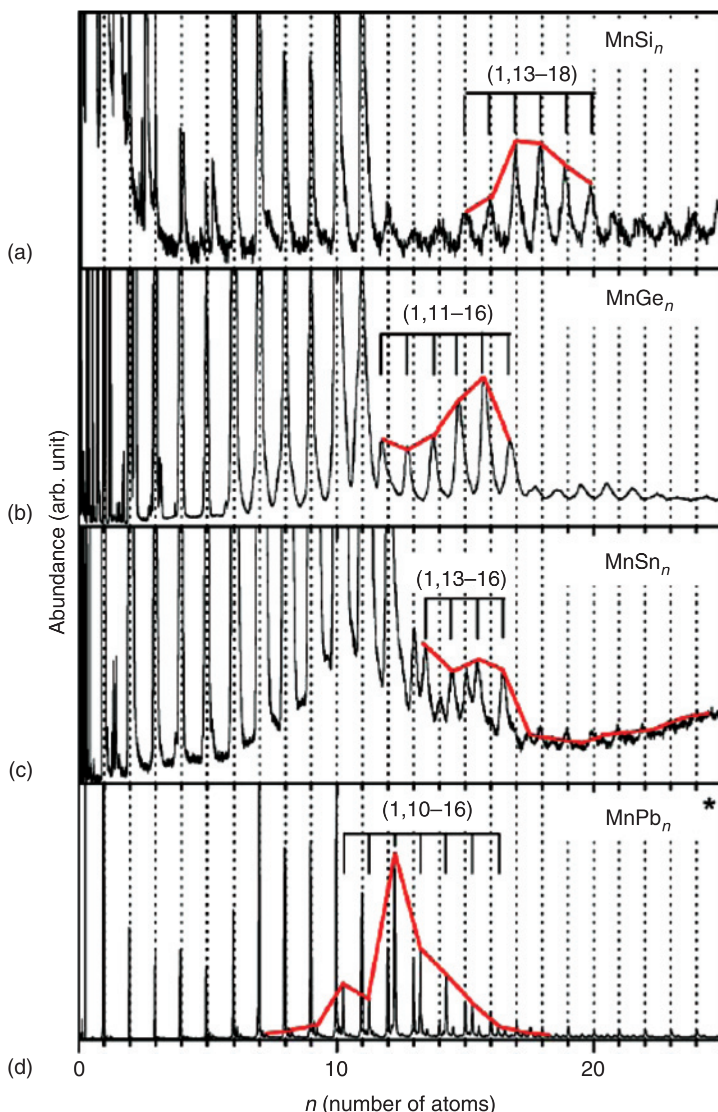

Figure 3.10 Mass abundance spectra of Mn doped clusters photoionized by 6.4 eV laser irradiation for Mn doped: (a) Si_n (400 μJ/cm^2), (b) Ge_n (500 μJ/cm^2), (c) Sn_n (390 μJ/cm^2) clusters and (*) photoionized by 7.9 eV laser light for Mn doped, and (d) Pb_n clusters (455 μJ/cm^2) (Reproduced with permission from Ref. [71], courtesy S. Neukermans and P. Lievens).

with 8 pentagons and 2 rhombi (Fig. 3.10a) are intermediate cases. For Si_{12} cage, three different competing structures (fullerene, chair shaped, and hexagonal prism) have been found (Fig. 3.11) and from the point of view of isolated rhombus rule, a fullerene cage with only 4 rhombi (Fig. 3.11a) is the best. However, a hexagonal prism structure is favoured for W@Si_{12} and Ta@Si_{12}^- and these clusters have large HOMO–LUMO GGA gaps of 1.24 and 1.96 eV. Electronically the two clusters

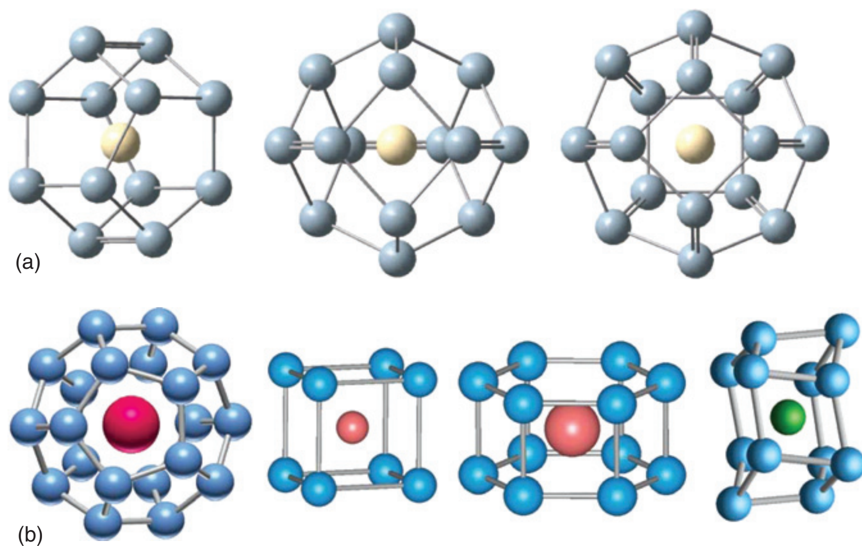

Figure 3.11 (a) Metal encapsulated fullerene cages of $Ni@Si_{12}$, $W@Si_{14}$, and $Zr@Si_{16}$ showing two, three, and eight double bonds, respectively. (b) The optimized structures of (from left to right) $Th@Si_{20}$ fullerene, $Be@Sn_8$ cubic, $W@Si_{12}$ hexagonal prism, and chair shaped $Be@Si_{12}$, respectively. For $Be@Si_{12}$ a fullerene-like isomer derived from $Ni@Si_{12}$ above has the lowest energy.

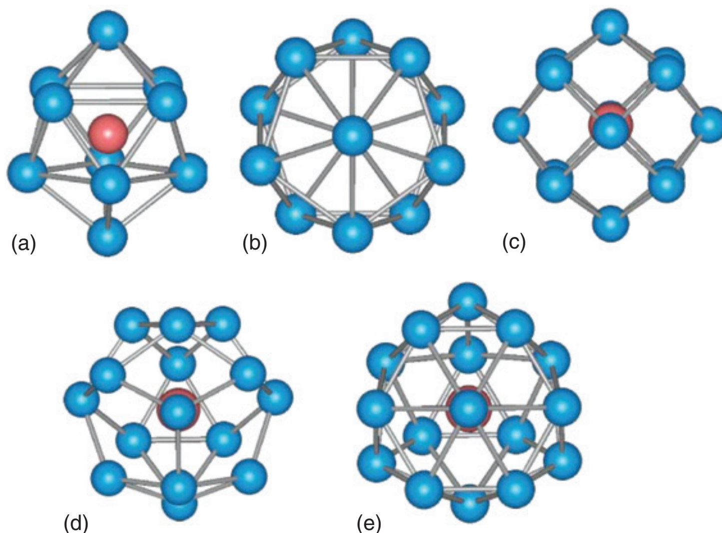

Figure 3.12 Closed packed structures of M encapsulated clusters of X atoms. (a) Bicapped tetragonal antiprism for $Be@Si_{10}$, $Ni@Ge_{10}$ and $Pt@Sn_{10}$, and $Al@Pb_{10}^{+}$, (b) icosahedral $Be@X_{12}$, $Mn@X_{12}$ (X = Ge and Sn), $Al^{+}@Pb_{12}$, and $Pt^{-2}@Pb_{12}$, (c) cubic $M@Si_{14}$ (M = Fe, Ru, and Os), (d) FK-$M@Si_{15}$ (M = Cr, Mo, W), and (e) FK-$Ti@Si_{16}$ and $Zr@Ge_{16}$. M atom is inside the cage (after Ref. [41]).

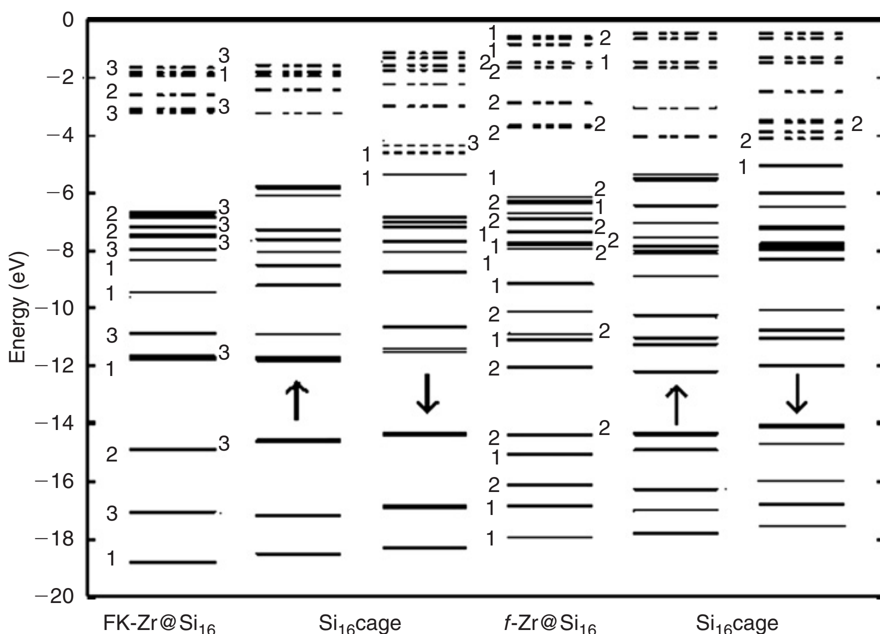

Figure 3.13 Electronic spectra of Frank-Kasper (FK) and fullerene isomers of Zr@Si_{16} and the corresponding empty centre Si_{16} cages. Note that most of the occupied states in the empty centre Si_{16} cage and after metal encapsulation remain nearly at the same energies except near the HOMO. The LUMO states are shown by broken lines. The degeneracies of the states are given by numbers. In the case of the Si_{16} cage of the FK isomer, the doubly degenerate HOMO-1 of the neutral cluster splits as it is occupied by 1 electron. This leads to small variations in all electronic states, but these are generally small in almost all cases except the highest occupied levels. Therefore, the degeneracies of the states have been maintained except for the HOMO and the LUMO states of the spin-down spectrum (Adopted from Ref. [57]).

are equivalent but the HOMO–LUMO gap differs significantly. This is likely to be due to the different effective atomic size of the dopant atom which affects the hybridization between the dopant and the cage orbitals. In the case of Ni doping, a smaller atom, the hexagonal prism structure distorts and it is nearly degenerate with the fullerene structure shown in Fig. 3.11a. In Si_{15} cage, 3 rhombi are nearest neighbours and it has significant strain. Therefore this is not the best choice from the stability point of view and a closed packed FK structure such as for Mo@Si_{15} (Fig. 3.12) becomes lower in energy.

Besides the above geometrical factor of the stability of metal encapsulated silicon clusters, the high abundance and high stability of metal encapsulated clusters arises from the large HOMO–LUMO gaps in the electronic structure. In the fullerene isomers with nearly sp^3 bonding, three lobs of the hybrid orbitals on each Si atom point towards three neighbouring silicon atoms and form σ bonds with the orbitals on the nearest Si atoms while the remaining sp^3 lob on each Si atom points outwards of the cage and it has weak π bonding with such lobs on neighbouring Si atoms. There are small variations in this description of the bonding in silicon fullerenes as the size is varied. Figure 3.13 shows the energy spectrum of the

Zr@Si_{16} fullerene. The π bonded states lie close to the HOMO. In order to understand the energy spectrum, an instructive way is to consider [41,57] the fullerenes as spheres and use a spherical potential model similar to the one used to understand the electronic structure of carbon fullerenes [96]. According to this model, the σ bonded states with nodeless orbitals are represented by principal quantum number n = 1. In Zr@Si_{16} fullerene there are 24 σ bonds with 48-valence electrons. In the simplified spherical model the low lying electronic states can be considered to be 1S, 1P, 1D, and 1F type that accommodate 32-valence electrons. The remaining 16-valence electrons in the σ bonds occupy 1G type orbitals. The latter can accommodate 18 electrons and therefore there are two holes in these states. The energy levels of the occupied π bonded states can be represented as 2S, 2P, and 2D type in the spherical potential model. They can accommodate 18-valence electrons. Out of the 16 electrons in the π bonded states, 2 electrons get transferred to the low lying 1G orbitals and make the 1G state fully occupied. Therefore four holes remain in the 2D state which forms the HOMO. *The angular character of the HOMO is important for doping and the stabilization of these metal encapsulated clusters.* The 4*d* atomic orbitals of Zr with the same angular character as the HOMO of the silicon cage, hybridize strongly with the D orbitals of the cage and have strong covalent bonding. This pushes the bonding states downwards and the HOMO of the empty silicon cage becomes fully occupied (Fig. 3.13) using the 4-valence electrons of Zr. The anti-bonding states are pushed up and are completely empty. This results in a large HOMO–LUMO gap. The covalent bonding between the metal atom and the cage also pacifies the dangling bonds partially. It is to be noted that the doping of another tetravalent atom such as Si, Ge, Sn, and Pb does not make this cluster magic [57] because these atoms do not have valence *d* electrons. The importance of the angular character of the dopant orbitals is also seen in clusters of metals. As an example Si@Al_{12} is known to be magic with a large HOMO–LUMO gap and electronic shell closure with 40-valence electrons. In this case the HOMO of the Al cage has 2P character within a spherical potential model and it hybridizes with the 3*p* orbitals of Si leading to a large gap. However, another tetravalent atom Ti with 3*d* valence orbitals does not lead [97] to a large gap.

The FK isomer of Ti@Si_{16} has a higher coordination of Si atoms and it is more compact. Such a polyhedron is found in complex metallic alloys and it has a nearly spherical shape with T_h symmetry. The tight bonding as well as higher symmetry in Ti@Si_{16} gives rise to a larger HOMO–LUMO gap of 2.35 eV within GGA as compared to the value of 1.58 eV for Zr@Si_{16} fullerene in which case the lower symmetry leads to the splitting of the states which can be seen in Fig. 3.13. A larger gap for $TiSi_{16}$ has been found recently in photoemission experiments [70]. Experiments were done on anion $TiSi_{16}$ clusters which showed a separation of 1.90 eV between the main emission peak and the weak HOMO peak. The adiabatic detachment energy of an electron (EA) from these experiments was obtained to be 2.03 $\pm$ 0.09 eV. This agrees very well with the calculated value of 2.05 eV by Kumar and coworkers [55,57]. In the case of the isoelectronic $ScSi_{16}^-$ the spectrum starts with the main peak (without any weak peak mentioned above) that is similar to the main peak in $TiSi_{16}$ suggesting the similarity of the electronic structure in the two cases and the closed electronic shell nature. The stability of these clusters can again be considered within a spherical potential model which is even a better

approximation for $Ti@Si_{16}$ and there is again 2D electronic shell closing at 68 electrons which is satisfied in this case and with 3*d* valence electrons of Ti, it leads to the high stability of this FK polyhedron. These results showed that though *Ti and Zr are isoelectronic, a small difference in size changes the structure and the electronic properties of metal encapsulated silicon clusters very significantly*. Further support on the relation of the stability with the number of valence electrons on this cluster was obtained from isoelectronic $ScSi_{16}^-$ and VSi_{16}^+ which also showed high abundances. Also $TiSi_{16}$ as well as VSi_{16}^+ were non-reactive towards F_2 but $VSi_{16}F$ complex could be formed suggesting that VSi_{16} behaved like an alkali atom and that $VSi_{16}F$ is an ionically bonded superatom complex where VSi_{16}^+ behaves like closed electronic shell specie. Furthermore the vertical detachment energy and the adiabatic detachment energy of $ScSi_{16}^-$ are 4.25 and 3.41 eV, respectively. This also suggests strong stability of this superatom. The EA of $ScSi_{16}$ is similar to than of a chlorine atom. Studies on the photoionization of the $TiSi_n$ neutral clusters show that one-photon ionization does not occur with the ArF laser (6.43 eV) but with F_2 laser (7.90 eV) indicating high IP of the neutral $TiSi_n$ clusters in the range of $n = 5$–16. Indeed the IP values of $Ti@Si_n$ clusters were calculated [55] to be greater than 6.59 eV in the range of $n = 8$–16 and in most cases the IP is greater than 7 eV but less than 7.6 eV. These results are in complete agreement with experiments. Chen *et al.* [65] have shown Si_{16}^{4-} fullerene and FK cages to be aromatic, the calculated nucleus-independent chemical shift (NICS) values being -40.9 and -22.9, respectively and are stabilized by the endohedral metal atom with 4-valence electrons such as Ti or Zr.

Smaller metal atoms such as Cr, Mo, and W favour a 15-atom silicon cage which has the highest binding energy per atom and is optimal for these metal atoms. The $M@Si_{15}$ (M = Cr, Mo, and W) fullerene cage does not have the lowest energy and a FK type isomer is favoured (Fig. 3.12). However, the symmetry is not high and the HOMO–LUMO gap for example for M = Cr is 1.33 eV within GGA and it is not the largest for these metal atoms. In the experiments of Beck, high intensities of MSi_{15} M = Cr, Mo, and W cations were observed. However, MSi_{16} cation was also nearly equally abundant (Fig. 3.1 as well as Fig. 3.9) and the intensity reduced dramatically beyond $n = 16$ suggesting good stability for $n = 16$ cluster for these metals. The structure of these $M@Si_{16}$ clusters [45,56] can be described as $M@Si_{15}$ fullerene cage with a face capping. Two electrons in the 3*p* orbitals of the capping Si atom can be considered to participate strongly in the bonding while the electrons in the 3*s* orbitals to be more localized. This can give an effective count of 68-valence electrons which can be related to the stability of this cluster. However, this aspect would need to be explored further. The $M@Si_{16}$ cluster does not have high symmetry and the HOMO–LUMO gap is 1.24 eV within GGA for M = Cr. Among the Cr doped clusters, $Cr@Si_{14}$ has the largest gap [45,56] of 1.54 eV within GGA. These clusters are not compact and have an element of covalent character in the bonding. The $M@Si_{15}$ cage with M = Fe, Ru and Os satisfies an electronic shell closure condition for 68-valence electrons and should be magic. Indeed for M = Ru and Os a FK type cage (Fig. 3.12) has a large HOMO–LUMO gap of about 1.5 eV. The *d* states of the metal atom hybridize strongly with the 1D and 2D states of the cage in a spherical model potential and lie about 2 eV below the HOMO while the hybridized 2D states are unoccupied. Therefore with an increasing number of *d* electrons on the transition metal atom, a smaller number of X

atoms is needed for an optimal cage, and the *d* states of the metal atom get mostly occupied. Depending upon the interaction between the metal atom and the X cage, the HOMO–LUMO gap is affected from the position of the LUMO states. Accordingly a smaller value of the HOMO–LUMO gap of 0.9 eV is obtained for Fe in GGA but 1.57 eV for Os@Si_{15}. For these metal atoms a body centred cubic cage of Si_{14} (Fig. 3.12) is favourable and is optimal. Also a fullerene cage (Fig. 3.11a) lies close in energy. In the cubic symmetry, the 2D cage states within a spherical potential model split into a t_{2g} and an e_g symmetry states. The 3*d* orbitals of the Fe atom hybridize strongly with the 2D orbitals of the cage and are occupied. On the other hand the t_{2g} type 2D hybridized states are occupied and e_g type states empty. The 1G states also spilt in the cubic symmetry and are only partly occupied with 8 electrons. This partial filling of the electronic shells also gives rise to a smaller HOMO–LUMO gap. Capping of 2 Si atoms on a Fe@Si_{14} cluster could lead to an effective valence count of 68 electrons (each capping Si atom contributing 2 electrons) leading to the stability of the Fe@Si_{16} cluster. Therefore, for M = Fe, Ru, and Os, $n = 14$, 15, and 16 clusters could be expected to show high abundances.

For the case of metal encapsulated X_{12} clusters, a few interesting structures have been obtained. The stability of the $Si_{12}W$ cluster (Fig. 3.11b) in the hexagonal prism form can be understood [40,52] from the 18-valence electron rule as 3-valence electrons from each Si atom are paired with neighbouring Si atoms in an approximate way. The remaining 12-unpaired electrons in the lobs pointing outwards of the hexagonal prism and 6-valence electrons of the metal atom form 18-valence electrons. This picture appeals but it is simplistic. In this case rather than a spherical potential model, a cylindrical potential is more appropriate. In the hexagonal symmetry the states are singly or doubly degenerate and the d_z^2 orbital of the metal atom does not hybridize strongly with the cage states. It forms the LUMO of this cluster. The other four 4*d* orbitals hybridize with the cage. The hybridized states lie about 1 eV below the HOMO. The HOMO arises from the cage and has little weight on the metal atom. $TaSi_{12}^-$ anion and $ReSi_{12}^+$ cation are isoelectronic to WSi_{12} and have similar consideration for stability. Also a $Si_{10}Fe$ cluster with pentagonal prism structure and Fe at the centre has been suggested [61] to satisfy 18-valence electron rule considering 10 electrons (one from each Si atom) and 8-valence electrons from Fe. However, the HOMO–LUMO gap in this structure is quite small. Therefore the general applicability of the 18-valence electron rule in the stability of these clusters is doubtful and a more detailed analysis of the electronic structure may be needed.

Kawamura *et al.* [56] have studied the growth behaviour of Cr doped silicon clusters and found that the metal atom is enclosed by silicon when the number of silicon atoms is 12. This is in contrast to Ti for which this number is 13 due to its larger size. Neutral Cr doped silicon clusters show magic behaviour for $n = 12$, 14, 15, and 16 within GGA. Magic behaviour of $n = 12$ cluster was also shown by Khanna *et al.* [52]. However, Kawamura *et al.* showed the magic behaviour to depend on the exchange-correlation used as well as on the charged state of the clusters. Within B3PW91, cluster with $n = 12$ remains strongly magic but 14 and 15 become weaker. Also among anion clusters, $CrSi_{12}^-$ was shown to be strongly magic but among cation clusters $CrSi_{13}^+$ and $CrSi_{15}^+$ become magic. The magic nature of the cluster with $n = 15$ agrees with experiments. Zheng *et al.* [72] have performed photoelectron spectroscopy on Cr doped anion clusters of silicon up to

$n = 12$ and have also measured the vertical detachment energies. For $n = 8$–12, these values are 2.71, 2.88, 2.87, 2.95, and 3.18 eV, respectively. For $n = 11$ and 12 the values are in good agreement with the calculation of Khanna *et al.* Kawamura *et al.* [56] have also calculated the adiabatic detachment energies in the range of $n = 8$–16 and for $n = 8$–12, these values are 3.24, 2.73, 2.88, 3.09, and 3.35 eV, respectively. Except for $n = 8$, the values are close to the measured ones and suggest that the relaxation effects are small. It is noteworthy that Zheng *et al.* [72] obtained a sharper peak in the photoelectron spectrum which was distinct from other clusters. Such a sharp feature has not been found for the case of M = Mo and W. It has been suggested that the smaller size of Cr could be responsible for the different behaviour of Cr doped silicon clusters. Recently Neukermans *et al.* [71] have produced Cr doped X = Si, Ge, Sn, and Pb cation clusters. They obtained different abundances of CrX_n clusters when X was changed. However, for silicon they also obtained high intensities for $n = 15$ and 16 as obtained earlier by Beck. The intensities of other Cr doped clusters were quite small. It is interesting that in these experiments as well as in the experiment of Beck, $CrSi_{12}$ cluster is not abundant. These results show dependence of the abundance on the nucleation condition. Also the abundance spectrum of Mn doped silicon cation clusters has been measured. Such cation clusters are isoelectronic to neutral Cr doped clusters. The abundance spectrum shows high intensities of $n = 15$ and 16 $MnSi_n^+$ clusters and relatively less abundances of $n = 17$ and 18 cation clusters. From this, one can conclude that neutral Cr doped Si clusters with $n = 15$ and 16 are magic. On the other hand for Ge, high abundances have been obtained for $n = 14$ and 15 due to the larger size of Ge atoms.

Doping of a divalent metal atom was found to lead to a chair shaped structure for $Si_{12}Be$ [46] (Fig. 3.11b) but later a fullerene-like structure was shown [41] to have lower energy. However, an icosahedral structure is most favourable [46,47] for Ge, Sn, and Pb (Fig. 3.12). Similar examples [98] are Si_{12}^{-2}, Sn_{12}^{-2}, Pb_{12}^{-2}, $[Pt@Pb_{12}]^{2-}$, and *closo* borane dianion, $B_{12}H_{12}^{2-}$ aromatic clusters. According to Wade's $2n + 2$ skeletal electron rule, clusters with 26-valence electrons are stable. King *et al.* [99] have used the idea of aromaticity in three-dimensional clusters such as the *closo* $B_nH_n{}^{2-}$ borane dianions and calculated the NICSs in their cage centres, NICS(0) which has large negative value for $5 \leqslant n \leqslant 12$. All these boranes are strongly aromatic. High symmetry clusters such as octahedral $B_6H_6{}^{2-}$ and icosahedral $B_{12}H_{12}^{2-}$ with a total of 26 (18 first shell + 8 second shell) and 50-valence electrons can be also understood from Hirsch's $2(N + 1)^2$ spherical aromaticity rule. However octahedral Si_6^{2-} and icosahedral Si_{12}^{2-} with 26- and 50-valence electrons, respectively have large positive NICS values and are therefore anti-aromatic. The difference between boranes and Si clusters arises due to different contributions to NICS from the HOMO which leads to their different NICS(0) values. Chen *et al.* [65] have recently calculated NICS values at the centres of X_n^{2-} (X = Si, Ge, Sn, and Pb) clusters with $5 \leqslant n \leqslant 12$. They obtained nearly the same values for all X in the range of $5 \leqslant n \leqslant 9$ and 11. However, for $n = 10$ and 12 the difference is more significant. NICS is negative for all X_{10}^{2-} with the highest negative value for X = Si. For $n = 12$ it is positive for X = Si and Ge, nearly zero for Sn, but negative for Pb. They performed experiments on Si, Ge, Sn, and Pb cation clusters doped with Al and obtained peaks for AlX_{10}^+ in the mass spectrum for all X. However, the features were more distinct for Ge and Sn. This suggested the role of the size of the dopant in

these clusters. As expected from NICS analysis, AlX_{12}^{+} had no special stability for X = Si and Ge, but high intensity was obtained for X = Pb. Chen *et al.* [65] also studied the stability of MPb_{12}^{+} (M = B, Al, Ga, In, and Tl) cation clusters from *ab initio* calculations and found $AlPb_{12}^{+}$ to have higher stability than other clusters. Strong abundances of icosahedral I_h-Al@Pb_{12}^{+} and bicapped tetragonal antiprism D_{4h}-Al@Pb_{10}^{+} were reported [69] earlier with little intensities of other clusters. The isoelectronic divalent metal atom doped icosahedral clusters of Ge and Sn [46,47] with $n = 12$ have been shown from *ab initio* calculations to have large HOMO–LUMO gaps and such clusters could be photoluminescent in the visible range. Recently experiments [71] on Zn doped Sn and Pb clusters showed highest intensities for $n = 12$ clusters. For Zn doped Sn clusters, $ZnSn_{10}$ is also magic (Fig. 3.14). Ten-atom clusters of elemental Si, Ge, and Sn are known to be magic [77,87] and it has been shown [54] that by metal encapsulation their stability can be enhanced further such as by doping with Ni or Pt as the *d* states of these transition metal atoms get fully occupied. Optimal combinations of Ni, Pd, and Pt have been studied with Si, Ge, Sn, and Pb and Ni@Ge_{10} as well as Pt@Sn_{10} have been predicted [54] to be the best with a bicapped tetragonal antiprism structure (Fig. 3.12). This structure has higher symmetry than the tetracapped prism of X_{10}. A solid form [100] of $Pb_{10}Ni$ has also been obtained showing the strong stability of this cluster as predicted [54]. These results suggest that both neutral as well as dianions of these clusters have strong stability. Fässler and Hoffmann [101] have characterized Pb_{10}^{2-} Zintl ion unambiguously in solid state as the first empty 10-atom closo cluster of group 14 elements and it is likely that in future such X_{10}^{2-} ions of X = Ge, Sn, and Si which are more strongly aromatic could be found in solid state. Also bulk quantities of doubly charged $Pb_{10}Ni^{2-}$ and M@Pb_{12}^{2-} (M = Ni, Pd, and Pt) have been produced [100].

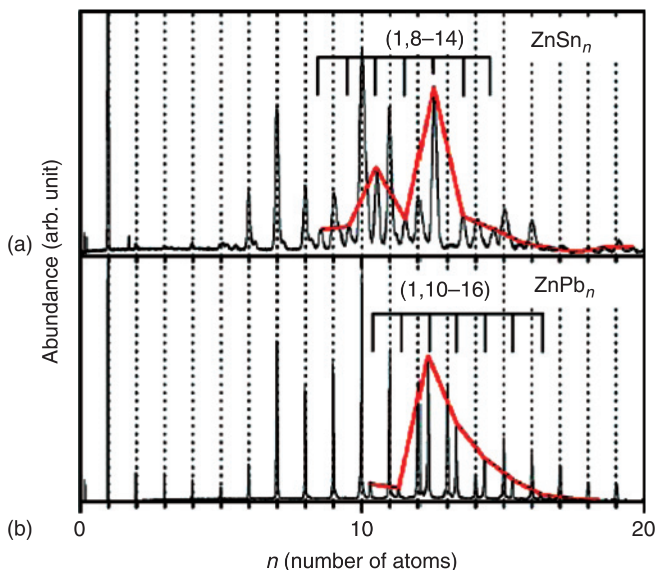

Figure 3.14 Mass abundance spectra of Zn doped (a) Sn_n (97.5 μJ/cm²) and (b) Pb_n (130 μJ/cm²) clusters radiated by 7.9 eV laser light (Reproduced with permission from Ref. [71], courtesy S. Neukermans and P. Lievens).

Pb_{12} has been shown [102] to be stable in empty cage icosahedral structure and this gets further stabilized by doping of a metal atom. Si_9^{2m-} (m = 2, 3, and 4) anion clusters have been formed [103] in solution.

Further analysis of the bonding nature in fullerenes showed that in Zr@Si_{16} (Fig. 3.11a), there are eight double bonds connecting the two square faces to the ring atoms in between the square faces such that each Si has a double bond and two single bonds similar to carbon fullerenes. The double bonds are the shortest. With the sp^3 bonding, the lobs pointing outwards of the cage on atoms connected with a double bond have more significant overlap compared with other atoms. Each pentagon has two double bonds that are shared by other pentagons. Similarly in the 3-fold symmetric Re@Si_{14}^+ fullerene isomer, there are three double bonds of length 2.32 Å (Fig. 3.11a) sharing 2 pentagons and connecting 2 rhombi while the other bond lengths have the values of 2.35 Å (sides of rhombi) and 2.40 Å (remaining bonds in pentagons) using the B3PW91 hybrid functional for the exchange-correlation energy and the Gaussian method with SDD basis set [104]. In the case of Ni@Si_{12} fullerene isomer which is a decahedron capped with a dimer (Fig. 3.11a), there are two double bonds of length 2.31 Å while the other bond lengths have values of 2.36, 2.38, and 2.44 Å. The doped magic cages have higher stabilities as compared to the elemental X clusters [30,77] and their electronic properties differ significantly depending upon the combination of the cage and the M atom making it possible to achieve tunable properties as well as size selectivity.

The Th@Si_{20} fullerene has predominantly sp^3 bonding and 60-valence electrons are accommodated in 30 Si–Si σ bonds along the edges on the fullerene cage. In a spherical potential model, 50 electrons occupy 1S, 1P, 1D, 1F, 1G states while the remaining 10 electrons are accommodated in the 1H states which split into a 5-fold (fully occupied) and two 3-fold degenerate (empty) states in the icosahedral symmetry of the cage. The remaining 20-valence electrons in the lobs pointing outwards of the cage are π bonded. Out of these 18 occupy 2S, 2P, and 2D states completely and the remaining 2 electrons occupy the 2F state that splits into a 4-fold and a 3-fold degenerate state in the icosahedral symmetry. The 3-fold state (HOMO) has four holes. Therefore, a tetravalent atom is most suitable to stabilize this cage. Furthermore the valence orbital of the dopant atom should have *f* character. Accordingly lanthanides and actinides are suitable from the point of view of the size as well as the electronic configuration and Th atom was found [58] to be a perfect choice. Though Ce is also a tetravalent atom, the icosahedral symmetry of the cage was shown to reduce to T_h symmetry. The most favourable oxidation state of other lanthanides and actinides is 2+ or 3+. Therefore fullerene anions of a trivalent atom such as M@Si_{20}^-, M = Y, La, and Ac are stabilized [59] with large binding energy and in these cases the fullerenes keep icosahedral symmetry. Similarly in the case of M = Pa, a fullerene cation Pa@Si^{20+} is stabilized but the symmetry of the cage reduces to T_h. In all these cases the embedding energy of the M atom is large as it is the case for smaller metal encapsulated silicon clusters. It is, however, to be noted here that Sun *et al.* [63] tried to stabilize Si_{20} fullerene cage by several large size atoms such as Ba, Sr, Ca, and Pb, but in all cases the energy to embed the metal atom in the Si_{20} cage as well as the HOMO–LUMO gap was small, as in all these atoms the valence orbital does not have *f* character which could hybridize strongly with the HOMO of the cage. Alkali or noble metal atoms can be used to form molecular structures such as La@Si_{20}Na

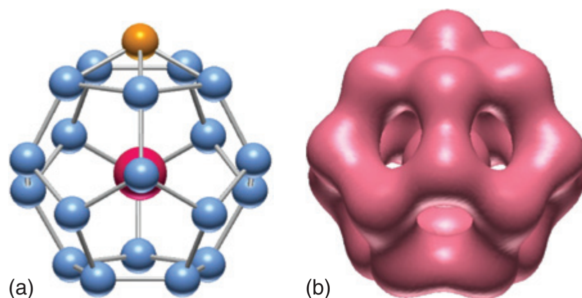

Figure 3.15 (a) Optimized structure of Cu–La@Si_{20} and (b) an isosurface of the total pseudocharge density. Cu is shown by brownish color. The density around Cu is mainly due to 3*d* electrons (after Ref. [59]).

or La@Si_{20}Cu as shown in Fig. 3.15. The alkali or noble metal atom transfers 1 electron to the silicon cage. As shown in the charge density distribution in Fig. 3.15 in the case of Cu, the density around Cu ion is mainly due to *d* electrons and therefore the bonding character between Cu and La@Si_{20} is predominantly ionic. The EA of La@Si_{20} is high and is nearly the same as for Cl and therefore it behaves like a halogen atom. Similar to fullerides of carbon, it may become possible to develop new salts of silicon [59] using the M@Si_{20} fullerenes.

3.3.4 Reactivity as a Probe of Metal Encapsulation

Studies on the reactivity of metal doped silicon clusters gave very useful information about the distribution of metal atom. The absence of hydrogen in Si_{12}W clusters when silane gas was reacted [40] with metal monomers and dimers was interpreted to be indicative of the encapsulation of the metal atom in a cage. Also reaction of water molecules on Ti doped silicon clusters showed [68] little abundance of adsorbed water molecule on $TiSi_n$ clusters with $n \geqslant 13$. Calculations [55] on $TiSi_n$ clusters gave a preference for basket structures (Fig. 3.7) for $n \leqslant 12$ so that the metal atom was available for interaction with a water molecule and there was a significant binding energy [95] as shown in Fig. 3.8. However for $n = 13$, the metal atom is encapsulated in a cage and is unavailable for reaction. This reduces the binding energy of a water molecule very significantly. Therefore adsorption of a water molecule gave clear indication of the encapsulation of the metal atom in a cage.

3.3.5 Vibrational Properties

Vibrational spectra of elemental silicon clusters have been measured [12,13] using infrared and Raman spectroscopy and it has been used to get information about the structures of clusters. For metal encapsulated silicon clusters, the strong bonding between the metal atom and the cage is expected to lead to high frequency modes which could distinguish them clearly from elemental silicon clusters. Moreover the structures of metal encapsulated clusters are completely different from those of the elemental silicon clusters and therefore the vibrational spectra can be expected to be quite distint as vibrational modes are sensitive to the bonding nature as well as to

the structure of a cluster. Since no experimental data on vibrational spectra is available yet on metal doped silicon clusters, it is important that the predictions be accurate. Kumar *et al.* [57] performed test calculations on a Si_7 cluster in the pentagonal bipyramid geometry using an all electron Gaussian method [104] with B3PW91 hybrid functional. They obtained two infrared modes at 421 cm^{-1} which were in excellent agreement with the experimental value [12] of 422.4 cm^{-1} obtained for Si_7 clusters in Ar matrix and 420.4 cm^{-1} obtained in Kr matrix. Also the calculated values for Raman-active frequencies 291, 342, 346 (all three doubly degenerate), 363, and 440 cm^{-1} were in very good agreement with the experimental values of 289, 340, 340, 358, and 435 cm^{-1}, respectively. In earlier calculations [91], in most cases the calculated frequencies were scaled down by 5% to obtain good agreement with experiments. The good agreement of calculated frequencies for elemental silicon clusters was used [57] to make predictions for metal encapsulated silicon clusters. For the fullerene Zr@Si_{16} and the FK Ti@Si_{16} clusters the infrared and Raman-active frequencies are shown in Fig. 3.16. For each isomer both Ti and Zr doping gives rise to similar frequency spectra. However, the frequency spectra in the two isomers are quite distinct. For the fullerene isomer, the double bonds lead to

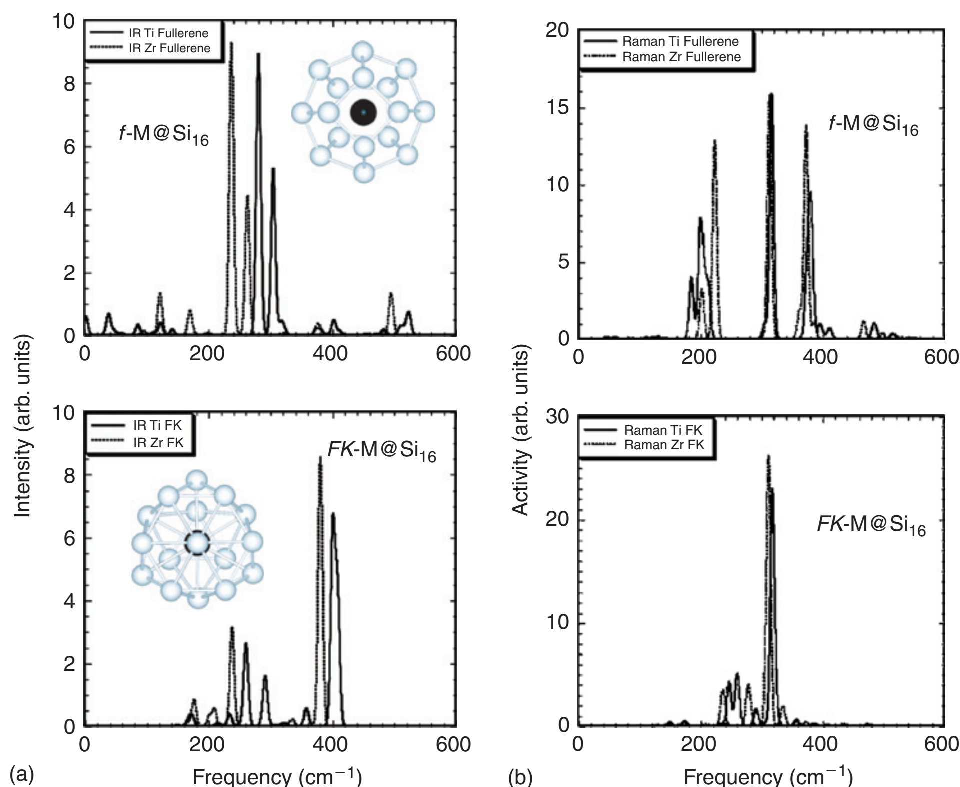

Figure 3.16 Gaussian broadened (width 3.5 cm^{-1}) infrared (a) and Raman (b) spectra of the FK and fullerene (f) isomers of the M@Si_{16} clusters. The inset shows the atomic structures of the fullerene and FK isomers. The metal atom is shown by the dark sphere and is at the center of the silicon cage (after Ref. [57]).

high frequency modes at 496 cm^{-1} corresponding to the stretching of the short bonds. Also the main peak in the Raman spectra corresponding to the breathing mode at 318 cm^{-1} for the FK Ti@Si_{16} isomer splits into two peaks for the fullerene isomer of Zr@Si_{16} due to the lower symmetry of the fullerene isomer. In the latter case there is a peak at 313 cm^{-1} which corresponds to the breathing mode of the 8 ring atoms while the higher frequency mode at 373 cm^{-1} corresponds to the breathing modes of the square atoms as these are more tightly bonded with the ring atoms. The bond lengths between the ring atoms are longer and there is a weaker bonding which leads to lower frequencies. Such distinctive features can be used to identify the structures of the metal encapsulated silicon clusters. This is in contrast to the polarizability [57] of these clusters which is much less sensitive to the details of the atomic structure. Similar calculations of the infrared and Raman-active modes have also been done for Cr encapsulated silicon clusters of different sizes by Kawamura *et al.* [56].

3.3.6 Empty and Endohedral Hydrogenated Fullerene Cages of Silicon

Hydrogen termination of the dangling bonds is a very common way to pacify silicon clusters. Often nanoparticles of silicon are produced from silane gas and in this case both hydrogen free and hydrogenated clusters could be produced. Among small hydrogenated clusters high abundance was obtained [105] for $Si_6H_{13}^+$ which corresponds to tetrahedrally bonded neutral cluster Si_6H_{12}. On the other hand from thermal decomposition of disilane gas, high abundance of Si_6H_{10} has also been obtained [106]. The structures of small hydrogenated Si clusters [107] and the optical absorption [108] have been studied. In tetrahedrally bonded small Si_nH_m clusters, the number of H atoms is greater than the number of Si atoms but this fraction decreases as the cluster size grows and finally the number of H atoms becomes less than Si in large nanoparticles. An interesting case occurs for $m = n$ where hydrogenated silicon clusters form cage structures. Recently a detailed study of such caged structures as well as their endohedral doping has been carried out [80]. For Si_nH_n ($n = 6$, 8, and 10), trigonal prism, cube, and pentagonal prism of silicon, respectively, are favoured. Each Si atom has 3 nearest Si atoms and one hydrogen atom associated with it. This trend is continued for $n = 12, 14, 16, 20, 24$, and 28, fullerene cages. A few selected examples have been shown in Fig. 3.17. As the size of the clusters grows, the bonding becomes close to tetrahedral which is most favoured by silicon and for $Si_{20}H_{20}$ fullerene cage the bonding is optimal as in the case of larger fullerenes with $n = 24$ and 28 there are two and four hexagonal faces, respectively and this partially induces sp^2 bonding in the cage. Therefore, the binding energy of the cages increases monotonically till $n = 20$ and beyond this, there is a slight decrease. Earley [109] has calculated strain in polyhedrane clusters X_nH_n, X = Si, Ge, and Sn, and $n = 4, 6, 8, 10, 12, 16, 20$, and 24 depending upon the type of rings present in the clusters and found that $n = 20$ fullerene is the least strained. For carbon, C_nH_n hydrocarbon species such as C_6H_6 prismane, C_8H_8 cubane, and $C_{10}H_{10}$ pentaprismane have been synthesized. It can therefore be expected that similar species of silicon and other group 14 elements could be produced. It is noteworthy that experiments [110] on $Si_{14}H_x$ clusters at different temperatures showed

a maximum in the abundance distribution for $x = 14$ at around 700 K. A cage structure was suggested for this cluster. However, it has been shown [80] that in the family of Si_nH_n cages, $n = 14$ cage is not magic and cages with $n = 16$ and 20 are particularly stable and magic. Therefore such fullerenes can be expected to have strong abundances. The hydrogenated cages of silicon have a large HOMO–LUMO gap of about 2.8 eV within GGA and the variation in the values for different cages is small. There is a local maximum for $n = 10$, 16, and 20. The nearly constant value of the HOMO–LUMO gap for different n is interesting as samples with a mixture of clusters of different sizes may have similar optical properties. Pichierri *et al.* [81] have shown that for $Si_{20}H_{20}$ cage the IP is high (8.10 eV) and the EA is low (1.54 eV) compared with the corresponding values of 7.58 and 2.67 eV for C_{60}, respectively. These results reflect high stability of the fullerene cages of silicon. The $n = 20$, 24, and 28 fullerene cages of silicon are found in silicon clathrates and are interlinked so that each Si is nearly sp^3 bonded. In isolated Si_nH_n cages, hydrogen atoms act similar to interlinks and therefore a study of the endohedral doping of such cages could be also useful in designing new clathrates. The silicon clathrates with metal atoms such as Na (Na_8Si_{46}) and Ba (Ba_8Si_{46}) have been synthesized. Connetable *et al.* [111] have studied doping of Xe in such cages and obtained even a larger band gap than for bulk Si.

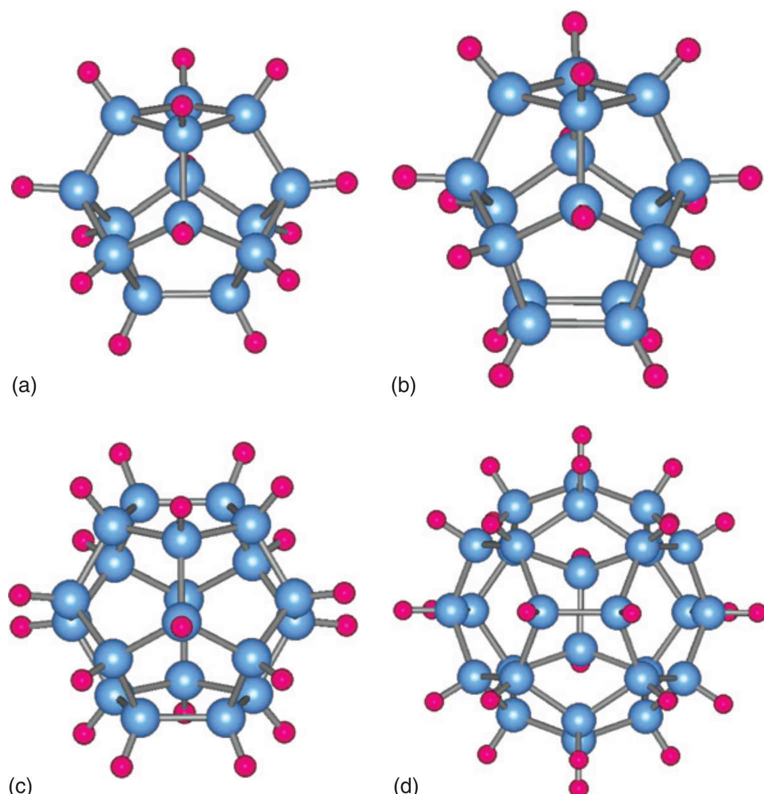

Figure 3.17 Empty cage Si_nH_n fullerenes: (a) $n = 14$, (b) $n = 16$, (c) $n = 20$, and (d) $n = 28$ (Adopted from Ref. [80]).

The fullerene cages with $n = 14, 16$, and 20 are large enough to accommodate a variety of atoms. The inner diameter of $Si_{20}H_{20}$ cage is similar to that of C_{60} which has been doped [112] endohedrally by different atoms. H capping leads to a slight expansion of the cage as compared to the metal encapsulated silicon cages and therefore slightly bigger atoms could be accommodated in such cages. Recently a detailed study [80] of the endohedral doping of a large variety of atoms in such cages has been done and many interesting aspects of the optical and magnetic properties have been studied. The LUMO of $Si_{20}H_{20}$ is localized [81] inside the cage while the HOMO has large weight on the cage. This is important for exohedral and endohedral doping of the cages. The HOMO and the LUMO states, and therefore the optical properties of these cages can be modified by doping in order to design materials with desired properties. Interestingly for some Ge cages, the HOMO–LUMO gap becomes larger than for Si cages. The guest atom in such cages interacts weakly with the cage because all the valence electrons on each Si/Ge atom are paired in covalent bonding. The endohedral doping energy is about 1 eV in most cases as compared to about 10 eV in the case of metal encapsulated silicon clusters without hydrogen. Therefore the guest atom in the cage can have nearly the same properties as a free atom. Thus hydrogenated cages of Si with slaved atoms could offer an interesting way to have a variety of new species with atomic like properties. It has been shown [80] that the magnetic moments of atoms such as Cr, Mn and Fe have the same values in the cage as in a free atom. Most interestingly the valence electronic level of the slaved atom may lie within the HOMO–LUMO gap of the empty cage. Therefore by changing the atom, the HOMO–LUMO gap and therefore the optical properties of the cages can be designed with absorption ranging from infrared to ultraviolet. Doping of rare gases leads to an increase in the HOMO–LUMO gap as found in clathrates [111] whereas for the case of Zn, the valence electronic levels of the atom lie in the occupied spectrum of the empty cage. Therefore, the HOMO of the occupied cage could arise from the guest atom or the cage itself. Figure 3.18 shows a few representative cases of endohedral doping of $n = 16$ and 20 cages by Ba, Zn and Be. Ba and Zn atoms occupy the centre of the cage. However, Be atom drifts towards the wall of the cage very similar to the case of carbon fullerenes. Pichierri *et al.* [79] have studied anions of halogen doped $Si_{20}H_{20}$ and found F doping to be optimal. Also exohedral doping by different chemical groups replacing an H atom have been studied [81]. Such derivatives keep

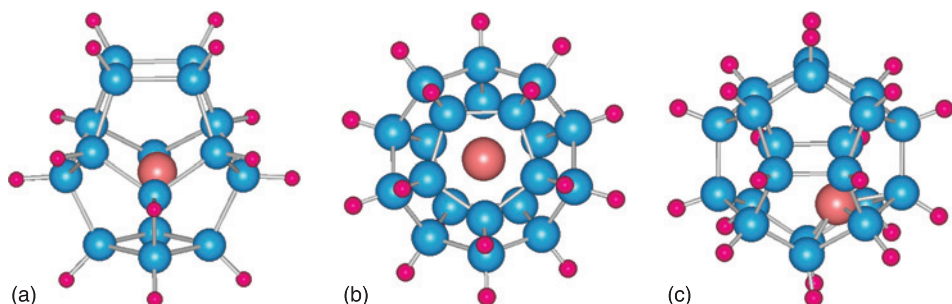

Figure 3.18 Endohedral doping of (a) $Si_{16}H_{16}$ with Ba, (b) $Si_{20}H_{20}$ with Zn, and (c) $Si_{20}H_{20}$ with Be (Adopted from Ref. [80]).

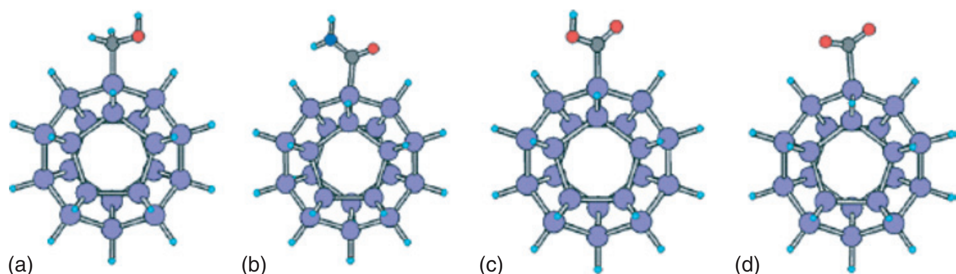

Figure 3.19 Optimized structures of: (a) $Si_{20}H_{19}(CH_2OH)$, (b) $Si_{20}H_{19}(CONH_2)$, (c) $Si_{20}H_{19}(COOH)$, and (d) $Si_{20}H_{19}(COO^-)$ (after Ref. [81]).

the fullerene structure intact as shown in Fig. 3.19 and the HOMO–LUMO gap also remains nearly the same as for the $Si_{20}H_{20}$ cage. Therefore the optical properties of the silicon fullerenes can be used for applications in sensors and biological applications such as cancer detection.

3.3.7 Absorption Spectra

The large HOMO–LUMO gaps of metal encapsulated silicon clusters and weak reactivity could be used for optical absorption and photoluminescence in the visible region. Kumar *et al.* [57] calculated the absorption spectra for Ti and Zr doped fullerene and FK isomers. The excitation of an electron creates an electron-hole pair and the exciton binding energy lowers the excitation energy. Accordingly the optical gap for the FK isomer of $Ti@Si_{16}$ was calculated to be 2.85 eV compared with the value of 3.44 eV for the HOMO–LUMO gap within B3PW91 hybrid functional for the exchange-correlation energy. This lies in the deep blue region of the optical spectrum. For the fullerene isomer of $Zr@Si_{16}$ the optical gap is 1.96 eV (HOMO–LUMO gap of 2.44 eV within B3PW91) which lies in the red region. The oscillator strengths for these transitions were calculated [57] to be 0.003 and 0.012, respectively. These values are comparable to those of 0.005–0.15 obtained [113] for small elemental silicon clusters terminated with hydrogen. Similar oscillator strength of 0.003 was obtained [114] for $Si_{29}H_{24}$ with a tetrahedral structure. This cluster is supposed to represent the structure of a magic cluster [39] that exhibits bright photoluminescence. Therefore similar behaviour is expected from the metal encapsulated silicon clusters. The optical gap for $Si_{29}H_{24}$ was calculated [57] to be 3.72 eV. Another allowed weak transition was obtained at ~3.5 eV, but the oscillator strength was very low. QMC calculation [114] on this structure gave the value of 3.5 eV in good agreement with the calculations within B3PW91. The absorption spectra obtained by Gaussian broadening (width 0.05 eV) of the transition energies and by multiplying with the oscillator strengths for different clusters are shown in Fig. 3.20.

3.3.8 Magnetic Clusters of Silicon

In general the magnetic moment of the metal atom is completely quenched in metal encapsulated silicon clusters. However, magnetic species of such systems are possible.

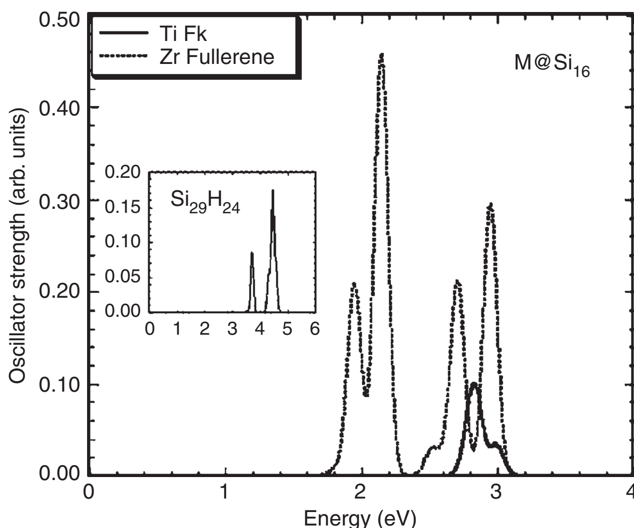

Figure 3.20 Gaussian broadened (width 0.05 eV) absorption spectra of the FK-Ti@Si_{16} and Zr@Si_{16} fullerene clusters. The inset shows the same for $Si_{29}H_{24}$ cluster (after Ref. [57]).

Icosahedral Mn@Ge_{12} and Mn@Sn_{12} (Fig. 3.12) were shown [47] to have large magnetic moments of 5 μ_B each arising from the 5-unpaired *d* electrons of Mn as it behaves like a divalent atom. The high symmetry of this cluster also leads to a large HOMO–LUMO gap of 1.10 and 1.15 eV for X = Ge and Sn, respectively making it likely that such species could be produced. Indeed very recently the prediction of the magic nature of Mn@Sn_{12} has been confirmed with the observation [71] of high abundance of this neutral cluster (Fig. 3.21), though $MnSi_{12}$ and $MnGe_{12}$ have not been found to be magic. In the case of Mn doped Si_{12} cluster a hexagonal structure was shown [47] to be lower in energy and in this case the magnetic moment is reduced to 1 μ_B. Experimentally the magnetic moments on these clusters are yet to be confirmed. For Cr doping, however, the highest abundance has been obtained [71] for $Sn_{10}Cr$ cation cluster (Fig. 3.21) which is expected to be magnetic. Metal doped 10-atom cluster of tetravalent atoms could have a D_{4h} structure for which X_{10}^{2-} is very stable. This cluster can therefore be stabilized [47] by a divalent atom and the remaining electrons could contribute to magnetic behaviour. Another possible way to generate magnetic clusters is by using rare earths that have localized *f* electrons. The atomic size of these metal atoms is appropriate to stabilize a Si_{20} fullerene cage [58,59] as discussed above. As 4 electrons are needed to fill the 3-fold HOMO state of the Si_{20} dodecahedral cage, it has been found that magnetic fullerenes with 4, 4, and 3 μ_B magnetic moments can be obtained for M = Sm, Pu, and Tm while highest magnetic moment of 7 μ_B can be obtained for Gd@Si_{20}^- in which case the *f* orbitals are half-filled. For these M atoms the symmetry of the cage is reduced to T_h and the *f* level splits into two 2-fold degenerate states and a 3-fold degenerate state. For Sm and Pu, four up-spin states are occupied while for Tm, seven up-spin and four down-spin *f* states are occupied and this leads to their symmetric structures. In the case of doping with other rare earths, the fullerenes are likely to be Jahn-Teller distorted and magnetic but it may be possible to have symmetric charged cages. For example anions with doping of trivalent Y, La, and Ac

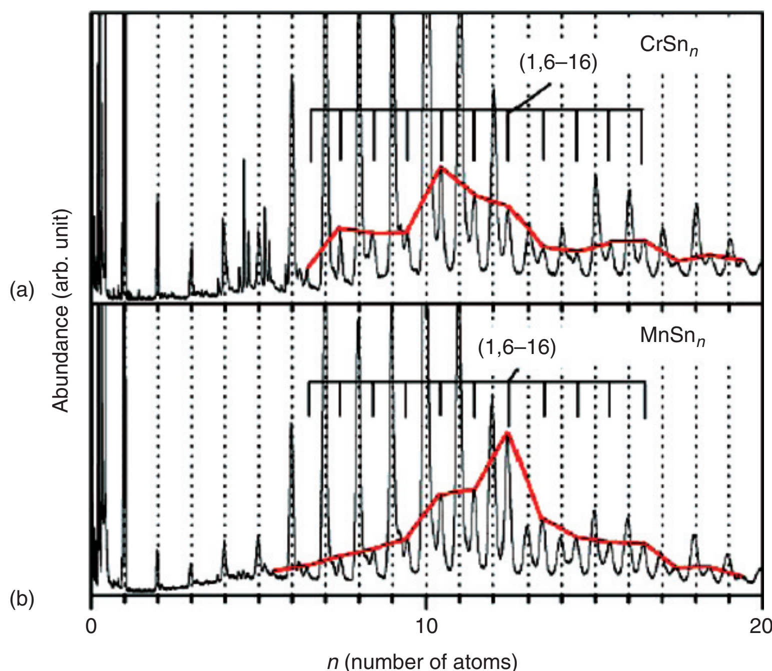

Figure 3.21 Mass abundance spectra of (a) Cr doped Sn_n (650 μJ/cm^2) and (b) Mn doped Sn_n (650 μJ/cm^2) clusters radiated by 7.9 eV laser light (Reproduced with permission from Ref. [71], courtesy S. Neukermans and P. Lievens).

have icosahedral structure. Similarly for M = Pa, cation of Pa@Si_{20} has been suggested [59] to be stable. As the magnetic moment on these cages are mostly localized on the M atom, it is likely that the moments will survive if assemblies of such species could be produced. This makes such species interesting for applications. Endohedral fullerenes of carbon are being considered for device development. In carbon fullerenes the metal atom has to be inserted as it is not required for the formation of fullerenes. However, for the formation of silicon fullerenes, it is necessary to have a metal atom inside the cage and it makes the silicon fullerenes very interesting. Another possible way to have magnetic species of silicon is using hydrogenated fullerene structure. As discussed above, atomic like behaviour of guest atoms is obtained in such fullerenes. This could be a nice way to have atomic like species with varying magnetic moments.

3.4 Summary

In summary, we have reviewed recent developments of metal encapsulated and hydrogenated clusters of silicon. The electronic structure and atomic stability of silicon fullerenes and other polyhedral forms have been discussed. The stronger stability of such nanostructures as compared to elemental clusters of similar size arises from the strong interactions between the encapsulated atom and the host as well as the closed shell electronic structure. This aspect could be very important for small scale devices.

These developments have opened up a new way to prepare nanostructures of silicon and other materials. Such species have drastically different structures and properties compared with elemental clusters and which could be tailored by using different metal atoms for encapsulation. Depending upon the size of the encapsulated atom and the host, different cages can be stabilized. This offers a possibility to design and produce nanostructures size selectively and with tunable electronic, magnetic, and optical properties. Similar to carbon fullerenes, empty cage silicon fullerenes are stabilized with hydrogen. We hope that these findings would stimulate further developments of the nanostructures based on silicon and their derivatives. Some of the predictions have been confirmed by recent experiments which illustrates the power of computer experiments. The rich variety of nanostructures and properties that are possible in mixed systems, have unfolded new possibilities for materials development that have potential for applications at the nanoscale.

Acknowledgments

I am grateful to Y. Kawazoe for all the support and cooperation at the Institute for Materials Research (IMR), Tohoku University where much of this work was done. I thankfully acknowledge discussions and fruitful collaborations with T.M. Briere, H. Kawamura, C. Majumder, F. Pichierri, and A.K. Singh, and the kind hospitality at the IMR, Tohoku University as well as the support of the staff of the Center for Computational Materials Science of IMR-Tohoku University for the use of SR8000/H64 supercomputer facilities. I also acknowledge with sincere thanks all the support received from K. Terakura and T. Ikeshoji at RICS, AIST and G. Baskaran at the Institute of Mathematical Sciences, Chennai where most of the parts of the review were written. Hospitality at these institutions and the support from NAREGI Nanoscience project funded by the Ministry of Education, Culture, Sports, Science and Technology, Japan, Hokkaido University, Sapporo as well as partial support from the Asian Office of Aerospace Research and Development are gratefully acknowledged.

REFERENCES

1. L.T. Canham, *Appl. Phys. Lett.* **57**, 1046 (1990).
2. J.R. Heath, Yuan Liu, S.C. O'Brien, Qing-Ling Zhang, R.F. Curl, F.K. Tittel and R.E. Smalley, *J. Chem. Phys.* **83**, 5520 (1985).
3. T.P. Martin and H. Schaber, *J. Chem. Phys.* **83**, 855 (1985).
4. L.A. Bloomfield, R.R. Freeman and W.L. Brown, *Phys. Rev. Lett.* **54**, 2246 (1985).
5. J.L. Elkind, J.M. Alford, F.D. Weiss, R.T. Laaksonen and R.E. Smalley, *J. Chem. Phys.* **87**, 2397 (1987).
6. Q.-L. Zhang, Y. Liu, R.F. Curl, F.K. Tittel and R.E. Smalley, *J. Chem. Phys.* **88**, 1670 (1988).
7. S. Maruyama, L.R. Anderson and R.E. Smalley, *J. Chem. Phys.* **93**, 5349 (1990).
8. J.M. Alford, R.T. Laaksonen and R.E. Smalley, *J. Chem. Phys.* **94**, 2618 (1991).
9. M.F. Jarrold, J.E. Bower and K. Creegan, *J. Chem. Phys.* **90**, 3615 (1989); J.E. Bower and M.F. Jarrold, *J. Chem. Phys.* **97**, 8312 (1992).
10. Y. Liu, Q.-L. Zhang, F.K. Tittel, R.F. Curl and R.E. Smalley, *J. Chem. Phys.* **85**, 7434 (1986); M.L. Mandich, V.E. Bondybey and W.D. Reents Jr., *J. Chem. Phys.* **86**, 4245 (1987); K. Fuke,

K. Tsukamoto, F. Misaizu and M. Sanekata, *J. Chem. Phys.* **99**, 7807 (1993); B. Liu, Z.-Y. Lu, B. Pan, C.-Z. Wang, K.-M. Ho, A.A. Shvartsburg and M.F. Jarrold, *J. Chem. Phys.* **109**, 9401 (1998); B. Liu, Z.-Y. Lu, B. Pan, C.-Z. Wang, K.-M. Ho, A.A. Shvartsburg and M.F. Jarrold, *J. Chem. Phys.* **109**, 9401 (1998).

11. T.N. Kitsopoulos, C.J. Chick, A. Weaver and D.M. Neumark, *J. Chem. Phys.* **93**, 6108 (1990); J. Müller, B. Liu, A.A. Shvartsburg, S. Ogut, J.R. Chelikowsky, K.W.M. Siu, K.-M. Ho and G. Gantefor, *Phys. Rev. Lett.* **85**, 1666 (2000); L. Kronik, R. Fromherz, E. Ko, G. Ganteför and J.R. Chelikowsky, *Nat. Mater.* **1**, 49 (2002); G. Meloni, M.J. Ferguson, S.M. Sheehan and D.M. Neumark, *Chem. Phys. Lett.* **399**, 389 (2004); O. Guliamov, L. Kronik and K.A. Jackson, *J. Chem. Phys.* **123**, 204312 (2005) and references therein.
12. E.C. Honea, A. Ogura, C.A. Murray, K. Raghavachari, W.O. Sprenger, M.F. Jarrold and W.L. Brown, *Nature* **366**, 42 (1993).
13. S. Li, R.J. Van Zee, W. Weltner Jr. and K. Raghavachari, *Chem. Phys. Lett.* **243**, 275 (1995).
14. M.F. Jarrold and V.A. Constant, *Phys. Rev. Lett.* **67**, 2994 (1991); A.A. Shvartsburg, B. Liu, M.F. Jarrold and K.-M. Ho, *J. Chem. Phys.* **112**, 4517 (2000); R.R. Hudgins, M. Imai, M.F. Jarrold and P. Dugourd, *J. Chem. Phys.* **111**, 7865 (1999); M.F. Jarrold and J.E. Bower, *J. Chem. Phys.* **96**, 9180 (1992).
15. K. Raghavachari and V. Logovinsky, *Phys. Rev. Lett.* **55**, 2853–2856 (1985); K. Raghavachari and C.M. Rohlfing, *J. Chem. Phys*. **94**, 3670 (1991); K. Raghavachari, *J. Chem. Phys.* **84**, 5672 (1986); G. Pacchioni and J. Koutecký, *J. Chem. Phys.* **84**, 3301 (1986).
16. D. Tománek and M.A. Schluter, *Phys. Rev. B* **36**, 1208 (1987).
17. P. Ballone, W. Andreoni, R. Car and M. Parrinello, *Phys. Rev. Lett.* **60**, 271 (1988).
18. E. Kaxiras and K. Jackson, *Phys. Rev. Lett.* **71**, 727 (1993); *ibid.* **71**, 2354 (1993).
19. U. Röthlisberger, W. Andreoni and M. Parrinello, *Phys. Rev. Lett.* **72**, 665 (1994).
20. J.C. Grossman and L. Mitás, *Phys. Rev. B* **52**, 16735 (1995).
21. M. Menon and K.R. Subbaswamy, *Phys. Rev. B* **51**, 17952 (1995).
22. X. Jing, N. Troullier, D. Dean, N. Binggeli, J.R. Chelikowsky, K. Wu and Y. Saad, *Phys. Rev. B* **50**, 12234 (1994).
23. A.A. Shvartsburg, M.F. Jarrold, B. Liu, Z.-Y. Lu, C.-Z. Wang and K.-M. Ho, *Phys. Rev. Lett.* **81**, 4616 (1998).
24. L. Mitas, J.C. Grossman, I. Stich and J. Tobik, *Phys. Rev. Lett.* **84**, 1479 (2000).
25. D.K. Yu, R.Q. Zhang and S.T. Lee, *Phys. Rev. B* **65**, 245417 (2002).
26. E.W. Draeger, J.C. Grossman, A.J. Williamson and G. Galli, *Phys. Rev. Lett.* **90**, 167402 (2003).
27. K.A. Jackson, M. Horoi, I. Chaudhuri, T. Frauenheim and A.A. Shvartsburg, *Phys. Rev. Lett.* **93**, 013401 (2004).
28. J. Wang, X. Zhou, G. Wang and J. Zhao, *Phys. Rev. B* **71**, 113412 (2005).
29. R.L. Zhou and B.C. Pan, *Phys. Rev. B* **73**, 045417 (2006).
30. S. Yoo and X.C. Zeng, *J. Chem. Phys.* **123**, 164303 (2005); S. Nigam, C. Majumder and S.K. Kulshreshtha, *J. Chem. Phys.* **125**, 074303 (2006); S. Yoo, X.C. Zeng, X. Zhu and J. Bai, *J. Am. Chem. Soc.* **125**, 13318 (2003); S. Yoo, N. Shao, C. Koehler, T. Fraunhaum, X.C. Zeng, *J. Chem. Phys.* **124**, 164311 (2006) and references therein.
31. A.J. Williamson, R.Q. Hood and J.C. Grossman, *Phys. Rev. Lett.* **87**, 246406 (2001); A. Puzder, A.J. Williamson, F.A. Reboredo and G. Galli, *Phys. Rev. Lett.* **91**, 157405 (2003).
32. D.V. Melnikov and J.R. Chelikowsky, *Phys. Rev. B* **69**, 113305 (2004); D. V. Melnikov and J.R. Chelikowsky; *Phys. Rev. Lett.* **92**, 046802 (2004).
33. Y. Zhao, Y.-H. Kim, M.-H. Du and S.B. Zhang, *Phys. Rev. Lett.* **93**, 015502 (2004).
34. K. Nishio, T. Morishita, W. Shinoda and M. Mikami, *Phys. Rev. B* **72**, 245321 (2005).
35. C. Delerue, M. Lannoo and G. Allan, *Phys. Rev. Lett.* **84**, 2457 (2000).
36. T. van Buuren, L.N. Dinh, L.L. Chase, W.J. Siekhaus and L.J. Terminello, *Phys. Rev. Lett.* **87**, 3803 (1998).
37. E.W. Draeger, J.C. Grossman, A.J. Williamson and G. Galli, *Phys. Rev. Lett.* **90**, 167402 (2003).
38. See review A.D. Yoffe, *Adv. Phys.* **50**, 1 (2001).
39. G. Belomoin, *et al.*, *Appl. Phys. Lett.* **80**, 841 (2002).
40. H. Hiura, T. Miyazaki and T. Kanayama, *Phys. Rev. Lett.* **86**, 1733 (2001).
41. See reviews V. Kumar, *Comput. mater. Sci.* **36**, 1 (2006); V. Kumar, *Comp. Mater. Sci*. **30**, 260 (2004).
42. V. Kumar and Y. Kawazoe, *Phys. Rev. Lett.* **87**, 045503 (2001); *ibid.* **91**, 199901 (E) (2003).
43. V. Kumar, C. Majumder and Y. Kawazoe, *Chem. Phys. Lett.* **363**, 319 (2002).

44. T. Miyazaki, H. Hiura and T. Kanayama, *Phys. Rev. B* **66**, 121403 (2002).
45. V. Kumar and Y. Kawazoe, *Phys. Rev. B* **65**, 073404 (2002).
46. V. Kumar and Y. Kawazoe, *Appl. Phys. Lett.* **80**, 859 (2002).
47. V. Kumar and Y. Kawazoe, *Appl. Phys. Lett.* **83**, 2677 (2003).
48. P. Sen and L. Mitas, *Phys. Rev. B* **68**, 155404 (2003). A detailed study of Ni@Si_{12} has been done by E.N. Koukaras, C.S. Garoufalis and A.D. Zdetsis, *Phys. Rev. B* **73**, 235417 (2006). For Fe doped Si clusters see also L. Ma, J. Zhao, J. Wang, B. Wang, Q. Lu and G. Wang, *Phys. Rev. B* **73**, 125439 (2006) and for Co doped Si clusters, L. Ma, J. Zhao, J. Wang, Q. Lu, L. Zhu and G. Wang, *Chem. Phys. Lett.* **411**, 279 (2005). For Zn, Cu and Ni encapsulated Si clusters see A.D. Zdetsis, *Phys. Rev. B* **75**, 085409 (2007); Cu, Mo and W in Si_{12} have also been considered by F. Hagelberg, C. Xiao, and W.A. Lester, Jr., *Phys. Rev. B* **67**, 035426 (2003).
49. F. Hagelberg, C. Xiao and W.A. Lester, Jr., *Phys. Rev. B* **67**, 035426 (2003).
50. J. Lu and S. Nagase, *Phys. Rev. Lett.* **90**, 115506 (2003).
51. Z. Chen, A. Hirsch, S. Nagase, W. Thiel and P. von Rague Schleyer, *J. Am. Chem. Soc.* **125**, 15507 (2003); J. Wang and J.-G. Han, *J. Chem. Phys.* **123**, 064306 (2005); and for temperature dependent properties of $TiSi_{16}$ see S. Zorriasatein, K. Joshi and D.G. Kanhere, *Phys. Rev. B* **75**, 045117 (2007).
52. S.N. Khanna, B.K. Rao and P. Jena, *Phys. Rev. Lett.* **89**, 016803 (2002).
53. V. Kumar and Y. Kawazoe, *Phys. Rev. Lett.* **88**, 235504 (2002).
54. V. Kumar, A.K. Singh and Y. Kawazoe, *Nano Lett.* **4**, 677 (2004).
55. H. Kawamura, V. Kumar and Y. Kawazoe, *Phys. Rev. B* **71**, 075423 (2005).
56. H. Kawamura, V. Kumar and Y. Kawazoe, *Phys. Rev. B* **70**, 245433 (2004).
57. V. Kumar, T.M. Briere and Y. Kawazoe, *Phys. Rev. B* **68**, 155412 (2003).
58. A.K. Singh, V. Kumar and Y. Kawazoe, *Phys. Rev. B* **71**, 115429 (2005).
59. V. Kumar, A.K. Singh and Y. Kawazoe, *Phys. Rev. B* **74**, 125411 (2006).
60. G. Li, X. Zhang, Z. Tang and Z. Gao, *Chem. Phys. Lett.* **359**, 203 (2002).
61. S.N. Khanna, B.K. Rao, P. Jena and S.K. Nayak, *Chem. Phys. Lett.* **373**, 433 (2003).
62. J.M. Pacheco, G.K. Gueorguiev and J.L. Martins, *Phys. Rev. B* **66**, 033401 (2002).
63. Q. Sun, Q. Wang, T.M. Briere, V. Kumar, Y. Kawazoe and P. Jena, *Phys. Rev. B* **65**, 235417 (2002).
64. G. Mpourmpakis, G.E. Froudakis, A.N. Andriotis and M. Menon, *Phys. Rev. B* **68**, 125407 (2003).
65. Z. Chen, S. Neukermans, X. Wang, E. Janssens, Z. Zhou, R.E. Silverans, R.B. King, P. von R. Schleyer and P. Lievens, *J. Am. Chem. Soc.* **128**, 12829 (2006).
66. D.-L. Chen, W.Q. Tian, W.-C. Lu and C.-C. Sun, *J. Chem. Phys.* **124**, 154313 (2006).
67. V. Kumar and Y. Kawazoe, *Phys. Rev. Lett.* **90**, 055502 (2003).
68. M. Ohara, K. Koyasu, A. Nakajima and K. Kaya, *Chem. Phys. Lett.* **371**, 490 (2003).
69. S. Neukermans, E. Janssens, Z.F. Chen, R.E. Silverans, P.v.R. Schleyer and P. Lievens, *Phys. Rev. Lett.* **92**, 163401 (2004).
70. K. Koyasu, M. Akutsu, M. Masaaki and A. Nakajima, *J. Am. Chem. Soc.* **127**, 4995 (2005); K. Koyasu, J. Atobe, M. Akutsu, M. Mitsui and A. Nakajima, *J. Phys. Chem. A* **111**, 42 (2007) and results presented in *3rd meeting of the Nanosociety*, Sendai 2005.
71. S. Neukermans, X. Wang, N. Veldeman, E. Janssens, R.E. Silverans and P. Lievens, *Int. J. Mass. Spec.* **252**, 145 (2006).
72. W. Zheng, J.M. Nilles, D. Radisic and K.H. Bowen Jr., *J. Chem. Phys.* **122**, 071101 (2005).
73. J.M. Goicoechea and S. Sevov, *J. Am. Chem. Soc.* **127**, 7676 (2005).
74. A. Negishi, N. Kariya, K. Sugawara, I. Arai, H. Hiura and T. Kanayama, *Chem. Phys. Lett.* **388**, 463 (2004).
75. S.M. Beck, *J. Chem. Phys.* **87**, 4233 (1987).
76. S.M. Beck, *J. Chem. Phys.* **90**, 6306 (1989).
77. V. Kumar, K. Esfarjani and Y. Kawazoe, in *Clusters and Nanomaterials*, Eds. Y. Kawazoe, T. Kondow and K. Ohno (Springer Series in Cluster Physics Springer-Verlag, Heidelberg, 2002), p. 9.
78. K. Jackson and B. Nellermoe, *Chem. Phys. Lett.* **254**, 249 (1996).
79. F. Pichierri, V. Kumar and Y. Kawazoe, *Chem. Phys. Lett.* **406**, 341 (2005).
80. V. Kumar and Y. Kawazoe, *Phys. Rev. B* **75**, 155425 (2007).
81. F. Pichierri, V. Kumar and Y. Kawazoe, *Chem. Phys. Lett.* **383**, 544 (2004).
82. H.W. Kroto, J.R. Heath, S.C. O'Brien, R.F. Curl and R.E. Smalley, *Nature* **318**, 162 (1985).
83. W. Krätschmer, L.D. Lamb, K. Fostiropoulos and D.R. Huffman, *Nature* **347**, 354 (1990).
84. K.-M. Ho, A.A. Shvartsburg, B. Pan, Z.-Y. Lu, C.-Z. Wang, J.G. Wacker, J.L. Fye and M.F. Jarrold, *Nature* **392**, 582 (1998).

85. T. Bachels and R. Schafer, *Chem. Phys. Lett.* **324**, 365 (2000).
86. M. Horoi and K.A. Jackson, *Chem. Phys. Lett.* **427**, 147 (2006).
87. C. Majumder, V. Kumar, H. Mizuseki and Y. Kawazoe, *Phys. Rev. B* **71**, 035401 (2005).
88. D.E. Bergeron and A.W. Castleman, Jr. *J. Chem. Phys.* **117**, 3219 (2002).
89. Li Ma, J. Zhao, J. Wang, B. Wang and G. Wang, *Phys. Rev. A* **73**, 063203 (2006).
90. J. Zhao, J. Wang, J. Jellinek, S. Yoo and X.C. Zeng, *Eur. Phys. J. D* **34**, 35 (2005).
91. K. Jackson, M.R. Pederson, D. Porezag, Z. Hajnal and T. Frauenheim, *Phys. Rev. B* **55**, 2549 (1997).
92. M. Ohara, Y. Nakamura, Y. Negishi, K. Miyajima, A. Nakajima and K. Kaya, *J. Phys. Chem. A* **106**, 4498 (2002); M. Harada, S. Osawa, E. Osawa and E.D. Jemmis, *Chem. Lett.* **1**, 1037 (1994); D.E. Jemmis, J. Leszczynski and E. Osawa, *Fullerene Sci. Technol.* **6**, 271 (1998); E.F. Sheka, E.A. Nikitina, V.A. Zayets and I.Y. Ginzburg, *Int. J. Quantum Chem.* **88**, 441 (2002); H. Tanaka, S. Osawa, J. Onoe and K. Takeuchi, *J. Phys. Chem. B* **103**, 5939 (1999); X.G. Gong and Q.Q. Zheng, *Phys. Rev. B* **52**, 4756 (1995); Q. Sun, Q. Wang, P. Jena, B.K. Rao and Y. Kawazoe, *Phys. Rev. Lett.* **90**, 135503 (2003), J. Song, S.E. Ulloa and D.A. Drabold, *Phys. Rev. B* **53**, 8042 (1996).
93. T. Kume, H. Fukuoka, T. Koda, S. Sasaki, H. Shimizu and S. Yamanaka, *Phys. Rev. Lett.* **90**, 155503 (2003) and references therein; J.S. Tse, S. Desgreniers, Z.-Q. Li, M.R. Ferguson and Y. Kawazoe, *Phys. Rev. Lett.* **89**, 195507 (2002) and references therein.
94. S.C. O'Brien, J.R. Heath, R.F. Curl and R.E. Smalley, *J Chem. Phys.* **88**, 220 (1988). J.B. Jaeger, T.D. Jaeger and M.A. Duncan, *J. Phys. Chem. A* **110**, 9310 (2006) have studied photodissociation of MSi_n^+ clusters with M = Cu, Ag, and Cr. For Cu and Ag photodissociation proceeds with the loss of metal atom suggesting that metal-Si bond is weaker, but for Cr with $n = 15$ and 16, the dissociation proceeds via the loss of silicon producing smaller metal-silicon clusters. This supports the stronger metal-silicon bonding.
95. H. Kawamura, V. Kumar and Y. Kawazoe, *Phys. Rev. B* **70**, 193402 (2004).
96. K. Jackson, E. Kaxiras and M.R. Pederson, *J. Phys. Chem.* **98**, 7805 (1994).
97. X.G. Gong and V. Kumar, *Phys. Rev. Lett.* **70**, 2078 (1993).
98. E.N. Esenturk, J. Fettinger, Y.-F. Lam and B. Eichhorn, *Angew. Chem. Int. Ed.* **43**, 2132 (2004); E.N. Esenturk, J. Fettinger and B. Eichhorn, *J. Am. Chem. Soc.* **128**, 9178 (2006); L.-F. Cui, X. Huang, L.-M. Wang, J. Li and L.-S. Wang, *Angew, Chem. Int. Ed.* **46**, 742 (2007); C. Rajesh and C. Majumder, *Chem. Phys. Lett.* **430**, 101 (2006); D.-L. Chen, W.Q. Tian and C.-C. Sun, *Phys. Rev. A* **75**, 013201 (2007).
99. R.B. King, T. Heine, C. Corminboeuf and P.v.R. Schleyer, *J. Am. Chem. Soc.* **126**, 430 (2004).
100. E.N. Esenturk, J. Fettinger and B. Eichhorn, *Chem. Comm.* **247**, (2005).
101. T.F. Fässler and D. Hoffmann, *Angew. Chem. Int. Ed.* **43**, 6242 (2004).
102. C. Rajesh, C. Majumder, M.G.R. Rajan and S.K. Kulshreshtha, *Phys. Rev. B* **72**, 235411 (2005).
103. J.M. Goicoechea and S.C. Sevov, *Inorg. Chem.* **44**, 2654 (2005); *J. Am. Chem. Soc.* **126**, 6860 (2004).
104. M.J. Frisch, *et al.*, Gaussian 98 (2001) Revision A.11.1, Gaussian Inc., Pittsburgh, PA.
105. M.O. Watanabey, N. Kawashimaz and T. Kanayama, *J. Phys. D: Appl. Phys.* **31**, L63 (1998); M.O. Watanabea, H. Murakami, T. Miyazakic and T. Kanayama, *Appl. Phys. Lett.* **71**, 1207 (1997).
106. K. Tonokura, T. Murasaki and M. Koshi, *J. Phys. Chem. B* **106**, 555 (2002).
107. D. Balamurugan and R. Prasad, *Phys. Rev. B* **64**, 205406 (2001).
108. M. Rohlfing and S.G. Louie, *Phys. Rev. Lett.* **80**, 3320 (1998).
109. C.W. Earley, *J. Phys. Chem. A* **104**, 6622 (2000).
110. G.A. Rechtsteiner, O. Hampe and M.F. Jarrold, *J. Phys. Chem. B* **105**, 4188 (2001).
111. D. Connetable, V. Timoshevskii, E. Artacho and X. Blase, *Phys. Rev. Lett.* **87**, 206405 (2001).
112. H. Shinohara, *Rep. Prog. Phys.* **63**, 843 (2000).
113. C.S. Garoufalis, A.D. Zdetsis and S. Grimme, *Phys. Rev. Lett.* **87**, 276402 (2001); I. Vasiliev, S. Ogut and J.R. Chelikowsky, *Phys. Rev. Lett.* **86**, 1813 (2001); S. Ogut, J.R. Chelikowsky and S.G. Louie, *Phys. Rev. Lett.* **79**, 1770 (1997).
114. G. Belomoin, J. Therrien, A. Smith, S. Rao, R. Twesten, S. Chaieb, M.H. Nayfeh, L. Wagner and L. Mitas, *Appl. Phys. Lett.* **80**, 841 (2002); L.X. Benedict, A. Puzder, A.J. Williamson, J.C. Grossman, G. Galli, J.E. Klepeis, J.-Y. Raty, and O. Pankratov, *Phys. Rev. B* **68**, 085310 (2003) have compared results of the optical absorption on a number of hydrogenated silicon clusters using Bethe-Salpeter equation and time-dependent LDA calculations. Effects of passivants other than hydrogen such as oxygen has been studied using quantum Monte Carlo calculations in Ref. 115.
115. A. Puzder, A.J. Williamson, J.C. Grossman and G. Galli, *Phys. Rev. Lett.* **88**, 97401 (2002).

CHAPTER FOUR

Porous Silicon – Sensors and Future Applications

James L. Gole and Stephen E. Lewis

Contents

4.1 Introduction 150
4.2 Kinds of PS 151
  4.2.1 Pore Structure in PS 151
  4.2.2 PL from PS 153
4.3 PS Sensors 157
  4.3.1 PS Humidity Sensors 157
  4.3.2 PS Chemical Sensors 161
  4.3.3 PS Gas Sensors 161
4.4 Future Technology 168
  4.4.1 Nanoparticle Photocatalytic Coating of PS 168
  4.4.2 Lithium Electrolyte-Based PS Microbattery Electrodes 170
4.5 Conclusions 172
References 172

Abstract

Current and future applications of porous silicon (PS) interfaces for the development of chemical sensors, microreactors, and lithium battery systems are considered. A brief overview of a diverse group of sensors, each with different applications, constructions, and benefits is used to provide a general understanding of the scope of PS sensors. A range of sensing mechanisms, methods of transduction, and fabrication methods for producing sensors for the detection of humidity, gas concentrations, and additional analytes are considered, indicating the diversity of PS sensors that can be developed as platforms for ever-increasing applications, especially as these devices are integrated into arrays with complementary metal-oxide semiconductor (CMOS), micro electro-mechanical system (MEMS), and nano electro-mechanical system (NEMS) technologies. Within this framework, we consider the variety of pore structures associated with the PS interface and the demonstration of a micro/nanoporous morphology to form optimized structures both in terms of available surface area (sensitivity) and selectivity, through nanostructure-based surface modification. We outline how the enhancement and stabilization of the photoluminescence (PL) from PS has been used to provide a means of generating low-resistance (20–100 Ω) contacts to the PS surface using PL-induced metallization from electroless

School of Physics, Georgia Institute of Technology, Atlanta, GA, USA

Nanosilicon
9780080445281

Copyright © 2007. Elsevier Ltd.
All rights reserved.

solutions and the extension of these efforts to nanostructure-based surface modification. A discussion of select humidity, chemical, and gas sensors is presented to convey the diversity of these devices. We indicate future applications with a short discussion of nanoparticle photocatalytic coatings placed on the nanostructured walls of a microsctructured scaffolding as a means of producing solar or electroluminescence-pumped microreactors that might also be used as solar pumped sensors. We conclude with a brief outline of PS-based lithium batteries.

4.1 Introduction

While porous silicon (PS) displays a UV light induced orange-red photoluminescence (PL) [1] which suggests its possible use in optoelectronics, displays, and photovoltaics (PVs) [2], a large internal surface area suggests that PS might best be considered for gas sensors [3], which can be effectively incorporated into the processing infrastructure of the silicon-integrated circuit industry.

A sensor should be sensitive, selective, rapid, reversible, inexpensive, and rugged. Within this framework, sensors developed with microfabrication technology can result in low-cost arrays of sensors which present an effective means for the discrimination of multiple analytes. Applications for PS sensors are multifarious, from the monitoring of cabin air quality in automobiles and transportation systems in general, to food analysis, and to medical diagnostic aids. The widespread use of these sensors will depend on their stability, ease of use, calibration, and manufacturing, and their ability to be readily integrated with CMOS electronics into arrays.

At a recent NSF/NIST "Process Measurement and Control Workshop" [4] several critical challenges for further sensor development were identified. Individual sensor systems should be produced cost effectively in any scale processes. Government and industry standards will require the operation of a device in a safely monitored and environmentally friendly manner. Key to developing these new capabilities must be the need for easier calibration models, methods to transfer calibration sensors with given performance properties and/or process parameters, calibration transfer among multiple-"like" sensors, and transitioning from laboratory development to plant operation.

Several potential applications can be envisioned for a PS sensor platform. These applications will require sensitive and selective devices, as well as reliably demonstrating performance under a range of operating conditions. Due to the many motivating applications for such devices, several groups worldwide are investigating PS-based sensors. Not all of these devices can be presented here;* however, a range of sensing mechanisms, methods of transduction, and fabrication methods for producing various sensors for the detection of humidity, gas concentrations, and additional analytes will be considered.

* This chapter focuses on chemical sensor development through the early months of 2005. The emphasis is on devices other than biosensors.

4.2 Kinds of PS

Interfaces and their modification will continue to play increasing roles in the development of device technologies. High surface area PS offers a versatile interface which can be obtained through the etching of either *p*- or *n*-type silicon.

The ability to control and transform the morphology and optical properties of the PS interface provides a framework for the development not only of sensors [5], but also microreactor and microbattery configurations [6,7]. The interactive sensing capabilities of PS can be varied as a function of pore size, pore morphology, and post-etch surface treatments [5,8,9].

4.2.1 Pore Structure in PS

Several groups have studied the development of pore formation in etched silicon surfaces. The electrochemical etching of silicon in a variety of electrolytes can produce a diverse range of pore diameters [9–19] which can be made to vary from the 1 to 10 nm range [11–14] (nanoporous silicon) to sizes in the 1–3 μm range [17] (microporous silicon). Further, mixtures of two pore types are possible [12,19], producing a hybrid micro-nanoporous structure. Additionally, "breakthrough pores" of order 100 nm can be obtained by using a short, high potential, etch of *n*-type silicon in darkness [9]. Further, "mesopores," typically 10 nm in diameter, can be obtained from heavily doped p^+—Si and n^-—Si under conditions that would produce nanopores in moderately doped silicon.

One common form of PS which has been used in the fabrication of devices is nanoporous silicon. This material is typically made through the electrochemical etch of a silicon wafer, using a mixture of ethanol and aqueous HF. In producing a nanoporous silicon film, a 1:1 (48% HF: ethanol) mixture (the etch solution) is prepared. This solution is contained in a Teflon cell, and exposed to the polished surface of a (100) Si wafer with a resistivity as low as 1 mΩ-cm. Electrical contact is made to the back side of the wafer through a metal foil, as a Pt mesh electrode (counter electrode) is also immersed in the etch solution. Anodization of the silicon wafer is established with a constant current density of 20 mA/cm^2 applied to the cell for 20 min. Figure 4.1 shows one possible configuration of an etch cell. The outlined etch procedure with a similar cell can result in a nanoporous sample approximately 12 μm deep with a porosity of near 75% [20].

While the vast majority of experiments conducted thus far on PS have involved primarily the characterization of nanoporous material. Christophersen, Carstensen, Föll, and others have recently studied the nature of micropore formation in *n*-type silicon (through backside illumination) as a function of doping, temperature, and potential, and in *p*-type silicon as a function of crystal orientation and electrolyte dependence; the former extends the studies of Lehmann and Föll [12] and Lehmann, *et al.* [15,21,22] and the latter establishes the important role played by hydrogen and oxygen in pore formation. Large up to 3 μm pores, "p-micropores," were first described for the non-aqueous etch of *p*-type silicon by Probst and Kohl [17] and subsequently by others [23,24]. Using a hybrid approach [25,26] it is possible to combine the microporous structure first generated by Probst and Kohl [17] with the advantages brought by a nanoporous framework.

It is clearly established that one can fabricate a range of hybrid structures between two limiting well-defined PS morphologies: (1) PS fabricated from aqueous electrolytes that consist of highly nanoporous, branched structures and (2) PS fabricated from non-aqueous electrolytes that is comprised of open and accessible microporous structures with deep, wide, well-ordered channels that display a crystalline Si (100) influenced pyramidal termination. The ability to control the interplay of these two regimes of porosity provides a means to exploit both the bulk and surface properties of the supporting membrane. The hybrid microporous/nanoporous structure etched into a silicon framework, as depicted in Fig. 4.2, represents an extrapolation of the Probst and Kohl [17] study, and provides a useful platform for the construction of a conductometric PS-based sensor.

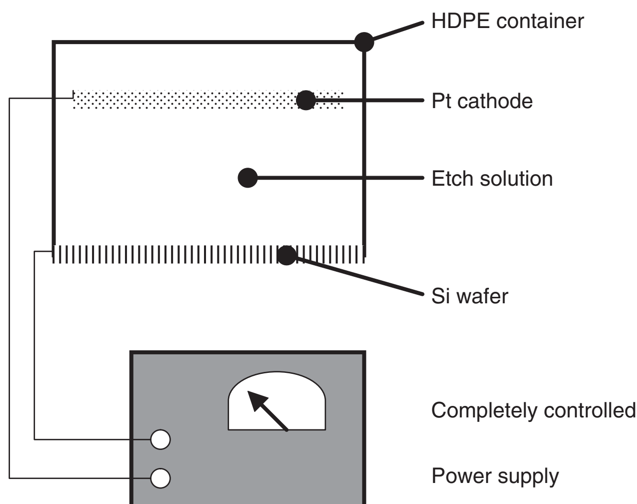

Figure 4.1 Schematic showing a possible electrochemical etch cell configuration used to produce a PS layer.

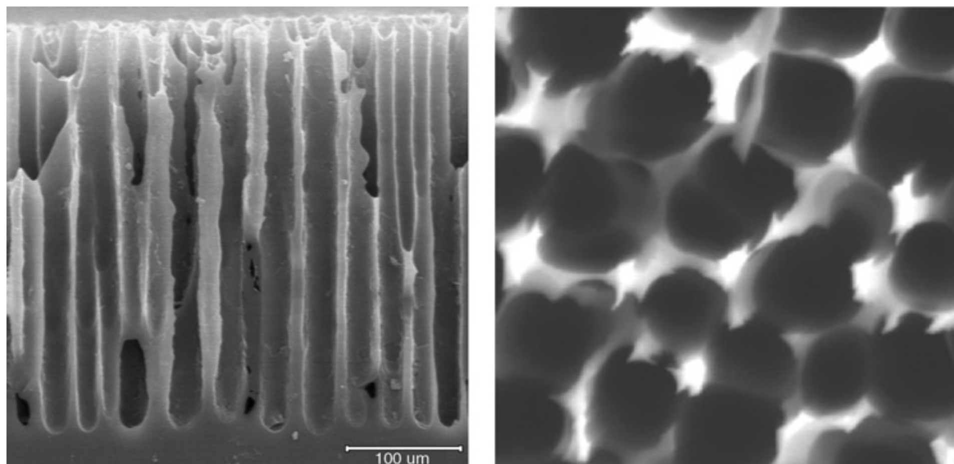

Figure 4.2 Closeup views of the hybrid PS film: side and top view.

Single-crystal (100) boron-doped *p*-type silicon wafers with resistivities of the order 1–20 Ω-cm have been used to form the hybrid structure depicted in Fig. 4.2. Hybrid nanopore-covered microporous *p*-type PS samples were fabricated in an electrochemical cell constructed from high-density polyethylene. A working electrode was attached to the back of the wafer and the counter electrode corresponded to a platinum foil placed in solution. The cell was sealed to the front of the wafer, using a clamp, as a 1 cm^2 section of the wafer made contact with the solution. A magnetic stir-bar was used to prevent the buildup of hydrogen at the surface of the silicon. The samples were etched in a solution of 1 M H_2O, 1 M HF, and 0.1 M tetrabutylammonium percholate (TBAP), all in acetonitrile. The hybrid samples were etched with a current density of 6 mA/cm^2 for between 50 and 75 min. Using this procedure, pores approximately 1 μm wide and 10–40 μm deep were formed, well covered by a coating of nanoporous silicon [25,27].

4.2.2 PL from PS

PS formed from the HF-based etch of a silicon wafer is characterized by an extensive visible PL which, when excited by UV radiation, displays a time dependent behaviour resulting primarily from surface-based oxidation processes. The development, enhancement, and evolution of this PL can be significantly influenced through the introduction of a variety of surface treatments with, e.g., HCl [26] and select dyes [28].

The light-induced PL from PS has been associated with a variety of mechanisms, including emission from quantum confined silicon crystallites [29–33] surface localized states [34], surface confined defects [35,36], or surface confined molecular emitters [37–40]. Stutzmann *et al.* have used the optical detection of magnetic resonance (ODMR) to establish that the PS "orange-red" emission results from the excitation of a triplet exciton. Prokes *et al.* [41] have suggested a source based in defect site localized oxyhydrides, having an Si–O core, as the origin of the red PL, following their high-temperature heating and electron spin resonance studies. A correlation with the manifold of electronic states associated with the silanone-based silicon oxyhydrides of the form 0 = Si–OH [42–44] or 0 = Si–$OSiH_3$ bound at the outer reaches of the PS skeleton is suggested. It has been suggested that the changes in bonding associated with electronic transitions involving the silanone-based oxyhydride ground electronic and low-lying triplet states, especially in the SiO-related bonds, and the substantial shift to larger SiO internuclear distance of these excited electronic states relative to their ground states, can be used to explain the observed character of the PL spectra [42, 45]. The excitation to a low-lying triplet state fluorophor, strongly bound to the surface of the PS substrate, whose effective potential is greatly shifted from the ground electronic state, does much to explain the significant red shift of the PL spectrum (550–800 nm) from the known absorption peak wavelength of the (PLE) excitation spectrum (∼350 nm) [46]. Further, calculated IR spectra are in excellent agreement with experimental Fourier Transfer Infrared Spectroscopy (FTIR) data [47].

This brief outline implies that controversy exists concerning the origin of the ubiquitous emission associated with PS. On the one hand there is significant support for a model which indicates that the emission is associated with an inhomogeneous distribution of quantum-confined crystallites (intrinsic) with which should

be associated a bandgap and phonon-like structure; on the other hand equally convincing evidence has been obtained to indicate that the emission should be associated with surface-bound emitters or fluorophors [45].

This question can be addressed through comparison of the PV response and photoluminescent emission from PS structures which are distinctly nanoporous with those which can be described as hybrid micro-nanoporous. The manifestation of differing electrical bandgaps was evaluated for samples which are characterized by distinct morphologies generated using diverse etch procedures. Those methods used for the direct etching of silicon to form open microporous structures [17] were extrapolated to form the micro/nanoporous interface depicted in Fig. 4.2. Crystallographic structure plays an important role in the fabrication of PS structures at room temperature as the rate of growth of the oxides and the porosity of the structure are also functions of solvent composition.

As Figs.4.3 and 4.4 demonstrate, the hybrid micro/nanoporous structure of Fig. 4.2 displays a dramatically different PV response versus either crystalline silicon or nanoporous silicon generated in an aqueous medium. In contrast, the relative responses of the corresponding time dependent PL from aqueous- and hybrid-etched samples (Fig. 4.4) are found to be quite similar. This suggests that the effective band gap for the distinctly different aqueous-etched and hybrid morphologies, as manifest in the PV response – a bulk characteristic, is not reflected in the observed PL from the aqueous- and hybrid-etched PS samples. While the PV response for nanoporous PS suggests a band gap of order 1.80 ± 0.02 eV [48,49], the results in Fig. 4.3 suggest a band gap for the hybrid PS surface of order 1.25 eV [25]. However, what is most relevant is not whether the peak in the PV response is at 1.25 eV but that the PV response is (1) quite distinct from that of aqueous PS and (2) intermediate to that of aqueous-etched PS and crystalline silicon. That the PL response for both the

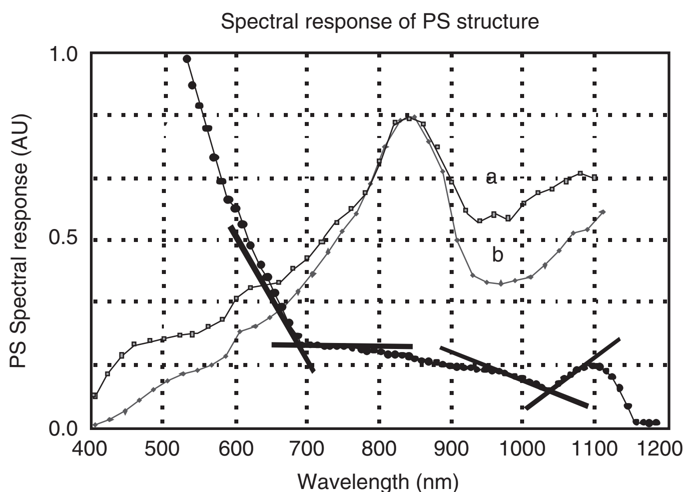

Figure 4.3 Comparison of the PV response (quantum efficiency) of a thick nanoporous silicon sample prepared from an aqueous etch [48,49] (dark full circles) with that of two distinct hybrid nano/microporous silicon samples (a and b) prepared from two mixed non-aqueous/aqueous etch solutions at 300 K [25].

aqueous- and hybrid-etched samples is virtually identical suggests that the PL, in contrast to the PV response, emanates from a surface localized source. These observations, while consistent with a surface-bound PL emitter, are not consistent with a quantum-confined emission from silicon nanocrystals. However, with a greatly increased time resolution compared to previous PS studies, they do provide an indication of the influence of the PS morphology on surface-based transformation.

4.2.2.1 Photoluminescent Enhancement and Stabilization

The development of devices based on the porous silicon PL, while a focus of considerable effort, has been slowed by (1) the inability to enhance and stabilize this PL for long periods and (2) difficulty in obtaining low-resistance contacts to the rough PS surface. In overcoming these primary limitations in the application of PS, a treatment has been created which is applicable to either nanoporous or hybrid micronanoporous PS structures that can be used to enhance and stabilize the PL. This process is applied through the treatment of the PS layer in an aqueous HCl/ methanol solutions [25,26,50].

4.2.2.2 PL-Induced Metallization

Based in part on this PL enhancement, a technique for the selective patterned metallization of a PS surface was developed using the photoluminescent surface as a reducing agent [51]. To accomplish this, a controlled PL-induced metallic ion reduction from an electroless solution [52] is made to occur in the intimate environment associated with the PL source at the PS surface. The basis of this method lies in the use of the stabilized "long-lived" PS luminescence [53] to enhance reduction at the PS surface. The formation of surface-bound electronically excited "centers," whose interaction

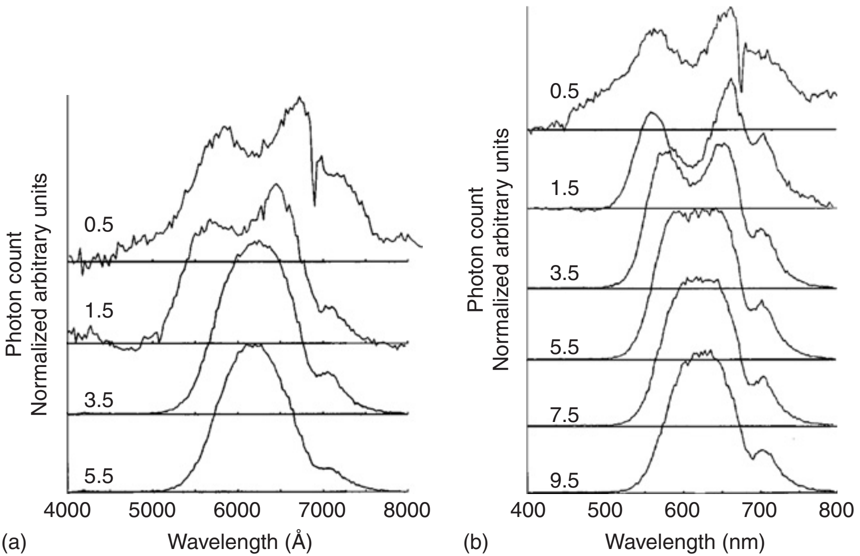

Figure 4.4 PV histograms of (a) a nanoporous PS sample for delay times after nitrogen laser pumping (337.1 nm) of 0.5–5.5 μs each with a 5 μs gate and (b) a hybrid micro/nanoporous PS sample for delay times after nitrogen laser pumping of 0.5–9.5 μs each with a 5 μs gate [25].

and reaction capability greatly exceeds that for the unexcited surface, provides a greatly enhanced and controllable reduction capability for electroless copper, silver, and gold solutions (see Fig. 4.5). This new mode of contact formation has been used to form gold-based contacts for conductometric PS sensors with contact resistances reduced to the 20–100 Ω range [52]. An HCl cleaning process appears to facilitate the surface metallization of the PS by increasing the density of activated sites.

This method of stabilization has also been used, in part, to develop an enhanced sensitivity and selectivity in conductometric PS sensors (which are discussed in detail below) [54]. An increased activity of the surface resulting from HCl cleaning gives the PS sensors an improved sensitivity. For the example shown in Fig. 4.6, a highly resistive sensor's response to 30 s 10 ppm pulses of ammonia was measured both before and after the sensor was treated with an HCl–MeOH solution. The sensor was cleaned by soaking in 1(HCl):5(MeOH) 44% HCl in methanol for 4 h and then immediately dried under N_2. This treatment roughly doubled the response of the device, as well as effecting a reduction in the device's baseline impedance. Additionally, this cleaning process further enables the deposition of thin, selective coatings to the device. The process of stabilization/metallization to establish a selective coating on the sensor

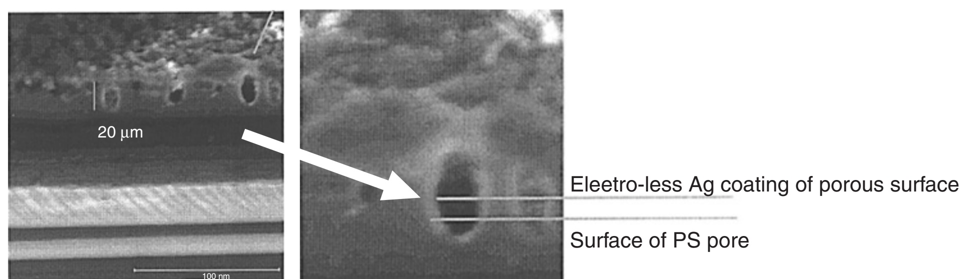

Figure 4.5 Electroless silver plating (metallization) of a hybrid micronanoporous silicon surface. The micropores are covered by a layer of metal which appears lighter in the scanning electron micrograph [51].

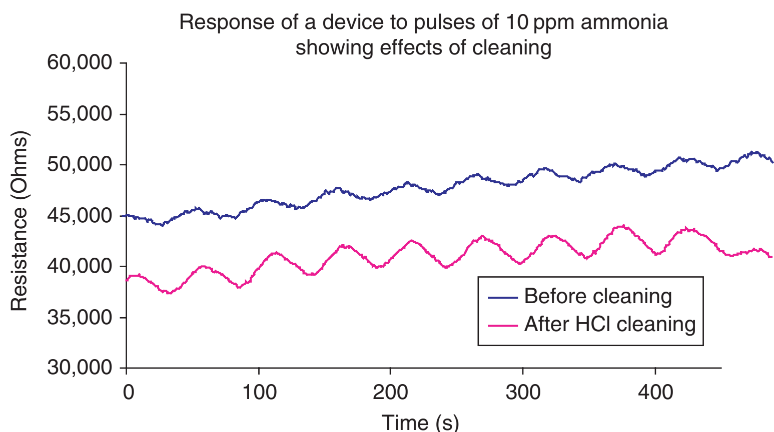

Figure 4.6 Response of a hybrid PS film-based sensor both before and after cleaning in a 1:5 HCl in methanol solution at room temperature [54].

results when the sensor is first treated with an HCl-based solution. The overall process results in the formation of metal and metal oxide nanoparticle centres on the surface of the nanopore-coated micropores depicted in Fig. 4.2.

4.3 PS sensors

Many kinds of sensors can be realized with PS materials. It has already been mentioned that PS is a viable sensor material because it provides a very high surface area in comparison to bulk silicon. This being said, there are many ways that the material can be manipulated to transduce the desired property or response.

Both the time of transduction and the recovery time are of paramount importance in most sensor applications, and both are governed by the diffusion equation. If the material is nanoporous, the diffusion coefficient is typically found from analysing Knudsen or zeolite diffusion, and not the faster Fickian diffusion, which is used to model open-air systems. When constructing a sensor system, if the adsorbtion reaction is undriven, the depth and width of nanoporous silicon must be analysed to ensure rapid transduction and recovery. The following represents the Diffusion equation:

$$\frac{dC(x,t)}{dt} = D_{ps}\frac{d^2C(x,t)}{dx^2} \tag{4.1}$$

In some instances, the sensing rate of PS is driven by factors other than diffusion. This occurs when the analyte is drawn to surface sites, either chemically or electrochemically. In the case of the humidity sensor, water vapour condenses from the atmosphere onto the surface of the sensor. In the case of the sodium ion sensor, an electrochemical cell collects sodium ions on the surface. In either case, the Nernstian behaviour of the configuration has a dramatic impact on sensing response. The Nernst equation (Equation (4.2)) describes the potential at which electrochemical equilibrium is achieved for a concentration of substance “X”.

$$E = E^0 + \frac{RT}{F}\ln([X]) \tag{4.2}$$

A brief overview of several kinds of sensors, each with different applications, construction, and benefits will provide the reader with a general understanding of the scope of PS sensors. While advances are being made through the integration of complementary metal-oxide semiconductor (CMOS), micro electro-mechanical system (MEMS), and other, newer technologies with existing sensors of all types, PS sensors of several types are now being developed as platforms for ever-increasing applications.

4.3.1 PS Humidity Sensors

PS is a common material in humidity sensors because of several enabling properties. In general, these sensors use the inherent high surface area of PS, in combination with a modified PS surface, to serve as the medium for transduction due to humidity. Water, present in the air, is collected onto the surface of the pores, changing the electrical properties of the bulk PS. The amount of water condensed is related to the

concentration of water in the air by the Nernst equation. Other factors, such as temperature and pressure also can affect the pore conductivity. Methods for measuring the electrical modification of the PS in addition to producing/treating the PS surface, account for most of the variations between different PS humidity sensors.

The most studied humidity sensors represent variations on a similar theme. The sensors use a (2–15 nm diameter) PS layer to measure the relative humidity (RH) of air. The adsorbed moisture effects the capacitance of the pores, which is typically measured with two gold electrodes either on the surface of the PS, or on the top and bottom of a treated wafer. A number of variations are possible with these common devices enabling improvements in performance to be realized.

A unique variation of the humidity sensor, constructed by Fürjes *et al.* is fabricated with the PS etch as the final step [55]. An n^{-} layer is used to define the location of the growth of a PS film, as it produces a large Shottkey barrier. Metal contacts are then deposited to produce interdigitated electrodes and a resistive heating structure. Finally, a PS etch is done, producing a nanoporous structure between the electrodes (Fig. 4.7). Capacitance is measured using this device, as with others, but the internal heating element allows slightly faster response times (approximately 1 min), by providing a driving force for desorption of the water (as shown in Fig. 4.8).

Another variation of the PS sensor, developed by Foucaran *et al.* couples a Peltier cooling device with the sensor [56]. This device uses gold contacts on the top and bottom of the sensor to measure the changing capacitance of a nanoporous film. The sensor is then affixed with a conductive epoxy to a thermoelectric cooler (TEC). The facility to cool the sensor allows one the ability to force condensation to occur rapidly on the PS layer. This humidity sensor has extremely fast response times which are on the order of seconds (see Fig. 4.9).

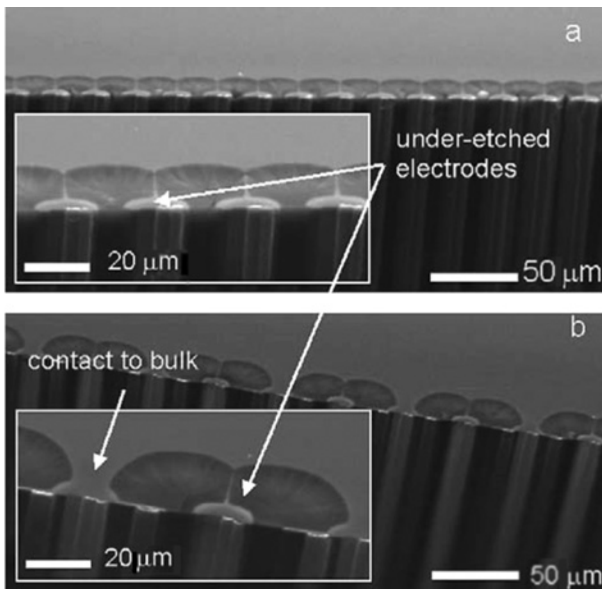

Figure 4.7 Scanning electro microscope (SEM) cross-sections of a cleaved humidity sensor. (a) Both electrodes (b) or one of the electrodes is under-etched [55].

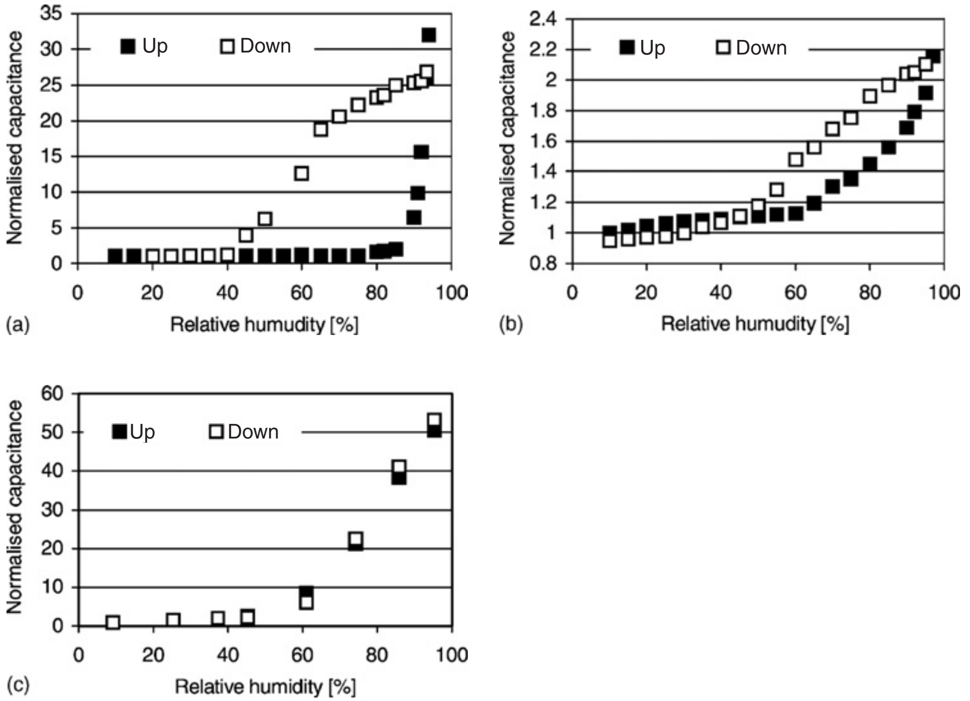

Figure 4.8 (a) Influence of heating conditions on sensor operation: without heating (b) with continuously self-heating at a power of 30 mW and (c) with refreshing before each measurement (20 s, 120 mW) [55].

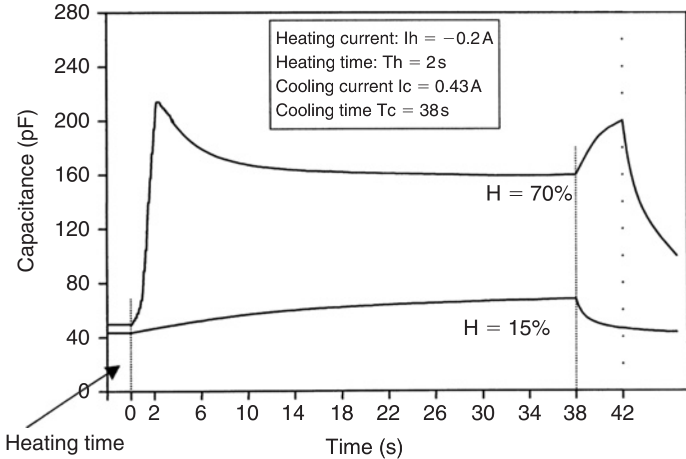

Figure 4.9 Typical curves of the TEC-integrated humidity sensor showing the capacitance variations versus time for a pulse current TEC [56].

An example of a PS humidity sensor using a modified coating is the thermally carbonized porous silicon (TC-PS) Humidity Sensor, created by Björkqvist *et al.* [57,58]. The fabrication of this sensor consists of the etching of *p*-type silicon with an HF-ethanol mixture to produce a 2.8 μm layer of pores which are an average of 6.1 nm in

diameter. This film is then carbonized at 520°C in a mixture of acetylene and nitrogen, producing a surface consisting of Si–C, Si–H, and C–H groups. 20 nm thick gold electrodes are sputtered, in the form of two rectangles, 0.5 mm apart, to produce electrical contact to the TC-PS surface. A schematic of the finished sensor is shown in Fig. 4.10. Humidity measurements are done at room temperature with impedance analysis at 100 mV and frequencies ranging from 35 to 100 Hz. Fig. 4.11 demonstrates the sensitivity and speed of the measurements. Capacitance is more sensitive at high humidity, while resistance is more sensitive at low humidity.

Additional unique humidity sensors have also been fabricated by several groups. The humidity sensor fabricated by Yarkin [59] is produced on an *n*-type silicon wafer, through the thermal oxidation of a PS film. The capacitance of the system is modulated following the diffusion of water into the porous layer, and measured between electrical contacts placed on the front and back sides of the wafer. A series of humidity sensors using porous polysilicon, and PS carbide were fabricated by Connolly *et al.* to produce devices for varying applications [60]. The porous polysilicon devices could be tuned using doping to eliminate temperature fluctuations in the capacitance of the sensor. This PS carbide sensor can operate in high-temperature environments where normal PS humidity sensors would be marginally functional.

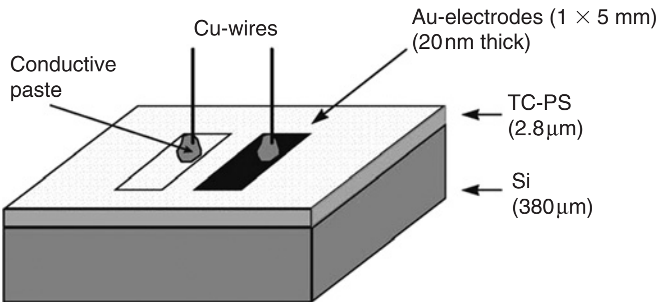

Figure 4.10 Schematic representation of a TC-PS humidity sensor [58].

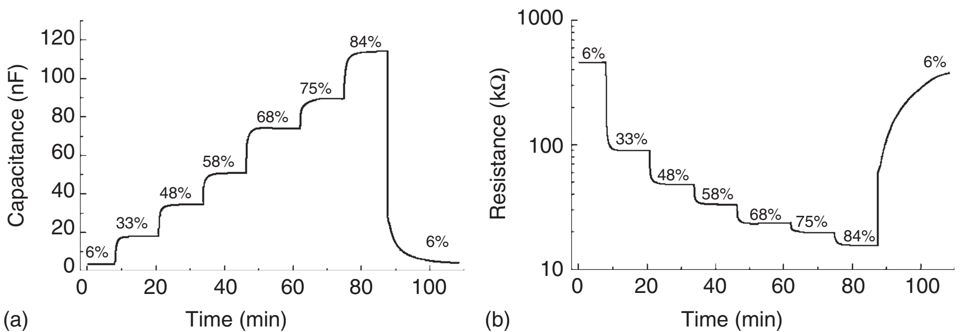

Figure 4.11 Dynamic response of (a) the capacitance and (b) the resistance of a TC-PS humidity sensor. Corresponding RH values are shown in the figures. Electrical parameters were measured using an 85 Hz frequency [58].

4.3.2 PS Chemical Sensors

PS sensors for chemical detection can utilize the optical or photoluminescent properties of PS for transduction [61] or, more simply, they can use the PS layer as the framework and electrode for detection. For example, the PS layer could have a reactive or selective layer deposited on it, and then the entire framework would be used as the counter electrode in an electrochemical cell. Bio-chemical sensors cover sensors produced to allow the detection of urea [62], glucose [63], and other biological molecules [64]. Chemical sensors which detect concentrations of either ionic solutions, or non-biological solutions constitute a second distinct group.

Exemplified below is the PS chemical ion sensor, developed by Ben Ali *et al.* [65]. Here, PS is used as a working electrode in an electrochemical cell. *P*-type silicon was etched with an HF-ethanol solution, which was subsequently oxidized to form a porous Si–O_X structure. This PS surface was used as a framework for the deposition of calix(4)arene, a sensitive material for sodium ion detection. A sensitivity of 240 mV/decade (see Fig. 4.12) to the concentration of sodium ions is demonstrated with this device. Analysis of wafer resistivity and of the depth of the PS film was used to demonstrate the effect each has on the sensitivity of the device. Further analysis of this sensor explains the Nernstian mechanism of the response in detail [66,67].

4.3.3 PS Gas Sensors

A wide range of PS gas sensors are presently being investigated by many groups. The interest in this field results as there are a large number of applications that require low cost, sensitive, and rapid discrimination between gases. Table 4.1 outlines several

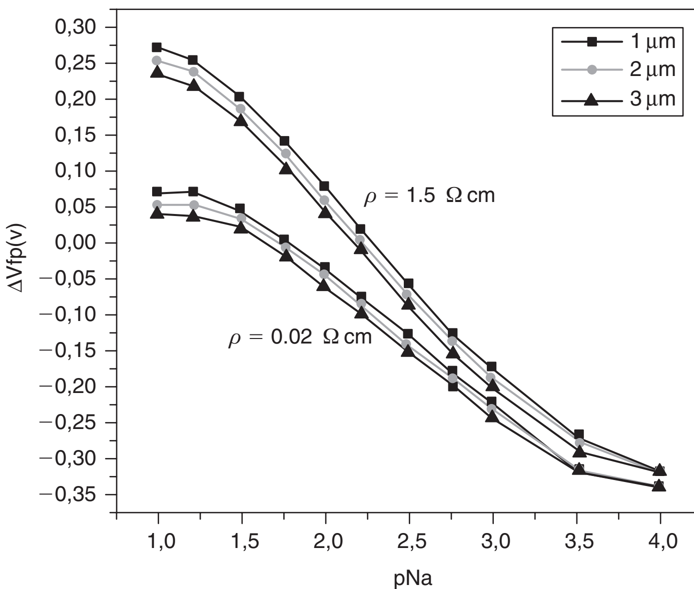

Figure 4.12 Calibration graph of functionalized PS samples for different PS layer thicknesses [66].

Table 4.1 Various gases and their detection limits for various applications [54].

Gas	LEL	Industry
Ammonia	800 ppb	Agriculture [74]
Ammonia	25 ppm	Health & Air Quality [75,76]
Carbon dioxide	0.5%	Air Quality [77]
Carbon monoxide	50 ppm	Automotive Emissions [78,79,80]/Health & Air Quality
Carbon monoxide	10 ppm	Fuel Cells [81]
Hydrogen	0.05%	ONR [82]/Fuel Cells/Hydrogen Economy
Hydrogen sulphide	20 ppm	Fuel Cells/Health & Air Quality
Hydrocarbons	500 ppm	Air Quality
Nitric oxide	20 ppm	Agriculture/Automotive Emissions [74,83]
Ozone	0.1 ppm	Air Quality
Sulphur dioxide	5 ppm	Fuel Cells/Air Quality

requirements and the lower exposure limit (LEL) needed for the detection of particular gases. The presence of amines [68] and ammonia [69] are indicators of infection whereas increased NO_x levels are correlated to inflammations including cystic fibrosis and acute asthma [70]. The food industry has a need for low-cost sensors to determine the quality/contamination of fish [71,72] and other foods [73]. Air quality monitoring is important in farming and for automotive systems. Gases which must be measured to insure air quality include carbon monoxide, carbon dioxide, sulphur oxides, nitrogen oxides, ammonia, and hydrogen sulphide.

4.3.3.1 NO_2 Sensors

NO_2 sensors in particular, of importance for air quality and emission testing, are being developed by three groups, each taking different approaches. Baratto *et al.* have fabricated a device by first producing 15 μm thick and 1–2 μm wide pores using an etch solution of 50% isopropanol/50% hydrofluoric acid [84]. These pores were then transferred to an alumina substrate, and the conductivity of the membrane was measured across pre-deposited platinum interdigitated contact (IDC) electrodes with a Solatron 1260 impedance analyzer. This system realized a sensitivity to 100 ppb of NO_2 with a response time of around 10 min (see Fig. 4.13).

Chakane *et al.* are also investigating an NO_2 PS sensor. This sensor is made through the deposition of Metallophthalocyanines (MPCs) on a nanoporous substrate 8–10 μm thick [85]. Metals tested for use with the MPCs consist of Cd, Al, and Co. These sensors produce a 70% to 100% resistance change (measured with a

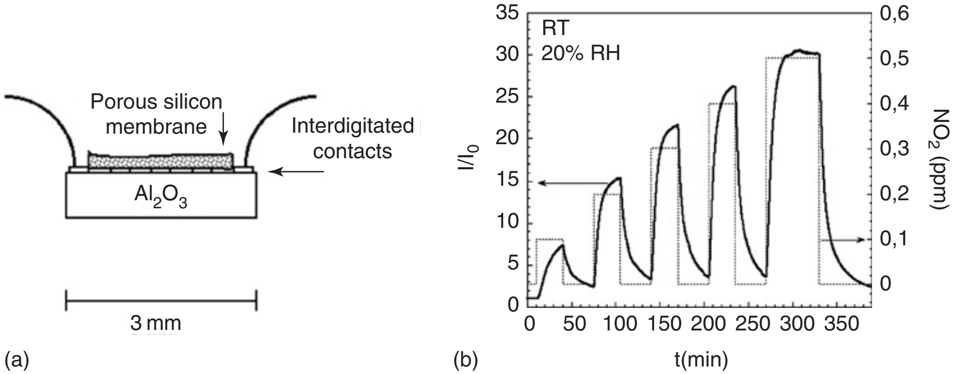

Figure 4.13 (a) Sketch of the NO_2 sensor of Baratto *et al.* (lateral view). The PS membrane is deposited on an alumina substrate. Sticking occurs with the IDC providing the electrical contacts. (b) Dynamic response of the sensor to sub-ppm concentrations of NO_2 at 20% RH and at room temperature. The continuous line represents the normalized current against time. The dotted line is the NO_2 concentration as a function of time [84].

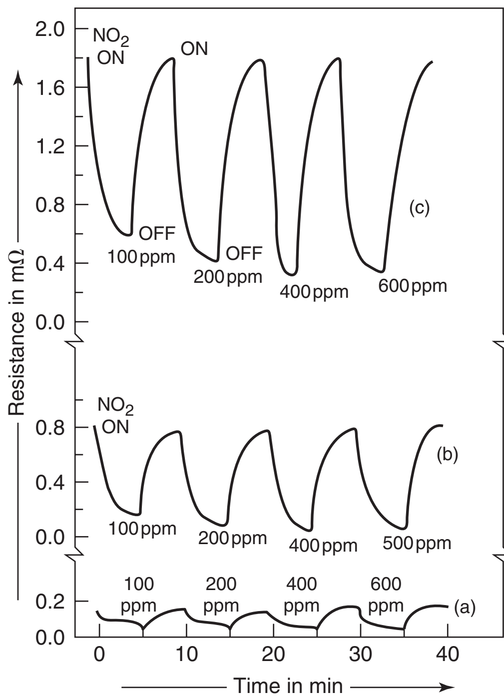

Figure 4.14 Dynamic response of (a) Al-PC, (b) Cd-PC, (c) Co-PC coated on PS towards different ppm concentrations of NO_2 [85].

Keithley-2000 electrometer) when exposed to 100 ppm of NO_2 with a response time of 4–5 min and a recovery time of 6–9 min (see Fig. 4.14). Boarino *et al.* [86], have also applied MEMS technology to form highly sensitive PS-based films for NO_2 detection.

4.3.3.2 Hydrocarbon Sensors

PS hydrocarbon gas sensors represent an additional subset of those devices being investigated. Angelucci *et al.* have constructed a sensor using integrated heating structures on a PS membrane [87]. A microporous structure was fabricated through backside illumination and electrochemical etching. This structure was then oxidized and coated with SnO_2 to form a sensitive layer (Fig. 4.15 (a)). The sensor was evaluated by measuring the current across the layer as a 1 V bias was applied to two sputtered Pt electrodes. This system senses sub-ppm C_6H_6 and CO with a response time of near 1 min (Fig. 4.15 (b)).

A second hydrocarbon gas sensor has been investigated by Liu *et al.* using polarization interferometry to detect the concentration of ethanol and heptane vapours [88]. The unique optical transduction mechanism which has been applied demonstrates optical sensitivity to ranges from 1 to 20 ppth of heptane, ethanol, and mixtures of the two. A response time of under 1 min is also seen for 2% heptane vapours. A similar sensor has also been developed by Rocchia *et al.* for reversible CO_2 sensitivity with the modification of a nanoporous surface with 3-amino-1-propanol [20]. This device is sensitive to 5 ppth of CO_2.

4.3.3.3 Low-Cost Multi-application Gas Sensors

PS gas sensors have been formed which present a unique integration of low-cost fabrication techniques to produce conductometric gas sensors [54,89]. The sensors are created through the integration of the hybrid PS electrochemical etch discussed above with standard microelectronic fabrication techniques (see Fig. 4.16). The majority of the sensors are formed as milli-scale devices to allow for rapid testing.

The sensors are fabricated on the polished surface of a test grade *p*-type (100) silicon wafer with a 1–20 Ω-cm resistivity. After an initial cleaning of the wafer, a silicon carbide layer is deposited selectively on the polished surface of the device to define the formation of PS during the etch process. The hybrid PS etch procedure discussed above is then used to produce a sensitive film. Following the etch process, the porous structure is rinsed in methanol and allowed to dry under N_2. Gold contacts can be

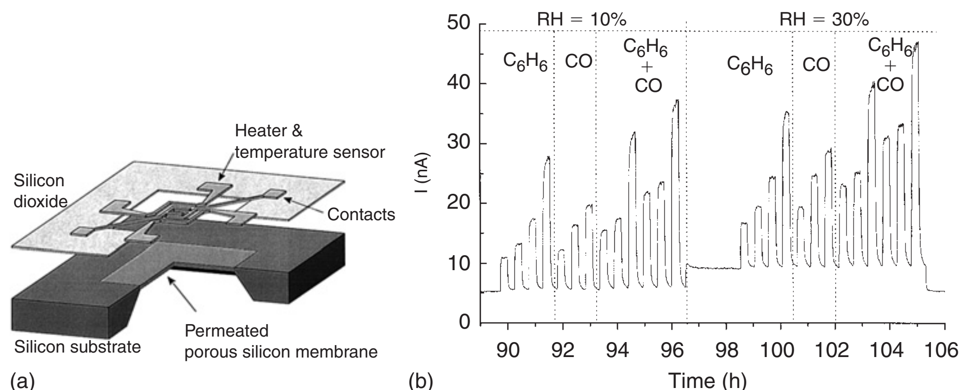

Figure 4.15 (a) Draft of a hydrocarbon sensor microstructure based on a suspended PS membrane. (b) Electrical response of the permeated suspended PS membrane sensor exposed to C_6H_6, CO, and a C_6H_6–CO mixture of differing composition, at 10% and 30% RH. $T = 370°C$, V bias = 1 V [87].

deposited by PL-induced metallization or defined by shadowmask and deposited through E-beam lithography to produce a resistive sensor. An HCl cleaning process is next used to maximize the activity of the PS surface. This process was developed as a method to optimize the PS photoluminescence [90–93]. Following a 4-h soaking in 1(HCl):5(MeOH) 44% HCl in methanol, the device is then rinsed through a brief immersion in methanol and dried under N_2.

The conductometric sensors can be evaluated with either an impedance analyzer (for higher accuracy) or with a standard voltage measurement (lower cost). A test configuration has been designed to modulate the delivery of calibrated concentrations of gas at 100 sccm [54]. Fig. 4.17 shows the resistance of a device successively exposed

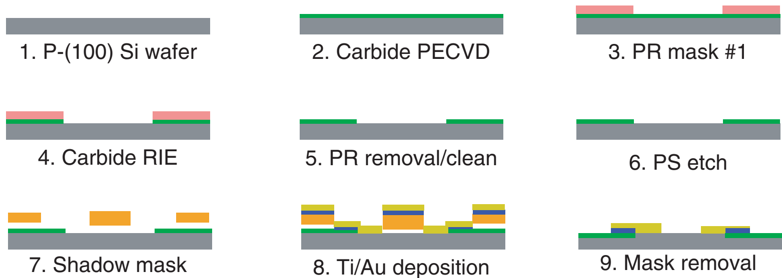

Figure 4.16 Summary of the fabrication steps for creating a PS gas sensor [54].

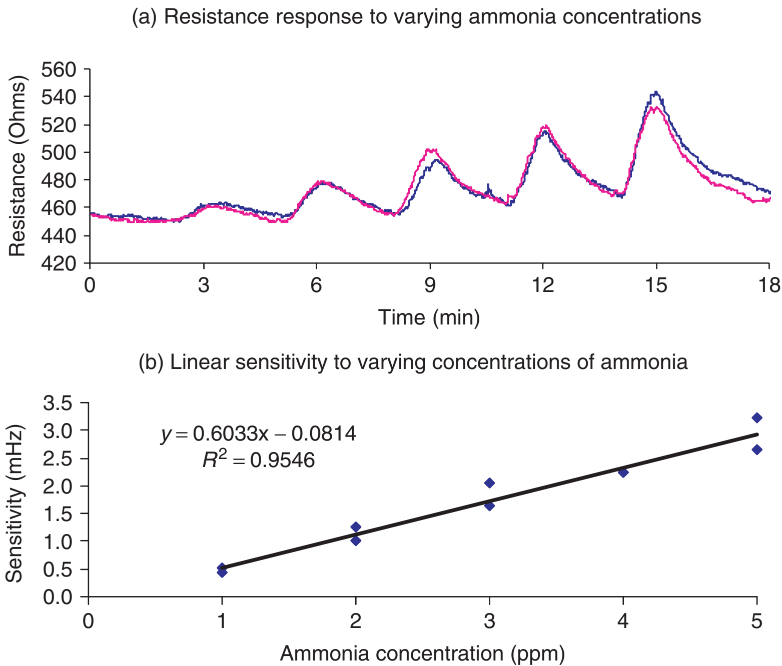

Figure 4.17 (a) Resistance of a conductometric PS sensor exposed to 1 min pulses of 1–5 ppm NH_3 in N_2 demonstrating a linear response profile. (b) A plot of the slopes of the data demonstrates the linearity and sensitivity of the response [54].

to 2 min of research grade N_2, followed by a 1 min exposure to 1, 2, 3, 4, and 5 ppm of NH_3. Each pulse of gas produces an impedance change whose slope is proportional to the concentration being delivered. The sensitivity is calculated, for a given pulse of gas, as the slope of the increase in the resistance, divided by the baseline impedance of the device. From this data, it can be established that an LEL for NH_3 of 403 ppb is achieved for this test configuration and device within a 95% confidence interval. Data depicting the relative sensitivity of a typical sensor to several gases is shown in Fig. 4.18.

Step 8 of the outlined fabrication process (Fig. 4.16) can be modified to create low-resistance 20 Ω contacts to the device by depositing electroless gold prior to the e-beam step. Electroless gold deposition can be accomplished on PS using PL-induced

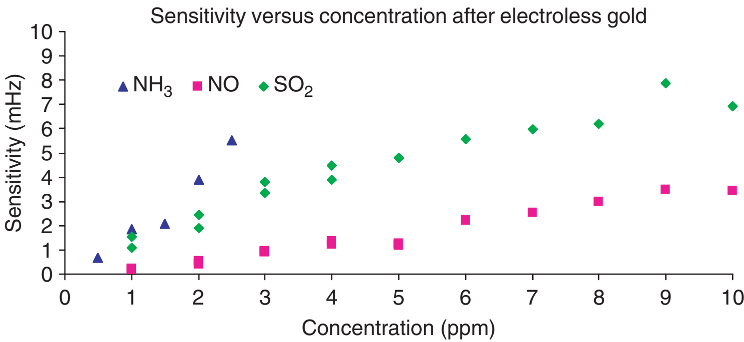

Figure 4.18 Sensitivity to NH_3, NO_x, and SO_2 for a typical conductometric PS gas sensor [54].

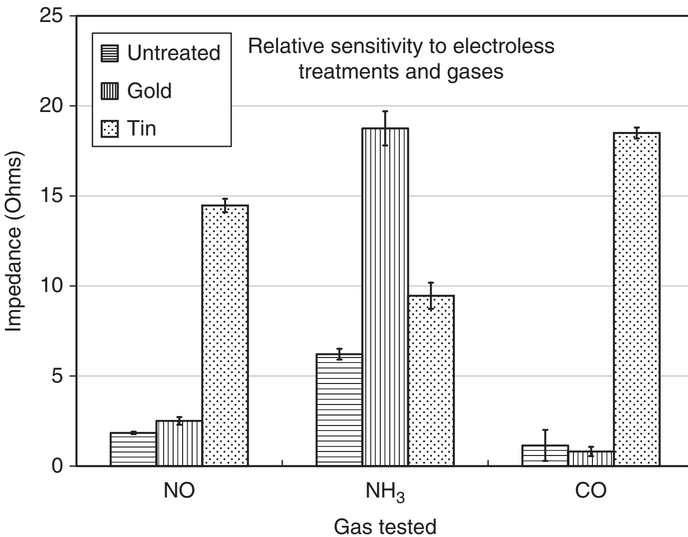

Figure 4.19 Comparison of response for sensors that are untreated, treated with electroless gold, or treated with electroless tin, and tested with 30 repeat pulses of 20 ppm NO_x, NH_3, or CO. Their average impedance change is given [54].

metallization to precipitate gold from an electroless solution at the photo-active sites on the surface of the PS pores [51,52]. These devices require less power to operate than do other kΩ contact resistance sensors, which is preferable for portable applications [53,94]. The shadow mask process was developed to minimize water contact on the sensors as it is believed to cause damage to the sensors resulting from a high rate of oxidation for the silicon microstructures [95,96]. The combinations of both processes to create more sensitive, low-power devices are continuing to be investigated.

It has been shown how the deposition of metal, using electroless metallization sources, can be enhanced by the presence of actively photoluminescing sites on the PS surface. In an effort to enhance not only sensor sensitivity but also selectivity at the sensor surface, it has been possible to deposit minimal amounts of metal to the sensor surface using a short exposure electroless metallization procedure. Here, e.g., an HCl-cleaned sensor was immersed in a commercially available (Transene) electroless gold metallization solution for 30 seconds. It was then rinsed by brief immersion in deionized (DI) water, followed by a 30 s rinse in methanol. The baseline impedance of the device decreases slightly through the deposition of additional conduction paths in the nanoporous regions of the sensor. A sensor, thus treated, resulted in a noticeably improved sensitivity to NH_3. A second electroless solution containing tin was used to deposit a layer of SnO_x. This coating, obtained as a non-uniform deposit of tin during a 20 s immersion, after rinsing in water and methanol, oxidizes to SnO_x and initiates a sensitivity to 10 ppm CO (which has since been lowered to < 5 ppm).

By saturating a sensor in 5 ppm NH_3 over 30 min, its response could be modeled with the diffusion equation as a metric for device performance. Fig. 4.20 depicts both

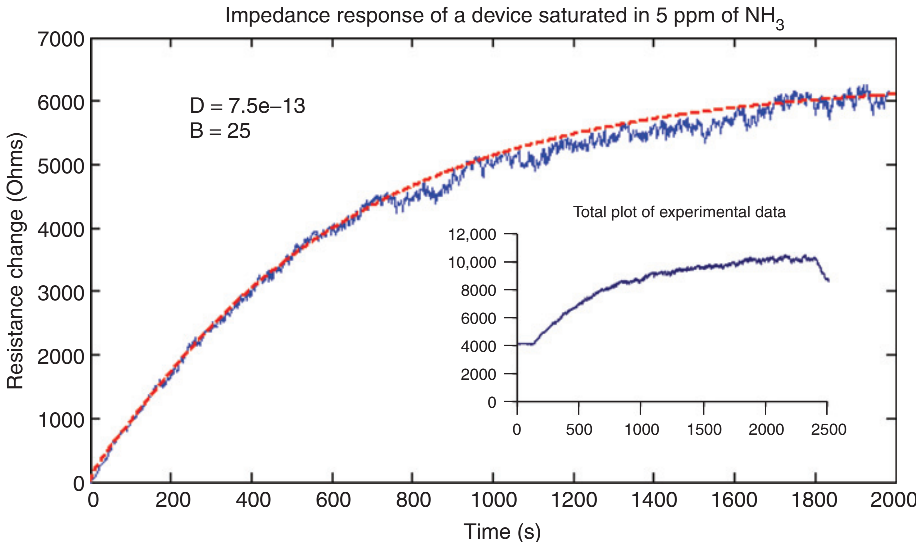

Figure 4.20 The response of a conductometric PS device (with baseline removed) under 5 ppm NH_3 saturation (solid line) compared to the value of the impedance change as given by the diffusion model discussed in the text (dashed line) [54].

the response of a typical device, which was not cleaned with HCl or coated in electroless gold, and a fitted model for the data. The correlation indicated in this figure suggests two factors. First, the sensor response appears to be driven by Knudsen diffusion, potentially within pores of nanometer size containing rough walls. This is suggested since the diffusion coefficient is of such a low order of magnitude [97]. Contrasting the fitted diffusion coefficient of $7.5 \times 10^{-13}\,m^2/s$, open air diffusion of NH_3 in air is $2.8 \times 10^{-4}\,m^2/s$, and Knudsen diffusion within a smooth pore of nanometer size is on the order of $10^{-7}\,m^2/s$. Second, the response appears to be transduced at chemically active nanoporous sites present at the walls and at the bottom of the hybrid structure micropores [54].

The described PS gas sensor uniquely combines sensitive, rapid, and reversible measurement with both a general method to achieve selectivity, and low-cost fabrication and operation. However, its realization into a fully functional gas discrimination system will require the development of arrayed sensors using an expanded combination of selective coatings.

4.4 Future technology

The PL from PS and its mode of excitation suggest that the PL and especially its electroluminescence (EL) counterpart might represent a means to create photocatalytic reactors. Here, it is suggested that the low-resistance contacts which are obtained with PL-induced metallization can allow a much more controlled and efficient EL process than is typically observed to take place [98]. Further, the PS structure depicted in Fig. 4.2 suggests the potential for developing photocatalyst supports and microreactors, as one introduces additional quantum dot (QD) structures into the PS framework. As a nanostructured framework is created, it must be emphasized that the expected enhanced activity brought by the nanoscale is, by no means, primarily the result of an enhanced surface/volume ratio. In fact, changes in the basic electronic structure of nanosized particles also play a fundamental role in the "orders of magnitude" improvement in sensitivity [99–101] and activity [102–107] which can be obtained at the nanoscale.

4.4.1 Nanoparticle Photocatalytic Coating of PS

The selectivity and sensitivity of a PS sensor could be improved and enhanced by introducing further QD structures into the pores of PS. These might include (Fig. 4.21) nitrided silica or titania nanostructures ($SiO_{2-x}N_x$, $TiO_{2-x}N_x$). When introducing nitrogen-doped visible light absorbing $TiO_{2-x}N_x$ photocatalysts [105–108] into the pores of the PS framework, it may be possible to create solar or room light pumped sensors based on this visible light adsorbing oxynitride photocatalyst.

Visible light absorbing $TiO_{2-x}N_x$ particles in a controlled size range (3–10 nm) can be produced in seconds at room temperature employing the direct nitridation of TiO_2 nanocolloids using alkyl ammonium compounds [104–109]. These titanium oxynitrides demonstrate a high quantum yield (>0.2) for reductive photocatalysis with methylene blue and for ethylene oxidation on a surface where the quantum yield in the visible is comparable to the quantum yield under UV irradiation.

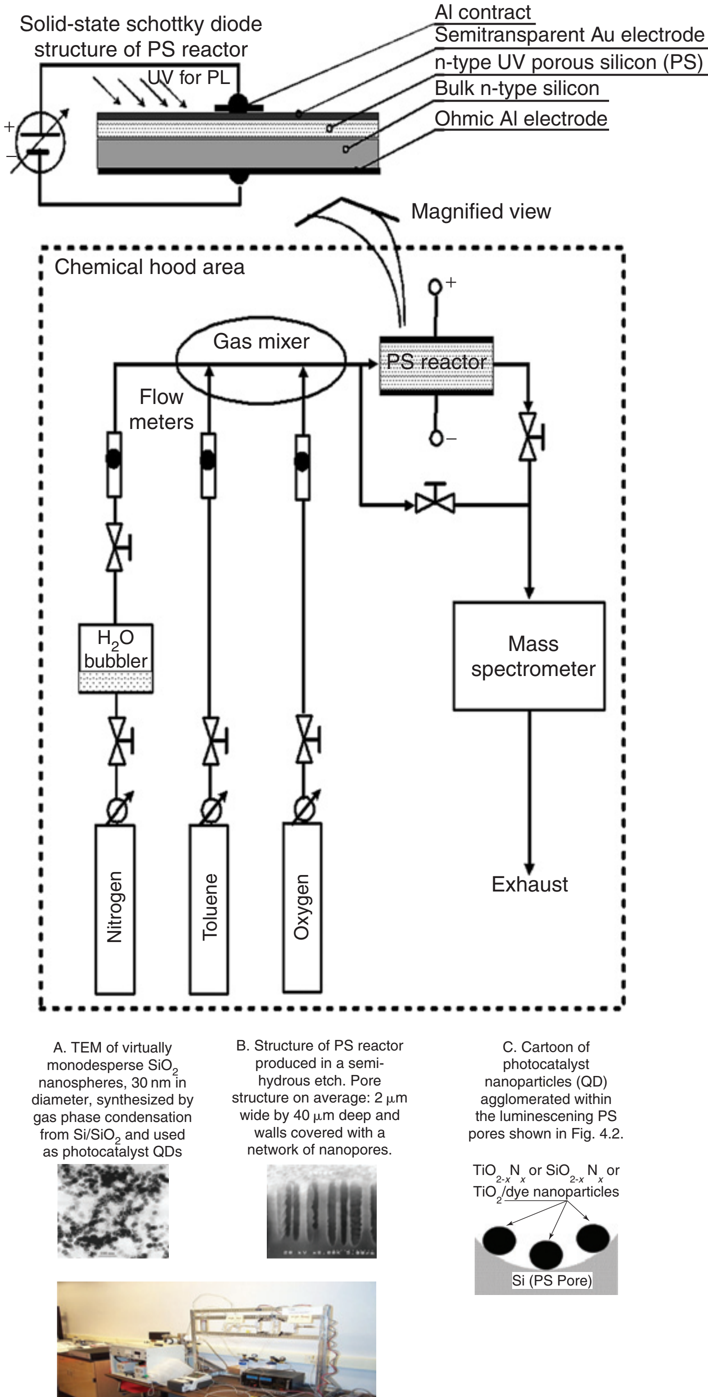

Figure 4.21 Principle: Use of nanostructured PS decorated with $TiO_{2-x}N_x$ nanoparticles as a conceptually new design for a portable photocatalytic device for the energy efficient oxidation of pathogenic bacteria and viruses (after Ref. [5]).

An advantage of the nanoscale doping procedure is that it produces slurries of the nitrided particles that form viscous solutions whose viscosity can be readily adjusted. This is of practical advantage as one places the agglomerates on a surface (e.g. a quartz reactor tube [109]) to create a film of photocatalytically active sites. A further advantage of these colloidal solutions is the unique property by which they can incorporate and uniformly disperse metallic compounds and the manner in which these metallic compounds can be introduced in concert with the nitriding process. In many instances this introduction produces a solution which, after some controlled period of time, can be transformed to a gel. This process can be accelerated by minimal heating (e.g. ~50°C).

The nitrided nanocolloids show an enhanced photocatalytic activity in the visible spectral range when used *in situ* or when prepared as films. A PS structure whose micron-size open pores are decorated with $TiO_{2-x}N_x$ nanostructures, by themselves, or impregnated with a noble metal, forming appropriate size photocatalyst Quantum Dots, constitutes a conceptually novel heterogeneous photocatalytic microreactor with possible superior performance. The reactor's success can be based on four factors. First, microporous silicon can provide a uniform and highly effective (i.e., tightly localized) illumination of the photocatalyst everywhere by UV–Vis light provided by solar radiation but also generated either from PS EL or PL. Second, PS, especially in the form of a hybrid microporous-nanoporous structure, can provide an extremely large specific (i.e. per unit volume) surface area owing to its highly porous structure and to the additional surface area made available via attached catalyst-based nanostructures. Third, photocatalysts in the form of nanoparticles have been shown to often possess superior catalytic properties as compared to a conventional bulk catalyst by virtue of the electronic modification of the catalysts through size quantization. Finally, because of the small characteristic size of the PS pores forming the reactor flow network, the significant reduction of diffusion limitations ($\sim 1/D^2$, where D is the pore diameter) can be achieved, improving the rate of the heterogeneous chemical reaction. This provides the potential to achieve reaction kinetics at its intrinsic rate while maintaining a sufficient reactor throughput using parallel chemical processing in many identical reactor units.

4.4.2 Lithium Electrolyte-Based PS Microbattery Electrodes

Because silicon can alloy with lithium electrochemically with up to 4.4 Li per Si, yielding an extremely large theoretical specific capacity of $4200\,mAhg^{-1}$ [110,111] and elemental Si shows a low voltage of $<0.3\,V$ versus Li/Li^+ [112], and high lithium ion diffusion coefficient ($\sim 7.2 \times 10^{-5}\,cm^2/s$ at 415°C) [113], it is not surprising that there is considerable recent interest in Si-based electrode materials [114–119]. Recently, the possibility of using PS as the negative electrode in rechargeable lithium batteries has been investigated, and it has been shown that PS has a high reactivity with lithium at room temperature [7]. Using the prescription to generate a hybrid PS morphology (Fig. 4.2) PS has now been used as the negative electrode in a rechargeable lithium battery. The peak current and the amount of charge transferred during cyclic-voltammetry (CV) increase with the channel depth of the PS (Fig. 4.22), indicating that the channel wall of the PS participates in the lithiation/delithiation process and thus that the capability for lithium storage

is improved with increasing channel depth. The channel structure of the PS electrodes remains essentially the same after 35 CV cycles in spite of the severe deformation of the channel wall and volume change during the repetitive lithium alloying/dealloying process. The specific capacity of the PS (Fig. 4.23) depends critically on the degree of activation of the PS before the galvanostatic charge/discharge experiment

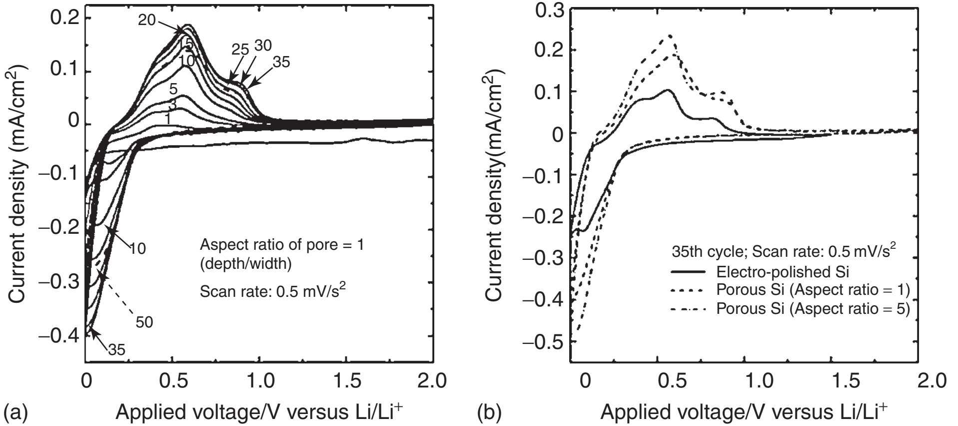

Figure 4.22 (a) Typical CVs of the PS electrodes and (b) variation of the CV with the channel depth of the PS [6,7].

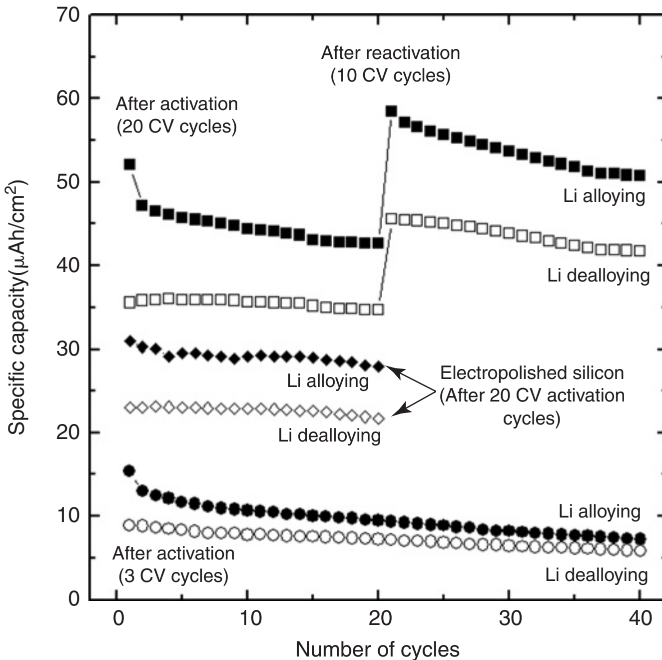

Figure 4.23 Dependence of the specific capacity on the number of cycles at a current density of $50\,\mu\text{A h/cm}^2$, obtained from the PS electrode [6,7].

and increases at the expense of cycling stability, indicating a tradeoff. In initial experiments, for an exemplary PS electrode pre-activated by 20 CV cycles, the reversible specific capacity of the PS reached 43 μAh cm^2. After a subsequent activation by 10 CV cycles, the capacity increased by 40% (60 μAh cm^2).

It is not easy to compare the specific capacity of this PS electrode with those in the literature (e.g. structured silicon formed as a pillar array [120]) because the size distribution, numerous coalescences of the pores, and the non-uniform thickness of the channel wall make a reasonable quantitative analysis (e.g. gravimetric capacity) for the PS electrodes quite difficult. Moreover, the strong dependence of the capacity on the electrochemical pre-treatment history complicates the situation. Nevertheless, in addition to its cost-effectiveness and the ease of formation of active sites, the electrochemical etching technique has the potential to create a variety of morphologies with different rate capabilities and specific capacities. Using the current etching process, not only the pore depth (Fig. 4.21) but also the density of pores can be tunable. Further, pore accessibility can be improved by using a combination of etching techniques including, e.g., the use of combined dimethylformamide (DMF) [121] and subsequent hybrid and aqueous etches to produce a more open-active pore volume. Thus, PS created by a relatively simple electrochemical etching process (versus, e.g. pillar formation), presents a viable possibility for constructing a three-dimensional negative electrode that has significant potential for a high-performance lithium microbattery.

4.5 Conclusions

Several recent advances in the field of PS have been discussed. PS presents a proven sensor technology for the measurement of humidity, chemical agents, biochemical molecules, and gas concentrations. The field will rapidly continue to expand as micro-sensor, MEMS, NEMS, and bio-technologies continue to be evaluated. PS represents an obvious avenue for the consideration of many applications that require high surface area combined with the most viable material for measurement, the silicon wafer.

REFERENCES

1. L.T. Canham, *Appl. Phys. Lett.* **57**, 1046 (1990).
2. M.J. Sailor and E.J. Lee, *Adv. Mater.* **9**, 783 (1997); L. Zeltner, M. Thoenissen, Th. Hierl, R. Brendl and M. Schulz, *Prog. Photovoltaics* **6**, 423 (1998); L. Stalmans, J. Poortmans, H. Bender, M. Caymax, K. Said, E. Vazsonyi, J. Nijs and R. Mertens, *ibid.* **6**, 233 (1998).
3. R. Halimaoui, in *Porous Silicon Science and Technology*, Eds. J.C. Vial and J. Derrien (Les Editions de Physique, Les Ulis, France, 1995), p.33; *J. Appl. Phys.* **91** (4), 2522 (15 February 2002). Downloaded 27 Feb 2004 to 130.207.165.29. Redistribution subject to AIP license or copyright, see http://jap.aip.org/jap/copyright.jsp.
4. *NSF/NIST Process Measurement and Control Workshop Report*. National Institute of Standards and Technology, USA.
5. J.L. Gole, A. Fedorov, P. Hesketh and C. Burda, *Phys. Stat. Sol.* (c) **1**, S2, S188 (2004).
6. H.-C. Shin, J. Corno, J.L. Gole and M. Liu, *J. Power Sources.* **139**, 314 (2005).
7. H.-C. Shin, Z. Shi, L.T. Seals, M. Liu and J.L. Gole, Solid state ionic devices III, *Proceedings of the Electrochemical Society*, Pennington, NJ, Ed. E. Wachman, *et al.*, Vol. **2002–26**, pp. 518–525 (2005).

8. M. Christophersen, J. Cartensen, A. Feuerhake and H. Föll, *Mater. Sci. Eng.* B **69–70**, 194 (2000) and references therein.
9. M. Hejjo, Al Rifai, M. Christophersen, S. Ottow, J. Carstensen and H. Föll, *J. Electrochem. Soc.* **147**, 627 (2000).
10. A.G. Cullis, L.T. Canham and P.D.J. Calcott, *J. Appl. Phys.* **82**, 909 (1997) and references therein.
11. M.J.J. Theunissen, *J. Electrochem. Soc.* **119**, 351 (1972).
12. (a) V. Lehmann and H. Föll, *J. Electrochem. Soc.* **137**, 653 (1990); (b) H. Föll, *Appl. Phys.* A**53**, 8 (1991).
13. P.C. Searson, J.M. Macaulay and F.M. Ross, *J. Appl. Phys.* **72** 253 (1992).
14. I. Berbezier and A. Halimasui, *J. Appl. Phys.* **74**, 5421 (1993).
15. V. Lehmann, *J. Electrochem. Soc.* **140**, 2836 (1993).
16. C. Levy-Clement, A. Lagoubi and M. Tomkiewicz, *J. Electrochem. Soc.* **141**, 958 (1994).
17. E.K. Probst and P.A. Kohl, *J. Electrochem. Soc.* **141**, 1006 (1994).
18. V. Lehmann and U. Gösele, *Adv. Mater.* **4**, 114 (1992).
19. S. Rönnebeck, S. Ottow, J. Carstensen and H. Föll, *Electrochem. Solid State Lett.* **2**, 126 (1999).
20. M. Rocchia, E. Garrone1, F. Geobaldo, L. Boarino and M.J. Sailor, *Phys. Stat. Sol.* (a) **197** (20), 365 (2003).
21. V. Lehmann, W. Hönlein, H. Reisinger, A. Spitzer, H. Wendt and J. Willer, *Solid State Technol.* **38**, 99 (1995).
22. V. Lehmann and U. Gruning, *Thin Solid Films*, **297**, 13 (1997).
23. E.A. Ponomarev and C. Levy-Clement, *Electrochem. Solid State Lett.* **1**, 1002 (1998).
24. R.B. Wehrspohn, J.-N. Chazalviel and F. Ozanam, *J. Electrochem. Soc.* **145**, 2958 (1998).
25. J.L. Gole, P. Lillehei, L. Seals, J.A. DeVincentis and S. Narasimba, *Phys. Rev. B* **61**, 7589 (2000).
26. J.L. Gole, L. Seals, J.A. DeVincentis, P. Lillehei, S.M. Prokes and D.A. Dixon, *Phys. Rev. B* **61**, 5625 (2000).
27. W.E. Carlos, S.M. Prokes, L. Seals and J.L. Gole, *Phys. Rev. B* **62**, 1878 (2000).
28. J.L. Gole, J.A. Devincentis and L. Seals, *J. Phys. Chem. B* **103**, 979 (1999).
29. See, for example, P.D.J. Calcott, K.J. Nash, L.T. Canham, M.J. Kane and D. Brumhead, *J. Phys. Condens. Matter.* **5**, L91 (1993).
30. P.D.J. Calcott, K.J. Nash, L.T. Canham, M.J. Kane and D. Brumhead, *J. Lumin.* **57**, 257 (1993).
31. K.J. Nash, P.D.J. Calcott, L.T. Canham and R.J. Needs, *Phys. Rev. B* **51**, 17698 (1995).
32. A.G. Cullis, L.T. Canham and P.D. Calcott, *J. Appl. Phys.* **82**, 909 (1997).
33. (a) S. Schuppler, S.L. Friedman, M.A. Marcus, D.L. Adler, Y.H. Xie, F.M. Ross, Y.J. Chabal, T.D. Harris, L.E. Brus, W.L. Brown, E.E. Chaban, P.J. Szajowski, S.B. Christman and P.H. Citrin, *Phys. Rev. B* **52**, 4910 (1995); (b) S. Schuppler, S.L. Friedman, M.A. Marcus, D.L. Adler, Y.H. Xie, F.M. Ross, T.D. Harris, W.L. Brown, L.E. Brus and P.H. Citrin, *Phys. Rev. Lett.* **72**, 2648 (1994).
34. Y.H. Xie, W.L. Wilson, F.M. Ross, J.A. Mucha, E.A. Fitzgerald, J.M. Macauley and T.D. Harris, *J. Appl. Phys.* **71**, 2403 (1992).
35. S. Prokes, O.J. Glembocki, V.M. Bermudez, R. Kaplan, L.E. Friedersdorf and P.C. Searson, *Phys. Rev. B* **45**, 13788 (1992).
36. S.M. Prokes, *J. Appl. Phys.* **73**, 407 (1993).
37. H.D. Fuchs, M. Rosenbauer, M.S. Brandt, S. Ernst, S. Finkbeiner, M. Stutzmann, K. Syassen, J. Weber, H.J. Queisser and M. Cardona, *Mat. Res. Soc. Proc.* **283**, 203 (1993).
38. M. Stutzmann, M.S. Brandt, M. Rosenbauer, H.D. Fuchs, S. Finkbeiner, J. Weber and P. Deak, *J. Lumin.* **57**, 321 (1993).
39. M.S. Brandt and M.S. Stutzmann, *Solid State Commun.* **93**, 473 (1995).
40. A.J. Steckl, J. Xu, H.C. Mogul and S.M. Prokes, *J. Electrochem. Soc.* **142**, L69 (1995).
41. S.M. Prokes and O.J. Glembocki, *Phys. Rev. B* **49**, 2238 (1994).
42. J.L. Gole, F.P. Dudel, D.R. Grantier and D.A. Dixon, *Phys. Rev. B* **56**, 2137 (1997).
43. J.L. Gole and D.A. Dixon, *Phys. Rev. B* **57**, 12002 (1998).
44. J.L. Gole and D.A. Dixon, *J. Phys. Chem. B* **109**, 14830 (2005).
45. J.L. Gole, E.C. Egeberg, E. Veje, A. Ferreira da Silva, I. Pepe and D.A. Dixon, *J. Phys. Chem B* **110**, 2064 (2005).
46. L.E. Brus, P.F. Szajowski, W.L. Wilson, T.D. Harris, S. Schuppler and P.H. Citrin, *J. Am. Chem. Soc.* **117**, 2915 (1995).
47. J.L. Gole and D.A. Dixon, *J. Phys. Chem.* **82**, 3125 (1997).

48. F.P. Romstad and E. Veje, *Phys. Rev. B* **55**, 5220 (1997).
49. O.K. Andersen and E. Veje, *Phys. Rev. B* **53**, 15 643 (1996).
50. J.L. Gole and F.P. Dudel, *J. Appl. Phys.* **82**, 402 (1997).
51. J.L. Gole, L. Seals and P. Lillehei, *J. Electrochemical Soc.* **147**, 3785 (2000).
52. L. Seals, L.A. Tse and P.J. Hesketh, *J. Appl. Phys.* **91**, 2519 (2002).
53. A. Foucaran, F. Pascalk-Delannoy, A. Giani, A. Sackda, P. Comette and A. Boyer, *Thin Solid Films* **297**, 317 (1997).
54. S. Lewis, J. DeBoer, J. Gole and P.J. Hesketh, *Sens. Actuator. B* **110**, 54 (2005).
55. P. Fürjes, A. Kovács, Cs. Dücső, M. Ádáma, B. Müller and U. Mescheder, *Sen. Actuators B* **95**, 140 (2003).
56. A. Foucaran, B. Sorli, M. Garcia, F. Pascal-Delannoy, A. Giani and A. Boyer, *Sensors Actuator A* **79**,189 (2000).
57. M. Björkqvist, J. Salonen and E. Laine, *Appl. Surf. Sci.* **222**, 269 (2004).
58. M. Björkqvist, J. Salonen, J. Paski and E. Laine, *Sens. Actuator. A* **112**, 244 (2004).
59. D.G. Yarkin, *Sens. Actuator. A* **107**, 1 (2003).
60. E.J. Connolly, P.J. French, H.T.M. Pham and P.M. Sarro, *Proceedings of IEEE Sensors* 2002, Part 1, Vol. **1**, p. 499.
61. M. Stewart and J. Buriak, *Adv. Mater.* **12**, 859 (2000).
62. J.H. Jin, N.K. Min, C.G. Kang, S.H. Park and S.I. Hong, *J. Korean Phys. Soc.* **39** (suppl. Pt. 1), S67 (2001).
63. S. Libertino and G. D'Arrigo, *Proceedings of the SPIE* **5119**, 149 (2003).
64. L. DeStefano, I. Rendina, L. Moretti, A. Lamberti, O. Longo and P. Arcari, *Proceedings of the SPIE* **5118**, 305 (2003).
65. M. Ben Ali, R. Mlika, H. Ben Ouada, R. M'ghaïeth and H. Maâref, *Sens. Actuator.* **74**, 123 (1999).
66. S. Zairi, C. Martelet, N. Jaffrezic-Renault, F. Vocanson, R. Lamartine, R.M'gaïeth, H. Maâref and M. Gamoudi, *Appl. Phys. A* **73**, 585 (2001).
67. S. Zairi, C. Martelet, N. Jaffrezic-Renault, R. M'gaïeth, H. Maâref and R. Lamartine, *Thin Solid Films* **383**, 325 (2001).
68. J.F. Hunt, E. Erwin, L. Palmer, J. Vaughan, N. Malhotra, T.A. Platts-Mills and B. Gaston, *Am. J. Respir. Crit. Care Med.* **165**, 101 (2002).
69. C.D.R. Dunn, M. Black, D.C. Cowell, C. Penault, N.M. Ratcliffe, R. Spence and C. Teare, *British J. of Biomedical Sci.* **58**, 66 (2001).
70. B. Fruhberger, N. Stirling, F.G. Grillo, S. Ma, D. Ruthven, R.J. Lad and B.G. Frederick, *Sens. Actuators B* **76**, 226 (2001).
71. C. DiNatale, G. Olafsdottir, S. Einarsson, E. Martinelli, R. Paolesse and A. D'Amico, *Sens. Actuators B* **77**, 572 (2001).
72. J. Hammond, B. Marquis, R. Michaels, B. Oickle, B. Segee, J. Vetelino, A. Bushway, M.E. Camire and K. Davis-Dentici, *Sens. Actuators B* **84**, 113 (2002).
73. J.E. Haugen, *Adv. Expt. Med. Biol.* **488**, 43 (2001).
74. R. Venterea and D. Rolston, *J. of Geophy. Res.* **105**, 15117 (2000).
75. Chemical Profile: Ammonia, Children's Health Environmental Coalition (2001) http://www.checnet.org/healthehouse/chemicals/
76. Toxicology Facts for Ammonia, Agency for Toxic Substances and Disease Control, September (2002) http://www.atsdr.cdc.gov/tfacts126.html
77. Occupational Health Guidelines for Chemical Hazards (1981-present): http://www.cdc.gov/niosh/81–123.html
78. Repairs and Passing, Georgia's Clean Air Force: Georgia Environmental Protection Division (2004): http://www.cleanairforce.com/passing2.htm.
79. Ward's Auto World, *Primedia Business Magazines* **35**, 21 (January 1999).
80. P. Andrian, *Sensor Business Digest* **11**, November 2002.
81. Fuel cell – Wikipedia, the free encyclopedia (2004): http://en.wikipedia.org/wiki/Fuel_cell
82. Correspondences between J.R. Wyatt, Office of Naval Research and J.L. Gole, Georgia Institute of Technology, School of Physics.
83. J.B. McCammon, W.D. Wagner, D. Groth, G. Hatfield and L. Reed, *Current Intelligence Bulletin 50: Carcinogenic Effects of Exposure to Diesel Exhaust*, (CDC Publication, August 1988) http://www.cdc.gov/.

84. C. Baratto, G. Faglia, E. Comini, G. Sberveglieri, A. Taroni, V. La Ferrara, L. Quercia and D. Di Francia, *Sens. Actuators B* **77**, 62 (2001).
85. S. Chakane, A. Gokarna and S.V. Bhoraskar, *Sens. Actuator B* **91**, 1 (2003).
86. R. Angelucci, A. Poggi, L. Boarino, L. Dori, G.C. Cardinali, A. Parisini, G. Pizzocchero, C. Critelli, F. Trifiro and F. Cavani, *Thin Solid Films*, **297**, 43 (1997); G. Benedetto, L. Boarino, N. Brunetto, A. Rossi, R. Spagnolo and G. Amato, *Phil. Mag.* **76**, 383 (1997).
87. R. Angelucci, A. Poggi, L. Dori, G.C. Cardinali, A. Parisini, A. Tagliani, M. Mariasaldi and F. Cavani, *Sens and Actuator A* **74**, 95 (1999).
88. R. Liu, T.A. Schmedake, Y.Y. Li, M.J. Sailor and Y. Fainman, *Sens. Actuator. B* **87**, 58 (2002).
89. L. Seals, L.A. Tse, P.J. Hesketh and J.L. Gole, *J. Appl. Phys.* **91**, 2519 (2002).
90. F. Dudel, D.R. Grantier, J.L. Gole and D.A. Dixon, *Phys. Rev. B* **56**, 2137 (1997).
91. J.L. Gole and D.A. Dixon, *J. Phys. Chem.* **101**, 8096 (1997).
92. J.L. Gole and D.A. Dixon, *J. Phys. Chem. B* **102**, 33 (1998).
93. J.L. Gole, J.A. Devincentis and L. Seals, *Phys. Rev. B* **61**, 5165 (2000).
94. I. Schechter, M. Ben-Chorin and A. Kux, *Anal. Chem.* **67**, 3727 (1995).
95. J.L. Gole, F.P. Dudel, L. Seals, M. Reiger, P. Kohl and L.A. Bottomley, *J. Electrochem. Soc.* **145**, 3284 (1998).
96. F.P. Dudel and J.L. Gole, *J. Appl. Phys.* **82**, 802 (1997).
97. K. Malek and M. Coppens, *J. Chem. Phys.* **119**, 5 (2003).
98. J.L. Gole and A.G. Fedorov, Work in progress.
99. J. DeBoer, S. Lewis, P.J. Hesketh and J.L. Gole, *205th ECS Spring Meeting*, San Antonio, TX, May 9–14, 2004 (accepted).
100. S. Lewis, J. DeBoer, J.L. Gole and P.J. Hesketh, accepted to 206th ECS Fall Meeting, Honolulu, HI, October 3–8, 2004.
101. J.L. Gole, L. Seals, L.A. Tse and P.J. Hesketh, *Proc. Electrochem. Soc.* **6**, 13 (2002).
102. J.L. Gole and M. White, *J. Catal.* **204**, 249 (2001).
103. J.L. Gole, B.D. Shinall, A.V. Iretskii, M.G. White, W.B. Carter and A.S. Erickson, *Chem. Phys. Chem.* **4**, 1016 (2003).
104. C. Burda, Y. Lou, X. Chen, A.C.S. Samia, J. Stout and J.L. Gole, *Nano Lett.* **3**, 1049 (2003).
105. J.L. Gole, J. Stout, C. Burda, Y. Lou and X. Chen, *J. Phys. Chem. B* **108**, 1230 (2004).
106. S.M. Prokes, W.E. Carlos, J.L. Gole, C. She and T. Lian, "Spatially resolved characterization of local phenomena in materials and nanostructures", *MRS Proceedings* **738**, 239 (2003).
107. D. Beydoun, R. Amal, G. Low and S. McEvoy, *J. Nanoparticle Res.* **1**, 439 (1999).
108. X. Chen, Y. Lou, A.C.S. Samia, C. Burda and J.L. Gole, *Adv. Func. Mater.* **15**, 41 (2005).
109. S. Kumar, J.L. Gole and A.G. Fedorov, "Photodegredation of Ethylene Using Visible-Light Responsive Surfaces Prepared from Titania Nanoparticle Slurries", Environmental Science and Technology. *J. Appl. Catal. B: Environmental* **57**, 93–107 (2005).
110. M. Winter, J.O. Besenhard, M.E. Spahr and P. Noval, *Adv. Mater.* **10**, 725 (1998).
111. B.A. Boukamp, G.C. Lesh and R.A. Huggins, *J. Electrochem. Soc.* **128**, 725 (1981).
112. A. Anani and R.A. Huggins, *J. Power Sources* **38**, 351 (1992).
113. C.J. Wen and R.A. Huggins, *J. Solid State Chem.* **37**, 271 (1981).
114. S.B. Ng, J.Y. Lee and Z.L. Liu, *J. Power Sources* **94**, 63 (2001).
115. H. Li, X. Huang, L. Chen, G. Zhou, Z. Zhang, D. Yu, Y.J. Mo and N. Pei, *Solid State Ionics* **135**, 181 (2000).
116. H. Li, X. Huang, L. Chen, Z. Wu and Y. Liang, Electrochem. *Solid State Lett.* **2**, 547 (1999).
117. S. Bourderau, T. Brousse and D.M. Schleich, *J. Power Sources* **81–82**, 233 (1999).
118. W.J. Weydanz and M. Wohlfahrt-Mehrens, *J. Power Sources* **81–82**, 237 (1999).
119. I.-S. Kim, P.N. Kumta and G.E. Blomgren, *Electrochem. Solid State Lett.* **3**, 493 (2000).
120. M. Green, E. Fielder, B. Scrosati, M. Wachtler and J.S. Moreno, *Electrochem. Solid State Lett.* **6**, A75 (2003).
121. Vyatkin, V. Starkov, V. Tzeitlin, H. Presting, J. Konle and U. König, J. *Electrochem. Soc.* **149**, G70 (2002).

CHAPTER FIVE

Silicon Nanowires and Nanowire Heterostructures

Zhaohui Zhong,[1] Chen Yang[1] and Charles M. Lieber[1,2]

Contents

5.1 Introduction 177
5.2 Silicon Nanowires 177
 5.2.1 Rational Synthesis and Structural Characterization of SiNW 177
 5.2.2 Electronic Properties of SiNWs 182
 5.2.3 SiNWs for Nanoelectronics 190
 5.2.4 Large-Scale Hierarchical Organization of SiNW Arrays 195
 5.2.5 SiNWs as Nanoscale Sensors 200
5.3 SiNW Heterostructures 204
 5.3.1 NiSi/SiNW Heterostructures 204
 5.3.2 Modulation Doped SiNWs 204
 5.3.3 Branched and Hyper-Branched SiNWs 209
5.4 Summary 213
References 214

Abstract

Silicon nanowires (SiNWs) and nanowire heterostructures are unique form of nanosilicon, which are grown by direct synthesis (bottom-up) rather than conventional lithography patterning (top-down) approach. Here we review key advances in SiNWs and SiNW heterostructures enabled by the bottom-up approach to nanoscience. First, we introduce a general method for the synthesis of SiNWs with precisely controlled physical dimensions and electronic properties, which is based on metal nanocluster catalysed vapour–liquid–solid growth. Second, we discuss fundamental low-temperature electrical transport studies that define key differences between our bottom-up SiNWs and top-down silicon nanostructures. Third, we describe the use of SiNWs as fundamental building blocks for a wide range of nanoscale electronic devices and circuits. Fourth, we describe rational strategies for large-scale hierarchical assembly of SiNWs and applications of unique assembly characteristics for macroelectronics. Fifth, we examine the potential of SiNWs as active elements in ultra-sensitive nanoscale sensors for chemical and biological detection. Last, we discuss SiNW heterostructures, which open up new and often unique dimensions of complexity and functionality.

[1] Department of Chemistry and Chemical Biology Harvard University, Cambridge, MA, USA.
[2] Division of Engineering and Applied Science, Harvard University, Cambridge, MA, USA.

Nanosilicon
9780080445281
Copyright © 2007. Elsevier Ltd.
All rights reserved.

5.1 Introduction

Reduction of the feature sizes in planar silicon devices has driven improvements in the performance and integration density for microelectronics over the past several decades [1,2]. In fact, microelectronics today could be called nanoelectronics since the critical dimensions of silicon devices have reached well below the 100 nm length scale. There are, however, two philosophically distinct approaches for creating nanoscale silicon structures and devices, which can be characterized as top-down and bottom-up. In the conventional top-down approach used by the microelectronics industry, silicon nanostructures are patterned in bulk materials by a combination of lithography, etching and deposition to form functional devices. While developments continue to push the resolution limits of the top-down approach, the improvements in resolution are associated with a near exponential increase in cost associated with each new generation of manufacturing facility. This economic constraint together with scientific and engineering issues faced by the top-down approach have motivated efforts worldwide to explore new strategies that could meet the demand for nanoscale structures today and in the future [2–4].

For example, nanosilicon can be produced directly and without lithography using the bottom-up approach, and then assembled into functional devices [5,6]. A key advantage of nanosilicon prepared by bottom-up approach is that critical nanoscale features are defined during synthesis, which eliminates some of the most challenging lithography-based fabrication steps, and moreover, can yield structures uniform at the atomic scale. Indeed, chemically synthesized SiNWs [7–10] and SiNW heterostructures [11–14] have shown exceptional properties, and demonstrated their potential as ideal building blocks for nanoscale electronic devices and circuits [4–16].

This chapter reviews recent research progress on SiNWs and SiNW heterostructures. The first part of the chapter will focus on the synthesis, properties and devices based on homogeneous SiNWs. We will first examine the synthesis and structural characterization of SiNWs, and then detailed electrical transport studies. Subsequently, we will review applications of SiNWs to a wide range of nanoscale electronic devices and circuits. Next, we will describe recent progress towards large-scale hierarchical assembly of SiNWs and electronics enabled by this bottom-up assembly approach. Last, SiNW nanoscale sensors for chemical and biological detection will be discussed. In the second part of the review, we will focus on the synthesis, characterization and device properties of several types of novel SiNW heterostructures, including NiSi/SiNW heterostructures, modulation doped SiNWs, and branched and hyper-branched SiNWs.

5.2 Silicon nanowires

5.2.1 Rational Synthesis and Structural Characterization of SiNW

The rational design and synthesis of SiNWs is critical to work directed towards understanding fundamental properties, creating nanostructured materials and developing nanotechnologies. To explore the diverse and exciting potential of one-dimensional (1D) SiNWs, it is essential to be able to control and systematically vary

their diameter, length and electronic properties. To meet these requirements we have focused our efforts on developing a general and predictive synthetic approach, much as molecular beam epitaxy has served as an all-purpose method for the growth of two-dimensional (2D) structures.

5.2.1.1 Overview of SiNW 1D Growth

In general, the preparation of nanowires requires that the addition of material during the growth process is constrained to occur along only one direction. In systems where atomic bonding is relatively isotropic, such as silicon, achieving 1D growth requires that the symmetry be broken during growth [17]. Over the past decade, considerable effort has been placed on the large-scale synthesis of nanowires, and several strategies have been developed to break the growth symmetry either "physically" or "chemically". One common scheme involves using a linear growth template to guide the material addition along only 1D [18–21]. This strategy has produced nanowires with diameters defined by the template, although the resulting materials are often polycrystalline and thus have significant limitations for high-performance electronics.

Another general strategy that has received increasing focus over the past several years involves exploiting a nanocluster "catalyst" to confine growth in 1D. The nanocluster or nanodroplet serves as the site that directs preferential addition of reactant to the end of a growing nanowire, much like a living polymerization catalyst directs the addition of monomers to a growing polymer chain. Several specific methods based on this underlying strategy have been developed for the synthesis of SiNWs, following the pioneering report of nanocluster catalysed nanowire growth [22]. These methods have used chemical vapour deposition (CVD) [23–25], laser ablation [7], physical evapouration [26] and supercritical fluids [27]. The most highly developed of these approaches is the CVD method, which enables ready and precise control of all key experimental properties, including the dopant incorporation [10]. For these reasons, we will focus our discussion on metal nanocluster catalysed CVD growth process.

Metal nanocluster catalysed CVD growth of SiNWs is accomplished by taking advantage of VLS growth mechanism [22,28,29], in which a liquid metal cluster acts as the energetically favoured site for vapour-phase reactant absorption and when supersaturated, the nucleation site for crystallization. An important feature of this approach for nanowire growth is that phase diagrams can be used to choose a catalyst material that forms a liquid alloy with the nanowire material of interest, i.e. silicon in this case [30]. Also, a range of potential growth temperatures can be defined from the phase diagram such that there is a coexistence of liquid alloy with solid nanowire phase. An example of Au nanocluster catalysed SiNW growth is illustrated in Fig. 5.1. The Au–Si binary phase diagram predicts that Au nanoclusters will form liquid alloy droplets with Si at temperatures higher than the eutectic point, 363°C. When the nanoclusters become supersaturated with silicon, a nucleation event occurs producing a solid/liquid Si/Au–Si alloy interface. In order to minimize the interfacial free energy, subsequent solid growth/crystallization occurs at this initial interface, which thus imposes the highly anisotropic growth constraint required for producing nanowires. Preferential 1D growth continues in the presence of reactant as long as the catalyst nanocluster remains in the liquid state.

A schematic illustrating key features of a CVD growth apparatus used for SiNW synthesis is shown in Fig. 5.2. Typically, growth substrates containing Au nanoclusters

Temperature (°C)
1600
1400
1200
1000
800
600
400
200
1404°
Au-Si (l)
1063°
Au-Si (l) + Si (s)
370°
31
0 10 20 30 40 50 60 70 80 90 100
Pure Au
Si content (atom%)
Pure Si
(a)

SiH_4
(b)
Au nanocluster
Nucleation
Silicon nanowire

Figure 5.1 Au nanocluster catalysed SiNW growth via VLS mechanism. (a) Binary phase diagram of Au–Si. (b) Nanocluster-mediated VLS nanowire growth process.

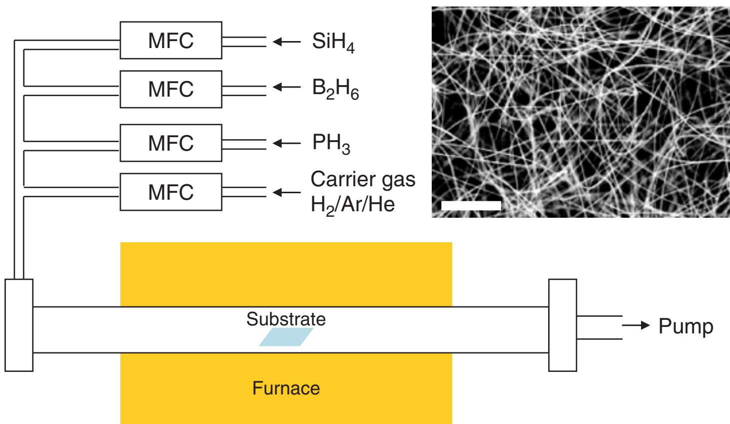

Figure 5.2 CVD reactor for SiNW growth. Inset, SEM image of SiNWs; scale bar, 10 μm.

are placed in a quartz reactor, and then SiNWs are grown at 435–460°C using silane as the silicon reactant, and diborane and phosphine as *p*- and *n*-type dopants, respectively [14,25,31]. The growth can be carried out using Ar, He or H_2 as the carrier gas, which enables an added level of control on the growth. For example, the use of H_2 as a carrier gas can passivate the growing solid surface and reduce the roughness [31], while Ar and He can enhance radial deposition of a specific composition shell. A representative growth substrate containing a large number of SiNWs is shown in Fig. 5.2, inset.

5.2.1.2 Structural Characterization of SiNWs

High-resolution transmission electron microscopy (HRTEM) has been used to define in detail the structures of these nanowires [25,31]. As synthesized SiNWs are single-crystalline nanostructures with uniform diameters. Studies of the ends of the nanowires show that they often terminate with gold nanoparticles (Fig. 5.3), thus providing strong evidence for proposed VLS growth mechanism [29]. In addition, the crystallographic growth directions of SiNWs have also been investigated using HRTEM, and systematic measurements reveal that the growth axes of SiNWs are related to their diameters

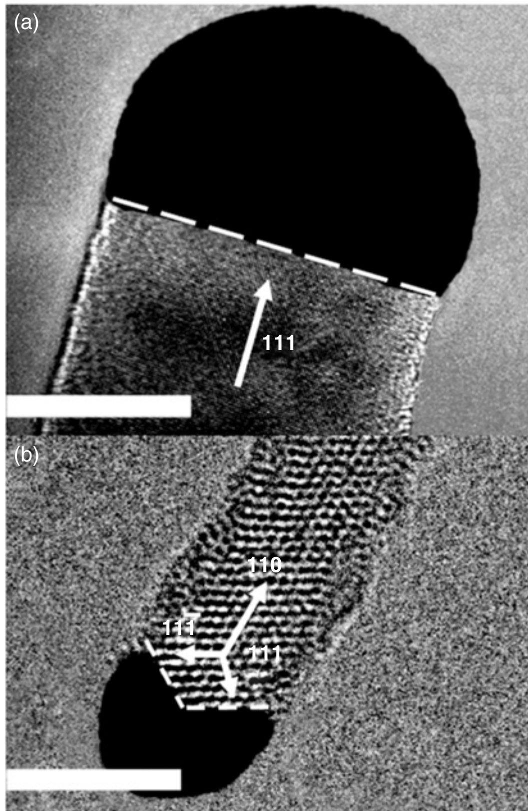

Figure 5.3 (a) HRTEM image of the gold catalyst/nanowire interface of a SiNW with a <111> growth axis. Scale bar, 20 nm. (b) HRTEM image of a gold catalyst/nanowire interface of a SiNW with a <110> growth axis. Scale bar, 5 nm (adapted from Ref. [31]).

[25,31]. For diameters between 3 and 10 nm, 95% of the SiNWs were found to grow along the <110> direction; for diameters between 10 and 20 nm, 61% of the SiNWs grow along the <112> direction; and for diameters between 20 and 30 nm, 64% of the SiNWs grow along the <111> direction. These results demonstrate a clear preference for growth along the <110> direction in the smallest SiNWs and along the <111> direction in larger SiNWs.

The observed preferences for growth directions can be understood in terms of the competition between the liquid catalyst alloy/solid SiNW interfacial energy and the SiNW surface energy. For large-diameter SiNWs, the growth axis is believed to be determined by the formation of a single lowest-free-energy solid–liquid interface, i.e. parallel to a single (111) plane [28]. In our studies, we observed that an increasing fraction of SiNWs grow along the <111> direction with increasing nanowire diameter, and that for SiNWs growing along the <111> direction there is a single catalyst–nanowire interface parallel to the (111) planes (Fig. 5.3a). For smaller-diameter SiNWs, the nanowire surface energy plays an increasingly important role in determining the growth direction. Indeed, consideration of the structure of a nanowire with a <110> growth axis suggests that it should be possible to terminate the solid/vacuum interfaces parallel to the axis with the lowest-free-energy (111) and (100) planes [32]. High-resolution imaging of the Au/SiNW interface in the smallest-diameter nanowires shows a well-defined V-shaped morphology (Fig. 5.3b). Crystallographic analysis shows that the interface consists of two {111} planes, whereby the <111> and <11-1> directions combine to yield a growth axis of <110> [31].

Cross-sectional HRTEM was used to further address these issues for molecular-scale SiNWs that grow along the <110> direction (Fig. 5.4) [31]. A cross-sectional

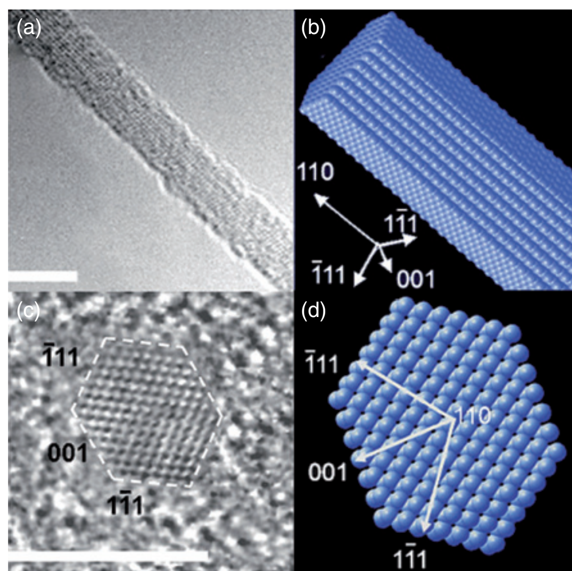

Figure 5.4 (a) TEM images of 3.8 nm diametre SiNWs with <110> growth axis, (c) HRTEM cross-sectional image, and equilibrium shapes for the (b) nanowire and the (d) nanowire cross sections predicted by Wulff construction. Scale bars, 5 nm (adapted from Ref. [31]).

image of a 3.8 nm SiNW with a <110> growth axis reveals that the nanowire has a hexagonal cross section with well-developed facets. An analysis of the lattice-resolved image shows that these facets correspond to the low-free-energy (111) and (100) family of planes, which is consistent with the equilibrium shape (Fig. 5.4d) predicted by a Wulff construction. The *d* spacings measured from the Fourier transform of the cross-sectional image, 3.103 Å for the (111) plane and 2.655 Å for the (200) plane, are within 2% of the expected values.

5.2.1.3 Rational Control of SiNW Diameters

The physical properties of nanowires can depend strongly on size due, for example, to quantum confinement. To explore size-dependent physical properties, requires the synthesis of SiNWs with well-defined and nearly monodisperse diameters. This goal can be conveniently achieved using the nanocluster catalysed growth mechanism by using metal nanoclusters with specific diameters to nucleate nanowire growth (Fig. 5.5a) [22,25]. Systematic characterization of the diameters of SiNWs grown from nanocluster catalysts with different diameters has been carried out by TEM [25], and histograms of the nanowire diameters obtained from different diameter nanoclusters are plotted in Figs. 5.5b–e. For SiNWs grown from 5 nm (4.9 ± 1.0 nm), 10 nm (9.7 ± 1.5 nm), 20 nm (19.8 ± 2.0 nm) and 30 nm (30.0 ± 3.0 nm) Au nanoclusters, the average nanowire diameters were 6.4 ± 1.2 nm, 12.3 ± 2.5 nm, 20 ± 2.3 nm and 31.1 ± 2.7 nm, respectively. Significantly, the dispersion of the SiNW diameters mirrors that of Au catalysts, suggesting that the dispersity of the SiNWs is limited only by the dispersity of diameters of Au nanocluster catalysts used to nucleate growth. The nanowire diameters were on average 1–2 nm larger than the starting nanocluster catalyst sizes. This observation is consistent with the formation of a Si/Au alloy prior to the nucleation and growth of the nanowire. In addition, post-growth oxidation of the SiNWs upon exposure to air could also increase the observed wire diameters. Overall, these results demonstrate size-controlled growth using our approach, and also show clearly the possibility of producing molecule-scale SiNWs with diameter as small as 3 nm [31].

Nanowires of well-defined length can also be prepared by controlling the growth time during synthesis, while the electronic properties of SiNWs can be precisely controlled by introducing dopant reactants during growth. Addition of different ratios of diborane or phosphine to silane reactant during growth produces *p*- or *n*-type SiNWs with effective doping concentrations directly related to the silane:dopant gas ratios [10,33,34]. The ability to prepare well-defined doped nanowire during synthesis distinguishes nanowires from other 1D nanostructures, such as carbon nanotubes, and endows nanowires with controllable electronic properties critical for assembly and fabrication of nanoelectronic devices discussed below.

5.2.2 Electronic Properties of SiNWs

Electrical transport measurements provide information about the electronic structure and behaviour of carriers in an electric field. We will describe transport studies carried out on SiNWs from 300 K to 1.5 K in this section.

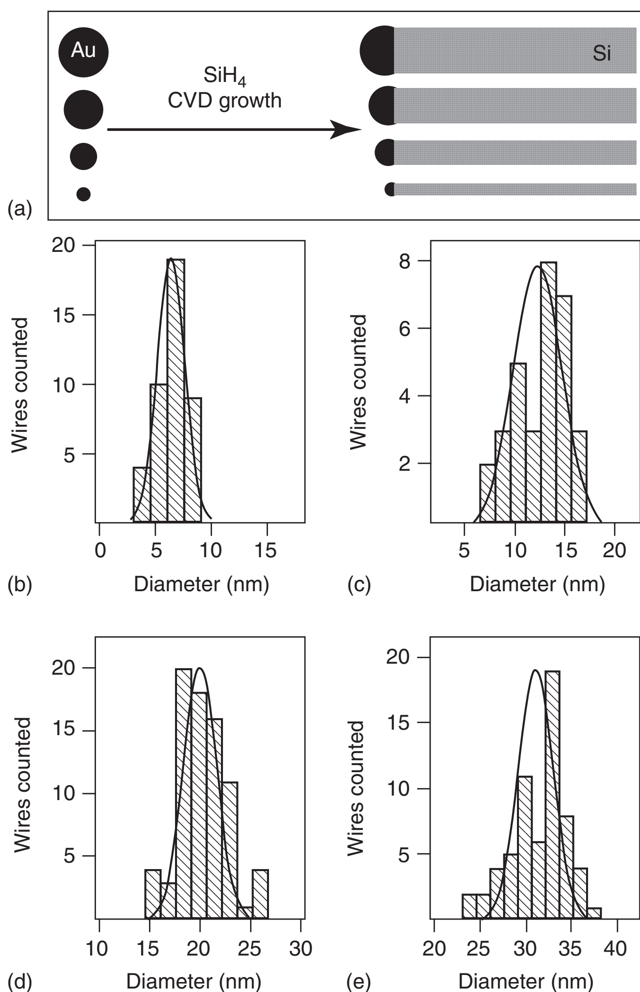

Figure 5.5 (a) Schematic illustration of size-controlled synthesis of SiNWs from Au nanoclusters. (b–e) Histograms of SiNW diameters grown from 5, 10, 20 and 30 nm diameter Au nanoclusters. The smooth curves are Gaussian fits of the distributions (adapted from Ref. [25]).

5.2.2.1 Room Temperature Electronic Properties of SiNWs

A flexible and powerful configuration for studying electrical transport is the SiNW field-effect transistor (FET) [8,10,35,36] as shown in Fig. 5.6. Individual SiNW FETs can be conveniently fabricated on oxidized silicon substrates where the underlying degeneratively doped silicon is used as a back-gate. Electrical contacts to individual SiNWs, which correspond to source and drain electrodes, are made using standard electron beam lithography methods, followed by metallization with Ti, Ni or Pd for *p*-type SiNWs and Ni for *n*-type SiNWs. Annealing is typically used to improve the contacts. We typically anneal contacts in forming gas (10% H_2 in He) at temperatures between 300 and 500°C. A schematic and scanning electron microscopy (SEM) image of a typical back-gated SiNW FET are shown in Fig. 5.6.

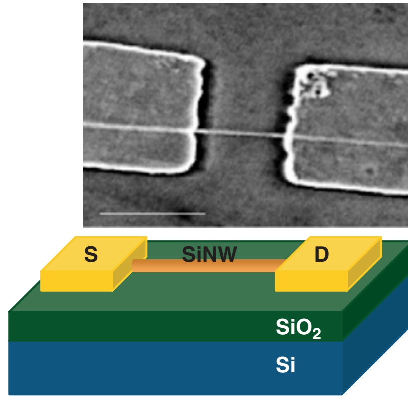

Figure 5.6 Schematic illustration and SEM image of a typical SiNW FET. Scale bar, 500 nm.

p-channel SiNW FETs Acceptor impurities can be introduced into SiNWs by adding diborane during synthesis [10]. Figure 5.7 shows electrical transport measurement data for ca. 20 nm diameter p-SiNW FETs prepared using a doping ratio of SiH_4:B_2H_6 of 4000:1 [35]. Two terminal source–drain current (I_{sd}) versus source–drain voltage (V_{sd}) curves are linear for small V_{sd} and saturate at larger negative voltages. Moreover, the conductance of the p-SiNW decreases with increasingly positive V_g (Fig. 5.7b), as expected for a p-channel metal–oxide–semiconductor FET (37). A linear plot of I_{sd} versus gate voltage (V_g) yields a peak transconductance, dI_{sd}/dV_g, of ca. 1250 nA/V, and a logarithmic plot demonstrates an on/off current ratio and a subthreshold slope of ca. 7×10^6 and 160 mV/decade, respectively. Moreover, studies of a large number of devices show that these results are reproducible. I_{sd} versus V_g plots for nine devices (Fig. 5.7c) all exhibit on/off current ratios greater than 10^6 and subthreshold slopes below 250 mV/decade, where the highest on/off ratio is 10^7 and the lowest subthreshold slope is 140 mV/decade. A histogram of the observed peak transconductance values for these and many other devices (Fig. 5.7c inset) shows a most probable value close to 1000 nA/V and a maximum value of 4300 nA/V.

The hole concentration in p-channel SiNW FETs has been estimated using the results from gate-dependent measurements. Specifically, the total nanowire charge can be expressed as $Q = C_g V_{th}$, where C_g is the nanowire gate capacitance and V_{th} the threshold gate voltage required to deplete completely the nanowire. The gate capacitance is estimated by $C = 2\pi\varepsilon\varepsilon_o L/ln(2h/r)$, where ε is the effective gate oxide dielectric constant, h is the thickness of the SiO_2 layer on the substrate, L is the nanowire length between the two electrodes and r is the nanowire radius [10,38]. The hole density, $n_h = Q/(e \cdot \pi r^2 L)$, is estimated to be $\sim 10^{18}\,cm^{-3}$ for the devices shown in Fig. 5.7. In addition, it is possible to estimate the carrier mobility of the SiNW FETs from the transconductance $dI/dV_g = \mu(C/L^2)V_{sd}$, where μ is the carrier mobility [37]. The peak transconductance value obtained in Fig. 5.7 corresponds to a calculated hole mobility of 307 $cm^2/V\,s$, around 10 times higher than the planar silicon value with similar dopant concentration [39].

In Table 5.1, key device parameters of SiNW FETs are compared with 50 nm gate length silicon FETs fabricated using silicon on insulator (SOI) substrates [40]

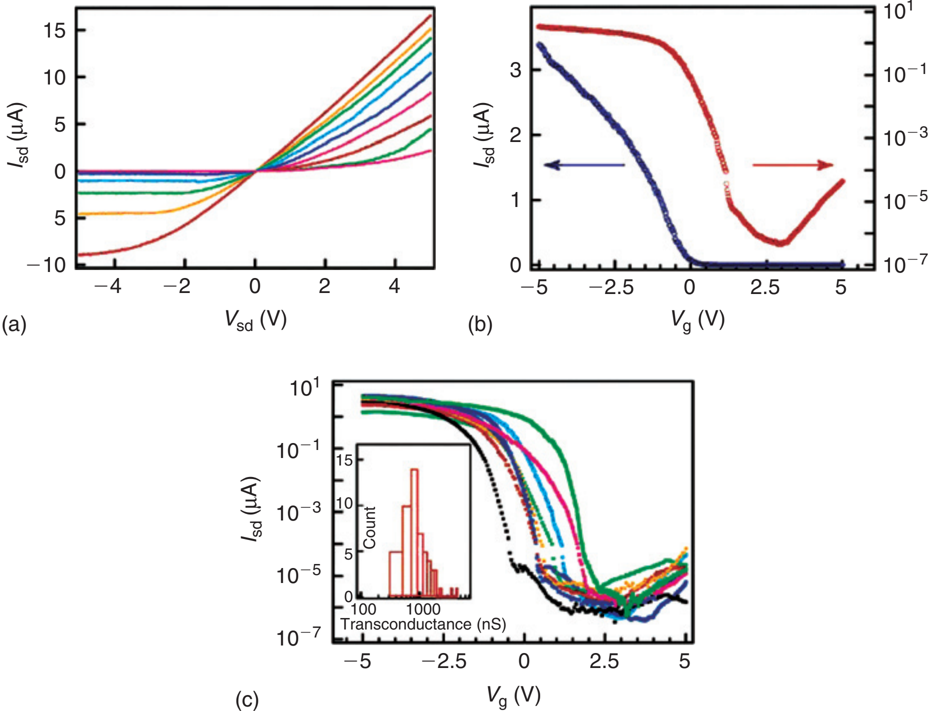

Figure 5.7 (a) I_{sd}–V_{sd} plots at different gate voltages for a typical p-SiNW FET. The red, orange, green, cyan, blue, magenta, red, green and magenta curves correspond to V_g values of −5, −4, −3, −2, −1, 0, 1, 2 and 3 V, respectively. (b) I_{sd}–V_g recorded for a typical device plotted on linear (blue) and log (red) scales at a V_{sd} of 1 V. (c) I_{sd}–V_g plots at a V_{sd} of 1 V for a sampling of devices. Inset: Histogram of the transconductance values observed for a sampling of devices (adapted from Ref. [35]).

and state-of-art carbon nanotube FETs [41]. For direct comparison, the transconductance of the SiNW FETs is scaled to 50 nm gate length. Notably, even with the much thicker gate oxide, SiNW FETs are better than the planar silicon FETs, and comparable with carbon nanotube FETs. Having both high transconductance and low off-state current makes SiNW FETs promising candidate as building blocks for future nanoscale electronics.

n-Channel SiNW FETs Phosphorous n-type dopant has been introduced into SiNWs by adding phosphine reactant during nanowire synthesis [34]. Figure 5.8 shows the typical electrical transport measurement results for n-SiNW FETs with doping ratio of SiH_4:PH_3 = 4000:1. Two terminal $I_{sd} - V_{sd}$ curves recorded with $V_g = -5$ to 5 V are linear for small V_{sd}, exhibit saturation at $V_{sd} \sim 2$ V, and show increase (decrease) in conductance as V_g becomes more positive (negative) as expected for n-channel FETs. A linear plot of $I_{sd} - V_g$ yields a peak transconductance of 350 nS, and a logarithmic plot demonstrates an on/off current ratio greater than 10^4 and a subthreshold slope of 300 mV/decade. Statistical studies on more than 50 devices yields an average transconductance value of 400 ± 100 nS, corresponding to a raw

Table 5.1 Comparison of the key device parameters between SiNW FETs [35], SOI silicon FETs (adapted from Ref. [40]) and carbon nanotube (CNT) FETs (adapted from Ref. [41]). Transconductance of SiNW FETs in parenthesis is scaled to 50 nm gate length for comparison.

	p-SiNW FET	*p*-type CNT-FET	Planar Si devices
Gate length (nm)	3000	50	50
Gate oxide thickness (nm)	60 (ZrO_2)	8 (HfO_2)	1.5 (SiO_2)
I_{ON} (μA/μm) (V_{sd} = 1V)	200	14,705	650
I_{OFF} (nA/μm)	~0.1	~5000	9
Subthreshold slope (mV/dec)	140	110	70
Transconductance (μS/μm)	215 (12,900)	17,647	650

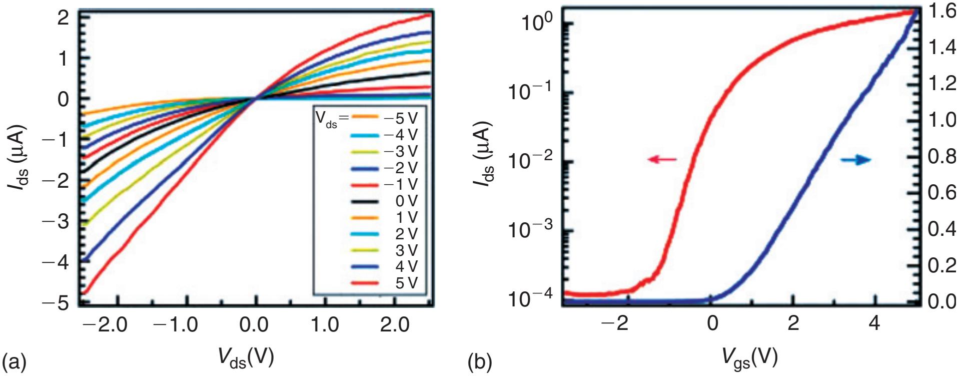

Figure 5.8 Electrical transport behaviour of an n-SiNW FETs. (a) I_{ds}–V_{ds} curves recorded for V_{gs} = −5–5 V. (b) I_{ds}–V_{gs} curves recorded at V_{ds} = 1 V. (adapted from Ref. [34]).

mobility value of 50 cm^2/V s. However, after subtracting the contact series resistance using four-probe transport measurement [42], the intrinsic electron mobility of n-SiNWs is found to be ~260 cm^2/V s, comparable with the value of planar silicon FETs with a similar doping level [43].

5.2.2.2 Fundamental Transport Studies of SiNWs

SiNWs have demonstrated potential as building blocks for nanoscale electronics: key device parameters of SiNW FETs can exceed planar silicon FETs, and the hole mobility for p-SiNW is approximately one order of magnitude higher than planar silicon at comparable doping levels [8,12,35]. Studies elucidating the fundamental transport properties of chemically synthesized SiNWs are essential for understanding these differences, and moreover, for moving beyond FETs to, for example, quantum electronic devices. In this section, we address the fundamental transport

properties through low-temperature measurements on molecular-scale SiNWs configured as single-electron transistors (SETs).

SiNW SET Single-crystalline p-type SiNWs with diameters of 3–6 nm were configured as back-gated transistors on silicon substrates with 50 nm thick oxide [9]. Current (I) versus gate voltage (V_g) data recorded with a 0.5 mV source–drain bias (V_{sd}) at 4.2 K from a device with source–drain separation of 400 nm exhibit regular oscillations in I over a broad range of V_g as shown in Fig. 5.9a. The current peaks are separated by regions of zero conductance with an average peak-to-peak separation of 0.015 ± 0.001 V. The heights of the observed peaks vary with V_g, although this variation has no obvious periodicity, whereas the positions and heights of the peaks are very reproducible on repeated V_g scans in this and similar devices. These observations indicate that the results are intrinsic to transport through the SiNWs, and moreover, are consistent with Coulomb blockade (CB) phenomena resulting from single charge tunnelling through a single quantum structure (e.g. the SiNW) with discrete energy levels [44,45].

To define better the length scale of the SiNW structure responsible for the CB oscillations, differential conductance ($\partial I/\partial V_{sd}$) versus V_{sd} and V_g was measured for the same device. The data shown in Fig. 5.9b exhibit 33 CB diamonds, where transport is "blocked" for values of $V_{sd} - V_g$ in the light-coloured regions. The regular closed diamond structure provides strong evidence for transport through a single quantum structure and not multiple quantum dots (QDs) connected in series, which would exhibit a more complex overlapping diamond structure [45]. Analysis of these

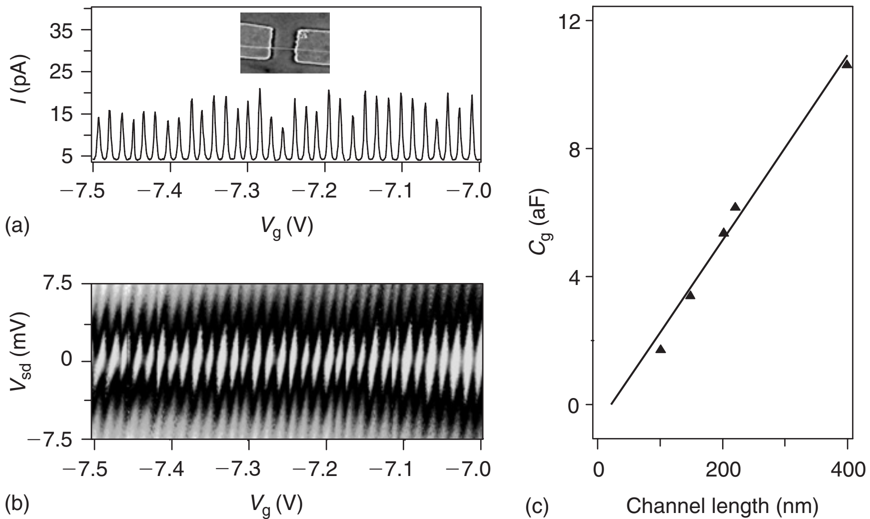

Figure 5.9 (a) CB oscillations observed at 4.2 K with $V_{sd} = 0.5$ mV. Inset: SEM image of the device. Scale bar, 500 nm. (b) Greyscale plot of $\partial I/\partial V_{sd}$ versus V_{sd} and V_g recorded at 4.2 K; the light (dark) regions correspond to low (high) values of $\partial I/\partial V_{sd}$; the dark colour corresponds to 3000 nS. (c) Gate capacitance versus source–drain separation (channel length) for five representative devices showing single-island CB behaviour. The line corresponds to a fit to the data with a slope of 28 ± 2 aF/μm (adapted from Ref. [9]).

results yields values for the gate capacitance, $C_g = e/\Delta V_g$, and gate coupling factor, $\alpha = C_g/C$, where C is the total capacitance, of 10.7 aF and 0.33, respectively.

Data exhibiting closed diamonds consistent with transport through single QDs were obtained on small-diameter SiNW devices with source–drain separations ranging from ca. 100–400 nm [9]. Importantly, these data show that C_g scales linearly with source–drain separation (Fig. 5.9c), and moreover, the average value of C_g determined from the data, 28 ± 2 aF/µm, agrees well with that calculated for a cylinder on plane model [38]. These results suggest that the relevant dot size is defined by source–drain electrodes, since a QD size scale set by structural variations or dopant fluctuations would give a smaller capacitance value, and be independent of the source–drain separation. The gate capacitance does deviate from the estimated value when the channel length is <100 nm, due to screening from the source/drain electrodes when the channel length becomes comparable to the thickness of the gate dielectric.

Coherent Single Charge Transport in SiNW Transistors The variations in the current peak height versus V_g in Fig. 5.9a suggest the formation of coherent energy states in the SiNW devices with energy level spacing, ΔE, larger than the thermal energy $k_B T$, where peak heights are determined by the coupling of the individual quantum states to the metal contacts at the Fermi level [44]. More clear data obtained at higher resolution for a 3 nm diameter SiNW device with a 100 nm source–drain separation are shown in Fig. 5.10a [9]. The data exhibit well-defined peaks in $\partial I/\partial V_{sd}$ that appear as lines running parallel to the edges of the CB diamonds, and consistent with discrete single particle quantum levels extending across the SiNW. Analysis of the data yields ΔE values for the first six levels spacings of 2.5, 1.9, 3.0, 2.0, 2.0 and 2.9 meV. These can be compared to ΔE estimated using a 1D hard wall potential: $\Delta E = (N/2)\hbar^2\pi^2/m^\star L^2$, where N is the number of holes, $m^\star$ is the silicon effective hole mass and L is the device length. ΔE estimated with this model ($N \approx 25$, $m^\star = 0.39\, m_e$ [46], $L = 100$ nm), 2.5 meV, agrees well with the observed values.

Temperature-dependent I–V_g measurements of the conductance peaks (Fig. 5.10b) show that peak current decreases rapidly as the temperature is increased from 1.5 to 10 K and is approximately constant above 30 K, consistent with coherent tunnelling through a discrete SiNW quantum level that is resonant with the Fermi level of the metal contacts [44,45]. Moreover, the temperature at which the peak height becomes constant, 30 K, yields an estimate of $\Delta E \approx 3$ meV that agrees with the value determined from the data and 1D model (see above). In addition, the temperature dependence of the conductance peak width (W) is related to the gate coupling factor, α, as $\alpha W = 3.52\, k_B T/e$ in the quantum regime, $k_B T < \Delta E$, and as $\alpha W = 4.35\, k_B T/e$ in the classical regime, $\Delta E < k_B T < U$, where U is the charging energy [44]. Notably, the value of α determined from the temperature-dependent data, 0.26, is consistent with that (0.26) obtained directly from Fig. 5.10a.

Coherent transport through a single island over length scales of several hundred nanometres indicates that these synthesized SiNWs are clean systems with little structural or dopant variation. Indeed, HRTEM shows that the SiNWs have a roughness of only ca. 1–2 atomic layers on 100 nm scale, which is much less than that produced during the lithography-based processing used to define the widths of planar nanowires. We also speculate that dopant introduced during nanowire growth may be driven to

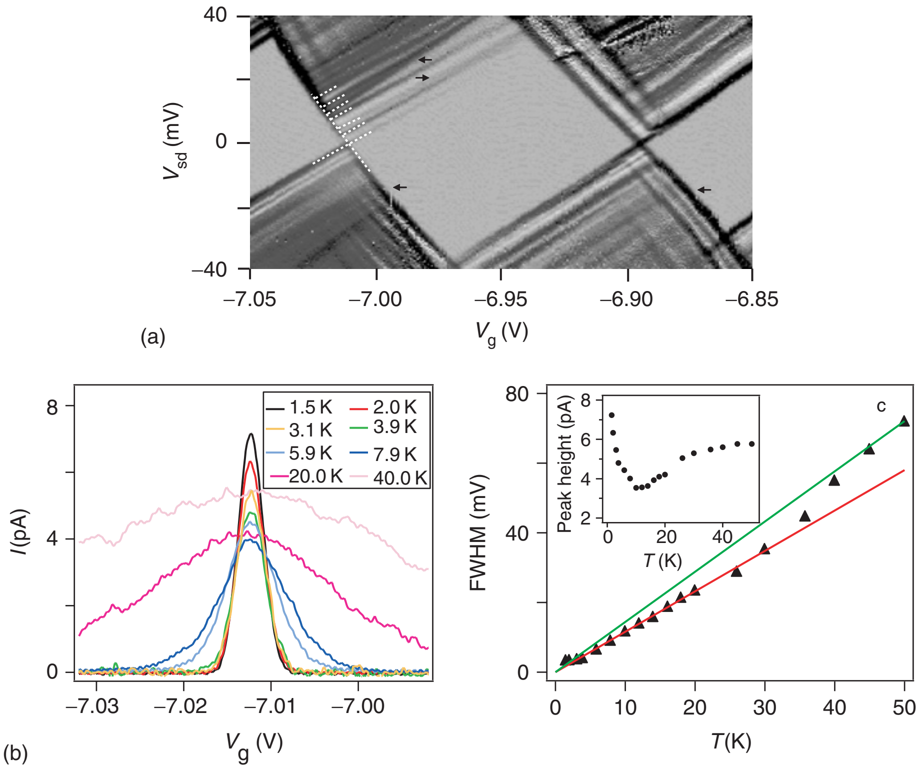

Figure 5.10 (a) $\partial I/\partial V_{sd}$–$V_{sd}$–$V_g$ data recorded at 1.5 K. (b) Temperature-dependant I–V_g curves recorded with $V_{sd} = 50\,\mu V$ at increasing temperature. (c) Conductance peak widths in (b) determined from the full width at half maximum of the peak height, versus temperature. Solid lines correspond to theoretical predictions for peak widths versus temperature in quantum regime ($\Delta E > k_B T$), $\alpha W = 3.52ek_B T$ (red), and classical regime ($\Delta E < k_B T$), $\alpha W = 4.35ek_B T$ (green) with $\alpha = 0.26$. Inset: Temperature dependence of the conductance peak height (adapted from Ref. [9]).

the surface of these molecular scale SiNWs as reported for semiconductor nanocrystals [47]. In contrast, low-temperature studies of nanowires with widths as small as ca. 10 nm fabricated by lithography on doped SOI substrates have been interpreted in terms of serially connected QDs arising from variations in the potential due to structural and/or dopant fluctuations that are intrinsic to these fabricated structures [48,49]. The length scale of the electronically distinct regions in these fabricated nanowires is on the order of 10 nm, and thus more than an order of magnitude smaller than chemically synthesized SiNWs.

Ground-State Spin Configuration of SiNW SETs Clean 1D systems represent unique platforms to study interactions in low-dimension systems. For example, the ground state (GS) of QDs defined in carbon nanotubes [50] was found to have the lowest possible spin, while recent studies on QDs defined in a 2D electron gas showed that higher-spin GS might also be possible [51]. The GS spin states of the SiNW SET devices were studied with the magnetic field parallel to the nanowire axis to minimize

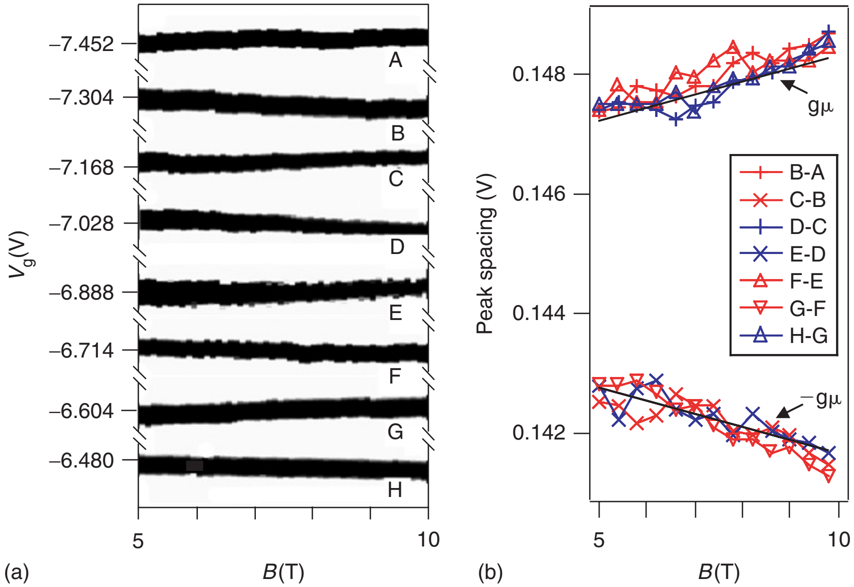

Figure 5.11 (a) Greyscale plot of the I as a function of V_g and parallel magnetic field B at 1.5 K. (b) Peak spacings from (a), offset to align into two branches. Solid black lines indicate expected B-dependence for spin transition from 1/2 to −1/2 (upward), and from −1/2 to 1/2 (downward) (adapted from Ref. [9]).

orbital effects [9]. Fig. 5.11a shows the greyscale plot of I as a function of V_g and magnetic field B taken from the same device as in Fig. 5.10. A small bias voltage (0.1 mV) was used so that only the GS contribute to transport. According to the constant interaction model, the GS spin in strictly 1D systems should alternate between $S = 0$ and $S = 1/2$. As a result, the addition energy as measured by the CB peak position will exhibit opposite slopes for adjacent peaks as governed by the Zeeman term, $-g\mu_B B\Delta S_Z$, with ΔS_Z alternating between 1/2 and −1/2 for adjacent charge states. Indeed, data taken from 8 consecutive charge states appear as 4 down-up pairs, as shown in Fig. 5.11a. The slope of the peak positions as a function of magnetic field is consistent with the Zeeman term, giving an average g value of 2.0 ± 0.2, which agrees with the bulk Si value [52]. Furthermore, peak spacings extracted from the data in Fig. 5.11a are clearly divided into two branches (Fig. 5.11b): an upward branch with slope of $g\mu$ corresponding to transition from spin 1/2–−1/2 states, and a downward branch with slope of $-g\mu$ corresponding to transition from spin −1/2–1/2 states. Furthermore, the simple GS spin configuration also suggests degeneracy between heavy and light holes is lifted, due to both strain and confinement effects.

5.2.3 SiNWs for Nanoelectronics

In the above sections, we have examined the controlled synthesis and properties of SiNWs, and have seen that this form of nanoscale silicon exhibits electrical properties that can exceed the performance of top-down fabricated silicon nanostructures at both room temperature and low temperature. In this section, we will extend this

fundamental understanding of growth and properties to a review of proof-of-concept nanoscale devices based on these SiNW building blocks.

5.2.3.1 Crossed Nanowire Structures and Devices

The crossed nanowire (cNW) architecture is a powerful strategy for both creation and integration of nanodevices [5,53–55]. Nanowires within a crossed array serve a dual purpose, i.e. they can function as both active devices and interconnects to the devices. Importantly, all key nanoscale metrics are defined during synthesis and subsequent assembly, and thus it is a true bottom-up approach. In addition, the cNW architecture provides natural scaling without additional complexity, as well as the potential for integration at the highest densities since the active device size is roughly the nanowire junction size.

Diodes and transistors, two important elements for logic, can be fabricated based on cNW structures. An example of a crossed SiNW p–n junction assembled from 20 nm diameter p- and n-type SiNWs is shown in Fig. 5.12a and b [33]. Current versus voltage (*I–V*) data recorded on the individual *p*- and *n*-type SiNWs are linear and indicate that metal–SiNW contacts are ohmic, and thus will not make a significant contribution to the nonlinear *I–V* behaviour of the junctions. Significantly, *I–V* measurements made on the p–n junction formed at the nanowire–nanowire cross show current rectification, exhibiting similar behaviour to bulk semiconductor p–n junctions. Examples of crossed SiNW FETs are also showed in Fig. 5.12c and d [55]. In this case, a SiO_2 shell, which can be prepared by deposition immediately following nanowire growth or by thermal oxidation, serves as an integral gate dielectric with controlled thickness [56]. Representative electrical transport data recorded on a single cNW–FET demonstrates excellent gate response. For depletion mode devices made in this way, the threshold voltage is also very reproducible with value of 5.4 ± 0.8 V.

5.2.3.2 Crossed Nanowire-Based Logic Gates

Complementary *p*- and *n*-type nanowires can be assembled into different crossed nanowire arrays, with each individual junction functionalized into a diode or transistor, working as logic gates. An example of a logic NOR gate assembled by using a 1(p-Si) by 3(n-GaN) cNW–FET array is shown in Fig. 5.13 [53]. The NOR gate is configured with 2.5 V applied to one cNW–FET to create a constant resistance of ~100 MΩ, and the p-SiNW channel is biased at 5 V. The two remaining n-GaN nanowire inputs act as gates for two cNW–FETs in series. In this way, the output depends on the resistance ratio of the two cNW–FETs and the constant resistor. The logic 0 is observed when either one or both of the inputs is high (Fig. 5.13a). In this case, the transistors are off and have resistances much higher than that of the constant resistor, and thus most of the voltage drops occurs across the transistors. A logic 1 state can only be achieved when both of the transistors are on, i.e. when both inputs are low. Analysis of V_o–V_i curve (Fig. 5.13b, inset) from this device and data from other similar structures demonstrate that these two-input NOR gates routinely exhibit gains in excess of five. High gain is a critical characteristic because it enables interconnection of arrays of logic gates without signal restoration at each stage. The truth table for this nanowire device (Fig. 5.13c) summarizes the V_o–V_i response and demonstrates that the device behaves as logic NOR gate. This multiple-input logic NOR gates can also function as NOT gates (simple inverters) by eliminating one of the inputs.

Figure 5.12 (a) Schematic and SEM image of a crossed SiNW p–n junction. Scale bar, 2 µm. (b) I–V behaviour of p–n, p–p and n–n junctions, respectively. I–V behaviour of individual p- and n-type SiNWs, and junctions are shown; the current values are multiplied by 10. The solid line corresponds to voltage drop measured between leads 3 and 4, and the dashed line to voltage between 3 and 2. (c) Schematic and SEM image of a crossed SiNW FET device. Scale bar, 1 µm. (d) Conductance versus gate voltage of a single cNW–FET. Inset: Histogram of the threshold voltages for 30 cNW–FETs (adapted from Refs. [33,55]).

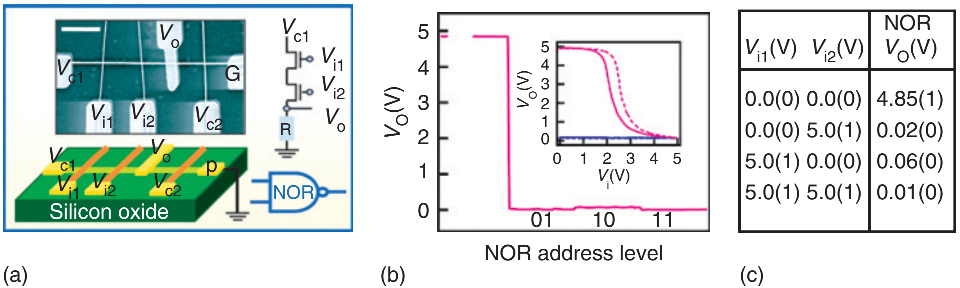

V_{i1}(V)	V_{i2}(V)	NOR V_O(V)
0.0(0)	0.0(0)	4.85(1)
0.0(0)	5.0(1)	0.02(0)
5.0(1)	0.0(0)	0.06(0)
5.0(1)	5.0(1)	0.01(0)

Figure 5.13 cNW Logic NOR gate. (a) Schematic of logic NOR gate constructed from a 1 by 3 cNW junction array. Insets: SEM image and symbolic electronic circuit. Scale bar, 1 µm. (b) Output voltage versus the four possible logic address level inputs. Inset: The V_o–V_i relation, where the solid and dashed A (B) lines correspond to V_o–V_{i1} and V_o–V_{i2} when the other input is 0 (1). The slope of the data shows that device voltage gain is larger than 5. (c) The measured truth table for the NOR gate (adapted from Ref. [53]).

5.2.3.3 Nanowire Crossbar Arrays as Address Decoders

The development of strategies for addressing arrays of nanoscale devices is central to implementing integrated nanosystems ranging from biological sensor arrays to nanocomputers. This quest can be approached based upon a scalable cNW–FET architecture in which molecular level modification of specific cross points within arrays is used to define an address code that enables nanowire input lines to turn on and off specific output lines [55]. This array structure functions as an address decoder with signal restoration at the nanoscale due to the inherent gain of the cNW–FET elements.

The underlying issue for addressing can be understood by considering a regular cNW–FET array (Fig. 5.14a) consisting of n-input ($I_1, I_2 \ldots I_n$) and m-output ($O_1, O_2 \ldots O_m$) nanowires where outputs are the active channels of FETs and the inputs function as gate electrodes that turn these output lines on and off [53,55]. When a voltage is applied to I_n in a regular array, it will affect each of the output nanowires in the same way, which precludes selective addressing of elements. This critical limitation can be overcome by differentiating cross points such that inputs affect only specific output cross points in the array. In the simplest scenario where one output nanowire is turned on/off by a single input, differentiation of diagonal elements of a square array (Fig. 5.14a) produces a code where $I_1, I_2 \ldots I_n$ address $O_1, O_2 \ldots O_n$, respectively. This idea can be generalized to enable a small number of input nanowires address a larger number of outputs if two or more inputs are used to turn on/off a given output [57],

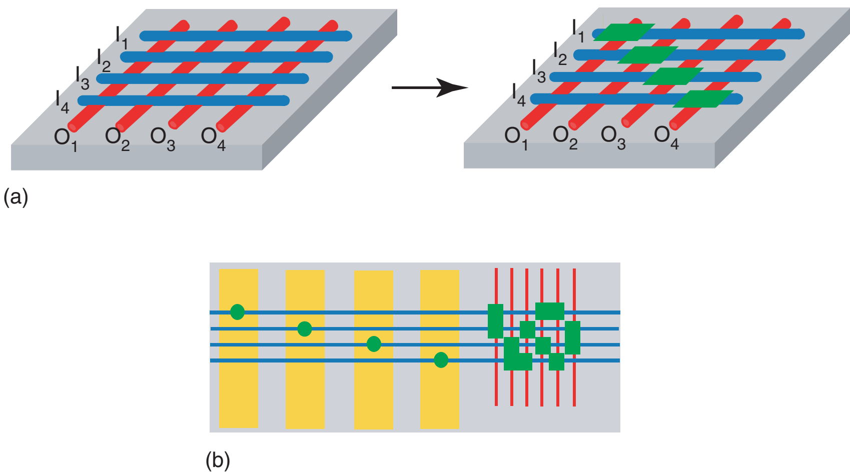

Figure 5.14 cNW array-based address decoders. (a) 4 × 4 cNW–FET array with four horizontal nanowires (I_1–I_4) as inputs and four vertical nanowires (O_1–O_4) as signal outputs. (Right) The four diagonal cross points in the 4 × 4 cNW–FET array were modified chemically (green rectangle) to differentiate their response to the input gate lines. (b) Bridging between mircoscale metal wires (yellow) and denser nanowires is achieved with a 2-hot code (green rectangles) whereby two inputs (blue nanowires) are required to address each output (red nanowires). The input nanowires can be turned on/off by specific microscale wires using a simple 1-hot code (adapted from Ref. [55]).

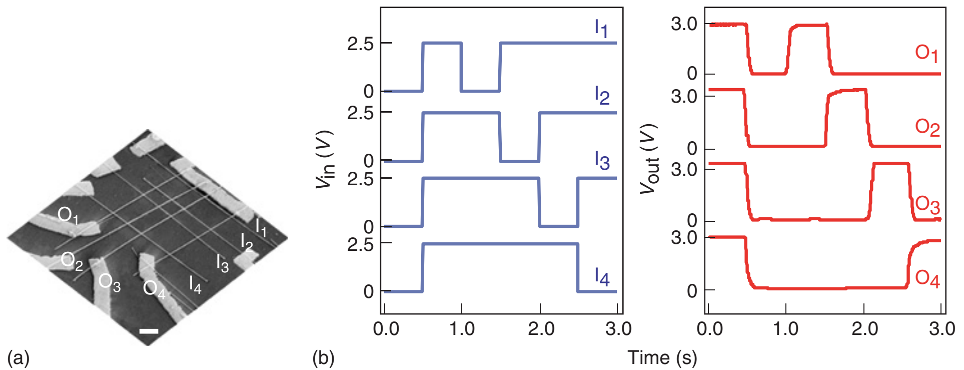

Figure 5.15 cNW FET decoders. (a) SEM image of a 4 × 4 cNW–FET decoder. The four diagonal cross points were chemically modified. Scale bar, 1 μm. (b) Real time monitoring of the gate voltage inputs (I_1, I_2, I_3, I_4) and signal outputs (O_1, O_2, O_3, O_4) for the 4 × 4 decoder (adapted from Ref. [55]).

or importantly, a small number of lithographically defined wires to address a much denser array of nanowires (Fig. 5.14b) as required to bridge between micro- and nanoscale features.

Surface modification at nanowire cross junctions with an aqueous or ethanol solution of tetraethylammonium chloride produces substantial and reproducible shifts in threshold voltage of cNW–FETs [8,55]. Thus it can be used to differentiate specific cNW–FET elements in an array to produce an address decoder circuit. A proof-of-principle demonstration based on a 4 × 4 cNW–FET array is shown in Fig. 5.15 [55]. All 16 cNW–FET elements remain on for gate voltages/input voltage >3 V prior to surface modification. Following specific modification of the four diagonal I_n/O_n elements, these four FETs can be selectively turned off by their respective inputs. Hence, by varying the nanowire input voltages (Fig. 5.15b) it is possible to address selectively each of the four output lines as required for multiplexing/demultiplexing signals. For example, when I_2, I_3 and I_4 were set to 2.5 V and I_1 was set to 0 V, only O_1 was active with an output of around 3 V and O_2, O_3, O_4 were off with an output of 0 V. Importantly, these nanowire FETs array-based decoders exhibit a large signal gain of more than one, which is distinct from results obtained with molecular diode switches [58,59], and suggest that it will be possible to achieve signal restoration with cNW–FET decoder at the nanoscale and not require external transistor devices for signal amplification.

5.2.3.4 SiNW Electronics on Non-conventional Substrates

The bottom-up approach separates high-temperature synthesis of single-crystal nanowires from ambient-temperature solution-based assembly, and thus enables the fabrication of single-crystal-like devices on virtually any substrate. The merging of nanoscale building blocks with flexible and/or low-cost substrates enables the development of high-performance electronic and photonic devices with the potential to impact a broad spectrum of applications [60,61]. There are three key features of this approach. First, the synthesis of nanowire building blocks is carried out under conditions optimized to yield high-quality single-crystal materials; there is no need to be

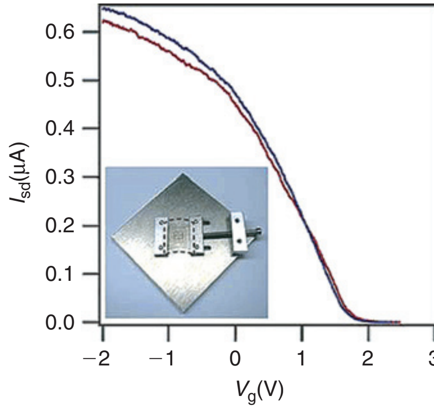

Figure 5.16 Effect of substrate bending on SiNW/plastic device performance. I_{sd} versus V_g for a nanowire transistor device measured when the substrate was flat (curve 1) and bent to a radius of curvature of 0.3 cm (curve 2). Inset: Photograph of the device used for bending the flexible plastic chip and securing it during measurement. The chip is highlighted with a black dashed line (adapted from Ref. [61]).

concerned with thermal and other substrate limitations, in contrast to direct thin-film deposition. Second, the nanowires can be readily isolated as stable solution suspensions that are then used for the deposition and patterning of devices. The use of nanowire suspensions has the same processing advantages as the use of organic semiconductors [62,63] and also enables us, via the sequential transfer of distinct nanowires, to introduce very different types of functions on the same substrate. Third, high aspect ratio nanowires can be interconnected without the need for advanced lithography, i.e. this approach takes advantage of the unique properties and processing of these nanoscale materials but does not require us to make ultra-small devices to achieve high performance.

A typical SiNW device fabricated on a plastic substrate is shown in Fig. 5.16 [61]. Significantly, the device performance is found to be comparable to SiNW FETs fabricated on conventional silicon substrates. Moreover, a comparison of I_{sd} versus V_g data recorded when the nanowire/plastic device was flat and bent to a radius of curvature of 0.3 cm (Fig. 5.16 inset) shows that there is only a slight decrease in current for the device in the bent configuration. This small change is notable given the large stress on the chip in the bent state, and clearly shows the robust nature of SiNW/plastic transistors and the potential for high-performance flexible devices.

5.2.4 Large-Scale Hierarchical Organization of SiNW Arrays

Individual semiconductor nanowire has been demonstrated as promising building blocks for nanoscale electronic and photonic devices [4]. However, any new technology starting from bottom-up will require hierarchical organization of nanoscale building blocks. Although small arrays of nanowires have been assembled using fluidic [54] and electric field alignment techniques [64], it remains a challenging task for assembly and integration of large-scale nanowire arrays with controlled orientation and spatial

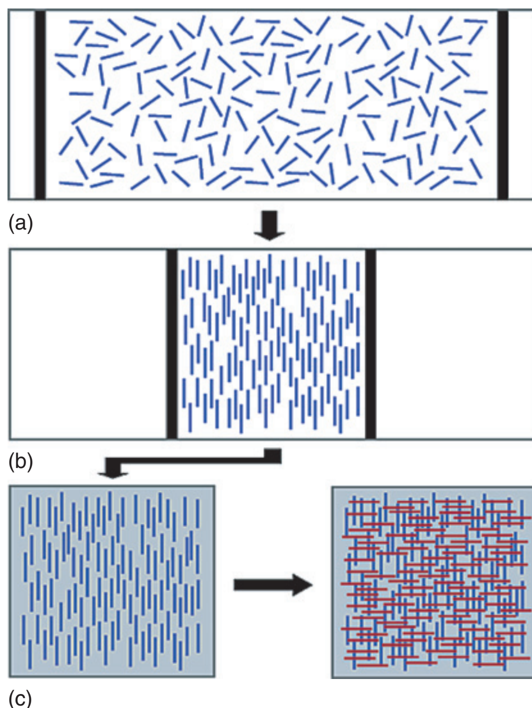

Figure 5.17 Nanowires in a monolayer of surfactant at the air–water interface are (a) compressed on a L–B trough to a specified pitch. (b) The aligned nanowires are transferred to the surface of a substrate to make a uniform parallel array. (c) cNW structures are formed by uniform transfer of a second layer of aligned parallel nanowires perpendicular to the first layer (adapted from Ref. [66]).

position [65,66]. Here, we focus our discussion on a general and controlled method for hierarchical assembly of nanowires from nanometre to centimetre scales [35,66,67].

5.2.4.1 Langmuir–Blodgett-Based Assembly of Nanowires

Langmuir–Blodgett (LB) assembly is a powerful technique that can be used to assemble a large-area monolayer of anisotropic building blocks [68], and thus represents an interesting approach for large-scale nanowire assembly. A schematic assembly of SiNWs using the LB technique is shown in Fig. 5.17 [66]. Stable SiNW suspensions in non-polar solvents made from the surfactant 1-octadecylamine, which coordinates reversibly to nanowire surfaces, were spread on the surface of the aqueous phase in an LB trough and uniaxially compressed. During compression, SiNWs become aligned along their long axes with the average spacing (centre-to-centre distance) controlled by the compression process. The compressed layer is then transferred in a single step to a planar substrate to yield parallel SiNWs covering the entire substrate surface. In addition, this sequence of steps can be repeated one or more times with controlled orientation to produce crossed and more complex nanowire structures, where the nanowires can be the same or different in sequential layers.

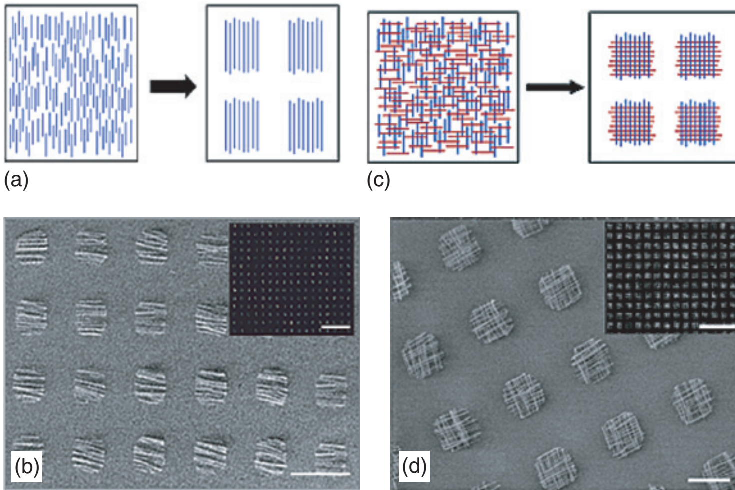

Figure 5.18 (a), (c) Hierarchical patterning of parallel and cNW arrays by lithography, respectively, where nanowires are removed from regions outside of the defined array pattern. (b) SEM image of patterned parallel nanowire arrays. Scale bar, 25 μm. Inset: Dark field optical image. The inset scale bar is 100 μm. (d) SEM image of patterned cNW arrays. Scale bar, 10 μm. Inset: Dark field optical image. The inset scale bar is 100 μm (adapted from Ref. [66]).

Hierarchical patterning of the transferred nanowire structures can be achieved by combining LB assembly with photolithography (Fig. 5.18) [66]. Following uniform transfer of nanowires of a specified spacing onto a substrate, photolithography is used to define a pattern over the entire substrate surface, which sets the array dimensions and array pitch, and then the nanowires outside the patterned array are removed by gentle sonication. An image of a 10 μm × 10 μm square array with a 25 μm array pitch (Fig. 5.18b) shows that this method provides ready and scalable access to ordered arrays over large areas. This array exhibits order on multiple length scales – 40 nm diameter nanowires, 0.5 μm nanowire spacing, 10 μm array size, 25 μm array pitch repeated over centimetres – that is representative of the substantial control enabled by our approach. This method also can be used to make crossed nanowire arrays by transferring sequential layers of aligned nanowires in an orthogonal orientation and then patterning the layers as described above (Fig. 5.18c). Images of crossed nanowire arrays (Fig. 5.18d), which were made by defining an array pattern with photolithography and then removing nanowires outside of the patterned areas, show that regular 10 μm × 10 μm square arrays with a 25 μm array pitch can be achieved over large areas and that each of the square arrays consists of a large number of crossed nanowire junctions.

5.2.4.2 Scalable Integration of Nanowire Devices

Parallel and scalable integration of nanowire devices over large areas can be implemented using the LB method to organize nanowires with controlled alignment and spacing, and using photolithography to define interconnects [35]. Centimetre-scale arrays containing thousands of single SiNW field-effect transistors can be readily fabricated in this way with unprecedented reproducibility and scalability to at least the 100 nm level. This concept is illustrated in Fig. 5.19 with the fabrication of large arrays

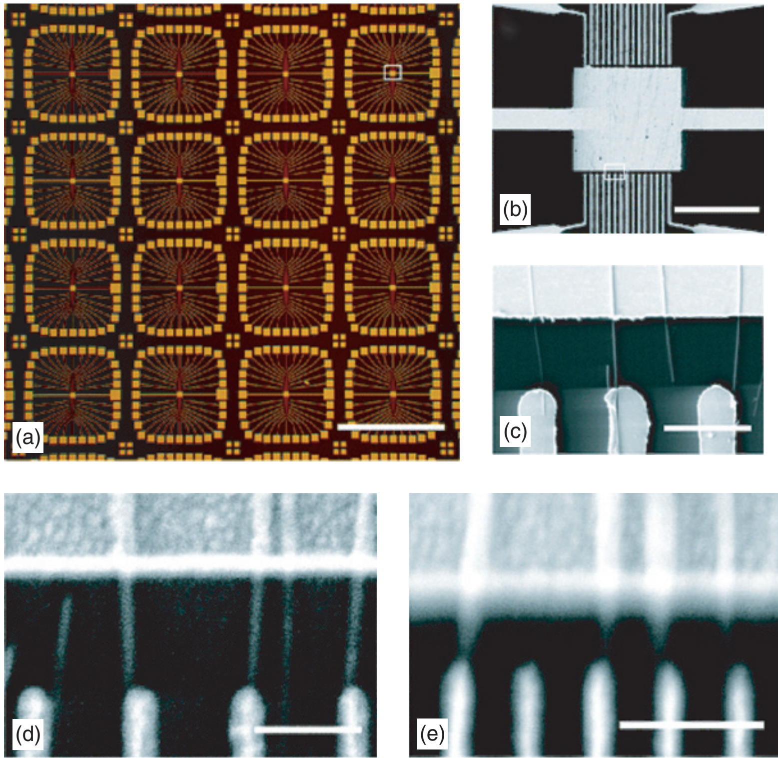

Figure 5.19 (a) Optical micrograph of integrated metal electrode arrays deposited on top of patterned parallel nanowire arrays defined by photolithography. Scale bar, 1 μm. (b) SEM image of the central active region of a repeat unit of the electrode array shown in part (a). Scale bar, 40 μm. (c) SEM image of three nanowire devices connected between the common and finger electrodes. Scale bar, 3 μm. (d, e) SEM images of higher-density nanowire devices defined by electron beam lithography. Scale bars, 300 nm (adapted from Ref. [35]).

of nanowire FETs in which each active device consists of a single *p*-type SiNW [35]. In general, the nanowire arrays are made on 1–10 cm^2 substrates, and then in the final metal electrode deposition step, the photolithography mask is aligned only to the position of the repeating nanowire arrays. Optical and electron microscopy images (Fig. 19a–c) demonstrate the key features and hierarchy of structures, including (1) FET subarrays with a 1 mm array pitch repeated over the entire substrate (Fig. 5.19a), (2) central electrode arrays on a 3-μm electrode pitch (Fig. 5.19b) and (3) individual 20 nm diameter SiNWs connected between the finger electrodes and the common electrode (Fig. 5.19c). Using this method, approximately 80% of the 3000 possible electrode connections available on a typical test chip could be bridged by nanowires when the spacing of the aligned nanowires was closely matched to the electrode width (ca. 1 μm in this demonstration).

This approach is scalable and thus can be used to produce devices in the nanometre size regime over large areas. Because the average nanowire spacing can be controlled down to the nanometre scale during the LB compression [66], a much smaller device size and a higher density of device integration can be readily achieved when

existing high-resolution parallel lithography techniques, such as submicron photolithography, extreme UV lithography [69] or nanoimprint lithography [70], are applied to define electrodes following this interconnection strategy. This key point of scaling is demonstrated using electron beam lithography to define regular nanometre-scale contact electrodes without registering them to individual nanowires [35]. Notably, electron microscopy images show clearly that individual nanowires are connected in high yield for electrodes with 300 nm (Fig. 5.19d) and 150 nm (Fig. 5.19e) pitch. There are also nanowires that fall between the electrodes, as expected statistically, although these are not expected to affect the interconnected active devices.

In addition, the electrical characterization of randomly chosen nanowire devices within the large arrays (Fig. 5.7) reveals excellent transistor characteristics and hole mobility up to 307 $cm^2/V\,s$, comparable with typical SiNW FETs. Thus, these results demonstrate that the solution-based assembly does not adversely affect the performance or reproducibility of the nanowire devices.

5.2.4.3 High-Frequency Nanowire Circuits

The high mobilities exhibited by FETs fabricated from single-crystal SiNWs [8], which are comparable to or exceed the best planar devices, and the potential for large-scale solution-based assembly [35,60] on virtually any substrate, including glass and plastics [61], enable the assembly of integrated circuits using nanowire building blocks [71]. Inverters, generated via the integration of two multi-nanowire transistors containing 80–100 p-SiNWs per device (Fig. 5.20a) [71], have been fabricated in a parallel process over entire glass substrates using standard photolithography techniques. These devices can be fabricated in high yield and exhibit reliable, well-defined signal inversion under DC conditions. Investigation of the AC response of these inverters (Fig. 5.20b) further demonstrates that the gain, or signal amplification, is greater than 1, and the expected phase inversion is achieved when these devices are driven by a 1 MHz sine wave at a supply of 15 V. The high reproducibility of the nanowire transistors and the achievement of gain at high frequencies allow for fully interconnected nanowire oscillators operating in the MHz regime to be implemented.

As an example, Fig. 5.20c demonstrates ring oscillators consisting of three inverters in series, where the input of each inverter is connected to the output of the previous device with a final feedback loop to complete the ring [71]. The necessary on-chip device integration is achieved during the fabrication and does not require any external wiring. Characterization of nanowire ring oscillators on glass substrates demonstrates stable and self-sustained output voltage oscillations. The devices exhibit a maximal oscillation frequency of 11.7 MHz, corresponding to a stage delay of 14 ns (Fig. 5.20d). Significantly, all devices measured on glass display oscillation frequencies at or above 10 MHz.

Studies of carbon nanotubes devices have shown oscillation frequencies from 5 to 220 Hz [72,73]. While these previous studies do not represent an intrinsic limit for nanotubes, they do highlight the importance of achieving reproducible material properties to enable fabrication of integrated, high-performance devices required for applications. It is also interesting to compare these nanowire device results to organic ring oscillators, since the active material in both the cases can be deposited at ambient temperatures from liquid solutions. Reported stage delay times for organic ring oscillators are typically >300 ns [74], and thus substantially (20×) slower than our

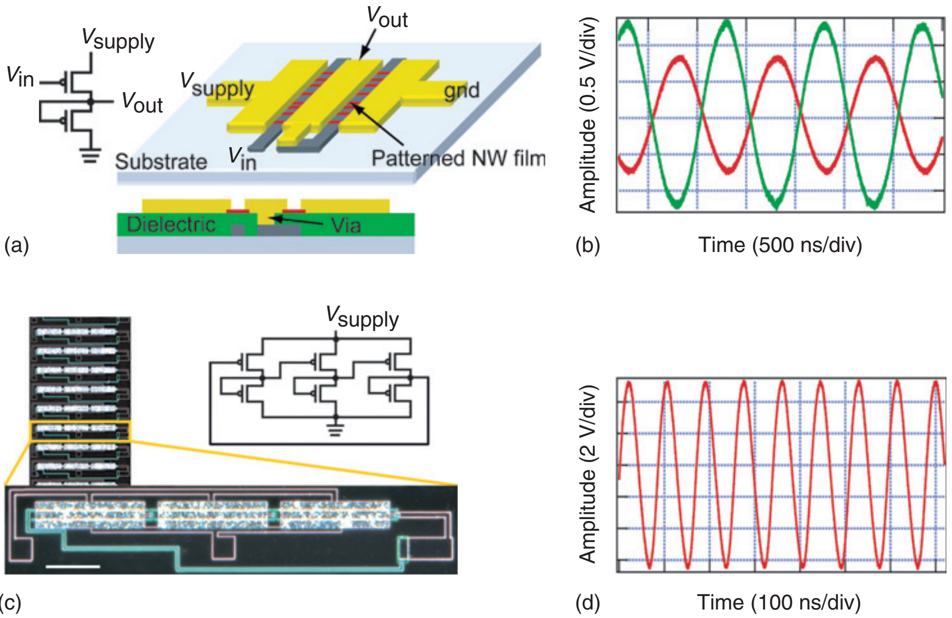

Figure 5.20 AC properties of integrated multi-nanowire circuits on glass. (a) Circuit diagram, perspective and cross-sectional schematics of the multi-nanowire inverters. The bias voltage (V_{supply}), input voltage (V_{in}), and output voltage (V_{out}) are labelled. The dielectric is omitted in the perspective schematic for clarity. (b) Output waveform (green) of an inverter fabricated on glass driven by a 1 MHz sine wave (red) with V_{supply} = 15 V. (c) Optical images and circuit diagram of three-stage nanowire ring oscillators fabricated on glass. The gate level edge, source–drain level edge, and nanowires appear green, pink and white, respectively, in dark field. Scale bar is 100 μm. (d) 11.7 MHz oscillation in a ring oscillator structure with V_{supply} = 43 V (adapted from Ref. [71]).

initial results on glass. Comparable results have been seen for other low-synthesis temperature semiconductors; the fastest reported stage delay for amorphous silicon ring oscillators we have located is 210 ns [75]. Overall, the stable oscillation frequencies observed for our nanowire-based devices on both glass and Si substrates are the highest reported for ring oscillators based on nanoscale building blocks. These results suggest significant promise for integrated nanowire-based transistors for a variety of electronic applications, such as radio frequency identification tags and flat-panel displays.

5.2.5 SiNWs as Nanoscale Sensors

The detection of biological and chemical species is central to many areas of health care and the life sciences, ranging from uncovering and diagnosing disease to the discovery and screening of new drug molecules. Hence, the development of new devices that enable direct, sensitive and rapid analysis of these species could impact in significant ways in humankind. Devices based on SiNWs offer new and sometimes unique opportunities in this rich and interdisciplinary area of science and technology [5,76]. The diameters of nanowires are comparable to the sizes of biological and

chemical species being sensed, and thus intuitively represent excellent primary transducers for producing signals that ultimately interface to macroscopic instruments.

5.2.5.1 Nanowire Field-Effect Sensors

The underlying mechanism for nanowire sensors is a field effect that is transduced using field-effect transistors [77,78], i.e. the binding and unbinding of charged molecules onto a nanowire surface leads to conductance changes. A general sensing device can be configured from the high-performance SiNW FET as illustrated in Fig. 5.21 [76], where specific sensing is achieved by linking recognition groups to the surface of the nanowire [79,80]. When the sensor device with surface receptor is exposed to a solution containing a macromolecule like a protein, which has a net positive charge in aqueous solution, specific binding of the macromolecule to the receptor will lead to an increase in the surface positive charge and a decrease in conductance for a p-type nanowire device. Practically, a very reliable and flexible integrated nanowire sensor device has been developed as shown in Fig. 5.21b, that incorporates SiNWs with well-defined *p*- or *n*-type doping, source–drain electrodes that are insulated from the environment (so that only processes occurring at the nanowire surface contribute to electrical signals) and a microfluidic device for delivery of solutions being examined [77,81–83].

Compared to conventional sensing schemes, SiNW FET-based electrical sensing offers variety of advantages. (1) High sensitivity: the large surface to volume ratio of SiNWs can dramatically increase the sensitivity compared to bulk devices. (2) High selectivity: well-understood silicon oxide chemistry enables SiNWs to be readily linked with virtually unlimited receptor molecules for highly selective detection. (3) Direct and label-free electrical readout: the electronically switchable properties of semiconducting nanowires provide a sensing modality – direct and label-free electrical readout – that is exceptionally attractive for many applications. (4) Device miniaturization: SiNWs have diameter as small as few nanometres, comparable to the sizes of molecules, and devices fabricated with SiNWs can be readily integrated into miniaturized systems. (5) High-density parallel detection: SiNWs can be readily assembled into high-density arrays, enabling high-density parallel detection. (6) SiNW

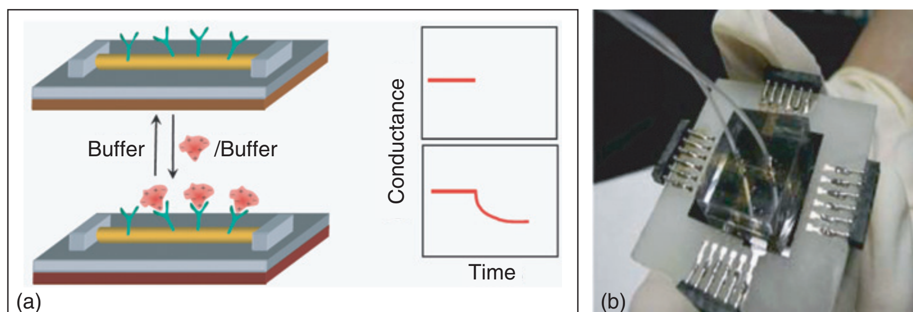

Figure 5.21 Nanowire FET sensor. (a) Schematic of a SiNW-based FET device configured as a sensor with antibody receptors, where binding of a protein with net positive charge (red) yields a decrease in the conductance. (b) Photograph of a prototype nanowire sensor biochip with integrated microfluidic sample delivery (adapted from Ref. [76]).

FET sensors fabricated on transparent substrates can also be readily integrated with optical detection method for simultaneous sensing. These characteristics together suggest that nanowire devices could revolutionize many aspects of sensing and detection in biology and medicine, and indeed, previous studies have demonstrated detection of ions [77], proteins [77], DNA [83], single viruses [82] and small-molecule – protein interactions [81]. Examples of single virus detection and multiplexed sensing will be discussed in the following sections.

5.2.5.2 Single Virus Detection

Viruses are among the most important causes of human disease [84] and an increasing concern as agents for biological warfare and terrorism [85,86]. Studies of the detection of viruses [82] have been carried out with the goal of determining whether the ultimate limit of one single entity could be detected reliably. Delivery of highly dilute influenza A virus solutions, on the order of 80 aM (10^{-18} M) or 50 viruses/μl, to p-type SiNW devices modified with monoclonal antibody for influenza A produces well-defined, discrete conductance changes (Fig. 5.22) that are characteristic of binding and unbinding of single negatively charged influenza viruses [82]. Simultaneous optical and electrical measurements using fluorescently labelled influenza viruses (Fig. 5.22) show that, as a virus diffuses near a nanowire device, the conductance remains at the baseline value, and only after binding at the nanowire surface does the conductance drop in a quantized manner; as the virus unbinds and diffuses from the nanowire surface the conductance returns rapidly to the baseline value. The two events in Fig. 5.22 also exhibit similar conductance changes when virus particles bind to distinct sites on the nanowire, and thus demonstrate that the detection sensitivity is relatively uniform along the length of the nanowire. These parallel measurements also show that a virus must be in contact with the nanowire device to yield an electrical response, suggesting that it will be possible to develop ultra-dense nanowire device arrays without crosstalk in future, where the minimum size scale is set by that of the virus.

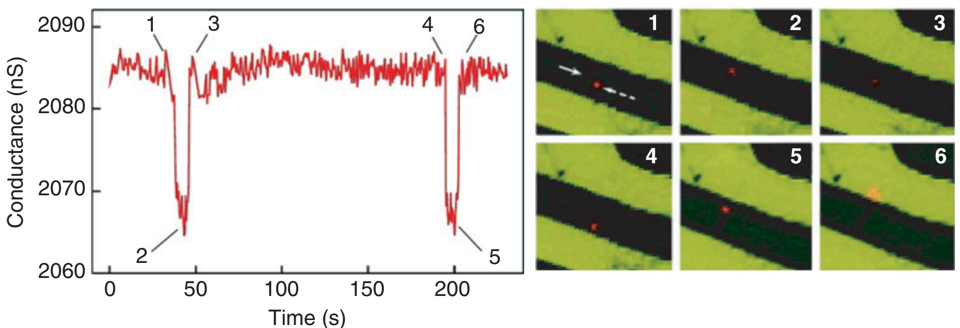

Figure 5.22 Single virus detection. Conductance (*left*) and optical (*right*) data recorded simultaneously versus time for a single SiNW device after introduction of influenza A solution. Combined bright field and fluorescence images correspond to time points 1–6 indicated in the conductance data; virus appears as a red dot in the images. The solid white arrow in image 1 highlights the position of the nanowire device, and the dashed arrow indicates the position of a single virus. Images are 8 × 8 μm. All measurements were performed with solutions containing 100 viral particles per μl (adapted from Ref. [82]).

5.2.5.3 Multiplexed Detection at the Single Virus Level

One extremely attractive feature of the nanowire FET sensors is their potential for integration into electrically addressable sensor arrays. In a previous section, we reviewed strategies that enable parallel and scalable integration of nanowire FET devices over large areas without the need to register individual nanowire–electrode interconnects [35,66,67], thus moving well-beyond methods in which a serial lithography is used to connect nanostructures one by one. The device arrays prepared in this way offer unique opportunities for label-free multiplexed detection of biological and chemical species.

Initial studies in this direction have demonstrated multiplexed detection of distinct viruses at the single virus level [82]. Experiments were carried out as illustrated in Fig. 5.23a, where two different nanowire sensor devices are modified with antibody receptors specific either for influenza A (nanowire 1) or adenovirus (nanowire 2). Simultaneous conductance measurements obtained when adenovirus, influenza A and a mixture of both viruses are delivered to the devices (Fig. 5.23b) show several key points. Introduction of adenovirus, which is negatively charged at the pH of the experiment, to the device array yields positive conductance changes for nanowire 2 with an on time of 16 ± 6 s. The magnitude of the conductance change for binding of single adenovirus particles differs from that of influenza A viruses because of differences in the surface charge densities for the two viruses. On the other hand, addition of influenza A yields negative conductance changes for nanowire 1. Nanowire 2 also exhibits short-duration negative conductance changes, which correspond to diffusion of influenza A viral particles past the nanowire device, and are readily distinguished from specific binding events by the temporal response. Significantly, delivery of a

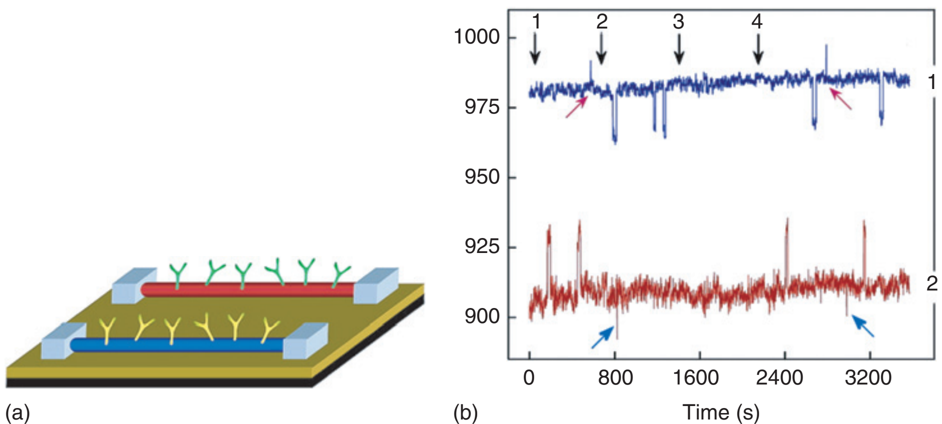

Figure 5.23 (a) Schematic of two SiNW devices; one nanowire (nanowire 1) was modified with anti-influenza type A antibody, and the other (nanowire 2) was modified with anti-adenovirus group III antibody. (b) Conductance versus time data were recorded simultaneously from two SiNW elements. Arrows 1–4 correspond to the introduction of adenovirus, influenza A, pure buffer and a 1:1 mixture of adenovirus and influenza A, where the virus concentrations were 50 viral particles per μl. Small arrows below curves 1 and 2 highlight conductance changes corresponding to diffusion of viral particles past the nanowire and not specific binding (adapted from Ref. [82]).

mixture of both the viruses demonstrates unambiguously that selective binding/unbinding responses for influenza A and adenovirus can be detected in parallel by nanowires 1 and 2, respectively, at the single virus level.

5.3 SiNW heterostructures

Planar heterostructures can provide functional properties [37] that have revolutionized both semiconductor industry and fundamental science. The concept of heterostructures is equally important in nanowires and could open up additional dimensions of structural complexity and corresponding functionality [6,87]. Incorporation of compositional and structural complexity into nanowires can be achieved by two approaches, either through integrating nanowire with top-down fabrication approach [12] or by purely bottom-up synthesis [6,87]. Here we will focus our discussion on SiNW heterostructures [12–14] with an emphasis on both the approaches.

5.3.1 NiSi/SiNW Heterostructures

SiNW heterostructures can be realized through selective material transformation using conventional lithography to define regions of transformation [12]. Examples are given for NiSi/Si heterostructures and superlattices (Fig. 5.24). Nickel metal is first patterned onto SiNWs, and then the nickel-containing regions are transformed to NiSi by annealing at elevated temperature. Excess Ni can be completely removed by subsequent etching. A dark-field optical image of a nanowire patterned in this way using 1 μm wide nickel regions on a 2 μm pitch (Fig. 5.24b) exhibits periodic variations in contrast extending over the full length of the 65 μm long nanowire. Analysis of the image shows that the average lengths of the Si and NiSi regions are both 1 μm, and in good agreement with the width and pitch of nickel metal deposited on the nanowire during fabrication. TEM images of similar NiSi/SiNW heterostructures (Fig. 5.24c) show a similar periodic variation in contrast that is consistent with NiSi (dark) and Si (light) materials within the heterostructure. This assignment was confirmed by EDS analysis: the dark and light regions correspond to a Ni:Si ratio of 1.02:1.00 and pure Si, respectively. Detailed examination of NiSi/Si heterostructure by HRTEM (Fig. 5.24d) also shows that the transformation yields an atomically abrupt interface.

The capability of transforming Si to NiSi in a spatially well-defined manner to form NiSi/SiNW heterostructures and superlattices with atomically sharp metal–semiconductor interfaces opens up the possibility of integrating both active devices and high-performance interconnects from a single nanoscale building block. In the next two sections, we will discuss two additional types of SiNW heterostructures [13,14], in which compositional and structural complexity are introduced during synthesis, and thus have the potential for nanoscale applications beyond the lithography limit.

5.3.2 Modulation Doped SiNWs

Direct synthesis can be exploited to prepare dopant modulated SiNW structures. These nanostructures provide unique opportunities for many areas of nanoscience and technology, and demonstrate clearly the power of the bottom-up approach.

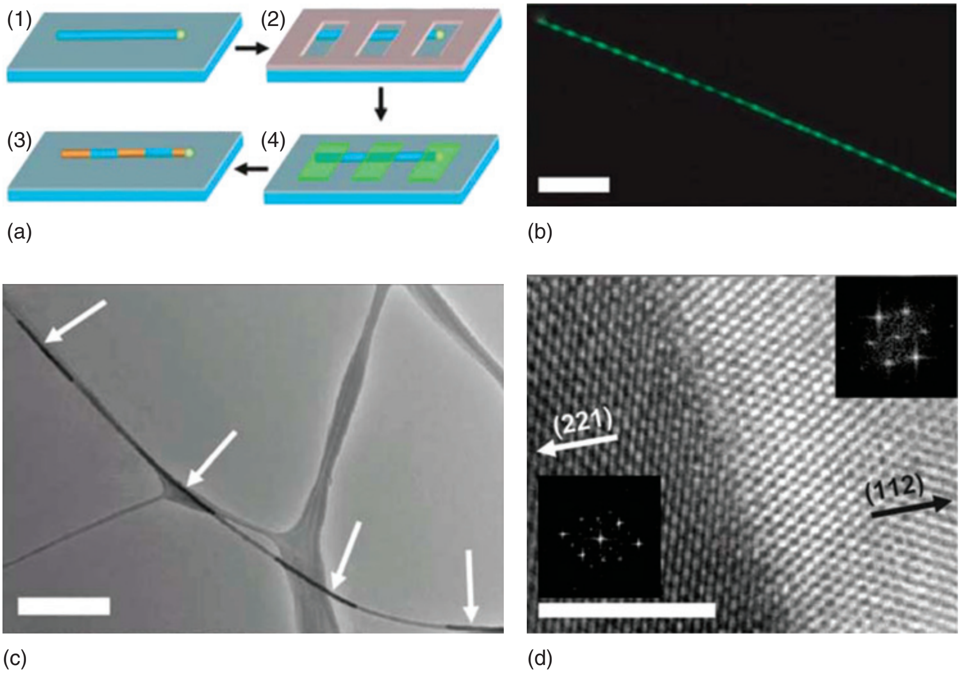

Figure 5.24 (a) Fabrication of NiSi/SiNW heterostructures and superlattices. (1) SiNWs (blue) dispersed on a substrate are (2) coated with photoresist (grey) and lithographically patterned, (3) selectively coated with Ni metal to a total thickness comparable to the SiNWs diameter and (4) annealed to form NiSi nanowires. (b) Dark field optical image of a single NiSi/SiNW heterostructure. The bright green segments correspond to silicon and the dark segments to NiSi. Scale bar, 10 μm. (c) TEM image of a NiSi/SiNW heterostructure. The bright segments of the nanowire correspond to silicon and the dark segments, which are highlighted with arrows, correspond to NiSi. Scale bar, 1 μm. (d) HRTEM image of the junction between NiSi and Si showing an atomically abrupt interface. Insets: 2D Fourier transforms of the image depicting the [110] and [111] zone axes of NiSi and Si, respectively, where the arrows highlight the growth fronts of the NiSi (221) and Si (112). Scale bar, 5 nm (adapted from Ref. [12]).

5.3.2.1 Synthesis and Characterization of Modulation Doped SiNWs

A general scheme for realizing dopant modulation in the frame of metal nanocluster catalysed nanowire synthesis involves varying the dopant reactant concentration in the vapour phase during growth. In this approach, it is essential to avoid radial overcoating (Fig. 5.25a) during growth since this could eliminate the desired electronic modulation in nanowire properties. This is a challenging problem distinct from planar growth due to the very large surface-to-volume ratio of nanowires. To meet the desired synthetic goals, we carried out growth in H_2, which suppresses the decomposition of silane, and slows growth rate by uncatalysed processes. In addition, a local substrate heater has been adopted to reduce reactant heating and possible homogeneous decomposition prior to delivery to the substrate and nanocluster catalyst. This further enhances selectivity for axial growth.

Dopant modulated structure were characterized by HRTEM and scanning gate microscopy (SGM), a localized electrical probing technique [11,88]. Data taken on

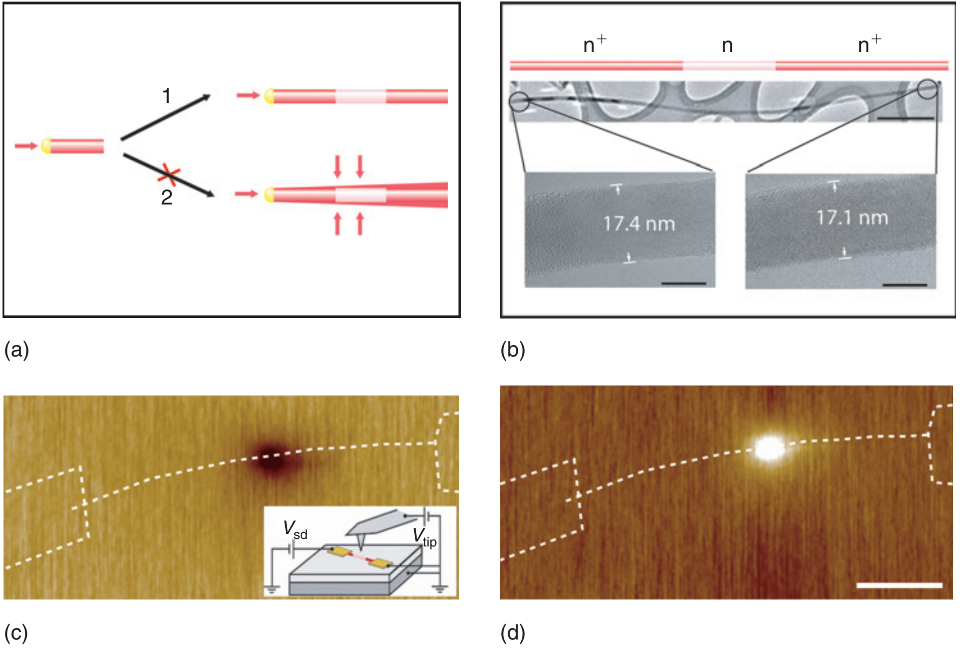

Figure 5.25 Synthesis and characterization of modulation doped SiNW. (a) Schematic of the synthesis of modulation doped SiNW. Au colloid (yellow) catalyses growth of a heavily doped region (red) and lightly doped region (pink) nanowire superstructures. (1) Pure axial growth, resulting in dopant modulated nanowire super structure. (2) Axial and radial growth, resulting in a layer of homogenous overcoating (red) and a taped nanowire structure. (b) Schematic and TEM images of a representative n^+–n–n^+ modulation doped SiNW. The scale bars in the upper and lower images are 500 and 10 nm, respectively. (c, d) SGM images of n^+–n–n^+ modulation doped SiNW recorded with tip biased at −9 and +9 V, respectively. Scale bar, 1 μm. Inset: A diagram illustrating electrical SGM characterization (adapted from Ref. [14]).

representative n^+–n–n^+ SiNWs, where n^+ and n represent the heavily and lightly doped SiNW sections, are shown in Fig. 5.25b–d [14]. Analysis of high-resolution TEM images, taken from two ends of a n^+–n–n^+ SiNW, show the diameters of 17.4 and 17.1 nm, respectively. The 0.3 nm diameter variation is on the order of one atomic layer, which corresponds to single lattice plane fluctuations, and demonstrates that growth is purely axial without overcoating. SGM measurements were made on a FET device in which the two n^+ ends of an n^+–n–n^+ SiNW were contacted, and show that the conductance is reduced (enhanced) when the scanned tip with negative (positive) applied voltage (V_{tip}) is scanned over the lightly doped region of the n^+–n–n^+ structure (Fig. 5.25c and d). In both cases, the SGM images confirm that the synthesis approach yields a spatially and electrically well-defined n^+–n–n^+ nanowire structure.

Rational control over dopant modulated structures can be achieved by tuning CVD synthesis parameters [14]. Representative SGM data taken on modulation doped n^+–(n–n^+)$_N$ SiNWs with N = 3, 6 and 8 are shown in Fig. 5.26a–c. The pitch spacings in these dopant modulated structures, which is defined as the separation between two nearest n regions, can be readily controlled by growth time, with the average values

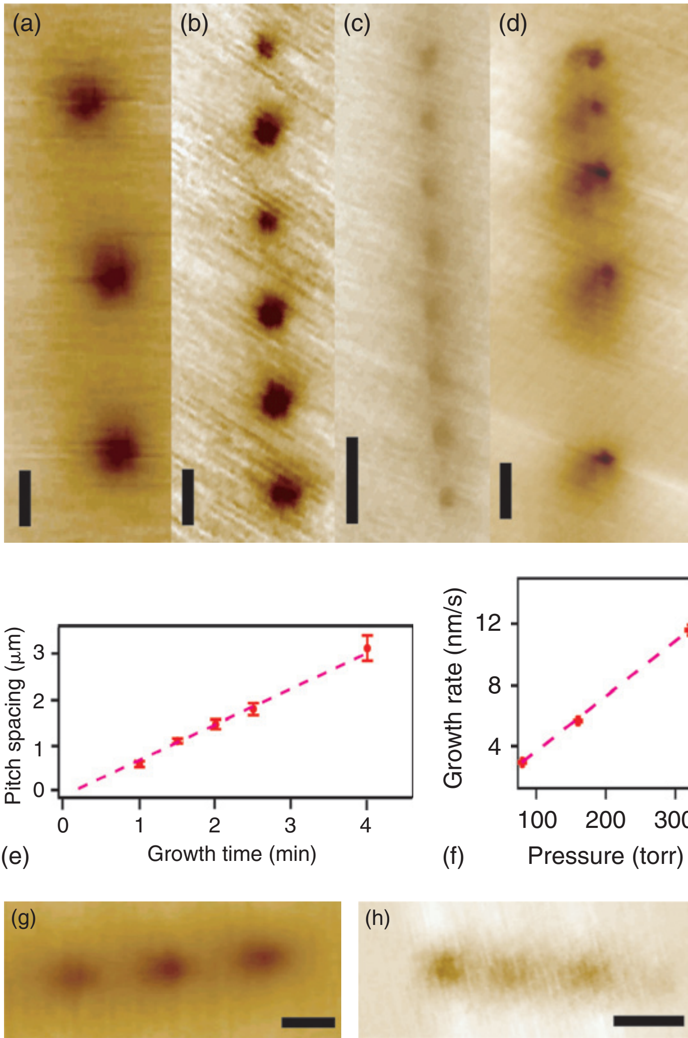

Figure 5.26 SGM images of SiNW n^{+}–$(n–n^{+})_N$ with (a) $N = 3$ (growth times for n and n^{+} regions are 1 and 3 min, respectively), (b) $N = 6$ (growth times for n and n^{+} regions are both 1 min), (c) $N = 8$ (growth times for n and n^{+} regions are both 30 s), and (d) $N = 5$ (growth times for n regions are 30 s and for n^{+} sections are 30 s, 1, 2 and 4 min). Scale bars are 1 μm. (e) Pitch spacing versus growth time under fixed growth conditions. (f) Growth rate versus growth pressure. SGM images of modulation doped SiNWs synthesized with total pressure of 160 (g) and 80 (h) torr with 30 s growth times for the n and n^{+} regions. Scale bars, 100 nm (adapted from Ref. [14]).

of 3.2 μm (Fig. 5.26a), 1.6 μm (Fig. 5.26b) and 0.8 μm (Fig. 5.26c), and additionally can be varied within single nanowire (Fig. 5.26d). More detailed studies reveal that the pitch spacing is directly proportional to growth time (Fig. 5.26e). Furthermore, systematic studies reveal that the growth rates decrease linearly with decreases in reactant pressure (Fig. 5.26f). Specifically, as the total pressure is reduced from 160 to 80 torr,

the average section length in each structure is reduced to 90 and 45 nm, respectively (Fig. 5.26g and h).

5.3.2.2 Novel Applications of Modulation Doped SiNWs

Lithography-Free Addressing The substantial conductance changes shown in the SGM measurements between n and n^+ sections within a modulation doped SiNW suggests that doping modulation can serve as bits for encoding. Compared to previous work [55], in which selective chemical modification at lithographically defined locations was used to define codes, coding during synthesis would enable lithography-free addressing at the nanoscale. To test this idea, top-gated FETs were fabricated on single n^+–n–n^+ modulation doped SiNWs (Fig. 5.27a) [14], where gate 2 was over the lightly doped region and gates 1 and 3 were over the heavily doped regions. Importantly, the nanowire transistor can be turned off by gate 2, while gates 1 and 3 have little effect. Since the three metal gates were fabricated in a parallel process, the selectivity can be attributed to modulated dopant concentration in the n and n^+ sections of the SiNW.

A 2 by 2 array assembled from the n^+–n–n^+ SiNWs was also characterized to provide proof-of-principle demonstration of addressing based on modulation doped nanowire FETs (Fig. 5.27b and c) [14]. Two metal top gates, In1 and In2, were defined on two parallel modulation doped SiNWs, which were configured as outputs, Out1

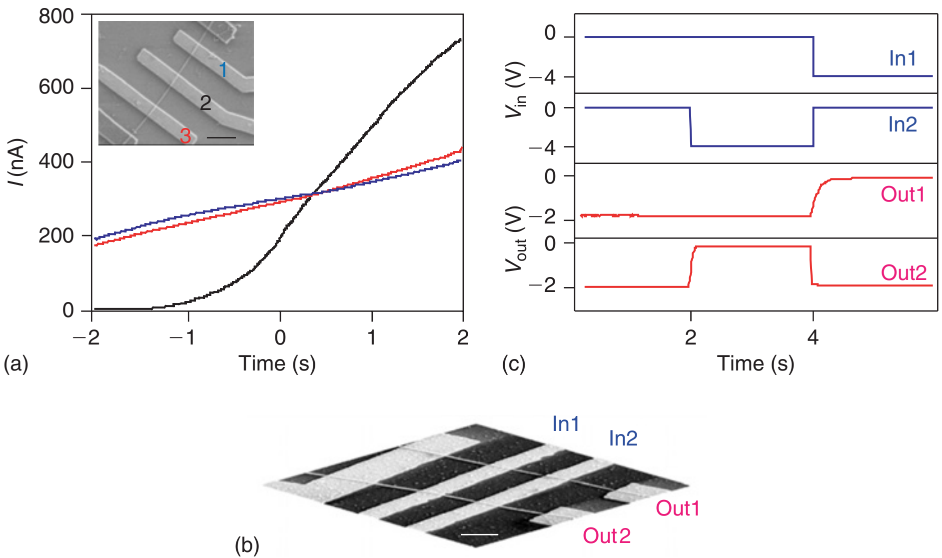

Figure 5.27 Address decoder based on modulation doped SiNW FET arrays. (a) Current versus gate voltage measured at three top gates on the n^+–n–n^+ modulation doped SiNW FET with V_{sd} = 1 V. Inset: SEM image of device. Scale bar, 1 μm. (b) SEM image of a 2 × 2 decoder based on top-gated modulation doped SiNW FETs. Scale bar, 1 μm. (c) Real time monitoring of the gate voltage inputs (IN1 and IN2) and signal outputs (OUT1 and OUT2) for the 2 × 2 decoder (adapted from Ref. [14]).

and Out2. Conductance versus applied gate voltage data measured at the four cross points show that Out1 and Out2 can only be turned off by In1 and In2, respectively, and thus the 2 by 2 array functions as an address decoder circuit for multiplexing and demultiplexing signals. Furthermore, this lithography-free decoding scheme can be readily scaled to larger arrays based upon a stochastic decoder scheme, in which modulation doped nanowires representing different codes are assembled in a fully random fashion [89]. Notably, this scheme does not require end-to-end alignment in nanowire arrays; in fact, lack of end registry can generate new rotating codes and reduce the required total number of distinct types of modulation doped nanowires.

Synthetically Defined QD Structures Modulation doped nanowire structures also provide a means for defining QDs within nanowires without the need for lithography [14,90]. Potential barriers, which define the QD, are created by the Fermi level offset resulting from dopant concentration differences in the modulated nanowire. This idea was demonstrated in five-section n^+–n–n^+–n–n^+ modulation doped SiNWs as shown in Fig. 5.28a [14]. Representative transport data (Fig. 5.28b) reveals well-defined Coulomb diamond structures, where charge transport is "blocked" for values of V_{sd}–V_g in the blue-coloured diamond regions. The single period diamond structures provide strong evidence for transport through a single QD structure. Key parameters of the CB transport can be estimated from this result. In particular, the gate capacitance C_g value of ≈23.5 aF is found to be consistent with that estimated from the QD size, ~500 nm, determined independently in SGM measurements (Fig. 5.28c).

In addition, this approach can be extended in a significant way to coupled QDs in which the inter-dot coupling strength can vary by the length of lightly doped barrier. The idea is demonstrated by the structure illustrated in Fig. 5.28d [14]. In addition to the two lightly doped sections acting as tunnelling barriers, one more n section is designed in the centre of n^+ region, which breaks the n^+ region into two QDs. I–V_g data taken from three devices with decreasing centre n section length (Fig. 5.28d) show the following: at large centre barrier widths (upper panel) a single period Coulomb oscillation with periodicity corresponding to the size of each individual dot. With reduced length (centre panel) the peaks start to split, and finally, the shortest length section (lower panel) yields single period oscillation peaks but with periodicity corresponding to one large QD equal to the sum of the two individual QDs. This phenomenon agrees well with previous theoretical [91] and experimental [92] studies on top-down fabricated double QD systems with increasing coupling strength. These studies suggest that our approach can open up exciting opportunities for fundamental studies and quantum electronics in the future.

5.3.3 Branched and Hyper-Branched SiNWs

Branched nanostructures represent an additional dimension for increasing structural complexity and potentially enabling greater function [93], and have been demonstrated for various material systems, including nanocrystals [94,95] and nanowire/nanoribbon structures [13,96–99]. The essence of this idea is the control over the density and size of nanoscale branches, which ultimately enables the rational design of building blocks for devices. To achieve this goal we developed an approach that is outlined in Fig. 5.29a. First, a nanowire backbone of specific diameter and composition

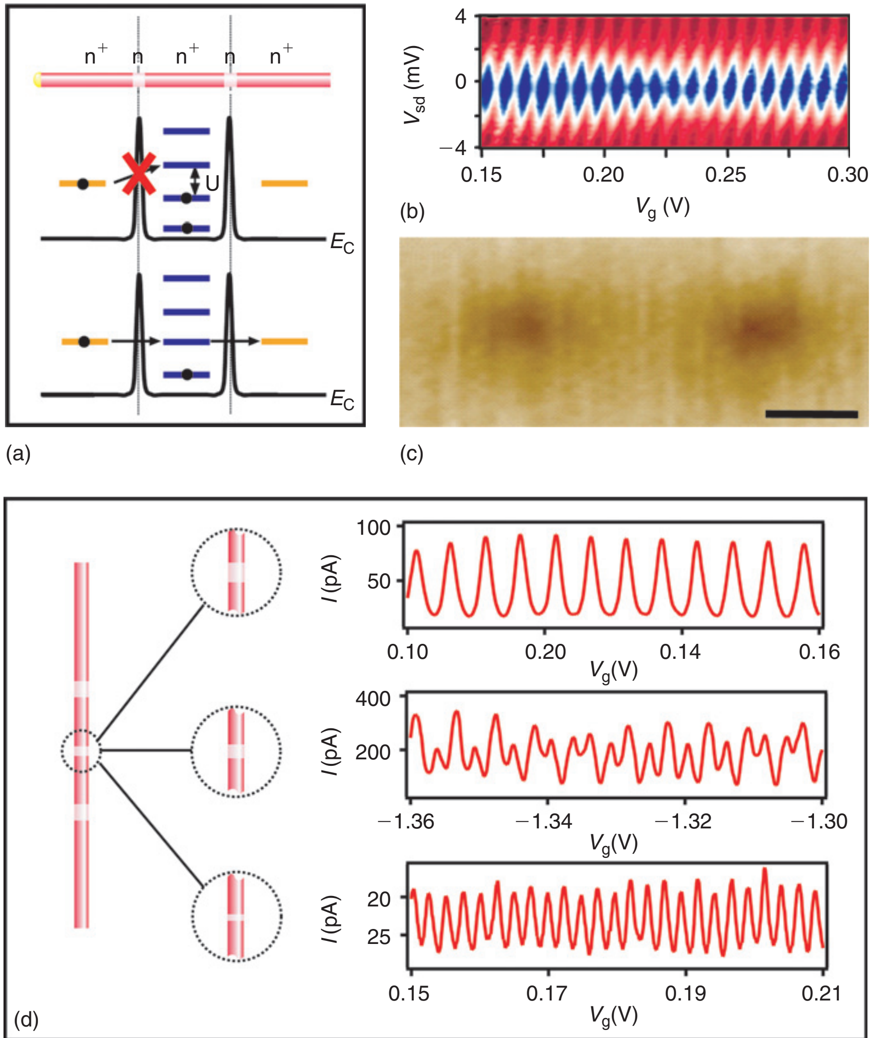

Figure 5.28 (a) Schematic of QD structure defined by two lightly doped barriers within a modulation doped SiNW. Red and pink colour-coded sections represent the n^+ and n sections, respectively. (b) 2D colour-scale plot of $\partial I/\partial V_{sd}$ versus V_{sd} and V_g recorded at 1.5 K on n^+–n–n^+–n–n^+ modulation doped SiNW device. The blue (red) regions correspond to low (high) values of $\partial I/\partial V_{sd}$. The middle n^+ section is grown at 80 torr for 3 min, while the two n sections are grown for 30 s. (c) SGM image of the same device. Scale bar, 200 nm. (d) Coupled double QD structures. (Left panel) A centre n section is introduced for tuning the coupling strength. I–V_g data taken at 1.5 K on three double dot devices with centre n sections grown for 15, 10 and 5 s from top to bottom, respectively (adapted from Ref. [14]).

is prepared by nanocluster-mediated VLS growth. Second, nanocluster catalysts of defined diameter are deposited on the backbone, and then first-order branches are grown by the VLS process. Third, the branch growth steps can be repeated one or more times to yield higher order or hyper-branched nanowire structures.

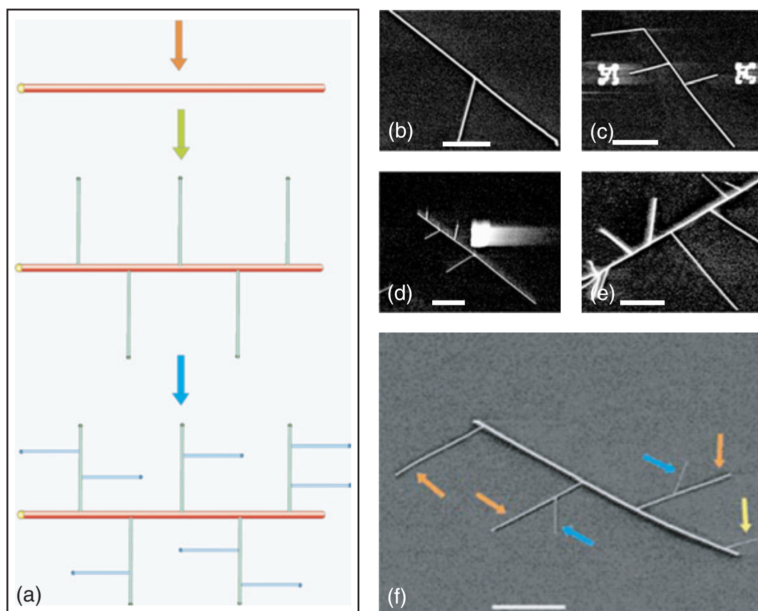

Figure 5.29 (a) Schematic illustrating the multi-step syntheses of branched and hyper-branched nanowire structures. Red, green, blue arrows/colours signify the growth of the backbone, first- and second-generation nanowires, respectively. (b–e) SEM images of branched SiNW structures. Branched SiNW structures prepared the following deposition of gold nanoclusters from (b) 1:20, (c) 1:8, (d) 1:3 and (e) 1:1 diluted stock solutions and subsequent growth. (f) SEM image of a hyper-branched SiNW structure. The first- and second-generation branches are indicated by orange and blue arrows, respectively. Yellow arrow indicates a 10 nm SiNW (from second-generation growth) grown from the backbone. Scale bars, 1 μm (adapted from Ref. [13]).

The basic features of this new approach were demonstrated with growth of silicon-based branched nanostructures [13]. First, SiNWs, which serve as backbones, were synthesized via gold nanocluster-mediated VLS growth process using silane as the reactant. Gold nanoclusters with diameters equal to or smaller than SiNW backbones produced in the first step were then deposited from solution onto the nanowire backbones, and SiNW branches were grown in the same way as the initial backbone. Figure 5.29b–e shows representative SEM images of branched SiNW structures prepared using increasing concentrations of gold nanoclusters during the deposition process. The images show that the nanowire branch density increases directly with the concentration of deposited gold nanoclusters, and hence, demonstrate the controllability over this important structural parameter. Last, the SEM images show that the SiNW branches grow within a range of angles, ca. 60–70°, with respect to the backbone, indicating that the growth is epitaxial.

This approach can be extended as suggested in Fig. 5.29a to produce more complex nanowire architectures. Hyper-branched SiNW structures were also synthesized by a three-step growth procedure in which 40, 20 and 10 nm gold nanoclusters were used to catalyse the VLS growth of the SiNWs comprising the backbone, first- and second-generation branches, respectively. Significantly, an image of a representative nanostructure prepared in this way (Fig. 5.29f) [13] shows clearly these

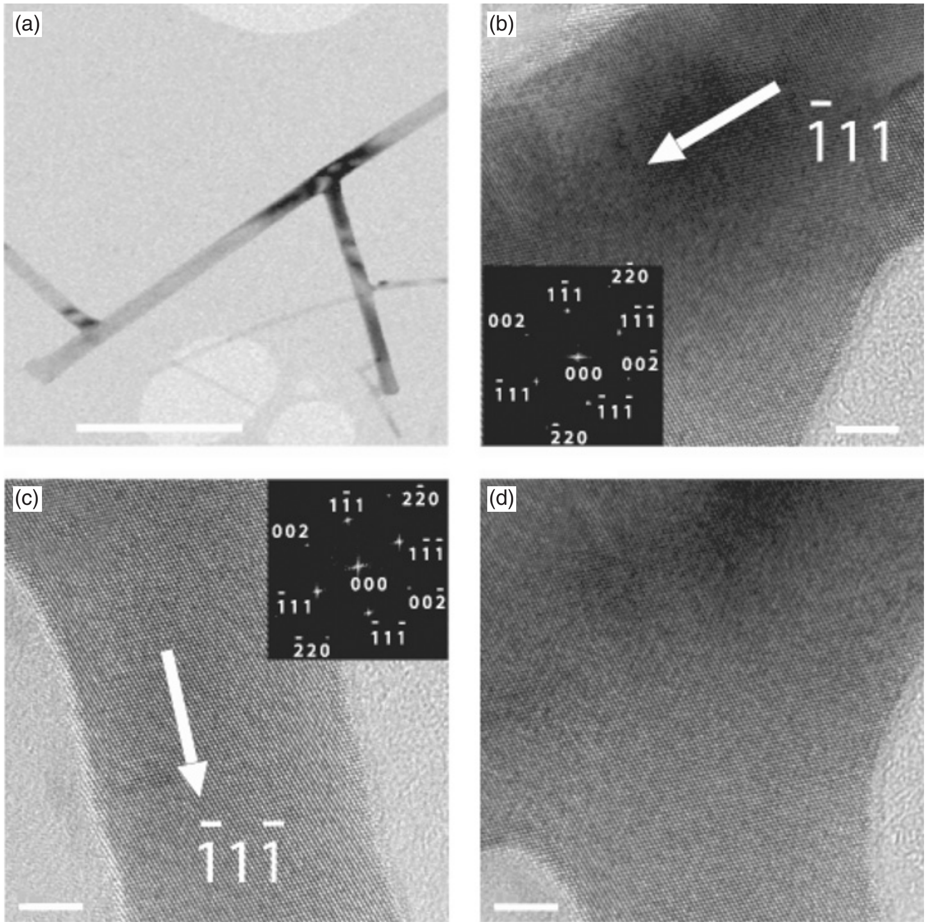

Figure 5.30 (a) TEM image of a branched SiNW structure showing two branches. Scale bar, 250 nm. (b–d) Lattice-resolved TEM images of the backbone (b), branch (c) and junction (d). The nanowires growth axes are indicated by the white arrows. Scale bars, 5 nm. Insets in (b) and (c) are reciprocal lattices determined from 2D Fourier transforms of the respective images (adapted from Ref. [13]).

first- and second-generation branches, which are unambiguous due to the differences in SiNW diameters nucleated using 20 and then 10 nm diameter nanoclusters. This image also shows a 10 nm branch on the backbone, which can be attributed to growth during the second branch step.

In addition, TEM characterization of the branched SiNWs demonstrate several key points (Fig. 5.30) [13]. First, the diameter of the branches, 22 nm, and backbone, 30 nm, are consistent with the diameters of the gold nanoclusters used to mediate their growth: 20 and 30 nm, respectively. Second, the lattice-resolved data (Fig. 30b–d) show that the branched SiNWs have single-crystal structures with clean backbone-to-branch junctions that are consistent with epitaxial branch growth. The indexed reciprocal lattices, from 2D Fourier transforms of the lattice-resolved images, show

that the [−111] direction was aligned with the backbone axis and the [−11−1] direction was aligned with the branch axis. The backbone–branch angle determined from the reciprocal lattice peaks, 72.3°, is consistent with the 70.5° angle between these two directions for the silicon crystal structure. These results demonstrate that SiNW branches are epitaxial, and thus might lead to interesting functional devices. For example, branched SiNWs structures consisting of p-type backbones and n-type branches could function as p–n diodes and junction FETs. The ability to introduce active electronic and optoelectronic junctions into branched and hyper-branched nanowire structures should open up many opportunities in the future, including 3D interconnected computing structures analogous to the brain.

5.4 Summary

In this chapter, we have reviewed recent research progress on chemically synthesized SiNWs and nanowire heterostructures. Overall, these examples illustrate a series of key advances that could potentially revolutionize future nanoscale science and technology. First, the general nanocluster catalysed VLS growth approach for the synthesis of SiNW enables rational control over physical dimensions and electronic properties of SiNWs. Second, electrical transport studies show that chemically synthesized SiNWs have much less structural and dopant fluctuations than top-down fabricated silicon nanostructures, which leads to exceptional device characteristics often outperforming existing planar silicon technology. Third, SiNWs can be assembled into a wide range of nanoscale electronic devices and circuits, and combined with large-scale hierarchical assembly technique, we have shown that great opportunities for applications ranging from high-density, scalable and integrated nanoelectronics to ultra-sensitive nanoscale sensors for chemical and biological detection. Last, novel SiNW heterostructures exhibit additional dimensions of complexities and functionalities for nanoelectronics applications and fundamental studies that make it difficult to predict just how far this form of nanosilicon can go.

We believe what we have seen is only the tip of the iceberg; broad aspects ranging from fundamental science to applications for these nanoscale silicon structures still await scientists to discover. Particularly, we envision the following areas will attract wide ranging attention from interdisciplinary research. (1) New materials synthesis: SiNWs can be used as backbone to generate heterostructures exhibiting diverse functionalities. (2) Fundamental scientific discovery: rational control over physical dimensions and properties of SiNWs and SiNW heterostructures make them promising systems for studying fascinating fundamental problems. (3) SiNW-based nanophotonics: quantum effects in nanoscale silicon could lead to fully integrated silicon optoelectronics circuits. (4) SiNW sensors: ultra-high sensitivity, large-scale and multiplexed sensor array will benefit many areas of health care and the life sciences, ranging from uncovering and diagnosing disease to the discovery and screening of new drug molecules. (5) Nanocomputing: advances on large-scale hierarchical organization of nanowires and novel computer architectures could make the dream of nanocomputing finally come true. In conclusion, by focusing on the fundamentals of nanoscience, we believe there is the potential to revolutionize some of the most important technologies we know today and most likely open unexpected areas in the future.

REFERENCES

1. R. Compañó, L. Molenkamp and D.J. Paul, *Technology Roadmap for Nanoelectronics, European Commission IST Programme: Future and Emerging Technologies*. http://nanoworld.org/NanoLibrary/nanoroad.pdf.
2. S. Polyviou and M. Levas, *The Future of Moore's Law*. http://www.iis.ee.ic.ac.uk/~frank/surp98/report/sp24.
3. J.D. Meindl, Q. Chen and J.A. Davis, *Science* **293**, 2044 (2001).
4. C.M. Lieber, *Sci. Am.* **285**, 58 (2001).
5. C.M. Lieber, *MRS Bull.* **28**, 486 (2003).
6. P. Yang, *MRS Bull.* **30**, 85 (2005).
7. A.M. Morales and C.M. Lieber, *Science* **279**, 208 (1998).
8. Y. Cui, Z. Zhong, D. Wang, W.U. Wang and C.M. Lieber, *Nano Lett.* **3**, 149 (2003).
9. Z. Zhong, Y. Fang, W. Lu and C.M. Lieber, *Nano Lett.* **5**, 1143 (2005).
10. Y. Cui, X. Duan, J. Hu and C.M. Lieber, *J. Phys. Chem. B* **104**, 5213 (2000).
11. M.S. Gudiksen, L.J. Lauhon, J. Wang, D.C. Smith and C.M. Lieber, *Nature* **415**, 617 (2002).
12. Y. Wu, J. Xiang, C. Yang, W. Lu and C.M. Lieber, *Nature* **430**, 61 (2004).
13. D. Wang, F. Qian, C. Yang, Z. Zhong and C.M. Lieber, *Nano Lett.* **4**, 871 (2004).
14. C. Yang, Z. Zhong and C.M. Lieber, *Science* **310**, 1304 (2005).
15. Y. Huang and C.M. Lieber, *Pure Appl. Chem.* **76**, 2051 (2004).
16. Y. Cui, X. Duan, Y. Huang and C.M. Lieber, *Nanowires and Nanobelts – Materials, Properties and Devices*, Ed. Z.L. Wang (Kluwer Academic/Plenum Publishers, New York, 2003), pp. 3–68.
17. C.M. Lieber, *Solid State Comm.* **107**, 607 (1998).
18. F.J. Himpsel, T. Jung, A. Kirakosian, J. Lin, D.Y. Petrovykh, H. Rauscher and J. Viernow, *MRS Bull.* **24**, 20 (1999).
19. W. Han, S. Fan, Q. Li and Y. Hu, *Science* **277**, 1287 (1997).
20. C.R. Martin, *Science* **266**, 1961 (1994).
21. H. Dai, E.W. Wong, Y.Z. Lu, S. Fan and C.M. Lieber, *Nature* **375**, 769 (1995).
22. R.S. Wagner and W.C. Ellis, *Appl. Phys. Lett.* **4**, 89 (1964).
23. J. Westwater, D.P. Gosain, S. Tomiya, S. Usui and H. Ruda, *J. Vac. Sci. Tech. B* **15**, 554 (1997).
24. N. Wang, Y. Zhang, Y.H. Tang, C.S. Lee and S.T. Lee, *Appl. Phys. Lett.* **73**, 3902 (1998).
25. Y. Cui, L.J. Lauhon, M.S. Gudiksen, J. Wang and C.M. Lieber, *Appl. Phys. Lett.* **78**, 2214 (2001).
26. D. Yu, Z. Bai, Y. Ding, Q. Hang, H. Zhang, J. Wang, Y. Zou, W. Qian, G. Xiong, H. Zhou and S. Feng, *Appl. Phys. Lett.* **72**, 3458 (1998).
27. J.D. Holmes, K.P. Johnston, R.C. Doty and B.A. Korgel, *Science* **287**, 1471 (2000).
28. R.S. Wagner, *Whisker Technology*, Ed. A.P. Levitt (Wiley, New York, 1970).
29. Y. Wu and P. Yang, *JACS* **123**, 3165 (2001).
30. J. Hu, T.W. Odom and C.M. Lieber, *Acc. Chem. Res.* **32**, 435 (1999).
31. Y. Wu, Y. Cui, L. Huynh, C.J. Barrelet, D.C. Bell and C.M. Lieber, *Nano Lett.* **4**, 433 (2004).
32. S.L. Hong, *J. Korean Phys. Soc.* **37**, 93 (2000).
33. Y. Cui and C.M. Lieber, *Science* **291**, 851 (2001).
34. G. Zheng, W. Lu, S. Jin and C.M. Lieber, *Adv. Mater.* **16**, 1890 (2004).
35. S. Jin, D. Whang, M.C. McAlpine, R.S. Friedman, Y. Wu and C.M. Lieber, *Nano Lett.* **4**, 915 (2004).
36. S.W. Chung, J. Yu and J.R. Heath, *Appl. Phys. Lett.* **76**, 2068 (2000).
37. S.M. Sze, *Physics of Semiconductor Devices* (Wiley, New York, 1981).
38. R. Martel, T. Schmidt, H.R. Shea, T. Hertel and P. Avouris, *Appl. Phys. Lett.* **73**, 2447 (1998).
39. O. Madelung, "Semiconductors: intrinsic properties of group IV elements and III–V and II–VI and I–VII compounds", in *LANDOLT-BÖRNSTEIN New Series: Vol III/22a*, Ed. O. Madelung (Springer-Berlin, Heidelberg, 1987).
40. R. Chau, J. Kavalieros, B. Doyle, A. Murthy, N. Paulsen, D. Lionberger, D. Barlage, R. Arghavani, B. Roberds and M. Doczy, *IEDM Tech. Digest* 29.1.1 (2001).
41. A. Javey, J. Guo, D.B. Farmer, Q. Wang, E. Yenilmez, R.G. Gordon, M. Lundstrom and H. Dai, *Nano Lett.* **4**, 1319 (2004).
42. M. Shur, *Physics of Semiconductor Devices* (Prentice Hall, Englewood, NJ, 1990).
43. D.A. Neamen, *Semiconductor Physics and Devices* (McGraw-Hill, New York, 1997).

44. H. Grabert and M.H. Devoret, Eds., *Single Charge Tunneling: Coulomb Blockade Phenomena in Nanostructures* (Plenum, New York, 1992).
45. L.P. Kouwenhoven, C.M. Marcus, P.L. McEuen, S. Tarucha, R.M. Westervelt and N.S. Wingreen, *Electron Transport in Quantum Dots*, Eds. L.L. Sohn, L.P. Kouwenhoven and G. Schön (Kluwer, Dordecht, 1997).
46. M.A. Green, *J. Appl. Phys.* **67**, 2944 (1990).
47. F.V. Mikulec, M. Kuno, M. Bennati, D.A. Hall, R.G. Griffin and M.G. Bawendi, *JACS* **122**, 2532 (2000).
48. A. Tilke, R.H. Blick, H. Lorenz and J.P. Kotthaus, *J. Appl. Phys.* **89**, 8159 (2001).
49. T. Altebaeumer and H. Ahmed, *Jpn. J. Appl. Phys. Part 1* **42**, 414 (2003).
50. D.H. Cobden, M. Bockrath, P.L. McEuen, A.G. Rinzler and R.E. Smalley, *Phys. Rev. Lett.* **81**, 681 (1998).
51. J.A. Folk, C.M. Marcus, R. Berkovits, I.L. Kurland, I.L. Aleiner and B.L. Altshuler, *Phys. Scripta* **T90**, 26 (2001).
52. G. Feher, J.C. Hensel and E.A. Gere. *Phys. Rev. Lett.* **5**, 309 (1960).
53. Y. Huang, X. Duan, Y. Cui, L.J. Lauhon, K.H. Kim and C.M. Lieber, *Science* **294**, 1313 (2001).
54. Y. Huang, X. Duan, Q. Wei and C.M. Lieber, *Science* **291**, 630 (2001).
55. Z. Zhong, D. Wang, Y. Cui, M.W. Bockrath and C.M. Lieber, *Science* **302**, 1377 (2003).
56. L.J. Lauhon, M.S. Gudiksen, D. Wang and C.M. Lieber, *Nature* **420**, 57 (2002).
57. A. DeHon, *IEEE Trans. Nanotech.* **2**, 23 (2003).
58. Y. Chen, G.Y. Jung, D.A.A. Ohlberg, X. Li, D.R. Stewart, J.O. Jeppesen, K.A. Nielsen, J.F. Stoddart and R.S. Williams, *Nanotech.* **14**, 462 (2003).
59. Y. Luo, C.P. Collier, J.O. Jeppesen, K.A. Nielsen, E. Delonno, G. Ho, J. Perkins, H.R. Tseng, T. Yamamoto, J.F. Stoddart and J.R. Heath, *Chem. Phys. Chem.* **3**, 519 (2002).
60. X. Duan, C. Niu, V. Sahi, J. Chen, J.W. Parce, S. Empedocles and J.L. Goldman, *Nature* **425**, 274 (2003).
61. M.C. McAlpine, R.S. Friedman, S. Jin, K. Lin, W.U. Wang and C.M. Lieber, *Nano Lett.* **3**, 1531 (2003).
62. J.A. Rogers, Z. Bao, K. Baldwin, A. Dodabalapur, B. Crone, V.R. Raju, V. Kuck, H. Katz, K. Amundson, J. Ewing and P. Drzaic, *PNAS* **98**, 4835 (2001).
63. H. Sirringhaus, T. Kawase, R.H. Friend, T. Shimoda, M. Inbasekaran, W. Wu and E.P. Woo, *Science* **290**, 2123 (2000).
64. P.A. Smith, C.D. Nordquist, T.N. Jackson, T.S. Mayer, B.R. Martin, J. Mbindyo and T.E. Mallouk, *Appl. Phys. Lett.* **77**, 1399 (2000).
65. A. Tao, F. Kim, C. Hess, J. Goldberger, R. He, Y. Sun, Y. Xia and P. Yang, *Nano Lett.* **3**, 1229 (2003).
66. D. Whang, S. Jin, Y. Wu and C.M. Lieber, *Nano Lett.* **3**, 1255 (2003).
67. D. Whang, S. Jin and C.M. Lieber, *Jpn. J. Appl. Phys. Part 1* **43**, 4465 (2004).
68. A. Ulman, *An Introduction to Ultrathin Organic Films: From Langmuir–Blodgett to Self-assembly* (Academic Press, New York, 1991).
69. G. Marsh, *Mater. Today* **6**, 28 (2003).
70. S.Y. Chou, P.R. Krauss and P.J. Renstrom, *Science* **272**, 85 (1996).
71. R.S. Friedman, M.C. McAlpine, D.S. Ricketts, D. Ham and C.M. Lieber, *Nature* **434**, 1085 (2005).
72. A. Bachtold, P. Hadley, T. Nakanishi and C. Dekker, *Science* **294**, 1317 (2001).
73. A. Javey, Q. Wang, A. Ural, Y. Li and H. Dai, *Nano Lett.* **2**, 929 (2002).
74. W. Clemens, W. Fix, J. Ficker, A. Knobloch and A. Ullmann, *J. Mater. Res.* **19**, 1963 (2004).
75. K. Hiranaka, T. Yamaguchi and S. Yanagisawa, *IEEE Electron Device Lett.* **7**, 224 (1984).
76. F. Patolsky and C.M. Lieber, *Mater. Today* **8**, 20 (2005).
77. Y. Cui, Q. Wei, H. Park and C.M. Lieber, *Science* **293**, 1289 (2001).
78. G.F. Blackburn, *Biosensors: Fundamentals and Applications*, Eds. A.P.F. Turner, I. Karube and G.S. Wilson (Oxford University Press, Oxford, 1987).
79. R.K. Iler, *The Chemistry of Silica* (John Wiley & Sons, New York, 1979).
80. P.N. Bartlett, *Handbook of Chemical and Biological Sensors*, Eds. R.F. Taylor and J.S. Schultz (IOP Publishing, Philadelphia, PA, 1996).
81. W.U. Wang, C. Chen, K. Lin, Y. Fang and C.M. Lieber, *PNAS* **102**, 3208 (2005).
82. F. Patolsky, G. Zheng, O. Hayden, M. Lakadamyali, X. Zhuang and C.M. Lieber, *PNAS* **101**, 14017 (2004).

83. J. Hahm and C.M. Lieber, *Nano Lett.* **4**, 51 (2004).
84. K. Stadler, V. Masignani, M. Eickmann, S. Becker, S. Abrignani, H.D. Klenk and R. Rappuoli, *Nat. Rev. Microbiol.* **1**, 209 (2003).
85. R.M. Atlas, *Nat. Rev. Microbiol.* **1**, 70 (2003).
86. E. Niiler, *Nat. Biotechnol.* **20**, 21 (2002).
87. L.J. Lauhon, M.S. Gudiksen and C.M. Lieber, *Phil. Trans. R. Soc. Lond. A* **362**, 1247 (2004).
88. A. Bachtold, M.S. Fuhrer, S. Plyasunov, M. Forero, E.H. Anderson, A. Zettl and P.L. McEuen, *Phys. Rev. Lett.* **84**, 6082 (2000).
89. A. DeHon, P. Lincoln and J.E. Savage, *IEEE Trans. Nanotech.* **2**, 165 (2003).
90. M.T. Bjork, C. Thelander, A.E. Hansen, L.E. Jensen, M.W. Larsson, L.R. Wallenberg and L. Samuelson, *Nano Lett.* **4**, 1621 (2004).
91. J.M. Golden and B.I. Halperin, *Phys. Rev. B* **53**, 3893 (1996).
92. F.R. Waugh, M.J. Berry, D.J. Mar, R.M. Westervelt, K.L. Campman and A.C. Gossard, *Phys. Rev. Lett.* **75**, 705 (1995).
93. D. Wang and C.M. Lieber, *Nature Mater.* **2**, 355 (2003).
94. D.J. Milliron, S.M. Hughes, Y. Cui, L. Manna, J. Li, L. Wang and A.P. Alivisatos, *Nature* **430**, 190 (2004).
95. L. Manna, D.J. Milliron, A. Meisel, E.C. Scher and A.P. Alivisatos, *Nature Mater.* **2**, 382 (2003).
96. P. Gao and Z.L. Wang, *J. Phys. Chem. B* **106**, 12653 (2002).
97. J.Y. Lao, J.G. Wen and Z.F. Ren, *Nano Lett.* **2**, 1287 (2002).
98. H. Yan, R. He, J. Johnson, M. Law, R.J. Saykally and P. Yang, *J. Am. Chem. Soc.* **125**, 4728 (2003).
99. K.A. Dick, K. Deppert, M.W. Larsson, T. Mårtensson, W. Seifert, L.R. Wallenberg and L. Samuelson, *Nature Mater.* **3**, 380 (2004).

CHAPTER SIX

Theoretical Advances in the Electronic and Atomic Structures of Silicon Nanotubes and Nanowires

Abhishek Kumar Singh,[1,2] Vijay Kumar[3,4,5] and Yoshiyuki Kawazoe[2]

Contents

6.1 Introduction 218
6.2 Computational Approach 220
6.3 Silicon Nanotubes 220
- 6.3.1 Metal Encapsulated Nanotubes of Silicon 222
- 6.3.2 Electronic Structure and Bonding Nature 225
- 6.3.3 Magnetism in Metal Encapsulated SiNTs 228

6.4 Germanium Nanotubes 231
- 6.4.1 Metallic and Semiconducting Nanotubes of Ge 233

6.5 Silicon Nanowires 235
- 6.5.1 Non-Crystalline Pristine SiNWs 237
- 6.5.2 Crystalline Pristine SiNWs 238
- 6.5.3 Band Structure of SiNWs 243

6.6 Hydrogenated Nanowires 244
- 6.6.1 Electronic Structure of Hydrogenated SiNWs 249
- 6.6.2 Effects of Doping and H Defects 251

6.7 Nanowire Superlattices 253
6.8 Conclusion and Perspective Remarks 254
Acknowledgements 255
References 255

Abstract

Nanotubular and nanowire structures of silicon are currently of great interest for miniature devices. Recently, using cluster assembly approach, nanotubular forms of silicon have been shown to be stabilized by encapsulation of metal atoms. Here we review these developments and discuss the stability of such nanostructures and their electronic properties

[1] Materials Department, University of California Santa Barbara, Santa Barbara, CA, USA.
[2] Institute for Materials Research, Tohoku University, Aoba-ku, Sendai, Japan.
[3] Dr. Vijay Kumar Foundation, 45 Bazaar Street, K. K. Nagar (West), Chennai, India.
[4] The Institute of Mathematical Sciences, Taramani, Chennai, India.
[5] Research Institute for Computational Sciences (RICS), National Institute of Advanced Industrial Science and Technology (AIST), AIST Tsukuba Central 2, Umezono, Tsukuba, Japan.

Nanosilicon
9780080445281

Copyright © 2007. Elsevier Ltd.
All rights reserved.

including metallic, semiconducting, and magnetic behaviours. Hydrogenated and oxygenated structures of silicon can also be made in tubular forms. These could be among the thinnest semiconducting nanostructures of silicon. Thicker quasi-one-dimensional structures of silicon have been grown in the form of nanowires which could be metallic or semiconducting. We discuss surface reconstruction in such nanowires and their electronic properties. Further effects of *p*- or *n*-type doping as well as hydrogen defects on the atomic and electronic structures of hydrogenated Si nanowires are presented. The metallic, semiconducting, and optical properties of silicon in such nanostructures could make it possible to develop novel silicon-based nanodevices.

6.1 Introduction

Nanoforms of silicon hold great promise for nanotechnology as bulk silicon has been for microelectronics. Silicon acquires a much desired advantage at the nanoscale that it could be luminescent in the visible range. In 1991, an important breakthrough happened when photoluminescence was discovered from porous silicon [1]. It was thought to be due to the formation of quasi-one-dimensional structures or the presence of nanoparticles. Since then much progress has been made in the understanding of the properties of nanoparticles and quasi-one-dimensional structures of silicon such as nanotubes and nanowires and new opportunities have opened up for novel applications in nanodevices. In recent years it has become possible to synthesize silicon nanowires (SiNWs) as well as nanoparticles with a control on size and several potentially important applications have been demonstrated in laboratory. The finding of bright luminescence in nanoforms of silicon in contrast to bulk, which is a bad emitter of light, could help in achieving a long standing goal of the integration of optoelectronic with microelectronics and this could offer entirely new applications of silicon.

Another strong reason for the intense research on nanoforms of silicon is that in the top-down approach it is perceived that the continuously shrinking size of the silicon-based device components will hit a road block due to the chemical and the physical limitations. Therefore, much research is being done to find alternate device components for future technologies. In the bottom-up approach, nanoparticles and quasi-one-dimensional structures of silicon, molecular electronics, and carbon nanotubes have been attracting much attention. The mechanical stability as well as ballistic transport properties of carbon nanotubes [2] are attractive and several possibilities of their applications [3–10] have been explored over the past decade. There is, however, a problem from the point of view of devices in that nanotubes of different diameters and chirality often coexist. As nanotubes with different chirality could be semiconducting or metallic, it is important to separate them for device applications and it is still a big problem for commercial application. On the other hand conventional silicon-based device fabrication technology is so well established that only overwhelmingly compelling new technology will be able to replace it. Therefore, continuous efforts are going on for understanding the properties of nanoforms of silicon as well as the miniaturization of silicon devices since they could prove to be more convenient and economical for commercialization than any other process as much is known about silicon and it could be possible to take advantage of the existing infrastructure. One such example is that

of a single electron transistor (SET) memory made up of silicon [11,12], whose fabrication process relies only on the technology already developed for MOSFETs (see Chapter Ten).

History of the SiNWs goes back to the finding of luminescence from porous silicon. Quasi-one-dimensional structures in the form of square or rectangular SiNWs were studied to understand the effects of quantum confinement [13–20]. These SiNWs were shown to have direct band gap which is important for luminescence. Progress has been more rapid in recent years and currently, it has become possible to produce SiNWs with a control on size and growth direction [21–26]. These developments have stimulated much theoretical and experimental research. Efforts are being made to develop a fundamental understanding of the electronic, optical, magnetic, thermal, and mechanical properties of such materials and their dependence on size and morphology as well as the changes due to interaction with other species. As a large fraction of atoms in a nanowire lies on the surface, the extensive knowledge available on the atomic and electronic structures of the surfaces of bulk silicon offers an advantage to understand the surface properties of SiNWs and to fabricate functional devices. Doping of SiNWs by boron and phosphorus has been achieved to develop [27,28] *p*- and *n*-type elements for active devices, and even integration of such devices to perform some of the basic computations [29] has been demonstrated (see Chapter 5). SiNWs are biocompatible and their potential for biological as well as chemical sensors even at the molecular scale has been demonstrated [30–35]. Boron-doped SiNWs have been shown [30] to be highly sensitive and selective nanosensors for biological and chemical species. SiNWs functionalized with amines and an oxide layer exhibit pH-dependent conductance due to the change in the surface charge during protonation and deprotonation. Biotin-modified SiNWs are used to detect streptavidin down to at least a picometer concentration range. Antigen functionalized SiNWs show reversible antibody binding and concentration-dependent detection in real time. The details of these developments are covered in Chapter Five.

Besides SiNWs, nanotubes are the other structures in quasi-one-dimensional form and several theoretical studies have been made on the stability of tubular forms of silicon similar to the carbon nanotubes [36–39]. It has been found that diamond-like nanowire structures are more favourable for silicon than nanotubes. There are experimental reports of tubular form of silicon where nanotubes [40–42] are formed with a very thick tube wall. However, these have not yet been well understood. A novel nanoform of silicon has recently emerged where metal encapsulation is used to realize silicon fullerenes [43–52] and nanotubes [53–56]. These are more stable than nanostructures formed from elemental silicon, have high symmetries, and potential for mass production with size selection. Their electrical, magnetic, and optical properties [57] can be changed by changing the metal atoms. Metal encapsulated silicon clusters could be assembled to form new varieties of silicon. Many different promising properties such as metallic behaviour [53], magnetism [54], vibrational, and optical properties have been found. The details have been covered by Kumar in a separate chapter. Here we shall discuss the assembly of metal encapsulated clusters that led to the discovery of metal encapsulated silicon nanotubes (SiNTs).

There are several important factors that differentiate nanoforms of a material from the corresponding bulk phases. The large fraction of atoms lying on the surface of a nanomaterial could lead to atomic structures that are different from bulk. A quantitative

understanding of these from experiments is difficult. For SiNWs, the presence of edges where two facets meet could lead to new reconstructions that are not known on flat bulk surfaces while thin SiNWs and SiNTs may have completely new structures. The dangling bonds on the surface could lead to states within the band gap and may dramatically affect the optical properties. For nanostructures with lateral dimensions of the order of the carrier de Broglie wavelength, quantum confinement could affect the gap energies leading to the possibility of visible photoluminescence and therefore new applications of silicon. The properties of such structures and their applications rely heavily on the electronic structure. Therefore, for the rapid development of this field, advances in the understanding of the atomic and electronic structures of SiNWs and SiNTs as well as the various possible ways to modify these are very important. Computer simulations can play a very important role in understanding the properties and phenomena under controlled conditions. It is also important that such calculations are performed using tools that have predictive capabilities. Here we review such theoretical developments on quasi-one-dimensional structures of silicon that are currently attracting much attention (see also Chapter Eight). A brief summary of the computational approaches that have been employed for the study of these system is given in the next section.

6.2 Computational approach

Theoretical results presented in this chapter have been mostly obtained using *ab initio* electronic structure calculations based on the solution of the Kohn–Sham equations within the density functional theory (DFT) [58]. DFT has been enormously successful using the local density approximation (LDA) and by taking into account gradient corrections within the generalized gradient approximation (GGA) [59] which often improves the LDA results by correcting the overbinding. Although different ways exist to solve the Kohn–Sham equations, a plane wave basis approach using pseudopotentials [60,61] is quite efficient for understanding the chemical bonding and associated properties of such systems. It seems to be most advantageous particularly in cases where ion dynamics needs to be performed and this is often the case for nanomaterials. The basis set is complete and the calculations can be performed on an equal footing for a variety of systems such as molecules, nanotubes, nanowires, quantum dots, perfect crystals, defects, and surfaces. Therefore, this method provides a possibility to understand the evolution of the properties of matter from atomic and molecular levels to the bulk phase with the same level of accuracy. Results obtained by such methods often agree with experiments closely and in some cases even predictions have received subsequent experimental support. Such simulations can be very advantageous in exploring different possibilities and to design new materials even before experiments are done.

6.3 Silicon nanotubes

The discovery of carbon nanotubes led to the curiosity if similar structures of silicon could be formed. However, unlike carbon, which can form *sp*, sp^2, and sp^3

bonded structures, silicon prefers predominantly sp^3 bonding and does not exist in sp^2 bonded form by itself. Puckered layers exist in AlB_2 type compound $Ca(Al_xSi_{1-x})_2$ or $Sr(Ga,Si)_2$ and this has been considered to be a possible system that could lead to the formation of nanotubes [62,63] (see Fig. 6.1). Seifert *et al.* have studied [62] the stability of such a nanotube by folding a puckered sheet. In these compounds large charge transfer takes place between Ca and Al/Si atoms and therefore Si atoms are in approximately Si^- configuration. The stability of such a charged hypothetical SiNT was studied by using a tight binding method and it was found to be stable [63]. In Si^- configuration, a Si atom can be replaced by a P atom and nanotubes of P with similar structure have also been found to be stable [64]. In another approach the dangling bonds in such a nanotube have been saturated by H atoms to form a nanotube of Si—H. Due to the puckered nature H atoms are on both the sides of a nanotube. A graphite type layer of Si with H atoms on one side is found to be unstable. However, small nanotubes with dangling bonds on the outer side passivated by H atoms are stable because the bonding in small nanotubes becomes more sp^3 type.

There are reports of the stability of (n,m) type SiNTs with hexagonal atomic structures similar to those of carbon nanotubes. However, a comparative study [65] of the hexagonal and puckered SiNTs showed puckered nanotubes to be more stable and it supports the preference for sp^3 bonding in tubular structures of silicon. The (n,n) SiNTs ($n = 5$–11) were found to be semiconducting. The band gap decreases with an increase in diameter. On the other hand $(n,0)$ SiNTs ($n = 10$–24) are semiconducting

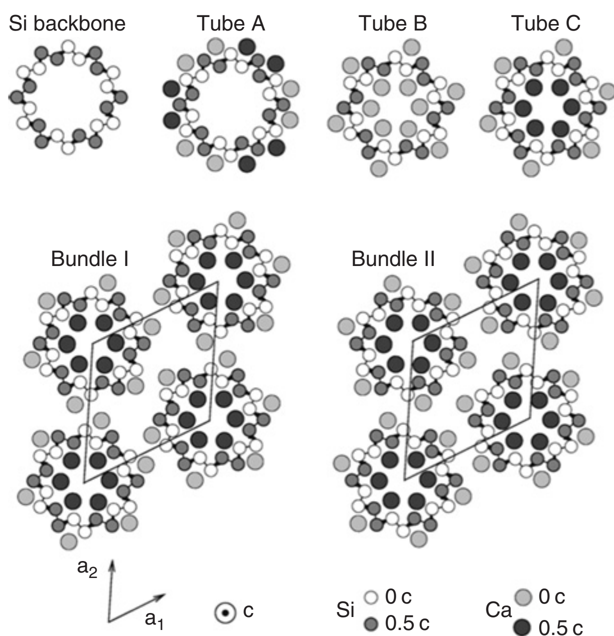

Figure 6.1 Schematic drawing of the cross-sections of nanotubes with different possibilities to accommodate 12 Ca atoms of the $CaSi_2$ in (6,6) tube. The bright Si and Ca atoms are located at 0 c and the dark ones at 0.5 c along the c-axis. The different packing schemes investigated in this study are also depicted in the lower part of the figure (Reproduced with permission from Ref. [63] copyright APS 2003).

but the band gap decreases in a period of 3. The (n,0) SiNTs with $n = 5$–9 are metallic as for small diameter nanotubes the mixing of $\sigma^\star$ and $\pi^\star$ states is strong. Fagan *et al.* [37] showed that the strain energy to fold a hexagonal sheet of Si into a nanotube is about 0.04 eV/atom which is similar to the value of carbon nanotubes. However, a graphene-like sheet of Si has 0.83 eV/atom lower binding energy (BE) as compared to the diamond structure and this makes the stabilization of a graphene-like sheet of Si difficult. The cohesive energy of a hexagonal nanotubes of Si is about 82% of the bulk value while for carbon nanotubes it is around 99%. There are reports [66] of the production of self-assembled SiNTs from a powder of silicon monoxide under supercritical hydrothermal condition with a temperature of 470°C and a pressure of 6.8 MPa. These multiwalled nanotubes have closed caps with a pore inside and 0.31 nm interplanar spacing. On the outer side there are 2–3 nm thick amorphous layers of SiO_2. SiNTs have also been grown [40] on a regular array of hexagonal porous alumina by molecular beam epitaxy (see Fig. 6.2). The outer layers of such nanotubes are also covered with an oxide layer.

An alternative approach to stabilize sp^2 bonding in silicon and to form nanotubes could be by doping Si with metal atoms. As briefly mentioned above, metal encapsulation has led to novel fullerene-like and other polyhedral clusters of silicon and germanium [67]. Assembly of metal encapsulated clusters has been shown [68] to lead to the formation of silicon and germanium nanotubes. The properties of such nanotubes are controlled by the metal atoms and it has been possible to develop metallic, semiconducting, and magnetic nanotubes. In the following we discuss these developments.

6.3.1 Metal Encapsulated Nanotubes of Silicon

Silicon has 6-membered rings in the bulk diamond structure. In an effort to develop quasi-one-dimensional structures of Si, stacking of such 6-membered chair-shaped units was considered [53]. The optimized structures of such assemblies (Fig. 6.3) were

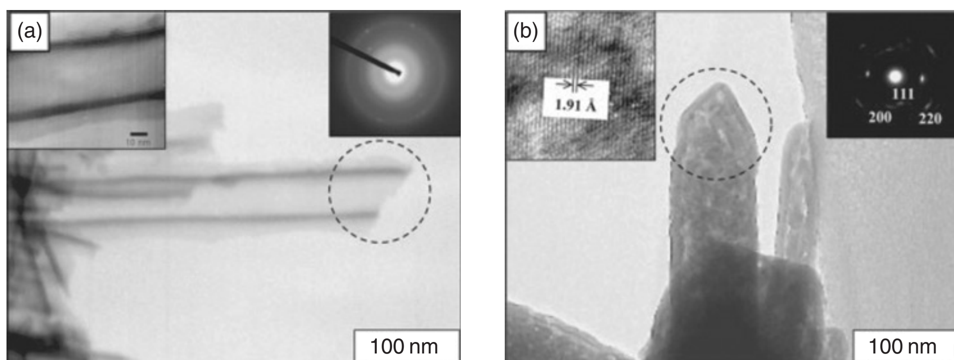

Figure 6.2 (a) Typical transmission electron microscope images (TEM) of the SiNTs. The dark and bright areas indicate Si and SiO_2 layers, respectively. The wall thickness of the SiNTs are 4–5 nm, shown in left inset. The dotted circle marked the tip morphology of the SiNTs. Inset left: High-magnification image of the SiNTs; right: the selected area electron diffraction pattern (SAED) rings taken from the SiNTs. (b) TEM image of SiNTs after HF treatment. Inset left: HRTEM image reveals that lattice fringe of the silicon wall is about 1.91 Å; right: the SAED pattern spot taken from the SiNTs (Reproduced with permission from Ref. [40]).

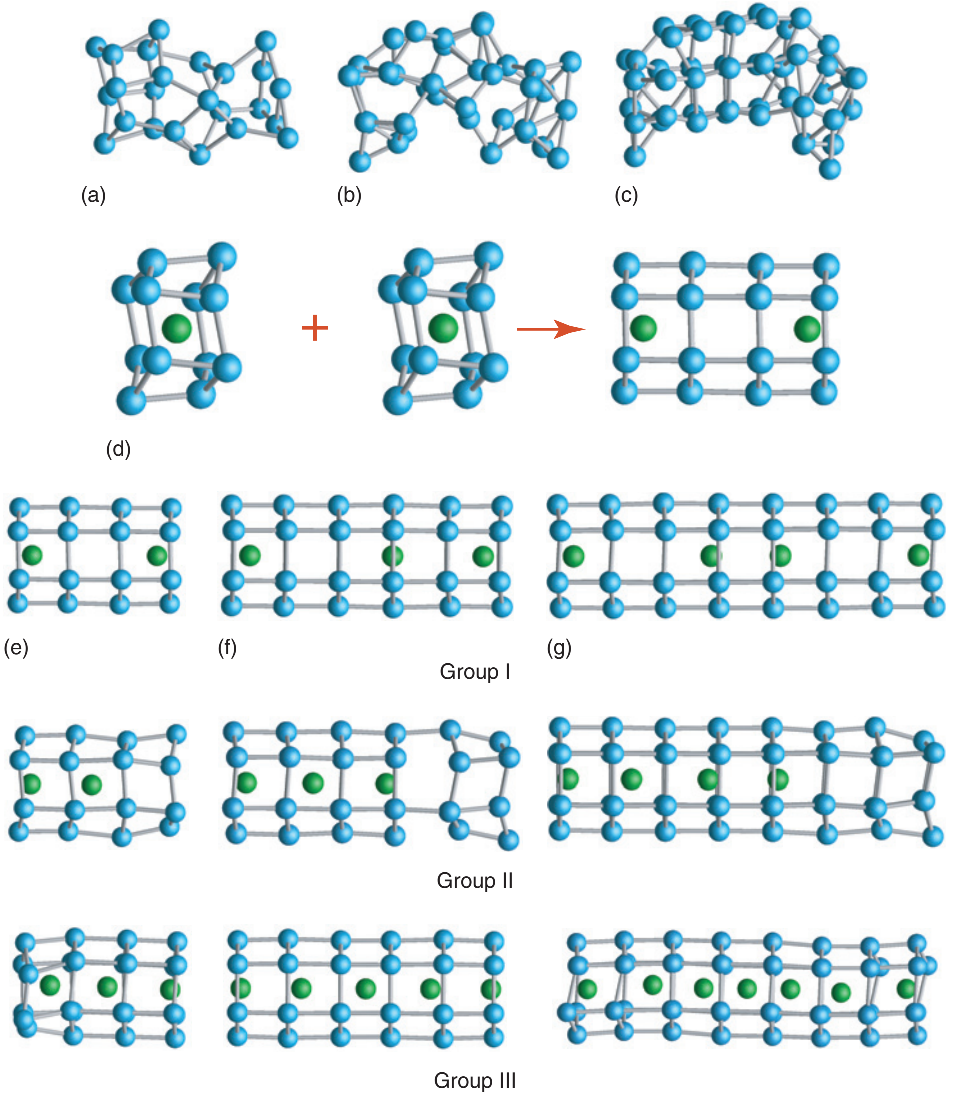

Figure 6.3 (a), (b), and (c) show optimized structures of SiNTs Si_{24}, Si_{36}, and Si_{48}, respectively, formed by stacking of hexagonal units. The structures show preference for transformation from quasi-one-dimensional to three-dimensional structures in the case of pure silicon. (d) Shows the structural transformation that occurs from the chaired structure of $Si_{12}Be$ cluster to a hexagonal shape when two units of $Si_{12}Be$ are brought together to form nanotube. (e), (f), and (g) show the finite-doped $Si_{24}Be_x$ (x = 2 and 3), $Si_{36}Be_x$ (x = 3 and 5), and $Si_{48}Be_x$ (x = 4 and 7) nanotubes, respectively. Groups I and II represent structures with the same number of Si and Be atoms but having different distributions of Be atoms, while the structures in Group III have higher concentrations of Be atoms. It can be clearly seen that undoped part of nanotubes are distorted showing the importance of Be atom doping. Group III shows an overdoping case which results in slight distortion in the nanotube (adopted from Ref. [53]).

found to show a tendency for agglomeration to three-dimensional structures. Several atoms tend to have tetrahedral coordination. This study showed the likelihood of long symmetric thin tubular forms of elemental Si to be doubtful. It has been also shown by Grossman *et al.* [69] that the elongated structures with the number of hexagonal units in the range of 10–29 can be stabilized by capping the ends with Si atoms. The stability could be further improved by replacing the capping element by B, Be, and N atoms. Also, similar to the case of hydrogen capped empty cage fullerene structures of silicon [70], simulations on growth dynamics of hydrogenated silicon nanostructures have shown that nanotubular hexagonal form of silicon [71] could be stabilized by H termination (see below) in a controlled way (Fig. 6.4).

Studies on reaction of silane gas with metal monomers and dimers showed a $Si_{12}W$ cluster with W atom at the centre of a hexagonal prism to be favoured without associating any H atoms [47]. This result suggested special stability of this cluster. Indeed the BE of H atom on this cluster was found [70] to be low and not favourable for dissociation of a hydrogen molecule. Assembly of such clusters were also considered to form a nanowire. However, it led to a distorted structure [70]. Further studies on encapsulation of a variety of metal atoms in Si cages showed a chair-shaped

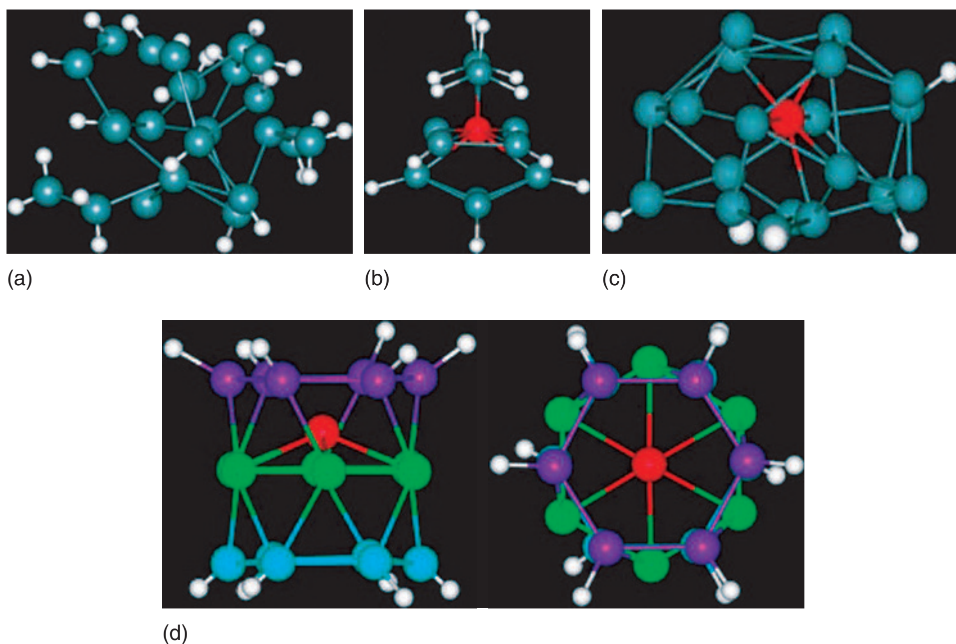

Figure 6.4 Typical structures of hydrogenated silicon nanoparticles created in a plasma reactor. (a) Typical example for an amorphous structure resulting from a growth mechanism in a pure silane plasma at room temperature; aggregation of those amorphous particles leads to the experimentally observed formation of dust particles; (b) typical example for a low atomic hydrogen flux giving rise to crystalline structures that are rich in hydrogen; (c) typical example for a high atomic hydrogen flux yielding crystalline structures relatively poor in hydrogen that are similar to those predicted for pure silicon clusters; (d) side and top view of a typical tube-like structure obtained with an intermediate atomic hydrogen flux. Hydrogen atoms are shown in white while the silicon atom inside is shown in red. The remaining atoms are Si atoms. The different colors of other atoms are to distinguish different hexagons (Reproduced with permission from Ref. [71] courtesy H. Vach).

structure (Fig. 6.3d) of $Si_{12}Be$ to be most stable. When two such $Si_{12}Be$ units were stacked together [50], surprisingly a transformation occurred from the chair-shaped units to a hexagonal shaped-nanotube as shown in Fig. 6.3d. In this nanotube form Be atoms are displaced from the centre of the hexagonal prism towards one of the hexagonal faces. Taking three units of $Si_{12}Be$, the rings were again found to be stable and hexagonal in shape but Be atoms were not symmetrically arranged and again displaced towards one of the hexagons in order to provide optimal bonding with the Si atoms. The third Be atom gets almost at the centre of the hexagonal prism. Studies on further doping and different arrangements of Be atoms showed the doped portion of the nanotube to be nearly symmetric and hexagonal in shape, while the undoped portion was distorted to chair-shaped structure, giving a clear indication of the stabilization of sp^2 bonding due to encapsulation of metal atoms. Further studies on nanotubes of different lengths showed $Si_{24}Be_2$ unit to be symmetric and the basic building block that could be repeated to form nanotubes of desired length. As shown in Fig. 6.3, the packing of two such units leads to a symmetric ($Si_{48}Be_4$) nanotube (Fig. 6.3g Group I) with very small sp^3 character. The BEs for different distributions of Be in a nanotube are rather similar. However, the highest occupied–lowest unoccupied molecular orbital (HOMO–LUMO) gap for finite nanotubes shows significant variation. It decreases as the length of the nanotube increases and finally the infinite nanotube becomes metallic. These results showed that in this quasi-one-dimensional structure, Peierls distortion does not take place and that nanotubes with stoichiometry $Si_{12}Be$ are quite stable with hexagonal rings of silicon. Such rings have predominantly sp^2 bonding and therefore offer the possibility of new nanostructures of Si stabilized by metal atoms. Further studies on the stability of doped infinite nanotubes with a unit cell of 24 Si atoms and 2, 3, or 4 Be atoms showed them to be stable. As in finite nanotubes, Be atoms in the lowest energy structures of $Si_{24}Be_2$, $Si_{24}Be_3$, and $Si_{24}Be_4$ infinite nanotubes were not exactly in between the hexagonal rings but slightly shifted towards one ring. Following these predictions, experiments have been performed on deposition of Be on Si(111)7 $\times$ 7 surface [72] and well-ordered structures have been obtained (Fig. 6.5) in a large area. These structures were interpreted in terms of the $Si_{24}Be_2$ units discussed above.

6.3.2 Electronic Structure and Bonding Nature

The electronic structure and the bonding nature of the metal encapsulated SiNTs can be understood by considering an effective unit cell Si_6Be of the $Si_{24}Be_4$ infinite nanotube (Fig. 6.6a and b). Figure 6.6c shows the band structures of a hypothetical Si_6 nanotube obtained by removing the Be atoms and the Si_6Be nanotube. A reasonable way to understand the electronic structure is to consider sp^2 bonding in hexagonal ring as shown in Fig. 6.6b. Such a ring of silicon consists of 24 valence electrons [73]. There are 6 σ bonds within the hexagonal ring which share 12 electrons. Considering the z-axis to be aligned with the nanotube axis, the p_z orbitals of Si atoms, lying perpendicular to the plane of the ring, form σ bonds with the neighbouring rings sharing six electrons. The bonding states corresponding to these σ bonds lie much below the HOMO and are fully occupied. The remaining six electrons lie in the six dangling bonds of the sp^2 orbitals projecting outwards of the ring. There is π bonding between these orbitals and the corresponding states lie close to the HOMO

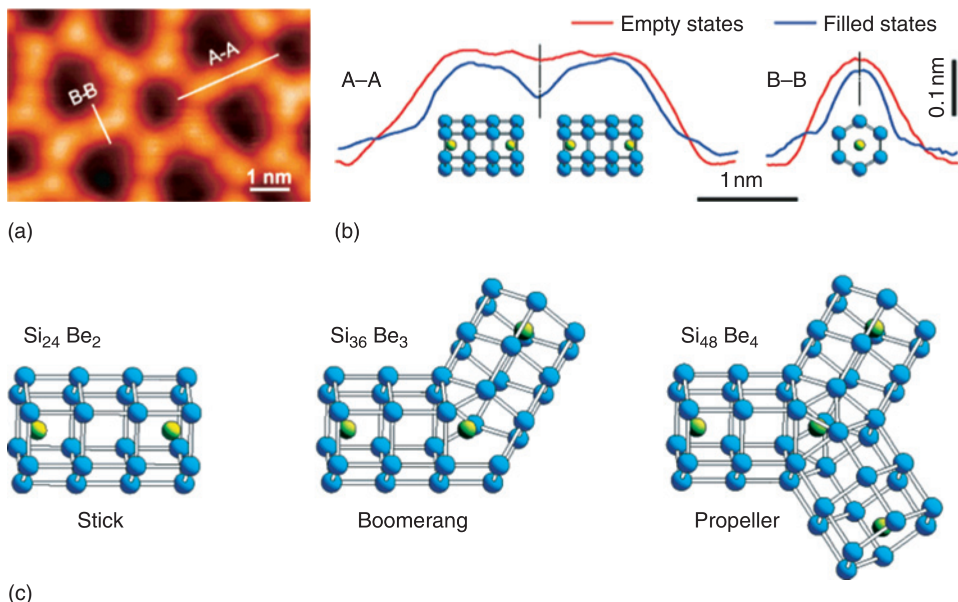

Figure 6.5 Atomic structure of the nanostructure building elements. (a) Fragment of the nanostructure array. (b) Line profiles along (A-A) and perpendicular (B-B) stick elements as indicated in (a). Red line for the empty states and blue line for the filled states. (c) Schematic diagram showing the hypothetical structure of the array building blocks: $Si_{24}Be_2$ for stick, $Si_{36}Be_3$ for boomerang, and $Si_{48}Be_4$ for propeller (Reproduced with permission from Ref. [72] copyright 2004 American Chemical Society).

(Fig. 6.6c). In an infinite nanotube, six deep lying bands arise from the 6 σ bonds within hexagons and another 3 bands arise from the σ bonds between the p_z orbitals. The three bands lying closest to the Fermi energy arise from the dangling bonds. Doping of Be leads to a strong hybridization between the p_z orbitals of Si and the p orbitals of Be atom which pushes the bands arising from the p_z orbitals down leading to a gain in energy. There is weak hybridization between the dangling sp^2 orbitals pointing outwards of the ring and the p orbitals of Be. The overall effect of this hybridization is a shift of the bands downward and the bands corresponding to p orbitals of Be get shifted upwards of the Fermi energy.

The above bonding picture is further confirmed by analysing the total and partial densities of states (DOS) of Si_6 and Si_6Be nanotubes (Fig. 6.6c). Clearly the states lying deeper are mostly from Si and the state in the middle are coming from Si and Be atoms whereas states near the Fermi energy are again from Si atoms. Therefore, conduction in this nanotube is predominantly through the SiNT. The metallicity of the nanotube is also due to the dangling bonds of silicon and not due to doping of metal atoms. The electronic charge density analysis of these nanotubes shows strong accumulation of charge within Si rings and between a metal atom and nearest Si ring whereas depletion of charge occurs between the metal atoms indicating no dimerization. There is a depletion of charge also from the p_z type orbitals of Si as well as a small depletion from the dangling sp^2 bonds. This is in line with the arguments given

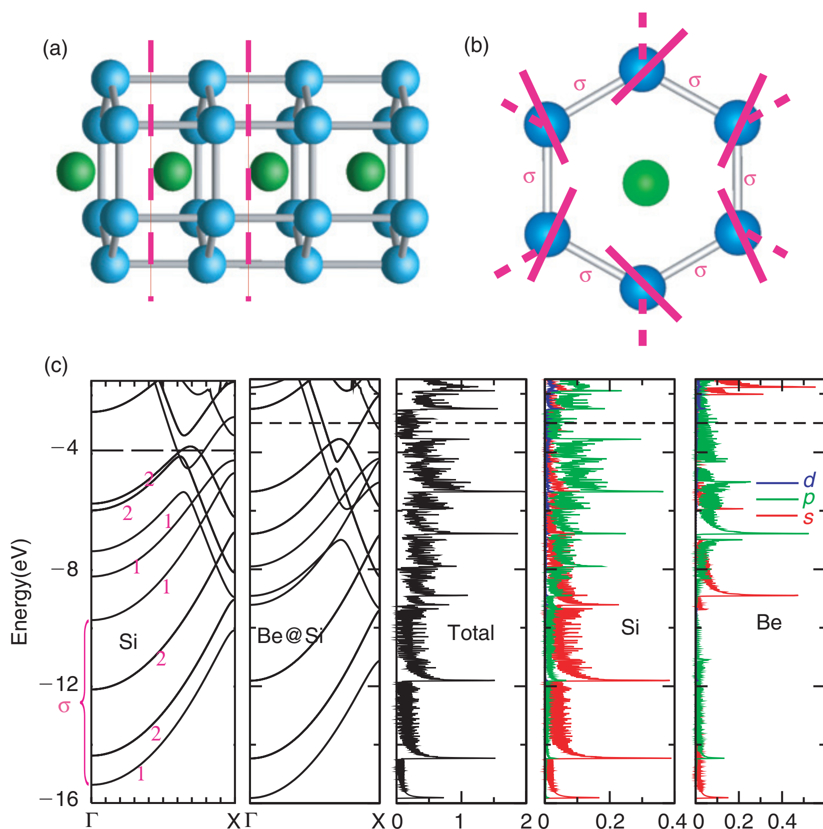

Figure 6.6 (a) Shows the unit cell of infinite nanotube $Si_{24}Be_4$. The broken lines indicate the effective Si_6Be unit cell. (b) Schematic representation of the bonding in the effective unit cell of the nanotube Si_6Be. Dotted lines represent six dangling bonds in the planar ring. Bonds between the Si atoms within the ring represent 6 σ bonds. Solid slanted lines represent six p_z orbitals, forming σ bonds with atoms in the adjacent unit cells. (c) Band structure of (i) Si_6 infinite nanotube obtained by removing Be atoms and keeping Si atoms fixed and (ii) Si_6Be nanotube. Numbers written in red represent the degeneracies of the bands. Corresponding total and partial DOS of Si_6Be infinite nanotube are also given for a better comparison. The typical feature of a one-dimensional system viz. the van Hove singularities, are present in the DOS.

above from the band structure and provides further evidence that strong interaction of Be atoms stabilizes hexagonal Si rings. These results should be contrasted with the possibilities of metal encapsulated carbon nanotubes as the bonding between carbon atoms in a nanotube is much stronger than between Si atoms and metal atom interaction with carbon nanotubes is generally weaker than in SiNTs. Therefore, doping of carbon nanotubes with metal atoms does not change its structure. However, for Si, metal doping has a very important role in controlling the structure as shown.

The above results very convincingly show that metal encapsulated nanotubes of silicon are one of thinnest most stable forms of quasi-one-dimensional nanostructure of silicon. They could find several interesting applications in nanodevices including those of spintronics.

6.3.3 Magnetism in Metal Encapsulated SiNTs

The fact that metal atoms can stabilize SiNTs opens up a possibility to develop magnetic nanostructures of silicon by using transition metal (TM) atoms. The latter have been shown to be particularly important for the stabilization of metal encapsulated silicon clusters. The embedding energy of TM atoms in silicon cages is large [43] due to very tight bonding which enhances the stability of elemental silicon clusters very significantly. Therefore, depending upon the size of the TM atom, cages of different sizes have been found to be optimal. Accordingly, doping of TM atoms could also lead to more stable SiNTs. Among TM atoms, 3*d* elements are relatively smaller in size and could lead to magnetism in nanotubes. Therefore, these atoms were considered to be most appropriate for doping of SiNTs. It is to be noted that encapsulation of W atoms [70] created distortions so that SiNT structure could not be obtained as mentioned before. Using smaller TM atoms the strain in Si—Si bonds can be minimized. Following the case of Be doping, the stability of $Si_{12}M$, M = Mn, Fe, Co, and Ni clusters was studied by Singh *et al.* [54] in order to explore the basic units that could be assembled in to nanotubes. As shown in Fig. 6.7a the hexagonal prism structure of $Si_{12}M$ was found to have the lowest energy for M = Mn, Fe, and Co as compared to the chair-shaped structure of $Si_{12}Be$ while in the case of Ni, the structure was found to be slightly distorted. Clusters with M = Mn, Fe, Co, and Ni have 1, 0, 1, and 0 μ_B magnetic moments, respectively, as the strong interaction with silicon atoms tend to quench the magnetic moments. Stacking of two units of the hexagonal prism clusters led to weak interaction and large separation (Fig. 6.7b) between the units particularly for $Si_{12}Mn$ due to its large HOMO–LUMO gap (Fig 6.7c). Doping of one more TM atom in between the units led to a structure that is slightly curved in a symmetric manner (Fig. 6.7b). However, continuation of the assembly and doping with a TM atom in between the prisms led to an increase in the BE of the nanotubes, an improved geometry with nearly planar Si hexagonal rings (Fig. 6.7b) and generally an enhancement in the magnetic moments as shown for M = Fe in Fig. 6.7c. The cohesive energy of the nanotubes lies in the range of 3.88–4.25 eV/atom as compared to 3.62–3.86 eV/atom for the Be-doped nanotubes (Fig. 6.7c). Therefore the stability of the nanotubes is enhanced more significantly by TM doping as it was expected.

The occurrence of magnetism in TM-doped SiNTs is an interesting aspect for developing nanoforms of silicon as this is in contrast to the behaviour in clusters. Studies on finite Fe- and Mn-doped SiNTs showed an increase in the local magnetic moments with an increase in the number of dopants for a given number of Si atoms (Fig. 6.7c). As the interaction between the TM atoms is also mediated via the silicon atoms, there is a possibility of the variation in the magnetic ordering with a change in doping. For Fe doping a transition occurs from antiferromagnetic to ferromagnetic coupling as the number of dopants is increased. Furthermore, the magnetic moments in a finite nanotube vary along the nanotube axis. The local moments in both the cases of Fe and Mn are highest towards the centre of the nanotubes and lowest at the ends. This is due to the fact that upon assembly of clusters, charge on silicon atoms gets shared with other Si atoms in the neighbouring ring at the cost of the interaction with the metal atom. This helps to enhance the magnetic moments on metal atoms away from the edges of the nanotube. The value of the local moments lies in the

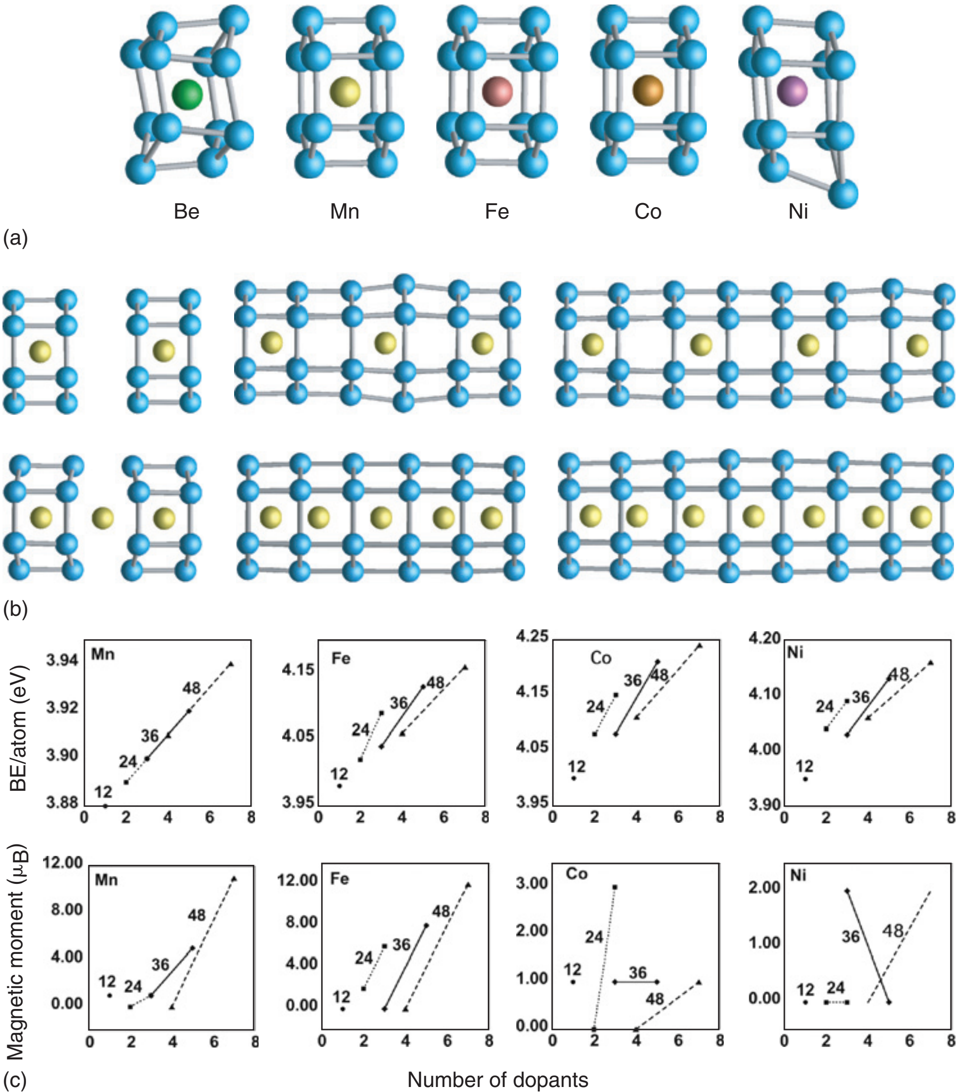

Figure 6.7 (a) Lowest energy structures of the finite nanotubes with stoichiometry $Si_{12}M$ (M = Be, Mn, Fe, Co, and Ni). (b) Structures of Fe-doped finite SiNTs with stoichiometries $Si_{24}Fe_2$, $Si_{36}Fe_3$, $Si_{48}Fe_4$, $Si_{24}Fe_3$, $Si_{36}Fe_5$, and $Si_{48}Fe_7$. (c) Plots of BE/atom and magnetic moment as a function of the number of dopant atoms for finite TM-doped Si nanotubes. The number of Si atoms is indicated above each line (adopted from Ref. [54]).

range of 1.0–2.6 μ_B for Fe and 0–3.6 μ_B for Mn-doped nanotubes. The magnetic moments in Co-doped nanotubes are lower, while in Ni-doped SiNTs these are in most cases completely quenched due to the lower value of the magnetic moments and small exchange splitting in a Ni atom. Therefore, as we go from Mn towards Ni in the 3*d* series, there is a general tendency of decreasing magnetic moments. This can in general be expected as the magnetic moments in TM atoms also show this trend.

When $Si_{12}M$ cluster units interact to form a nanotube, there is an increase in the Si—Si and TM—Si bond lengths. A similar increase in the cage size was obtained [70] due to the capping of H atoms on metal encapsulated clusters of silicon such as $Si_{12}Cr$. It led to the development of magnetic moments in this cluster due to the weakening of the interaction between the cage and the metal atom. H termination of these clusters has a similar effect as the linking between the clusters in nanotubes. This is further supported from the fact that a small or zero local magnetic moment is found on metal atoms that lie towards the edges of the finite nanotubes while large moments occur on atoms that are away from the edges of the nanotubes. The high magnetic moments of $Si_{48}Fe_7$ (1.7 μ_B per Fe atom) and $Si_{48}Mn_7$ (1.6 μ_B per Mn atom) suggest that such nanotubes could be useful for magnetic device applications.

The infinite nanotubes with the stoichiometry $Si_{24}M_4$ and $Si_{24}M_2$ show enhanced stability due to doping of M atoms. An interesting finding has been the change in the position of the dopant atom for different M. In the ferromagnetic phase of the infinite $Si_{12}M$ nanotube, M = Mn, Fe, and Co, the M atom lies at 0.98, 0.79, and 0.27 Å away from a hexagonal ring, respectively, while Ni atoms lie at the centres of the hexagons as shown in Fig. 6.8a. The BEs of all the infinite SiNTs are higher than the values for the corresponding finite nanotubes. The infinite Fe-doped SiNT has ferromagnetic coupling with a high magnetic moment of 2.4 μ_B per Fe atom. This value is nearly the same as in bulk Fe. The antiferromagnetically coupled Fe-doped SiNT is 0.70 eV higher in energy, indicating that the ferromagnetic phase is quite stable. The quasi-one-dimensionality of this nanotube along with its high magnetic moments makes it attractive for use as a nanoscale magnet. On the other hand Mn atoms prefer an interesting spin arrangement in which pairs of ferromagnetically coupled Mn atoms are antiferromagnetically coupled with their neighbouring pairs, resulting in zero net moment. The ferromagnetically coupled pairs are 2.55 Å apart as compared to 2.40 Å for the antiferromagnetically coupled pairs. Therefore, there is a dimerization of the antiferromagnetically coupled Mn atoms such that these are 1.12 and 1.18 Å away from the hexagons. The local magnetic moments on the Mn atoms range from 2.4–2.7 μ_B. This configuration, however, is only 0.03 eV lower in energy than

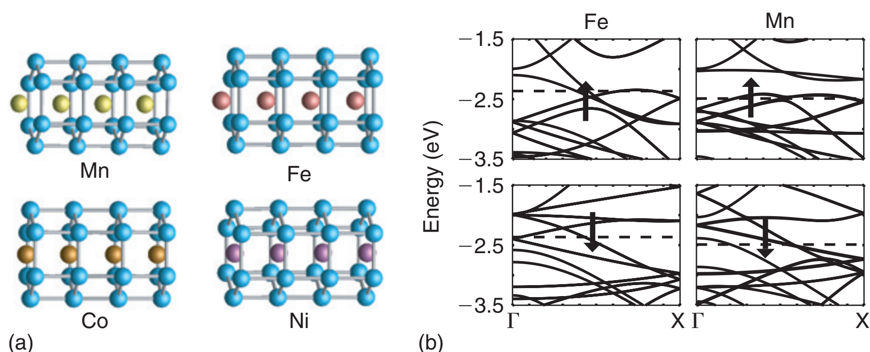

Figure 6.8 (a) Structures of infinite $Si_{24}M_4$ (M = Mn, Fe, Co, and Ni) nanotubes. (b) Band structures of the infinite $Si_{24}Fe_4$ and $Si_{24}Mn_4$ ferromagnetic nanotubes along the nanotube axis. Both the spin-up and spin-down band structures are shown. The Fermi energies are represented by dashed lines. In both cases the nanotubes are metallic (after Ref. [54]).

the corresponding ferromagnetically coupled SiNT. This result shows that a transformation from antiferromagnetic to ferromagnetic coupling in the Mn-doped nanotubes may be achieved by application of a weak magnetic field and suggests that spin-polarized current flow could be controlled by applying a magnetic field. The BE for the Mn-doped nanotube is almost 90% of the bulk cohesive energy of Si within GGA. For the Co- and Ni-doped infinite SiNTs, ferromagnetic and antiferromagnetic starting configurations converge to non-magnetic solutions and therefore in these cases the SiNTs are non-magnetic.

Figure 6.8b shows the band structures of Fe- and Mn-doped SiNTs. In all cases there is band crossing at the Fermi level for both the spin-up and spin-down components, indicating metallic behaviour. The band structure of the Mn-doped ferromagnetic nanotube shows a gap just above the Fermi energy for the spin-up component and therefore there could be interesting possibilities of making half-metallic nanotubes by inducing a small shift in the Fermi energy such as by doping. The antiferromagnetic Mn-doped nanotube shows a quite different band structure, as the periodicities in the two cases are different. Thus, doping of TM atoms leads to enhanced stability of SiNTs and new possibilities of magnetic nanostructures of silicon.

It is interesting to mention here that the hexagonal SiNTs have similarity with the rare earth-doped SiNWs grown on a Si substrate [74–77]. In this case the hexagonal tubes are linked and form a strip. Andriotis *et al.* [56] have shown that V doping could also lead to the formation of SiNTs with similar structure. The nanotubes obtained by Andriotis *et al.* were also metallic and have slight magnetic moment. Furthermore, Dumitric *et al.* [78] have studied the stability of metal encapsulated SiNTs with several TM atoms as well as various other structural variations (see also Chapter Eight). They also concluded hexagonal ring-based SiNTs to be the most stable among various phases. Similar to the results of the previous studies [53,54], they also found these nanotubes to be metallic. Further studies on the mechanical properties of the SiNTs showed high mechanical stability.

6.4 Germanium nanotubes

Similar to SiNTs, metal encapsulated clusters of Ge can be used as building blocks for novel nanoforms of Ge. An important aspect here is that Ge atom is about 4% bigger in size as compared to Si. This could lead to the possibility of doping with slightly bigger atoms as well as making different structures of Ge nanotubes (GeNTs) while the more extended nature of Ge valence orbitals may give rise to different properties. In order to find suitable building blocks of GeNTs, Singh *et al.* [68,79] performed a search for the most favourable structure of $Ge_{12}Mn$ cluster by optimizing icosahedral, decahedral, hexagonal prism, and hexagonal antiprism structures. Unlike $Si_{12}Mn$ cluster that has the hexagonal prism structure [80], $Ge_{12}Mn$ favours a perfect icosahedral structure, which has high coordination and high magnetic moment of $5\,\mu_B$. However, another nearly degenerate isomer with hexagonal antiprism structure has a small magnetic moment of $1\,\mu_B$. Both the icosahedral and hexagonal isomers were found to possess large HOMO–LUMO gaps of 1.11 and 1.13 eV, respectively and therefore are very stable, suggesting the possibility of their assemblies into nanotubes and other forms.

A stacking of pentagonal antiprisms (icosahedral isomer without two opposite capping atoms) of Ge (Fig. 6.9a) led to the formation of finite symmetric GeNTs with Mn doping. However, because of the $3d^54s^2$ electronic configuration of Mn atom, the *d*–*d* interaction between the Mn atoms was found to be very strong. It leads to very short Mn—Mn bond lengths with weak or no net magnetic moment in short $Ge_{15}Mn_2$ nanotubes. With an increase in the nanotube length, Mn—Mn bond lengths also increase and this reduces the Mn—Mn interaction leading to an enhancement in the local magnetic moments on Mn atoms. An infinite pentagonal antiprism nanotube with $Ge_{20}Mn_4$ unit cell (Fig. 6.9a) was found to be ferromagnetic with 2.40 (≈0) μ_B magnetic moments on each Mn (Ge) atom. Interestingly, compression of this nanotube along its axis led to a transition to a ferrimagnetic state (Fig. 6.9c) in which the magnetic moment of the nanotube decreased to an average value of 1.1 μ_B per Mn atom with the local moments of 2.17, 2.00, −1.81, and 2.58 μ_B at the equilibrium value of the cell length (9.9 Å). These results showed that competing long-range ferromagnetic and short-range antiferromagnetic interactions develop in the GeNT due to magnetic stress on compression. The magnetic moments on Mn and Ge atoms in this nanotube are similar to those obtained in dilute magnetic bulk [81,82] Ge doped with Mn. Further calculations on nanotubes with larger unit cells ($Ge_{30}Mn_6$ and $Ge_{40}Mn_8$) confirmed ferrimagnetic coupling. The magnetic configuration can be

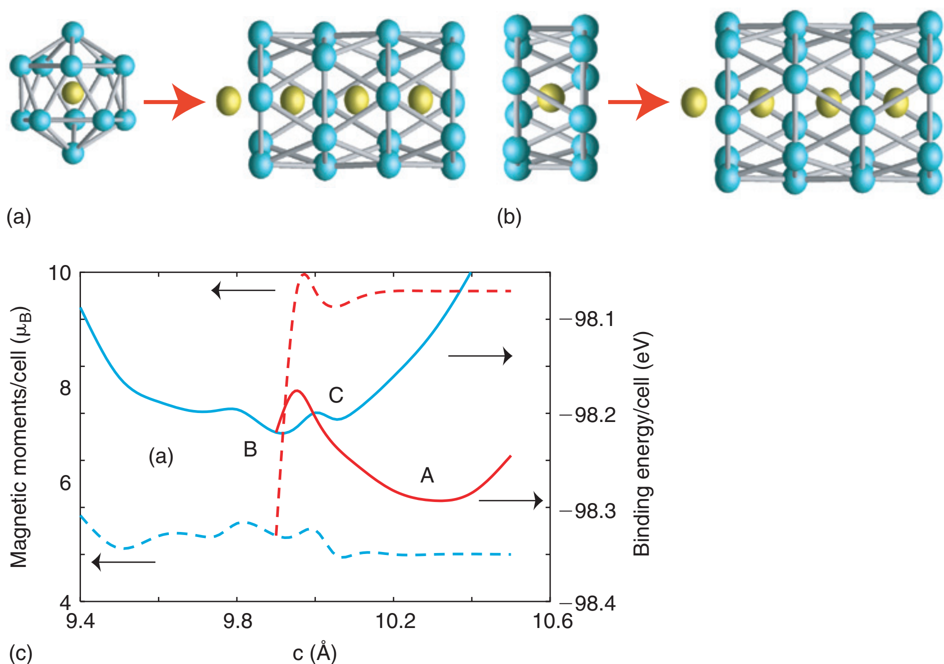

Figure 6.9 (a) Icosahedral and (b) hexagonal antiprism isomers of $Ge_{12}Mn$. Assemblies of pentagons and hexagonal clusters lead to the formation of GeNTs doped with metal atoms. (c) Magnetic phase diagram for the infinite pentagonal nanotube. A corresponds to the ferromagnetic state while B and C, to ferrimagnetic states. B is marginally metallic while C is semiconducting (adopted from Ref. [79]).

described in terms of ferromagnetically coupled nano-domains and patches of anti-ferromagnetically coupled spins. The antiferromagnetically coupled Mn atoms have shorter Mn—Mn bond lengths compared with ferromagnetically coupled Mn atoms leading to a reduction in the magnetic stress of the nanotubes on compression.

The band structures of GeNT in different phases with a $Ge_{20}Mn_4$ unit cell show that the ferromagnetic phase (A in Fig. 6.9c) is metallic, but the ferrimagnetic phase at the equilibrium cell length of 9.9 Å is only marginally metallic with few holes in the valence band and a few electrons in the conduction band for spin-up and spin-down states, respectively. Further calculations with an expanded lattice constant in the ferrimagnetic phase showed a shallow minimum (C) in which the nanotube is semiconducting with a small band gap and 1 μ_B magnetic moment per Mn atom. As the GGA underestimates the band gap, it was suggested that the true ground state of the ferrimagnetic phase (B) could also be semiconducting. Compression of the nanotube beyond the cell length 9.9 Å leads to more metallic behaviour of the ferrimagnetic GeNT in which the local magnetic moments change, though the net magnetic moment per cell remains nearly the same leading to a relatively shallow region in the phase diagram.

A stacking of hexagonal rings in an antiprism structure also leads to highly symmetric GeNT (Fig. 6.9b) with significantly higher magnetic moments on Mn atoms than in the case of the pentagonal nanotubes. The behaviour of these hexagonal GeNTs is very similar to SiNTs as there is a weak interaction between the clusters due to the magic nature of $Ge_{12}Mn$ and its large HOMO–LUMO gap. This also leads to large intercluster separation for the dimer and makes ferromagnetic (2 μ_B) as well as antiferromagnetic (0 μ_B) spin isomers nearly degenerate. Doping of an Mn atom in between two hexagonal $Ge_{12}Mn$ clusters leads to antiferromagnetic coupling between the Mn atoms and a reduction in the Ge—Ge intercluster separation. Similar to the case of the SiNTs, the enhanced interaction between the clusters due to the reduction in the intercluster Ge—Ge bond lengths leads to an increase in the local magnetic moments on Mn atoms. As the length of the nanotube increases, there is further shortening of the intercluster Ge—Ge bond lengths and delocalization of electrons in the nanotubes. The ferromagnetic and antiferromagnetic spin-isomers generally lie close in energy for the finite nanotubes but the infinite GeNT favours ferromagnetic ordering. An infinite nanotube with a unit cell of $Ge_{24}Mn_4$ is very symmetric and the local magnetic moments are the highest among the M-doped nanotubes with the value of 3.41 μ_B on each Mn atom. There is a small-induced polarization of opposite spin (0.05 μ_B) on each Ge atom leading to 3.06 μ_B average magnetic moment per Mn atom. This behaviour remains even when the nanotube is compressed suggesting that it is a good nanomagnet. The band structure of the infinite hexagonal antiprism nanotube shows band crossing at the Fermi level for the spin-up as well as spin-down components, indicating metallic behaviour.

6.4.1 Metallic and Semiconducting Nanotubes of Ge

In the case of Ge it is possible to stabilize nanotubes with a variety of TM atoms. Studies on the structural stability of $Ge_{12}M$, M = Nb, Mo, and W showed a hexagonal antiprism structure to be of lowest energy [83,84]. However, nanotube-shaped $Ge_{18}M_2$ (M = Nb, Mo, and W) clusters have an antiprism–prism structure (Fig.

6.10a) which is 0.44, 0.55, and 0.59 eV lower in energy for M = Nb, Mo, and W, respectively compared to a biprism structure which was found to be lowest in energy for $Si_{18}W_2$. A prism–prism structure of GeNT lies second in energy with a longer M—M bond while an antiprism–antiprism structure lies highest in energy with shorter M—M bond. The prism–antiprism structure optimizes M—M as well as Ge—Ge and Ge—M interactions. The HOMO–LUMO gap for this finite nanotube with M = Nb and W is 0.33 and 1.03 eV, respectively. Infinite GeNTs were obtained by assembling $Ge_{18}M_2$ clusters. When two clusters of $Ge_{18}Nb_2$ are assembled together with a Nb atom in between ($Ge_{36}Nb_5$), then the antiprism–prism structure remains stable as shown in Fig. 6.10b. This structural growth also got support from a calculation in which an antiprism–antiprism stacking of hexagons transformed to the antiprism–prism structure. Therefore, the preference for prism–antiprism structure did not change with an increase in the length of the nanotube. Further addition of a $Ge_{12}Nb$ cluster keeps this structure very symmetric (Fig. 6.10d) but with increasing length, a slightly different stacking in which the central four hexagons are in the antiprism structure, lies only 0.05 eV higher in energy. These results showed that the rotation of a hexagon costs little energy as the length of the nanotube increases, though for an infinite nanotube the antiprism–prism staking remains lowest in energy (Fig. 6.10d). The BE of the nanotube was found to increase with an increase in the number of clusters and therefore nanotubes can be formed with a large aspect ratio. The HOMO–LUMO gap in finite

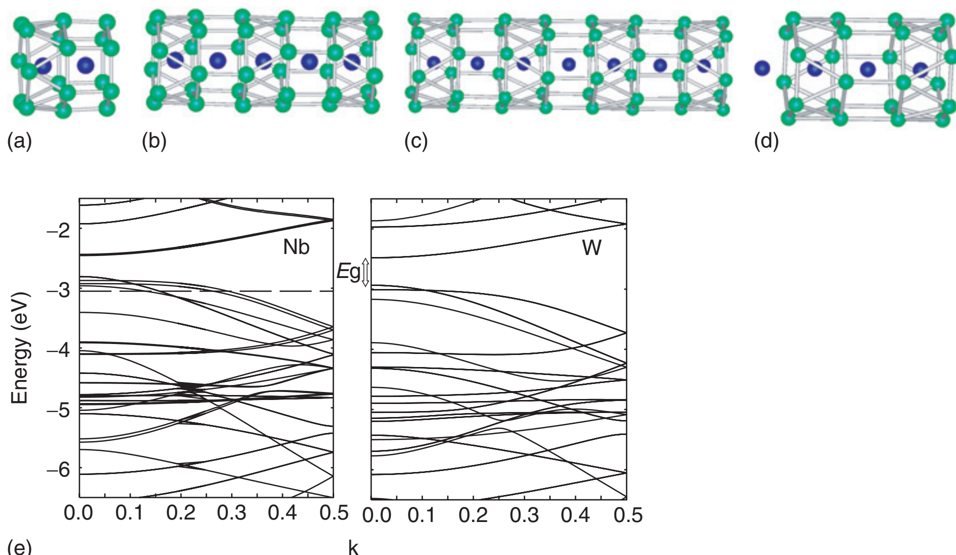

Figure 6.10 (a), (b), and (c) show optimized structures of finite nanotubes $Ge_{18}M_2$, $Ge_{36}M_5$, and $Ge_{48}M_7$, respectively. These structures are similar for M = Nb, Mo, and W though Nb-doped nanotubes are slightly distorted while Mo- and W-doped nanotubes are very symmetric. (d) shows the optimized unit cell of infinite nanotube $Ge_{24}M_4$ with $Ge_{12}M$ clusters stacked in prism and antiprism structures. (e) Band structures of Nb- and W-doped infinite nanotubes. Dashed line shows the Fermi energy. E_g is the band gap for the W-doped semiconducting nanotube (adopted from Ref. [83]).

nanotubes is small and the infinite GeNT becomes metallic with a unit cell of $Ge_{24}Nb_4$.

The band structure of an infinite $Ge_{24}Nb_4$ nanotube shows (Fig. 6.10e) a gap just above the Fermi level indicating the possibility of the formation of a semiconducting nanotube by the filling of these states. Indeed when all Nb atoms were replaced with Mo, the extra electron filled the empty states near the Fermi level and the nanotube became 6-fold symmetric and semiconducting with a band gap of 0.38 eV (Fig. 6.10e). Similar results were also obtained for W-doped GeNT. Therefore, unlike SiNT, doping of Mo or W in GeNT led to the formation of a semiconducting nanotube with a direct band gap. The band gap is higher for W doping with the GGA value of 0.5 eV. The $Ge_{18}Mo_2$ and $Ge_{36}Mo_5$ finite nanotubes were also found to have smaller HOMO–LUMO gaps of 0.96 and 0.75 eV as compared to 1.03 and 1.01 eV, respectively for W doping. The true values of the band gap in the infinite nanotubes is expected to be around 1 eV which is comparable to the value for bulk silicon. Therefore, W-doped GeNT could open up new possibilities for device development at the smallest scale. The BE for the W-doped infinite nanotube is 4.04 eV/atom as compared to 3.81 eV/atom for Mo doping. Therefore, W doping is better from energetic point of view as well.

The partial DOS of the $Ge_{24}M_4$ infinite nanotubes (Fig. 6.11) shows that the two non-equivalent M atoms, one lying in the antiprism environment and the other in the prism environment, have quite different local DOS. The states near the Fermi energy arise mostly from the Ge 4*p* orbitals and the *d* orbitals of the M atom that lies in the prism environment (Fig. 6.11). The contribution to the states near the Fermi energy from the *d* orbitals of the M atom lying in the antiprism environment is negligibly small (Fig. 6.11). In the antiprism geometry Ge—M bond lengths are shorter and give rise to stronger hybridization of the M *d* and Ge 4*p* states which pushes the *d* states to higher BEs. However, in the prism geometry Ge—Ge and Ge—M interactions are weaker. The density of states also shows the van Hove singularities expected for such quasi-one-dimensional structures. These studies showed for the first time that thinnest metal stabilized semiconducting nanotubes of Ge could be possible by doping of Mo or W atoms, knowing that elemental structures of this dimension are unstable. A significant advantage here would be that by changing the M atom in the growth process it can be possible to grow metallic or semiconducting nanotubes making novel possibilities for miniature devices.

6.5 Silicon nanowires

In contrast to SiNTs, nanowire form of silicon have been attracting attention for more than a decade. Early studies have been to explain visible luminescence from porous silicon. Also bar type nanostructures of Si have been studied by electron beam lithography in an effort to prepare the smallest possible structures of Si in the traditional top-down approach. In recent years fabrication techniques of SiNWs such as metal nanocluster-catalyzed vapour–liquid–solid growth have advanced to a level that allow greater control in growth direction and the diameter of the nanowires. Furthermore, the possibilities of using such nanowires as chemical as well as biological sensors have been demonstrated. The bright prospects of device developments have

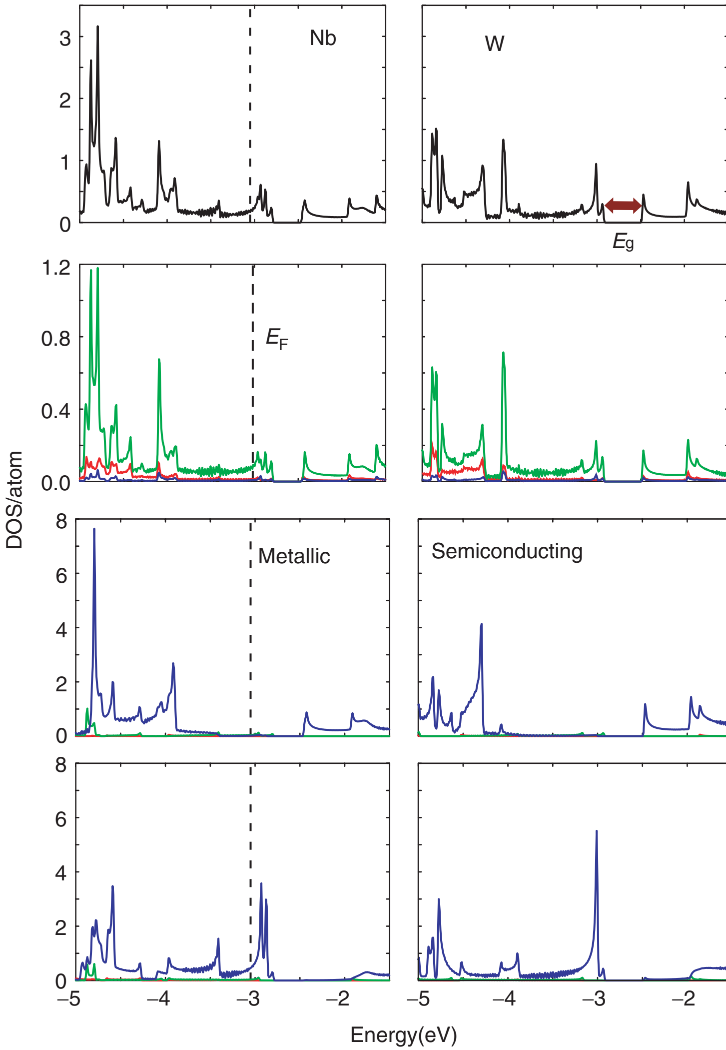

Figure 6.11 Total and partial DOS for Nb- and W-doped infinite GeNTs. (a) Total DOS, (b) partial DOS of Ge, (c) partial DOS for Nb atom in the antiprism environment, and (d) partial DOS for the Nb atom in the prism environment of Ge. Red, green, and blue lines represent contributions from *s*, *p*, and *d* orbitals, respectively. Dashed line shows the Fermi energy (E_F), while for the W-doped semiconducting nanotube the band gap is indicated by an arrow (adopted from Ref. [83]).

led to the fabrication of SiNWs in many laboratories and in recent years their applications have also been explored extensively. More details about the experimental developments can be found in Chapter Five as well as by Durrani and Ahmad (Chapter Ten) who also discuss SiNW-based SET. In the subsequent sections we present a review of theoretical studies on the atomic and electronic structures of these systems and show how first principles studies can help to the development of this class of materials.

Theoretical studies on SiNWs can be classified into two categories: (1) Novel structures formed from assembly of clusters and (2) nanowires having bulk silicon-like structure. In the latter case the properties could depend sensitively on the morphology and the direction of the axis along which the cut is made. In experiments surfaces of SiNWs of category (2) are generally passivated with hydrogen or oxygen and the atomic structure is mostly crystalline at least inside the nanowires while some changes may take place on the surface depending upon the morphology and the growth conditions used. On the other hand properties of pristine SiNWs could depend strongly on surface reconstructions. In this section we focus on (1) non-crystalline pristine SiNWs that are based on assembly of novel clusters of Si, (2) crystalline pristine SiNWs, and (3) hydrogenated SiNWs. Finally we discuss some studies on Si/Ge core-shell nanowires as well as nanowire superlattices.

6.5.1 Non-Crystalline Pristine SiNWs

Similar to metal encapsulated Si/GeNTs where metal encapsulated clusters are assembled to form tubuler structures, nanowire structures of pristine silicon could be produced by assembly of stable elemental Si clusters and they could offer a new form of silicon with novel properties. A few possibilities of such assemblies have been explored. Experimentally at least 100 nm long SiNWs of 3–7 nm diameter have been prepared by depositing silicon vapour onto highly oriented pyrolytic graphite [85]. These nanowires were assembled parallel in bundles and their atomic structure was modelled in terms of aggregation of small Si clusters whose size is much smaller than the diameter of the nanowires. From total energy calculations on a few selected cluster assembled SiNWs, it was shown that the atomic structure based on an assembly of fullerene-shaped Si_{24} clusters was lowest in energy. These structures are inherently metastable as pure Si_n clusters with $n > 20$ prefer elongated or three-dimensional structures [86,87] rather than empty cage fullerenes. The stabilization of SiNW with Si_{24} fullerene cages could be similar to the stabilization of fullerene cages of silicon with H termination. For pure silicon clusters, a transition to nearly spherical three-dimensional compact structures at $n \approx 27$ is related to the onset of the formation of structures [87,88] that are composed of fullerene-like cages with a small number of silicon atoms inside. These results also give a clear indication of the difficulty in forming very thin nanowires or nanotubes of silicon which require conditions that allow only one-dimensional growth such as in vapour–liquid–solid growth using metal clusters as seeds.

Theoretical studies have been done on a few assemblies of clusters. Thin SiNWs with length up to 26 Å formed [89] from an assembly of Si_9 tricapped trigonal prism (TTP) units and uncapped trigonal prisms as the building blocks were shown to be stable using full-potential linear muffin-tin orbital calculations. The HOMO–LUMO gap of these finite nanowires approaches zero value with increasing length. Menon and Richter [90] have studied quasi-one-dimensional structures of Si using a generalized tight binding molecular dynamics method and shown that SiNW structures could be stable if the core atoms are 4-fold coordinated and are surrounded by 3-fold coordinated surface atoms. The latter are arranged in such a way so as to form one of the most stable reconstructions known on bulk silicon surfaces such as the buckled dimer formation on Si(100) surface or the (7×7) reconstruction on Si(111) surface.

Because of the presence of dangling bonds, surface of such a nanowire was suggested to be reactive. The building blocks of these SiNWs are multiply connected clusters with a small hollow region in the middle. The electronic structure of such as infinite nanowires showed them to be semiconducting with a slightly smaller band gap compared with bulk Si.

6.5.2 Crystalline Pristine SiNWs

Studies on crystalline pristine SiNWs have been done by considering a cut from bulk silicon such as a square-shaped [001] oriented SiNW. The fraction of atoms lying on the surface of such a thin nanowire is quite large and the properties of such nanowires could be affected significantly by changes on the surface such as by reconstruction and adsorption. This is also a reason for the molecular level sensitivity of the SiNWs in contrast to bulk whose properties are affected little by the presence of surface. Similar to the reconstructions on bulk Si surfaces, reconstruction could be expected on pristine SiNW surface. However, such studies are only few and the physics and chemistry of SiNW surfaces are yet to be fully developed. There are several natural questions that need to be addressed. Among these, the effects of large surface to bulk ratio on the structural, electrical, mechanical, vibrational, and doping behaviour of the nanowires are very prominent. As compared to bulk surfaces, nanowires have facets that have infinite extent only in one of the lateral directions and finite in the other. The edges, i.e. the intersection of two facets could have significant effect on surface reconstruction of a nanowire and the morphology. Such effects become more important as the diameter of nanowire decreases because surface states may be responsible for conductance in such SiNWs and it may itself be larger than expected from doped SiNWs. Therefore, pristine SiNWs may not need doping for conduction. In general appropriate doping ways may be needed to tailor the electrical properties of SiNWs and control statistical fluctuations in doping concentration as well as distribution from one wire to another. Answering these questions by experiments alone could be difficult and *ab initio* studies could prove to be an important tool in this regard.

A comprehensive study to identify the importance of edges and their effects on the properties of SiNWs was carried out by Ismail-Beigi and Arias [91] on SiNWs oriented along the [001] axis. A nanowire with octagonal cross-section was constructed using Wulff construction by removing corner atoms from an initially square-shaped nanowire. At the edges of such a nanowire $\{110\}$ facets meet $\{100\}$ facets. All atoms on the surface of this nanowire are 2-fold coordinated without atomic relaxation. Studies on bulk Si (001) surface have shown 2×1 (or $p(2 \times 2)$) and $c(2 \times 2)$ reconstructions to be competitive, though $p(2 \times 2)$ reconstruction has the lowest energy [92]. When the structure of SiNW was relaxed, two competing low-energy reconstructions on the $\{100\}$ surface of SiNWs were found: (1) that best satisfies the system in terms of the total number of bonds with optimal bonding along the edges and (2) that best satisfies the system in terms of the lowest energy configuration of the surfaces. For a given size of the nanowires, a balance has to be made between the two and therefore the reconstructions are size dependent. They found a unique surface atom with which each edge atom may bind to become 3-fold coordinated, but it affects reconstruction on $\{100\}$ facets which favour $c(2 \times 2)$ type reconstruction. Therefore an edge-driven transition from $p(2 \times 2)$ reconstruction on

large diameter nanowires (similar to the one favoured on bulk (001) surface) to the c(2 × 2) reconstruction occurred as the cross-section of the nanowire was decreased below the value of around 3.0 × 3.0 nm. The c(2 × 2) reconstruction maximizes the number of bonds in the system and it overcomes the cost in changing the natural tendency of the surfaces. In SiNWs with the p(2 × 2) surface reconstruction there is a doubling of the periodicity along the nanowire axis and half the atoms on edges are 2-fold coordinated. Because of bonding restrictions into the interior of the structure, the dimer rows in alternate faces have patterns of 2 × 1 reconstruction as shown in Fig. 6.12. The reconstruction was shown to have an effect on the electronic structure as the surface states could depend on the type of reconstruction, but little change in the elastic properties of the nanowires.

The effects of edges on the atomic structure of SiNWs have also been considered by Zhao and Yakobson [93] who studied SiNWs with large diameters using a tight binding molecular dynamics method. Nanowires with pentagonal cross-section ({100} facets) and hexagonal cross-section (four {111} and two {100} facets) were considered. The ground state of the nanowires with diameters (d) <6 nm was found to be polycrystalline with 5-fold rotational symmetry. Also a nanowire made of Si_{20} fullerenes was found to have lowest energy in this family of structures.

Recently, Rurali and Lorente have studied SiNWs [94,95] of ≈1.5 nm diameter oriented along the [100] direction. The core of the nanowires was considered to have the bulk structure but reconstruction was allowed on the surface. There is evidence that core of nanowires has bulk structure. Similar to the studies of Zhao and Yakobson [93], the formation of {100} facets was found to be favoured. However, they obtained two types of surface reconstructions. Among them facets with an even number of atoms per cell were found to have dimerization which lowers the energy. Such facets are therefore favoured over facets with an odd number of atoms in a cell. Two competing geometries for the {100} facets were found: (1) A reconstruction

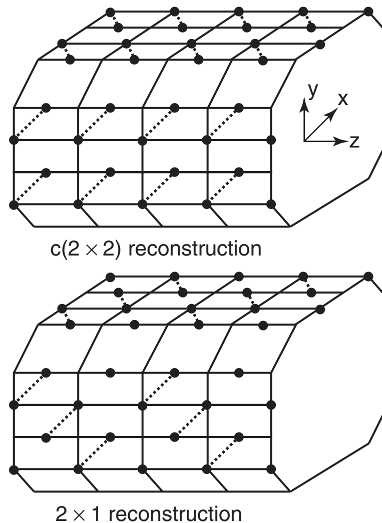

Figure 6.12 A schematic view of SiNW and the bonds formed on the surface of the nanowire in the c(2 × 2) reconstruction (top) and in the (2 × 1) reconstruction (bottom) (Reproduced with permission from Ref. [91] copyright 1998 APS).

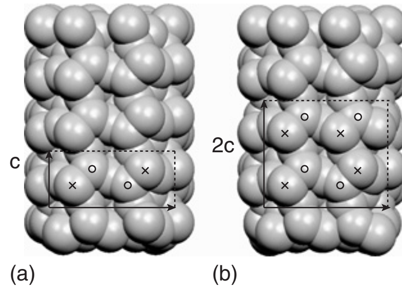

Figure 6.13 {100}-facet reconstructions. (a) 1c and (b) 2c dimerization of the surface dangling bonds. Lattice vectors of the facet unit cell are sketched to underline the different periodicity along [100] axis (c is the bulk lattice parameter) (Reproduced with permission from Ref. [94] copyright 2004 APS).

(see Fig. 6.13a) with the same periodicity as the cell along the unreconstructed wire, has a trough in the middle of the facet and it turns out to be the most stable and (2) a reconstruction (see Fig. 6.13b) with twice the periodicity of (1) which is only 3 meV/atom higher indicating that both reconstructions are likely to coexist. The trough in reconstruction (1) is determined by the buckled dimer sequence which presents a double chain of low atoms (labeled with a circle in Fig. 6.13). This is observed in only one of the two sides in reconstruction (2) while on the other side, one out of every two dimers is flipped. Interestingly, no direct correspondence was found with infinite surface reconstructions. Hence the two minimum-energy possibilities are differentiated according to the size of the periodicity along the nanowire axis. Despite the energetic near equivalence of the two reconstructions, (1) is found to be strongly metallic while (2) is semimetallic. The bands near the Fermi energy arise from the surface states originating from the dimer dangling bonds. This electronic-structure behaviour is attributed to the particular surface states of each reconstruction. The flipping of the dimer in reconstruction (2) leads to localization of electrons and to semimetallic behaviour. These authors suggested competition between the coordination at the surface recovering the full tetrahedral bonding as in reconstruction (2) and the delocalization of a Bloch state along the nanowire axis as in reconstruction (1). The bulk-like core of the nanowires confer them with a Young modulus close to the value for bulk Si. On the other hand, the Poisson ratio indicates good lateral elastic properties of these nanowires.

Very recently Singh *et al.* [96] have performed *ab initio* calculations on pristine SiNWs oriented along the [110] direction and showed them to be indirect band-gap semiconductors. The nanowires were cut from bulk silicon in a rectangular shape and were bounded by two {100} and two {110} facets in lateral directions (Fig. 6.14). They considered large unit cells with 12 or more layers of Si along the nanowire axis to allow for possible reconstructions on the surface and eliminate artifacts of periodic boundary conditions. In this family of SiNWs, the initial structure of a thin SiNW had an array of Si atoms with three dangling bonds due to the presence of {100} facets and the way the facets meet at the edges. Consequently, this nanowire underwent severe reconstruction, strongly driven by the tendency of Si atoms to reduce the number of dangling bonds at the surface (Fig. 6.14). Such severe reconstructions of very thin SiNWs could change their overall structure. However, the important aspects

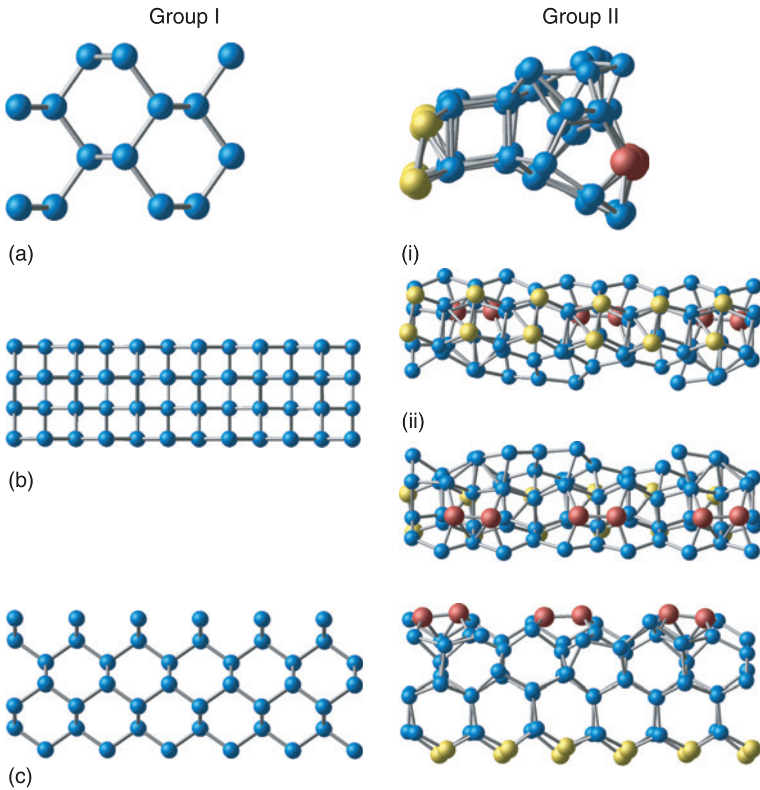

Figure 6.14 Optimized unit cell of a thin [110] SiNW. Group I and Group II represent the initial and final structures, respectively. (a), (b), and (c) show the view along the nanowire principal axis, and {100} and {110} facets, respectively. Yellow and brown colour balls show dimer formation on the two opposite {100} facets of the SiNW (after Ref. [96]).

of this thin nanowire were the semiconducting nature and the formation of Si dimers at the {100} facets such that the dimers on the two opposite {100} facets were perpendicular to each other and buckled similar to the reconstruction observed on infinite Si(100) surface. Studies on different diameter SiNWs showed these features to be quite common in this family and could be realized even in nanowires with diameters in sub-nanometer range.

Calculations on thicker SiNWs with the same orientation and facets showed a slightly different behaviour. Unlike the thin SiNW with [110] orientation, none of the Si atoms in the initial structure of the thicker nanowires (Fig. 6.15a) had three dangling bonds. Atoms on the {100} facets of the unrelaxed SiNWs have two neighbours and therefore each of these has two dangling bonds. After optimization two dangling bonds per dimer are removed by dimerization. This leads to a significant reduction in the energy of the nanowires. Similar to the thin SiNW, in this case also one of the dimer layers shown by yellow balls in Fig. 6.15b(i) lies along the nanowire axis and it resembles very closely the reconstruction found on the (100) surface of bulk Si. The dimers are buckled symmetrically. On the opposite {100} facet, there are three dimer arrays in the unit cell, each with two dimers as shown in Fig. 6.15b(ii) by brown balls. Unlike

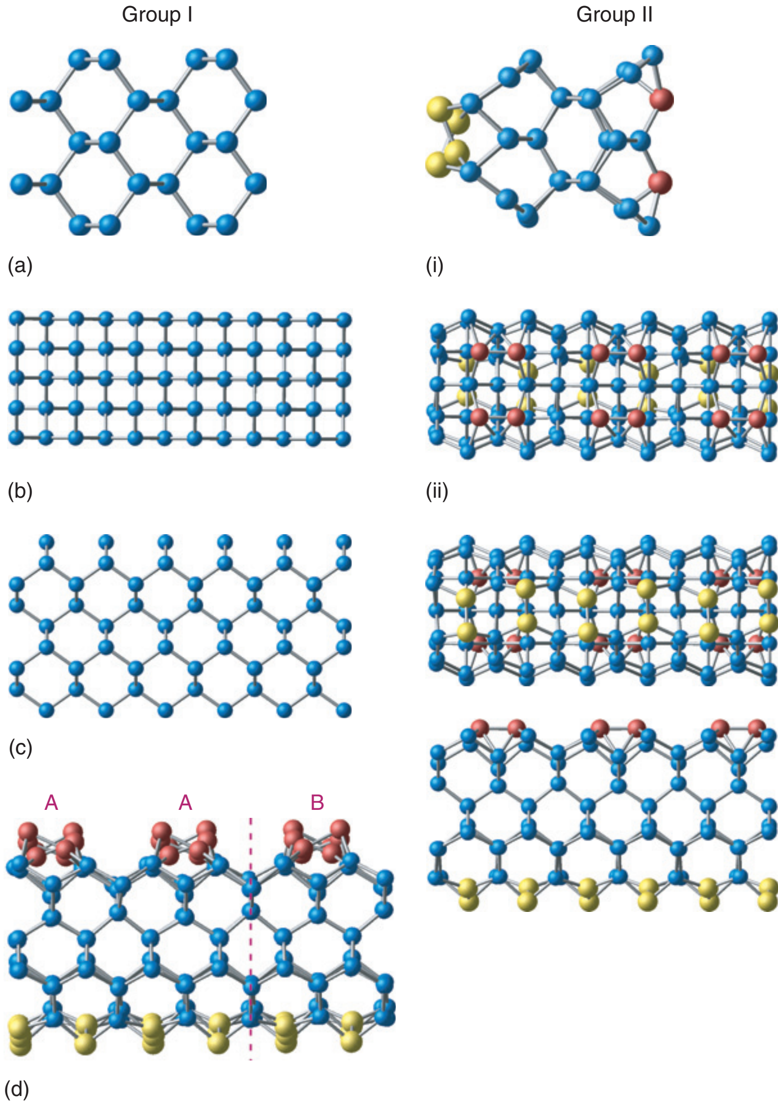

Figure 6.15 The initial and final atomic structures (Group I and II, respectively) in the unit cell of SiNWs. (a) shows the cross-section along the nanowire axis while (b) and (c), the {100} and {110} facets, respectively. Twelve layers of Si atoms can be seen in the unit cells shown in (b) and (c). For clarity, the surface Si atoms that form dimers are shown in brown and yellow on the two opposite {100} facets (i) and (ii) in (b). The orientation of the dimers on the two facets is perpendicular to each other. The brown balls can be seen in (c) to lie in a plane so that there is no buckling of these dimers. Also the {110} facets of the nanowire do not reconstruct but have significant relaxation near the edges. (d) Similar to (c) but for a thicker nanowire. There are different reconstructions of brown atoms and these are marked with A and B. B is the reflection of A and the plane of reflection is shown by the line (after Ref. [96]).

bulk surfaces, these dimer arrays do not have an infinite extent and are terminated at the edges of the nanowire. The pair of Si atoms forming a dimer on this face makes an additional bond with the Si atom in the adjacent {110} facet. This way the remaining dangling bonds on the dimer atoms are weakened and it lowers the energy further. Consequently, the dimers are not buckled and remain planar (see Fig. 6.15c). The {110} facets, however, do not reconstruct but relaxation occurs which is more significant for the edge atoms. It is partly due to the fact that most of the atoms on these facets are already tricoordinated and any additional bond formation requires large strain energy that is not compensated by the bond formation energy. The optimized structure showed the unit cell to consist of four Si layers along the nanowire axis.

With increasing thickness of the SiNWs, the number of dimers in an array perpendicular to the nanowire axis on a {100} facet increases to four or more (Fig. 6.15d) and this leads to buckling of the dimers on this face as well (Fig. 6.15d) and an expansion in the mean diameter of the nanowires. The dimers that are in the middle of these arrays are tricoordinated and the Si atoms in the core of the nanowires are tetracoordinated as in bulk. This leads to buckling features similar to infinite surfaces. Also the edge dimers are tricoordinated and buckled with slightly longer (2.42 Å) bond lengths as compared to the value (2.34 Å) for the two inner dimers. These results showed that the atomic structure of thick SiNWs is not significantly affected by edges. The effects of terminating the facets are more and more localized on the edges and elsewhere the reconstruction resembles one of the low energy reconstructions observed on the (100) surface of bulk Si. However, an interesting finding was the occurrence of two consecutive arrays of dimers (marked A and B in Fig. 6.15d) on a {100} facet that had mirror symmetry in a plane perpendicular to the axis of the nanowire. Further calculations [96] on nanowires with eight Si layers in a unit cell with two different configurations (i) having two dimer arrays with a reflection symmetry (Fig. 6.16a and c) and (ii) having two dimer arrays with similar consecutive arrangements (Fig. 6.16b and d), showed them to be nearly degenerate in energy, though in the case (i) the energy was 0.04 eV lower than the value for the case (ii). Therefore, a possibility of polytypism in the growth of these nanowires with different sequences of A and B type blocks of layers was suggested. Interestingly, in all the cases, the nanowires were found to be semiconducting with nearly the same value of the band gap. Therefore, such a polytypism will not affect the properties of SiNWs significantly.

6.5.3 Band Structure of SiNWs

The band structures of the [110] SiNWs show that the nanowires are indirect bandgap semiconductors (Fig. 6.17a and b). The electronic charge density in Fig. 6.17c shows that the topmost valence band originates from sp^3 type orbitals on the edge atoms. The lobes pointing outside of the surface have large separation (3.77 and 3.83 Å) along the nanowire axis and overlap weakly. This leads to a relatively flat band. The electronic charge density from the bottom of the conduction band states comes from p_z type orbitals on atoms in the nearly flat facets (Fig. 6.17c). The bonding within such facets can be described in terms of sp^2 type orbitals. The separations between the lobes of p_z type orbitals are 3.69 and 3.92 Å. Therefore, again the dispersion of the corresponding band is small and the band is narrow. Similar results have been obtained for thicker nanowires. It is to be noted that the bands corresponding to the conduction

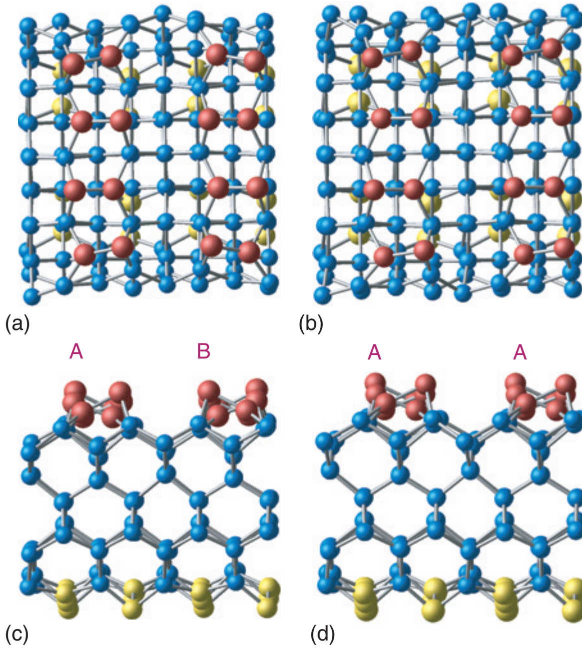

Figure 6.16 Optimized atomic structure of a [110] SiNW with eight silicon layers in the unit cell. The nanowire is bounded by two {100} and two {110} facets. Two ways of reconstruction are shown such that the dimer sequences are AA or AB type. (a) and (c), ((b) and (d)) show the {100} and {110} facets, respectively of the AB (AA) sequence. AB sequence has the lowest energy but AA is almost degenerate (after Ref. [96]).

band minimum (CBM) and valence band maximum (VBM) of these SiNWs originate at two different facets. This is in contrast to the metallic/semimetallic nature of the nanowires grown along the [100] direction, where they lie invariably on the dimer atoms as observed by Rurali and Lorente [94]. These results indicate that the semiconducting gap is inherent to this particular family of the [110] SiNWs and there is a possibility of the formation of thicker semiconducting SiNWs. Preliminary studies [97] on other shapes of SiNWs oriented along [110] direction and involving {100} facets show them to be semiconducting irrespective of the morphology of other facets. This could be important in developing semiconducting nanowires of pristine silicon.

6.6 Hydrogenated nanowires

The surfaces of SiNWs are often passivated with an oxidized layer or the dangling bonds are terminated with hydrogen. This provides stability to the nanowires and a big gain in their optical properties compared with the pristine SiNWs due to a change in the band gap. Most of the theoretical studies consider hydrogen-terminated nanowires as it is relatively easy to model them. An oxide layer on nanowires could be more than an atomic layer thickness and could involve matching at the interface which is very complex. The effects of the confinement can, however, be understood by

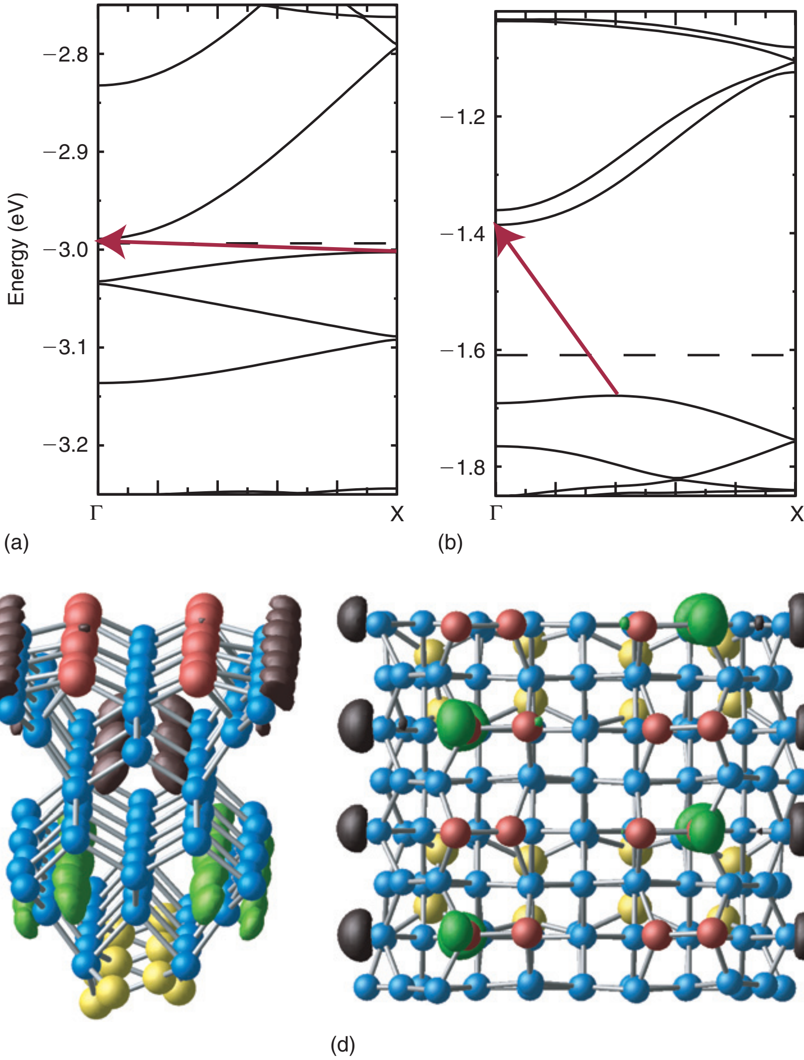

Figure 6.17 (a) and (b) show the band structures of [110] oriented SiNWs with different thickness. The arrows show the indirect band gap. Dashed line shows the Fermi level. Band decomposed electronic charge densities for the corresponding two SiNWs. Brown and green show band decomposed electronic charge density isosurfaces from the top of the valence band and the bottom of the conduction band, respectively (after Ref. [96]).

considering hydrogenated nanowires. In this section we review such studies and highlight their important role in understanding the structural, electronic, sensing, and mechanical properties of SiNWs.

Historically, H terminated SiNWs with rectangular cross-section (widths ≈ 1–2.3 nm) and oriented along [100] direction were studied to understand photoluminescence from porous silicon. These nanowires were found to have a direct band gap that increased with a decrease in the mean diameter of the nanowire due to quantum confinement. Buda *et al.* [14] studied similar nanowires with diameter 1.5 nm

and obtained a very similar conclusion. In many studies quantum confinement effects have been considered within an effective mass approximation. However, Read *et al.* [13] observed deviations from the effective mass theory in nanowires thinner than 2.3 nm (see later part also). Thicker nanowires have been studied by empirical and semiempirical methods. Using an empirical method Sanders and Chang [15] and Chin Yu *et al.* [18] showed that exciton oscillator strengths could be as large as the value for GaAs.

In contrast to most theoretical studies on [100] oriented SiNWs, experimentally grown nanowires are often oriented along [110] or [112] direction [98]. The orientation of nanowires has been found to be thickness dependent. Nanowires with diameter larger than 13 nm grow along [111] direction, while those having diameter between 13 and 7 nm have preference to grow along the [112] direction. SiNWs having diameters in the range of 7–3 nm grow almost exclusively along the [110] direction and the thinner nanowires are oriented along the [112] direction [99]. The thinnest nanowires grown so far have diameters of about 1.3 nm and are oriented along the [112] direction [98]. The surface of these SiNWs is passivated by H atoms. *n*- or *p*-type nanowires have also been grown for device development. These studies have shown that the physical and chemical characteristics of SiNWs including the mean diameter, composition, and electronic properties can, in principle, be controlled during synthesis.

Zhao *et al.* [100] have investigated the atomic and electronic structures, and optical properties of hydrogen-terminated SiNWs from first principles. The nanowires were cut from bulk Si along [110] and [111] directions with diameter, d, up to 4.2 nm and passivated with H such that there was no SiH_3 complex, i.e. the maximum number of dangling bonds per Si atom was two. The size and orientation dependence of the band gap was studied and a power law dependence of the HOMO–LUMO gap was obtained as a function of d, and it was suggested to be the same for nanowires with different orientations. Furthermore, they corrected the LDA band gap using many-body perturbation method based on the GW approximation. All the [110] nanowires were found to have a direct fundamental band gap at the Γ point due to band folding. The [111] nanowires were, however, found to exhibit a transition from an indirect band gap in large d nanowires to a direct one in small d nanowires. They observed the band gap to increase sub-quadratically with decreasing d. Similar to the studies on porous silicon, quantum confinement was found to become significant for $d < 2.2$ nm. However, strong anisotropy in dielectric function was observed in this range of d and new low-energy absorption peaks were found in the imaginary part of the dielectric function for polarization along the nanowire axis. Similar anisotropy was also found in a previous semiempirical tight-binding study for a SiNW of $d = 0.77$ nm oriented in the [100] direction. In another theoretical study on [001] SiNW ($d < 1.56$ nm), certain peaks were found not to change with the system size and were assigned to bulk-like excitations. However, after including the size-dependent quasi-particle gap correction, such features were not observed.

The GW-corrected band gaps for [110] SiNWs as obtained by Zhao *et al.* [100] is in good agreement with the experimental value, though for small d nanowires the discrepancy became appreciable. This was due to the fact that the orientation of nanowires for small d was different in experiments. This result supported the orientation dependence of the band gap that becomes more significant in small d

nanowires, e.g. nanowires with $d = 2.2$ nm. This has been shown from *ab initio* calculations on [112] SiNWs by Singh *et al.* [101] who also found the scaling of the band gap with mean diameter to be significantly dependent on the morphology. Recently Chan *et al.* [102] have used a genetic algorithm approach combined with *ab initio* calculations to study the structure of hydrogenated [110] SiNWs. As the number of atoms per length increases, they find that the cross-section of the nanowire evolves from chains of six-atom rings to fused pairs of such chains to hexagons bounded by {001} and {111} facets. They further predicted the stability of hexagonal wires starting at about 1.2 nm diameter. This is consistent with the recent experimental report of hexagonal SiNWs with diameters of about 3 nm.

Singh *et al.* [101] have studied the electronic and atomic structures of hydrogenated SiNWs by changing the mean diameter, morphology, and orientation to compare the properties and understand possible reasons for the preferential growth behaviour. Five different classes of nanowires oriented along [110], [100], and [112] crystallographic directions and having different surface morphologies were considered. In Fig. 6.18 these are referred to as NWn ($n = 1$–5). The nanowires were cut from a bulk silicon crystal such that these were bounded by low index surfaces. The geometry of NW1 is the same as inferred from experiments on larger d nanowires. It is oriented along the [110] direction and has a hexagonal cross-section with four

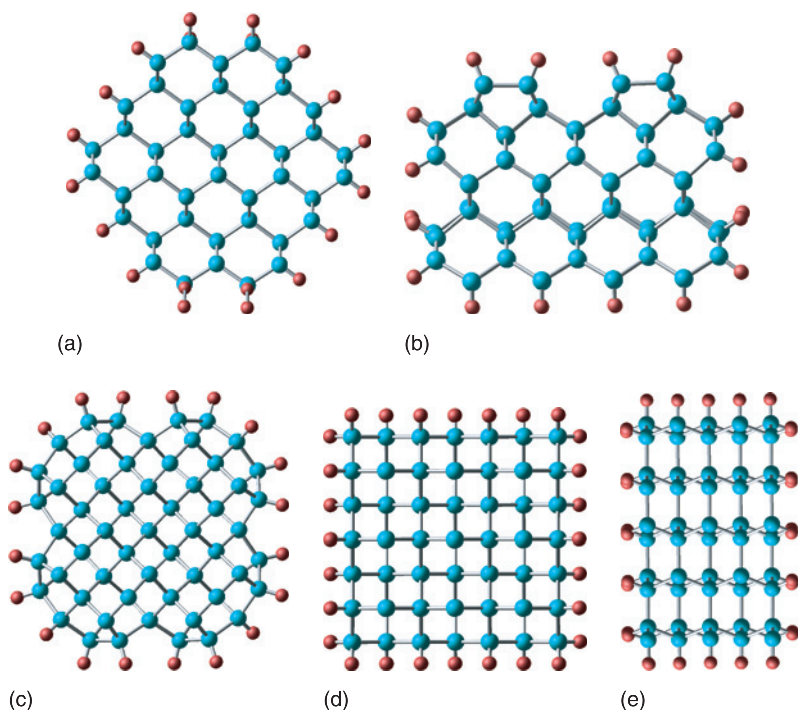

Figure 6.18 Cross-sections of the optimized structures of SiNWs. (a) NW1, (b) NW2, (c) NW3, (d) NW4, and (e) NW5. Brown and blue balls represent H and Si atoms, respectively. NW1 and NW2 are oriented along [110], NW3 and NW4 along [100] while NW5 is oriented along the [112] direction (after Ref. [101]).

{111} and two {100} facets. NW2 is also oriented along [110]. However, it is bounded by two {100} and two {110} facets in lateral directions. NW3 differs from NW2 only in orientation because it is bounded by similar facets as NW2 but oriented along [100]. NW4 is bounded by {110} facets in all lateral directions and it is oriented along the [100] direction. Finally, the geometry of NW5 is similar to the thinnest experimentally observed SiNW. It is oriented along the [112] direction and bounded by two {110} and two {111} facets in lateral directions. The dangling bonds on the surface are terminated with H atoms so that each Si atom lying on the surface of the nanowires is tetracoordinated. However, in NW2 and NW3, the tetravalency of Si atoms lying on Si(100) facets is ensured by taking into account Si dimer formation, which is usually observed on bulk Si(100) surface.

The optimized structures of hydrogenated SiNWs are highly symmetric (Fig. 6.18a–e) and in general lack any surface reconstruction due to the passivation of the dangling bonds by H except for the case of NW2 and NW3 in which the tricoordinated Si atoms on Si {100} surfaces get dimerized as shown in Fig. 6.19a. For NW2, the dimer layers on the two opposite facets are perpendicular to each other as it was also found in the case of the pristine SiNWs but the dimers are planar (Fig. 6.19a). This is in contrast to the {100} surface of bulk Si and pristine SiNWs where the Si atoms remain tricoordinated even after dimer formation and are buckled. An exception, however, occurs in the case where the dimer forming atoms get tetracoordinated and become planar. These results therefore agree well with the finding on hydrogenated SiNWs. The reconstructions on the {100} facets of hydrogenated

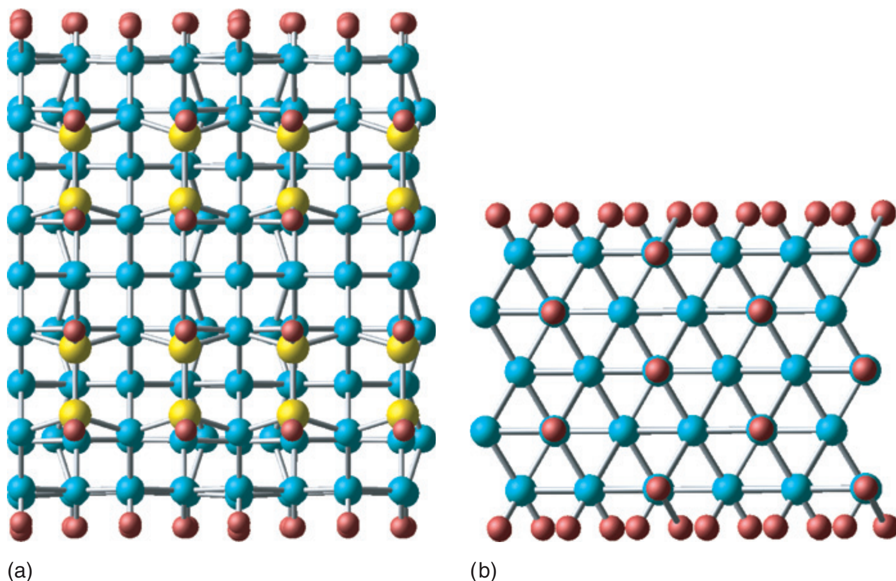

Figure 6.19 (a) Shows the dimerization of those Si atoms (yellow balls) that have only one terminal H on the (100) surface. On one {100} facet (front side in the figure) of NW2 the dimerization is perpendicular to the nanowire axis but on the opposite {100} facet (back side) it is along the nanowire axis. Similar Si dimers are formed on the {100} facets of NW3 also. (b) Shows the (111) surface of NW5. The main features of the structure are the same as observed in experiments except that in calculations, each surface Si atom is terminated with one H (after Ref. [101]).

SiNWs are very similar to monohydride formation on the H adsorbed (100) 2 × 1 surface of bulk Si. The morphology of the optimized hydrogenated NW3 has Wulff construction (Fig. 6.18c). The dimer formation induces curvature on the facets and it leads to a beautiful reconstruction where four semicircular parts get joined together such that the structure becomes 4-fold symmetric along the nanowire axis. The core of the nanowire has the bulk Si structure along the [100] direction. Similar to NW2, the dimers on {100} facets of NW3 are also planar. These reconstructions have important consequences on the electronic structure of the nanowires.

The {100} facets of NW1 resemble the dihydrated (100) 1 × 1 surface of bulk Si. It has been shown that with an increase in H chemical potential monohydride 2 × 1 Si(100):H can transform to a dihydride surface. In the case of NW5, the thinnest experimentally observed SiNW, the structure of the (111) facet (Fig. 6.19b) is very similar to the STM images [98]. The calculated Si—Si and Si—H bond lengths (3.85 and 1.5 Å) on the (111) facet were found to agree well with experiments (3.80 and 1.5 Å). However, the STM data was interpretated to suggest the dots on the top of the silicon atoms to be SiH_3 complexes. In the calculations of Singh *et al.* each Si atom on the surface had only one H because each Si atom had only one dangling bond (Fig. 6.19b). Any additional H atom will induce strain in the structure and could lead to distortions. However, the STM image showed no sign of distortions on this facet.

6.6.1 Electronic Structure of Hydrogenated SiNWs

The electronic structures of the nanowires are shown in Fig. 6.20. Except for NW3 and NW4, the nanowires are direct band-gap semiconductors which make them very interesting for silicon-based nano-optoelectronic devices and lasers. The band gap changes with the orientation and thickness of the nanowires (Fig. 6.20). In all cases the band gap increases with decreasing *d* because of quantum confinement but the scaling is dependent on the morphology of the SiNWs. NW1 and NW2 are oriented along the same direction and have similar band gaps (≈1.34 eV). However, the band gaps for NW3 and NW4 differ by as much as 0.40 eV though both are oriented along the same direction and have nearly the same mean *d* but the surface morphologies are different. Also, the scaling of the band gap with *d* depends strongly on the nanowire morphology. The band gap increases more strongly for NW4 with decreasing mean *d* than in the case of NW3 even though both of the nanowires are oriented along the same direction. Therefore it is not possible to fit them in a universal function, as it was reported by Zhao *et al.* The band gap for NW5 oriented along the [112] direction was calculated to be the largest (1.80 eV) among all the SiNWs with comparable mean *d*. The actual band gap, though, can be expected to be significantly higher because of the underestimation within the GGA. For [110] and [111] SiNWs of small *d*, Zhao *et al.* calculated a correction to the band gap using the GW method and found it to be about 100% of the LDA value. Accordingly, the true band gap was suggested to lie close to the experimental value of 3.53 eV. The band gap in this case is direct (not determined in experiments) and it is detrimental to the optical applications of the SiNWs.

The band structures of NW3 and NW4 hydrogenated SiNWs are similar because they are oriented along the same direction. Near the top of the valence band, two bands cross and their maxima lie at nearly the same energy. These two nanowires are

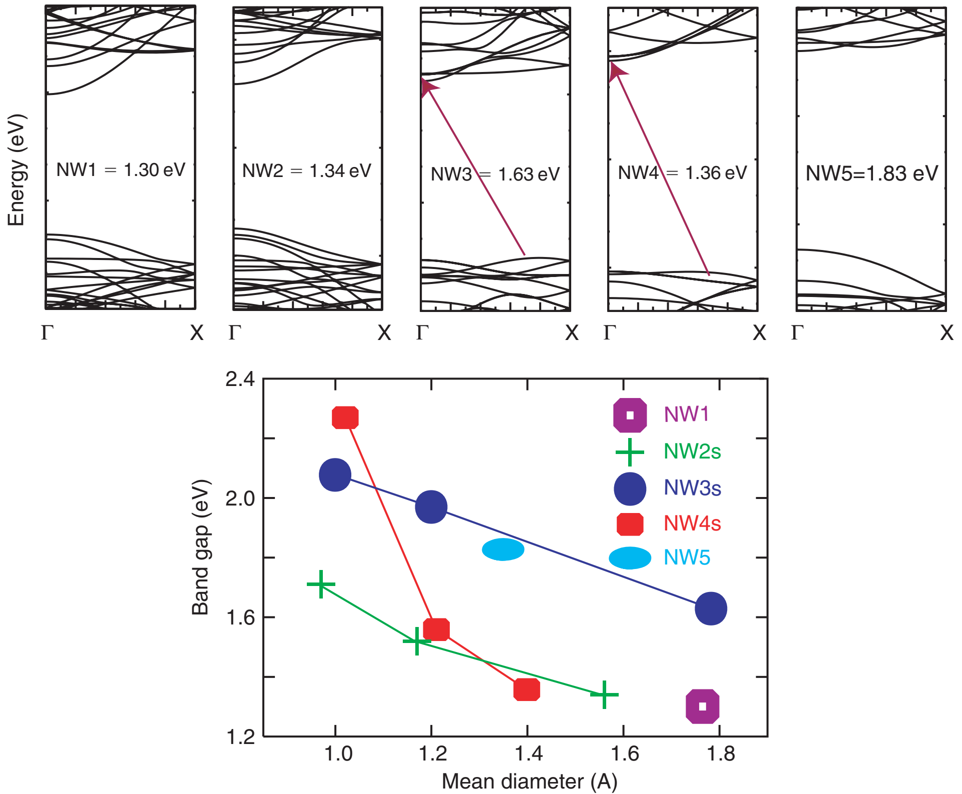

Figure 6.20 The electronic band structures and band gaps of NWn (n = 1–5) SiNWs with comparable mean diameters. Arrows are drawn to show the indirect band gaps in NW3 and NW4. Major ticks on the y-axis are equivalent to 1 eV. Plot of the band gap versus mean diameter of the nanowires shows that in general the gap increases with decreasing diameter and it depends on the orientation of the nanowire. The dependence on mean diameter is similar for NW2 and NW3 but very different for NW4 showing a strong dependence on the morphology of the nanowire (adopted from Ref. [101]).

indirect band-gap semiconductors. The profile of the band structure does not change when d is decreased. However, the thinner nanowires are direct band-gap semiconductors. The band gap of the nanowires increases monotonically with decreasing thickness (Fig. 6.20). This is due to the quantum confinement of the carriers, which is particularly strong in the range of diameters shown here. The largest GGA band gap (2.27 eV) is found for the thinnest nanowire (mean diameter 1.02 nm) in the NW4 family, for which the actual band gap is expected to lie in the ultraviolet region. This result shows that a band-gap engineering is possible and SiNWs could be prepared with desired band gaps by varying thickness, orientation, and morphology. It could open up avenues for their potential applications in optoelectronics, photonics, and miniaturized lasers. These results also showed that though orientation and surface morphology modify the band gap, the change is more systematic with the variation of d. Other possible ways of band-gap engineering could be by alloying and nanowire superlattice formation (see below).

6.6.2 Effects of Doping and H Defects

Besides optical applications, SiNWs have been shown to hold great promise for label-free detection of biological and chemical species [30–34]. The electrical detection of species by SiNW sensors is based on the principle of solid-state field effect transistor (FET) in which p- or n-doped nanowires are used and the gating is achieved chemically by a change in the surface charge when a species binds on the surface leading to a change in the conductance. For the detection of specific biological molecules, the surface of SiNWs in such devices is modified by attaching receptors that bind selectively the species to be detected. In another setup the surface of a SiNW was modified for measuring pH so that it could undergo protonation and deprotonation. Such a change in the surface charge gates the nanowire without applying any voltage and again a change in conductance could be used for detection. In contrast to bulk surfaces where the changes in the electronic structure are confined to the surface, the effects of receptor-legend chemistry on the surface of a nanowire go deeper into the core of the nanowire and this further increases the sensitivity of the sensors to the point of single molecule detection. Unlike oxidized nanowires where the layers of silica are generally thick, the surfaces of hydrogenated nanowires have only one layer of H to pacify the dangling bonds. Therefore, surfaces of hydrogenated nanowires could be even more sensitive and any changes in surface chemistry could have a pronounced effect on the sensing capability of nanowires. A variation in hydrogen concentration on the surface could affect the sensing capabilities of different surface morphologies and the associated surface reconstructions. On {100} facets deficiency of H was found to lead to dimer formation and therefore H deficiency does not have a strong effect. However, on other facets deficiency of H leads to states which appear in the band gap. Any attachment to such sites can affect the transport properties very significantly. Singh *et al.* studied the effects of changing the concentration of H on the surface of NW4 SiNWs because they involve only {110} facets. Removal of one H atom from each of the corner Si atoms of the NW4 nanowire (8H atom/unit cell) has an effect of creating unpaired electrons on the surface which leads to a drastic change in the band structure (Fig. 6.21). The electronic states associated with defects have energies lying within the band gap and it leads to a dramatic reduction in the band gap of the SiNWs. The origin of the defect states is seen from the charge density arising from the defect states (inset in Fig. 6.21). It is seen that the charge densities arising from the VBM and CBM are strongly localized on the eight corner Si atoms, showing clearly that these bands originate from hydrogen defect sites. Importantly, these sites can act as centres of attraction for various receptors. In contrast to this result, it is found that SiNWs with {100} facets can easily offset the effects of H deficit on the surface by dimerization as we discussed in the case of NW2 and NW3 earlier. Therefore, on such surfaces the band gap and electronic properties are unlikely to be affected by H defects. On the other hand nanowires with {110} or {111} facets could be ideal for sensors because their electronic properties could be modified drastically by changing H concentration.

Most of the electronic or sensing applications of SiNWs have been shown for p- or n-doped nanowires having thicknesses in the range of 10–30 nm and with oxidized layers on the surface. With the development of hydrogenated thin SiNWs, it is important to know the effects of doping on the electronic structure of such nanowires. Since there are significant differences in the electronic properties of NW1 and NW4,

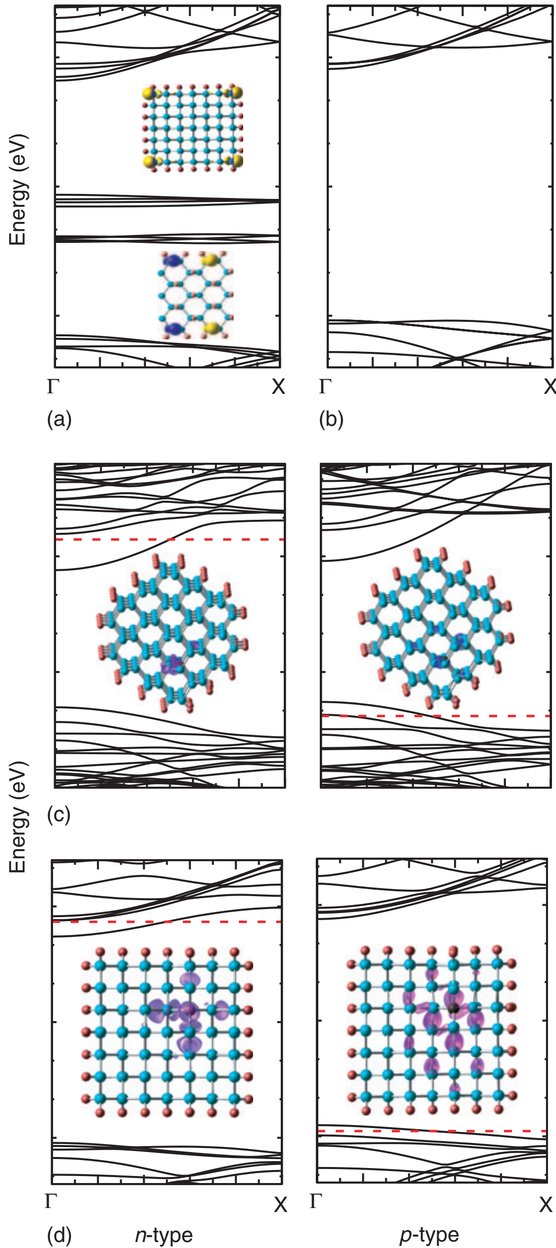

Figure 6.21 The band structures of a NW4 SiNW with (a) H defects and (b) no defect. The inset shows the cross-section and side views of the nanowire with band decomposed charge density isosurfaces. Yellow and purple colours correspond to VBM and CBM for nanowire with H defects. (c) and (d) show the band structures of *n*- as well as *p*-type NW1 and NW4 SiNWs, respectively. Red dotted line shows the Fermi energy. Inset shows the charge density decomposed on the donor and acceptor bands crossing the Fermi energy. For NW1 the charge density around the dopant site spreads to several neighbours but it is more along the nanowire axis (adopted from Ref. [101]).

Singh *et al.* considered these as prototypes to study the effects of doping. Boron and phosphorous atoms were doped to study p- and n-type SiNWs, respectively. After optimization, the band structures of the doped nanowires showed (Fig. 6.21) a shift of the Fermi level towards the valence and conduction band for *p*- and *n*-type SiNW, respectively. This behaviour is quite universal and is observed in both types of nanowires (Fig. 6.21) irrespective of their orientation and surface morphology. However, few subtle differences were observed that arise not because of doping but because of the difference in the surface morphologies of the nanowires. For example, the dispersion in the valence band of p-NW1 is more than that in the case of p-NW4, implying heavier holes in p-NW4 in comparison to p-NW1. Likewise, better conduction properties are expected in p-NW1. A comparison of the band structures of the doped and undoped nanowires (Figs. 6.20 and 6.21) shows that the dispersion of the conduction or valance bands does not change much upon doping. However, the band structure of the nanowires could be tailored by growing them in different orientations and with different surface morphologies. This could be used to design doped SiNWs with better conduction properties.

The doping concentrations in these doped SiNWs correspond to a case of heavy doping as one dopant in the unit cell represents about 0.4% dopant concentration. The band structures show that the Fermi level lies in the acceptor (donor) bands for the *p*- (*n*-) type nanowires. The electronic charge density decomposed on CBM for the n-type and VBM for the *p*-type nanowires shows that these bands originate from the dopant sites. For the *p*-type nanowire the electronic charge extends up to 3rd and 4th nearest neighbours and it can be expected even for lower doping concentrations a similar effect would be observed. It can enhance the sensing capabilities of thin nanowires further. Therefore, thin hydrogenated SiNWs could have potential for silicon-based device development at the smallest scale.

Conductance of cluster assembled short SiNWs passivated by H and connected to aluminium electrodes has been studied from DFT calculations [103]. The short ($\approx$0.6 nm) nanowires were found to be fully metallized due to the metal-induced gap states while longer (2.5 nm) nanowires form a nanoscale Schottky barrier with heights larger than the bulk value by 40–90%. Using *ab initio* calculations, Durandurdu [104]. very recently also predicted a stable small diameter SiNW. The wire is constructed from expanded phases of silicon namely clathrate Si_{34} and Si_{46} structures, and found these to be energetically more favourable than the diamond type nanowires with the same diameters. Furthermore, the wires are semiconducting with the band-gap energy of 0.22 and 0.34 eV.

6.7 Nanowire superlattices

Apart from the *n*- and *p*- type materials the other important component of the semiconductor industry which is most often used to bring the versatilities in electronic and photonic properties of devices are compositionally modulated structures, which are also known as superlattices. Nanowire-based superlattices are quite promising to achieve bulk-like functionalities at the nanoscale. Nanowire superlattices from Group III–V, II–VI and Group IV materials have already been synthesized [105–107]. Besides, superlattices another way to develop variation in the properties is by preparing

core-shell heterostructures. These can be formed by growing crystalline overlayers on nanocrystals or nanowires and offer enhanced emission efficiency [108].

Planar modulations in nanowires have been developed mostly for the III–V or II–VI materials to have variations in optical properties which are interesting in bar coding. Some of the experimental developments could be found in Chapter Five by Zhou *et al.* However, modulation of the radial composition has received much less attention until recently. Lauhon *et al.* [109] have recently synthesized SiGe core-shell nanowires. Such nanowires are quite thick and are difficult to model by first principles calculations within the current available resources. However, peculiarities of structural and electronic properties of large core-shell nanowires can be understood by studying thin nanowires or atleast a trend could be found which can be applied to larger diameter nanowires. Mustin and Wang have recently carried out a detailed first-principles DFT study of the composition dependence of the structural and electronic properties of the core-shell type SiGe nanowire heterostructures [110]. They analysed the relationship between structural characteristics and chemical composition in these core-shell structured systems and obtained a quantitative estimation of the degree of deviation from the linearity assumed by the Vegard's law [111] which states that the relaxed lattice parameter of a two component system is a linear function of the composition. The analysis of the changes in the local and global geometry and electronic structure of the epitaxial SiGe hydrogen-passivated core-shell structured nanowires revealed strong core-specific features for both the structural and electronic properties. They also observed the existence of both negative and positive deviations from the linear behaviour of the calculated structural parameters of the nanowires with the tensile strained Si core and compressive strained Ge core, respectively. They further observed [109] direct-to-indirect transition for the fundamental band gap in Ge-core/Si-shell nanowires. Based on the weak size dependence of the critical composition for direct-to-indirect gap transition they suggested [109] Ge-core/Si-shell nanowires with 5 and 15 nm shell diameter to have direct and indirect fundamental gaps, respectively. A smooth synthesis process could be expected by adding Ge shell onto Si core, as the calculation indicated a gradual increase in the tensile strain, whereas the strain relaxation for compressively strained Ge cores is much involved [109]. They observed direct band-gap practically over the whole compositional range for Si-core/Ge-shell nanowire heterostructures. This along with the possibility of the band-gap variation with change in composition, diameter of nanowire, and/or shell thickness suggests a promising perspective for band-gap engineering and the fabrication of novel nanoarchitectures for optoelectronic applications. Theoretical studies on this technologically important aspect of nanowires are still in a very nascent stage and demands for more involved studies which can include planar modulated superstructure.

6.8 Conclusion and perspective remarks

The developments and achievements in the field of synthesis and applications of the Si nanowires have brought them as strongest candidates in the arena of ever evolving area of nanotechnology. They have emerged as most important and smallest circuit elements for electronic applications as well as the smallest and precise sensors for the

detection of chemical and biological species at molecular scale. The possibilities of forming nanotubular structures of silicon with metal encapsulation have open up novel possibilities of quasi-one-dimensional structures of silicon which could be both metallic and semiconducting. A long-standing goal of the integration of electronic with optoelectronic in silicon-based devices appears to be realizable for the first time in nanosilicon-based devices. Theoretical studies are giving way to develop a microscopic understanding of the properties of such nanostructures of silicon and are complimenting experimental studies as often at this scale a detailed knowledge of structure from experiments is difficult. This is one of the research areas where complimentary theoretical and experimental research can be helpful in atomic scale design of silicon nanostructures. The full potentials of SiNW and nanotube applications are yet to be unfolded and we expect to see many developments and rapid progress both theoretically and experimentally in the years to come.

Acknowledgements

We thankfully acknowledge the support of the staff of the Center for Computational Material Science, IMR, Tohoku University for allowing the use of the Hitachi SR8000/64 supercomputing facilities. AKS is thankful for the support of a JSPS fellowship. AKS also thankfully acknowledges partial support of the MRSEC Program of the National Science Foundation under Award No. DMR05-20415. VK gratefully acknowledges support at RICS from NAREGI Nano Science Project, Ministry of Education, Culture, Sports, Science and Technology, Japan and the hospitality at IMR, Tohoku University, RICS, AIST and the Institute of Mathematical Sciences.

REFERENCES

1. A.G. Cullis and L.T. Canham, *Nature* **353**, 335 (1991).
2. S. Iijima, *Nature* **354**, 56 (1991).
3. W. Liang, *et al.*, *Nature* **411**, 665 (2001).
4. S.P. Franh, P. Poncharal, Z.L. Wang and W.A. de Heer, *Science* **280**, 1744 (1998).
5. M.J. Biercuk, *et al.*, *Appl. Phys. Lett.* **80**, 2767 (2002).
6. Y. Chen, *et al.*, *Appl. Phys. Lett.* **78**, 2128 (2001).
7. A.C. Dillon and M.J. Heben, *Appl. Phys. A.* **72**, 133 (2001).
8. N.S. Lee, *et al.*, *Diamond Relat. Mater.* **10**, 265 (2001).
9. H. Sugie, *et al.*, *Appl. Phys. Lett.* **78**, 2578 (2001).
10. P.G. Collins, K. Bradley, M. Ishigami and A. Zettel, *Science* **287**, 1801 (2000).
11. L. Guo, E. Leobandung and S. Chou, *Science* **275**, 649 (1997).
12. S. Tiwari, *et al.*, *Appl. Phys. Lett.* **68**, 1377 (1996).
13. R.J. Read, *et al.*, *Phys. Rev. Lett.* **69**, 1232 (1992)
14. F. Buda, J. Kohanoff and M. Parrinello, *Phys. Rev. Lett.* **69**, 1272 (1992).
15. G.D. Sanders and Y-C. Chang, *Phys. Rev. B* **45**, 9202 (1992).
16. M.S. Hybertsen and M. Needels, *Phys. Rev. B* **48**, 4608 (1993).
17. C. Delerue, G. Allan and M. Lannoo, *Phys. Rev. B* **48**, 11024 (1993).
18. C-Y. Yeh, S.B. Zhang and A. Zunger, *Phys. Rev. B* **50**, 14405 (1994).
19. B. Delley and E.F. Steigmeier, *Appl. Phys. Lett.* **67**, 2370 (1995).
20. J-B. Xia and K.W. Cheah, *Phys. Rev. B* **55**, 15688 (1997).
21. A.M. Morales and C.M. Lieber, *Science* **279**, 208 (1998).

22. J.D. Holmes, K.P. Johnston, R. Doty and B.A. Korgel, *Science* **287**, 1471 (2000).
23. V. Schmidt, S. Senz and U. Gosele, *Nano Lett.* **5**, 931 (2005).
24. Y. Wu, Y. Cui, L. Huynh, C.J. Barrelet, D.C. Bell and C.M. Lieber, *Nano Lett.* **4**, 433 (2004).
25. X.-Y. Zhang, *et al., Adv. Mater.* **13**, 1238 (2001).
26. S. Ge, *et al., Adv. Mater.* **17**, 56 (2005).
27. Z. Zhong, *et al., Science* **302**, 1377 (2003).
28. Y. Cui and C.M. Lieber, *Science* **291**, 851 (2001).
29. Y. Huang, X. Duan, Y. Cui, L.J. Lauhon, K.-H. Kim and C.M. Lieber, *Science* **294**, 1313 (2001).
30. Y. Cui, Q. Wei, H. Park and C.M. Lieber, *Science* **293**, 1289 (2001).
31. P. Alivisatos, *Nat. Biotechnol.* **22**, 47 (2004).
32. Z. Zheng, *et al.*, *Nat. Biotechnol.* **23**, 1294 (2005).
33. J. Hahm and C.M. Lieber, *Nano Lett.* **4**, 51 (2003).
34. F. Patolsky, G. Zheng, O. Hayden, M. Lakadamyali, X. Zhuang and C.M. Lieber, *Proc. Natl. Acad. Sci. USA* **101**, 14017 (2004).
35. U.W. Wang, C. Chen, K. Lin, Y. Fang and C.M. Lieber, *Proc. Natl. Acad. Sci. USA* **102**, 3208 (2005).
36. R.Q. Zhang, S.T. Lee, C.K. Law, W.K. Li and B.K. Teo, *Chem. Phys. Lett.* **364**, 251 (2002).
37. S.B. Fagan, *et al.*, *Phys. Rev. B* **61**, 9994 (2000).
38. S.B. Fagan, R. Mota, R.J. Baierle, G. Paiva, A.J.R. da Silva and A. Fazzio, *J. Mol. Struct.* (Theochem) **539**, 101 (2001).
39. A.S. Barnard and S.P. Russo, *J. Phys. Chem. B* **107**, 7577–7581 (2003).
40. S.Y. Jeong, J.Y. Kim, H.D. Yang, B.N. Yoon, S.H. Choi, S.J. Eum, C.W. Yang and Y.H. Lee, *Adv. Mater.* **15**, 1172 (2003).
41. M. De Crescenzi, *et al.*, *Appl. Phys. Lett.* **86**, 23190 (2005).
42. Y-W Chen, Y-H. Tang, L-Z. Pei and C. Guo, *Adv. Mater.* **15**,1172–1176 (2003).
43. V. Kumar and Y. Kawazoe, *Phys. Rev. Lett.* **87**, 045503 (2001); *ibid.* **91** 199901(E) (2003).
44. V. Kumar and Y. Kawazoe, *Phys. Rev. B* **65**, 073404 (2002).
45. V. Kumar and Y. Kawazoe, *Phys. Rev. Lett.* **88**, 235540 (2002).
46. V. Kumar and Y. Kawazoe, *Appl. Phys. Lett.* **86**, 859 (2002).
47. H. Hiura, T. Miyazaki and T. Kanayama, *Phys. Rev. Lett.* **86**, 1733 (2002).
48. V. Kumar, C. Majumder and Y. Kawazoe, *Chem. Phys. Lett.* **363**, 319 (2002).
49. V. Kumar, *Eur. Phys. J. D* **24**, 227 (2003).
50. A.K. Singh, V. Kumar and Y. Kawazoe, *Phys. Rev. B* **71**, 115429 (2005).
51. M. Ohara, K. Koyasu, A. Nakajima and K. Kaya, *Chem. Phys. Lett.* **371**, 490 (2003).
52. K. Koyasu, M. Akutsu, M. Mitsui and A. Nakajima, *JACS* **127**, 4998 (2005).
53. A.K. Singh, V. Kumar, T.M. Briere and Y. Kawazoe, *Nano Lett.* **2**, 1243 (2002).
54. A.K. Singh, T.M. Briere, V. Kumar and Y. Kawazoe, *Phys. Rev. Lett.* **91** 146802, (2003).
55. M. Menon, A.N. Andriotis and G.E. Froudakis, *Nano Lett.* **2**, 301 (2002).
56. A.N. Andriotis, G. Mpourmpakis, G.E. Froudakis and M. Menon, *New J. Phys.* **4**, 78 (2002).
57. V. Kumar, T.M. Briere and Y. Kawazoe, *Phys. Rev. B* **68**, 155412 (2003).
58. W. Kohn and L. Sham, *Phys. Rev.* **140**, A1133 (1965).
59. J.P. Perdew, *Electronic Structure of Solids '91*, Eds. P. Ziesche and H. Eschrig, (Akademie Verlag, Berlin 1991); J.P. Perdew, S. Kurth, A. Zupan and P. Blaha, *Phys. Rev. Lett.* **82**, 2544 (1999); J.F. Dobson and J. Wang, *Phys. Rev. B* **62**, 10038 (2000).
60. G. Kresse and J. Furthmuller, *Phys. Rev. B* **54**, 11169 (1996); *Comput. Mater. Sci.* **6**, 15 (1996).
61. G. Kresse and J. Joubert, *Phys. Rev. B* **59**, 1758 (1999).
62. G. Seifert, T. Kohler, H.M. Urbassek, E. Hernandez and T. Frauenheim, *Phys. Rev. B* **63**, 193409 (2001).
63. S. Gemming and G. Seifert, *Phys. Rev.* **68**, 075416 (2003).
64. G. Seifert and T. Frauenheim, *J. Korean Phys. Soc.* **37**, 89 (2000).
65. X. Yang and J. Ni, *Phys. Rev. B* **72**, 195426 (2005).
66. Y.H. Tang, L.Z. Pei, Y.W. Chen and C. Guo, *Phys. Rev. Lett.* **95**, 116102 (2005).
67. V. Kumar, *Comp. Mater. Sci.* **36**, 1 (2006).
68. A.K. Singh, V. Kumar and Y. Kawazoe, *J. Mater. Chem.* **14**, 555 (2004).
69. J.C. Grossman and L. Mitas, *Phys. Rev. B* **52**, 16735 (1995).
70. V. Kumar and Y. Kawazoe, *Phys. Rev. Lett.* **90**, 055502 (2003).

71. H. Vach and Q. Brulin, *Phys. Rev. Lett.* **95**, 165502 (2005).
72. A.A. Saranin, *et al.*, *Nano Lett.* **4**, 1469 (2004).
73. A.K. Singh, Ph.D. Thesis, 2004.
74. G. Mederios-Ribeiro, A.M. Bratkovski, T.I. Kamins, D.A.A. Ohlberg and R.S. Williams, *Science* **279**, 353 (1998)20.
75. C. Preinesberger, S.K. Becker, S. Vandr, T. Kalka and M. Dhne, *J. Appl. Phys.* **91**, 1695 (2002).
76. Y. Chen, D.A.A. Ohlberg, G. Mederios-Ribeiro, Y.A. Chang and R.S. Williams, *Appl. Phys. Lett.* **76**, 4004 (2000); Y. Chen, D.A.A. Ohlberg and R.S. Williams, *J. Appl. Phys.* **91**, 3213 (2002).
77. J. Nogami, B.Z. Liu, M.V. Katkov, C. Ohbuchi and N.O. Birge, *Phys. Rev. B* **63**, 233305 (2001).
78. T. Dumitric, M. Hua and B.I. Yakobson, *Phys. Rev.* **70**, 241303 (2004).
79. A.K. Singh, V. Kumar and Y. Kawazoe, *Phys. Rev. B* **69**, 233406 (2004).
80. V. Kumar and Y. Kawazoe, *Appl. Phys. Lett.* **83**, 2677 (2003).
81. Y.D. Park, *et al., Science* **295**, 651 (2002).
82. Y. Zhao, T. Shishidou and A.J. Freeman, *Phys. Rev. Lett.* **90**, 47204 (2002).
83. A.K. Singh, V. Kumar and Y. Kawazoe, *Phys. Rev. B* **71**, 075312 (2005).
84. A.K. Singh, V. Kumar and Y. Kawazoe, *Eur. Phys. J. D* **71**, 075312 (2005).
85. B. Marsn and K. Sattler, *Phys. Rev. B* **60**, 11593 (1999).
86. K. Ho, A.A. Shvartsburg, B. Pan, Z. Lu, C. Wang, J.G. Wacker, J.L. Fye and M.F. Jarrold, *Nature* **392**, 582 (1998).
87. L. Mitas, J.C. Grossman, I. Stich and J. Tobik, *Phys. Rev. Lett.* **84**, 1479 (2000).
88. U. Rothlisberger, W. Andreoni and M. Parrinello, *Phys. Rev. Lett.* **72**, 665 (1994).
89. B. Li, P. Cao, R.Q. Zeng and S.T. Lee, *Phys. Rev. B* **65**, 125305 (2002).
90. M. Menon and E. Richter, *Phys. Rev. Lett.* **91**, 792 (1999).
91. S. Ismail-Beigi and T. Arias, *Phys. Rev. B* **55**, 11923 (1998).
92. M.S. Hybertsen, M. Needels, N. Roberts and R.J. Needs, *Surf. Sci.* **236**, 112 (1990); J. Fritsch and P. Pavone, *ibid.* **344**, 159 (1995).
93. Y. Zhao and B.I. Yakobson, *Phys. Rev. Lett.* **83**, 035501 (2003).
94. R. Rurali and N. Lorente, *Phys. Rev. Lett.* **94**, 026805 (2005).
95. R. Rurali and N. Lorente, *Nanotechnology* **16**, S250 (2005).
96 A.K. Singh, V. Kumar, R. Note and Y. Kawazoe, *Nano Lett.* **5**, 2302 (2005).
97. A.K. Singh, V. Kumar and Y. Kawazoe, Unpublished.
98. D.D.D. Ma, C.S. Lee, F.C.K. Au, S.Y. Tong and S.T. Lee, *Science* **299**, 18742003 (2003).
99. Y. Wu, Y. Cui, L. Huynh, C.J. Barrelet, D.C. Bell and C.M. Lieber, *Nano Lett.* **4**, 433 (2004).
100. X. Zhao, C.M. Wei, L. Yang and M.Y. Chou, *Phys. Rev. Lett.* **92**, 236805 (2004).
101. A.K. Singh, V. Kumar, R. Note and Y. Kawazoe, *Nano Lett.* **6**, 920(2006).
102. T.-L. Chan, C.V. Ciobanu, F.-C. Chuang, N. Lu, C.-Z. Wang and K.-M. Ho, *Nano Lett.* **6**, 277 (2006).
103. U. Landman, R.N. Barnett, A.G. Scherbakov and P. Avouris, *Phys. Rev. Lett.* **85**, 1958 (2000).
104. M. Durandurdu, *Phys. Stat. Sol. B* **243**, R7 (2006).
105. M.S. Gudiksen, *et al.*, *Nature* **415**, 617 (2002).
106. M.T. Bjork, *et al.*, *Appl. Phys. Lett.* **80**, 1058 (2002).
107. Y.Y. Wu, R. Fan and P.D. Yang, *Nano Lett.* **2**, 83 (2002).
108. M. Nirmal and L. Brus, *Acc. Chem. Res.* **32**, 407 (1999).
109. L.J. Lauhon, *et al.*, *Nature* **420**, 57 (2002).
110. R.N. Musin and Xiao-Qian Wang, *Phy. Rev. B* **71**, 155318 (2005).
111. L. Vegard, *Z. Phys.* **5**, 17 (1921).

CHAPTER SEVEN

Phonons in Silicon Nanowires

Kofi W. Adu[1], Humberto R. Gutierrez[1] and Peter C. Eklund[1,2]

Contents

7.1 Introduction 259
7.2 Theoretical Models for Confined Phonons 261
7.2.1 Lattice Dynamics of Si Nanowires 261
7.2.2 The Richter Model for Raman Scattering from Confined Phonons 267
7.3 Experimental Evidence of Confined Phonons in Silicon 269
7.3.1 Acoustic Phonons 269
7.3.2 Optical Phonons 273
7.3.3 Thermal Conductivity 275
7.4 Effects of Inhomogeneous Laser Heating on Raman Lineshape 278
7.4.1 Stokes–AntiStokes Ratio as a Probe of Laser Heating of Si Nanowires 279
7.4.2 Evolution of the Raman Band Asymmetry with Laser flux 280
7.4.3 Modification of Richter's Lineshape Function to Include Inhomogeneous Heating 282
7.5 Summary and Conclusions 285
Acknowledgements 285
References 286

Abstract

Cubic silicon in bulk form has changed the modern landscape of electronics and electro-optics. The physical and chemical properties of Si are perhaps the best understood of any crystalline solid. It is therefore a crucial crystalline material to research and understand the possibilities for new devices at the nanoscale where quantum confinement phenomena drive the formation of new electronic and phonon states. In this chapter, we focus on phonon properties expected for "confined" Si in the form of nanowires. We review calculations of the phonon dispersion in small diameter nanowires as well as experiments that seek to probe the change in the phonon dispersion and the associated physical properties. Discussion is presented on the observation and interpretation of data on inelastic light scattering from nanowire phonons (Raman and Brillouin Spectroscopy), thermal conductivity and specific heat.

[1] Department of Physics, Pennsylvania State University, University Park, PA, 16802 USA.
[2] Materials Science and Engineering Deptartment and Materials Research Institute, Pennsylvania State University, University Park, PA, 16802 USA.

Nanosilicon
9780080445281
Copyright © 2007. Elsevier Ltd.
All rights reserved.

7.1 Introduction

In this chapter, we will review the phonon properties of Si nanowires. We will consider how quantum confinement in the waist of the nanowire leads to new phonon dispersion. We will also review experimental work that probes how the physical properties related to phonons change with decreasing wire diameter (e.g. Raman and Brillouin scattering, thermal conductivity, specific heat). Many of the concepts that we discuss should be perfectly general and apply to other semiconducting nanowire systems as well. Our knowledge of the bulk physical properties of crystalline and amorphous Si since the 1950s has led to a wide landscape of electronic, electro-optic and photovoltaic devices. These devices have been, and will continue to be, of tremendous importance to society [1–4]. In the past 10 years, considerable effort has been expended to find new properties of semiconductors that can be obtained by reducing the dimension (D) of the system from the bulk (i.e. 3D), to ultra-thin films (2D) [2–4], to small diameter nanowires (1D) [2–24] and finally to small particles or "quantum dots" (0D) [2–4]. Si nanosystems have certainly been at the centre of many of these studies.

For electronic devices, the geometry of a long wire is ideal. Standard device fabrication techniques can then be used to add contacts and lead wires to electronically interrogate them. The discovery of the growth of small diameter semiconducting nanowires [25–32] has therefore led to widespread research activity driven by the anticipation of many applications, e.g. transistors and logic gates [20,21,28,31–45], electro-optic devices [46–51] and sensors [18–24]. A variety of nanowires have been synthesized by methods usually identified with the so-called vapour–liquid–solid (VLS) growth mechanism [7,8,25,52]. In particular, silicon nanowires with diameter in the range $\sim 2 \leqslant d \leqslant 20$ nm have been prepared via this route [53–74]. The wires have been found to grow along several directions (e.g. 111, 001, 110, 112), depending on the wire diameter and growth conditions.

Calculations of quantum confinement effects on the electronic states of small diameter Si nanowires have been carried out [53,75–80]. For example, small diameter (110) Si wires have been found to exhibit a direct rather than an indirect band gap [53, 75–80]. With decreasing wire diameter d, the gap is found to increase as $\sim d^{-1.7}$ [53,75,76,79,80]. These predictions have been verified in Si by scanning tunnelling spectroscopy (STS) [81]. The phonon spectrum, or phonon dispersion (frequency versus wavevector), and how it depends on d, is also of fundamental importance to nanowire devices. Phonons will be the dominant scattering mechanism for electrons at elevated temperature. Interestingly, there have been a few reports of *ballistic* transport in 5–10 nm diameter semiconducting wires [82] and it is not yet known if the nanowire geometry reduces the importance of electron–phonon scattering. Calculations of the changes in phonon dispersion in confined systems have also been reported [83–99] and they will be reviewed here. We describe below two different approaches to calculate the phonon dispersion in small diameter Si nanowires. One calculation is based on wires periodically embedded in a crystalline medium [91,92,95–97], while the other is for a free standing nanowire [83–86,93].

Several groups have reported observing phonon confinement effects in nanowires via Raman scattering [7,8,52,57,100–115]. They have interpreted their results in

terms of a phenomenological model originally developed by Richter, *et al.* for Raman scattering from nanoparticles [102]. This model was extended by Campbell and Fauchet to the case of nanowires and thin films [103]. The so-called "Richter" model has been found quite useful to experimentalists, since it provides an expression for the Raman lineshape that is sensitive to nanoparticle or nanowire diameter. We will discuss the application of this model to experimental spectra in some detail and also consider its application to situations where the laser field is particularly intense and causes inhomogeneous heating in the scattering volume.

Bulk silicon has two atoms per primitive cell. Therefore, there must be six phonon branches, including three acoustic and three optic branches. The phonon dispersion calculated for bulk Si (solid curves) is shown in Fig. 7.1 [116,117]. The results are plotted for the full range of wavevectors q ($q = 2\pi/\lambda$, where λ is the wavelength of the

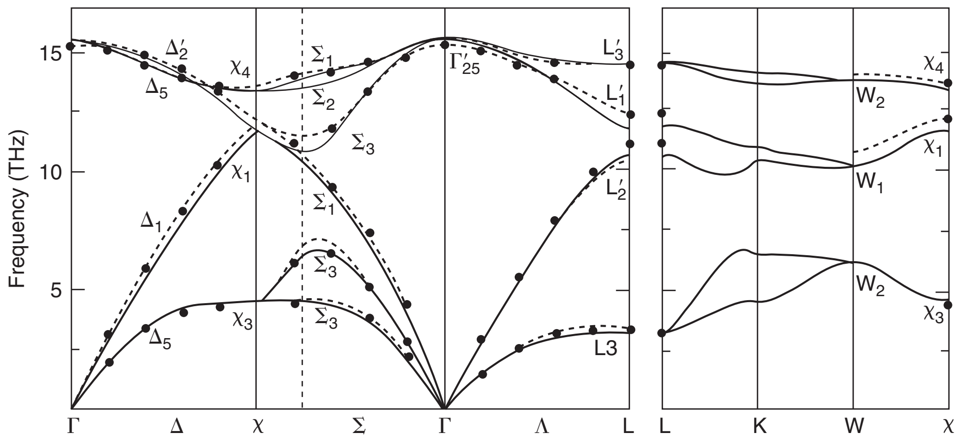

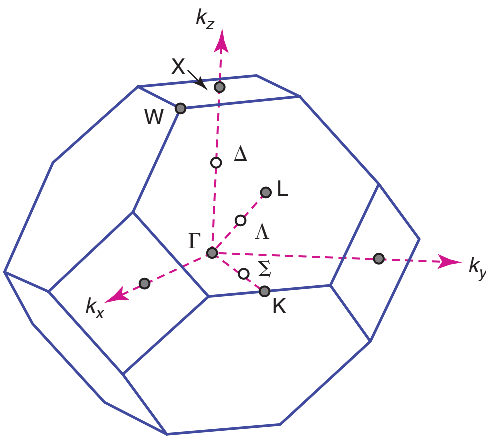

Figure 7.1 (a) Phonon dispersion curves for bulk Si. Solid lines show the bond charge model results. The experimental values (solid circles) are from Refs. [118,119]. Dashed lines represent the valence force potential calculation of Refs. [116,117]. (b) Brillouin zone for the fcc lattice (Reproduced with permission from Ref. [116] copyright 1977 APS and from Ref. [117] copyright 1972 AIP).

lattice wave or phonon along various high symmetry directions in the first Brillouin zone). The phonon dispersion of bulk Si is remarkably simple compared to that calculated for small Si nanowires). The data in the figure (solid points) are from inelastic neutron scattering experiments [118,119]. Acoustic branches involve phonons (lattice waves) where the nearest neighbour atoms vibrate in phase. Optic branches, on the other hand, involve phonons where these atoms vibrate out of phase. Two of the acoustic branches are associated with atomic motion primarily transverse to the direction of propagation (i.e. transverse acoustic or TA) and the remaining acoustic branch describes a longitudinal displacement of the atoms primarily parallel to the direction of phonon propagation (LA). The same designation can be made for the out-of-phase or optic (O) phonon modes, i.e. there is one LO branch and two TO branches. The acoustic branches exhibit the property $\omega \rightarrow 0$ as $q \rightarrow 0$, whereas the optic phonons exhibit $\omega \rightarrow \omega_o$ as $q \rightarrow 0$. Normally, the acoustic branches exhibit linear dispersion at small wavevectors. The slope of the dispersion curve at small q is known as the sound velocity. The longitudinal sound velocity is normally larger than the transverse sound velocity. Even though Si is a simple cubic solid with the minimum number of atoms per unit cell (2) required to support optic phonons, it is clear from Fig. 7.1 that Si has an anisotropic sound velocity. Because no formal charge separation exists between the two inequivalent Si atoms in the primitive cell (i.e. the primitive cell does not support a static electric dipole moment), the LO and TO branches are degenerate at the centre ($q = 0$) of the Brillouin zone. Note that the LA and LO branches are degenerate at the zone boundary ($q = \pi/a$) along the [100] direction (X-point). This degeneracy occurs because of the cubic symmetry of the Si lattice and the fact that both atoms in the primitive cell have the same mass.

However, the primitive cell of the infinite crystal is no longer the fundamental structural unit for a nanowire. Strictly speaking, the formal primitive cell of the nanowire involves all the atoms in the volume defined by the cross section of the wire and contained within the fundamental repeat distance along the wire axis. Of course, the formulation of a larger unit cell affects both the electron and phonon states. Intuitively, we expect that as the wire diameter increases, the physical properties will eventually return to that of the bulk Si.

The organization of the chapter can be summarized as follows. A discussion of "confined" phonon dispersion and the Richter model is presented in Section 7.2. In Section 7.3, we present experimental studies on confined phonons in Si. In Section 7.4, we discuss the effects of inhomogeneous laser heating during Raman scattering studies of Si nanowires. In Section 7.5, we summarize the main results in this chapter and make suggestions for future research in phonon confinement.

7.2 Theoretical models for confined phonons

7.2.1 Lattice Dynamics of Si Nanowires

The phonon dispersion of low dimensional nanostructures has been studied over the past 25 years [83–99,120]. Classical theories date back even further to the late 1800s [121]. Recent calculations have been carried out in both the continuum approximation as well as with atoms on a discrete lattice. A rather complete discussion of the acoustic modes in nanostructures based on elastic continuum theory has been

presented by Stroscio and Dutta [95]. To understand the impact of the physical boundary of the nanowire on the phonon properties, we review two recent calculations, one by Thonhauser and Mahan [85,86] for free standing Si nanowires and another by Hepplestone and Srivastava [91,92] for Si nanowires periodically embedded in a crystalline medium.

We start with the calculations of Thonhauser and Mahan. They computed the phonon dispersion in Si [111] nanowires using the Stillinger–Weber potential [116,122] which contains terms for bond stretching and bond bending. This potential has been widely used, and fits the experimental phonon dispersion obtained by inelastic neutron scattering [123]. The cross section of Si nanowire with a [111] wire axis along the z direction is shown in Fig. 7.2a. Confinement of electrons and phonons therefore takes place in the (x, y) plane. As shown in the figure, the nanowires are chosen to have a hexagonal cross section, i.e. they are faceted. The atoms in the (111) planes can be thought of as residing in rings about a central atom. Therefore, a particular diameter Si (111) wire can be described by the number of rings of Si atoms that exist in the wire cross section. The primitive cell requires six layers of atoms along the

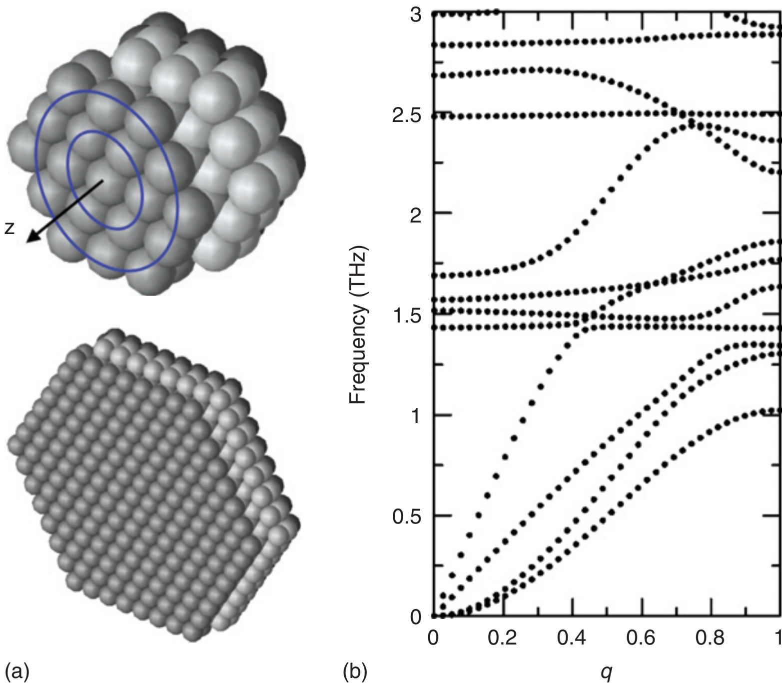

Figure 7.2 (a) Unit cell of a Si nanowire with axis along the [111] direction. Each unit cell consists of six layers in the hexagonal structure. Depicted are a unit cell with two rings of atoms (top) and with seven rings of atoms (bottom). The groups of different layers are coloured in different grey scales. (b) Some low frequency branches of the phonon spectrum for a Si [111] 7-ring nanowire. q thereby refers to the reduced wavevector. Four acoustic branches are clearly visible. Two acoustic modes linear in q (longitudinal and transversal), but also two modes proportional to q^2, which are characteristic for wires (Reproduced with permission from Ref. [86] copyright 2004 APS).

[111] axis (Fig. 7.2a) and this number is independent of the number of rings of atoms in a layer. The new (longer) periodicity along the nanowire axis generates a significantly larger primitive cell. For example, a seven-ring Si [111] nanowire of lateral dimension $7a$ ($a_{\mathrm{Si}} = 0.5431$ nm) has 1014 atoms in its six-layer primitive cell. The dynamical matrix therefore has dimension 3042×3042. Bulk Si, on the other hand, has 2 atoms per primitive cell and six degrees of freedom. The phonon wavevector can only be along the wire axis.

The complexity in the phonon dispersion curves generated by the introduction of the nanowire surface can be formidable. A seven-ring Si [111] nanowire has 3042 phonon branches and is quite complicated. At high frequency, the optic mode branch density is extremely dense relative to the bulk. In Fig. 7.2b, we show only the lowest 12 branches calculated by Thonhauser and Mahan for a seven-ring Si [111] nanowire (3 THz corresponds to $\sim$100 cm^{-1}) [86]. It can be seen that eight of the lowest lying branches are optical and *four* are acoustic. Infinite solids normally exhibit three acoustic branches with linear dispersion (i.e. $\omega \sim q$) at long wavelength ($q \sim 0$). However, as can be seen in the figure, only the two upper acoustic branches exhibit linear dispersion. The lower two acoustic branches exhibit an unusual quadratic dispersion (i.e. $\omega \sim q^2$) at small q, as is also calculated for a carbon nanotube [124]. The uppermost acoustic branch in the figure corresponds to the LO branch in the bulk and the sound velocity is close to that of the bulk LA mode. The next lower acoustic branch is a (transverse) rotary mode branch. Finally, the lowest two ($\omega \sim q^2$) acoustic branches are transverse "snake-like" phonon branches, i.e. the nanowire wiggles when these modes are excited. If the wire is pinned to a substrate these modes are probably strongly damped. As the diameter of the wire becomes very large, we suspect that the rotary mode loses its rotary character and becomes a TA mode similar to the bulk. The two transverse "snake" branches should become degenerate and form the other bulk-like TA branch. Mahan and Thonhauser reported that the sound velocity v_s for the two lower acoustic branches, i.e. $v_s = (\mathrm{d}\omega/\mathrm{d}q)_q \sim 0$, exhibits a significant dependence on the number of atomic rings n in the nanowire. The veloci-ties were found to increase by $\sim$20–30% as n increases from 1 to 7. The appearance of *four* acoustic phonon branches in a nanowire is a very interesting result and apparently is a general property of free standing nanowires. Four acoustic phonon branches were first predicted by Nishiguchi *et al.*, although they did not provide a complete mapping of the phonon dispersion [125].

The existence of the low lying *optical* branches in small diameter nanowires is also very interesting. Eigenvectors ($q = 0$) calculated for some of these low frequency optical branches in 7-ring Si [111] nanowires are shown in Fig. 7.3. Modes labelled (a) and (b) in the figure correspond to L modes (displacement parallel to [111]) and the modes labelled (c) and (d) exhibit atomic displacement transverse (T) to the [111] nanowire axis. Of particular importance, Thonhauser and Mahan [85] have also reported a low frequency "radial" optical mode in which all atoms exhibit a nearly radial in-phase displacement with decreasing amplitude as the atoms approach the surface of the nanowire. The radial mode was also shown to exhibit Raman activity [85]. Interestingly, a Raman-active radial (or breathing) mode, with frequency $\omega \sim 1/d$ is the hallmark of single walled carbon nanotubes.

For comparison to the low frequency optical mode eigenvectors (Fig. 7.3), we display in Fig. 7.4 six more of the family of optical modes, but with frequency near

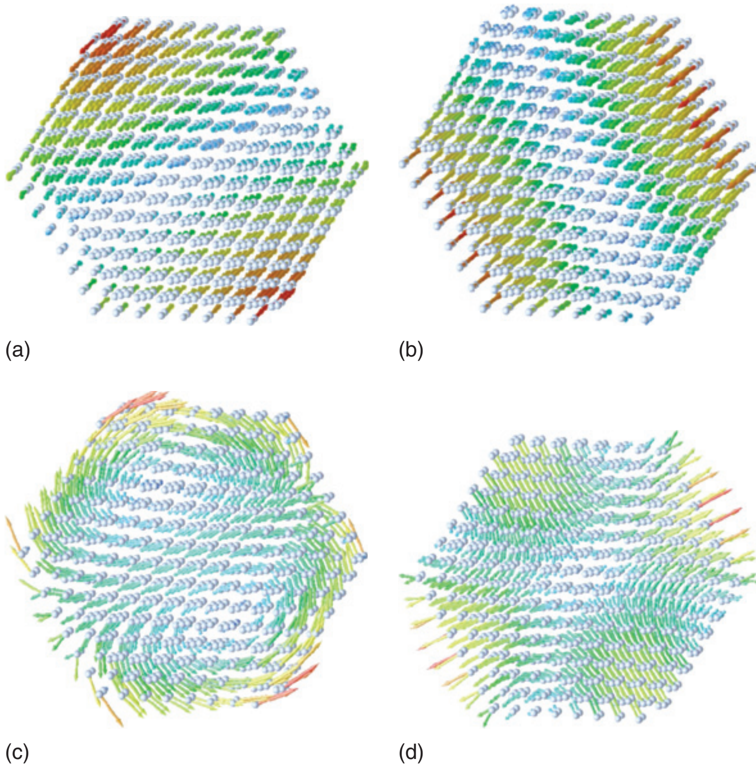

Figure 7.3 Eigenvectors of the four lowest lying optic modes around 1.5 THz for $q = 0$. The line of sight is slightly off the [111] direction in order to better view the mostly longitudinal modes in (a) and (b) (Reproduced with permission from Ref. [86] copyright 2004 APS).

the Raman-active optical modes (LO–TO) in bulk Si (i.e. $\omega \sim 520\,\text{cm}^{-1}$) [85]. As Thonhauser and Mahan point out, the displacement pattern can have a variety of symmetries that is not necessarily dominated by the 6-fold wire cross section of the nanowire. Figure 7.4 indicates that the amplitude of vibration of the surface atoms involved in the optical modes is very small (or zero) compared to the maximum displacement in the mode. This is clear support for a "clamped" boundary condition for the optical modes in nanowires. This should be a general result for all nanosystems [86].

We next turn to highlights of related Si nanowire phonon calculations by Hepplestone and Srivastava [91,92]. Their calculations are based on square cross section Si [100] nanowire that is periodically embedded in a (fictitious) lattice (supercell approach). The atoms in the fictitious lattice are also organized on the same cubic (Si) lattice. However, the fictitious atoms are assigned a mass 10^{-6} that of Si. This mass assignment separates the phonon modes associated with the fictitious medium from the nanowire phonon modes. The calculation is therefore designed to provide information on a free standing nanowire. A bond charge potential developed by Weber [116] was used to describe the force between all atoms (in the nanowire and the medium atoms).

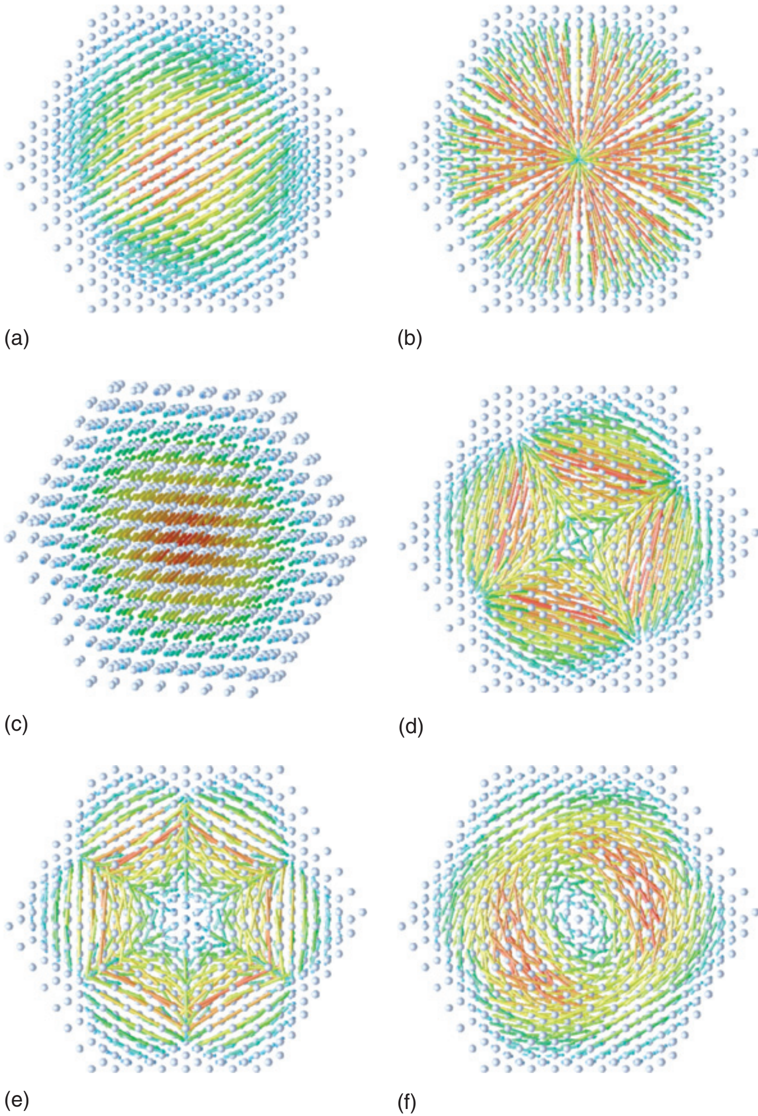

Figure 7.4 Eigenvectors of some optical phonon modes around 15.3 THz for $q = 0$. The line of sight parallels the [111] direction, except in case (c), where it is slightly of the [111] direction, so that the mostly longitudinal mode is better to see (Reproduced with permission from Ref. [86] copyright 2004 APS).

The "supercell" approach of Hepplestone and Srivastava also confirms the existence of "clamped" surface atoms for the optic modes. However, the supercell model fails to generate *four* acoustic branches. This may stem from the finite coupling to the fictitious medium. It is nevertheless interesting to compare their supercell results with those of the Thonhauser and Mahan for free standing nanowires [86]. This comparison is most easily done below $\sim 100\,\text{cm}^{-1}$, where the density of phonon branches is low enough to distinguish one branch from another. The supercell results for a

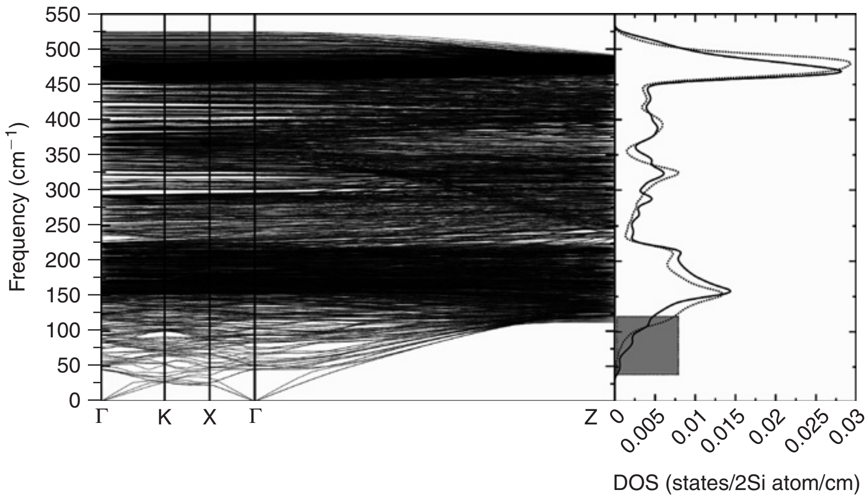

Figure 7.5 The phonon dispersion curves and density of states for a silicon nanowire of cross section 3.8 nm × 3.8 nm. The Γ−X direction is considered to be perpendicular to the direction of propagation of the wire, the Γ−Z direction is parallel to the direction of propagation of the wire and Γ−K is along the face diagonal in the Brillouin zone for the wire. Also shown are the density of states for the wire (bold line) and the density of states of bulk silicon (dashed line) (Reproduced with permission from Ref. [92]).

$7a \times 7a$ Si [100] nanowire are shown in Fig. 7.5. The directions (ΓX, ΓK and KX) are perpendicular and the direction (ΓZ) is parallel to the nanowire axis. Whereas the Thonhauser–Mahan [86] dispersion curves in Fig. 7.2b (n = seven-ring [111] wire) relate only to the lowest 12 branches below $\sim$100 cm^{-1}, the Hepplestone and Srivastava [92] dispersion curves in the figure are presented for the entire set of branches in the $7a \times 7a$ Si (100) wire. The numerous high frequency optical branches can be seen to form a tangled "spaghetti" of modes. Note that only three acoustic branches are produced by the supercell model. On the basis of Thonhauser and Mahan's results, we would have expected two $\omega \sim q^2$ branches (snake modes) and that they would be degenerate along the nanowire axis.

It is also interesting to identify a benchmark optical phonon frequency assigned to the lowest frequency optical mode ($q = 0$). We label this optical mode frequency as ω_0. From Figs. 7.2b and 7.5, respectively, we can estimate that $\omega_0 \sim 40$ cm^{-1} [92] for a $7a \times 7a$ Si [100] nanowire and $\omega_0 \sim 45$ cm^{-1} [86] for the seven-ring hexagonal Si [111] wire. These frequencies are in quite good agreement, despite the fact that the direction of the wire axis and the wire cross sectional shape are different.

One can compare a few of the eigenvectors obtained from these two calculations. The eigenvectors for the lowest three $q = 0$ optic modes of the $7a \times 7a$ (100) [92] embedded nanowires are reproduced in Fig. 7.6 [92]. The amplitude of the displacement is represented in the figure by the size of the "atom" in the lattice (large displacement, large atom). The impact of the square cross-sectional shape of the nanowire on the symmetry of the eigenvector is interesting. The eigenvectors for hexagonal and square cross section wire results should be studied by examining Figs. 7.3, 7.4 and 7.6.

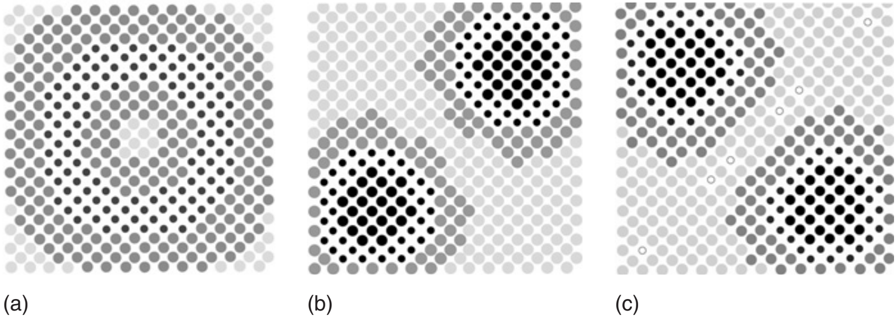

Figure 7.6 **The amplitude of atomic vibration of the three lowest optic modes near the zone centre for a nanowire of cross section 3.8 nm × 3.8 nm. The darker the atom, the higher its relative amplitude of vibration compared to other atoms: (a) lowest frequency optic mode, (b) next higher frequency optic mode and (c) third highest frequency optic mode (Reproduced with permission from Ref. [92]).**

The one-phonon density of states (pdos) for the $7a \times 7a$ Si [100] nanowire and bulk Si (bold line) are plotted for comparison to the right of the supercell phonon dispersion curves in Fig. 7.5. As can be seen, the overall pdos for the nanowire and the bulk is similar, yet the additional structure in the nanowire pdos is clearly visible.

7.2.2 The Richter Model for Raman Scattering from Confined Phonons

The model of Richter *et al.* [102] to compute Raman line profiles in small nanoparticles was extended by Campbell and Fauchet [103] to nanowires and films. It uses a superposition of bulk phonon states to describe phonons in a confined geometry. Their approach leads to a prediction of an asymmetric Raman lineshape for confined phonons that is related to a particular Raman-active *bulk* phonon. The smaller the confined system, the larger is the distortion of the Raman band from the Lorentzian lineshape of the bulk phonon.

Consider a long wavelength ($q = 0$) (Raman-active) optical phonon in an infinite system such as silicon. The displacement of the atoms would be independent of position in the system. Atoms in every primitive cell are engaged in the same displacement. To describe how the confinement due to physical boundaries (surface of the nanowire) affects this phonon mode, Richter *et al.* proposed a confined phonon wavefunction that is the simple product of the bulk phonon wavefunction and a Gaussian envelope function $G(r)$, where r is the radial coordinate in the nanowire. The factor $G(r)$ causes the atomic displacement in the confined phonon wavefunction to decay radially with increasing radial position measured from the axis of the nanowire or the centre of the nanoparticle. An expansion of this confined phonon wavefunction in Bloch phonon wavefunctions of the bulk is carried out and the spectral weight ($|C(0, q)|^2$) of each particular bulk phonon of wavevector q in the expansion of the $q = 0$ phonon is thereby determined. Their analysis shows that $|C(0, q)|^2$ is just the Fourier transform of $G(r)$ and is therefore also a Gaussian function. $C(0, q)$ defines the range of transverse bulk wavevectors (δq) needed to describe the confined phonon and the Raman scattering from the nanowire. From the form of $C(0, q)$ it is easy to show that for a nanowire with diameter d, $(d)(\delta q) \sim 1$, i.e. this is same form as the "uncertainty" principle. The Richter model is a phenomenological

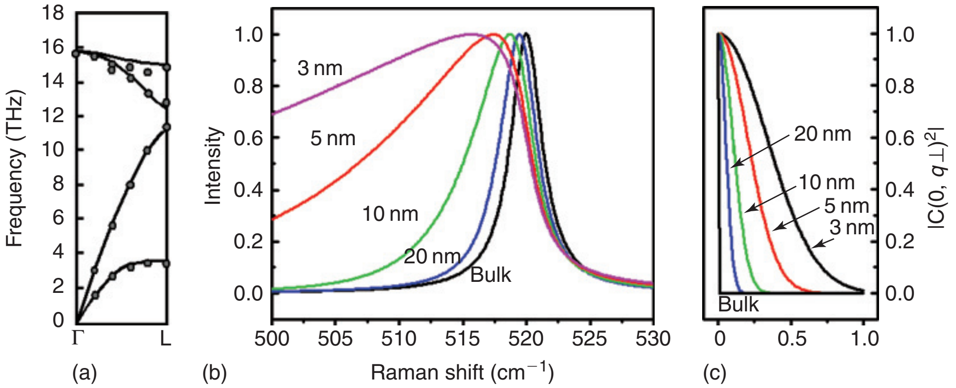

Figure 7.7 (a) Phonon dispersion for Si along Γ→L direction. (b) Calculated Raman lineshapes for individual Si nanowires with diameters from 3–20 nm, as predicted by the phonon confinement model of Richter *et al.* (Eq. 7.1) [102]. The lineshape develops asymmetry and downshifts with decreasing nanowire diameter. (c) Spectral weighting function (Eq. 7.2) for different nanowire diameters.

theory. Nevertheless, it seems to work very well, as we show later when analysing Raman scattering data on confined phonons in Si nanowires.

For a nanowire, the form of the Richter model Raman lineshape function for confined phonons related to the bulk q = 0 mode takes the following form [7,8,102,103]:

$$I_{\mathrm{NW}}(\omega) = A_{\mathrm{o}} \int_{\mathrm{o}}^{q_{\mathrm{MAX}}} \frac{|C(0, q_{\perp})|^2}{[\omega - \omega(q_{\perp})]^2 + (\Gamma/2)^2} 2\pi q_{\perp} \mathrm{d}q_{\perp} \tag{7.1}$$

where ω is the scattered photon frequency measured relative to the laser line, $\omega(q_{\perp})$ and Γ are, respectively, a bulk phonon frequency for transverse wavevector $q_{\perp}$ and the related inverse phonon lifetime. The notation $C(0, q)$ in Eq. (7.1) reminds us that we are calculating the confined phonon spectrum derived from the $q = 0$ bulk phonon. Note that the integral in Eq. (7.1) is taken over the confined transverse wavevectors $q_{\perp}$, i.e. the "parallel" wavevector ($q_{||}$) is in the direction of the nanowire axis. As can be seen in Eq. (7.1), the Raman lineshape is built from Lorentzian contributions from bulk phonons. The spectral weighting function $|C(0, q_{\perp})|)^2$ is given by:

$$|C(0, q_{\perp}|^2 \sim \exp\left[-\frac{1}{2}\left(\frac{q_{\perp} d}{\alpha}\right)^2\right] \tag{7.2}$$

The knowledgeable reader may notice that there is an additional factor α introduced into the denominator of the exponent in Eq. (7.2) that does not appear in the original article by Richter *et al.* or in the follow-up article by Campbell and Fauchet [103]. We have introduced α to set the length scale for phonon confinement. A value for α should be determined by experiment. In Fig. 7.7, we display in three panels: (a) bulk Si phonon dispersion along (111) direction, (b) the evolution of the Raman lineshape for Si nanowires from 20 to 3 nm (Richter model) and (c) the corresponding

spectral weighting function $|C(0,q_{\perp})|^2$. The wavevector is normalized to $q_{\perp} = 1$ at the zone boundary.

It may also be noticed from Eq. (7.1) that the Raman matrix element $|M_{q_{\perp}}|^2$ for scattering contribution from the infinite crystal phonon with frequency $\omega(q_{\perp})$ has been set equal to a constant and incorporated into the constant prefactor A_o. As an approximation, Γ represents the natural FWHM of all the bulk phonons contributing to the lineshape. To fit experimental data, we should convolute the natural phonon lineshape with the spectrometer function. We therefore use $\Gamma = 4.5\,\text{cm}^{-1}$ in Eq. 7.1 which is the FWHM value for the Raman band in bulk Si at $\sim 520\,\text{cm}^{-1}$ that we obtain under identical optical conditions to those used to acquire the Si nanowire Raman spectrum. The natural full width at half maximum of this phonon is known to be $\sim 3\,\text{cm}^{-1}$ at room temperature [126–129]. It should also be mentioned that the confined phonon Raman lines shown in Fig. 7.7b are calculated for $\alpha = 6.3$. This value is justified by our experiments in Si nanowires (see below) [8].

In many cases, Raman scattering from a single nanowire is too weak to observe. An ensemble of nanowires is therefore studied and the Richter analysis should be extended to include the diameter distribution for the ensemble. We can easily amend Eq. (7.1) to include a diameter distribution $F(d)$ by adding a second integral:

$$I_{\text{NWD}}(\omega, \bar{d}) = \int_0^{\infty} F(d) I_{\text{NW}}(\omega, d)\,\text{d}d \tag{7.3}$$

where $I_{\text{NW}}(\omega,d)$ is the Richter lineshape function for scattering from a single nanowire of diameter d, and $\bar{d}$ is the most probable nanowire diameter in the distribution $F(d)$.

The Richter lineshape function can also be easily equipped to handle temperature by introducing the temperature dependence of the relevant bulk phonon parameters, i.e. frequency $\omega(q_{\perp})$ and inverse phonon lifetime Γ. From Raman scattering experiments on bulk Si, the temperature dependence of ω and Γ for the $q = 0$ phonons have been determined; they are shown in Fig. 7.8, [7,126]. With increasing T, the *inverse* optical phonon lifetime Γ increases due to anharmonic interactions [126] and the phonon frequency decreases due to thermal expansion of the lattice [7,126]. In calculating the confined Raman lineshape at a particular temperature, we assume that all optical phonons ($q \neq 0$) in the same optical branch have the same T-dependence as observed for the $q = 0$ optical mode. In this limit, with increasing T, the optical branch makes a rigid, downward displacement. It can be shown that the effect of a uniform increase of temperature along the nanowires would be to homogeneously broaden the Raman line [130]. We will consider below the more general case of inhomogeneous laser heating, where a temperature distribution $T(z)$ is induced in the nanowire by the incident laser beam exciting the Raman scattering.

7.3 Experimental Evidence of Confined Phonons in Silicon

7.3.1 Acoustic Phonons

In inelastic light scattering by phonons, the total wavevector in the scattering process (i.e. phonon + photon) is conserved, i.e. $\Delta(k + q) = 0$, where k and q are,

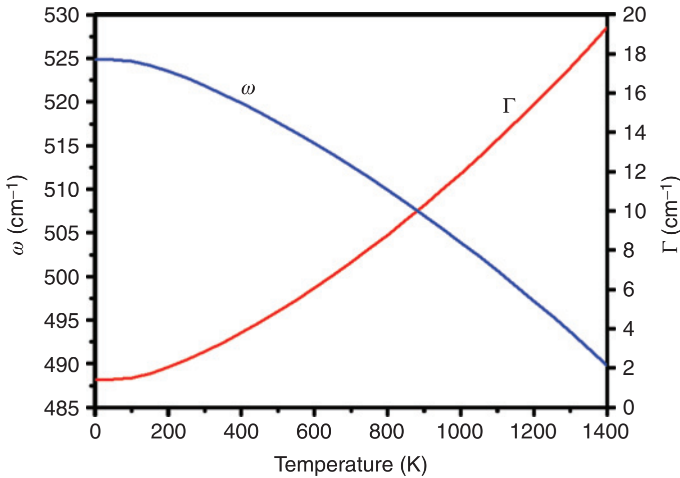

Figure 7.8 Temperature dependence of the $q = 0$ Si phonon frequency and inverse optical phonon lifetime (Γ). Γ also refers to the FWHM of the Si 520 cm^{-1} band in the bulk [7,126].

respectively, the wavevectors of the photons and phonons. Therefore, in a backscattering event, the wavevector of the phonon produced is $q = 2nk_i$, where n is the refractive index of the solid and k_i is the incident photon wavevector (for Si, $n \sim 3.9$ at 2 eV). This wavevector "selection rule" holds for acoustic or optical phonon scattering. Application of this selection rule to the excitation of *acoustic* phonons therefore predicts a narrow peak in the scattered light spectrum at a frequency shift $\omega = v_s q = 2v_s nk_i$, where v_s is the sound velocity of the phonon. These peaks are typically observed in the range ~20–200 GHz (0.7–7 cm^{-1}) which is very close in frequency to the laser line. A multi-pass Fabry–Perot interferometer, rather than a grating spectrometer, is used to detect the scattered radiation. The technique of detecting low frequency excitations in solids and liquids is called Brillouin spectroscopy.

In Fig. 7.9, we display the Brillouin spectrum of bulk Si [131]. Note that the frequency units are in GHz. The sharp peaks that are fully revealed are found in Stokes/antiStokes pairs and are assigned to longitudinal (L), transverse (T) and surface acoustic waves (S). The strong offscale peaks in the figure are artifacts [131]. Finally, a broad central "quasi-elastic" peak is observed which was found to contain two broad components that have been tentatively assigned to two-phonon difference scattering [131].

Given the more complex acoustic phonon spectrum of nanowires produced by quantum confinement in the waist of the nanowire, the Brillouin spectrum of Si nanowires would certainly be very interesting to observe. Unfortunately, to date, there have not been any reports of Brillouin scattering from nanowires. As described in the previous section, small diameter Si nanowires should support four (acoustic) phonon branches [86]. Two of these branches are predicted to exhibit the usual linear dispersion (sound waves) and should produce Brillouin peaks in the backscattering geometry at $\omega = 2v_s nk_i$, where the particular values of the sound velocity should be used. The other two branches ("snake-like" modes) are predicted to exhibit a quadratic dispersion at small q; they should produce Brillouin peaks at $\omega = cq^2 = 4c(nk_i)^2$. Since

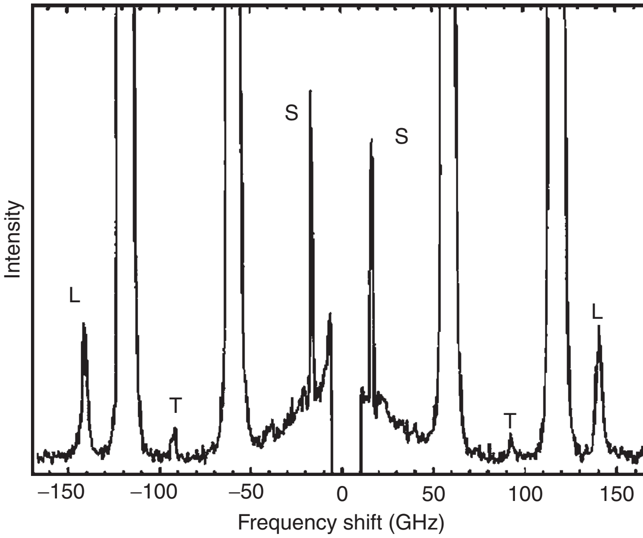

Figure 7.9 The Brillouin spectrum of silicon displays a broad quasi-elastic peak between −50 and 50 GHz. The central elastically scattered peak has been removed. Peaks corresponding to the surface acoustic wave (*S*), bulk transverse mode (*T*) and longitudinal mode (*L*) can also be observed (Reproduced with permission from Ref. [131] copyright 2000 APS).

these quadratic modes involve macroscopic wiggling of the nanowires, they may not be observed when the wires are supported directly on substrates (i.e. they might be severely damped by contact with the substrate). Thus Brillouin scattering experiments should be carried out on wires suspended over trenches in substrates or contained in loose powders. Finally, according to Thonhauser and Mahan, the acoustic mode dispersion is sensitive to nanowire diameter and nearly monodisperse nanowire samples should be preferred in these studies. Otherwise, line broadening due to the diameter distribution will be observed.

Raman spectroscopy has been used as a successful probe of low frequency modes in semiconducting nanoparticles [132–135]. These modes are the analogue of new optical modes predicted for nanowires. They are reviewed here as they give insight to the physics of confined phonons.

In the case of nanoparticles, the system is fully bounded by the external surface in all three dimensions. The vibrational modes of a fully confined small system (e.g. $d <$ phonon mean free path) are not described in terms of propagating phonons, but rather in terms of non-propagating normal modes. The low frequency normal modes of vibration of elastic solid spheres were first worked out by Lord Rayliegh in 1880 and Lamb [121] in 1882. These classical calculations are reviewed by Love [136]. These normal modes are related to the longitudinal and transverse sound waves in the bulk, or more exactly, their frequencies depend on the bulk elastic constants that define the various sound velocities. The normal modes are either spheroidal or torsional in nature and they are classified according to the symmetry group of the sphere by the labels (ℓ, m) defining the spherical harmonics $Y_{\ell m}$. Only the

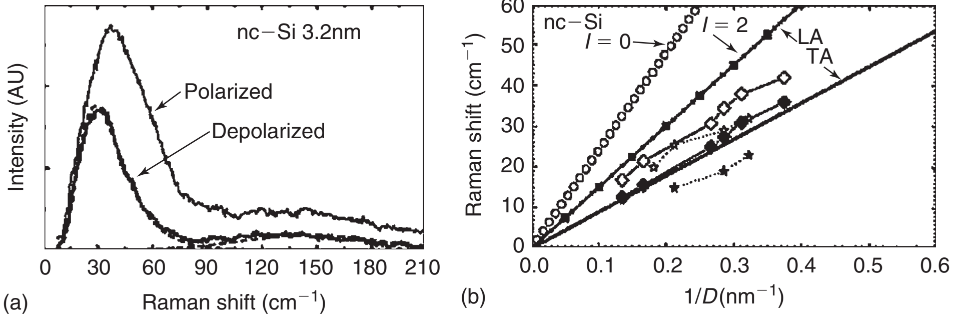

Figure 7.10 (a) Low frequency Raman spectra of nc-Si (Si nano-crystals) with average diameter of 3.2 nm as obtained from the XRD analysis. These spectra were taken under excitation with the 514.5 nm line of an Ar+ laser in the backscattering geometry. Two spectral lines with log-normal (peak $\sim 30\,\mathrm{cm}^{-1}$) and Gaussian (peak $\sim 135\,\mathrm{cm}^{-1}$) shapes were used to simulate the depolarized spectra (solid line). (b) Raman peak frequencies of polarized (open diamond) and depolarized (filled diamond) spectra versus the inverse particle diameter for nc-Si. Open circle and filled circle lines are the theoretical calculations for a free elastic sphere–spheroidal modes $l = 0$ and 2, using average sound velocities. The thin line and thick line are bulk LA and TA modes, respectively. The stars are the experimental data of nc-Si in silica from Fujii *et al.* [139,140] (adopted from Ref. [139] copyright 2005 AIP).

spheroidal modes are found to be Raman-active and the two lowest modes are $\ell = 0$ (symmetric) and $\ell = 2$ (quadrapolar). For a free standing sphere, the frequency ν_ℓ for the $\ell = 0, 2$ modes is given by [137]:

$$\nu_\ell = \frac{S_\ell v_\ell}{cD} \tag{7.4}$$

where S_ℓ are constants of the order unity ($S_0 = 0.76, S_2 = 0.84$), v_0 is the bulk longitudinal sound velocity (8790 m/s for Si), v_2 is the transverse sound velocity (5410 m/s for Si), c is the speed of light and D is the nanoparticle diameter. Note that the plots of ν versus $1/D$ then should yield straight lines whose slope is related to the respective sound velocity. The classical theory has been confirmed by recent lattice dynamical calculations by Cheng *et al.* [138]. Results for Si nanocrystals ($2 < D < 7$ nm) embedded in Silica films reported by Yang *et al.* [139] are shown in Fig. 7.10. They report that the intensity of the Raman peaks can be as strong as those identified with optical phonon modes. The Raman spectrum for $D = 3.2$ nm nanocrystals (as measured by Transmission Electron Microscopy, TEM) is shown in Fig. 7.10a. The spectrum contains two asymmetric peaks at ~ 30 and $\sim 36\,\mathrm{cm}^{-1}$. Each peak is seen in a different polarization configuration, i.e. either in polarized (||, ||) or depolarized (||, $\perp$) scattering, where the symbols in parentheses indicate the mutual alignment of the incident and scattered electric fields. The broad diameter-independent symmetric Raman peak observed at $\sim 146\,\mathrm{cm}^{-1}$ was assigned to disorder-induced zone-boundary TA phonon scattering [139]. The asymmetric shape of the low frequency peaks has been connected with inhomogeneous line broadening due to the nanoparticle diameter distribution which is well described by an asymmetric log-normal distribution [137,139]. In Fig. 7.10b [139], the peak positions of these two

low frequency peaks are plotted versus inverse diameter ($1/D$) and they are indicated in the figures as open and closed diamonds. Consistent with the classical theory, one can see that an approximate $1/D$ dependence of the mode frequency is observed. However, these frequencies lie significantly below the exactly linear results predicted for $\ell = 0$ and $\ell = 2$ that are plotted in the figure as the open and closed circles. Two other solid straight lines are plotted in the figure and are indicated by LA and TA. These lines are drawn based on the relation $\omega = vq$, the average sound velocity v of the LA and TA branch, and the assumption that $q = \pi/D$. The assumption amounts to assuming the particle size activates a particular bulk acoustic phonon whose q-vector is inversely proportional to particle diameter. The stars in the figure represent data on another set of Si nanoparticles embedded in silica by Fuji *et al.* [140]. The source of disagreement between the classical theory and experiment can reside in many factors. First, the Si particles are not free standing and they are also not spherical. Calculations by Zi *et al.* [141] predict that the coupling of the nanoparticles to the medium (silica) should soften the modes observed in polarized and depolarized scattering. Further work on Raman scattering from small crystalline nanoparticles in general, and in Si and Ge in particular, will be needed to resolve the discrepancies between experiment and theory.

7.3.2 Optical Phonons

Raman scattering from nanowires (unless resonant) is usually sufficiently weak as to prevent a spectrum from being collected on a single small diameter nanowire. In this case, the spectrum is usually collected from an ensemble of randomly oriented wires. We have found the scattering to be weak for Si nanowires [7,8] and the results summarized here are for an ensemble of our Si nanowires randomly oriented on an indium substrate.

Our Si nanowires were grown by pulsed laser vapourization (PLV) of Si:10%Fe targets maintained in heated quartz tube in flowing $Ar:H_2$. Details are presented in Ref. [108]. The growth process is known as the VLS growth mechanism and involves a small metal particle to capture semiconductor vapour to form a liquid metal–semiconductor alloy (e.g. $Si_{1-x}Fe_x$) and the wire grows in solid crystalline form from the surface of the alloy droplet. Our synthesis approach produces small diameter Si nanowires ($3 < d < 30$ nm) several μm in length. As grown, they have a few nm thick oxide coating which may form after they are handled in air.

To "tighten" the diameter distribution and also produce ensembles of nanowires with different average diameter, we have developed a means for separating the wires produced by PLV–VLS growth according to their diameter. The tubes are first harvested from the walls of the quartz tube in the PLV reactor and they are agitated in isopropanol in an ultrasonic bath followed by a short exposure to an ultrasonic horn. The suspension was then centrifuged at ~5000 rpm for a few minutes. The largest wires are driven to the bottom of the centrifuge tube and the remainder of the wires in suspension is decanted. The centrifugation of the decanted suspension is then repeated to drive down the next set of wires to the bottom of the tube. This procedure is repeated several times; each time the sediment in the bottom of the tube contains a smaller set of wire diameters. In this way, we have gathered four samples from the primary batch with successively smaller diameter Si nanowires for study. More details of this separation process are given in Refs. [7,8,142].

Ensembles of tens of Si nanowires per square micron were prepared for micro-Raman experiments by placing two to three drops of the nanowire suspension (in iso-propanol) onto indium foil and allowing the solvent to evaporate under ambient conditions.

Low resolution TEM images of Si nanowires are shown in Fig. 7.11a and b for two separate precipitates in the centrifugation process. These particular samples were found to have most probable diameter $\bar{d} = 23$ and 6.5 nm respectively, by fitting the TEM histogram data of the crystalline core to a log-normal distribution shown as the solid line in Fig. 7.11c and e. A log-normal diameter distribution is often found in nanosystems and stems from the relative importance of the surface and volume energies of the wire (or particle) [143]. The insert in Fig. 7.11a is a Scanning Electron Microscopy (SEM) image of the as-grown wires. The TEM images (Fig. 7.11a and b) show that the wires are long ($>2\,\mu$m), most have long straight sections. High resolution TEM (HRTEM) images (Fig. 7.11d and f) reveal an outer SiO_2 shell that is typically 2–4 nm thick in the as-grown wires. The oxide presumably forms when the wires are removed from the PLV apparatus and are exposed to laboratory air. The HRTEM images (JEOL 2010F @ 200 kV) of Si nanowires show individual wires: diameter $d \sim 6$ nm ((100) growth direction) (Fig. 7.11d) and $d \sim 16$ nm ((011) growth direction) (Fig. 7.11f). The growth directions were determined by correlating the electron diffraction pattern, the Fourier transform of the image and the lattice fringe spacing [7].

In Fig. 7.12, we display Raman spectra for the Si 520 cm^{-1} band in four nanowire samples. The spectra were obtained at *low* laser flux ($\Phi \sim 8\,\mu W/\mu m^2$) using an Ar^+ ion laser (514.53 nm) and a triple grating spectrometer. All data were collected at room temperature under identical optical conditions. The data are for four ensembles of nanowires whose diameter distribution $F(d)$ is fitted well by a log-normal function. The most probable nanowire diameter $\bar{d}$ for each Si nanowire ensemble is indicated above each spectrum. The asymmetric Raman bands are the signature of phonon confinement as predicted by Eq. (7.1). For comparison, we show at the bottom of the figure the one-phonon band measured in the same optical apparatus for bulk Si (001). The Raman data are represented by open circles while the solid curves are the result of least squares lineshape analyses for the nanowire spectra using the Richter model with α (Eq. 7.3) and A_o (intensity scale factor) as the only adjustable parameters. It is clear from Fig. 7.12 that with decreasing $\bar{d}$, the first order Raman band at $\sim$520 cm^{-1} band develops an increasing asymmetry to lower frequency and the peak position downshifts. The fitting to the Richter lineshape function Eq. (7.3) (solid line) is seen to be excellent. On the other hand, the lineshape for bulk Si (bottom band) is well fitted by a symmetric Voigt function which is the convolution of Gaussian spectrometer function (FWHM = 1.5 cm^{-1}) and a Lorentzian representing the natural phonon lineshape.

To the best of our knowledge the data and analysis in Fig. 7.12 represent the first systematic study of phonon confinement in nanowires as a function of diameter [8]. The analysis of the Raman lineshape associated with all four samples results in value for $\alpha = 6.3 \pm 0.2$ which is independent of diameter. From the quality of the fits, it is clear that the phonon confinement model of Richter *et al.* [102] describes very well the shape of the $\sim$520 cm^{-1} Raman bands for diameters down to $\sim$4 nm. This is somewhat surprising because $d = 4$ nm is equivalent to only $\sim$8 lattice constants.

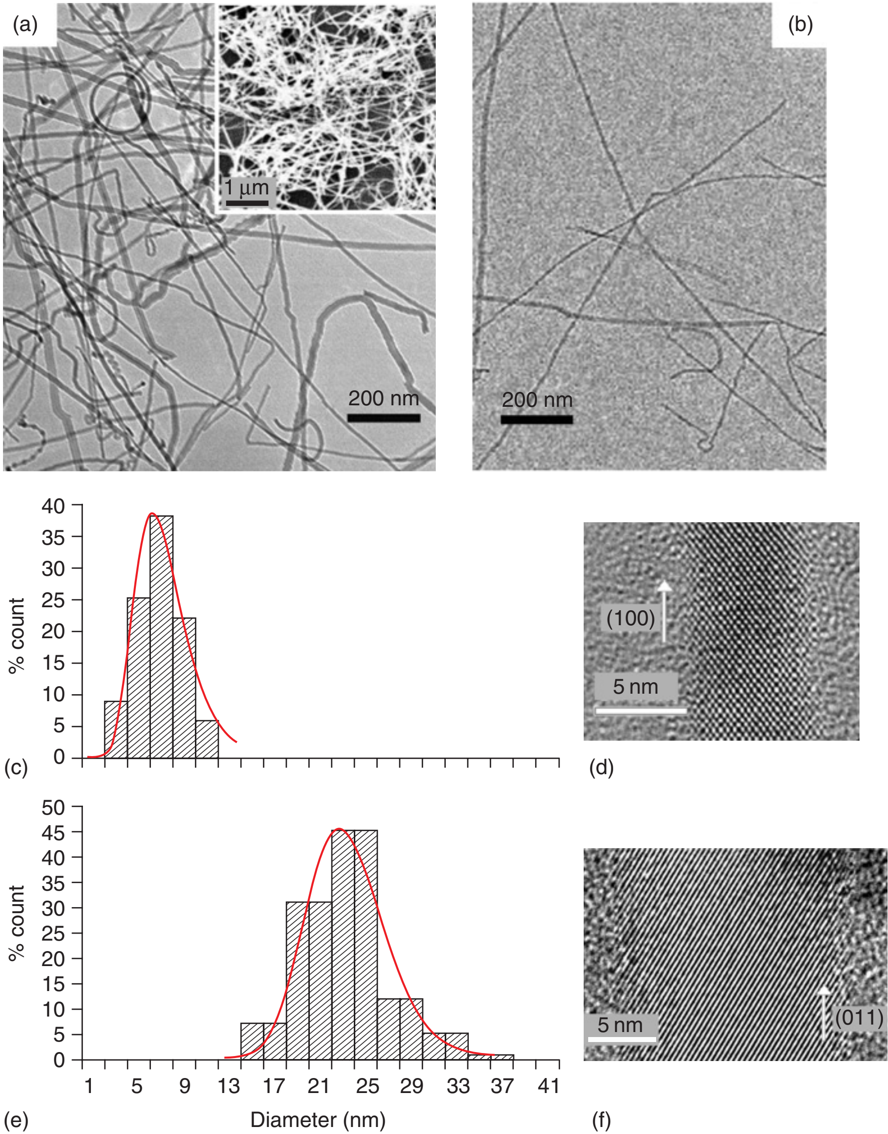

Figure 7.11 Typical TEM images of two Si (bottom) and nanowires with most probable diameter (a) $\bar{d} = 23$ nm and (b) $\bar{d} = 6.5$ nm. The inset in (a) is the SEM image of the wires on an indium foil substrate. (c) and (e) are the diameter distribution of the Si crystalline core for (b) and (a), respectively. The solid curve in (c) and (e) is a log-normal fit to the distribution. (d) and (f) show HRTEM lattice images of a 6 and 16 nm wire, respectively.

7.3.3 Thermal Conductivity

Some progress has been made in understanding how the lattice thermal conductivity κ of small diameter Si nanowires may be different from the bulk. By "lattice", we mean the contribution to κ from phonons. For temperatures below ~100°C, the acoustic

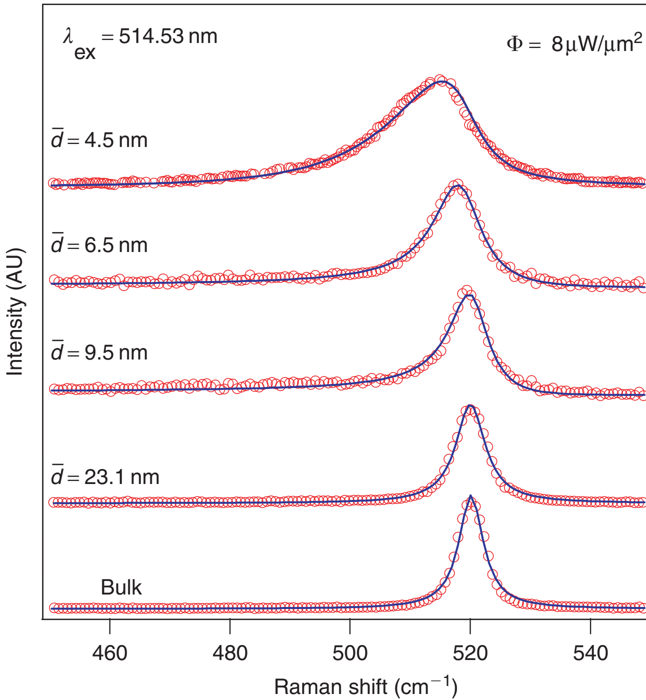

Figure 7.12 Raman spectra taken at very low laser power showing the evolution of the 520 cm^{-1} first order Raman band in Si nanowires with increasing confinement. Data for bulk Si (bottom) and nanowires with most probable diameters $\bar{d}$ = 4.5 ± 0.2 nm, 6.5 ± 0.3 nm, 9.5 ± 0.3 nm and 23.0 ± 0.7 nm are shown. We have introduced a confinement length factor α in the lineshape function (see text). The parameters α and A_o Eqs. (7.1 and 7.2) are adjusted to obtain the fit. The value of $\alpha = 6.3$ is found independent of the wire diameter. Open circles represent the experimental data and solid *curves* represent a least squares fit using Eq. (7.3) in which both the Richter's lineshape and the diameter distribution function $F(d)$ are taken in account.

phonons are known to carry most of the heat. The general relationship between the lattice thermal conductivity and the acoustic phonon parameters is given by:

$$\kappa = \frac{1}{3} C v l \tag{7.5}$$

where v is sound velocity, C is the specific heat per unit volume and l is the phonon mean free path. The relationship describes the contribution from one acoustic branch. The net thermal conductivity is the sum of contributions from two TA branches and one LA branch. To appreciate the temperature regime where size effects might become important for the lattice thermal conductivity (i.e. the temperature where $l \sim d$ and d is the nanowire diameter), we list values for l obtained from a careful analysis of thermal conductivity of bulk Si [144] ($l \sim 40$ nm @ 273 K; $l \sim 3$ µm @ 77 K; $l \sim 400$ µm @ 20 K). It is interesting to note that these values can be quite large compared to a typical nanowire diameter synthesized today (e.g. 4–20 nm), i.e. even at room temperature we can see that $l > d$.

The thermal conductivity κ for bulk Si is shown in Fig. 7.13 [145] and references therein. The increase in K with increasing T in the low T region is primarily due to

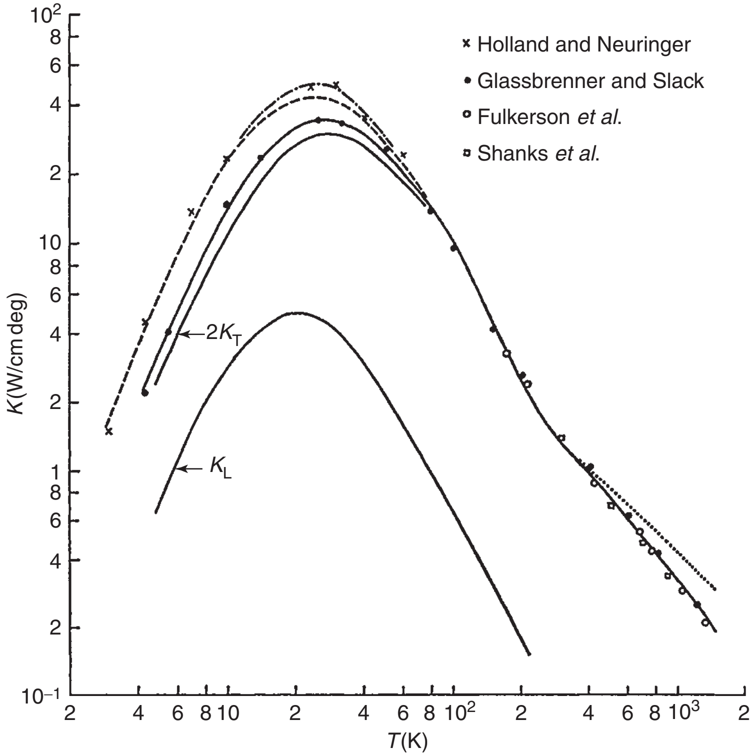

Figure 7.13 Lattice thermal conductivity of bulk silicon. The solid curves are the analysis of the data of Glassbrenner and Slack. Curves marked K_L and $2K_T$ represent the contribution of the longitudinal and the transverse phonons, respectively. The third solid curve represents the total lattice conductivity and is equal to $K_L + 2K_T$. The dashed and dot-dashed curves are the analysis of the data of Holland and Nueringer in reference [145] and the references therein.

the specific heat factor (i.e. $C \sim T^3$) and κ is seen to reach a maximum value of ~40 W/cm-s at 25 K. Above this temperature, the decrease in κ is due to phonon–phonon scattering involving umklapp processes [146]. It is interesting to compare this bulk data to that of nanowires and to diamond which is isostructural to Si. Diamond is the best (lattice) thermal conductor known and has the max $\kappa = 3000$ W/cm-s at ~90 K [147].

Recently, Li *et. al.* [148–150] have reported κ for individual crystalline Si nanowires. The measurements were made with the wires suspended above a substrate and thermally anchored at their ends on two platforms containing heaters and thermisters. They found that the wire thermal conductivity was approximately two orders of magnitude *lowe*r than reported for bulk Si. Their results for $\kappa(T)$ for Si nanowires with diameter $d = 22$, 37, 56 and 115 nm [150] are shown in Fig. 7.14. The T-dependence is consistent with a strongly limited phonon mean free path derived from phonon scattering from the nanowire surface, as they describe [150]. For all but the smallest diameter wire, κ was found to exhibit a pronounced maximum whose position downshifts with decreasing wire diameter. However, the smallest ($d = 22$ nm) wire does not exhibit a peak within the experimental temperature range. Their data

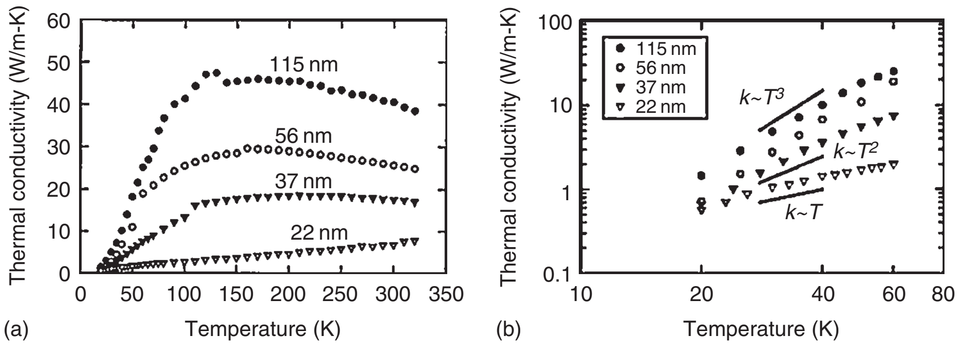

Figure 7.14 **(a) Measured thermal conductivity of different diameter Si nanowires. The number beside each curve denotes the corresponding wire diameter. (b) Low temperature experimental data on a logarithmic scale. Also shown are T^3, T^2 and T^1 curves for comparison (adopted from Ref. [150] copyright 2003 AIP).**

are qualitatively consistent with Eq. (7.5) above, setting $l \sim d$. That is, at low T, $l \sim d$, and $C \sim T^3$. As T increases, eventually l becomes less than d, C tends to saturate and, as is generally expected, l continues to decrease as $\sim 1/T$ in the high temperature limit. The downshift of the κ maximum with decreasing nanowire diameter suggests that the phonon boundary scattering increasingly dominates over phonon–phonon umklapp scattering. Eventually, for the smallest nanowire ($d = 22$ nm), surface scattering dominates over the entire experimental temperature range and no maximum is observed. Even the low $T \sim T^3$ behaviour is lost.

As we have discussed, lattice mode calculations indicate that for Si nanowire with $d \sim 5$ nm, changes in the acoustic phonon dispersion should be introduced, i.e. there should be diameter-dependent sound velocity. Furthermore, the "snake-like" acoustic modes with $\sim q^2$ dispersion are predicted. In principle, these changes in the acoustic modes should affect the T-dependence of κ and the specific heat in nanowires.

No reports appear in the literature regarding the lattice specific heat of small diameter nanowires. Based on the discussion above, specific heat measurements, Brillouin scattering and thermal conductivity should all provide important tests for dramatic changes predicted in the acoustic modes of nanowires. Specific heat measurements on loose powders of nanowires might support the thermal activation of the "snake-like" modes. Since the acoustic mode dispersion depends on nanowire diameter, some care must be taken to consider the effects of the diameter distribution on the results.

7.4 Effects of Inhomogeneous Laser Heating on Raman Lineshape

Recently, two Raman scattering studies on Si nanowires have reported a second mechanism, other than phonon confinement, that can induce an asymmetric broadening of the Si 520 cm^{-1} Raman line profile [7,100]. Both of these studies reported that the band asymmetry can increase with increasing laser power density on the sample [7,100]. Interestingly, a similar observation was made in bulk Si just

after the introduction of high power Ar ion lasers in the early 1960s [130]. Our observations will be shown below to indicate *inhomogeneous* laser heating within the Raman volume. Intuitively, we expect that the reduced thermal conductivity of small diameter nanowires would increases the chance of observing inhomogeneous heating effects. We will also show that large diameter nanowires, i.e. too large to exhibit confinement-related asymmetry in their one-phonon Raman band, can exhibit an asymmetric Raman band under high laser illumination. Unfortunately, in the limit of small diameters, the Raman band asymmetry can be due to simultaneous contributions from phonon confinement and inhomogeneous laser heating. This underscores the importance of determining the experimental lineshape in the illumination regime where the lineshape is independent of laser power.

The ability of a strongly focused laser beam to induce a significant temperature distribution in a nanowire lying on a substrate depends on the optical power density in the beam, the thermal conductivity of the nanowire and underlying substrate, and the efficiency of the thermal anchoring of the nanowire to the substrate. We have measured the Stokes/antiStokes Raman intensity ratio (I_S/I_{AS}) that is sensitive to the average temperature in the Raman volume and the data indicate that a few mWs of laser power can increase the temperature in the wire by 300–700°C. We have chosen a primitive means of providing significantly different thermal anchoring conditions. We have fabricated either a submonolayer coverage of nanowires on the substrate ("low coverage") that promotes good thermal anchoring or a higher coverage per unit area deposition of nanowires ("high coverage", cf. SEM image in Fig. 7.11a) where the nanowires are more often suspended by one another from the substrate and in poor thermal contact with the substrate. We chose a good thermal conductor, i.e. indium foil for the substrate material.

7.4.1 Stokes–AntiStokes Ratio as a Probe of Laser Heating of Si Nanowires

The Stokes–antiStokes intensity ratio I_S/I_{AS} is related to the average temperature T_{eff} in the Raman scattering volume by [151]:

$$I_S/I_{AS} = \beta \exp(h\nu/k_B T_{eff}) \tag{7.6}$$

where ν is the frequency of the phonon and (h, k_B) are the Planck and Boltzmann constants, respectively, and β is a factor that is chosen to fit experiment at low flux where $T_{eff} = T_a$, where T_a is ambient temperature. In Fig. 7.15, we plot results of a Stokes/antiStokes study of laser heating on a large diameter Si nanowires ($\bar{d} = 23$ nm) in poor thermal contact with the substrate (high coverage). Phonon confinement effects are not significant in this sample, i.e. the 520 cm^{-1} band has a Lorentzian shape at low laser flux (Fig. 7.15a). In Fig. 7.15b, we plot the incident laser flux Φ(mW/µm^2) versus T_{eff} obtained from Eq. (7.6). The data show that with increasing Φ, the initial Lorentzian band takes on an increasingly asymmetric shape. As can be seen from the data in Fig. 7.15(b), there is an approximately linear relationship between Φ and T_{eff} for these poorly anchored Si nanowires. Furthermore, it can be seen that $\Phi \sim 4$ mw/µm^2 induces effective nanowire temperatures in excess of 1000 K. This magnitude of laser power density can be easily achieved in microRaman spectrometers.

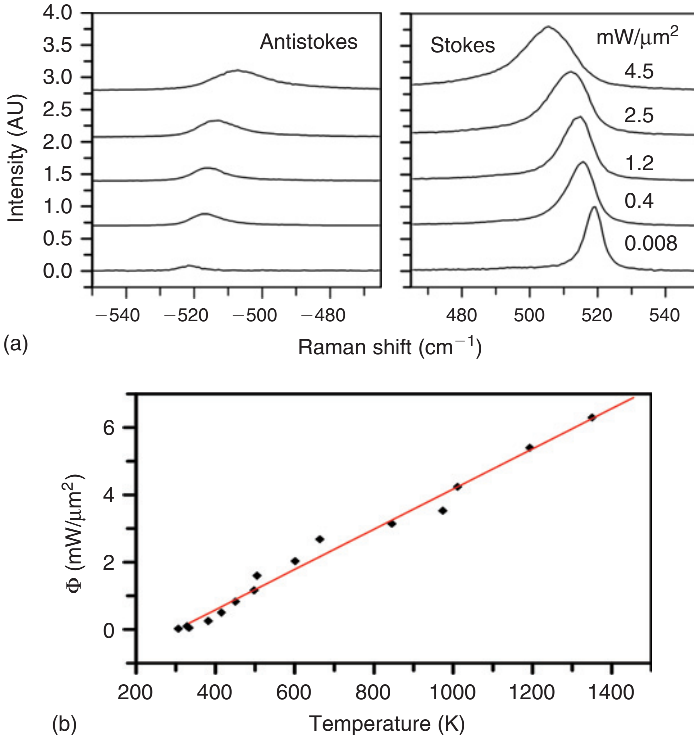

Figure 7.15 (a) Stokes–antiStoke Raman spectra of $\bar{d} = 23\,\text{nm}$ Si nanowires collected from a region of high wire coverage on the indium substrate that leads to poor thermal anchoring. (b) Flux versus average temperature in the Raman volume calculated from the measured Stokes–anti-stoke intensity ratio.

7.4.2 Evolution of the Raman Band Asymmetry with Laser Flux

It is interesting to follow the evolution of the shape of the $520\,\text{cm}^{-1}$ Si Raman band in small and large diameter nanowires with increasing laser flux Φ. The data are shown in four panels in Fig. 7.16. The upper two panels Fig. 7.16(a and b) refer to results on large diameter $\bar{d} = 23\,\text{nm}$ wires, and the lower two panels Fig. 7.16(c and d) refer to $\bar{d} = 6.5\,\text{nm}$ wires. Conversely, the left-hand panels (a, c) refer to nanowires at high coverage and easily heated by the laser field, and the data in the right-hand panels (b, d) refer to wires deposited at low coverage that are in significantly better thermal contact with the substrate. The spectra in each panel are stacked from bottom to top according to increasing laser flux measured at the sample. The spectrum of bulk Si (taken at low laser flux under identical optical conditions) is also shown for comparison. For a visual guide, a vertical-dashed reference line is drawn at $520\,\text{cm}^{-1}$ so that the small shift in the Raman band maximum is more apparent.

To observe the subtle changes in the Raman band with laser flux and without recourse to a lineshape analysis, we define the Raman band asymmetry A [152]:

$$A = \frac{\Delta\omega_{\text{L}}}{\Delta\omega_{\text{R}}} = \frac{\omega_{\text{m}} - \omega_{-}}{\omega_{+} - \omega_{\text{m}}} \tag{7.7}$$

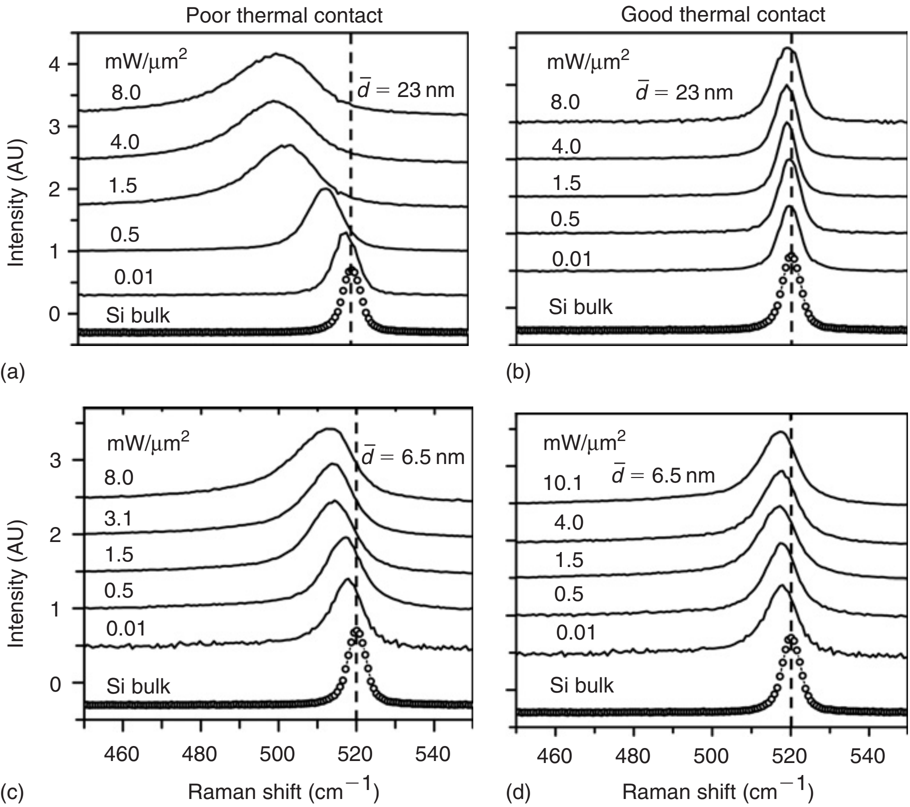

Figure 7.16 Flux (Φ) dependent Raman spectra of Si nanowires collected under poor thermal anchorage (a, c) and good thermal anchorage (b, d) for 23 nm wires (a, b) and 6.5 nm wires (c, d). The wires were located on an indium substrate.

where the subscript L, R refer to the line width measured to the left and right of the band maximum, respectively. The frequencies ω_- and ω_+ locate the positions at the 10% intensity on the low and high frequency sides of the band maximum located at ω_m. Of course, $A = 1$ is obtained for a symmetric lineshape (e.g. Lorentzian).

The values for A obtained directly from the observed Raman band are plotted versus log-flux Φ in Fig. 7.17: $\bar{d} = 23$ nm (left panel) and $\bar{d} = 6.5\,nm$ nanowires (right panel). The open squares and the solid circles refer, respectively, to "low" and "high" coverage of the nanowires on the indium foil. Interesting behaviour, sometimes non-monotonic can be observed depending on whether the wires are small enough in diameter to exhibit phonon confinement. For the (large) $\bar{d} = 23$ nm nanowires (Fig. 7.17a), we can see two behaviours, depending on the nature of the thermal anchoring: poor thermal contact allows asymmetry to develop at low flux, whereas good thermal contact delays the development of asymmetry to higher T. Recall that $A \sim 1$ is observed for these large diameter wires at low flux (i.e. they exhibit a Lorentzian lineshape). In this case, the observed Raman band asymmetry at high flux clearly has nothing to do with phonon confinement.

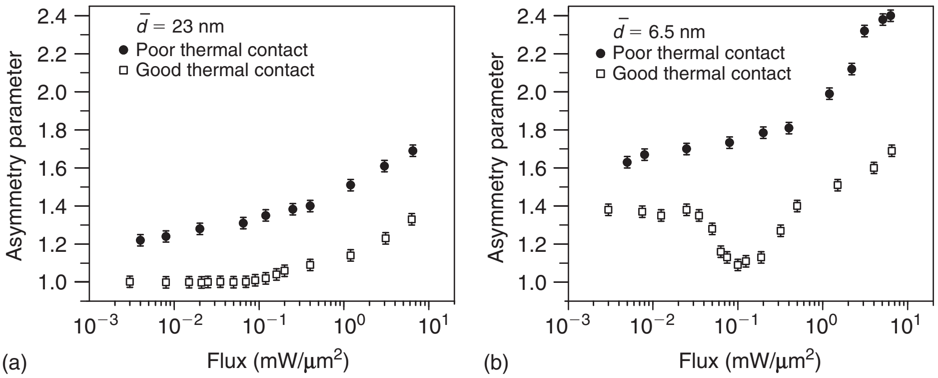

Figure 7.17 Flux (Φ) dependence of the asymmetry parameter A for Si nanowires under poor thermal contact (solid circles) and good thermal contact (open squares) for (a) 23 nm, (b) 6.5 nm Si nanowires.

In Fig. 7.17b, for wires small enough to show phonon confinement asymmetry, we can observe two distinct behaviours for $A(\Phi)$. Poor thermal contact allows an early increase in A with increasing flux, whereas small diameter wires in good thermal contact with the substrate exhibit an interesting non-monotonic behaviour with Φ. A careful lineshape analysis including inhomogeneous heating can reproduce the range of behavior observed (see Ref. [7] for more details).

7.4.3 Modification of Richter's Lineshape Function to Include Inhomogeneous Heating

Let us now consider quantitatively Raman scattering from a volume that is inhomogeneously illuminated. We can analyse this situation in one dimension for nanowires within the framework of the Richter model [7]. Heating of the Raman volume stems from the Gaussian focal spot of the incident laser beam in the plane of the sample. Projected onto a single nanowire the flux is therefore described by:

$$I(z) = I_o \exp\left(-\frac{z}{a}\right)^2 \tag{7.8}$$

where z is the distance along the wire measured relative to the centre of the laser focal spot of diameter ~$2a$. To proceed with the Richter analysis, we shall assume that a Gaussian temperature distribution $T(z)$ is induced along the wire as a response to the Gaussian laser flux distribution. $T(z)$ is the result of a competition between laser heating and thermal cooling, the latter due to ambient convective cooling and the thermal coupling of the nanowire to the substrate. The form of $T(z)$ is therefore assumed to be given by:

$$T(z) = \Delta T \exp\left(-\frac{z}{b}\right)^2 + T_a \tag{7.9}$$

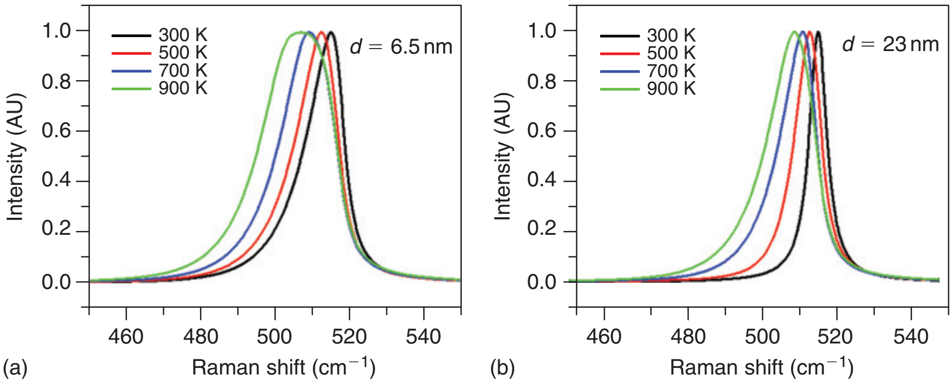

Figure 7.18 **Calculated Raman lineshape for Si nanowires using eq. 7.10 and $\alpha = 6.3$, $a = 0.5\mu$, $b = 0.25\mu$ for various $T^\star = T_a + \Delta T$ listed.**

where ΔT is the maximum temperature rise above the ambient temperature $T_a \sim 300\,\mathrm{K}$, and the parameter b determines the width of the induced temperature profile along the nanowire axis (z). Including both the position dependence of the laser flux $I(z)$ in the nanowire *and* the induced temperature response $T(z)$ in the Richter model leads to the following form for the Raman lineshape:

$$I(\omega) = \int_{-c}^{+c} \mathrm{d}z\, I_o \mathrm{e}^{-(z/a)^2} A_o \int_{o}^{q_{\mathrm{MAX}}} 2\pi q_\perp \mathrm{d}q_\perp \frac{|C(q_\perp)|^2}{[\omega - \omega_o(q_\perp, T(z))]^2 + [\Gamma(T(z))/2]^2} \tag{7.10}$$

$|C(q_\perp)|^2$ is the same confinement envelope function as shown in Eq. (7.2). The integral in z is calculated over the average length of a nanowire ($l = 2c$) from which Raman scattered radiation can be imaged through the slit of the spectrometer (in our case, $l \sim 1\,\mu\mathrm{m}$). The explicit T-dependence of the inverse phonon lifetime Γ and the phonon frequency, shown in Fig. 7.8, is built into Eq. (7.10).

Using Eq. (7.10), it can easily be shown that an increase in the Raman line asymmetry A is primarily due to the temperature dependence of the phonon frequency (ω). The contribution from the temperature dependence of the inverse phonon lifetime (Γ) actually tends to offset the contribution from ω. In Fig. 7.18 we show the evolution with temperature of the calculated shape of the Raman band for $\bar{d} = 23\,\mathrm{nm}$ (little or no phonon confinement) and $\bar{d} = 6.5\,\mathrm{nm}$ (significant phonon confinement) wires. The results are plotted for various $T^\star$, i.e. the maximum temperature induced in the nanowire at the centre of the laser focal spot ($T^\star \sim \Delta T + T_a$) For both $\bar{d} = 23$ and $\bar{d} = 6.5\,\mathrm{nm}$ Si wires, a growing asymmetry A with increasing $T^\star$ is apparent.

We next use the modified Richter lineshape function (Eq. (7.10)) to directly fit the experimental $520\,\mathrm{cm}^{-1}$ band for $\bar{d} = 6.5\,\mathrm{nm}$ nanowires at $\Phi = 0.01$, 0.5 and $2.5\,\mathrm{mW}/\mu\mathrm{m}^2$ and for $\bar{d} = 23\,\mathrm{nm}$ nanowires at $\Phi = 0.01$, 2.0 and $4.0\,\mathrm{mW}/\mu\mathrm{m}^2$.

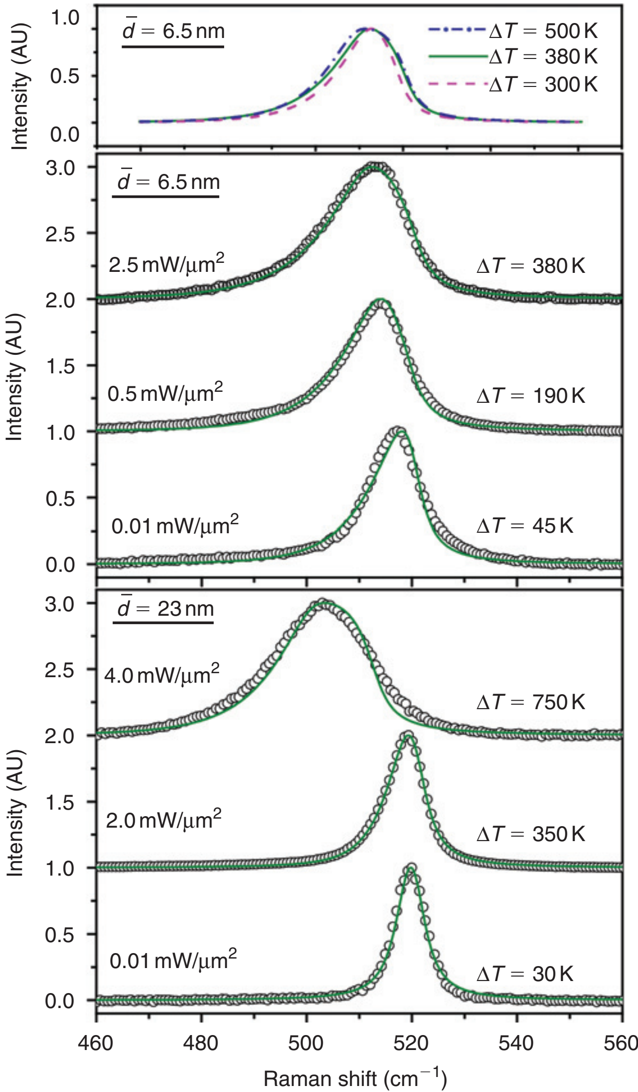

Figure 7.19 Raman spectra (open circles) for the d = 6.5 nm (middle panel) and d = 23 nm (bottom panel) Si nanowires collected at 514.5 nm excitation. The solid lines are calculated according to Eq. (7.10). ΔT is the maximum increase in the sample temperature due to the laser heating. Values for the experimental laser flux are indicated. The top panel shows the sensitivity of the calculated lineshape function to the values of ΔT (Eq. 7.10); all other parameters are fixed ($\alpha = 6.3$, $a = 0.5\,\mu$m, $b = 0.25\,\mu$m.)

We have fixed $a = 0.5\,\mu$m, $b = 0.25\,\mu$m, $\alpha = 6.3$. A_0 and ΔT are the only adjustable parameters in our lineshape analysis. The data (open circles) and least squares fit (solid line, Eq. (7.10)) for $\bar{d}$ = 6.5 and 23 nm Si wires are shown in Fig. 7.19. For the $\bar{d}$ = 6.5 nm wires (middle panel, Fig. 7.19), we obtained $\Delta T = 45$, 190 and 380 K for $\Phi = 0.01$, 0.5 and 2.5 mW/μm^2, respectively. Similarly, for the 23 nm wires (bottom panel, Fig. 7.16), we obtained $\Delta T = 30$, 350 and 750 K for

$\Phi =$ (0.01, 2.0 and 4.0 mW/μm^2), respectively. As can be seen from the least squares fit to the experimental spectra, the modified Richter lineshape function (Eq. (7.10)) provides a reasonably good fit to the Raman data.

Finally, we should mention that our experimental diameter distributions are narrow enough that we have neglected them in the Raman lineshape calculations regarding inhomogeneous heating. A test calculation showed that the changes in the calculated results for these narrow diameter distributions were small enough to not justify the increase in the complexity of the analysis.

7.5 Summary and conclusions

In this chapter, we have considered how the physical confinement of the lattice vibrations in the waist of Si nanowires affects the basic phonon dispersion. We have presented theoretical results that demonstrate that four, rather than three, acoustic phonons are expected, and that the appropriate boundary condition for the optical modes is that atoms are frozen in position at the free surface of the nanowire. The confinement necessitates using a much larger primitive cell that, in turn, creates a plethora of optical phonons. For very small diameter nanowires, this change in the phonon dispersion is predicted to significantly alter the physical properties of the phonon system, i.e. the sound velocity becomes a function of diameter and new "snake-like" vibrational modes with $a \sim q^2$ dispersion are created. Sensitive experiments that can probe these new phonon properties in "confined" nanowires are still needed, e.g. Brillouin scattering thermal conductivity and specific heat measurements. The phonon mean free path in Si can be quite large (e.g. microns at low T) and it should be anticipated that the thermal conductivity of nanowires should be strongly suppressed. This has been observed experimentally.

Raman scattering from optical phonons in Si has been investigated rather thoroughly. It has been found that the Lorentzian lineshape of the 520 cm^{-1} band in bulk Si evolves to a broadened asymmetric shape in nanowires of diameter $d < 10$ nm. Studies versus laser power have shown that inhomogenous laser heating can occur. This is an expected outcome of the poorer thermal conductivity of the nanowire and possible poor thermal coupling to the substrate. Inhomogeneous laser heating adds a second contribution to the line asymmetry. Therefore, it is important that phonon confinement effects be demonstrated to be independent of the laser flux. A phenomenological model due to Richter *et al.* has been discussed in some detail and shown to describe the asymmetric shape of the one-phonon Raman band, if an additional parameter (α) that sets the scale of the phonon confinement is introduced into the original model. The Richter model has also been shown to handle the incorporation of temperature effects and inhomogeneous heating in the scattering volume and gives a satisfactory account of laser heating effects in Si nanowires.

Acknowledgements

The authors gratefully acknowledge stimulating conversations with Prof. Gerald Mahan (Pennsylvania State University) and (José Menéndez, Arizona State

University). This work was supported, in part, by funding from the NSF (NIRT # DMR-0304178).

REFERENCES

1. S. Guha and J. Yang, *J. Non-Crystal. Solid.* **352**, 1917 (2006).
2. A.D. Yoffe, *Adv. Phys.* **42**, 173 (1993).
3. A.D. Yoffe, *Adv. Phys.* **50**, 1 (2001).
4. A.D. Yoffe, *Adv. Phys.* **51**, 799 (2002).
5. O.J. Pallotta, G.T.P. Saccone and R.E. Woolford, *Med. Bio. Eng. Comp.* **44**, 250 (2006).
6. K.M. Sawicka, A.K. Prasad and P.I. Gouma, *Sensor Lett.* **3**, 31 (2005).
7. K.W. Adu, H.R. Gutiérrez, U.J. Kim and P.C. Eklund, *Phys. Rev. B* **73**, 155333 (2006).
8. K.W. Adu, *et al.*, *Nano Lett.* **5**, 409 (2005).
9. Y. Li, *et al.*, *Nano Lett.* **6**, 1468 (2006).
10. F. Patolsky, G.F. Zheng and C.M. Lieber, *Anal. Chem.* **78**, 4260 (2006).
11. P.V. Radovanovic, *et al.*, Abstracts of Papers of the American Chemical Society **230**, U2042 (2005).
12. J. Xiang, *et al.*, *Nature* **441**, 489 (2006).
13. O. Hayden, R. Agarwal and C.M. Lieber, *Nat. Mater.* **5**, 352 (2006).
14. Z.H. Zhong, *et al.*, Abstracts of Papers of the American Chemical Society **229**, U703 (2005).
15. C. Yang, Z.H. Zhong and C.M. Lieber, *Science* **310**, 1304 (2005).
16. F. Qian, *et al.*, *Nano Lett.* **5**, 2287 (2005).
17. S. Gradecak, *et al.*, *Appl. Phys. Lett.* **87**, 173111 (2005).
18. V.V. Dobrokhotov, *et al.*, *Nanotechnology* **17**, 4135 (2006).
19. S.S. Sridharamurthy, *et al.*, *Lab Chip* **6**, 840 (2006).
20. Z. Fan and J.G. Lu, *Appl. Phys. Lett.* **86**, 123510 (2005).
21. K. Sivakumar and B. Panchapakesan, *J. Nanosci. Nanotechnol.* **5**, 313 (2005).
22. W. Wan, *et al.*, *Appl. Phys. Lett.* ***84***, 3654 (2004).
23. A. Kolmakov and M. Moskovits, *Annu. Rev. Mater. Res.* **34**, 151 (2004).
24. R. Byrne and D. Diamond, *Nat. Mater.* **5**, 421 (2006).
25. A.M. Morales and C.M. Lieber, *Science* **279**, 208 (1998).
26. H.J. Fan, P. Werner and M. Zacharias, *Small* **2**, 700 (2006).
27. Y. Huang and C.M. Lieber, *Pure Appl. Chem.* **76**, 2051 (2004).
28. L. Samuelson, *et al.*, *Phys. E Low Dimen. Sys. Nanostruct.* **25**, 313 (2004).
29. M. Law, J. Goldberger and P.D. Yang, *Annu. Rev. Mater. Res.* **34**, 83 (2004).
30. N.S. Xu and S.E. Huq, *Mater. Sci. Eng. R Rep.* **48**, 47 (2005).
31. Y.N. Xia, *et al.*, *Adv. Mater.* **15**, 353 (2003).
32. G.C. Yi, C.R. Wang and W.I. Park, *Semicond. Sci. Technol.* **20**, S22 (2005).
33. D. Vashaee, A. Shakouri, J. Goldberger, T. Kuykendall, P. Pauzauskie and P. Yang. *J. Appl. Phys.* **99**, 054310 (2006).
34. S.M. Koo, *et al.*, *Nano Lett.* **5**, 2519 (2005).
35. S.H. Ju, K. Lee and D.B. Janes, *Nano Lett.* **5**, 2281 (2005).
36. K. Nishiguchi *et al.*, Jpn. *J. Appl. Phys. Part 1 Regular Papers Brief Communications and Review Papers* **44**, 7717 (2005).
37. R. Chau, *et al.*, *IEEE Trans. Nanotechno.* **4**, 153 (2005).
38. D.H. Kang, *et al.*, *J. Appl. Phys.* **96**, 7574 (2004).
39. H.T. Ng, *et al.*, *Nano Lett.* **4**, 1247 (2004).
40. D.H. Kim, *et al.*, *IEEE Trans. Nanotechnol.* **1**, 170 (2002).
41. M.T. Bohr, *IEEE Trans. Nanotechnol.* **1**, 56 (2002).
42. M. Yumoto, S. Kasai and H. Hasegawa, *Microelectron. Eng.* **63**, 287 (2002).
43. S. Kasai and H. Hasegawa, *IEEE Electron Dev. Lett.* **23**, 446 (2002).
44. J.Y. Juang and D.B. Bogy, *Microsystem Technol. Micro. Nanosys. Informat. Storage Process. Syst.* **11**, 950 (2005).
45. M. Willander, *et al.*, *Microelectron. J.* **36**, 940 (2005).
46. A.B. Greytak, *et al.*, *Appl. Phys. Lett.* **87**, 151103 (2005).
47. C.P. Li, *et al.*, *Solid State Commun.* **139**, 355 (2006).

48. H. Yamada, *et al.*, *Jpn. J. Appl. Phys. Part 1 Regular Papers Brief Communications and Review Papers* **44**(9A), 6541 (2005).
49. L. Chen and E. Towe, *Appl. Phys. Lett.* **87**, 103111 (2005).
50. C.X. Xu, X.W. Sun, C. Yuen, B.J. Chen, S.F. Yu and Z.L. Dong, *Appl. Phys. Lett.* **86**, 011118 (2005).
51. J.C. Johnson, *et al.*, *J. Phys. Chem. B* **107**, 8816 (2003).
52. Y.F. Zhang, *et al.*, *Appl. Phys. Lett.* **72**, 1835 (1998).
53. Y. Zheng, *et al.*, *IEEE Trans. Electron Dev.* **52**, 1097 (2005).
54. J.D. Carter, *et al.*, *Chem. Commun.* Vol. 17, 2274 (2005).
55. H.Y. Tuan, *et al.*, *Nano Lett.* **5**, 681 (2005).
56. S. Bhattacharya, *et al.*, *Appl. Phys. Lett.* **85**, 2008 (2004).
57. S. Bhattacharyya and S. Samui, *Appl. Phys. Lett.* **84**, 1564 (2004).
58. Y.H. Yang, *et al.*, *J. Phys. Chem. B* **108**, 846 (2004).
59. Y.J. Xing, *et al.*, *Chinese Phys. Lett.* **20**(5), 700 (2003).
60. Y.J. Xing, *et al.*, *Appl. Phys. A Mater. Sci. Process.* **76**, 551 (2003).
61. S. Hofmann, *et al.*, *J. Appl. Phys.* **94**, 6005 (2003).
62. C.P. Li, *et al.*, *Adv. Mater.* **15**, 607 (2003).
63. X.M. Lu, *et al.*, *Nano Lett.* **3**, 93 (2003).
64. J.Y. Yu, S.W. Chung and J.R. Heath, *J. Phys. Chem. B* **104**, 11864 (2000).
65. S.W. Chung, J.Y. Yu and J.R. Heath, *Appl. Phys. Lett.* **76**, 2068 (2000).
66. Y.F. Zhang, *et al.*, *J. Cryst. Growth* **212**, 115 (2000).
67. Y.F. Zhang, *et al.*, *Phys. Rev. B* **61**, 8298 (2000).
68. S.T. Lee, *et al.*, *J. Mater. Res.* **14**, 4503 (1999).
69. Y.H. Tang, *et al.*, *Chem. Phys. Lett.* **314**, 16 (1999).
70. F.C.K. Au, *et al.*, *Appl. Phys. Lett.* **75**, 1700 (1999).
71. Y.F. Zhang, *et al.*, *Appl. Phys. Lett.* **75**, 1842 (1999).
72. Y.H. Tang, *et al.*, *J. Appl. Phys.* **85**, 7981 (1999).
73. N. Wang, *et al.*, *Chem. Phys. Lett.* **299**, 237 (1999).
74. G.W. Zhou, *et al.*, *Appl. Phys. Lett.* **73**, 677 (1998).
75. H. Scheel, S. Reich and C. Thomsen, *Phys. Status Solidi B Basic Solid State Phy.* **242**, 2474 (2005).
76. X.Y. Zhao, C.M. Wei, L. Yang and M.Y. Chou, *Phys. Rev. Lett.* **92**, 236805 (2004).
77. B.X. Li, P.-L. Cao, R. Q. Zhang and S. T. Lee, *Phys. Rev. B* **65**, 125305 (2002).
78. J. Li and A.J. Freeman, *Phys. Rev. B* **74**, 075333 (2006).
79. C. Harris and E.P. O'Reilly, *Phys. E Low Dimen. Syst. Nanostruct.* **32**, 341 (2006).
80. I. Ponomareva, M. Menon, D. Srivastava and A.N. Andriotis, *Phys. Rev. Lett.* **95**, 265502 (2005).
81. D.D.D. Ma, *et al.*, *Science* **299**, 1874 (2003).
82. W. Lu, *et al.*, *Proc. Natl. Acad. Sci. USA* **102**, 10046 (2005).
83. B.K. Ridley, *Phys. Rev. B* **44**, 9002 (1991).
84. B.K. Ridley, *Phys. Rev. B* **47**, 4592 (1993).
85. T. Thonhauser and G.D. Mahan, *Phys. Rev. B* **71**, 081307 (2005).
86. T. Thonhauser and G.D. Mahan, *Phys. Rev. B* **69**, 075213 (2004).
87. Y.F. Chen *et al.*, *J. Heat Transfer- Transact. ASME* **127**, 1129 (2005).
88. E.P. Pokatilov, D.L. Nika and A.A. Balandin, *Superlattice. Microstruct.* **38**, 168 (2005).
89. D. Lacroix, *et al.*, *Appl. Phys. Lett.* **89**, 103104 (2006).
90. X. Lu and J. Chu, *J. Appl. Phys.* **100**, 014305 (2006).
91. S.P. Hepplestone and G.P. Srivastava, *Appl. Phys. Lett.* **87**, 231906 (2005).
92. S.P. Hepplestone and G.P. Srivastava, *Nanotechnology* **17**, 3288 (2006).
93. C. Trallero-Giner, *et al.*, *Phys. Rev. B* **45**, 11944 (1992).
94. M. Babiker, *J. Phys. C Solid State Phys.* **19**, 683 (1986).
95. M.A. Stroscio and M. Dutta, *Phonons in Nanostructures* (Cambridge University Press, Cambridge, 2001).
96. M.A. Stroscio, *et al.*, *J. Appl. Phys.* **76**, 4670 (1994).
97. M. Stroscio, *et al.*, *Physica B* **316**, 8 (2002).
98. M. Dutta, *et al.*, *Phys. E Low Dimen. Syst. Nanostruct.* **11**(2–3), 277 (2001).
99. S.M. Komirenko, *et al.*, *Phys. Rev. B* **59**, 5013 (1999).
100. S. Piscanec, M. Cantoro, A.C. Ferrari, J.A. Zapien, Y. Lifshitz, S.T. Lee, S. Hofmann and J. Robertson, *Phys. Rev. B* **68**, 241312 (2003).
101. S. Piscanec, *et al.*, *Mater. Sci. Eng. C Biomimetic Supramol. Syst.* **23**, 931 (2003).

102. H. Richter, Z.P. Wang and L. Ley, *Solid State Commun.* **39**, 625 (1981).
103. I.H. Campbell and P.M. Fauchet, *Solid State Commun.* **58**, 1835 (1986).
104. D.P. Yu, *et al.*, *Appl. Phys. Lett.* **72**, 3458 (1998).
105. B.B. Li, D.P. Yu and S.L. Zhang, *Phys. Rev. B* **59**, 1645 (1999).
106. J.X. Liu, *et al.*, *Phys. E Low Dimen. Syst. Nanostruct.* **23**, 221 (2004).
107. R.P. Wang, *et al.*, *Phys. Rev. B* **61**, 16827 (2000).
108. R. Gupta, *et al.*, *Nano Lett.* **3**, 627 (2003).
109. N. Fukata, T. Oshima, N. Okada, K. Murakami, T. Kizuka, T. Tsurui and S. Ito, *J. Appl. Phys.* **100**, 024311 (2006).
110. J.J. Niu, J. Sha and D.R. Yang, *Scripta Mater.* **55**, 183 (2006).
111. N. Fukata, *et al.*, *Phys. B Condens. Matter* **376**, 864 (2006).
112. Z.X. Su, *et al.*, *Phys. Status Solidi A Appl. Mater. Sci.* **203**, 792 (2006).
113. Z.X. Su, *et al.*, *J. Phys. Chem. B* **110**, 1229 (2006).
114. N. Fukata, *et al.*, *Appl. Phys. Lett.* **86**, 213112 (2005).
115. T. Xu, *MRS Bull.* **30**, 266 (2005).
116. W. Weber, *Phys. Rev. B* **15**, 4789 (1977).
117. R. Tubino, G. Zerbi and L. Piseri, *J. Chem. Phys.* **56**, 1022 (1972).
118. G. Nilsson and G. Nelin, *Phys. Rev. B* **6**, 3777 (1972).
119. G. Dolling, *Inelastic Scattering of Neutrons in Solids and Liquids* (IAEA, Vienna, 1963).
120. Y.S. Ju and K.E. Goodson, *Appl. Phys. Lett.* **74**, 3005 (1999).
121. H. Lamb, *Proc. Math. Soc. Lond.* **13**, 187 (1882).
122. F.H. Stillinger and T.A. Weber, *Phys. Rev. B* **31**, 5262 (1985).
123. J. Wang, K.M. Zhang and X.D. Xie, *Solid State Commun.* **86**, 731 (1993).
124. M.S. Dresselhaus, G. Dresselhaus and P.C. Eklund, *Science of Fullerenes and Carbon Nanotubes* (Academic Press, New York, 1996).
125. N. Nishiguchi, Y. Ando and M.N. Wybourne, *Superlattice. Microstruct.* **22**, 213 (1997).
126. M. Balkanski, R.F. Wallis and E. Haro, *Phys. Rev. B* **28**, 1928 (1983).
127. J. Menendez and M. Cardona, *Phys. Rev. B* **29**, 2051(1984).
128. T.R. Hart, R.L. Aggarwal and B. Lax, *Phys. Rev. B* **1**, 638 (1970).
129. M. Grimsditch and M. Cardona, *Phys. Status Solidi B Basic Rese.* **102**, 155 (1980).
130. J. Raptis, E. Liarokapis and E. Anastassakis, *Appl. Phys. Lett.* **44**, 125 (1984).
131. P.R. Stoddart and J.D. Comins, *Phys. Rev. B* **62**, 15383 (2000).
132. A. Dieguez, *et al.*, *Appl. Phys. Lett.* **71**, 1957 (1997).
133. E. Duval, *et al.*, *Phys. Rev. B* **63**, 075405 (2001).
134. P. Verma, *et al.*, *Phys. Rev. B* **60**, 5778 (1999).
135. F.Q. Liu, *et al.*, *Phys. Rev. Lett.* **76**, 604 (1996).
136. A.E.H. Love, *A Treatise on Mathematical Theory of Elasticity* (Dover, New York, 1994).
137. M. Ivanda, *et al.*, *J. Raman Spectrosc.* **37**, 161 (2006).
138. W. Cheng, S.F. Ren and P.Y. Yu, *Phys. Rev. B* **68**, 193309 (2003).
139. Y.M. Yang, X.L. Wu, L.W. Yang, G.S. Huang, G.G. Siu and P.K. Chu, *J. Appl. Phys.* **98**, 064303 (2005).
140. M. Fujii, *et al.*, *Phys. Rev. B* **54**, R8373 (1996).
141. J. Zi, K.M. Zhang and X.D. Xie, *Phys. Rev. B* **58**, 6712 (1998).
142. K.W. Adu, H.R. Gutierrez and P.C. Eklund (to be published).
143. Y. Maeda, *Phys. Rev. B* **51**, 1658 (1995).
144. R. Berman, *Cryogenics* **5**, 297 (1965).
145. Y.P. Joshi and G.S. Verma, *Phys. Rev. B* **1**, 750 (1970).
146. J.S. Blackmore, *Solid State Physics* (W.B. Saunders Company, Philadelphia, PA, 1969).
147. R. Berman, P.R.W. Hudson and M. Martinez, *J. Phys. C Solid State Phys.* **8**, L430 (1975).
148. D.Y. Li, *et al.*, *J. Heat Transfer Trans. ASME* **127**, 108 (2005).
149. L. Shi, *et al.*, *J. Heat Transfer Trans. ASME* **125**, 881 (2003).
150. D.Y. Li, *et al.*, *Appl. Phys. Lett.* **83**, 2934 (2003).
151. M. Cardona, Light scattering in solids, Springer-Verlag (1975).
152. J.J. Kirkland, *et al.*, *J. Chromatogr. Sci.* **15**, 303 (1977).

CHAPTER EIGHT

Quasi-One-Dimensional Silicon Nanostructures

Yu Lin[1], Nevill Gonzalez Szwacki[1,2] and Boris I. Yakobson[1]

Contents

8.1 Introduction 290
8.2 Silicon Nanowires 290
  8.2.1 Pentagonal Silicon Wires 290
  8.2.2 Hydrogen-Passivated Silicon Wires 297
8.3 Metal Silicide 300
  8.3.1 Endohedral Silicon Nanotubes 301
  8.3.2 Yttrium Silicide NW 307
  8.3.3 Energy Decomposition 308
Acknowledgements 311
References 312

Abstract

Great interest to silicon nanostructures is not only a tribute to the advanced silicon technology, but is also driven by the inherently rich behaviour. Nearly one-dimensional material arrangements in the form of elongated clusters or nanowires have to be explored for their stability, atomic makeup, electronic structure and electronic transport properties. An overview of our recent work is mostly focused on determining the lowest-energy structural ground state for pure silicon nanowires. One remarkable finding is that the balance of the surface and edge contributions leads to the unusual pentagonal shape internally polycrystalline but possessing the minimum energy for the thinnest wires (up to 5–6 nm in diameter). Another class of wires discussed here is derived from metal-endohedral silicon nanotubes, and their identity to the thinnest metal-silicide nanowires is demonstrated. We discuss how the energy decomposition into the contributions from the bulk, surface, and edges, with their different size-scaling behaviours, permits to propose an efficient way of the energy computations for arbitrarily thick wires, without the taxing computational load. A simple relationship between the cohesive energy and the stoichiometry of the wire is discussed and verified through direct first principles energy analysis.

[1] Department of Mechanical Engineering & Materials Science, and Department of Chemistry, Rice University, Houston, TX, USA.
[2] Institute of Physics PAS, Warsaw, Poland.

Nanosilicon
9780080445281
Copyright © 2007. Elsevier Ltd.
All rights reserved.

8.1 Introduction

Continuous advances of computer engineering technologies drive the size of silicon-based electronic devices towards the limit, where quantum mechanics confinement effects become dominant. Nanostructures of silicon draw ever growing attention from both theoretical and experimental workers. In this chapter, we focusing on quasi-one dimensional nanostructures of silicon, such as silicon nanowires (SiNW) [1,2] and metal-endohedral silicon nanotubes (M@SiNT) closely related to silicide nanowires (MSNW), which posses novel and unique properties. The discussion proceeds approximately as following, and covers mainly our own work with no attempt to offer comprehensive review of the rapidly growing field.

Relative simplicity and compatibility with traditional techniques, makes nanowires (NW) one of the promising building blocks for the next generation electronic circuits. However, some of the basic structural issues remain unsettled. One important parameter is the most stable shape of the cross-section of a given thickness wire (i.e. a number N of atoms in a cross-section of diameter $d \sim N^{1/2}$). Recently, the edge energy E_e has been appended to the classical Wulff construction energy, because E_e is comparable to the bulk energy in mesoscopic scale and is no longer negligible. Pentagonal cross-section turns out to be the ground state shape for SiNW thinner than about 6 nm. Interestingly, the band gap of pentagonal SiNW changes linearly with mechanical strain, while the single crystal hexagonal SiNW does not respond to deformation this way.

Tubular structures have shown fascinating properties with carbon nanotubes (CNT). Although silicon and carbon are both in the same column in the periodic element table, and share similar structural and electronic properties, silicon tends to form sp^3 bonding networks rather than two-dimensional (2D) silicon "graphite". The reason stems from the smaller energy splitting between 3*s* and 3*p* orbitals in silicon comparing to the energy splitting between 2*s* and 2*p* in carbon; in addition, the weaker π bond is formed among silicon atoms [3] than among carbon atoms due to silicon's larger radius. While pure silicon tubes appear not sufficiently stable, in order to prevent the collapse, structures can be "propped" by encapsulating metal atoms (Me) inside. Such M@SiNT are stable structurally and show electrical conductivity, associated not with the rather spaced metal chain but from the silicon side wall. It can be further noticed that the (2, 2) M@SiNT has the AlB_2-type structure and is identical to the thinnest metal-disilicide NW, as can be grown on the Si(001) substrate. This observation bridges an interesting artificial design of the metal-endohedral tubes with the realistic silicide wires grown in the laboratory.

8.2 Silicon nanowires

8.2.1 Pentagonal Silicon Wires

As recent research indicates, ultra-thin SiNW might have properties that make them competitive choice in nanoelectronics; e.g. different surface reconstructions render SiNW either metallic or semimetallic [4], and strong polarization-dependent photoluminescence of SiNW fibres [5]. As known, silicon has relatively reactive

properties which facilitate doping [6]. Faster and lower energy-consuming electronic devices have been suggested and circuits of arrays of SiNW have been demonstrated experimentally [7].

8.2.1.1 Wulff's Construction Generalized

Different from the nanotube (NT), which has cylindrical cross-section and homogeneous surface, SiNW cross-section shapes are determined by the atomic details, including crystal facets, and thickness. This poses a question, for a given thickness (i.e. a number N of atoms in a cross-section of diameter $d \sim N^{1/2}$) what shape corresponds to the lowest energy and is likely to be the most stable [8]? For macroscopic silicon wires ($N \rightarrow \infty$) Wulff construction provides a classical recipe [9], relating equilibrium shape with the surface energies γ_s of different facets. By minimizing $\sum s\gamma_s$ at $N = const$ (surface being measured by a number s of appropriate unit cells), one can find the cross-section shape for the most stable silicon wire with a given thickness. In this approach, one will notice that the energy of the edges E_e ($\sim d^0 \sim N^0$) between the facets is quite negligible compared to the surface contribution ($\sim s \sim d \sim N^{1/2}$), while the bulk ($\sim d^2 \sim N$) is assumed already at its minimum and thus invariant. However, when N becomes smaller, e.g. only a few dozens, the energy of the edges matching the adjacent facets, E_e, cannot be neglected any longer. It can affect the reconstruction [10], and can even favour certain changes in the bulk as reflected by E_b (including possibly internal granularity or elastic strain, if such would lower the energy overall). Therefore, the Wulff energy must be generalized as,

$$F = \sum E_e + \sum s\gamma_s + E_b \tag{8.1}$$

8.2.1.2 Pentagonal Shape SiNW

Following the modification (8.1), identifying the ground-state structure of a NW should again be based on minimizing the edge energy, the number of the edges, and reducing the surface area, since there is no much room to vary the bulk energy. Intuitively, one can cut the wire from silicon bulk, and several possible pristine SiNW structures [10–15] have previously been discussed. Stepping aside from single crystal NW, a family of quasi-crystalline NW can be proposed. Figure 8.1(a) shows the Si-lattice structure projected to the (110) plane.

The optimal design comes from a prism cut along the [110] direction in bulk Si with a (100) and two {111} planes. The angle between these two {111} planes, $\theta = 2\tan^{-1}(1/\sqrt{2})$ is very close to $2\pi/5$, with $\delta = \theta - 2\pi/5 = 0.025$. Therefore, with very little shear strain ε and inexpensive {111} stacking faults, five such prisms can form a pentagonal SiNW P, shown in Fig. 8.1. All surfaces of these pentagonal SiNW are (100) facets, which has relatively low-energy [16,17] and permit low-energy reconstruction with characteristic dimer row. The complex (111)-(7 $\times$ 7) reconstruction is not considered here because the matching at edges would lead to complicated defects with many dangling bonds. The alignment of the dimer rows is known to alternate between two orthogonal directions when the bulk lattice grows in consecutive layers [18]. The degeneracy of these row patterns is lifted since their orientation with respect to the wire becomes important. Moreover, depending on the number of layers (i.e. thickness) NW are divided into three different categories.

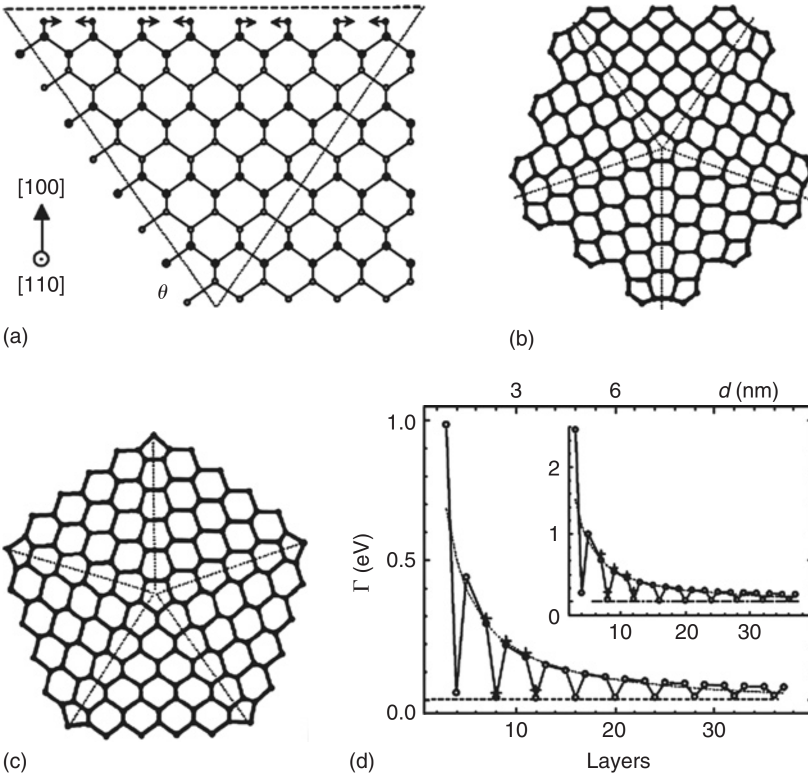

Figure 8.1 (a) Si lattice viewed along the [110] axis shows the dark and light atoms displaced by $a/2$ in the axial direction, so that the slanted off-plane bonds appear shorter than the in-plane bonds; arrows indicate dimerization of surface atoms. Five prisms outlined by the triangle can join in pentagonal wire with the surface dimer rows either (b) parallel, (c) or perpendicular, to the wire axis; shown are 12-layer thick $P_{||}$ and 11-layer $P_{\perp}$. (d) Energy dependence on NW thickness computed with classical EP (circles) and TB (crosses). The inverse-linear curve (dotted) is fitted to the sample points at 7 and 17 layers. The inset is for carbon.

First of all, the wires which have $4l$ atomic layers will form dimer rows parallel to these $P_{||}$ NW, Fig. 8.1b. For those wires with $(2l - 1)$ layers, the dimer rows on the (100) surface are circumferential and perpendicular to the $P_{\perp}$ wires, Fig. 8.1c. Lastly, the wires with $2(2l - 1)$ layers are not energetically favourable, since there is one surface atom column left unpaired in each facet.

8.2.1.3 Ground State of the Thinnest SiNW

In order to illustrate the heuristically useful but approximate decomposition described in Eq. (8.1), one can conduct a comparison of all these pentagonal silicon and the single crystalline wires with many-body empirical potentials (EP) [19,20]. For more convenient comparison between $P_{||}$ and $P_{\perp}$, one can split the bulk energy into three terms: the unperturbed bulk energy, the stacking fault [21] and the bulk shear [22], and rewrite the Eq. (8.1) as follows:

$$F - Ne_{\mathrm{b}} - s\gamma_{\mathrm{s}} = E_{\mathrm{e}} + s\gamma_{\mathrm{f}} + \frac{1}{2}NK\varepsilon^2 \tag{8.2}$$

Since all pentagonal silicon rods have only (100) facet, summation over surface energies becomes total surface area times uniform surface energy density γ_s; the number of surface atoms in P-type NW equals that of atoms at the interface, thus the area of interface is substituted by the area of the surface, and γ_f is stacking-fault energy per interface atoms which is known as 0.06 eV for silicon. Here, s is counted as a number of three-fold coordinated atoms (one per surface cell). For convenience of comparison, the *excess surface energy*, $\Gamma = (F - Ne_b - s\gamma_s)/s$, is plotted in Fig. 8.1d versus number of atomic layers. The deduction of a large trivial contribution ($Ne_b + s\gamma_s$) reduces the error in absolute value of surface energies computed by different methods. Clearly, the computed points shown in Fig. 8.1d are fitting to a horizontal straight line (dashed line, $\Gamma = 0$) and an inverse-linear curve (dotted line, $\Gamma \sim 1/d$), which are corresponding to $P_{||}$ and $P_{\perp}$ silicon rods, respectively. The inverse-linear behaviour is indicating the edge energy overwhelms over the almost negligible stacking fault and elastic strain energies, and plays the major role in the excess surface energy.

To demonstrate the robustness of Eq. (8.1), we performed analysis of pentagonal isomorphic carbon wires. The inset in Fig. 8.1d plots Γ for isomorphic carbon wires, very similar to the case of Si, in spite of different inter-atomic forces. Since the surface-counting method (s as a number of three-fold coordinated atoms) is identical for $P_{||}$ and $P_{\perp}$, Fig. 8.1d can be interpreted as evidence of very low edge energy in $P_{||}$, at least in comparison with the $P_{\perp}$ series. This originates from their structures, Fig. 8.1b and c: little strain is added to the edges of $P_{||}$, while the $P_{\perp}$wire is rather strained in the corner-pentagons. (Putting in one more atomic column to change the pentagon into a hexagon places the steps on both sides of the edge, which raises the energy.)

For series of rather large systems (up to 10^4 atoms in the computation cell, $4a$ in length) and to reveal the general dependencies, EP [19,20] are used to compute the energies faster. They are also used below in molecular dynamics (MD) tests. Further, when only sample-wires are needed for evaluating parameters in the Eq. (8.1), they are computed using tight-binding approximation [23] (TB). Bulk, (100)-(2 × 1) surface, and wire structures were calculated with 3D, 2D, and 1D periodic boundary conditions (PBC), respectively, with the box periods optimized.

In the following, we extend a comparison of the $P_{||}$ wires with others of hexagonal (H) and square (S) shapes, as most feasible 1D structures. Indeed, since both the (100) and {111} surfaces have the lowest energies [16,17], a competitive family is the hexagonal bars with these facets, sized according to Wulff theorem, that is equilateral. The (100) facets with axially aligned dimer rows match the {111} facets in Fig. 8.2b: two of the {111} facets follow the normal π-bond chain model [24] while the other two have incomplete reconstruction leaving two rows of atoms similar to an unreconstructed surface. S-bars cut out by four {100} planes have been discussed [10] with two possible reconstructions, i.e. (2 × 1) [or p(2 × 2)] and c(2 × 2) denoted here as $S_{\square}$ and $S_{\diamond}$, according to the reconstruction patterns.

Comparison between the $S_{\square}$, $S_{\diamond}$, H, and $P_{||}$ should be based on their energies $F(N)$, whose direct computation is, however, not practical given the numerous (a hundred) structures of interest and the large size of each (up to $\sim 10^4$ atoms). Equation (8.1), reduced to $F = E_e + s\gamma_s$ for the mono-crystalline S and H bars, offers an efficient way. First we define a method to count s, evaluate the corresponding $E_e = F - s\gamma_s$ from computed sample structures, and find E_e to be almost invariant within the isomorphic

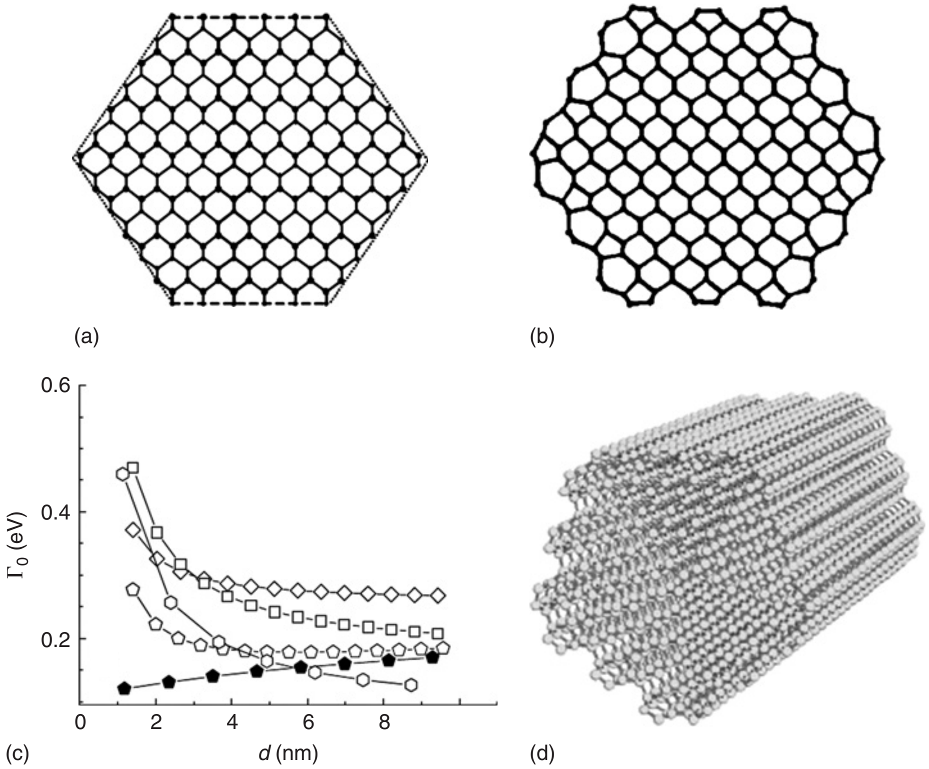

Figure 8.2 Hexagonal wire with four {111} and two {100} (a) unreconstructed and (b) reconstructed facets. (c) Size-dependent energy of different types of wires obtained as extrapolation based on several sample-point large-scale computations. The lowest-energy line (solid pentagons) makes the ground state for $d < 6$ nm evident as $P_{||}$ structure, shown in (d). Added here for completeness, $P_{\perp}$ plot (open pentagons) differs from $P_{||}$ due to significant edge energy, $E_e = 4.3$ eV. Curves with open hexagons, squares, and diamonds denote, respectively, H, $S_{\square}$, and $S_{\diamond}$ wires. The shaded circle corresponds to the chain of fullerene-like Si_{20} clusters, whose energy is the lowest among this variety; see Fig. 5c in Ref. [12].

families. Then the free energies for the whole group are evaluated as $F = E_e + s\gamma_s$ without repetitive full computations. Indeed, the number of cross-sectional atoms N and the surface area s are explicitly counted and given in Table 8.1. Obtained from TB computations, the edge energies E_e agree with the estimates [25] by modelling complex surface in terms of simpler surfaces, which are calculated by *ab initio* method. For example, in each edge of $S_{\diamond}$, there is a 3-coordinated atom in a length of $\sqrt{2}a$. Such edge atom is not a standard (100) surface atom hence was not counted in s. Its formation energy from the bulk is the surface energy of the relaxed (111) per surface atom (1.37 eV); therefore, $E_e = 4 \times 1.37/\sqrt{2}a = 3.88$ eV per length a, and close to our TB result, 3.56 eV per length a, for $S_{\diamond}$.

All parameters were obtained from only TB-computations of several sample energies $F(N)$ then followed by solving coupled linear algebraic equations within each family to determine the edge, surface, etc. energy parameters. We found that our TB computations underestimate the stacking fault γ_f and strain energy (although TB

Table 8.1 Parameters (measured per length of *a*) used to calculate energy of SiNW: $l = 1, 2, 3, \ldots, N$ is the number of all atoms, *s* is a number of surface atoms. The surface energy $\gamma_o = 1.32$ eV for (100)- and (111)-(2×1) is based on Ref. [16], while that of (2×2) relative to (2×1) is based on Ref. [10]. The area $\sqrt{3}a^2/2$ per (111) surface atom is used to define *s* for the *H* bars.

	N	s	E_e	$\gamma_s - \gamma_o$
$S_{\square}$	$(8l^2 + 12l + 1)/\sqrt{2}$	$8l/\sqrt{2}$	5.58	0
$S_{\diamond}$	$(8l^2 + 12l + 1)/\sqrt{2}$	$8l/\sqrt{2}$	3.56	0.077
H	$4l(6l + 1)$	$2l(2 + 2\sqrt{3})$	1.96	0
$P_{\|\|}$	$10l(2l + 1)$	$10l$	0	0

results are higher than EP). Therefore, in order to make a more fair conservative comparison of $P_{||}$ with other wires in Fig. 8.2c by showing a smaller gap between them, we use the TB-computed E_e's and *ab initio* surface energies; for the $P_{||}$ family, we use *ab initio* computed stacking fault [21] $\gamma_f = 0.06$ eV and experiment-based shear modulus, $K = 48$ GPa $= 5.9$ eV/atom for Si in the corresponding direction [22].

Table 8.1 can be readily used for energy evaluation at arbitrary size. By generalizing the Γ-plot in Fig. 8.1d, we plot now $\Gamma_0 = (F - s_0\gamma_0)/s_0$ as a function of the effective diameter *d*, Fig. 8.2c. Here $\gamma_0 = 1.32$ eV per a^2-area is the surface energy [16,17] of Si(100)-(2×1) or (111)-(2×1), and the effective surface area $s_0 = 2.11\ N^{1/2}$ corresponds to the cylinder of diameter *d*, containing *N* atoms in unit length.

Obtained with the decomposition–extrapolation approach (8.1), Fig. 8.2c represents well the energies of the wires, e.g. the asymptotic levels at $d \to \infty$ correspond to their relative shape-determined surface areas (lowest for the *H* and highest for the *S*-types) or surface energies. Notably, the curves here also reproduce more subtle features, like a crossover point for the two types of square *S*-bars, obtained in large-scale computation [10]. Unsurprisingly, for the smallest range $d < 1.5$ nm decomposition (8.1) shows its limitations, as the strain-overlap between the edges makes the energy higher than simple addition. Direct calculation for the $P_{||}$ of $d = 1.1$ nm yields energy almost as high as that of one fullerene cluster-wire in Fig. 8.2c, while all the thicker SiNW results fall well on the line. The energies for other cluster-chains [11–13,26] are yet higher due to dangling bonds and/or substantial strain, if hydrogen terminated [26].

Turning to the ground-state issue, it is useful to corroborate the evidence of Fig. 8.2c with a more transparent estimate. In the spirit of earlier analysis [25], for all the whiskers here, the edge energy is roughly ~1 eV (dangling bond energy) per edge or 4–5 eV total (The apparent edge energy for *H* is lower because the extra density of dangling bonds at the edges is contained in *s*.) The $P_{||}$ wire is unique in its edge reconstruction almost indistinguishable from the facets and thus $E_e = 0$; instead there is a cost of the stacking fault and elastic shear $(0.06s + 0.002N)$ eV. It will surpass the edge energy only for *s* and *N* at about 20 layers, i.e. $d \sim 6$ nm , while a $3 \sim 4$ nm $P_{||}$ wire remains well below its competitors in energy.

To further verify stability, we performed a MD test for ~1 ns at $T = 1000$ K. Fig. 8.3 shows that after 10 ps C wires gradually transform into the tube-like patterns,

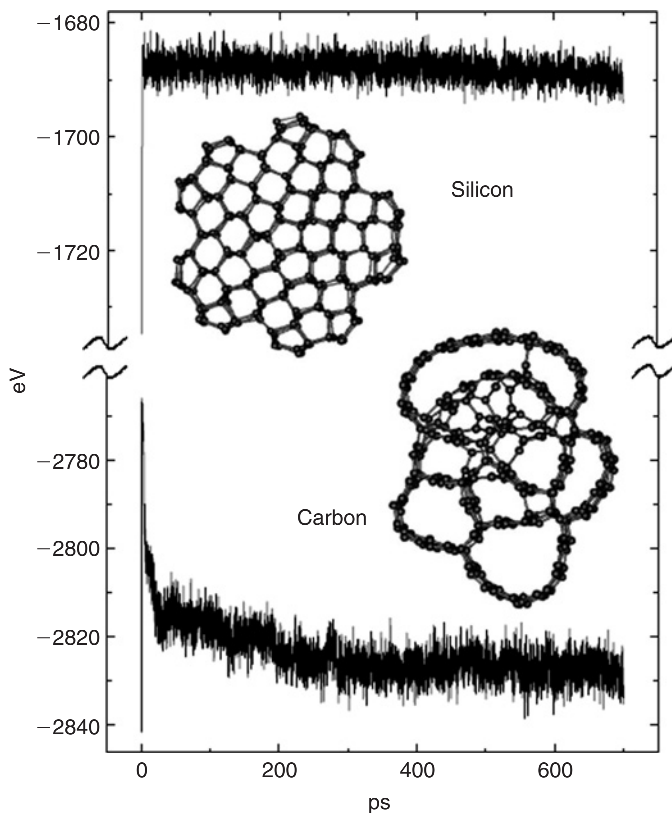

Figure 8.3 Potential energy and structural changes of 8-layer $P_{||}$ wires in MD simulations at $T = 1000\,\mathrm{K}$. The insets show the final structures of relatively stable Si (top) and of C transforming into sp^2 tubular-graphitic foam (bottom) (after Ref. [27]).

while the Si wires remain stable. At much longer times capillary instability should not be neglected [28].

8.2.1.4 Kinetic Advantages of $P_{||}$ SiNW

Besides the lower energy, the $P_{||}$ structures also kinetically favour the whisker growth due to highly anisotropic diffusion of adatoms on the Si(100)-(2 × 1) surface. It is about 1000 times faster along the flat dimer rows than across the row-groove corrugation [29]. On the surface of a $P_{||}$, circumferential diffusion facilitates an accretion of the next layer, transforming it into a $P_{||}$ type. Such thickness-growth may be accompanied by shape-oscillations [30], which is beyond the scope of the present report; we simply emphasize the kinetic advantages of the $P_{||}$ wires for unidirectional growth. At $T = 550\,\mathrm{K}$, diffusion rate [29] $D = 10^{-9}\,\mathrm{cm}^2/\mathrm{s}$, and deposition rate of less than 0.015 ML/s (monolayer, $1\,\mathrm{ML} = 1/a^2$), an adatom propagates along a 1 μm wire faster to the ends than an addimer or an island can emerge. Even a dimer vacancy, which often occurs on the normal (100)-(2 × 1) surface, is more likely to migrate to this whisker's end [31]. This kinetics favours a $P_{||}$ structure. In contrast, all other wires do not support such an enhanced axial diffusion.

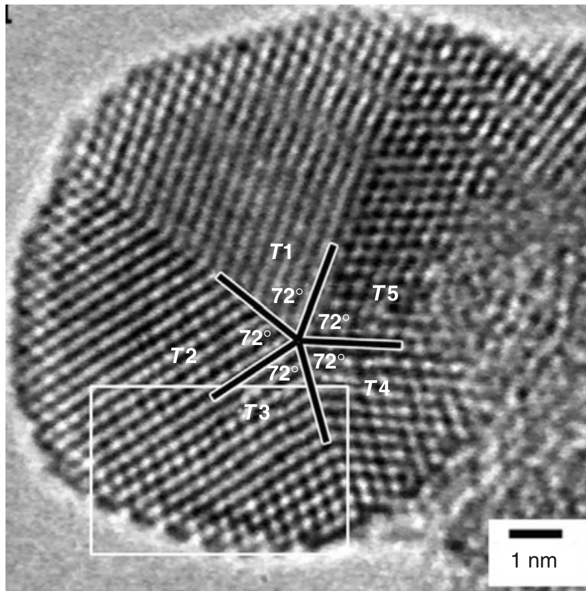

Figure 8.4 HRTEM image of a silicon multiply-twinned nanoparticle (MTP) with five-folded pentagonal-like cross-section grown in an ultrahigh vacuum chamber (after Ref. [32]).

Besides all these theoretical analysis of both energy and kinetics, several experimental facts are indicating that these pentagonal SiNWs are practically synthesizable. The silicon multiply-twinned nanoparticles (MTP) [32], synthesized by K. Furuya and his colleagues using the electron-induced SiO_2-decomposition technique inside an ultrahigh vacuum transmission electron microscope (UHV-TEM), has five-folded pentagonal-like cross-section, shown in Fig. 8.4. The surface reconstruction on the sides of the nano-particle is showing the dimer rows parallel to the direction of the pentagonal-like surface, which is exactly the same as the $P_{||}$-type SiNWs we proposed above. Another experimental evidence [12] suggest that high-vacuum growth of SiNW offers an efficient practical way complementary to vapor–liquid–solid growth [33].

In summary, we have compared several families of SiNWs and singled out a very stable type. With lower ground-state energy, reasonable thermal stability, and the surface diffusion kinetics favourable for axial growth, these NW appear to be promising 1D pristine silicon structures. Small SiNWs obtained by acid-thinning of a bulk-structured Si core have been reported [1], but could not be of *P*-family; the *H*-type appears as the next by energy (Fig. 8.2a–c) and is consistent with the reported hexagonal shape with four {111} and two {100} facets [1].

8.2.2 Hydrogen-Passivated Silicon Wires

At any practical ambient conditions, pristine SiNW must be passivated prior to any use. Passivated SiNW have been observed in experiments [1] and studied by computational modelling [34–38]. When surface passivation follows the growth, it effectively seals the wire as it was grown (e.g. in high vacuum). Depending on the

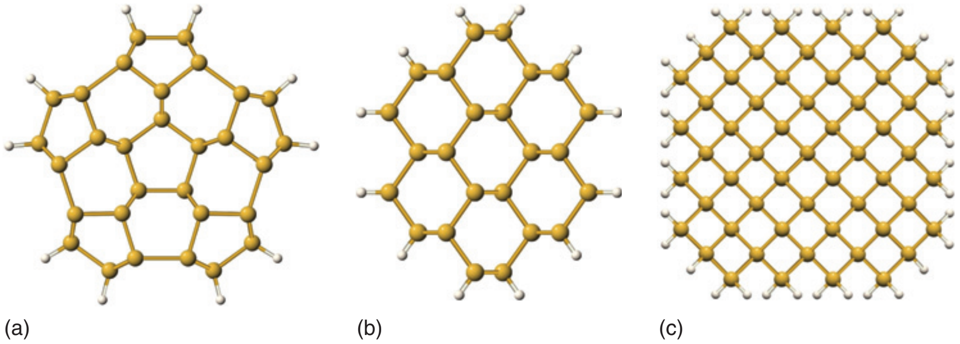

Figure 8.5 Hydrogen-passivated (a) 4-layer $P_{||}$ SiNW, (b) hexagonal [110] SiNW and (c) square [100] SiNW.

procedures of synthesis, SiNW can be passivated in many different ways and by variety of agents, e.g. hydrogen, oxygen, fluorine or hydroxyl groups. For simplicity, we only briefly discuss hydrogen-passivated NW in this section.

In addition to structural stability, we discuss the electronic properties of the pentagonal wires. All the calculations were performed with the Khan's non-orthogonal tight-binding model [39], which is much faster than *ab initio* calculations, yet reasonably accurate in band gap calculations. As a benchmark, we studied a completely hydrogen-passivated 3-layer thick hexagonal SiNW, which has four {111} and two (100) facets, and is shown in Fig. 8.5. The pseudo-diameter of the single crystalline SiNW (before passivation) was defined as $d = (32\sqrt{3}/9\ Nb_{\mathrm{Si}}^3/\pi \mathrm{L})^{1/2}$, where N is the number of silicon atoms, b_{Si} is the length of Si—Si bond, and L is the periodic length of the Si wire. Thus, the pseudo-diameter of the 3-layer Si wire is 1.3 nm. The tight-binding calculation shows that the band gap of the passivated 3-layer hexagonal SiNW is 2.2 eV, which is reasonably close to the experimental result [1]. To test the robustness of this tight-binding model for the electronic density of states (DOS) calculations, another single crystalline SiNW with a pseudo-diameter 1.6 nm was studied, which is shown in Fig. 8.5 as well. The cross-section of this SiNW is a roughly 8×8 square; all the four sides are (100) facets, and four corners are truncated, forming four narrow [110] facets. The band gap for this SiNW is also 2.2 eV, which shows the band gap of passivated SiNW doesn't depend on the shape of cross-section shape much but the pseudo-thickness, and our calculation results are reasonably consistent with the experiments [1].

We first consider $P_{||}$ wire, discussed in the previous section as lowest energy structure. Furthermore, to avoid the rather large systems and to reveal basic physics, the 4-layer pentagonal SiNW $P_{||}$ can be explored. Since there are many ways to passivate this pentagonal SiNW $P_{||}$, we consider fully passivated SiNW, with no dangling bonds left. Moreover, the pentagonal SiNW $P_{||}$ surface has been dimerized prior to passivation. The structure of this pentagonal SiNW $P_{||}$ is shown in Fig. 8.1. Within the tight-binding approximation, we got the electronic band gap of this passivated 4-layer $P_{||}$, $E_g = 2.2$ eV, which is close to the band gap of the single crystalline SiNW mentioned previously. It also turns out that the shape of the cross-section of the SiNW doesn't make much difference for the band gap, but the diameter or thickness play a substantial role to it.

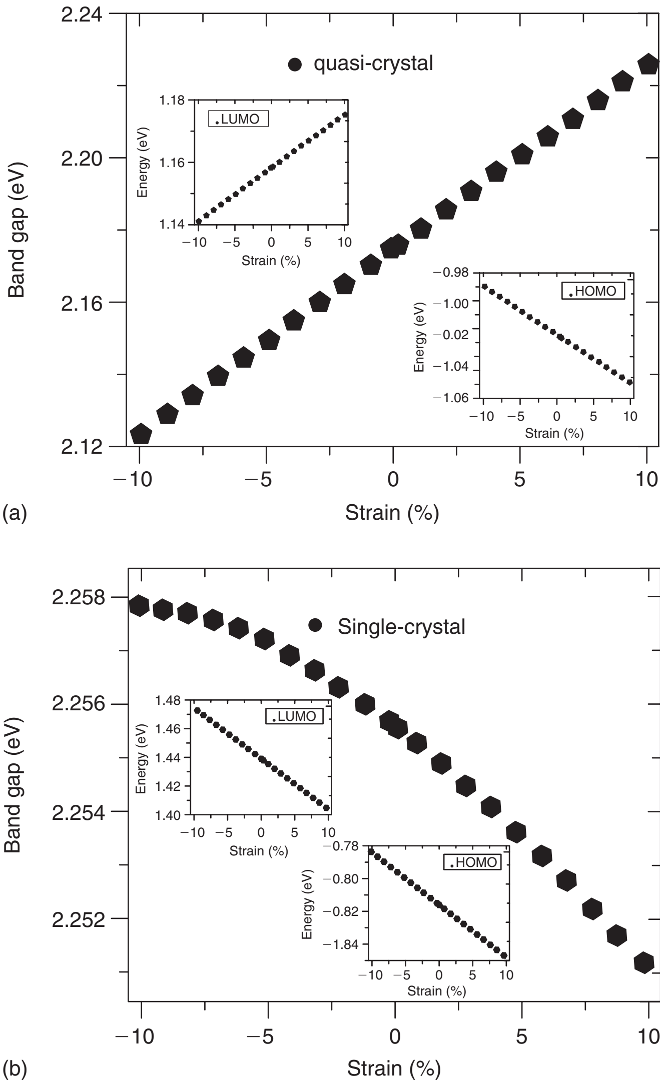

Figure 8.6 Tensile strain dependence of the band gap for the hydrogen-passivated (a) 4-layer $P_{||}$ SiNW and (b) hexagonal [110] SiNW; the insets are the strain dependence of the HOMO and LUMO energies, respectively.

All the results illustrated so far are for the equilibrium structures of different SiNW, which have no any external stress or compression. The strain effect on the electronic band structure is well known and has been studied both theoretically [40] and experimentally [41] for decades. For 1D structures, among recent examples is the band gap change of CNTs tunable by varying the external strain [42]. We have recently investigated the strain effect on the electronic band gap of SiNW, based on which the strain-controlled switch could be proposed. In Fig. 8.6a, the band gap of the passivated 4-layer pentagonal SiNW $P_{||}$ is plotted against the strain applied

along the axis of the SiNW. The band gap of this $P_{||}$ SiNW has a nearly linear response to the unaxial strain applied on the NW,

$$E_g = E_0 + \kappa\varepsilon \tag{8.3}$$

where E_0 is the band gap of the equilibrium structure, $\kappa = -0.51$ eV, and ε is the external strain. The band gap of passivated $P_{||}$ varies by about 120 meV within $\pm 1\%$ strain. For more details, the energies of the highest-occupied molecular orbital (HOMO) states and the lowest-unoccupied molecular orbital (LUMO) states are plotted respectively in the insets of Fig. 8.6a. Although both the HOMO and LUMO energies depend linearly on external strain, the corresponding slopes have different sign: LUMO energy increases when the NW is stretched, while the HOMO energy linearly decreases.

In contrast, the strain effect to the electronic band gap of the hexagonal single crystalline SiNW with a similar diameter is different. Here, Fig. 8.6b, both HOMO and LUMO energies decrease linearly with tension, their slopes have the same signs and are very similar in magnitude. Upon subtraction, the linear term in the band gap is nearly cancelled out, and fitting the gap up to quadratic term yields:

$$E_g = E_0 + \kappa\varepsilon + \gamma\varepsilon^2 \tag{8.4}$$

where γ is the second order coefficient of Taylor expansion of $E_g(\varepsilon)$. Here, $\kappa = -0.03$ eV is 20 times less than for the $P_{||}$ wire, $\gamma = -0.11$ eV becomes relatively significant, and makes the band gap dependence nonlinear, although small compared to the $P_{||}$ wire: the band gap varies only by 7 meV between $+1\%$ and -1% strain. Therefore, although both the passivated polycrystalline $P_{||}$ SiNW and the passivated single crystalline hexagonal SiNW have band gap tunable by the axial strain, only the band gap in $P_{||}$ changes linearly and significantly, and thus might be of interest for designing an intact nano-sensor of strain, by remotely observing the changing wavelength of light emission.

The Young's modulus of passivated silicon SiNW can be estimated from the second derivative of the energy-strain curve. To define the cross-section, one can treat the surface hydrogen atoms as part of bulk silicon as well.

8.3 Metal silicide

Metal silicide nanowires (MSNW) find their relevance in nanotechnology as the potential building blocks for nano-electronics since their morphology, size, and electronic properties make them suitable for fabricating both nanoscale devices and interconnects [43,44].

Growth of a variety of epitaxial self-assembled rare-earth MSNWs, has been reported [43,45–51]. When a sub-monolayer metal film is deposited on Si(001) surface and annealed it forms compounds $MSi_{1.7}$ in the hexagonal AlB_2-type structure with the *c*-axis parallel to the surface. The self-assembled MSNW can be grown on Si if the magnitude of the lattice mismatch between the epilayer and substrate is large along one crystal axis and small along the perpendicular axis, leading to the formation of long, straight wires due to the effects of strain. This was first observed for

dysprosium Dy [43,45–48] and later for erbium, Er [45,49], holmium, Ho [46,50], gadolinium, Gd [51], and, though not a rare-earth metals, scandium, Sc [45] and yttrium, Y [52]. These NW have widths and heights in the range of 1.5–11 and 0.2–4 nm, respectively, depending on the lattice mismatch. The average lengths of the NW are in the range 150–450 nm and are determined primarily by the kinetics issues [45]. MSNW exhibit atomically flat surfaces, are also straight, robust, and conductive, which are necessary properties for any potential usage in nanodevice architectures [43].

Here we present some of our effort to understand the structural, elastic and electronic properties of selected metal silicide NW. There is only limited mentioning of the work by other groups, discussed in the other chapters.

8.3.1 Endohedral Silicon Nanotubes

The long-standing interest in fine hair-like crystals-whiskers has shifted over the last decade towards yet thinner filaments, NT and NW. This is largely due to their electronic properties and the advances in synthetic methods, both driven by further device miniaturization for nano- and molecular electronics [7,53–55]. While carbon can form narrow NT cylinders [56,57], another critical element, silicon, so far, could only be produced [1,58] as NW, but not in tubular form. Calculations show that even though SiNT might correspond to local minima [59], they cannot sustain perturbations and collapse into sp^3 aggregates. Moreover, sp^3-bulk-based NW thinner than 1.2 nm lack stability [27].

Compelled to stabilize the thinnest SiNT, we "propped" them up by placing metal (M) inside. Here we present such M@SiNT, isomorphic to rescaled carbon tubules of (2, 2) and (3, 0) symmetry. Computations for a series of metals show that M@SiNT are stable, and have substantial cohesive energies (E_c) and elastic moduli. They appear to be the thinnest 1D silicon forms, since other reconstructions always lead to thicker wires. Electronic DOS show no band gap, which implies good conductivity. Plotting cohesive energies as a function of stoichiometry (molar fraction, x) permits formation energy comparison with other known M_xSi_{1-x} structures at different conditions. Finally, there is a remarkable correspondence between these thinnest M-endohedral nanotubes and the synthesized [45,46,48,49,60] subnanometer disilicide wires.

The structures were fully optimized within unrestricted density functional theory (DFT) with the PBC algorithm [61] of GAUSSIAN 98 [62]. We used the gradient-corrected functional of Perdew, Burke, and Ernzerhof [63] (PBE) and the 3–21 G Gaussian basis set to represent both the valence and core orbitals. We verified that this framework, previously used for 1D (carbon NT (CNT) and boron nitride NT (BNNT)) [64,65] and 3D (UO_2) [66] systems, gives for bulk silicon a bond length of 2.38 Å and E_c of 4.64 eV, in agreement with experiments [67].

Pure SiNT of zigzag (3, 0) and armchair (2, 2) types were unstable in our calculations but both could be underpinned by M atoms inserted along NTs axis. In the (3, 0) case, M atoms were placed between consecutive zigzag motif rings. For the (2, 2) SiNT, M atoms were put at the centres of every other Si rectangle, as shown in Fig. 8.7. Consequently, we used in our PBC calculations unit cells with stoichiometry M_2Si_{12} and MSi_8, for the (3, 0) and (2, 2) SiNT, respectively. Convergence was achieved by employing between 116 and 178 **k** points.

The optimized geometries of Fig. 8.7 (left), where M = Zr, demonstrate that the reinforcement by internal M–Si bonding stabilizes both zigzag and armchair SiNT topologies. Both possess large E_c values of 4.34 eV for the (3, 0) and 4.26 eV for (2, 2) Zr@SiNT, and stiffness around 200 GPa (see below). We explored other M choices, such as the 3*d* elements Sc, Ti, Cr, Fe, and Ni, and the alkaline earth Be and Ca. The performed optimizations indicated that the (3, 0) and (2, 2) SiNT cages can be stabilized with M from different groups of the Periodic Table. The E_c values (Table 8.2) show a slight increase with the group number. As the M's elemental radii decreases with the group number [67], the relaxed M—Si bonds get shorter. For example, in the (2, 2) series there is a 7% bond length decrease, from $l_{Ca—Si} = 2.92$ Å to $l_{Ti—Si} = 2.72$ Å. This bonding effect appears as a limiting factor for the M choices, as $l_{M—Si}$ can become too short to stabilize the SiNT cage. Calculations identify Cr and Ti as the limiting 3*d* metals for the (2, 2) and (3, 0) series, respectively.

To ensure that stability is retained at finite length as well, we considered the termination caps shown in Fig. 8.7 (right). For the (3, 0), an additional Si atom was placed on the axis to reduce the number of dangling bonds. For the (2, 2) no additional atoms were needed, as the end atoms reconstruct naturally to form a square cap. Computations performed for clusters Zr_3Si_{28} for armchair and Zr_4Si_{32} for zigzag lead to stable configurations, with large E_c of 4.09 and 4.12 eV, and HOMO–LUMO gaps

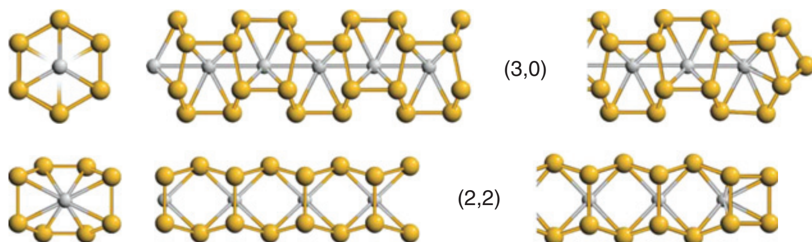

Figure 8.7 The thinnest (3, 0) and (2, 2) SiNT are stabilized by endohedral metals (smaller ball). The infinite (axial and side views, left) and end-cap (right) structures were optimized for M = Zr at the PBE/3–21 G level (after Ref. [68]).

Table 8.2 Cohesive energies E_c (eV/atom) for the (2, 2) and (3, 0) M@SiNT families.

Metal	Be	Ca	Sc	Ti	Zr	Cr
(3, 0)	3.74	3.11	4.05	4.24	4.34	–
[6, 0]	3.74	3.18	4.10	4.33	4.39	4.49
[6, 0]′	3.71	2.90	3.85	4.11	4.16	4.36
(2, 2)	3.65	3.34	4.02	4.15	4.26	4.13
[4, 4]	–	3.19	3.97	–	4.23	–
(4, 0)	–	3.59	4.12	–	4.30	–

of 0.95 and 0.60 eV, respectively. Thus, both NT types are stable not only as infinite tubes, but also can sustain the intrinsic strain (surface tension) associated with the tip ends.

To thoroughly investigate the configurational vicinity of our M@SiNTs, other nearly 1D structures were considered. Starting from the (3, 0) and (2, 2) structures, Fig. 8.8a sketches the lattice changes that lead, through DFT optimizations, to the new 1D stable structures shown in Fig. 8.8b. For the (3, 0) M@SiNT, the three hexagons were transformed into six surface rectangles. Analogous to the hexagon-lattice wrapping indexing, we label this tube as [6,0], where the square brackets stand for rectangular surface units. Further, we noticed that a half-period axial shift of the M chain leads to a previously proposed 1D structure [69,70], confirmed as stable and labelled [6,0]′. For the (2, 2) shell, the alternative longitudinal shifts of the zigzag motifs accompanied by the bonding of Si atoms 2 and 5 in Fig. 8.8a, lead to a [4,4] NT. Next, the hexagonal wall pattern can be regained in the (4, 0) zigzag orientation through alternating circumferential shifts.

The E_c values for all wires, stabilized with different M choices, are plotted in Fig. 8.9 as a function of optimized unit-cell lengths l. Clearly, the (2, 2) and (3, 0) NTs emerge as the longest (or thinnest (of smallest diameter, d)) NTs within their stoichiometric families. When compared with reconstructed NTs, the energy differences appear notably low, in spite of an obviously larger energy contribution of specific surface, which scales as $\sqrt{l}$ or $1/d$, and therefore favours shorter and thicker

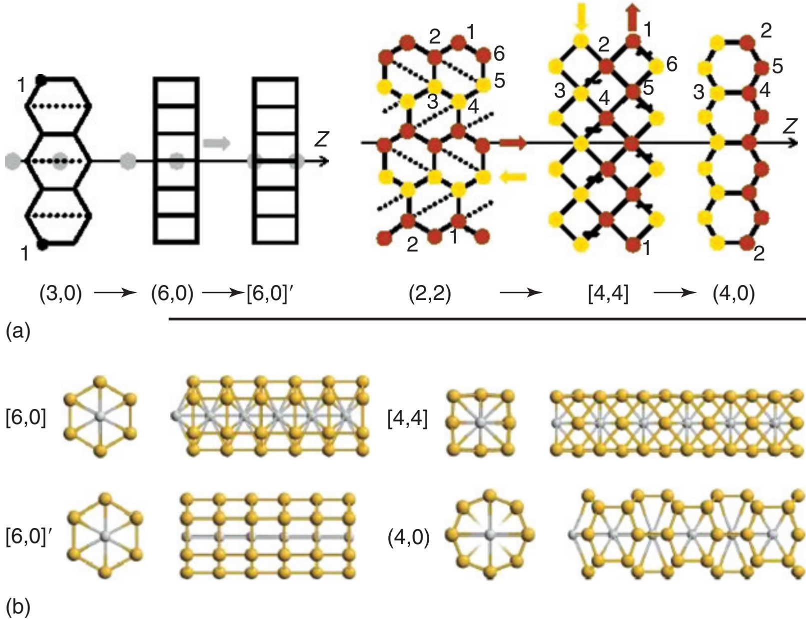

Figure 8.8 (a) Possible atomic rearrangements, in 2D geodesic projection: (3, 0) → [6, 0] → [6, 0]′and (2, 2) → [4, 4] → (4, 0). Arrows indicate collective displacements of same coloured atoms. Dotted lines and "∼" denote the incipient and breaking bonds. (b) Axial and side views of actual reconstructed NT: "sharp pencil" [6, 0], "blunt pencil" [6, 0]′ (also discussed in Ref. [24]), 1D fcc [4, 4], and zigzag (4, 0) (after Ref. [68]).

types (and ultimately of course favours bulk material over any filaments). For instance, for M = Zr we obtained that the [6,0] structure is by 12% shorter than (3, 0) NT, but its E_c is only 1% larger. By separately computing the energies of the Si and Zr subsystems we could divide this energy difference into separate contributions over the whole Zr_2Si_{12} unit cell. While the binding strengthens within both the Si cage (by 2.3 eV) and internal Zr chain (by 1.3 eV, as $l_{Zr—Zr}$ shrinks from 2.94 to 2.59 Å, the embedding of the Zr chain into the Si cage (a measure of Zr—Si binding) decreases from 15.6 to 12.8 eV. Next, along this family we found that the internal M-chain shift by half-period into [6, 0]′ is unfavourable, and E_c decreases to 4.16 eV for M = Zr. Turning now to the (2, 2) M@SiNT, the transformation into [4,4] is uphill, in spite of 12% length shrinkage; further, (4, 0) M@SiNT is the lowest in energy for all considered metals, but it is 19% shorter than the initial (2, 2). We have attempted other transformation possibilities besides the ones shown in Fig. 8.8, which did not, however, lead to stable 1D structures. For example, bonding the Si atoms in the 1 and 4 positions (Fig. 8.8a) of the (2, 2) cage could lead to a [4,0] M@SiNT; our calculations proved it unstable, as also suggested by cluster analysis [71].

Considering the length-changing transformations of Fig. 8.9, one can conjecture if they could be induced by applied force F. For example, to evaluate the tension required for the [6,0] ⟶ (3, 0) transformation, we calculated the energy versus *elastic* elongation curves. We obtained that both [6,0] and (3, 0) Zr@SiNT are quite stiff, with the Young's moduli of 220 and 160 GPa, respectively (assuming cross-sectional areas as 41 and 38 Å^2, to include Si radii). Thermodynamically, the transformation occurs at critical force F_t when the enthalpies $H = E - Fl$ of the two NTs are equal. The tension estimate $F_t = \delta E/\delta l$ (where $\delta E = 0.79$ eV and $\delta l = 0.71$ Å are the energy and unit-cell length differences between the stress-free phases [65]) yields 1.1 eV/Å, which corresponds to a small 2% strain, suggesting that such transition is viable.

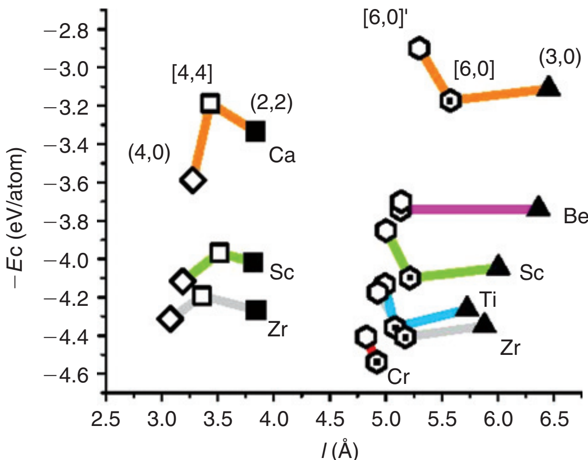

Figure 8.9 Cohesive energy E_c versus unit-cell length l for the two MSi_8 and M_2Si_{12} NT families. Polygons represent different structures (after Ref. [68]).

While primarily focused on structural stability, our calculations also provided the M@SiNT electronic characterization. Taking into account 128 **k** points, Fig. 8.10 presents the band structure and the DOS of (3, 0) Zr@SiNT. The DOS shows a series of van Hove peaks and maintains a nonzero value at the Fermi level $E_F = -5.54$ eV due to the contribution of four electronic bands. Further insight is gained by separately analysing the *projection* of the total DOS on the metal chain and SiNT structure. One notices a dominant contribution at E_F from the silicon shell, which explains the metallic character of all other M@SiNT including for M = Cr (an indirect low band gap semiconductor in the $CrSi_2$ bulk form). DOS analysis for (2, 2) Zr@SiNT revealed similar metallic behaviour at $E_F = -5.24$ eV. The possibility of Peierls distortion and a small gap opening is not excluded by this analysis.

For a broader perspective, MSi_6 and MSi_8 structures discussed above might be compared with previously reported $Zr@Si_{16}$ ($E_c = 4.16$ eV, Ref. [72]) and $Zr@Si_{12}$ ($E_c = 3.4$ eV, Ref. [73]) clusters, with 5-Å-narrow (4, 0) pure-Si tubules ($E_c = 3.75$ eV, Ref. [59]), and MSi_5 pentagonal wire [74]. For the latter, our DFT calculations confirmed its stability, with $E_c = 4.15$ eV for M = Zr. However, E_c's computed per "average" atom bear little significance for structures of different compositions. Their relative stability depends on the constituents' chemical potentials, μ_M and μ_{Si}, which in turn represent environmental conditions. To account for this, we follow the approach customary in binary phase thermodynamics and define a molar (per atom) Gibbs free energy of formation δG for composition M_xSi_{1-x}, as

$$\delta G(x) = -E_c(x) - x\mu_M - (1 - x)\mu_{Si} \tag{8.5}$$

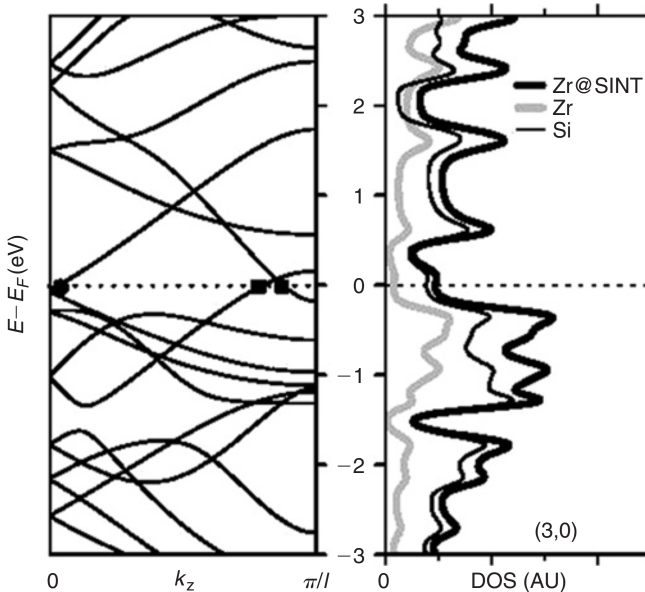

Figure 8.10 Electronic band structure (left) and DOS (right) of the (3, 0) Zr@SiNT. Squares (circles) mark single (doubly degenerate) Fermi-level crossings. The grey and thin black lines are the projection of the total DOS (thicker black line) on the Zr and Si atoms, respectively (after Ref. [68]).

where the E_c term neglects thermal contribution for the solid phase. Accordingly, Fig. 8.11 plots the E_c's of all nanostructures, along with the values for the bulk Si, Zr and disilicide $ZrSi_2$, as a function of Zr molar fraction $0 < x < 1$. This allows one to conveniently compare the thermodynamics of the *range* of M—Si binary structures, based on the altitude of each $-E_c(x)$ point from the line connecting the reference μ_{Si} and μ_M values at $x = 0$ and $x = 1$. For instance, when choosing the constituent chemical potentials in Fig. 8.11 at the bulk values $\mu_{Si} = \mu_{Si}^{bulk} = -E_c[Si]$ and $\mu_{Zr} = \mu_{Zr}^{bulk} = -E_c[Zr]$, crystal $ZrSi_2$ appears thermodynamically stable. Indeed, the straight line of slope $\mu_{Zr}^{bulk} - \mu_{Si}^{bulk}$ clears above the $ZrSi_2$ point, with $\delta G(1/3) = -0.56\,\text{eV}$ [75,76]. On the other hand, all nanostructures appear above this line and are metastable (mainly due to great excessive surface), while δG still characterizes their relative stability. The (3, 0) Zr@SiNT ($ZrSi_6$ with $\delta G(1/7) = 0.52\,\text{eV}$) appears to be slightly better than the (2, 2) Zr@SiNT ($ZrSi_8$ with $\delta G(1/9) = 0.54\,\text{eV}$), and both of these proposed Zr@SiNT remain more favourable than other clusters, than the $ZrSi_5$ NT of Ref. [74] ($\delta G(1/6) = 0.74\,\text{eV}$), or the pure (4, 0)-SiNT of Ref. [59] ($\delta G(0) = 0.93\,\text{eV}$).

After establishing the thermodynamic advantage of the proposed M@SiNT, a connection can be made with experiment. At a first glance, M@SiNT have stoichiometries ($x = 1/7$ and $x = 1/9$) very different from disilicide ($x = 1/3$) or the disilicide NW [45,48,49] synthesized recently by controlled deposition [60]. As wires become thinner, their formal composition M_xSi_{1-x} changes towards Si

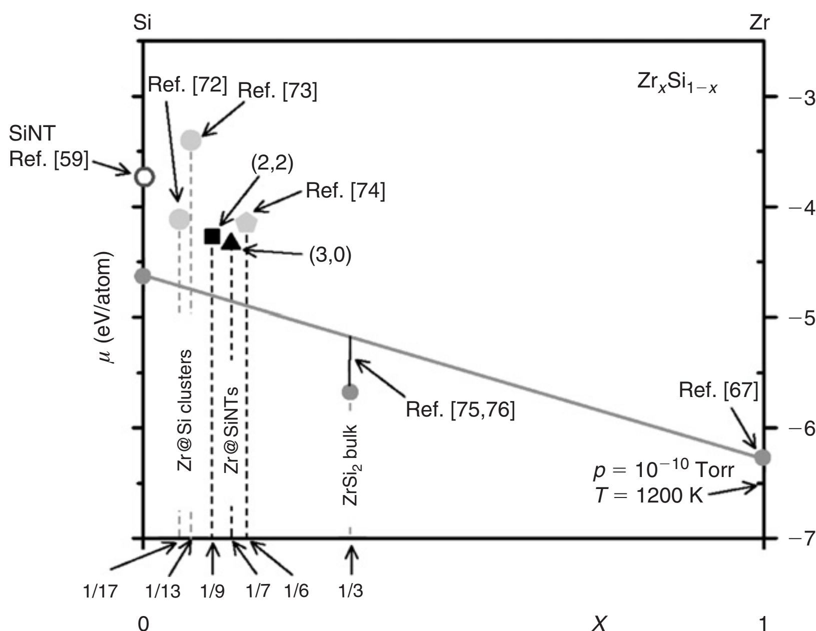

Figure 8.11 Cohesive energies E_c for the (2, 2) $ZrSi_8$NT (■) and (3,0) $ZrSi_6$NT (▲) plotted as a function of Zr fraction x. For a broader comparison we included the $ZrSi_5$NT of Ref. [74] and the pure (4,0) SiNT of Ref. [59], along with the clusters $ZrSi_{16}$ of Ref. [72] and $ZrSi_{12}$ of Ref. [73]. The bulk −Ec values for Si, $ZrSi_2$ and Zr are also shown at $x = 0, 1/3$, and 1 (after Ref. [68]).

(merely due to Si termination of the exterior). Structurally, Fig. 8.12 shows a schematic for such Sc–silicide NW with $x = 1/5$ grown in the [110] direction on Si substrate. The wire's top surface exhibits usual dimerization. Notably, the framed portion has exact $x = 1/9$ Sc fraction and, if lifted off, would make exactly a free-standing (2, 2) Sc@SiNT (upper right). (Similarly, the (3, 0) Sc@SiNT can be viewed as a cut from a hexagonal silicide NW grown in perpendicular [110] direction.) Formally, it shows identity of the introduced here "metal-endohedral nanotubes" with thinnest silicide wires, likely precursors of experimentally observed thicker types. Further, although the synthesis process is nonequilibrium, a thermodynamic analysis is still instructive: to adjust to the M-depleted conditions [45,49], the μ_{Zr} value in Fig. 8.11 must be lowered. Under such steeper slope $\mu_{\mathrm{Zr}}^{\mathrm{gas}} - \mu_{\mathrm{Si}}^{\mathrm{bulk}}$, the (2, 2) Zr@SiNT ($ZrSi_8$) appears as the most favourable NW (e.g. with $\mu_{\mathrm{Zr}}^{\mathrm{gas}} =$ 6.5 eV for ideal gas at $T = 1200°\mathrm{C}$ and $p = 10^{-10}$ Torr, its $\delta G(1/9) = 0.57$ eV).

In summary, M@SiNT are shown to be stable, yet structurally versatile [68]. Within the stoichiometric families, armchair (2, 2) and zigzag (3, 0) are the thinnest structures. Unexpected morphological similarity with the thicker disilicide NW grown on substrate, makes these conducting filaments of ~0.3 nm radii the realistic mini-aturization limit for Si-based electronic junctions.

8.3.2 Yttrium Silicide NW

As mention in the introduction yttrium silicide NW are already produced experimentally. Although yttrium has no *f* electrons, it is generally associated with the rare earths due to its similar physical and chemical properties. Therefore the study of yttrium silicide NW can give us an idea of the properties of the whole group of rare-earth silicide NW [77].

As a first step we analysed the structures similar to that presented in Fig. 8.7 for (2, 2) Sc@SiNT. As previously for Sc the (2, 2) SiNT is stabilized by Y atoms. The resulting structure of stoichiometry YSi_8 possesses large cohesive energy of 4.57 eV (the

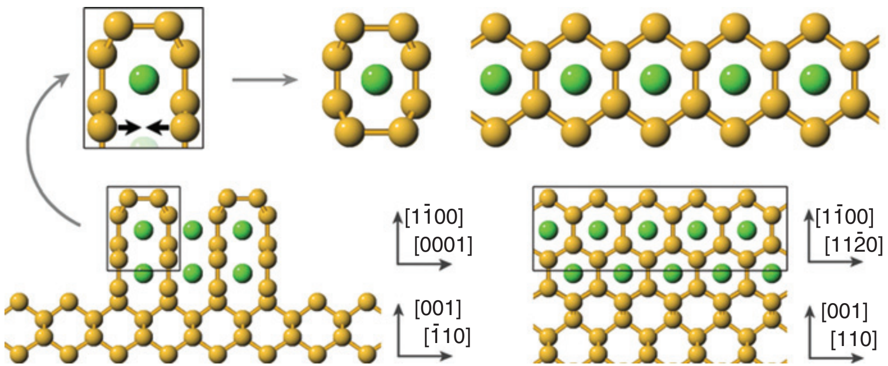

Figure 8.12 Bottom part shows the axial (left) and side (right) views of a two-monolayer-high $ScSi_2$-NW grown in the [110] direction of the Si substrate (Refs. [45,48,49]). Following the arrows, the upper left shows a magnified detail of the framed portion, which upon detachment and bottom dimerization (thick horizontal arrows) leads to the unsupported (2, 2) Sc@SiNT (upper right) (after Ref. [68]).

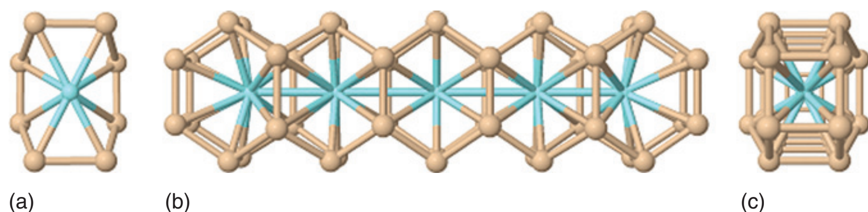

Figure 8.13 (a) Axial view of the thinnest endless NW of AlB_2-type structure. (b) Side and (c) axial view of a Y_5Si_{44} cluster (after Ref. [77]).

calculated cohesive energy E_{bc} for the bulk structure YSi_2 is 5.46 eV), and is quite stiff, with the Young's modulus of 144 GPa (assuming cross-section area as 44 Å^2, to include Si radii). The tension was estimated to be 1.2 eV/Å for a 2% strain. The axial view of the infinite structure is shown in Fig. 8.13a. To ensure that stability is retained at finite length as well, we considered finite clusters Y_3Si_{28} and Y_5Si_{44}, which were found to be also stable with cohesive energies equal to 4.45 and 4.50 eV, respectively. In Fig. 8.13b we have shown the side view of the Y_5Si_{44} cluster. The end atoms of the cluster reconstruct naturally to form a square cap as can be clearly seen from the axial view in Fig. 8.13c. Turning now to electronic properties, the infinite NW was found to be metallic with substantial DOS at the Fermi level. The Y_3Si_{28} and Y_5Si_{44} clusters have HOMO–LUMO gaps of 107 and 57 meV, respectively.

8.3.3 Energy Decomposition

Let us now consider the YSi_8 infinite NW with small cross-sections as building blocks of wires with larger cross-section. Each NW can be then decomposed schematically into $n \times m$ smaller NW. Every two neighbouring NW share silicon atoms and the yttrium chains lie on wire axes parallel one to each other. We will call the arrangement of building blocks in the n and m "directions" as a "vertical" and "horizontal", respectively. In the special case of infinite n (m) we get a vertical (horizontal) slab of "thickness" m (n). For simplicity we consider here only NW with rectangular cross-sections, but our study can be extended to NW with any desired cross-section. The $n \times m$ wire has $Y_{nm}Si_{2nm+2n+2m+2}$ stoichiometry, where we distinguish $3nm$ bulk atoms from $2n + 2m$ surface atoms and 2 edge atoms. The surfaces and edges are monoatomic and composed of Si – the vertical surface has $2n$ and the horizontal one $2m$ atoms. The bulk atoms instead can be divided into $2nm$ silicon atoms and nm yttrium atoms. In Fig. 8.14a–c we have shown three examples of those wires with shapes $1 \times 5, 3 \times 1$ and 3×3, respectively. Following the logic of the energy expansion in Eqs. (8.1 and 8.2), total energy of $Y_{nm}Si_{2nm+2n+2m+2}$ wire can be expressed by the formula

$$E_t(n, m) = 3n \cdot m \cdot E_b + 2n \cdot E_1 + 2m \cdot E_2 + 2 \cdot E_e, \tag{8.6}$$

where E_b, E_1, E_2, and E_e are the energy contributions per atom to the total energy of the system from bulk YSi_2, vertical surface, horizontal surface, and edge atoms, respectively. The question which arises now is if the energy parameters in Eq. (8.6) have universal values for any pair n, m (wire size). The four parameters, E_b, E_1, E_2

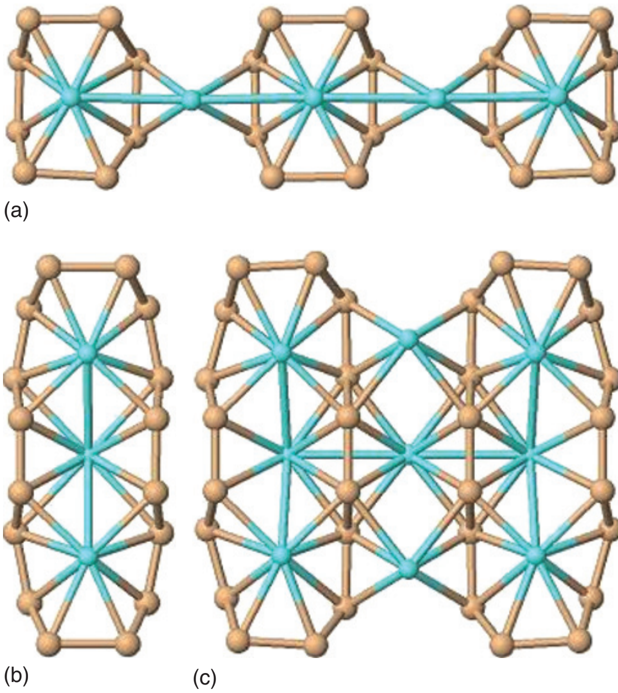

Figure 8.14 Axial view of NW with three different cross-sections: (a) 1×5, (b) 3×1 and (c) 3×3 (after Ref. [77]).

and E_e, can be easily derived calculating the total energies of four different NW, but it is not obvious that we can use then these values to calculate $E_t(n, m)$ of any other desired NW. In the next part we will describe how to find such universal parameters and also we will try to answer the question how accurate Eq. (8.6) can be. For this purpose let's define the system cohesive energy (per atom),

$$E_c(n, m) = [N_Y \cdot E_Y + N_{Si} \cdot E_{Si} - E_t(n, m)]/N_t \tag{8.7}$$

where $E_t(n, m)$ is given by Eq. (8.6), E_Y and E_{Si} are the metal and silicon atomic energies, respectively, $N_Y = nm$ and $N_{Si} = 2nm + 2n + 2m + 2$ are the number of metal and silicon atoms, respectively, and $N_t = N_Y + N_{Si}$ is the total number of atoms. Using Eqs. (3.6) and (3.7) we can define now the total NW surface energy as a difference between bulk and wire cohesive energies per atom multiplied by N_t

$$E_s(n, m) = N_t \cdot [E_{bc} - E_c(n, m)] = 2n \cdot \gamma_1 + 2m \cdot \gamma_2 + 2 \cdot \gamma_e \tag{8.8}$$

where $E_{bc} = (E_Y + 2 \cdot E_{Si} - 3 \cdot E_b)/3$ is the bulk cohesive energy and $\gamma_i = E_i - E_{Si} + E_{bc}$, where $i = 1, 2$ and e, are surface and edge energies per atom, respectively. In Fig. 8.15a we plotted the surface energy given by Eq. (8.8) as a function of the number n of YSi_8 NW ordered vertically and the number m of the same NW ordered horizontally. We used for E_{bc} the value obtained from calculations for the bulk YSi_2 structure. As could be seen from the figure in both cases the

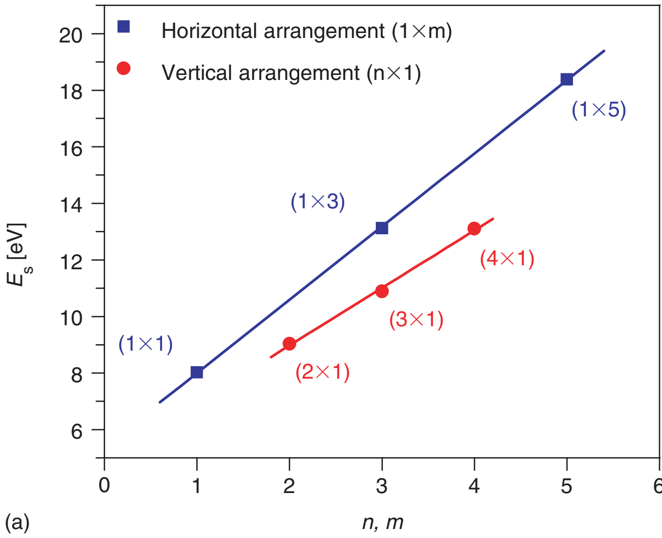

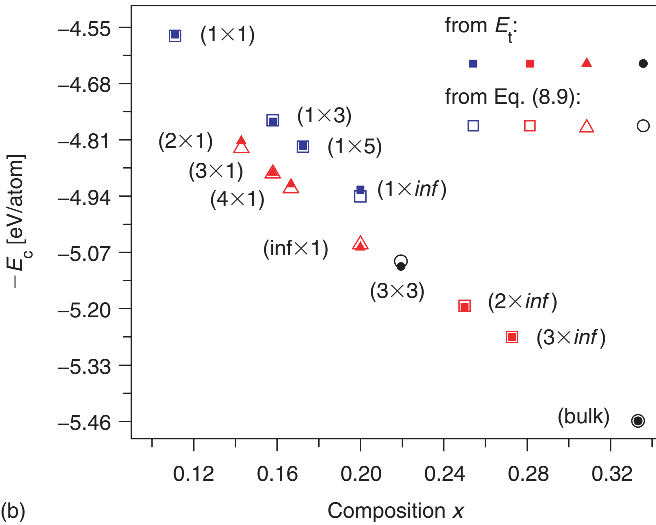

Figure 8.15 (a) Surface energy E_s described by Eq. (8.8) versus the number n of YSi_8 NW ordered vertically and the number m of the same NW ordered horizontally. (b) Cohesive energy E_c per atom as a function of composition $x = N_Y/N_t$. The open and filled symbols correspond to values obtained from Eqs. (8.9) and Eq. (8.7), respectively. Two different sets of surface and edge energies where used (see text) for blue and red points (after Ref. [77]).

relation is linear (as suggested by Eq. (8.8)), and from the slope of the curves we can derive the values for γ_1 and γ_2. This result is very important since we can define the same vertical surface energy for each wire from the family of $n \times 1$ NW. The same is true for the horizontal surface energy and NW ordered in the horizontal direction ($1 \times m$ family). From the linear fitting to the data of Fig. 8.15a we obtained that the values for γ_1 and γ_2 are 1.018 and 1.295 eV, respectively. Surface energies can also be

obtained independently from more accurate calculations for slab systems. The corresponding surface energies for the thinnest slabs in both directions are 1.001 and 1.334 eV for γ_1 and γ_2, respectively. The agreement with previously obtained values is remarkably good, especially if we take into account the fact that only few data points (see Fig. 8.15a) were used to calculate the slopes.

It is well known that for thin slabs γ_1 and γ_2 will depend on the slab thickness [78]. It was also demonstrated that the value for E_{bc} calculated from the bulk structure may lead to errors in surface energies [78]. Since our goal in this work is to explore the existence of universal parameters, which are useful for predicting the cohesive energy of NW, we aim to estimate the values for γ_1 and γ_2 rather than calculate them to extreme accuracy. The vertical slab consists of a set of graphene-like horizontal sheets of sp^2 bonded silicon atoms separated by yttrium layers. We do not expect the silicon monolayers too strongly interact with each other, and as a consequence γ_1 should not depend significantly on the thickness of the slab even for small m. This is not the case of horizontal slabs, in which the silicon atoms do not form bonds in plains parallel to slab surfaces but are rather arranged in plains perpendicular to them, consequently, stronger dependence on slab thickness n can be expected. Indeed, for the slab with thickness $n = 2$, γ_2 was calculated to be 1.064 eV (for $n = 1, \gamma_2 = 1.334$ eV), however, farther increase of slab thickness does not change γ_2 significantly.

Summarizing the results, we can say that the estimated value for γ_1 is nearly the same and equals 1.001 eV for all NW. The horizontal surface energy decreases from $\gamma_2 = 1.334$ eV, for the NW family $1 \times m$, to the value of 1.064 eV, for NW with $n > 1$. The value of γ_e in Eq. (8.8) was calculated (fitted to data) to be 1.304 eV and is the same for all NW except those from the $1 \times m$ family for which $\gamma_e = 1.686$ eV. (It is important to note that one cannot confirm the value of γ_e from independent calculations.)

The values for surface, edge, and bulk energies can be used now to calculate the cohesive energy for any $n \times m$ NW. Indeed, from Eq. (8.8) we can defined E_{c} (per atom) as

$$E_{\mathrm{c}}(n, m) = E_{\mathrm{bc}} - (2n \cdot \gamma_1 + 2m \cdot \gamma_2 + 2 \cdot \gamma_e)/N_{\mathrm{t}} \tag{8.9}$$

In Fig. 8.15b we depicted $E_{\mathrm{c}}(n, m)$ as a function of composition $x = N_{\mathrm{Y}}/N_{\mathrm{t}}$ for all studied NW. The open points correspond to values predicted from Eq. (8.9) and the filed points represent values obtained from the total energy (see Eq. (8.7)). As can be seen from the figure, the predicted values are very accurate. In all cases the error does not exceed 20 meV. More precise calculations of surface energies will farther improve the accuracy of Eq. (8.9), what is important especially for larger NW, for which cohesive energies are very close in values.

Acknowledgements

Work on nanowires was supported by the Robert Welch Foundation, and partially by NASA URETI of Texas and the NSF Center for Biological and Environmental Nanotechnology (CBEN).

REFERENCES

1. D.D.D. Ma, C.S. Lee, F.C.K. Au, *et al.*, *Science* **299**, 1874 (2003).
2. D.D.D. Ma, C.S. Lee, L. Lifshitz and S.T. Lee, *Appl. Phys. Lett.* **81**, 3233 (2002).
3. R.Q. Zhang, S.T. Lee, C.-K. Law, *et al.*, *Chem. Phys. Lett.* **364**, 251 (2002).
4. R. Rurali and N. Lorente, *Phys. Rev. Lett.* **94**, 26805 (2005).
5. D.D.D. Ma, S.T. Lee and J. Shinar, *Appl. Phys. Lett.* **87**, 33107 (2005).
6. D.D.D. Ma, C.S. Lee and S.T. Lee, *Appl. Phys. Lett.* **79**, 2468 (2001).
7. D. Appell, *Nature* **419**, 553 (2002).
8. C.-P. Li, C.-S. Lee, X.-L. Ma, *et al.*, *Adv. Mater.* **15**, 607 (2003).
9. C. Herring, *Phys. Rev.* **82**, 87 (1951).
10. S. Ismail-Beigi and T.S. Arias, *Phys. Rev. B* **57**, 11923 (1999).
11. B.-x. Li, P.-l. Cao, R.Q. Zhang, *et al.*, *Phys. Rev. B* **65**, 125305 (2002).
12. B. Marsen and K. Sattler, *Phys. Rev. B* **60**, 11593 (1999).
13. M. Menon and E. Richter, *Phys. Rev. Lett.* **83**, 792 (1999).
14. A.K. Singh, V. Kumar, R. Note, *et al.*, *Nano Lett.* **5**, 2302 (2005).
15. I. Ponomareva, M. Menon, D. Srivastava, *et al.*, *Phys. Rev. Lett.* **95**, 265502 (2005).
16. A.A. Stekolnikov, J. Furthmuller and F. Bechstedt, *Phys. Rev. B* **65**, 115318 (2002).
17. Y.F. Zhao, Z.H. Zhang, H.Q. Yang, *et al.*, *J. Vac. Sci. Technol. A* **18**, 320 (2000).
18. D.J. Chadi, *Phys. Rev. Lett.* **59**, 1691 (1987).
19. D.W. Brenner, *Phys. Rev. B* **42**, 9458 (1990).
20. J. Tersoff, *Phys. Rev. B* **38**, 9902 (1988).
21. D. Vanderbilt, *Phys. Rev. Lett.* **59**, 1456 (1987).
22. J.J. Wortman and R.A. Evans, *J. Appl. Phys.* **36**, 153 (1965).
23. C.Z. Wang, B.C. Pan and K.M. Ho, *J. Phys. Condens. Mat.* **11**, 2043 (1999).
24. K.C. Pandey, *Phys. Rev. Lett.* **49**, 223 (1982).
25. D. Vanderbilt, *Phys. Rev. B* **36**, 6209 (1987).
26. U. Landman, R.N. Barnett, A.G. Scherbakov, *et al.*, *Phys. Rev. Lett.* **85**, 1958 (2000).
27. Y. Zhao and B.I. Yakobson, *Phys. Rev. Lett.* **91**, 035501 (2003).
28. D.J. Srolovitz and S.A. Safran, *J. Appl. Phys.* **60**, 255 (1986).
29. Y.W. Mo, J. Kleiner, M.B. Webb, *et al.*, *Phys. Rev. Lett.* **66**, 1998 (1991).
30. J. Tersoff, A.W.D. van der Gon and R.M. Tromp, *Phys. Rev. Lett.* **70**, 1143 (1993).
31. Z. Zhang, H. Chen, B.C. Bolding, *et al.*, *Phys. Rev. Lett.* **71**, 3677 (1993).
32. M. Takeguchi, M. Tanaka, H. Yasuda, *et al.*, *Surf. Sci.* **493**, 414 (2001).
33. A.M. Morales and C.M. Lieber, *Science* **279**, 208 (1998).
34. A.J. Read, R.J. Needs, K.J. Nash, *et al.*, *Phys. Rev. Lett.* **69**, 1232 (1992).
35. H. Yorikawa, H. Uchida and S. Muramatsu, *J. Appl. Phys.* **79**, 3619 (1996).
36. A.K. Singh, V. Kumar, R. Note, *et al.*, *Nano Lett.* **6**, 920 (2006).
37. X. Zhao, C.M. Wei, L. Yang, *et al.*, *Phys. Rev. Lett.* **92**, 236805 (2004).
38. R.Q. Zhang, Y. Lifshitz, D.D.D. Ma, *et al.*, *J. Chem. Phys.* **123**, 144703 (2005).
39. F.S. Khan and J.Q. Broughton, *Phys. Rev. B* **39**, 3688 (1989).
40. H. Zhu, S. Feng, D. Jiang, *et al.*, *Jpn. J. Appl. Phys.* **1**, 6264 (1999).
41. G.E. Pikus and G.L. Bir, *Sov. Phys. Solid State* **1**, 136 (1959).
42. E.D. Minot, Y. Yaish, V. Sazonova, *et al.*, *Phys. Rev. Lett.* **90**, 156401 (2003).
43. B.Z. Liu and J. Nogami, *J. Appl. Phys.* **93**, 593 (2003).
44. J.R. Heath, P.J. Kuekes, G.S. Snider, *et al.*, *Science* **280**, 1716 (1998).
45. Y. Chen, D.A.A. Ohlberg and R.S. Williams, *J. Appl. Phys.* **91**, 3213 (2002).
46. J. Nogami, B.Z. Liu, M.V. Katkov, *et al.*, *Phys. Rev. B* **63**, 233305 (2001).
47. C. Preinesberger, S. Vandré, T. Kalka, *et al.*, *J. Phys. D Appl. Phys.* **31**, L43 (1998).
48. C. Preinesberger, S.K. Becker, S. Vandré, *et al.*, *J. Appl. Phys.* **91**, 1695 (2002).
49. Y. Chen, D.A.A. Ohlberg, G. Medeiros-Ribeiro, *et al.*, *Appl. Phys. Lett.* **76**, 4004 (2000).
50. C. Ohbuchi and J. Nogami, *Phys. Rev. B* **66**, 165323 (2002).
51. D. Lee and S. Kim, *Appl. Phys. Lett.* **82**, 2619 (2003).
52. M. Katkov and J. Nogami, *Bull. Am. Phys. Soc.* **47**, 283 (2002).
53. C. Joachim, J.K. Gimzewski and A. Aviram, *Nature* **408**, 541 (2000).
54. D.H. Cobden, *Nature (News and Views)* **409**, 32 (2001).

55. M.S. Gudiksen, L.J. Lauhon, J. Wang, *et al.*, *Nature (London)* **415**, 617 (2002).
56. L.-M. Peng, Z.L. Zhang, Z.Q. Xue, *et al.*, *Phys. Rev. Lett.* **85**, 3249 (2000).
57. X. Zhao, Y. Liu, S. Inoue, *et al.*, *Phys. Rev. Lett.* **92**, 125502 (2004).
58. Y. Wu, Y. Cui, L. Huynh, *et al.*, *Nano Lett.* **4**, 433 (2004).
59. A.S. Barnard and S.P. Russo, *J. Phys. Chem. B* **107**, 7577 (2003).
60. G. Medeiros-Ribeiro, A.M. Bratkovski, T.I. Kamins, *et al.*, *Science* **279**, 353 (1998).
61. K.N. Kudin and G.E. Scuseria, *Phys. Rev. B* **61**, 16440 (2000).
62. M.J. Frisch, G.W. Trucks, H.B. Schlegel, *et al.*, *GAUSSIAN 98, Revision A.5* (Gaussian, Inc., Pittsburgh, PA, 1998).
63. J.P. Perdew, K. Burke and M. Ernzerhof, *Phys. Rev. Lett.* **77**, 3865 (1996).
64. K.N. Kudin, G.E. Scuseria and B.I. Yakobson, *Phys. Rev. B* **64**, 235406 (2001).
65. T. Dumitrică, H.F. Bettinger, G.E. Scuseria, *et al.*, *Phys. Rev. B* **68**, 085412 (2003).
66. K.N. Kudin, G.E. Scuseria and R.L. Martin, *Phys. Rev. Lett.* **89**, 266402 (2002).
67. C. Kittel, *Introduction to Solid State Physics* (Wiley, New York, 1996).
68. T. Dumitrica, M. Hua and B.I. Yakobson, *Phys. Rev. B* **70**, 241303 (2004).
69. A.K. Singh, V. Kumar, T.M. Briere, *et al.*, *Nano Lett.* **2**, 1243 (2002).
70. A.K. Singh, T.M. Briere, V. Kumar, *et al.*, *Phys. Rev. Lett.* **91**, 146802 (2003).
71. T. Miyazaki, H. Hiura and T. Kanayama, *Phys. Rev. B* **66**, 121403(R) (2002).
72. V. Kumar and Y. Kawazoe, *Phys. Rev. Lett.* **87**, 045503 (2001).
73. J. Lu and S. Nagase, *Phys. Rev. Lett.* **90**, 115506 (2003).
74. M. Menon, A.N. Andriotis and G.E. Froudakis, *Nano Lett.* **2**, 301 (2002).
75. C.J. Först, P.E. Blöchl and K. Schwarz, *Comput. Mater. Sci.* **27**, 70 (2003).
76. C.J. Först, private communication.
77. N. Gonzalez Szwacki and B.I. Yakobson, *Phys. Rev. B* **75**, 035406 (2007).
78. V. Fiorentini and M. Methfessel, *J. Phys. Condens. Matter* **8**, 6525 (1996).

CHAPTER NINE

Low-Dimensional Silicon as a Photonic Material

N. Daldosso and L. Pavesi

Contents

9.1 The Need of a Silicon-Based Photonics 314
9.2 Various Approaches to a Silicon Light Source 316
  9.2.1 Silicon Raman Laser 317
  9.2.2 Bulk Silicon Light Emitting Diodes 319
9.3 Optical Gain in Silicon Nanocrystals 321
  9.3.1 CW and TR Measurements 322
  9.3.2 Gain Model: Four-Level System 325
  9.3.3 Other Key Ingredients 327
9.4 Er Coupled Si Nanocrystal Optical Amplifiers 328
  9.4.1 Er^{3+} Internal Transition 329
  9.4.2 Er^{3+} and Si-nc Interactions 330
  9.4.3 Er^{3+} Cross Sections 330
9.5 Conclusions 332
Acknowledgements 333
References 333

Abstract

In this chapter the state-of-the-art on the development of low-dimensional silicon for application in photonics is presented with the aim to settle the status and try to weight out the perspectives. The necessity for Si-based photonics is introduced, and special emphasis is dedicated to the subject which is at the forefront of the today discussion: the route to a silicon light source. Two examples are detailed: silicon nanocrystals and Er-doped silicon nanocrystals.

9.1 The Need of a Silicon-Based Photonics

The recent developments in silicon technology continue to advance the frontiers of device integration, complexity, and speed of the microelectronics devices. This advance has been driven by application requirements in switching technology (e.g. computers), in stocking data (e. g. memories), and in high-speed electronics

Dipartimento di Fisica, Università di Trento (Trento), Italy.

Nanosilicon
9780080445281
Copyright © 2007. Elsevier Ltd.
All rights reserved.

(e.g. wireless telecommunications). However, some concerns about the evolution of the microelectronic industry have been raised in terms of speed, signal delay, packaging, fanout, and power dissipation because of the combination of ever-increasing chip sizes, decreasing feature sizes, and increasing clock frequencies. As an example, it is worth noting that for a gate length shorter than 200 nm, the delay is no longer dictated by the gate switching time but by the wiring delay. In addition, the length of interconnects on a single chip are getting longer and longer. Nowadays we are at the 90 nm technology node and chips have an active interconnect length of 700 m/cm^2 of chip area (excluding global interconnects) with a chip area of 280 mm^2 where 386 millions of transistors are interconnected with 10 metal levels, while in 10 years from now we will be at the 32 nm technology node with chip area of 280 mm^2 where 1391 millions of transistors will be interconnected by using 13 metal levels and interconnect lengths of 3203 m/cm^2 of chip area [1]. The problem is not only related to the length of interconnects but also to the complexity of their architecture. All these facts introduce problems related to the delay in signals propagation caused by RC coupling, signal latency, signal crosstalk, and RL delays. Finally, there is the problem of power consumption and heat dissipation, which causes the thermal power generated within the chip to reach a density in excess of a conventional hot plate and within few years to reach the level typical of nuclear reactors.

Moreover, for interconnection with everyday appliances such as telephones, faxes, and computers optics is used on the long distances while in short distances electricity is used. This means that at the premises we have electrical signals which have to be converted into optical signals on the long haul and back again to electrical signals, with signal distribution via the local electronic network. For current and near-future data traffic demands, the present network is both cost-effective and adequate. However, widespread demand is predicted to reach terabit levels (10^{12} bits/s), at which rates existing and easily foreseeable electronic technologies will be unable to operate, implying the urgent need for an integrated optical solution. Wireless cannot be used at this speed and hence radio will not be the final but only an intermediate solution.

A possible answer to these problems could be optics [2–4]. In fact, by manipulating photons instead of electrons, some of the limitations placed on electronic devices by, e.g. device capacitance, scaling difficulties, increased density, precision of synchronization, voltage isolation, crosstalk, may be overcome. Integrated optics should be capable of signal splitting and combining, switching and amplification; the last function being a key component in compensating transmission, insertion, and distribution losses.

Till now, the reliability and compatibility of many optical interconnect systems are quite far from a real integrated system and are based on hybrid approaches, which make the fabrication difficult and costly: i.e. optical interconnects through optical fibres and III–V laser sources [5]. No single material or single technology is leading the market. Some convergence is appearing towards the use of InP as the substrate material to integrate different optical functions. However, other materials are potential candidates for overcoming the limitations of InP. For some the future of Si-based photonic lies in hybrid solutions, for others the most satisfactory solution would be optoelectronic and photonic devices created entirely from Si-based

materials, where the extensive experience in Si fabrication and processing could be put to best use [4].

To achieve a monolithically integrated silicon photonics, the basic components have been already demonstrated [4,6–8], but for any practical Si-based light sources: either efficient light emitting diode (LED) or a Si laser [9]. Hence in this chapter we will concentrate mostly on the various approaches followed to produce a reliable and efficient light source. Among all, we will review in details low-dimensional silicon where important results have been reported recently.

9.2 Various approaches to a silicon light source

As a light source for integrated optics a laser will be ideal. Easy of focusing, brilliance, monochromaticity, coherence, fast modulation are all good laser properties. However an incoherent light emitting source, such as a LED, will be also an option. The general requirements for the sources are: wavelengths in the range 0.4–1.6 μm to cover both full colour displays and the 1.3–1.6 μm transparency windows of optical fibres, emitting power in the mW range, operating voltage lower than 5 V, modulation frequency of a few kHz (display) or higher than few GHz (communication), ... Specific applications for such sources include: fibre-optic transmitters, optical interconnects within and between chips, optical interconnects among boards, optical controllers for phased-array microwave antennas, information display screens, printing elements in xerography, and writing and readout of optical compact disc information. The market for such an optical source will be enormous.

The main limitation of silicon is related to its energy band diagram, i.e. to the indirect band gap. This band structure implies very long spontaneous lifetimes (ms range) while the usual non-radiative lifetimes are short (few ns). If we quantify the emission property of a material with its internal quantum efficiency η_{int} (the ratio of the radiative recombination probability to the total recombination probability) these different lifetimes result in a very low internal quantum efficiency ($\eta_{\text{int}} \approx 10^{-6}$) which prevented silicon to be a luminescent material [3]. Moreover, when population inversion is looked for to achieve lasing high excitation is needed. In this case, other fast non-radiative processes turn on such as Auger recombination (three particles non-radiative processes) or free carrier absorption.

Despite this, many different strategies have been employed to overcome the silicon limitations and are currently followed to build an efficient silicon source [10]. Some, such as SiGe quantum well or Si/Ge superlattice structures, rely on band structure engineering, while others rely on quantum confinement effects in low-dimensional structures. Still another approach is impurity-mediated luminescence from, e.g. isoelectronic impurities or rare earth ions. In early 2000 a series of papers appeared that questioned the common belief that silicon cannot be used to form a laser [11–14]. In October 2004, the first report on a silicon Raman laser appeared [15], while in January 2005 the first all-continuous wave (CW) silicon Raman laser was reported [16]. Moreover, it is worth noting the demonstration of a LED with a power efficiency in excess of 1% in porous silicon [17] or as high as 10% in Er-doped silicon rich oxide [18]. Recently, evidence of lasing at cryogenic temperatures have been reported in nanometer size holes of a silicon thin film [19];

and stimulated emission at room temperature in a nanostructured silicon pn junction [20].

9.2.1 Silicon Raman Laser

As the first silicon laser has been reported by using stimulated Raman Scattering (SRS), we will firstly describe this achievement. It should be remarked from the start, that this laser is not an injection laser (i.e. an electrically pumped laser) and is not using interband transitions which are mostly affected by the silicon indirect band gap structure. It is based on the Raman scattering, a non-linear optical effect discovered in the early 1930s by Sir. Raman. In a quantum-mechanical picture a photon can be scattered at a different energy by a non-linear interaction with the material. This interaction can be pictured by using the concept of phonons and hence applying the energy conservation principle at the scattering event:

$$\hbar\omega_{\mathrm{in}} = \hbar\omega_{\mathrm{out}} \pm h\nu_{\mathrm{ph}}$$

where $\hbar\omega_{\mathrm{in}}$ is the energy of the photon before the scattering event, $\hbar\omega_{\mathrm{out}}$ is the energy of the photon after the scattering event and $h\nu_{\mathrm{ph}}$ is the energy of the phonon which has been absorbed or created by the scattering. When the power of the light beam is higher than a critical value, SRS occurs. A stimulated process favours the scattering of the in-photon to the energy of the out-phonon. This process is described by a Raman gain coefficient and can be used to realize an all-optical amplifier where the out-photon becomes the signal beam which is amplified and the in-photon the power beam whose optical power is transferred to the signal beam.

Optical Raman fibre amplifiers are already deployed in the field. It appears that the Raman gain cross-section in Si is five order of magnitude larger than in silica due to the difference between crystalline and amorphous materials. Thus silicon waveguide could be used to make amplifiers which should be only a few cm long while in optical fibre amplifiers some km long fibres are needed to have the same gain. Clearly, the frequency of the light should be smaller than the silicon band gap (1.1 μm) and the phonon frequency in silicon is 15.6 THz.

Unfortunately when an intense light beam is travelling through silicon two-photon absorption occurs and electrons and holes are created. A cloud of free carriers forms in the waveguide channel and the optical losses of the waveguide increases dramatically due to free carrier absorption which weakens both the pump and signal beam: in this situation no SRS is possible. In the first example of a silicon amplifier, to avoid free carrier absorption, a pulsed pump beam with pulses shorter than the typical lifetime of the free carriers was used. Then by using a 8 m long single mode optical fibre the exit of a 3 cm long waveguide was looped back into the entry: the signal photons recycled into the waveguide to form an optical cavity and achieve lasing. Thus the signal got multiple amplifications and, eventually, the laser threshold was overcome and laser light exited from the waveguide. The first pulsed silicon laser with a fibre loop cavity was fabricated [15].

Shortly after this successful report, the first all-silicon-pulsed Raman laser was demonstrated [21]. Here the cavity was realized by forming mirror on the facets of an S-shaped silicon rib waveguide resting on a silicon on insulator (SOI) wafer. The

S-shape was used to have a 4.8 cm long waveguide while maintaining a small foot-print as real estate on a silicon chip is extremely expensive. The exact emission wavelength is determined by the pump wavelength and the cavity details. By changing the cavity length it is possible to get various wavelengths out of a single pump wavelength within a very narrow interval.

Following this result, the same team reported a CW all-silicon Raman laser [16]: the free carrier generated by two photon absorption in the waveguide channel are driven away by using an electric field generated by a reverse biased p–i–n diode (Fig. 9.1). The two electrodes collect the free carrier generated by the two photon absorption allowing CW and stable laser emission. Interestingly the micro-electronic properties of silicon (a current can flow through) are applied to drive its non-linear optical properties. The same idea was used to chop on and off a pulsed Raman laser by injection of free carriers in the silicon waveguide with a forward bias p–i–n diode formed across the silicon waveguide [22]: free carriers absorb light and switch off the laser. Direct modulation is useful as one can code-in data stream electrically on the optical beam instead of using an external modulator.

The main open question about the Raman silicon laser is to what is it worth. For applications in microelectronics, electrical injection is a must. One could think about an external laser source to pump various Raman amplifier distributed along the optical circuit on top of a chip. Or one could think about medical applications where the silicon Raman laser will replace other more expensive systems. Or one could think of the Raman silicon laser as a secondary source in dense wavelength division multiplexing (DWDM) applications, where a pump laser is pumping various Raman silicon laser which are used as the signal source. However the real killer application is an injection silicon laser. In the following we will review the main promising approaches.

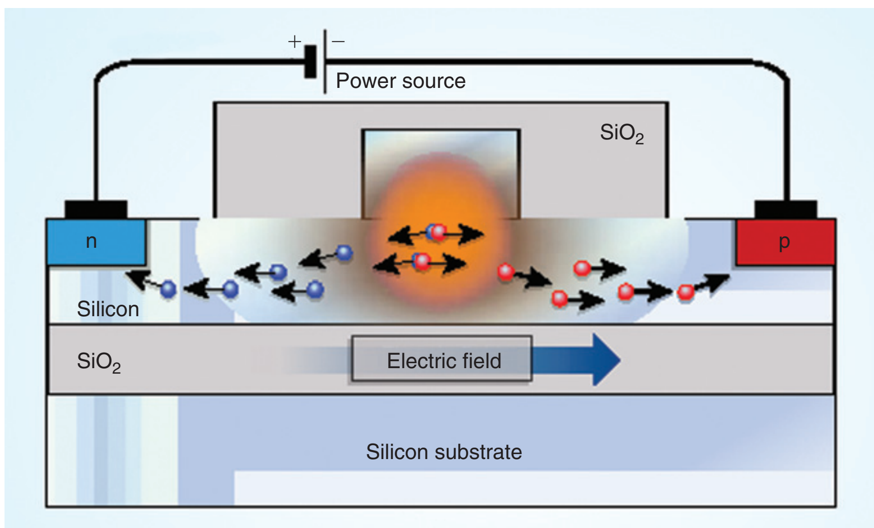

Figure 9.1 Cross-section of the silicon laser realized at Intel (after Ref. [16]).

9.2.2 Bulk Silicon Light Emitting Diodes

The common belief that bulk silicon cannot be a light emitting material has been severely questioned by a series of different approaches. The first one is based on the results achieved in high-efficiency solar cells and on the consideration that, within thermodynamic arguments, absorption and emission are two reciprocal processes [13]. Green *et al.* noticed that world record solar cells are characterized by extremely long carrier recombination lifetimes of the order of some milliseconds. That is for these solar cells the recombination lifetime is of the order of the radiative lifetime, hence their η_{int} is of the order of 1. Then, if the solar cell is biased in the forward regime instead of the usual reverse regime, the solar cell behaves as a very efficient LED. In order to achieve the highest to date power efficiency for Si-based LED, approaching 1%, the non-radiative rates are reduced by using: (i) high-quality intrinsic Si substrates, float-zone (FZ) being preferred over Czochralski (CZ); (ii) passivation of surfaces by high-quality thermal oxide, in order to reduce surface recombination; (iii) small metal areas; and (iv) by limiting the high doping regions to contact areas, to reduce the Shockley–Read–Hall recombinations in the junction region and to minimize free carrier absorption. Finally, the extraction efficiency of light from the solar cell is enhanced by suitably texturizing the Si surface. Figure 9.2 shows a schematic of the device and a room temperature emission spectrum.

In addition a fully integrated opto-coupler device (LED coupled to a photodetector) was also demonstrated on the basis of this technology [23]. The main drawbacks of this approach for an integrated laser or LED are: (i) the need of both high purity (low doping concentration) and of surface texturing which renders the device processing not compatible with standard complementary metal-oxide semiconductor (CMOS) processing; (ii) the strong and fast free carrier absorption typical of bulk Si that can prevent reaching the condition for population inversion is not addressed; (iii) the suitable integration of the active bulk Si into an optical cavity to achieve the required optical feedback to sustain a laser action can be a problem; (iv) the modulation speed of the device which can be limited by the long lifetime of the excited carriers (ms) and the need of a large optical cavity.

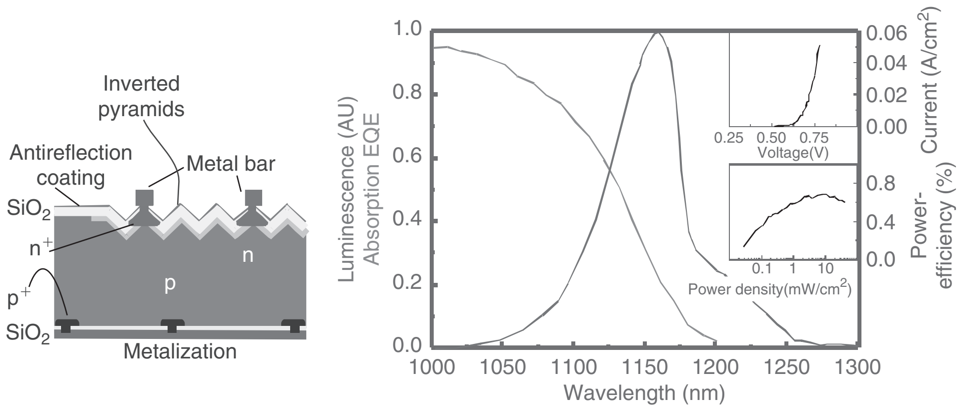

Figure 9.2 Sketch of the LED geometry. Luminescence and absorption spectrum, power efficiency versus injected electrical power density and *I–V* characteristics (inset) at room temperature (after Ref. [9]).

The same research group published also a theoretical paper [24] which questioned one common belief that indirect band gap materials could not show optical gain because of parasitic absorption processes due to free carrier [25]. Indeed they demonstrate that optical gain is theoretically possible and pointed out that the most suitable energy region is the sub-band gap region where processes involving phonons could help in achieving gain.

These theoretical arguments have been partially confirmed in a recent study where stimulated emission has been observed (see Fig. 9.3) [20]. As the limit to efficient light generation in Si is the short non-radiative lifetime, the idea was to avoid carrier diffusion and to spatially localize free carriers in a small device region where non-radiative recombination centres can be easily saturated. To localize carriers, in a previous study ion implantation has been used to induce dislocation loops at the junction of a p–n diode [14]. The dislocation loops cause local strain fields which in turn increase locally the energy gap causing a potential barrier for carrier diffusion. LED based on this idea were realized.

Other researchers [20] realized carrier localization by spin-on doping of small silica nanoparticles at the junction of a p–n diode (Fig. 9.3). The current–voltage (I–V) characteristic of the diode shows rectifying behaviour with a clear threshold in the light–current (L–I) characteristic. A change from a broad emission spectrum characteristic of band-to-band emission below threshold to sharp peaks due to stimulated emission above threshold is observed too. Stimulated emission is observed for a two-phonon indirect transition as it was theoretically predicted. Furthermore, when the injection current significantly exceeds the threshold, a single peak dominates. All these results are very encouraging since the proposed system has excellent electrical qualities as they are p–n junctions. The main problem

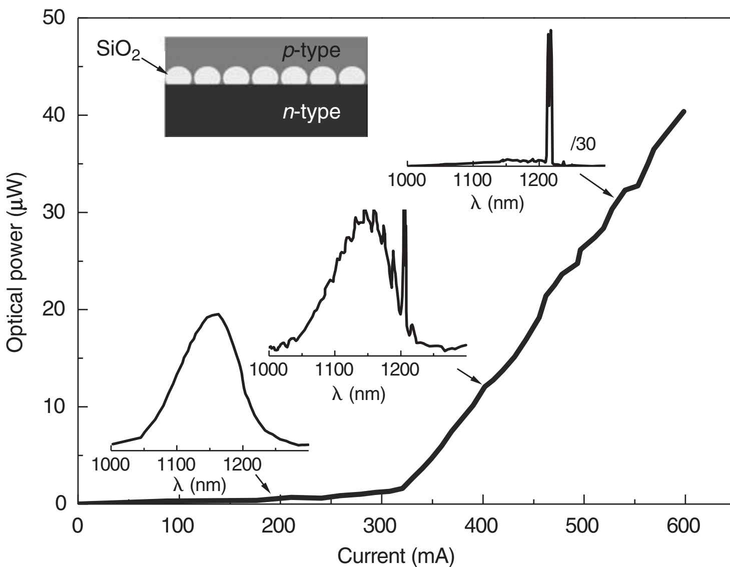

Figure 9.3 Optical power versus injected current for a LED containing SiO_2 nanoclusters in the junction region (inset). Also shown are a few electroluminescence spectra for different injection rate (arrows). The data have been redrawn from Ref. [20].

with the bulk Si approach is related to the presence of a large enough gain to overcome possible free carrier losses which to date is still unclear. However in the light of the present state-of-the-art, a laser made with bulk silicon seems accessible.

9.3 Optical gain in silicon nanocrystals

The most promising approach is based on nanostructured silicon, where the optoelectronic properties of silicon are modified by quantum confinement effects. Within this approach one maximizes carrier confinement, improves the radiative probability by quantum confinement, shifts the emission wavelength to the visible and controls the emission wavelength by silicon nanocrystal (Si-nc) dimension, decreases the confined carrier absorption due to the decreased emission wavelength, and increases the light extraction efficiency by reducing the dielectric mismatch between the source materials and the air.

This approach has been pioneered by the studies on porous silicon [26,27], which showed that once silicon is reduced to nanometric dimensions (as a porous quantum sponge of nanoparticles and/or nanowires) because of the electrochemical etching in an HF solution, bright red luminescence at room temperature occurs. Unless microelectronics compatibility of porous silicon has been demonstrated and integration of driving circuits with light emitting element has been performed, the disordered distribution of nanocrystal sizes, interconnectivities and surface reactivity to chemical agents hamper a real engineering of porous silicon properties. The enormous and active inner surface causes time-dependent properties, ageing effects, and uncontrolled deterioration of device performances. At the same time microcavities with improved light emission properties have been produced and can be used as optical filters and as a trap for delay a travelling light [28]. No optical gain was reported in bulk porous silicon. In oxidized porous silicon gain has been reported even though the emitting centre responsible for the amplification could be not Si-nc [29].

In comparison with porous silicon, Si-nc embedded in amorphous silica (a-SiO_2) are better candidates for photonics, because of their robustness and stability and their full compatibility with the mainstream CMOS technology [30]. The generation of visible light from Si-nc embedded in a-SiO_2 matrix has been extensively studied to obtain optically tuneable quantum systems by modifying the dimensions of the nanoparticles [3].

Various techniques are used to form Si-nc, the size of which can be tailored to a few nanometres [3]. Starting with a Si-rich oxide, which can be formed by deposition, sputtering, ion implantation, cluster evaporation, etc., partial phase separation is induced by thermal annealing. The duration of the thermal treatment, the annealing temperature, and the starting excess Si content all determine the final size of the cluster, the size dispersion, and the crystalline nature. Recently, thermal anneal of amorphous SiO/SiO_2 superlattices has been proposed to better control the size distribution: almost monodispersed size distribution has been demonstrated [31].

The Si-nc system is very promising to achieve a laser and many breakthroughs have been recently demonstrated in this field [11,18,32,33]. In recent papers [34,35] we have shown amplified spontaneous emission (ASE) from Si-nc grown by a wealth

of different techniques (Plasma-enhanced chemical vapour deposition (PECVD), superlattices, magnetron sputtering) by means of VSL (variable stripe length) technique in the CW (continuous wavelength) and TR (time-resolved) regime and we have discussed in detail experimental methods and critical issues to be addressed in order to avoid undesired experimental artefacts due to pump diffraction, light coupling and focal plane effects, and edge irregularities of sample edges.

9.3.1 CW and TR Measurements

TR experiments performed in the one-dimensional amplifier configuration, i.e. by pumping through the surface and collecting the guided light from one edge of the sample as a function of the excitation (pumping) length, are used to investigate the amplification of Si-nc. Figure 9.4 shows an example, where the time resolved ASE spectra at two observation time scales have been measured. For long integration times (500 μs) the usual broad emission lineshape centred around 900 nm is measured. This emission has similar spectral feature as the usual luminescence from Si-nc. On the contrary, when the first 100 ns are considered, a fast recombination component appears in the decay dynamics and the spectral shape of the ASE signal appears strongly blue shifted, as shown in Fig. 9.4a.

The fast component disappears when either the excitation length ℓ is decreased at a fixed pumping power density J_p or when J_p is decreased for a fixed ℓ. These observations rule out the non-radiative Auger processes as the origin of the observed fast component, since the J_p intensity does not depend on ℓ, whereas the

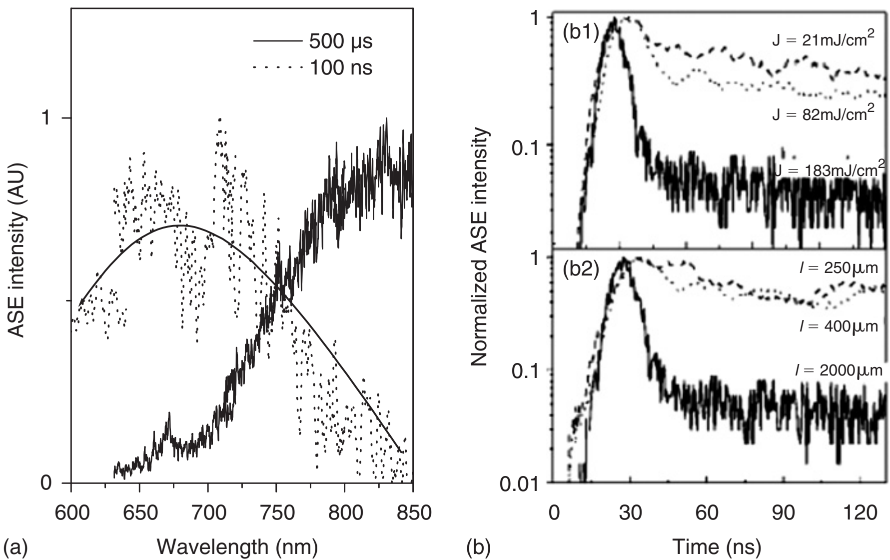

Figure 9.4 (a) ASE lineshapes measured with the 500 μs time window (black continuous line) and with the 100 ns time window (dotted line) at the pump fluence of 200 mJ/cm^2. The stripe length ℓ was 2000 μm. (b) Time resolved ASE decay measured as (b1) a function of pump fluence for a fixed excitation length and (b2) pump length under VSL configuration for a fixed pump fluence. Detection wavelength was 750 nm.

fast recombination peaks are critically dependent on the pumping length, keeping fixed the excitation conditions. Moreover, the peak intensity of the fast component shows a super linear increase versus ℓ for high J_p, which can be fitted with the usual one-dimensional amplifier equation yielding a net optical gain of $12 \pm 3\,\text{cm}^{-1}$ at 760 nm (Fig. 9.5a). Modal gain values ranging between $8\,\text{cm}^{-1}$ and $20\,\text{cm}^{-1}$ are measured depending on the detection wavelength. When the same fit is performed on the slow emission component, optical losses in the range $10–30\,\text{cm}^{-1}$ can be extracted.

The fast component peak intensity shows a threshold behaviour versus J_p: at low J_p the emission is sub linear to a power 0.5, suggesting a strong Auger limited regime; while for higher J_p, population inversion is achieved and a super linear increase to a power ≈ 3 is measured, suggesting the onset of the stimulated regime (Fig. 9.5b). Moreover, the lifetime of the fast component significantly shortens when the stimulated regime is entered. The emission threshold therefore separates two different regimes (Auger limited and stimulated emission) where more likely two distinct physical recombination mechanisms are present: either two different recombination centres in the same Si-nc (defect centres and quantum confined excitons) or two different emission centres in the system (distinct Si-nc populations, SiO_2 defects pumped efficiently through the smallest Si-nc). The presence of different recombination mechanisms in our samples is also evidenced by the clear difference in the spectral lineshape of the fast and slow emission components.

The fast recombination dynamic without threshold behaviour versus J_p can be explained by the Auger mechanisms. In fact, the fast dynamics of its own is not enough to claim for optical amplification. A strong competition between Auger fast processes and stimulated emission is present in Si-nc. For some samples Auger can prevail.

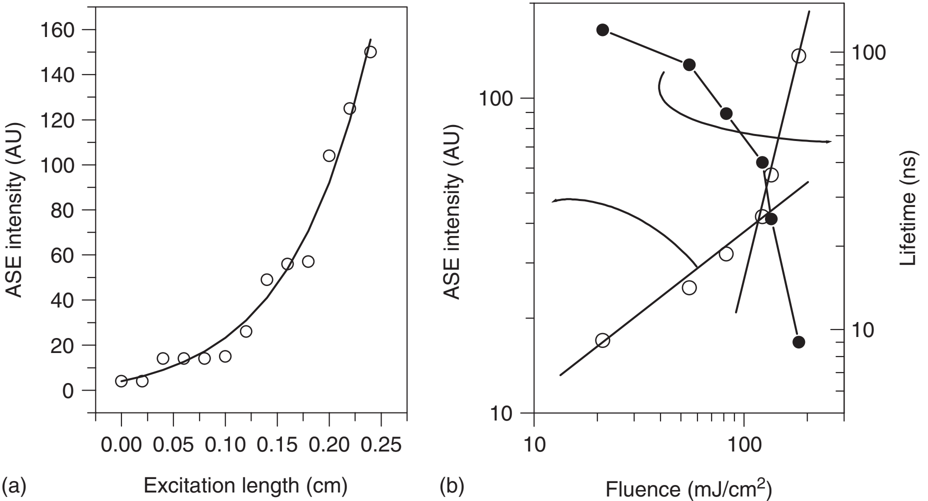

Figure 9.5 (a) ASE intensity versus excitation length at 760 nm. Pump fluence of 200 mJ/cm^2; (b) ASE intensity (open circles) of the fast emission peak versus pump fluence, (black circles) fast luminescence lifetime versus pump fluence. The lifetime has been extracted from the experimental decays as the $1/e$ intensity time. Excitation length was 2 mm.

Having demonstrated that probe amplification is possible in Si-nc and that the dynamics of the amplification is extremely fast and, within the time resolution of our experimental set-up, coincident with the time dynamics of the stimulated emission, and that TR transmission measurements as a function of the pumping intensity have shown a net amplification of the probe signal with respect to the incident probe signal [36], we present here the spectral dependence of the gain in CW pump and probe experiments.

Careful alignment of the pump and probe beam on the sample surface is needed to avoid spurious effects such as those caused by sample heating. CW probe beam is provided by a monochromatized short-arc air-cooled 1000 W Xe lamp in presence of the chopped CW pump beam (457 or 365 nm lines of an UV-extended Ar laser). A large area detector is used here in order to avoid possible artefacts caused by non-linear effect such as lensing of the probe beam. At high pumping power density, a strong modulation of the transmitted signal is observed which follows the on–off modulation of the pump beam. No such effect is observed at low pumping power. After the initial transient (1 ms) the transmitted intensity signal is constant excluding major heating problems or damaging of the sample. On these bases we attributed the transmission enhancement to probe beam amplification.

As an example, Fig. 9.6 reports the spectral dependence of transmittance spectra (T_{OFF}, when the sample is not optically pumped, and T_{ON}, when the sample is optically pumped) measured. It should be noted that these are absolute transmittance measurements, normalized with respect to the intensity of the probe beam

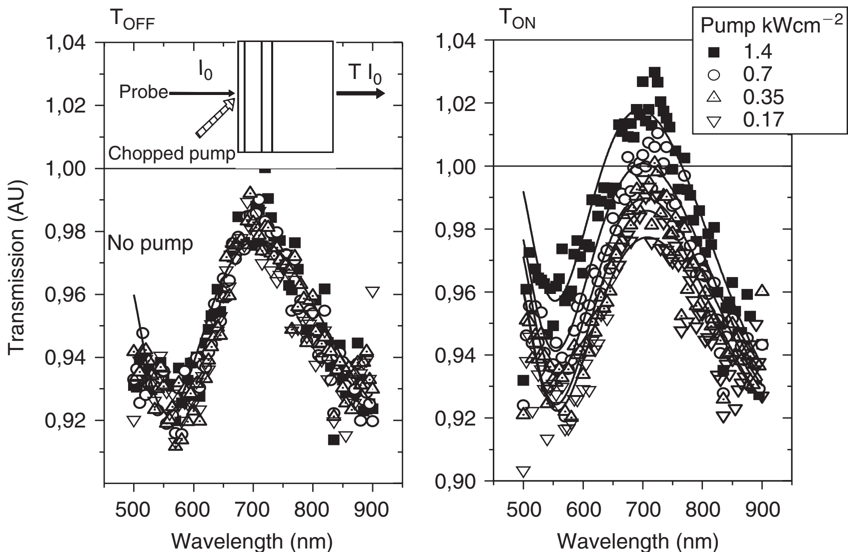

Figure 9.6 Transmission spectra (points) for increasing pumping power densities integrated during the time interval when the pump beam is off (left panel) or is on (right panel). The various pump powers and the relative symbols are given as legend in the graph. The lines are guides for the eyes of the experimental data for the various power densities. The thick line in the left panel is the no pump results of the simulation of right panel. (Inset) Sketch of the experiment scheme and of the sample structure (after Ref. [36]).

incident on the sample, which was measured by the same apparatus in absence of the sample. As shown in the left panel of Fig. 9.6, T_{OFF} does not depend on J_P. T_{OFF} shows clear interference fringes in the transparency region of the sample, which are caused by the multilayered structure of the sample. T_{ON} shows the same interference fringes (no dramatic heating effect on the real part of refractive indices). In addition, in a region centred at about 700 and 100 nm wide T_{ON} increases significantly with increasing J_P and reaches the transparency threshold ($T_{ON} = 1$) at about 0.5 kW/cm^2. Note that the interference fringes structure is not affected by the pump power, i.e. the maxima and minima do not shift with J_P. For even greater J_P, T_{ON} is larger than 1. In this region the probe beam is amplified with respect to its value before the sample, i.e. the sample shows high values of the optical gain, which compensates even for the losses caused by probe beam propagation in the quartz substrate. No similar effect is observed in a reference quartz substrate without the Si-nc. Other samples show an increase in the transmitted intensity up to the transparency. In conclusion, net optical amplification of a probe beam through a sample where Si-nc have been formed has been measured.

9.3.2 Gain Model: Four-Level System

Although a full theoretical model of the stimulated emission processes in Si-nc is still lacking and a clear understanding of the microscopic gain mechanism is still under debate, it has been suggested that interface radiative states associated with oxygen atoms can play a crucial role in determining the emission properties of Si-nc systems [37–40], in particular localized state recombinations either in the form of silicon dimers or in the form of Si = O bonds formed at the interface between the Si-nc and the oxide or within the oxide matrix. We have proposed an effective four-level model to treat qualitatively the strong competition among losses, Auger recombination and stimulated emission (Fig. 9.7 and 9.8). Two different kinds of Auger recombinations are considered to explain population inversion that can be studied on the basis of rate equations of the relaxation dynamics. This which has explained the fast recombination component with the power threshold behaviour observed in our time resolved VSL measurements. In fact, we have shown that the effect of pumping on the recombination dynamics results in a fast recombination component, as the pumping rate becomes high enough to create population inversion. The very same presence of the fast emission component together with the occurrence of a threshold intensity behaviour and a superlinear ASE increase represent a strong indication that the fast emission is related to the stimulated emission of Si-nc. Optical gain is observed whenever the stimulated emission rate is greater than the Auger recombination rate. It is possible to define a stimulated emission lifetime τ_{se} and an equivalent Auger recombination time τ_A as follows:

$$\tau_{se} = \frac{1}{Bn_{ph}} = \frac{4}{3}\pi R_{nc}^3 \frac{1}{\xi\sigma c n_{ph}} \qquad \tau_A = \frac{1}{2C_A N_3}$$

where $B = \sigma c/V$, is the stimulated transition rate, σ the gain cross section at 750 nm, n_{ph} is the emitted photons numbers, R_{nc} is the mean radius of the nanocrystals and ξ

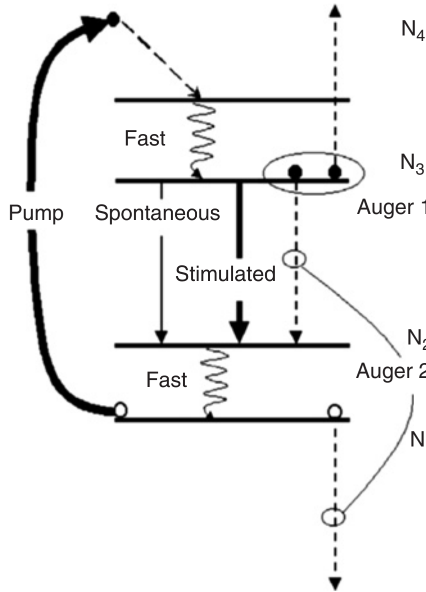

Figure 9.7 Effective four-level system introduced to model qualitatively the recombination dynamics under gain conditions.

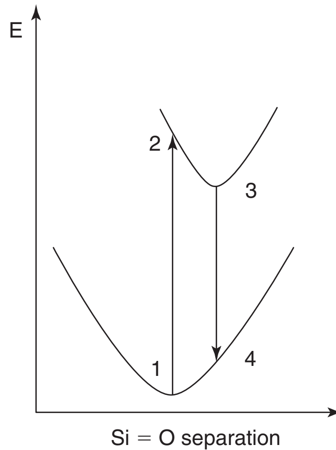

Figure 9.8 Energy configuration diagram of the silicon nanocrystals in an oxygen-rich matrix. Level labelling refers to transitions in Fig. 9.7.

the Si-nc volume fraction; C_A is the effective Auger coefficient and N_3 the population of the emitting level 3. It is worth noticing the inverse dependence of τ_{se} on ξ and on σ. It is clear that to observe optical gain $1/\tau_{se} \geq \tau_A$. This poses a condition on the volume fraction, which could explain different results among different samples. In addition, a critical role is played by the n_{ph}, the photon flux density inside the active medium. It can be increased by optical amplification and strong emission and it can be decreased by optical absorption and optical propagation losses inside the waveguide. This in turn

means that the balance between stimulated emission and Auger recombination is ruled also by the waveguide/optical cavity optical properties.

The four-level model of Fig. 9.7 is still a phenomenological model, which does not refer to a developed theory of the optical properties of Si-nc in SiO_2 and of their interfaces. However, we can suggest a possible nature for this four-level model. X-ray measurements [40] reported the presence of a modified SiO_2 region around the Si-nc participating to the light emission process, but not extending to the whole silica matrix. Thus we proposed a structural model, where the Si-nc are capped by a modified SiO_2 region, which plays an active role in the luminescence. The model involves three regions: the core Si-nc, the capping modified SiO_2 shell, and the embedding bulk SiO_2. The size of this intermediate region has been evaluated about 1 nm. *Ab initio* calculations have been performed for the Si_{10} nanocrystals in SiO_2 showing that the entire structure moves to a minimum-energy configuration, where a rearrangement of the starting crystalline surrounding SiO_2 both in bond lengths and angles is achieved. Thus the dots result to be surrounded by a cap-shell of about 0.8–0.9 nm thick modified SiO_2 which goes towards a pure crystalline matrix. The spatial distribution of the highest occupied (HOMO) and lowest unoccupied (LUMO) Kohn-Sham orbitals clearly show that the distribution is totally confined in the Si-nc region with some weight on the interface O atoms confirming the dot nature of the near band-edge states but showing also the contribution of the surrounding SiO_2 cap-shell. The calculation of the absorption spectrum shows that these new states originate strong features in the optical region, which can be at the origin of the photoluminescence observed for Si-nc immersed in a SiO_2 cage.

These experimental and theoretical analyses point out, for the first time, the important role played not only by the Si-nc but also by a modified silica host region in determining the optoelectronic properties of this system. Its relevance for the observed optical gain in Si-nc is to be associated with the four levels. In fact, one can speculate that this stressed SiO_2 shell enhances the formation of interface oxygen-related states (silanone?) on the surface of Si-nc or decreases the non-radiative Auger rate because of the resulting smoothing of the potential barriers.

9.3.3 Other Key Ingredients

In the previous sections, we have detailed one of the most interesting properties for a Si-nc based laser, the active material. Other key ingredients for a laser have been demonstrated too. As the Si-nc rich region has an effective Si content larger than SiO_2, its refractive index is larger than the one of silica (1.45). Refractive index ranging between 1.45 and 2.2 at 780 nm have been reported. Hence, Si-nc rich SiO_2 can be used to form the core region of a waveguide where the cladding is made by SiO_2. Rib waveguides or stripe loaded waveguides have been fabricated. Low losses in these Si-nc based waveguides have been reported [41]. Losses as low as 10 dB/cm have been measured at 780 nm and attributed mainly to scattering and absorption.

Vertical optical micro-cavities based on a Fabry–Perot structure with mirrors constituted by Distributed Bragg Reflectors (DBR) and where the central layer is

formed by Si-nc dispersed in SiO_2 have been already fabricated [42]. The presence of thick SiO_2 layer needed to form the DBR can be a problem for electrical injection when current has to flow through the DBR. Lateral injection schemes can avoid these problems. On the other hand the electrical injection into the Si-nc is a delicate task by itself. Bipolar injection is extremely difficult to achieve. Despite some claims, most of the reported Si-nc LED are impact ionization devices: electron–hole pairs are generated by impact ionization by the energetic free carriers injected through the electrode. By exploiting impact ionization Si-nc LED have been demonstrated with electroluminescence spectra overlapping luminescence spectra, onset-voltage as low as 5 V and efficiencies in excess of 0.1% [43]. Another recent work reports on a field-effect transistor (FET) structure where the gate dielectric is a thin oxide with a layer of Si-nc [44]. In this way by changing the sign of the gate bias, separate injection of electrons and holes in the Si-nc is achieved. Luminescence is observed only when both electrons and holes are injected into the Si-nc. By using this pulsing bias technique, bipolar injection is achieved which should lead to high efficiency in the emission of the LED.

All these different experiments have still to be merged in a laser cavity structure to demonstrate a Si-nc based laser.

9.4 Er coupled Si nanocrystal optical amplifiers

The Si-nc we discussed previously are potential sources for visible, i.e. the wavelength region nowadays covered by gallium arsenide (GaAs) based vertical cavity surface-emiltiry laser (VCSEL) and which is used for short-distance communication such as board-to-board or chip-to-chip. As it is well know-another wavelength region worth of interest is the one of the maximum transparency for optical fibre: the wavelength region spanning from 1.3 to 1.6 μm. It is attractive a source in this wavelength region to take fibre optics down to the chip. Indeed, a major limitation of present-day optical networks is the difficulty of exploiting the enormous bandwidth available in local area networks. While erbium-doped fibre amplifiers (EDFA) are well established in long-haul transmission [45], reducing their size and cost for widespread integration presents major difficulties: ion pair interactions, combined with the small excitation cross-section of the Er^{3+} ion, necessitate the use of long lightly doped fibre. Moreover, high power (and therefore expensive) laser diodes tuned to specific electronic transitions are required as pump sources. Nonetheless, in the past few years, several Er-doped waveguide amplifiers (EDWAs) have been developed, and in some cases optical gain has been achieved [46]. The main difficulty in constructing an EDWA lies in providing suitably high gain in a short length, which requires high Er^{3+} doping without concentration-dependent effects. Existing EDWAs and lossless splitters have been formed by ion exchange in silicate or phosphate glass matrices and by ion implantation into Al_2O_3. Internal gains of 4.1 dB/cm have been achieved in ion-exchanged phosphate glass and 0.6 dB/cm in Er-implanted Al_2O_3. While other glass matrices have been proposed to reduce the concentration quenching effects, and co-doping with Yb^{3+} has also been used to extend the choice of excitation wavelengths, the challenge today is to develop a low-cost integrated device that is compatible with conventional silicon CMOS processing.

Clearly, a breakthrough in optical material design and fabrication that removes many of the constraints of the current EDFA gain medium could have a considerable impact on the industry. In particular, a new gain medium that enables broadband optical or electrical excitation of rare-earth ions, with a potential 100-fold reduction in pump costs, and provides order-of-magnitude enhancements in effective absorption cross-sections, with corresponding reductions to amplifier length dimensions could revolutionize optical amplification, and optical networking architectures. It would have an equally significant impact on the field of solid-state laser sources, enabling the realization of novel laser configurations. Recent work on rare-earth-doped silica containing silicon nanoclusters suggests that this may hold the key to the required material.

9.4.1 Er^{3+} Internal Transition

The radiative transitions in the internal 4*f* shell of Erbium ions (Er^{3+}) are exploited in EDFA, see Fig. 9.9. These energy levels are screened by the 5*s* and 5*p* states which make them insensitive to the host matrix where the Er ions are inserted. For this reason, during the 1990s several experimental efforts have been spent in order to develop an efficient and reliable light source by using Er^{3+} in Si [3]. The idea was to excite the Er^{3+}, which emits 1.535 μm photons, by an energy transfer from the electrically injected e–h pairs in a p–n Si diode. The most successful results have been the demonstration of room temperature emission with an external quantum efficiency of 0.1% in a MHz modulated Er^{3+} based LED [47]. The main problem associated to Er^{3+} in Si is the back transfer of energy from the Er^{3+} ions to the Si host, which causes a lowering of the emission efficiency of the diode [48]. This is due to a resonant level which appears in the Si band gap due to the Er^{3+} doping and which couples with the Er^{3+} levels.

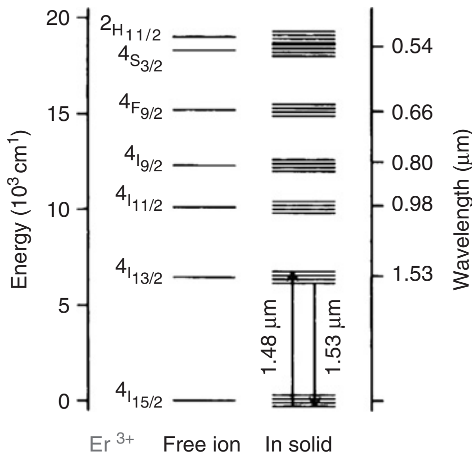

Figure 9.9 Schematic energy level diagram of Er^{3+}. In the free ion the energy levels are sharp; in a solid the levels are split due to the Stark effect. Pump (~1.48 μm) and signal (~1.53 μm). wavelengths are indicated, together with the Russell–Saunders notation of the energy levels (after Ref. [48]).

9.4.2 Er^{3+} and Si-nc Interactions

In order to reduce this back-transfer process it was proposed to enlarge the band gap of the Er^{3+} host so that the resonance between the defect level and the internal Er^{3+} levels is lost [49]. Si-nc in a SiO_2 dielectric were thus proposed as the host. Indeed it turns out that Si-nc are very efficient sensitizers of the Er^{3+} luminescence with typical transfer efficiency as high as 70% and with a typical transfer time of 1 μs. In addition, the Er^{3+} are dispersed in a SiO_2, where they found the most favourable chemical environment. Quite interestingly the transfer efficiency gets maximized when the Si-nc are not completely crystallized but still in the form of Si nanoclusters. Some reports claim even that the Er^{3+} can be excited through defects in the matrix. Still under debate is the number of Er ions that can be excited by a single Si-nc: a few or many ions.

The use of broadband sensitizers relaxes the stringent conditions for the pump source and raises the efficiency of the optical amplifier [50]. A sensitizer is another chemical species or another active centre which is inserted into the host matrix together with Er ions in order to improve the excitation of Er themselves. Usually the pumping energy is absorbed by the sensitizer which efficiently transfers it to the Er ions, making the ions optically active and prone to emit photons. A good sensitizer has to have an high absorption cross section and has to transfer efficiently energy to Er^{3+}. Si-nc have typical absorption spectra that depend on the average size of the Si-nc but that usually start to be appreciable near 600 nm and grow towards shorter wavelengths. The absorption cross sections are of the order of $10^{-16}\,cm^2$ around the 488 nm region, that is five orders of magnitude higher than the absorption cross section of Er^{3+} in stochiometric silica samples ($8 \times 10^{-21}\,cm^2$ at 488 nm). In addition, it has been demonstrated that Er^{3+} doped silica containing Si-nc produced by cosputtering, PECVD or ion implantation exhibits a strong energy coupling between Si-nc and Er^{3+}. Thus, the presence of the Si-nc strongly enhances the effective excitation cross section of Er^{3+}, which is comparable to the absorption cross section of Si-nc alone. It has been also seen that the shape of the Er^{3+} photoluminescence spectra at low pumping powers when placed in a SiO_2 matrix is almost independent of the presence of the Si-nc on the matrix, which indicates that Er is surrounded by oxide.

9.4.3 Er^{3+} Cross Sections

Figure 9.10 summarizes the various mechanisms and defines the related cross-sections for this system. Excitation of Er^{3+} occurs via an energy transfer from photoexcited e–h pairs which are excited in the Si-nc: the overall efficiency of light generation at 1.535 μm through direct absorption in the Si-nc is described by an effective Er^{3+} excitation cross section σ_{exc}. On the other hand, the direct absorption of the Er^{3+} ions, without the mediation of the Si-nc, and the emission from the Er ions are described by an absorption σ_{abs} and an emission σ_{em} cross section, respectively. The typical radiative lifetime of Er^{3+} is of 9 ms, which is similar to the one of Er^{3+} in pure SiO_2. Figure 9.11 (a) reports the luminescence and the absorption spectra measured in an Er^{3+} coupled Si-nc ridge waveguide at room temperature [51].

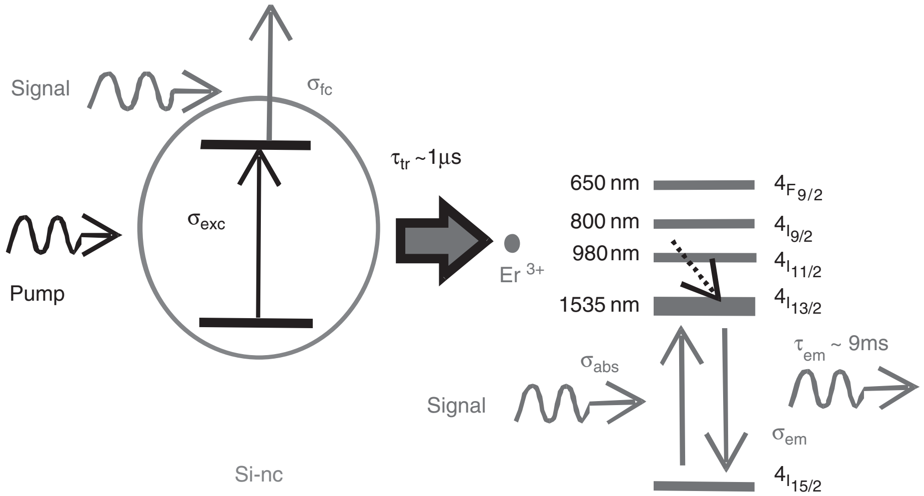

Figure 9.10 Diagram of the excitation process of Er^{3+} ions via a Si-nc, with the main related cross-sections. On the left the main internal energy levels of the Er^{3+} are shown. (Reproduced with permission from Ref. [33] copyright 2002 AIP).

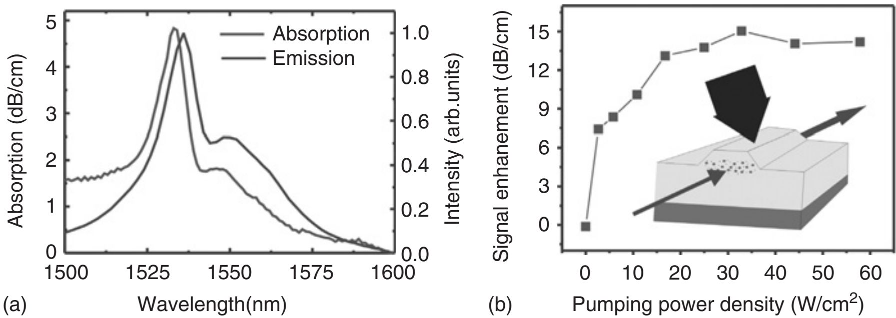

Figure 9.11 (a) Absorption and luminescence spectra of an Er^{3+} coupled Si-nc waveguide. Data after Ref. [52]. (b) Signal enhancement at 1.535 μm in an Er^{3+} coupled Si-nc waveguide versus the pumping power density by using top pumping as shown in the inset (after Ref. [33]).

Table 9.1 summarizes the best results for the various cross sections reported in the literature. It is important to notice the five order of magnitude increase in σ_{exc} and the fact that this value is conserved also when electrical injection is used to excite the Si-nc [32]. In addition, despite erroneous literature reports on an enhanced σ_{abs} [51] more reliable data shows that its values are almost the same as that of Er in silica [53].

If one places the Er^{3+} ions in a Si-nc ridge waveguide (see inset of Fig. 9.11b) one can perform experiments on signal amplification at 1.535 μm with the aim to demonstrate an EDWA. The main advantage of an EDWA with respect to an EDFA is the reduced size, the decreased pump power to achieve the same gain, and the wide spectrum range to optically pump the system. A few groups have performed such an experiment. The most successful result was reported in Ref. [33], see Fig. 9.11b. In this work a very low Si-nc concentration has been used and an internal gain of

Table 9.1 Summary of the various cross sections related to Er^{3+} in various materials. The best reported results are shown and are taken in the reference listed in the last column.

	Er in SiO_2 (cm^2)	Er in Si (cm^2)	Er in Si-nc (cm^2)	Reference for Er in Si-nc
Effective excitation cross section of luminescence at a pumping energy of 488 nm	$1 - 8 \times 10^{-21}$	3×10^{-15}	$1.1 - 0.7 \times 10^{-16}$	[54,55]
Effective excitation cross section of electroluminescence		4×10^{-14}	1×10^{-14} by impact ionization	[32]
Emission cross section at 1.535 μm	6×10^{-21}		2×10^{-19}	[33]
Absorption cross section at 1.535 μm	4×10^{-21}	2×10^{-20}	5×10^{-21}	[52,53]

7 dB/cm has been deduced. A successful experiment of pumping the EDWA with a LED battery was also reported. In other experiments, with a large Si-nc concentration, no or weak signal enhancement has been observed [52]. The reason is attributed to the presence of a strong confined carrier absorption which introduces a loss mechanism at the signal wavelength and prevents the sensitizing action of the Si-nc. Indeed, the energy transfer is in competition with confined carrier absorption at the signal wavelength (see Fig. 9.10). A confined carrier cross section of $10^{-18}\,cm^2$ is usually assumed. Propagation losses, saturation of Er^{3+} excitation, up-conversion of the pumped light and confined carrier absorption make difficult the proper design of EDWA where optical amplification can be observed.

Having got internal gain, electrically injected LED [18, 32] and optical cavities [42] a laser which uses the Er^{3+} coupled Si-nc system as active material seems feasible.

9.5 Conclusions

Silicon photonics is a reality but is not yet a killer applications. The development of a reliable silicon injection laser which can outperform similar III–V based devices and can be easily integrated with modern ULSI microelectronics will transform silicon photonics in the killer applications which will help take face with the fast improvement predicted by Moore's law.

To get an injection laser, we have outlined in this chapter the three most interesting approaches: bulk silicon, silicon nanocrystals, and Er-coupled silicon nanoclusters. Which one will be the first successful is at this moment unknown.

It is clear that the three are covering different wavelength ranges all appealing for different applications. Research should be more focused to this end and an injection silicon laser will finally be demonstrated.

Acknowledgements

We acknowledge fruitful collaborations and discussions with the partners in the European project SINERGIA, SEMINANO, and PHOLOGIC. The financial support by EC through these projects and by MIUR through the FIRB projects (RBNE01P4JF and RBNE012N3X) is gratefully acknowledged.

REFERENCES

1. International Technology Roadmap for Semiconductors 2005 update MPU Interconnect Technology Requirements.
2. D.A. Miller, *Proc. of IEEE* **88**, 728 (2000).
3. S. Ossicini, L. Pavesi and F. Priolo, *Light Emitting Silicon for Microphotonics. Springer Tracts in Modern Physics*, Vol. 194 (Springer-Verlag, Berlin, 2003).
4. L. Pavesi and D. Lockwood, *Silicon Photonics, Topics in Applied Physics*, Vol. 94 (Springer-Verlag, Berlin, 2004).
5. S.K. Moore, *Spectrum of IEEE* (31 July 2002).
6. G. Masini, L. Colace and G. Assanto, *Mater. Sci. Eng. B* **89**, 2 (2002).
7. O. Bisi, S.U. Campisano, L. Pavesi and F. Priolo, *Silicon Based Microphotonics: From Basics to Applications* (IOS Press, Amsterdam, 1999).
8. L. Pavesi and G. Guillot, *Optical Interconnects the Silicon Approach. Springer Series in Optical Science,* Vol. 119 (Springer-Verlag, Berlin, 2006).
9. L. Pavesi, *Mater. Today* **8**(1), 18–25 (January 2005).
10. L. Pavesi, S. Gaponenko and L. Dal Negro, *Towards the First Silicon Laser, NATO Science Series* (Kluwer Academic Publishers, 2003).
11. L. Pavesi, L. Dal Negro, C. Mazzoleni, G. Franzò and F. Priolo, *Nature* **408**, 440 (2000).
12. G. Dehlinger, L. Diehl, U. Gennser, H. Sigg, J.Faist, K. Ensslin and D. Grützmacher, *Science* **290**, 2277 (2000).
13. M.A. Green, J. Zhao, A. Wang, P.J. Reece and M. Gal, *Nature* **412**, 805 (2001).
14. W.L. Ng, M.A. Lourenço, R.M. Gwilliam, S. Ledain, G. Shao and K.P. Homewood, *Nature* **410**, 192 (2001).
15. O. Boyraz and B. Jalali, *Optics Express* **12**, 5269 (2004).
16. H. Rong, A. Liu, R. Jones, O. Cohen, D. Hak, R. Nicolaescu, A. Fang and M. Paniccia, *Nature* **433**, 292 (2005).
17. B. Gelloz and N. Koshida, *J. Appl. Phys.* **88**, 4319 (2000).
18. M.E. Castagna, S. Coffa, M. Monaco, L. Caristia, A. Messina, R. Mangano and C. Buongiorno, *Physica E* **16**, 547 (2003).
19. S.G. Cloutier, P.A. Kossyrev and J. Xu, *Nature Mater.* **4**, 887 (2005).
20. M.J. Chen, J.L. Yen, J.Y. Li, J.F. Chang, S.C. Tsai and C.S. Tsai, *Appl. Phys. Lett.* **84**, 2163 (2004).
21. A. Liu, H. Rong, M. Paniccia, O. Cohen and D. Hak, *Opt. Express.* **12**, 4261 (2004).
22. O. Boyraz and B. Jalali, *Optics Express* **13**, 796 (2005).
23. J. Zhao, M.A. Green and A.J. Wang, *J. Appl. Phys.* **92**, 2977 (2002).
24. T. Trupke, M.A. Green and P. Wurfel, *J. Appl. Phys.* **93**, 9058 (2003).
25. W.P. Dumke, *Phys. Rev.* **127**, 1559 (1962).
26. L.T. Canham, *Appl. Phys. Lett.* **57**, 1046 (1990).
27. O. Bisi, S. Ossicini and L. Pavesi, *Surf. Sci. Rep.* **38**, 1 (2000).

28. M. Ghulinyan, Z. Gaburro, L. Pavesi, C.J. Oton, N.E. Capuj, R. Sapienza, C. Toninelli, P. Costantino and D.S. Wiersma, "Optical superlattices: where photons behave like electrons" *Progress in Laser and Electro-Optics Research* (Nova Science Publishers, 2005).
29. M. Cazzanelli, D. Kovalev, L. Dal Negro, Z. Gaburro and L. Pavesi, *Phys. Rev. Lett.* 93, 207402 (2004).
30. W.L. Wilson, P.F. Szajowski and L.E. Brus, *Science* **262**, 1241 (1993).
31. M. Zacharias, J. Heitmann, R. Scholz, U. Kahler, M. Schmidt and J. Bläsing, *Appl. Phys. Lett.* **80**, 661 (2002).
32. F. Iacona, D. Pacifici, A. Irrera, M. Miritello, G. Franzó, F. Priolo, D. Sanfilippo, G. Di Stefano and P.G. Fallica, *Appl. Phys. Lett.* **81**, 3242 (2002).
33. H.-S. Han, S.-Y. Seo, J.H. Shin and N. Park, *Appl. Phys. Lett.* **81**, 3720 (2002).
34. L. Dal Negro, M. Cazzanelli, N. Daldosso, Z. Gaburro, L. Pavesi, F. Priolo, D. Pacifici, G. Franzò and F. Iacona, *Physica E* **16**, 297 (2003).
35. M. Cazzanelli, D. Navarro-Urrios, R. Riboli, N. Daldosso, L. Pavesi, J. Heitmann, L.X. Yi, R. Scholz, M. Zacharias and U. Gosele, *J. Appl. Phys.* **96**, 3164 (2004).
36. L. Dal Negro, M. Cazzanelli, B. Danese, L. Pavesi, F. Iacona, G. Franzò and F. Priolo, *J. Appl. Phys.* **96**, 5747 (2004).
37. M.V. Wolkin, J. Jorne, P.M. Fauchet, G. Allan and C. Delerue, *Phys. Rev. Lett.* **82**, 197 (1999).
38. A.B. Filonov, S. Ossicini, F. Bassani and F. Arnaud d'Avitaya, *Phys. Rev. B* **65**, 195717 (2002).
39. M. Luppi and S. Ossicini, *J. Appl. Phys.* **94** (2003).
40. N. Daldosso, M. Luppi, S. Ossicini, E. Degoli, R. Magri, G. Dalba, P. Fomasini, R. Grisenti, F. Rocca, L. Pavesi, S. Boninelli, F. Priolo, C. Spinella and F. Iacona, *Phys. Rev. B* **68,** 085327 (2003).
41. P. Pellegrino, B. Garrido, C. Garcia, J. Arbiol, J.R. Morante, M. Melchiorri, N. Daldosso, L. Pavesi, E. Schedi and G. Sarrabayrouse, *J. Appl. Phys* **97**, 074312 (2005).
42. F. Iacona, G. Franzò, E.C. Moreira and F. Priolo, *J. Appl. Phys.* **89**, 8354 (2001).
43. G. Franzò, A. Irreira, E.C. Moreira, M. Miritello, F. Iacona, D. Sanfilippo, G.F. Di Stefano, F. Fallica and F. Priolo, *Appl. Phys. A* **74**, 1 (2002).
44. R.J. Walters, R.I. Bourianof and H. Atwater, *Nat. Mater.* **4**, 143 (2005).
45. E. Desurvire, *Erbium-Doped Fiber Amplifiers: Principles and Applications* (Wiley, New York, 1994).
46. A. Polman, *J. Appl. Phys.* **82**, 1 (1997).
47. G. Franzò, S. Coffa, F. Priolo and C. Spinella, *J. Appl. Phys.* **81**, 2784 (1997).
48. F. Priolo, G. Franzò, S. Coffa and A. Carnera, *Phys. Rev. B* **57**, 4443 (1998).
49. A.J. Kenyon, P.F. Trwoga, M. Federighi and C.W. Pitt, *J. Phys. Condens. Mater.* **6**, L319 (1994).
50. A. Polman and F.C.J.M. van Veggel, *J. Opt. Soc. Am. B* **21**, 871 (2004).
51. P.G. Kik and A. Polman, *J. Appl. Phys.* **91**, 534 (2002).
52. N. Daldosso, D. Navarro-Urrios, M. Melchiorri, L. Pavesi, F. Gorbilleau, M. Carrada, R. Rizk, C. Garcia, P. Pellegrino, B. Garrido and L. Cognolato, *Appl. Phys. Lett.* **86,** 231103 (2005).
53. N. Daldosso, D. Navarro-Urrios, M. Melchiorri, L. Pavesi, C. Sada, F. Gourbilleau and R. Rizk, *Appl. Phys. Lett.* **88,** 161901 (2006).
54. F. Priolo, G. Franzò, D. Pacifici, V. Vinciguerra, F. Iacona and A. Irrera, *J. Appl. Phys.* **89**, 264 (2001).
55. A.J. Kenyon, C.E. Chryssou, C.W. Pitt, T. Shimizu-Iwayama, D.E. Hole, N. Sharma and C.J. Humphreys, *J. Appl. Phys.* **91**, 367 (2002).

CHAPTER TEN

Nanosilicon Single-Electron Transistors and Memory

Z.A.K. Durrani [1,2] and H. Ahmed [3]

Contents

10.1 Introduction 335
10.1.1 Single-Electron and Quantum Confinement Effects 337
10.2 Nanosilicon SETs 341
10.2.1 Conduction in Continuous Nanocrystalline Silicon Films 341
10.2.2 Silicon Nanowire SETs 343
10.2.3 Point-Contact SETs: Room Temperature Operation 346
10.2.4 "Grain-Boundary" Engineering 350
10.2.5 Single-Electron Transistors Using Silicon Nanocrystals 351
10.2.6 Comparison with Crystalline Silicon SETs 352
10.3 Electron Coupling Effects in Nanosilicon 352
10.3.1 Electrostatic Coupling Effects 354
10.3.2 Electron Wavefunction Coupling Effects 354
10.4 Nanosilicon Memory 356
References 358

Abstract

Nanosilicon materials are promising systems for the fabrication of single-electron transistor (SET) and memory devices in silicon. In these devices, precise control over the charging of a nanometre-size "island" by just one electron raises the possibility of low power, highly scaled integrated circuits with one electron per bit. Nanosilicon materials, consisting of crystalline silicon grains ~10 nm in size, provide a means to fabricate ultra-small charging islands using growth techniques rather than high-resolution lithography. It is then possible to fabricate single-electron devices operating at room temperature. This review introduces electron transport in nanosilicon and considers the design and fabrication of SETs, quantum-dot transistors, and few-electron memory cells in these materials.

10.1 Introduction

Nanoscale silicon materials [1–12], consisting of crystalline silicon grains ~10 nm in size separated by amorphous silicon or silicon oxide grain boundaries

[1] Electronic Devices and Materials Group, Engineering Department, University of Cambridge, Cambridge, UK.
[2] SORST, Japan Science and Technology Corporation, Tokyo, Japan.
[3] Corpus Christi College, Cambridge, UK.

Nanosilicon
9780080445281
Copyright © 2007. Elsevier Ltd.
All rights reserved.

(GBs), have raised the possibility of the fabrication of advanced single-electron devices and circuits in silicon. In these devices, the single-electron charging or "Coulomb blockade" effect [13–17] is used to control precisely the transfer of individual electrons onto a nanoscale conducting island, isolated by tunnel barriers. Single-electron devices are promising candidates for advanced logic and memory circuits where the bits can be defined using only a few electrons, leading to circuits with immunity from statistical fluctuations in the number of electrons per bit and very low power consumption. In addition, the inherently small size of these devices, and the potential for high scalability in comparison with conventional complementary metal oxide semiconductor (CMOS) devices, raises the possibility of very low power, highly integrated large-scale integrated (LSI) circuits.

The continuous reduction in size of microelectronic devices has been the key to rapid improvement in the performance of CMOS LSI circuits. In 2004, the MOS transistor minimum feature size (transistor gate length) was ~45 nm [18]. It is predicted that by 2010, this will fall to 18 nm and that it may be possible to accommodate ~1 billion transistors on a microprocessor chip. With each design generation, it has been possible to incorporate ever greater numbers of transistors and memory cells on to a single memory or logic chip, accompanied by a rapid increase in the operating speed of the chip. However, increasing the speed and number of transistors on the chip has lead to a sharp rise in the total power consumption of the chip. For example, in microprocessors, although the power consumption of the industry-standard metal oxide semiconductor (MOS) transistor has been reduced by a factor of ~2 every 5 years, due to a reduction in size and improved operating parameters, the rise in the number of transistors per chip has more than negated this improvement. The result has been a ~3.5-fold increase in the total power consumption of the microprocessor during the same period.

A reduction in the number of electrons necessary to define the storage "bits" would automatically lead to smaller operating currents and lower power consumption. Unfortunately, a reduction in the number of electrons per bit in a conventional MOS transistor to well below ~100 is difficult because "$\sqrt{n}$" fluctuations in the electron number cause unacceptable statistical fluctuations in the sub-threshold characteristics of the MOS transistors [19]. In addition, if the size of the device falls to below ~10 nm, then quantum effects can influence strongly the device characteristics. Perhaps, the most significant of these effects for conventional MOS devices is the quantum tunnelling of electrons across thin potential barriers. This can lead to increasing gate leakage currents in MOS transistors, with an accompanying loss of gain and an increase in the power consumption.

An additional problem, especially significant for memory circuits, arises in both storing and sensing small numbers of electrons per bit, well below ~1000. If we consider scaling trends in dynamic random-access memories (DRAMs) [20], after the 1 Mbit generation, it has become increasingly difficult to maintain a continuous decrease in the charge per bit. This is because the signal associated with this charge becomes difficult to sense, and is less immune to leakage current, internal noise and soft errors. There has been a strong effort to scale down the cell area while maintaining the number of stored electrons at ~50,000. As a result, the design of the standard one-transistor, one-capacitor, DRAM cell has become increasingly complex. In this regard, a "gain-cell" approach, where a transistor integrated in each cell

amplifies the stored charge directly (e.g. a high-speed analogue of a “FLASH” type memory cell), may be promising [21,22].

Silicon single-electron devices can help in overcoming the power consumption, charge fluctuation and charge sensing problems in LSI circuits scaled into the ~10 nm size regime. In these devices, the precise definition of bits by a few or even single electrons using the Coulomb blockade effect directly leads to immunity from charge fluctuations and low power consumption. The performance of single-electron devices can also improve with a reduction in device size. The devices also retain compatibility with LSI fabrication techniques, which would allow integration with CMOS technology for those sections of the circuit where conventional MOS devices would still be appropriate [4]. It would then be possible to fabricate highly scalable, inherently low power, few-electron LSI circuits.

Nanosilicon materials provide a highly promising approach for the fabrication of CMOS compatible single-electron devices and circuits. Using nanoscale silicon grains and the surrounding GBs to define the critical components of the device, i.e. the charging “island” and the surrounding tunnel barrier, can allow the “natural” fabrication of devices using growth techniques rather than high-resolution lithography. We note that if the grains are ~10 nm or less in size, and the GB tunnel barriers are ~100 meV or higher, then the single-electron charging energy and tunnel resistances can be large enough for room temperature operation of the nanosilicon SETs [5,13,23]. In devices of this scale, quantum confinement of electrons is also likely, raising the possibility of quantum-dot devices [24,25] in silicon. This may be more easily realizable using nanosilicon material rather than using high-resolution lithography. It is also possible to control the size and shape of the nanosilicon grains in these materials, with precision greater than is possible with high-resolution lithographic techniques, by carefully tailoring the material growth process [7,8,10,11]. This would help to obtain reproducibility between the operating characteristics of the large numbers of devices necessary in LSI circuit applications.

In this review, we will introduce briefly single-electron charging, Coulomb blockade and quantum effects with reference to nanosilicon. We will then consider the design and operation of single-electron and quantum-dot nanosilicon transistors, Finally, we review work on nanosilicon memory devices, where silicon nanocrystals can be used to store charge consisting of only a few or even single electrons.

10.1.1 Single-Electron and Quantum Confinement Effects

We now introduce briefly single-electron charging effects in silicon. Detailed general introductions to single-electron charging effects can be found in Ref. [13–16]. Consider a system where electrons tunnel across a small conducting “island”, isolated between source and drain electrodes by tunnelling potential barriers (Fig. 10.1a). We assume that the tunnel barrier resistances R_1 and R_2 (circuit diagram, Fig. 10.1b) are large enough such that the electronic states on the island are relatively localized. This condition exists if R_1 and R_2 are greater than the quantum of resistance $R_K \sim h/e^2 = 26\,\mathrm{k}\Omega$. If the capacitances associated with the tunnel barriers are C_1 and C_2, and the total capacitance of the island $C_1 + C_2 = C \sim 10^{-15}\,\mathrm{F}$ or less, then the charging energy $E_c = e^2/2C$ associated with the addition of even a single electron onto the island may be larger than the thermal energy $k_B T$ at low

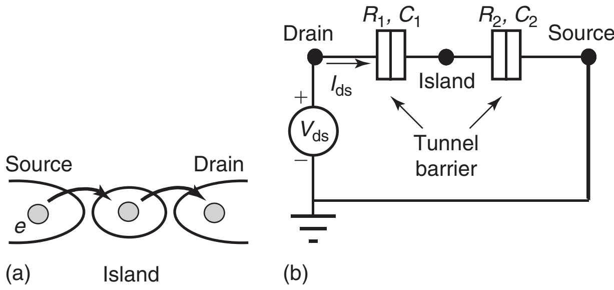

Figure 10.1 Single island, double tunnel junction. (a) Schematic diagram. (b) Circuit diagram.

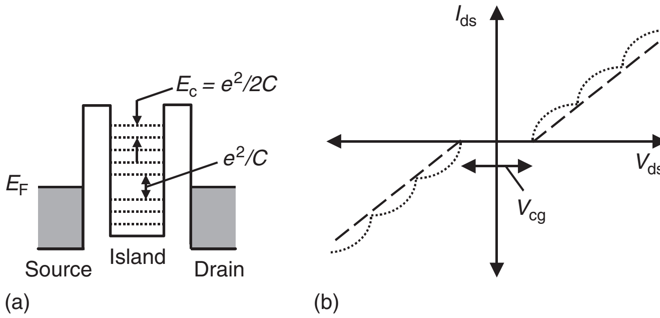

Figure 10.2 (a) Single-electron energy levels in a double tunnel junction. (b) Coulomb blockade *I–V* characteristics.

temperature. This implies that electronic conduction can begin across the system at low temperature only if the applied voltage across the drain and source electrodes V_{ds} is larger than $2E_c/e$ (assuming that an equal voltage drop occurs across each tunnel junction). This is the well-known "Coulomb blockade" of conduction, leading to a low current voltage gap in the *I–V* characteristics.

Once the Coulomb blockade is overcome, electrons can transfer onto and off the island, a drain-source current I_{ds} begins to flow and the average number of electrons on the island increases by one. As the applied voltage equals multiples of $2E_c/e$, the charging energy for additional electrons on the island is overcome, and the average number of electrons on the island can increase one by one. There is a set of discrete energy levels on the island, separated by the single-electron charging energy $e^2/2C$ (Fig. 10.2a) If the source- and drain-island tunnel resistance are similar, then electrons can tunnel off the island at the same rate as they tunnel on to the island, and the current increases linearly with voltage outside a central Coulomb blockade region $V_{cg} = 2e/C$ (dashed lines, Fig. 10.2b). However, if the tunnel resistances are very different then electrons can persist on the island, influencing the tunnelling probability of additional electrons and leading to current steps periodic in voltage. This is called the Coulomb staircase (dotted lines, Fig. 10.2b), and each step corresponds to the addition of an extra electron onto the island. We note that the drain-source conductance shows a peak at each current step in the staircase.

It is also possible to use an additional gate electrode to control the island charging (Fig. 10.3a). If the gate voltage V_{gs} is varied, the charging energy is periodically

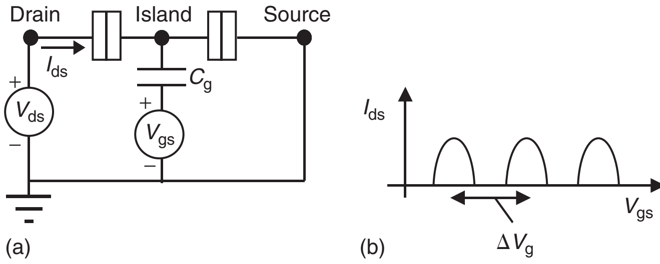

Figure 10.3 (a) Single-electron transistor. (b) Single-electron current oscillations in a SET.

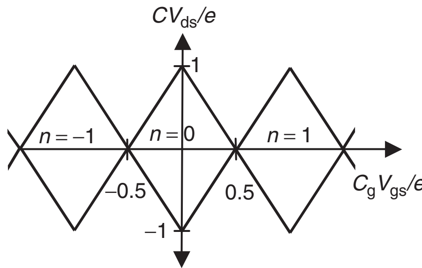

Figure 10.4 Charge stability diagram of a SET.

overcome and drain-source current or conductance oscillations periodic in gate voltage are observed (Fig. 10.3b). Each oscillation corresponds to resonance of the single-electron levels with the Fermi energy of the drain. Passing through an oscillation changes the number of electrons on the island by one, e.g. if the gate voltage becomes more positive at an oscillation, the single-electron level energy is lowered relative to the drain Fermi energy, and an electron can occupy the level. The oscillation period is given by $\Delta V_g = e/C_g$. Such a device is known as a SET, demonstrated first by Fulton and Dolan [26] in 1987, used an $Al/Al_2O_3/Al$ multilayer structure operating at 4.2 K. Here, both the drain-source voltage and the gate voltage can control the number of electrons on the island.

Figure 10.4 shows schematically the "charge stability diagram" of a SET, where the electron number on the island of the SET is plotted as a function of the drain-source voltage and the gate voltage. It is seen that this number is constant within trapezoidal regions of charge stability, often referred to as "Coulomb diamonds". The edges of the charge stability regions trace the position of the single-electron conductance oscillation peaks, as a function of the gate and drain-source voltage. The electron number is seen to change by one from a charge stability region to the next.

We note that the single-island SET can be very sensitive to changes in the charge on the gate capacitor, or simply the background charge (often called the "offset" charge) nearby the island. A change in this charge of $e/2$ can shift the SET operating point from the middle of the Coulomb gap to the edge of the Coulomb gap. This sensitivity can be a potential problem for single-electron circuits, leading to unwanted switching of the SET, but can be overcome by using silicon SETs, where most traps serving as the source of offset charge may be passivated using oxidation.

In addition, a multiple tunnel junction (MTJ) SET may be used, where there are a number of charging islands in series. Any fluctuation in a local "offset" charge then switches only one of the islands of the SET, but not the others, reducing sensitivity of the entire device to the "offset" charge.

Single-electron charging effects were first observed in a silicon system in 1989, when Scott-Thomas *et al.* [27] observed conductance oscillations at 2 K in the inversion layer of a narrow channel MOSFET as a function of the gate voltage. This behaviour was explained by single-electron charging effects in a segment of the inversion layer, isolated by potential barriers associated with scattering centres [28]. Single-electron charging effects were then observed in other silicon-based systems, e.g. Coulomb blockade characteristics persisting up to 50 K were observed in a device with a nanometre-scale island fabricated in δ-doped silicon germanium [29], and in a nanometre-scale island defined using high-resolution electron-beam lithography in the heavily doped crystalline silicon top layer of silicon-on-insulator (SOI) material [30]. These observations opened the way for the development of silicon SETs compatible with CMOS technology.

If the island in a SET in SOI is scaled down to very small island sizes ~12 nm, then single-electron conductance oscillations can be observed even at room temperature [31]. It is also possible to obtain room temperature SETs using ~10 nm size nanoscale islands isolated by pattern-dependent oxidation [32]. Single-electron effects can also occur in conduction through etched nanowires defined in SOI where there is no lithographically defined island. Ishikuro *et al.* [33] have observed single-electron effects at room temperature in ~10 nm wide and 100 nm long anisotropic wet-etched nanowires. It is believed that in a manner similar to single-electron effects in narrow inversion layers in Si MOSFETs, potential fluctuations isolate segments along the nanowire, creating an MTJ device. These fluctuations have been associated with disorder in the local doping level or surface potential [34], and with lateral confinement effects or regions of SiO_x [35]. Heavily doped gated nanowires have been modelled as an MTJ with a combination of single-electron effects and a field effect induced by the gate voltage [36]. These devices are easier to fabricate because precise, high-resolution lithography to define the charging island is unnecessary. However, the random nature of the MTJ leads to more complicated electrical characteristics.

In nanosilicon films, the grains can be <10 nm in size and the grain capacitance can be extremely small, ~1 aF. We may estimate the order of magnitude of the charging energy for a nanoscale dot of radius $r = 5$ nm embedded in SiO_2, using the self-capacitance of a sphere $C = 4\pi\varepsilon r = 2$ aF. This implies that the single-electron charging energy, $E_C = e^2/2C = 40$ meV, which is greater than $k_B T = 25$ meV at room temperature ($T = 300$ K). This implies that single-electron charging effects may be observed even at room temperature in these materials [5,23].

In nanosilicon films with grains ~10 nm or less in size, an additional effect is the quantum confinement [24,25] of electrons on the grain by the GB potential barriers, leading to the formation of discrete electron energy levels. For example, if we consider a grain of radius "*r*" with parabolic potential barriers, the electrons then occupy equally spaced energy levels within the well, where the energy level spacing is equal. Such a system forms a "quantum dot", leading to strong peaks in the electron tunnelling probability across the grain when the levels align with the Fermi energy. Placing the

quantum dot between source and drain contacts provides a means to observe resonant tunnelling through these levels. Strong tunnelling peaks are observed when the energy levels in the dot align with the Fermi level in the source as a function of the source-drain or gate bias. We note that usually, a combination of single-electron and quantum confinement effects can occur. Here, the energy of each level is given by the sum of the quantum confinement and single-electron charging energies.

10.2 Nanosilicon SETs

10.2.1 Conduction in Continuous Nanocrystalline Silicon Films

We will consider first the electronic conduction mechanism in a doped, physically continuous polycrystalline or nanocrystalline silicon (nc-Si) thin film, before extending this picture to include single-electron and quantum confinement effects associated with nanoscale grain sizes. Conduction through a nc-Si film is strongly affected by potential barriers at the GBs, associated with the large density of trapping states caused by defects at the GBs. These states trap free carriers from the grains, reducing the carrier density within the grain. The space charge distribution near the GB also leads to an electric field, which causes a "Schottky-like" potential barrier at the GBs [37–40]. The height and width of the potential barrier is a function of the doping concentration in the grains. The carrier density in the grains may also be reduced if any segregation of dopant atoms occurs at the GBs [39,41,42].

Consider a one-dimensional chain of n-type nc-Si grains (Fig. 10.5a), where the GB thickness is small relative to the grain size "D". We assume a uniform donor concentration N_D (per unit volume) in the grain, and GB traps with a density N_t (per unit area) at an energy E_t w.r.t. the intrinsic Fermi level. We note that in large grained polycrystalline silicon films, N_t is often $\sim 10^{11}–10^{12}/cm^2$ [40,43]. Charge trapped at the GBs leaves ionized donors in the grains (Fig. 10.5b). For small N_D, all the electrons contributed by the dopants are trapped in the GBs and the grain is fully depleted. The trapped charge and the ionized dopants generate an electric field extending from the GB into the grains, leading to a double Schottky-like potential barrier of height E_{GB} (Fig. 10.5c). As N_D increases, more charge is trapped

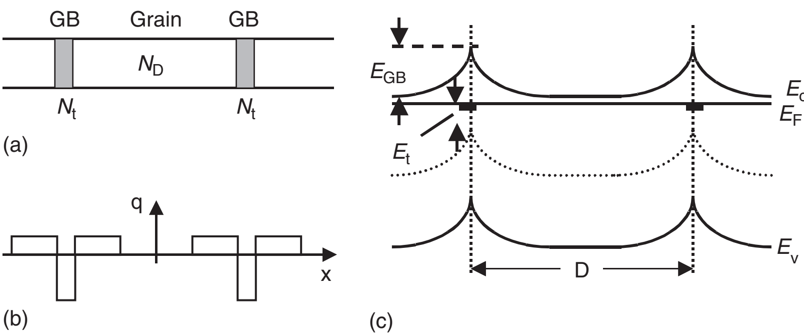

Figure 10.5 Energy bands in a one-dimensional chain of n-type nanocrystalline silicon (nc-Si) grains. (a) Schematic diagram, with a grain isolated by GBs. (b) Charge distribution. (c) Energy bands across the grain and GBs.

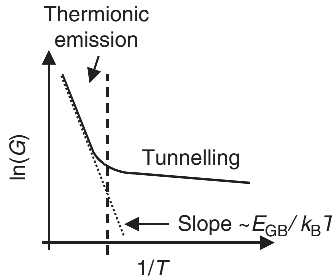

Figure 10.6 Arrenhius plot (shown schematically) of conductance G versus inverse temperature $1/T$ in nc-Si.

at the GB, increasing the electric field and potential barrier height until at $N_D = N_D^\star \approx N_t/D$, the conduction band in the centre of the grain lies near the Fermi energy E_F. Free carriers can now exist in the grain and E_{GB} is at its maximum value. Any further increase in N_D reduces E_{GB}. In the above discussion, we have assumed that N_t is high enough such that all the traps are not filled if N_D is increased. In addition, in a real nc-Si film, the grain size, GB trap density, and local doping concentration is likely to vary from grain to grain, leading to a distribution of GB barrier heights and widths across the film [44].

Electron transport across the GBs at room temperature, and at moderately low temperature, can occur by thermionic emission. With this mechanism, the temperature dependence of the conductance, plotted as an Arrenhius plot, $\ln(G)$ versus $1/T$, will be linear. However, the conduction mechanism may be assisted by tunnelling via defect states within the barrier, e.g. by empty states at the GB, or by tunnelling across the entire barrier if the barrier width is small. As the temperature is reduced, the thermionic emission current falls and tunnelling effects begin to dominate the conduction process, leading to a largely temperature-independent section of the Arrenhius plot. This is shown schematically in Fig. 10.6. The slope of the temperature-dependent section of the plot can be used to extract the activation energy, which is a measure of the barrier height. At low temperatures, a variable range hopping transport mechanism may also contribute to the overall conduction in a nanocrystal solid [45,46]. In addition, any variation in the barrier heights and widths across the film can result in a network of percolation paths for current flow across the film [44,45], where low resistance paths through GBs with low potential barriers dominate the conduction.

In the preceding discussion, we have ignored single-electron charging effects in the silicon grains. A thermionic emission model is valid if the grain size in the nc-Si is large enough, or the temperature is high enough such that the thermal fluctuations $k_B T$ are greater than the single-electron charging energy $E_c = e^2/2C$. The thermionic emission model will also be valid if the GB barrier height and width is small enough that the associated tunnel resistance R_{GB} is comparable to or smaller than the quantum resistance $R_Q = h/e^2 \sim 25.8\,\mathrm{k}\Omega$, i.e. electrons can be delocalized across the grains.

We will now consider the influence of reducing the grain size in a polycrystalline silicon film to the nanometre scale. Typically, "quantum effect" nc-Si devices have grain sizes from $\sim$50 nm to less than 10 nm. As the grain size is reduced to the

nanometre scale, the local or "microscopic" properties of the GBs, single-electron charging effects and quantum-confinement effects all begin to affect the electron transport mechanism [13,25,47,48]. We have seen that the nc-Si film may be regarded as an array of nanoscale conducting grains, isolated from each other by potential barriers at the GBs. We have also seen that at cryogenic temperatures, electron transport can occur by tunnelling through the GB potential barriers. The nc-Si film under these conditions can then be considered to form a nanoscale tunnel capacitor network, which can show single-electron charging effects. If the grains are ~10 nm in size, then it is possible for the capacitance C to be as low as 10^{-18} F. The charging energy E_C can then be larger than $k_B T$~25 meV even at room temperature. However, for the observation of room temperature single-electron charging, it is also necessary for the GB barrier height to be considerably larger than the thermal energy $k_B T$, and the GB tunnelling resistance $R_{GB} > R_Q$, so that electrons can be quasi-localized on the grains at room temperature. Coulomb blockade then occurs in the I_{ds}–V_{ds} characteristics across the grain, and current can flow only if $|V_{ds}| > |V_C|$, corresponding to the voltage necessary to overcome E_C. In addition, with grains ~10 nm or less in size, quantum confinement of electrons on the grains by the GB potential barriers is also possible, leading to the formation of discrete electron energy levels. A parabolic potential well picture may be expected from a simple extension of the polycrystalline silicon model discussed earlier. The electrons then occupy equally spaced energy levels within these wells and the grains form silicon "quantum dots". The I–V characteristics through these systems can then show current peaks associated with resonant tunnelling through the energy levels.

It is clear that single-electron and quantum-confinement effects may be of considerable importance in individual grains in an nc-Si film. However, in a large area film, variation in the grain size and in the tunnel barriers at the GB leads to percolation through the lowest resistance transport paths [47,48]. This would tend to bypass the higher resistance paths associated with the grains behaving as quantum dots, and prevent the observation of single-electron and quantum confinement effects. Therefore, it has been necessary in most demonstrations of single-electron charging and quantum-dot devices to reduce the number of current paths by defining nanowires and "point contacts" (i.e. a short nanowire where the length ≈ width). Depending on the geometry, one or multiple grains can contribute to single-electron charging effects, leading to single-island or an MTJ devices.

10.2.2 Silicon Nanowire SETs

The silicon nanowire SET in a continuous nc-Si film is an analogue of the widely investigated silicon nanowire SET fabricated in crystalline SOI material (Section 10.1.1 and Refs. [30–35]). Crystalline silicon nanowire SETs mostly use a nanowire <50 nm wide, defined by trench isolation between large source and drain regions in the top silicon layer of the SOI material, ~50 nm or less in thickness and heavily doped n-type (~10^{18}/cm^3–10^{20}/cm^3) or p-type (~10^{20}/cm^3). Disorder associated with the doping and with surface states results in a chain of conducting silicon islands along the nanowire, separated by depleted silicon potential barriers. At low temperature, the nanowire forms an MTJ system where conduction across the potential barriers occurs via single-electron tunnelling [34]. The position of the

depleted silicon potential barriers can be controlled by patterning notches in the nanowire [30], or by forming potential barriers associated with self-limiting oxidation at the ends of the nanowire [32]. The nanowire current can be gated using a variety of techniques, e.g. trench isolated side-gates [34], deposited polycrystalline silicon or metal top gates [33], or a back gate formed by the substrate of the SOI material [30].

Nanocrystalline silicon nanowire SETs, very similar in geometry to these crystalline silicon SETs, can be defined in polycrystalline or nc-Si films less than ~50 nm thick. The different variations of gate structures for SOI nanowires can also be applied here. However, the presence of GBs creates tunnel barriers intrinsically along the nanowire, isolating charging islands at the grains, and any doping or surface disorder effects are likely to be subsidiary to this. Disorder can however affect the GB potential barrier shape, by altering the local space charge distribution.

Lateral, side-gated nanowire SETs have been fabricated in solid-phase crystallized (SPC) polycrystalline silicon films, deposited on SiO_2 layers grown on silicon substrates [49,50]. Figure 10.7a shows a schematic of a typical device. The polycrystalline silicon material was prepared using a standard LSI process, as follows: A 50 nm thick amorphous silicon film was first deposited at 550°C by plasma enhanced chemical vapour deposition (PECVD), onto a 10 or 40 nm thick gate quality silicon oxide layer grown on a crystalline silicon substrate (p doped, at $5 \times 10^{14}/cm^3$). Phosphorous ion-implantation was used to heavily dope the film *n*-type to $5 \times 10^{19}/cm^3$. The film was then crystallized into polycrystalline silicon using thermal annealing at 850°C for 30 min. TEM analysis indicated that the grains varied from ~5 to 50 nm in size, and the average grain size was ~20 nm. Side-gated nanowires of various geometry were defined in the film using electron-beam lithography and reactive-ion-etching in a $SiCl_4/CF_4$ plasma. Nanowires of various dimensions, and with argon annealing or oxidation treatments were fabricated. Figure 10.7b shows an SEM image of this type of device after oxidation, where the nanowire is 1 μm long and 40 nm wide. The oxidation process reduces the cross-sectional area of the nanowire by ~10 nm and passivates surface states. The annealing process modifies the defect state density at the GBs, at the Si/SiO_2 interface and along the etched surfaces, and increases the grain size.

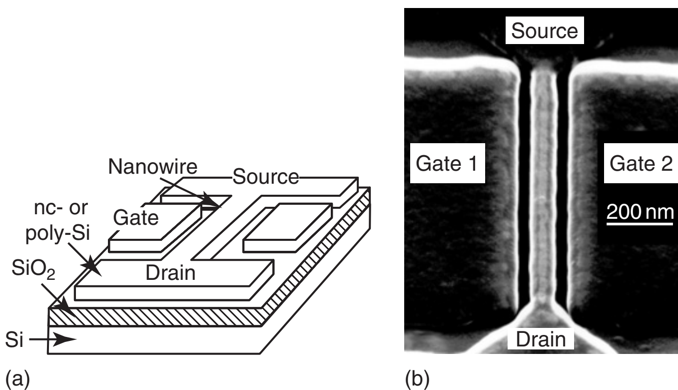

Figure 10.7 (a) Nanowire SET. (b) Scanning electron micrograph of nanowire SET.

The drain-source I_{ds}–V_{ds} characteristics at 4.2 K, from an oxidized nanowire where the pre-oxidized width was 50 nm and length was 1.5 μm, are shown in Fig. 10.8a [49]. The characteristics show single-electron charging effects associated with the charging of the crystalline silicon grains along the nanowire, isolated by tunnel barriers at the GBs [49,50]. A zero current Coulomb gap, and the steps of a Coulomb staircase can be identified. Single-electron current oscillations are observed in the I_{ds}–V_{gs} characteristics (Fig. 10.8b), corresponding to the addition of single electrons on to a dominant charging island. The single-electron current oscillations in various devices can be complex, due to multiple periods associated with an MTJ and to changes in the gate capacitance with voltage. This device had a rather low maximum operating temperature of ~15 K, due to the large grain size and low GB tunnel barrier heights.

The single-electron characteristics of these devices are dependent on the nanowire dimensions [50]. The oscillation periods increase when the nanowire length is increased from 500 nm to 1.5 μm, and decrease when the nanowire width is increased from 50 to 60 nm. Wider wires show only Ohmic conduction. This is because the longer the nanowire, the higher is the probability of smaller grains existing along the nanowire, with smaller gate capacitances and larger observed oscillation periods. The decrease in the oscillation period with increasing width, which implies an increase in the lateral area of the charging island, can be associated with the electric field through the buried oxide, below the plane of the side-gates and nanowire.

The effect of the grain size in nc-Si SETs can be observed directly in the single-electron characteristics, as this is proportional to the island capacitance and therefore determines the Coulomb gap and the current oscillation period. However, the GB tunnel barrier must be investigated by other means, e.g. by an Arrenhius plot measurement of the SET conductance as a function of temperature (Fig. 10.6). This allows an extraction of the thermal activation energy, which may be associated with the barrier height. This technique has been used to investigate the effect of restricting the multiple current paths in nc-Si nanowire SETs, by varying the dimensions of the nanowire. Furuta *et al.* [47,51] have investigated the electrical properties of a single GB at the microscopic scale using nanowires defined by electron-beam lithography in 50 nm thick polycrystalline silicon films with grain size from 20 to 150 nm, created by

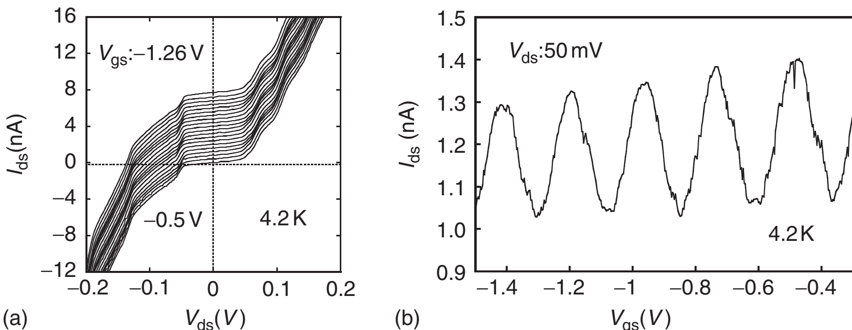

Figure 10.8 Electrical characteristics of a nc-Si nanowire SET at 4.2 K. (a) I_{ds}–V_{ds} characteristics. The curves are offset 4 nA/40 mV gate step for clarity. (b) I_{ds}–V_{gs} characteristics.

SPC of low-pressure chemical vapour deposition (LPCVD) deposited amorphous silicon. Furuta *et al.* fabricated nanowires of varying width and length, from 30 to 50 nm, and measured the distribution of the potential barrier height from the Arrenhius plots. They observed that any local variation in the potential barrier height of a GB provided a low-resistance path for current transport across the GB. If the nanowire width was increased, a lower barrier height was measured because of the increased likelihood of a low section of the GB across the nanowire. If the nanowire length was increased, a higher barrier height was observed because more than one GB could lie in series, and the GB with the highest barrier was dominant.

We observe that the barrier height can vary even at various points along a single GB. This has strong implication for the fabrication of nanometre-scale electronic devices in nanocrystalline and polycrystalline silicon films. It is clear that disorder in the GB potential barrier can lead to considerable variation in the *I–V* characteristics of different devices, and that a means of control over the GBs may be essential for the practical fabrication of LSI circuits using nc-Si devices of small size. Careful optimization of the polycrystalline silicon film growth or deposition processes may help to control the composition of the GBs.

10.2.3 Point-Contact SETs: Room Temperature Operation

The maximum operating of nc-Si nanowire SETs may be raised up to room temperature if the grain size and the corresponding total grain capacitance is reduced. If the length and width of the device is also reduced to ~50 nm or less to form a "point contact" (Fig. 10.9a) then only a few grains can exist within the active area of the device at most, improving the electrical characteristics of the device. Such films have been deposited using VHF PECVD, where the film thickness was ~20 nm and the grain size was <10 nm [5], by using LPCVD where the film thickness was ~40 nm and the grains varied from ~10 to 30 nm in size [52], and by using extremely thin (<10 nm thick) granular and non-uniform films [5]. We will discuss SETs in granular films later (Section 10.2.5). In this section, we discuss the fabrication and characterization of point-contact SETs in VHF PECVD nc-Si films, and the improvement of the operating temperature of these SETs to room temperature by selective oxidation of the GBs.

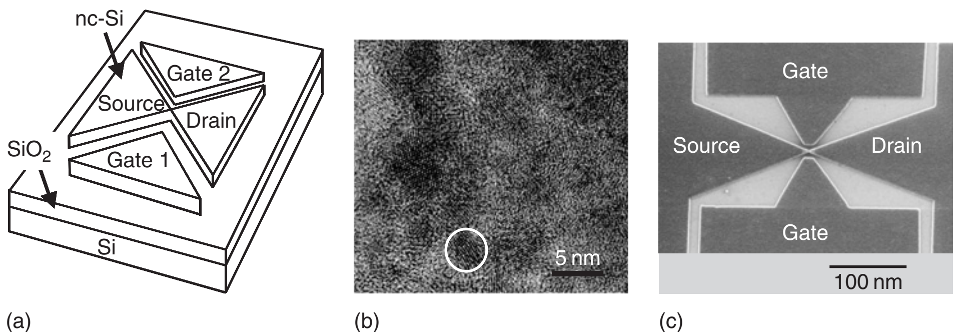

Figure 10.9 Nanocrystalline silicon point-contact SET. (a) Schematic diagram. (b) Transmission electron micrograph of the nc-Si film. (c) Scanning electron micrograph of a device.

Point contact SETs which can operate up to 60 K have been fabricated in a ~30 nm thick nc-Si, with grains <10 nm in size [53]. The films were deposited using VHF PECVD from a SiF_4:H_2:SiH_4 gas mixture, onto a 150 nm thick silicon oxide layer grown thermally on n-type crystalline silicon. The carrier concentration and electron mobility, measured at room temperature by Hall measurements, were $3\times10^{20}/cm^3$ and $1.8\,cm^2/Vs$, respectively. Figure 10.9b shows a TEM image of the film, where uniformly distributed crystalline silicon grains can be seen (e.g. circled area). The grain size ranges from ~4 to 8 nm and the GBs were formed by amorphous silicon ~1 nm thick. The crystalline volume fraction, determined by Raman spectroscopy, was 70%. Point-contact SETs were defined in these films using electron-beam lithography in polymethyl methacrylate resist, and reactive ion etching in a mixture of $SiCl_4$ and CF_4 gases, in a manner similar to longer nanowire SETs. The point-contact width was ~20 nm and two side-gates could be used to control the device characteristics. Figure 10.9c shows a scanning electron micrograph of a device. These devices show Coulomb gaps ~40 mV which could persist up to a temperature of ~60 K. The single-electron current oscillations showed a main oscillation with a period of 500 mV in gate voltage. Finer superimposed oscillations were also observed, attributed to additional islands and the formation of an MTJ.

The operating temperature in these SETs is limited not only by the grain size and the associated inter-grain capacitances, but also by the tunnel resistance and height of the GB potential barriers. The low operating temperature of these SETs, even though the grain size was small enough and the charging energy large enough to observe high-temperature effects, could be associated with a comparatively low barrier height. The barrier height could be estimated using Arrenhius plots of the conductance of the device as a function of inverse temperature (Fig. 10.10). Above a transition temperature T_1~60 K, the conduction mechanism could be attributed to thermionic emission across a distribution of potential barrier heights with various activation energies. The maximum gradient obtained in this region corresponded to an activation energy E_A ~40 meV, which could be associated with the maximum height of the amorphous silicon GB tunnel barriers. This is not high enough, relative to k_BT~25 meV at room temperature, to confine electrons on the grains.

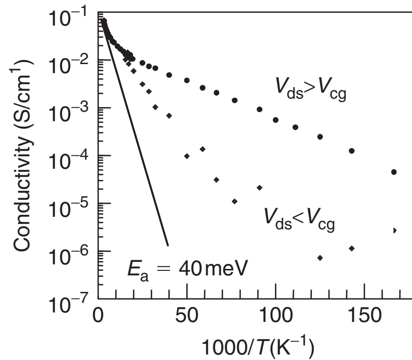

Figure 10.10 Arrenhius plot of conductivity versus inverse temperature in nc-Si point-contact SET, for V_{ds} = 50 mV>V_{cg}, and V_{ds} = 0 V<V_{cg}. Here V_{cg}~10 mV.

The operating temperature of point-contact SETs in VHF PECVD nc-Si can be raised to room temperature by raising the GB tunnel barrier height, using selective oxidation of the amorphous silicon GBs into SiO_x [54–56]. These devices were again prepared in an n-type VHF PECVD nc-Si film with crystalline silicon grains 4–8 nm in size, and amorphous silicon GBs. However, the film thickness was only ~20 nm and in comparison with earlier work, the point-contact dimensions could be as small as 20 nm×20 nm×20 nm.

After defining the SET, a low-temperature oxidation and high-temperature annealing process was used to oxidize the GBs selectively. This process was performed after defining the SETs, in order to maximize the surface area for oxygen diffusion, and to passivate simultaneously the surface states in the device. A relatively low oxidation temperature of 750°C for 1 h was used, in order to take advantage of the higher rate of diffusion of oxygen atoms at these temperatures into the GBs than in the crystalline silicon grains. The devices were then annealed at 1000°C for 15 min to improve the tunnel barrier height. Figure 10.11 shows an SEM image of a device. Microscopy of the SET before and after the thermal processing did not show significant change in the grain shape and size, due to encapsulation of the grains by SiO_x.

The selective oxidation of the GBs provides a method to engineer GB tunnel barriers with increased potential energy high enough to observe room temperature single-electron effects [54]. The source-drain current I_{ds}, measured with respect to the gate voltage V_{gs}, at temperatures from 23 to 300 K, is shown in Fig. 10.12a. Single-electron current oscillations with a single oscillation period of 3 V are seen, which can be associated with a single dominant charging island. The oscillations persist up to 300 K with an unchanged period. However, there is a fall in the peak-valley ratio as the temperature increases, due to a thermally activated increase in the tunnelling probability. Figure 10.12b shows the device I_{ds}–V_{ds} characteristics at 300 K, where a non-linearity corresponding to the Coulomb gap can be observed.

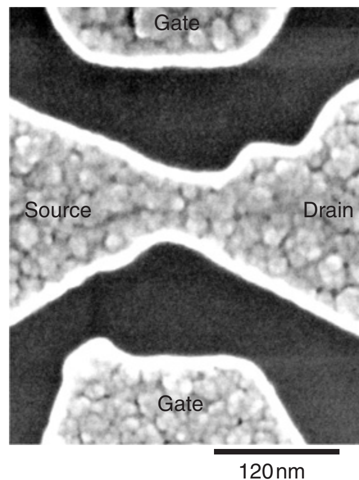

Figure 10.11 Scanning electron micrograph of a nc-Si point-contact SET with GB oxidation, for room temperature operation of the device.

The room temperature operation of these devices can be attributed to the formation of SiO_x at the GBs, which leads to an increase in the tunnel barrier height and better confinement of electrons on the grains even at room temperature. The tunnel barrier height, measured using Arrenhius plots of the device conductance, is ~170 meV. This is approximately seven times higher than $k_B T$ at room temperature and considerably larger than the maximum barrier height of ~40 meV for a similar device in the as-deposited nc-Si film. The oxygen incorporation in the oxidized and annealed nc-Si film can be investigated using secondary-ion mass spectroscopy (SIMS) to measure the oxygen depth profile [54]. It is seen that in a 30 nm wide point contact, SiO_x with $x = 0.67$ was formed. Greater amounts of oxygen could be incorporated into the GBs in smaller point contacts, due to diffusion from the sidewalls of the point contact. It is then possible for single-electron charging to occur on grains at the point contact centre even at room temperature. This is shown schematically in Fig. 10.13.

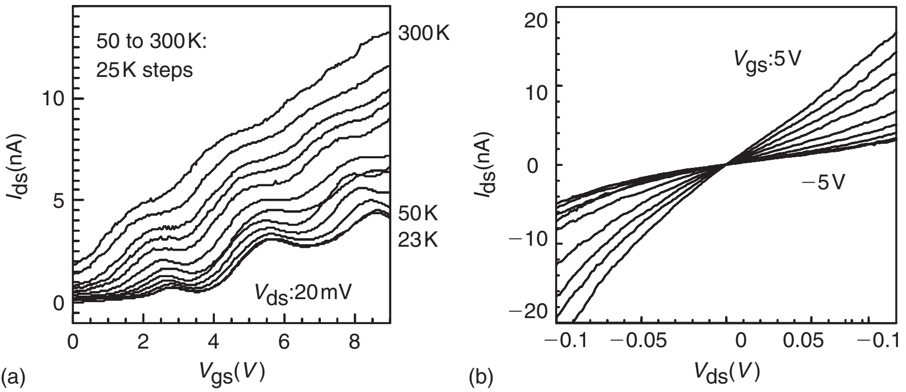

Figure 10.12 Electrical characteristics of a nc-Si point-contact SET with oxidized GBs (a) Temperature dependence of I_{ds}–V_{gs} oscillations. The oscillations persist to 300 K. (b) I_{ds}–V_{ds} characteristics at 300 K.

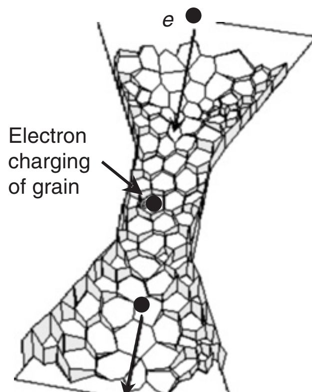

Figure 10.13 Schematic diagram of GB oxidation in a nc-Si point-contact.

In the preceding discussion, we have concentrated on single-electron effects only. However, in nc-Si SETs, quantum-confinement effects can also occur where the nc-Si grains not only exhibit single-electron charging phenomena but also show energy level quantization. Such a combination of single-electron and quantum-confinement effects, along with resonant tunnelling through the discrete energy levels, is common in GaAs/AlGaAs two-dimensional electron gas (2-DEG) devices at milli-Kelvin temperatures [13,25]. The existence of discrete energy levels within silicon nanocrystals has been inferred from observations of light emission from the nanocrystals [57–59]. In the electrical characteristics of a nc-Si quantum-dot transistor, these energy levels would lead to a complex series of resonant tunnelling peaks in the gate dependence of the transistor drain-source current. The peak separation corresponds to a sum of the single-electron and quantum-confinement energy level separation and the peak height corresponds to the coupling to the contacts of the electron wavefunction associated with each energy level. Natori *et al.* [60] have theoretically investigated this behaviour for silicon dots. Interactions between two or more quantum dots are also possible, and both electrostatic and electron wavefunction coupling effects can be observed. We will discuss these effects in detail in Section 10.3.

Vertical transport polycrystalline and nc-Si SET designs have also been demonstrated. Single-electron effects have been observed at 4.2 K in 45–100 nm diameter pillars formed in a material consisting of layers of polycrystalline silicon and Si_3N_4 [61]. In this device, the Si_3N_4 layers form the tunnel barriers and the polycrystalline silicon layers form the charging island. The lateral dimensions of the charging islands are defined not by the grain size but by the pillar sidewalls, i.e. lithographically. While the device does not show single-electron effects at room temperature, it can still be used as a vertical transport switching device at room temperature. A vertical transport device has considerable advantages in device integration, e.g. it can be stacked on top of the gate of a MOSFET to form a random-access memory gain cell where the number of stored electrons can be as small as $\sim$1000 [62]. This is a large reduction over the number of electrons used in a conventional one-transistor, one-capacitor DRAM cell and holds considerable promise for future advanced DRAM applications.

10.2.4 “Grain-Boundary” Engineering

The previous sections have discussed the significance of the GB potential barrier in SETs in continuous nc-Si films. Control of the height of this barrier is crucial to the confinement of electrons on the grains at higher temperatures, and the operation of room temperature SETs. By contrast, the reduction of the GB potential barrier is important in reducing the film resistivity, and improving the effective carrier mobility in the nc-Si. Different “GB engineering” processes can be used for these requirements.

The effect of oxidation and annealing on the electrical properties, and the structure of the GBs in heavily doped SPC polycrystalline silicon, has been characterized in detail using bulk films, and using 30 nm wide nanowires [63]. Oxidation at 650–750°C was seen to oxidize selectively the GBs, and subsequent annealing at 1000°C was seen to increase the associated potential barrier height and resistance.

These observations were explained by structural changes in the Si—O network at the GBs, and the competition between surface oxygen diffusion and oxidation from the GBs in the crystalline grains. This work suggested that a combination of oxidation and annealing provided a method for better control of the GB potential barrier height and width in the polycrystalline silicon and nc-Si thin films.

In contrast, hot H_2O-vapour annealing effectively reduces the GB barrier height [64]. Experiments on nanowire devices fabricated in LPCVD polycrystalline silicon thin films showed that hot H_2O-vapour annealing effectively reduced the GB dangling bonds and the corresponding potential barrier height. In addition, the process narrowed the distribution of the barrier height value across different devices significantly. These effects could be attributed to oxidation in the vicinity of the film surface, and hydrogenation in the deeper regions of the film. These results suggested that H_2O annealing could improve the carrier transport properties by opening up shorter percolation paths, and by increasing the effective carrier mobility and density.

10.2.5 Single-Electron Transistors Using Silicon Nanocrystals

The preceding sections have concentrated on SETs fabricated in continuous nc-Si films. In such a film, the GBs are narrow (~1 nm) and if the material is heavily doped, the SET has a comparatively moderate resistance (~100 kΩ or greater) outside the Coulomb blockade region. However, we have seen that single-electron charging effects can be overcome thermally by increasing electron delocalization with temperature. The electrons can be localized far more strongly in a discontinuous nc-Si film with higher potential barriers between the grains. One of the earliest observations of single-electron effects at room temperature was by Yano *et al.* [5], in nanowires fabricated in ultra-thin (~3 nm), strongly granular, nc-Si layers with grains ~1 nm in size (Fig. 10.14a). In these materials, the grains can be separated by gaps of comparable size. Such a system can show strong single-electron effects in the *I*–*V* characteristics even at room temperature. However, the large tunnel gap resistance leads to a low device current, ~10 fA. In a similar room temperature SET design, Choi *et al.* [65] have used a thin, discontinuous, PECVD deposited film with 8–10 nm diameter silicon grains. Metal source and drain electrodes separated by

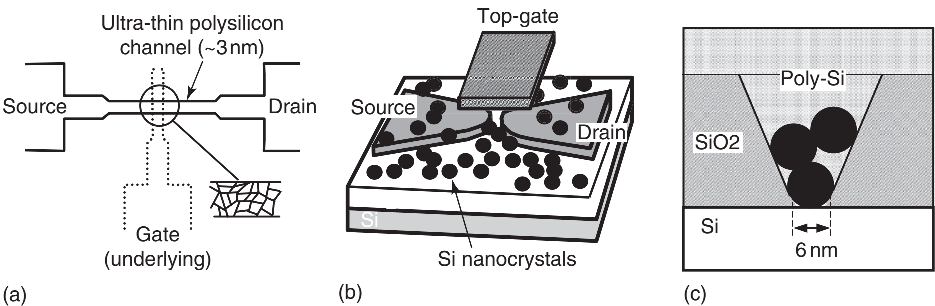

Figure 10.14 Single-electron transistors using silicon nanocrystals. (a) Device using an ultra-thin nc-Si film [5]. (b) Device using deposited nanocrystals [68]. (c) Vertical transport device with deposited nanocrystals [69].

a gap of <30 nm were deposited on top of the film and used to apply a voltage across the grains.

Silicon nanocrystals provide a means to form precisely the SET islands using growth techniques. A very promising technique for this purpose is to grow the silicon nanocrystals using plasma decomposition of SiH_4, e.g. $\sim 8 \pm 1$ nm size crystals with a surface oxide ~ 1.5 nm thick can be prepared [7,8]. A number of different configurations of SET designs are possible using these techniques [66–69]. These include planar devices where the nanocrystals are deposited on source and drain contacts defined in SOI material, separated by a narrow 30 nm gap (Fig. 10.14b). A top gate supported on a deposited oxide layer is used to control the current. In this configuration, it is possible to observe single-electron charging effects in the device transconductance up to room temperature [68]. An alternative is to deposit the nanocrystals in a nanoscale hole etched in a silicon dioxide layer, and then top-fill the hole with polycrystalline silicon [69]. This is shown schematically in Fig. 10.14c.

10.2.6 Comparison with Crystalline Silicon SETs

We observe that while nc-Si nanowire and point-contact SETs (Sections 10.2.2 and 10.2.3) appear to be similar superficially to crystalline Si nanowire SETs [30–35], the mechanism for formation of the tunnel barriers is very different. The tunnel barriers in the nc-Si devices are defined by the GBs. While additional disorder effects associated with the device surface conditions or the non-uniformity of the dopant distribution (the proposed mechanism for crystalline silicon nanowire SETs) can also occur, they are less significant. We have seen that careful preparation of the nc-Si film can be used to control the tunnel barrier properties more accurately. This implies that the active regions of the device, i.e. the grains and GBs within the nanowire or point contact, can be defined precisely by material processing techniques rather than high-resolution lithography or disorder, and very large numbers of quantum dots can be formed simultaneously over the entire chip area if necessary. Silicon nanocrystals also provide a means for this (Section 10.2.5). Such a process is an extremely attractive alternative to high-resolution lithography at the nanometre scale over a large area. The SET islands can also be grown or deposited at any convenient stage of the process, greatly increasing in flexibility the fabrication process, e.g. a nc-Si room temperature SET could be incorporated within the gate of a scaled Si MOSFET to define a room-temperature few-electron random access memory cell.

10.3 Electron coupling effects in nanosilicon

It is possible to use the nc-Si point-contact SET to investigate electronic interactions between two or more nanosilicon grains. By varying the dimensions of the point contact, the number of grains taking part in the single-electron transport process can be varied, and by tailoring the GB selective oxidation process (Section 10.2.4), the strength of the inter-grain electron coupling can be controlled. It is then possible to operate the device at low temperature as a double- or multiple-quantum-dot device with electron interactions between the quantum dots formed at the grains.

Electrostatic coupling effects have been investigated in great detail at milli-Kelvin temperatures in double quantum dots formed in GaAs/AlGaAs 2-DEG materials (a review may be found in [70]). In these experiments, two gates are used to change the potentials of two quantum dots quasi-independently, and a plot of the Coulomb oscillations versus two gate voltages forms hexagonal regions of constant electron number on the quantum dots, associated with single-electron interactions between the dots. This forms a "charge stability" diagram where the total electron number changes by one between neighbouring hexagons. If the quantum dots are strongly tunnel coupled, then the electron wavefunctions on the two dots can also interact with each other, forming new "quasi-molecular" states, analogous to a covalent bond. Resonant tunnelling through these states leads to additional peaks in the device conductance. These states have been observed near ~50 mK temperature in measurements on GaAs/AlGaAs double quantum dots [71].

We now discuss electron coupling effects in nc-Si point-contact SETs [52,72]. The devices used point contacts ~30 nm × 30 nm × 40 nm in size, with two side-gates, and were fabricated in a ~40 nm thick heavily doped LPCVD film with grain size from ~10 to 30 nm and ~1 nm thick amorphous Si GBs. Only a few grains existed within the channel at most, and different grains contributed in varying degrees to the device conduction. A scanning electron micrograph of the device is shown in Fig. 10.15. By modifying the inter-grain coupling by selective oxidation of the GBs, only electrostatic, or combined electrostatic and electron wavefunction coupling effects between two quantum dots could be observed at 4.2 K in the Coulomb oscillation pattern as a function of the two gate voltages. Different grains influenced the Coulomb oscillations in different ways, e.g. a single or two grains could dominate the Coulomb oscillations, or nearby grains could electrostatically switch the oscillations without taking part directly in conduction across the device.

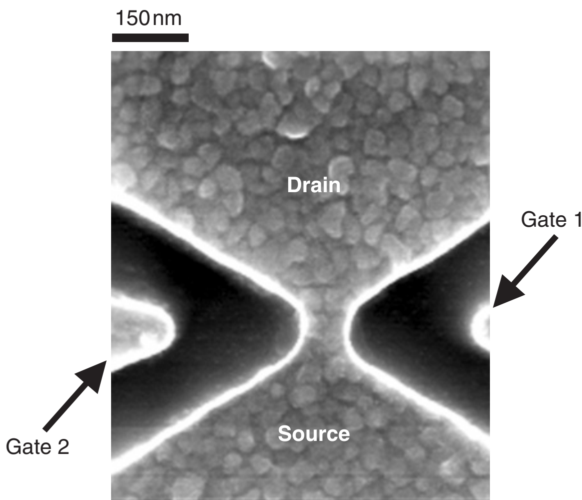

Figure 10.15 Scanning electron micrograph of a nc-Si point-contact transistor for the measurement of electron coupling effects.

The GB properties in these devices were controlled by varying the duration of the selective oxidation process, and by subsequent argon annealing. If the device was oxidized at 650–750°C, followed by annealing in argon at 1000°C, then this created a high- and wide-GB tunnel barrier (>100 meV) where electrostatic coupling effects dominated. If the device was oxidized only, without annealing, then the GB tunnel barriers remained low (~40 meV) and narrow and the grains were more strongly coupled. These devices showed both electrostatic and electron wavefunction coupling effects.

10.3.1 Electrostatic Coupling Effects

Figure 10.16a shows a three-dimensional grey-scale plot of the drain-source current I_{ds} in a device with electrostatically coupled grains at 4.2 K, as a function of the voltages on gate 1 and gate 2 (V_{g1} and V_{g2}, respectively) and $V_{ds} = 2$ mV. The maximum value of the current (white regions in the plot) is relatively low ($I_{ds} = 1.2$ pA). A series of lines (marked using dotted lines) are formed by shifts in the Coulomb oscillation positions as a function of both V_{g1} and V_{g2}. These oscillation lines occur when the single-electron energy levels in the point-contact align with the Fermi energy in the source. As both the gates couple to the grain, the energy of a single-electron level relative to the source Fermi energy depends on a linear combination of the two gate voltages. This leads to the oscillation peaks and valleys tracing diagonal lines across the plot. Switching of the position of the oscillation lines is also observed, which implies an abrupt change in the energy of the corresponding single-electron level. The behaviour can be attributed to single-electron charging of a nearby grain, coupled electrostatically to the dominant grain [52].

The characteristics of Fig. 10.16a can be understood using the circuit of Fig. 10.16b. The circuit uses a grain (QD1), connected to the source and drain by tunnel junctions T_1 and T_2 and coupled capacitively to the two gates by the capacitors C_{g1} and C_{g4}. A nearby grain (QD2), coupled to QD1 by the tunnel capacitor C_f, can be charged with electrons from the source via tunnel junction T_3. QD2 is also coupled capacitively to the gates. In such an arrangement, the Coulomb oscillations of QD1 form a series of lines as a function of the two gate voltages due to the capacitive coupling of the energy levels of QD1 to both gates. The solid lines in Fig. 10.16c show this schematically. The electron number on QD1 differs by one between regions on either side of a line and this number increases as the gate voltages become more positive. The lines switch in position when the gate voltages overcome the Coulomb blockade of QD1 and the Coulomb blockade of QD2 (along the dotted lines) simultaneously, i.e. at the intersection of the solid and dotted lines. Here, an electron transfers from the source onto QD2, and this change in charge switches (via C_f) the current through QD1. Note that there is no conduction path from source to drain across QD2. The overlap between the single-electron oscillation lines in the experimental characteristics is a function of the cross capacitances C_{g3} and C_{g4} between the grains and the gates.

10.3.2 Electron Wavefunction Coupling Effects

In contrast to the device characteristics discussed in Fig. 10.16, which show only electrostatic coupling effects between grains, additional wavefunction coupling

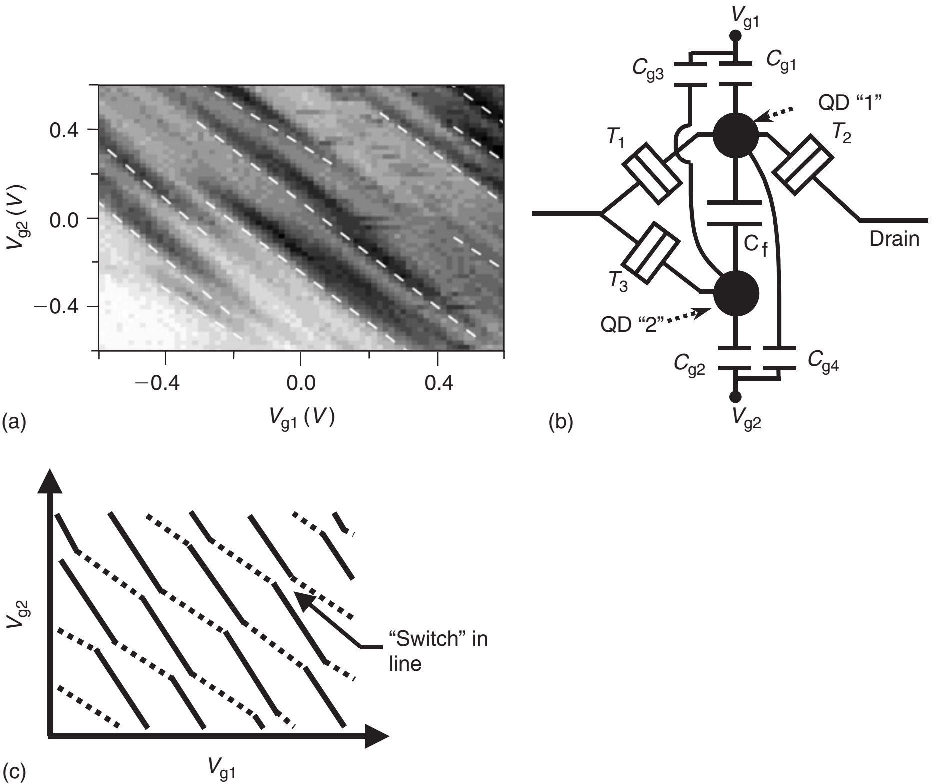

Figure 10.16 Electrostatic coupling effects in a nc-Si point-contact. (a) Grey-scale plot of the current at 4.2 K, as a function of two gate voltages. $V_{ds} = 2$ mV and the maximum value of $I_{ds} = 1$ nA (white). (b) Double quantum-dot model. (c) Schematic of Coulomb oscillation lines.

effects can be observed in devices that are oxidized only. In these devices, the GB tunnel barriers remain low and narrow. In a region (Fig. 10.17a) where the Coulomb oscillation lines from two quantum dots QD1 and QD2 (solid and dotted lines, respectively) intersect, the corresponding energy levels from each quantum dot are resonant at two points "1" and "2". With strong coupling between these levels, due to the weak GB tunnel barriers, additional "quasi-molecular" states can be formed. This is shown schematically in Fig. 10.17b.

Khalafalla *et al.* [72] have observed the formation of quasi-molecular states at 4.2 K in an nc-Si point-contact SET, oxidized at 750°C for 30 min only. In a measurement of the device conductance across a region where the oscillation lines from two QDs intersected, i.e. at the two points "1" and "2" (Fig. 10.17a), a set of four peaks was observed. These peaks could be fitted using the sum of four Lorentzian peaks. The position of the peaks, i.e. near the points "1" and "2", where two energy levels in adjacent grains were resonant, and their strongly coupled nature, suggested that they were quasi-molecular states formed by the delocalization of the electron wavefunctions over adjacent tunnel-coupled grains. By comparison, in devices with oxidation and annealing, electron delocalization was inhibited because of the higher and wider GB-tunnel barriers.

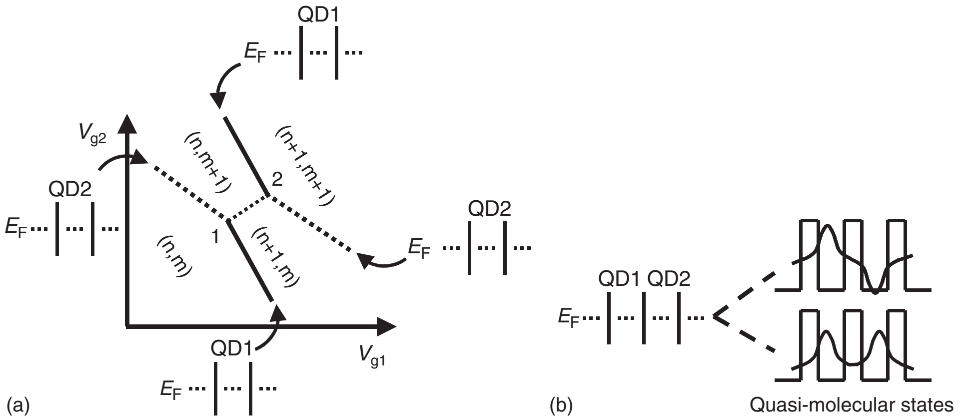

Figure 10.17 Electron wavefunction coupling effects in a nc-Si point-contact. (a) Resonance (at points "1" and "2") between energy levels on two quantum dots, in a plot of the Coulomb oscillations versus the gate voltages V_{g1} and V_{g2}. (b) Quasi-molecular states.

10.4 Nanosilicon memory

Single-electron effects provide a means to control precisely small amounts of charge down to a single electron, raising the possibility of single- or few-electron memory circuits with high potential for scaling. In these memories, either the Coulomb blockade effect in a SET is used to trap electrons on a storage capacitor or the capacitor is scaled to an extent that only single or a small number of electrons can be stored on it. Following the early development of single-electron memory using an MTJs defined in GaAs delta-doped layers [19], other memorie cells were demonstrated in both crystalline SOI [73–76] and nanosilicon materials. In the following, we introduce nanosilicon few-electron memory cells.

There has been considerable interest in the development of few-electron memory cells using silicon nanocrystals to store charge (5,6,77–83). A number of these memory cells [6,77–81] are analogues of non-volatile "FLASH" memory cells, where the charge is stored on a "floating gate" formed by a discontinuous layer of silicon nanocrystals. Figure 10.18a shows a schematic diagram of such a memory cell. The silicon nanocrystals can be grown in silicon-rich oxide, by direct seeding on an oxide, by high-density silicon ion-implantation into an oxide or by plasma decomposition of SiH_4. The nanocrystals are sandwiched in the gate stack of a silicon MOSFET, separated from the channel by a thin layer of oxide and from the gate by an additional, thicker layer of oxide. Charge can be injected into the nanocrystals by direct tunnelling from the channel across the thin oxide, using a large voltage on the gate. This charge can be sensed by a shift in the threshold voltage of the MOSFET.

In conventional FLASH memory cells, a thicker oxide layer is used above the channel and a high voltage is necessary to transfer electrons on to the gate by Fowler–Nordheim tunnelling or by hot-electron injection. The high electric field and current in the Fowler–Nordheim tunnelling process degrades the oxide over numerous operations of the cell by generating traps, leading to an increasing leakage

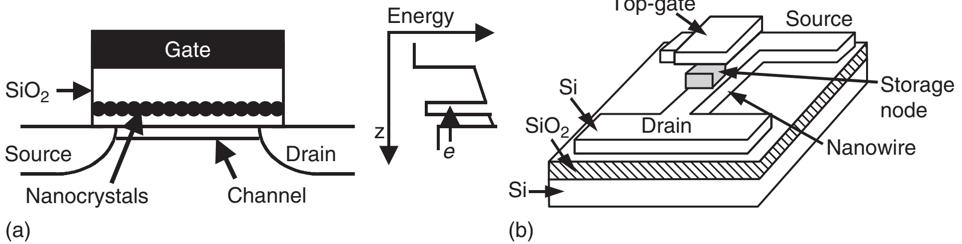

Figure 10.18 Nanosilicon memory cells. (a) Silicon nanocrystal memory cell. (b) Memory cell with a single nanoscale storage node.

current which limits the lifetime of the memory. The problem becomes even more severe in a scaled FLASH memory cell, where the stored charge is small and any leakage path quickly discharges the stored charge. In a nanocrystal memory cell, the electric field can be smaller and any leakage paths affect only a small number of nanocrystals. Charge is retained in the remaining nanocrystals and it is less easy to fully discharge the cell. A typical example of such a memory cell, fabricated by Hanafi *et al.* [78], uses 3 nm diameter silicon nanocrystals at a density of $1\times10^{12}/\text{cm}^3$. The nanocrystals are separated from each other by ~7 nm and the lower oxide layer is ~1 nm thick. If a charge corresponding to one electron per nanocrystal is stored, then the threshold voltage shifts by 0.35 V, which can change the underlying MOSFET threshold current by 4–5 orders of magnitude. The retention time of such a memory cell can be $\sim10^5$ s. In alternative designs [77], where the nanocrystals are created by plasma decomposition of SiH_4, the nanocrystal size can also be well controlled.

Single-electron charging and quantum-confinement effects can influence the electric field at which electrons are injected into the nanocrystals. These effects also lead to the stored electrons being separated in energy, providing a means to operate the cell with a precise number of electrons by controlling the magnitude of the writing voltage. These effects can be observed more clearly in highly scaled analogues of discontinuous gate FLASH memories [82,83], where only a single-silicon nanocrystal defines the floating gate. This nanocrystal is defined by using high-resolution lithography to fabricate a nanoscale silicon island in a polycrystalline silicon layer, deposited on the gate oxide of a nanoscale MOSFET (Fig. 10.18b). Such a memory cell can show discrete charging steps in the MOSFET current as a function of the gate voltage, where each step corresponds to the addition of single electrons onto the nanocrystal. The cell can then be operated with a precisely known number of electrons, down to a single electron. The write time can be less than 1 μs and the retention time can be as long as 5 s at room temperature.

In contrast to these FLASH type memories, Yano *et al.* have used their room temperature SET [5], fabricated in an ultra-thin, strongly granular and non-uniform (~3 nm) nc-Si layer (Fig. 10.14a), as the basis of a prototype 128 Mbit memory operating at room temperature [4]. Memory operation occurs due to the tunnelling of single or small numbers of electrons on to storage nodes formed by the grains in the nc-Si layer. The write-erase times are ~10 μs and the retention time is up to 1 month.

REFERENCES

1. G.F. Grom, D.J. Lockwood, J.P. McCaffery, N.J. Labbe, P.M. Fauchet, B. White Jr., J. Diener, D. Kovalev, F. Koch and L. Tsybeskov, *Nature* **407**, 358 (2000).
2. W.L. Wilson, P.F. Szajowski and L.E. Brus, *Science* **262**, 1242 (1993).
3. K.A. Littau, P.F. Szajowski, A.J. Muller, A.R. Kortan and L.E. Brus, *J. Phys. Chem.* **97**, 1224 (1993).
4. K. Yano, T. Ishii, T. Sano, T. Mine, F. Murai, T. Hashimoto, T. Kobayashi, T. Kure and K. Seki, *Proc. IEEE* **87**, 633 (1999).
5. K. Yano, T. Ishii, T. Sano, T. Hashimoto, T. Kobayashi, F. Murai and K. Seki, *Appl. Phys. Lett.* **67**, 828 (1995).
6. S. Tiwari, H. Hanafi, A. Hartstein, E.F. Crabbé and K. Chan, *Appl. Phys. Lett.* **68**, 1377 (1996).
7. S. Oda and M. Otobe, *Mater. Res. Soc. Symp. Proc.* **358**, 721 (1995).
8. M. Otobe, T. Kanai and S. Oda, *Mater. Res. Soc. Symp. Proc.* **377**, 51 (1995).
9. A. Nakajima, Y. Sugita, K. Kawamura, H. Tomita and N. Yokoyama, *J. Appl. Phys.* **80**, 4006 (1996).
10. T. Kamiya, K. Nakahata, K. Ro, C.M. Fortmann and I. Shimuzu, *Mater. Res. Soc. Symp. Proc.* **557**, 513 (1999).
11. T. Kamiya, K. Nakahata, Y.T. Tan, Z.A.K. Durrani and I. Shimuzu, *J. Appl. Phys.* **89**, 6265 (2001).
12. K. Nakahata, K. Ro, A. Suemasu, T. Kamiya, C.M. Fortmann and I. Shimuzu, *Jpn. J. Appl. Phys. Part 1* **39**, 3294 (2000).
13. H. Grabert and M.H. Devoret, Eds., *Single Charge Tunneling – Coulomb Blockade Phenomena in Nanostructures*, NATO ASI Series B (Plenum Press, New York, U.S.A., 1991).
14. D.K. Ferry, *Transport in Nanostructures* (Cambridge University Press, New York, 1996).
15. K.K. Likharev, *Proc. IEEE* **87**, 606 (1999).
16. U. Meirav and E.B. Foxman, *Semicond. Sci. Technol.* **10**, 255 (1995).
17. H. Ahmed, *J. Vac. Sci. Technol. B* **15**, 2101 (1997).
18. International Technology Roadmap for Semiconductors, (2005) available at: http://www.itrs.net
19. K. Nakazato, R.J. Blaikie, J.R.A. Cleaver and H. Ahmed, *Electron. Lett.* **29**, 384 (1993).
20. B. Prince, *Semiconductor Memories*, 2nd edition (John Wiley and Sons, New York, 1996).
21. H.P. Wong, D.J. Frank, P.M. Solomon, C.H.J. Wann and J.J. Welser *Proc. IEEE* **87**, 537 (1999).
22. K. Nakazato, K. Itoh, T. Sakata, H. Mizuta, H. Ahmed, T. Kisu and M. Kato, ISSCC2000, 132 (2000).
23. Y.T. Tan, T. Kamiya, Z.A.K. Durrani and H. Ahmed, *J. Appl. Phys.* **94**, 633 (2003).
24. M.A. Kastner, *Phys. Today* **46**, 24 (1993).
25. L.P. Kowenhoven, C.M. Marcus, P.L. McEuen, S. Tarucha, R.M. Westervelt and N.S. Wingreen, *Mesoscopic Electron Transport*, Ed. L.L. Sohn, *et al.* (Kluwer Academic Press, Dordrecht, Netherlands, 1997).
26. T.A. Fulton and G.L. Dolan, *Phys. Rev. Lett.* **59**, 109 (1987).
27. J.H.F. Scott-Thomas, S.B. Field, M.A. Kastner, H.I. Smith and D.A. Antoniadis, *Phys. Rev.* Lett. **62**, 583 (1989).
28. H. Van Houten and C.W.J. Beenakker, *Phys. Rev. Lett.* **63**, 1893 (1989).
29. D.J. Paul, J.R.A. Cleaver, H. Ahmed and T.E. Whall, *Appl. Phys. Lett.* **63**, 631 (1993).
30. D. Ali and H. Ahmed, *Appl. Phys. Lett.* **64**, 2119 (1994).
31. L. Zhuang, L. Guo and S.Y. Chou, *Appl. Phys. Lett.* **72**, 1205 (1998).
32. Y. Takahashi, H. Namatsu, K. Kurihara, K. Iwadate, M. Nagase and K. Murase, *IEEE Trans. Electron Dev.* **43**, 1213 (1996).
33. H. Ishikuro, T. Fujii, T. Saraya, G. Hashiguchi, T. Hiramoto and T. Ikoma, *Appl. Phys. Lett.* **68**, 3585 (1996).
34. R.A. Smith and H. Ahmed, *J. Appl. Phys.* **81**, 2699 (1997).
35. H. Ishikuro and T. Hiramoto, *Appl. Phys. Lett.* **74**, 1126 (1999).
36. H.O. Müller, D.A. Williams, H. Mizuta, Z.A.K. Durrani, A.C. Irvine and H. Ahmed, *Physica B* **272**, 85 (1999).
37. T.I. Kamins, *J. Appl. Phys.* **42**, 4357 (1971).
38. J.Y.W. Seto, *J. Appl. Phys.* **46**, 5247 (1975).
39. G. Baccarani, B. Ricco and G. Spandini, *J. Appl. Phys.* **49**, 5565 (1978).

40. J. Levinson, F.R. Shepard, P.J. Scanlon, W.D. Westwood, G. Este and M. Rider, *J. Appl. Phys.* **53**, 1193 (1982).
41. M.E. Cower and T.O. Sedgwick, *J. Electrochem. Soc.* **119**, 1565 (1972).
42. A.L. Fripp, *J. Appl. Phys.* **46**, 1240 (1975).
43. T.I. Kamins and P.A. Pianetta, *IEEE Electron Dev. Lett.* **1**, 214 (1980).
44. J.W. Tringe and J.D. Plummer, *J. Appl. Phys.* **87**, 7913 (2000).
45. B.I. Shklovskii and A.L. Efros, *Electronic Properties of Doped Semiconductors* (Springer, Berlin, 1984).
46. Y. Dong, C. Wang, B.L. Wehrenberg and P. Guyot-Sionnest, *Phys. Rev. Lett.* **92**, 216802 (2004).
47. Y. Furuta, H. Mizuta, K. Nakazato, Y.T. Tan, T. Kamiya, Z.A.K. Durrani, H. Ahmed and K. Taniguchi, *Jpn. J. Appl. Phys.* **40**, L615 (2001).
48. Y. Furuta, H. Mizuta, K. Nakazato, T. Kamiya, Y.T. Tan, Z.A.K. Durrani and K. Taniguchi, *Jpn. J. Appl. Phys.* **41**, 2675 (2002).
49. A.C. Irvine, Z.A.K. Durrani, H. Ahmed and S. Biesemans, *Appl. Phys. Lett.* **73**, 1113 (1998).
50. Y.T. Tan, Z.A.K. Durrani and H. Ahmed, *J. Appl. Phys.* **89**, 1262 (2001).
51. Y. Furuta, H. Mizuta, K. Nakazato, T. Kamiya, Y.T. Tan, Z.A.K. Durrani and K. Taniguchi, *Jpn. J. Appl. Phys.* **41**, 2675 (2002).
52. M.A.H. Khalafalla, H. Mizuta and Z.A.K. Durrani, *IEEE Trans. Nanoelectron.* **2**, 271 (2003).
53. Y.T. Tan, T. Kamiya, Z.A.K. Durrani and H. Ahmed, *Appl. Phys. Lett.* **78**, 1083 (2001).
54. Y.T. Tan, Z.A.K. Durrani and H. Ahmed, *J. Appl. Phys.* **89**, 1262 (2001).
55. Z.A.K. Durrani, T. Kamiya, Y.T. Tan and H. Ahmed, *Microelectron. Eng.* **63**, 267 (2002).
56. Z.A.K. Durrani, *Physica E* **17**, 572 (2003).
57. Y. Kanemitsu, *Phys. Rep.* **263**, 1 (1995).
58. Y. Kanemitsu, S. Okamoto, M. Otobe and S. Oda, *Phys. Rev. B* **55**, 7375 (1997).
59. L.E. Brus, P.F. Szajowski, W.L. Wilson, T.D. Haris, S. Shuppler and P.H. Citrin, *J. Am. Chem. Soc.* **117**, 2915 (1995).
60. K. Natori, T. Uehara and N. Sano, *Jpn. J. Appl. Phys.* **39**, 2550 (2000).
61. D.M. Pooley, H. Ahmed, H. Mizuta and K. Nakazato, *Appl. Phys. Lett.* **74**, 2191 (1999).
62. H. Mizuta, M. Wagner and K. Nakazato, *IEEE Trans. Electron Dev.* **48**, 1103 (2001).
63. T. Kamiya, Z.A.K. Durrani and H. Ahmed, *Appl. Phys. Lett.* **81**, 2388 (2002).
64. T. Kamiya, Z.A.K. Durrani, H. Ahmed, T. Sameshima, Y. Furuta, H. Mizuta and N. Lloyd, *J. Vac. Sci. Tech. B* **21**, 1000 (2003).
65. B.H. Choi, S.W. Hwang, I.G. Kim, H.C. Shin, Y. Kim and E.K. Kim, *Appl. Phys. Lett.* **73**, 3129 (1998).
66. A. Dutta, M. Kimura, Y. Honda, M. Otobe, A. Itoh and S. Oda, *Jpn. J. Appl. Phys.* **36**, 4038 (1997).
67. A. Dutta, S.P. Lee, Y. Hayafune, S. Hatatani and S. Oda, *Jpn. J. Appl. Phys.* **39**, 264 (2000).
68. A. Dutta, S. Oda, Y. Fu and M. Willander, *Jpn. J. Appl. Phys.* **39**, 4647 (2000).
69. K. Nishiguchi and S. Oda, *J. Appl. Phys.* **88**, 4186 (2000).
70. W.G. Van der Wiel, S. De Franceschi, J.M. Elzerman, L.P. Kouwenhoven, T. Fujisawa and S. Tarucha, *Rev. Mod. Phys.* **75**, 1 (2003).
71. R.H. Blick, D. Pfannkuche, R.J. Haug, K.K.V. Klitzing and K. Eberl, *Phys. Rev. Lett.* **80**, 4032 (1998).
72. M.A.H. Khalafalla, Z.A.K. Durrani and H. Mizuta, *Appl. Phys. Lett.* **85**, 2262 (2004).
73. N. Stone and H. Ahmed, *Appl. Phys. Lett.* **73**, 2134 (1998).
74. Z.A.K. Durrani, A.C. Irvine, H. Ahmed and K. Nakazato, *Appl. Phys. Lett.* **74**, 1293 (1999).
75. A.C. Irvine, Z.A.K. Durrani and H. Ahmed, *J. Appl. Phys.* **87**, 8594 (2000).
76. Z.A.K. Durrani, A.C. Irvine and H. Ahmed, *IEEE Trans. Electron Dev.* **47**, 2334 (2000).
77. B.J. Hinds, K. Nishiguchi, A. Dutta, T. Yamanaka, S. Hatanani and S. Oda, *Jpn. J. Appl. Phys.* **39**, 4637 (2000).
78. H.I. Hanafi, S. Tiwari and I. Khan, *IEEE Trans. Electron Dev.* **43**, 1553 (1996).
79. P. Normand, E. Kapetanakis, P. Dimitrakis, D. Tsoukalas, K. Beltsios, N. Cherkashin, C. Bonafos, G. Benassayag, H. Coffin, A. Claverie, V. Soncini, A. Agarwal and M. Ameen, *Appl. Phys. Lett.* **83**, 168 (2003).
80. S. Tiwari, F. Rana, K. Chan, L. Shi and H. Hanafi, *Appl. Phys. Lett.* **69**, 1232 (1996).
81. I. Kim, S. Han, K. Han, J. Lee and H. Shin, *IEEE Electron Dev. Lett.* **20**, 630 (1999).
82. J.J. Welser, S. Tiwari, S. Rishton, K.Y. Lee and Y. Lee, *IEEE Electron Dev. Lett.* **18**, 278 (1997).
83. L.J. Guo, E. Leobung and S.Y. Chou, *Appl. Phys. Lett.* **70**, 850 (1997).

Index

A
Acoustic phonons, in silicon, 269–273
Air quality, detection of gases for, 162
Alkenes in colloid dispersion of H-terminated Si particles, thermal hydrosilylation of, 14
Amperometric detection, Si nanoparticles applications in, 70–71
Auger electron spectroscopy (AES) analysis, 21

B
$Ba_8@[Ag_xSi_{46-x}]$ clathrates, superconductivity, 107
$Ba_8@[Au_xSi_{46-x}]$ clathrates, superconductivity, 107
$Ba_8@[Cu_xSi_{46-x}]$ clathrates, superconductivity, 107
$Ba_8@[Ga_{16}Ge_{30}]$ clathrates, superconductivity, 107
Band structure of SiNWs, 243–244
Bardeen-Cooper-Schrieffer (BCS) theory, of phonon-mediated superconductivity, 107
$Ba_8@Si_{46}$ clathrates, 105
  superconductivity, 107–109
$Be@Si_{10}$ cluster, 129
$Be@Si_{12}$ cluster, 129
$Be@Sn_8$ cluster, 127, 129
Bethe-Salpeter equation, 44
Biochemical sensors, 161
Biophotonic imaging, nanoparticles use in, 68–70
Breast cancer cells, imaged by fluorescence microscope, 69
Butylamine, Si nanoparticles functionalization with, 11–15

C
Carbon fullerenes, 121, 127
Carbon nanotubes (CNTs), 186
  ballistic transport properties of, 218, 290
Cathodoluminescence, in Si nanoparticles, 27–29
CdS nanoparticles, 9
Chemical sensors, porous silicon in, 161
Complementary metal-oxide semiconductor (CMOS) technology, 149–150, 157, 319, 321, 328, 336–337, 340
Conduction band minimum (CBM), 243–244, 251–252
Coulomb blockade (CB) effect, 56, 187, 336–338, 356
Cr doped clusters, mass abundance spectra of, 124, 127, 144
Crossed nanowire (cNW)
  array-based address decoders, 193–194
  logic NOR gate, 191–192
  structures and devices, 191, 196
$CrSi_{12}$ cluster, 134
$Cr@Si_{14}$ cluster, 132
$CrSi_n$ clusters, photoionization mass spectrum of, 115–116
Crystalline pristine SiNWs, atomic structures of, 238–243
Crystalline silicon SETs and SiNW SET, 352
C_{60}Si-cluster-assembled films, 96
$C_{58}Si_2$ structures, 95–96
Cu-La@Si_{20} cluster, structure of, 137

D
Density functional theory (DFT), 43–44, 220
Deposition-diffusion-aggregation (DDA) model, 86
Diffusion Monte Carlo (DMC) method, 46
Distributed Bragg Reflectors (DBR), 327–328
Doped clathrates
  compressibility and pressure stability of, 109–110
  superconductivity in, 107–109
  tayloring band gap by doping, 105–107
Dye markers, 8
Dynamic random-access memories (DRAMs), 336

E
Electrodeposition, reconstitution of Si nanoparticles in films by, 31
Electroluminescence (EL), 168
  in Si nanoparticles, 27–29
Electronic structure of nanoclusters
  computational methods for
    applications to Si clusters, 46–49
    DFT methods, 44–45
    diffusion Monte Carlo method, 46
    Quantum Monte Carlo method, 45
    variational Monte Carlo method, 45–46

18-electron rule, 47
Electrophoresis, 31
Eleetro-less Ag coating of porous surface, 156
Elemental silicon clusters, 117
vibrational spectra of, 137–139
Encapsulated silicon structures, metal size dependence, 122–124
Endohedral doping, in silicon clathrates, 104–110, *See also* Doped clathrates
Endohedral silicon nanotubes, 301–307
cohesive energies E_c, 301–302, 304, 306
Erbium-doped fibre amplifiers (EDFA), 328–329, 331
Er-doped waveguide amplifiers (EDWAs), 328, 331–332
Escherichia coli bacteria, incubated in silicon nanoparticles, 70

F
Fe-doped SiNTs, 228–231
Fe@Si_{14} cluster, 133
Fe@Si_{16} cluster, 133
Fickian diffusion, 157
Field-effect transistors (FETs), *See* SiNW FETs
First principles molecular dynamics (FPMD), 54
FK-Ti@Si_{16} cluster, 138–139
absorption spectra, 143
FLASH memory cells, 356–357
Fluorescent markers, 9
Fourier transform infrared spectroscopy (FTIR) analysis, 17–19
Fowler-Nordheim tunnelling process, 356
Frank-Condon principle, 53
Frank-Kasper (FK) Zr@Si_{16} cluster, electronic spectra, 130

G
Gases, lower exposure limit (LEL) for detection by sensors, 162
Gel permission chromatography (GPC) analysis, 20
$Ge_{18}Mo_2$ nanotube, 235
$Ge_{36}Mo_5$ nanotube, 235
Ge nanotubes (GeNTs), 231–235
band structures of, 232–233
DOS for Nb- and W-doped infinite GeNTs, 236
metallic and semiconducting nanotubes, 233–235
$Ge_{18}Nb_2$ clusters, 234
$Ge_{36}Nb_5$ clusters, 234
$Ge_{24}Nb_4$ nanotube, 235
Grain-Boundary (GB) engineering process, 350–351

H
Hartree-Fock theory, 59
High-frequency nanowire circuits, 199–200
High-resolution transmission electron microscopy (HRTEM), image of Au/SiNW interface, 180
H_2O_2 effect, on Si nanoparticles surface reconstruction, 51–52
Humidity sensors
heating conditions influence on, 158–159
porous silicon in, 157–160
SEM cross-sections of, 158
thermoelectric cooler integrated, 158–159
Hybrid gold-silicon nanoparticle inks, 73
Hydrocarbon gas sensors, 164
Hydrogenated particles (supermolecule), 49–51
Hydrogenated silicon nanoparticles, structures, 224
Hydrogenated silicon nanowires, 244–253
atomic and electronic structures, 246–247, 249–250
band structures of, 249–250
doping and H defects effects, 251–253
Hydrogen-passivated SiNW, 297–300

I
Infrared radiation, photostability of Si nanoparticles under, 29
I_6@Si-34 clathrates, DFT-LDA band structure of, 106
I_8@Si_{46} clathrates, 105–107, 109
Isolated silicon clusters, *See* Si clusters

K
Kidney cells, imaged by laser scanning microscopy, 69
Knudsen diffusion, 157, 168
Kohn-Sham equations, 220

L
Langmuir-Blodgett (LB) assembly of SiNWs, 196–197
Laplace's law, 80
Large-scale integrated (LSI) circuits, 336–337
La@Si_{20}Na cluster, structure of, 137
Lattice dynamics of SiNWs, 261–267
Light emitting diode (LED), 316, 319–321
Lithium electrolyte-based PS microbattery electrodes, 170–172
Local density approximation (LDA), 44–45, 220
Low-energy cluster beam deposition (LECBD) technique, 79, 84–85, 86
Luminescent Si nanoparticles, *See* Silicon nanoparticles

M

Mass abundance spectra of
  Cr doped clusters, 124, 127, 144
  Mn doped clusters, 124, 128, 144
  Zn doped Sn_n and Pb_n clusters, 135
Metal encapsulated silicon clusters, 117
  absorption spectra, 142, 143
  closed packed structures, 129
  electronic configuration and isolated rhombus rule, 124–137
  empty and endohedral hydrogenated cages of, 139–142
  fullerene cages of, 121–122, 129, 139–142
  magnetic moment of metal atom, 142–144
  metal size dependence, 122–124
  reactivity of, 137
  vibrational properties, 137–139
Metal encapsulated silicon nanotubes, 222–225
  electronic structure and bonding nature, 225–227
  magnetism in, 228–231
Metallic and semiconducting Ge nanotubes, 233–235
Metal oxide
  semiconductor transistor, 336
  silicon memory devices, 66–68
Metal silicide nanowires (MSNW), 300–311
  cohesive energies E_c, 301–302, 304, 306
  endohedral silicon nanotubes, 301–307
  energy decomposition, 308–311
  yttrium silicide NW, 307–308
Microcrystallites, incident beam interaction with, 36–38
Micro electro-mechanical system (MEMS) technology, 149, 157
Mn doped clusters, mass abundance spectra of, 124, 128, 144
Mn-doped SiNTs, 228–231
$Mn@Ge_{12}$ cluster, magnetic moments, 143–144
$Mn@Sn_{12}$ cluster
  magnetic moments, 143–144
  stability of, 124
MOSFET, 73, 219, 356–357
$Mo@Si_{15}$ cluster, structure for, 130
$MoSi_n$ clusters, photoionization mass spectrum of, 115–116

N

$Na_xBa_{8-x}@Si_{46}$ clathrates, superconductivity, 107
Nanocapacitor, 66
Nanoclusters electronic structure, *See* Electronic structure of nanoclusters
Nanocrystalline silicon (nc-Si) films
  conduction in, 341–343
  silicon nanowire SETs, 343–346
Nanocrystalline silicon point-contact SET, 346–350, *See also* SiNW SET
  electrical characteristics of, 348–349
  with GB oxidation, 348–349
Nano electro-mechanical system (NEMS) technology, 149
Nanoelectronics
  crossed nanowire
    array-based address decoders, 193–194
    logic NOR gate, 191–192
    structures and devices, 191
  SiNWs for, 190–195
Nanoink printing, 73
Nanoparticles, *See* Silicon nanoparticles
Nanosilicon
  electron coupling effects, 352–356
    electron wavefunction coupling, 354–356
    electrostatic coupling, 354
  memory cells, 356–357
  SETs, 341–352, *See also* SiNW SET
Nano-silicon-organic ink, 73
Nanosolar cell, 71–72
Nanostructure building elements, atomic structure of, 226
Nanowire circuits, 199–200
Nanowire field-effect sensors, 201–202
Nanowire superlattices, 253–254
$Na_8@Si_{46}$ clathrates, 106, 109
N-channel SiNW FETs, 185–186
Ni-doped SiNTs, 229–231
$Ni@Ge_{10}$ cluster, 129, 135
$Ni@Si_{12}$ cluster, metal encapsulated fullerene cages of, 129
Non-crystalline pristine SiNWs, 237–238
NO_2 sensors, 162–163
Novel silicon-carbon phases, 79
Nuclear magnetic resonance (NMR) analysis, 19–20

O

Optical detection of magnetic resonance (ODMR), 153
Optical gain media, 39
Optical phonons, in silicon, 273–275
$Os@Si_{15}$ cluster, 133

P

$Pa@Si_{20}$ cluster, magnetic moments, 144
P-channel SiNW FETs, 184–185, 186
Pentagonal SiNW, 290–297
  ground state of, 292–296
  kinetic advantages of, 296–297
  shape, 291–292
  Wulff construction for, 291

Pentene, Si nanoparticles functionalization with, 14
Phonon density of states (ph-DOS), of silicon diamond, 101–103
Phonon-mediated superconductivity, BCS theory of, 107
Phonons
acoustic phonons, 269–273
dispersion in SiNWs, 262–267
optical phonons, 273–275
Richter model for Raman scattering from, 267–269
in silicon, 269–278
structure of Si nanoparticles, 59–60
theoretical models for, 261–269
thermal conductivity and, 275–278
Photoluminescence (PL), 150
induced metallization, 155, 168
from porous silicon, 153–155
Photostability, of Si nanoparticles under UV and infrared radiation, 29
Photovoltaic Si solar cells, 71
Polycrystalline Si solar cells, 71–72
Porous silicon (PS)
applications of, 149–150
chemical sensors, 161
electrochemical etch cell configuration used to produce film of, 152
eleetro-less silver coating of, 156
gas sensors, 161–168
humidity sensors, 157–160
hybrid films, 152, 156
lithium electrolyte-based microbattery electrodes, 170–172
morphologies, 152
nanoparticle photocatalytic coating of, 168–170
photoluminescent enhancement and stabilization, 155
PL from, 153–155
PL-induced metallization, 155, 168
pore structure, 151–153
PV response, 154–155
quantum dot (QD) structure introduction into, 168
sensors, 157–168
Post-Hartree-Fock methods, 45
Precipitation spray, for reconstitution of Si nanoparticles in films, 30
PS gas sensors
fabrication steps for, 165
hydrocarbon gas sensors, 164
low-cost multi-application gas sensors, 164–168
NO_2 sensors, 162–163
resistance and sensitivity responses, 165–167
Pt@Sn_{10} cluster, 129, 135

Q
Quantum dot of silicon, 120–121
Quantum Monte Carlo (QMC) methods, 45–46, 57

R
Raman band asymmetry with laser flux, 280–282
Raman scattering studies of SiNWs, 267–269, 278–282
Resonant tunnelling, 56
Richter model for Raman scattering from phonons, 267–269

S
Scanning tunnelling microscope (STM), 55
Schottky barrier formation, 117
$ScSi_{16}$ anions, size-selective formation of, 123
Second harmonic generation, in Si nanoparticles, 39
Self-assembly formations, of Si nanoparticles, 33–34
Si-34
cohesive energy and stability under pressure, 103–104
DFT-LDA band structure of, 106
Si@Al_{12} cluster, electronic spectra of, 131
Si_6Be infinite nanotube, unit cell and DOS of, 227
SiC-cluster film, TMAFM image of, 87
SiC heterofullerenes, 95
Si-cluster-assembled films
electronic structure, 90–91
gas-phase synthesis of, 83–85
HRTEM micrograph of, 88
hybridization of silicon atoms, 93–97
C_{60}-Si-based nanostructures, 95–97
SiC heterofullerenes, 95
optical properties, 92–93
Raman spectra of, 92
structure and morphology, 86–90
TMAFM image of, 87
vibrational structure, 90–92
Si clusters
assembled materials
films, 83–97
from fullerenes, 97–110
large clusters, 82–83
medium-sized clusters, 82
photoionization mass spectrum of, 115–116
role of metal encapsulation in stabilization, 117
small Si_n clusters, 81–82
structure of, 81–83

Si_4 clusters, Raman spectra of, 81
Si_5 clusters, 82
Si_6 clusters, Raman spectra of, 81
Si_9 clusters, Raman spectra of, 81
Si_{33} clusters, 82
Si_{39} clusters, 82
Si_{45} clusters, 82
$Si_{15}Cr$ cluster, 117
$Si_{16}Cr$ cluster, 117
Si crystallites, *See also* Silicon nanoparticles
functionalized surfaces with organic layers, 9–11
HRTEM micrograph of, 6
Si_2C_{58} structures, 95–96
SiC_{59} structures, 96
Si dodecahedral fullerenes, 79
$Si_{10}Fe$ cluster, 133
Si_{50} film, HRTEM micrograph, 88
$Si_{29}H_{24}$
silicon–hydrogen prototype of, 51
structure of, 50, 54–55, 57
$Si_{20}H_{19}(CH_2OH)$, structure of, 142
$Si_{16}H_{16}$ cluster, endohedral doping with Ba, 141
$Si_{20}H_{20}$ cluster, endohedral doping with Zn and Be, 141
$Si_{20}H_{19}(CONH_2)$, structure of, 142
$Si_{20}H_{19}(COO^-)$, structure of, 142
$Si_{20}H_{19}(COOH)$, structure of, 142
Silicon
acoustic phonons, 269–273
based photonics, 314–316
evidence of phonons in, 269–278
laser, 316–318
light source, 316–321
silicon LED, 319–321
silicon Raman laser, 317–318
magnetic clusters of, 142–144
multiply-twinned nanoparticles (MTP), 297
optical phonons, 273–275
phonon dispersion curves for, 260–261
quantum confinement effects, 337, 340–341
research on nanoforms of, 218–220
single-electron charging effects in, 337–341
thermal conductivity, 275–278
Silicon clathrates, 79
cohesive energy and stability under pressure, 103–104
electron density of states in, 101
electronic properties, 100–101
endohedral doping in, 104–110
phonon density of states, 101–103
structures, 98–100
synthesis, 100
vibrational properties, 101–103
Silicon clusters, *See* Si clusters
Silicon diamond (Si-2)
electron density of states in, 100–101
phonon density of states, 101–103
Silicon fullerenes, 121–122, 129, 139–142
Silicon nanocrystals
Er coupled optical amplifiers, 328–332
Er^{3+} and Si-nc interactions, 330
Er^{3+} cross sections, 330–332
Er^{3+} internal transition, 329
optical gain in, 321–328
CW and TR measurements, 322–328
energy configuration, 326
LED, 328
model-four-level system, 325–327
waveguides, 327
Silicon nanoparticles
alkylated particles, 11–15
applications
amperometric detection, 70–71
biophotonic imaging, 68–70
metal oxide silicon memory devices, 66–68
nanoink printing, 73
nanosolar cell, 71–72
single electron transistor devices, 73
UV photodetectors, 64–65
band gap, 63
CL spectrum for film of, 27–28
collective molecular surface, 57–59
collective molecular vibration modes, 59–60
composite films of metal and, 31
computational methods for electronic structure, 43–49
detection of, 22–26
dielectric constant and effective mass, 55–56
electronic structure, 43–49
emission intensity of reconstructed thin film of, 36
excited states, 57
frozen in gel, 29
functionalization
aggregation and solubility, 15–17, 20
with alcohol, 11–13
with alkene, 14
with alkylamine, 13–14
with alkyl and alkoxy groups, 15
with carboxylic groups, 14–15
effect on emission, 41
with organic layers, 9, 12–13
surface condition, 9–11
GPC plots of dispersions of, 16–17
hydrogenated particles prototype, 49–51
incident beam interaction with, 36–38
luminescence models, 42–43
microlasing, 36
molecular-like bands, 57

Silicon nanoparticles (*Contd.*)
molecular-like behaviour, 52–54
molecular-like emission, 60–61
nonlinear optical properties
optical nonlinearity and gain, 39–41
second harmonic generation, 39
stimulated emission, 34–38
nonlinear optical response in, 40–41
optical properties
cathodoluminescence and electroluminescence, 27–28
photostability under UV and infrared radiation, 29
PL and detection of single nanoparticles, 22–25
PL lifetimes, 26
partial energy-level diagram of surface dimers, 53
phonon structure, 59–60
photoelectric conversion applications, 64–65
properties, 55–56
prototype structural stability, 54–55
reconstitution in films by
electrodeposition:, 31
precipitation spray, 30
self-assembly formations, 33–34
silicon sheet roll into tubes, 32–33
reconstitution into crystals, 30
signatures of, 74
Si-Si bonds, 52–54
spectroscopic characterization
AES, 21, 22
FTIR, 17–19
GPC, 20
NMR, 19–20
TEM, 21–22
XPS, 21
stability in acid, 17
structure of, 41–63
surface reconstruction, H_2O_2 effect on, 51–52
synthesis of, 3–8
chemical techniques, 4
discretely sized, 6–8
electrochemical techniques, 4–6
physical techniques, 3–4
physico-chemical techniques, 4
X-ray diffraction for structure of, 61–63
Silicon nanotubes (SiNTs)
electronic structure and bonding nature, 225–227
magnetism in, 228–231
metal encapsulated, 222–225
stability, 221–222
structures, 220–223
TEM images, 222
Silicon nanowires (SiNWs)
atomic structures of, 237–244
band structure of, 243–245, 249–250
biotin-modified, 219
boron doped, 219
branched and hyper-branched, 209–213
crystalline pristine, 238–243
CVD reactor for, 179
1D growth, 178–180
diameters control, 182, 235
edges effects on atomic structure of, 238–239
electronic properties, 182–190, 238, 298
electronics on non-conventional substrates, 194–195
electronic structures, 249–250
energy decomposition, 308–311
field-effect sensors, 201–202
field-effect transistors (FETs), 182–190
n-channel, 185–186
p-channel, 184–185
SEM image of, 184
heterostructures, 204–213
hierarchical organization of arrays
high-frequency nanowire circuits, 199–200
LB assembly of, 196–197
scalable integration of devices, 197–199
history of, 219–220
HRTEM image of Au/SiNW interface, 180–181
hydrogenated nanowires, 244–253
hydrogen-passivated, 297–300
inhomogeneous laser heating on Raman lineshape for, 278–285
Langmuir-Blodgett assembly of, 196–197
lattice dynamics of, 261–267
modulation doped
applications of, 208–209
lithography-free addressing, 208–209
synthesis and characterization of, 205–208
synthetically defined QD structures, 209
for nanoelectronics, 190–195, 213
NiSi/SiNW heterostructures, 204–205
non-crystalline pristine, 237–238
pentagonal, 290–297
phonon dispersion in, 262–268
phonon properties, 259–260
Raman band asymmetry with laser flux, 280–282
Raman scattering studies, 267–269, 278–285
Richter's lineshape function for inhomogeneous heating, 282–285
scalable integration of devices, 197–199
SEM image of, 179

sensors, 200–204, 213, 236
multiplexed detection, 203–204
single virus detection, 202
single-electron transistors (SETs), 187–190, 219, 237, 343–346, *See also* SiNW SET
stabilization of, 237
Stokes-antiStokes intensity ratio for laser heating, 279–280
structural characterization of, 180–182, 220
synthesis, 177–180
TEM images of, 181
VLS growth mechanism, 179–180, 210–211
Silicon Raman laser, 317–318
$Si_{15}Mo$ cluster, 117
$Si_{16}Mo$ cluster, 117
Si-nc, *See* Silicon nanocrystals
Si_n clusters
binding energy, 118–119
gas-phase synthesis of, 83–85
representative structures of small, 118–119
Single electron transistor (SET), *See also* SiNW SET
using silicon nanocrystals, 73, 351–352
Si_nH_m fullerene cages, 139–142
SiNW FETs, 182–190
based electrical sensing, 201–202
electrical transport measurement, 184–185
n-channel, 185–186
p-channel, 184–185
SEM image of, 184
transconductance of, 186
SiNWs, *See* Silicon nanowires (SiNWs)
SiNW SET, 187–190, 219, 237, 343–346
CB oscillations, 187
coherent single charge transport in, 188–189
crystalline silicon SETs and, 352
electrical characteristics of, 345
Grain-Boundary engineering, 350–351
ground-state spin configuration of, 189–190
low-temperature measurements on, 187–190
point-contact SETs, 346–350
room temperature operations, 346–350
use of silicon nanocrystals, 73, 351–352
SiNW transistors, coherent single charge transport in, 188–189
Si_{28} T_d fullerene, 82
$Si_{12}W$ cluster, 117, 133, 137
$Si_{15}W$ cluster, 117
$Si_{16}W$ cluster, 117
$Si_{16}Zr$ fullerene, 117
$Sn_8@Si_{46}$ clathrates, 109
$Sr_xBa_{8-x}@Si_{46}$ clathrates superconductivity, 107
Staining cells, with Si nanoparticles, 69
Stimulated emission, in Si nanoparticles, 34–39
Stokes-antiStokes intensity ratio, for laser heating SiNWs, 279–280
Supermolecule (Hydrogenated particles), 49–51

T
$Ta@Si_{12}$ cluster, 128
Thermal hydrosilylation, of alkenes in colloid dispersion of H-terminated Si particles, 14
Thermally carbonized porous silicon (TC-PS) humidity sensor, 159–160
Thermoelectric cooler (TEC) integrated humidity sensors, 158–159
$Th@Si_{20}$ cluster, 126, 136
metal encapsulated fullerene cages of, 126, 129
Tight binding (TB) method, 43
Time-dependent density functional theory (TDDFT), 43, 45, 57
$TiO_{2-x}N_x$ photocatalysts, 168–169
$Ti@Si_{16}$ clusters, 117, 124
electronic spectra of, 131–132
Frank-Kasper polyhedral structure of, 122–123
growth behaviour of, 124–125
$Ti@Si_n$
binding energy, 126
structures and differences of total energies, 124–125
$TiSi_{16}$ neutrals, size-selective formation of, 123–124
Titania nanostructures, 168–169
$TM@Si_{12}$ clusters, 47–49
Transition metal (TM)-doped SiNTs, magnetism in, 228–231
Transmission electron microscopy (TEM) analysis, 21–22

U
Urbach's tail, 83
UV photodetectors, 64–65
UV radiation, photostability of Si nanoparticles under, 29

V
Valence band maximum (VBM), 244, 251–252, 253
Variational Monte Carlo (VMC) method, 45–46
Vertical cavity surface-emiltiry laser (VCSEL), 328
VSi_{16} cations, size-selective formation of, 123

W
$W@Si_{14}$ cluster, metal encapsulated fullerene cages of, 126, 129

W@Si_{12} fullerenes, 128–129
WSi_n clusters, photoionization mass spectrum of, 115–116

X
Xe_6@Si-34 clathrates, DFT-LDA band structure of, 106–107
Xe_8@Si_{46} clathrates, 106–107
X-Ray Photospectroscopy (XPS) analysis, 21

Y
YSi_8 NW, energy decomposition in, 308–311
Yttrium silicide NW, 307–308

Z
Zeolite diffusion, 157
Zn doped Pb_n clusters, mass abundance spectra of, 135
Zn doped Sn_n clusters, mass abundance spectra of, 135
$ZnSn_{10}$ cluster, 135
Zr-encapsulated Zr@Si_{20}, 122
Zr_3Si_{28} cluster, 302
Zr_4Si_{32} cluster, 302
Zr@Si_{12} cluster, 305
Zr@Si_{16} cluster, 136, 138–139, 305
  absorption spectra of, 143
  electronic spectra of, 130–131
  metal encapsulated fullerene cages of, 126, 129
  structures of, 121–123
Zr@Si_{17} cluster, 122
Zr@Si_{19} cluster, 122
Zr@Si_{20} cluster, 122
Zr@Si_{16} fullerenes, 126
Zr@SiNT, 302, 305–307